

# Hydra: Computer Vision for Data Quality Monitoring

---

**Thomas Britton,<sup>1</sup> Torri Jeske, David Lawrence, Kishansingh Rajput**

*Thomas Jefferson National Accelerator Facility,  
Newport News, VA, USA*

*E-mail:* [tbritton@jlab.org](mailto:tbritton@jlab.org)

**ABSTRACT:** Hydra is a system which utilizes computer vision to perform near real time data quality management, initially developed for Hall-D in 2019. Since then, it has been deployed across all experimental halls at Jefferson Lab, with the CLAS12 collaboration in Hall-B being the first outside of GlueX to fully utilize Hydra. The system comprises back end processes that manage the models, their inferences, and the data flow. The front-end components, accessible via web pages, allow detector experts and shift crews to view and interact with the system. This talk will give an overview of the Hydra system as well as highlight significant developments in Hydra's feature set, acute challenges with operating Hydra in all halls, and lessons learned along the way.

---

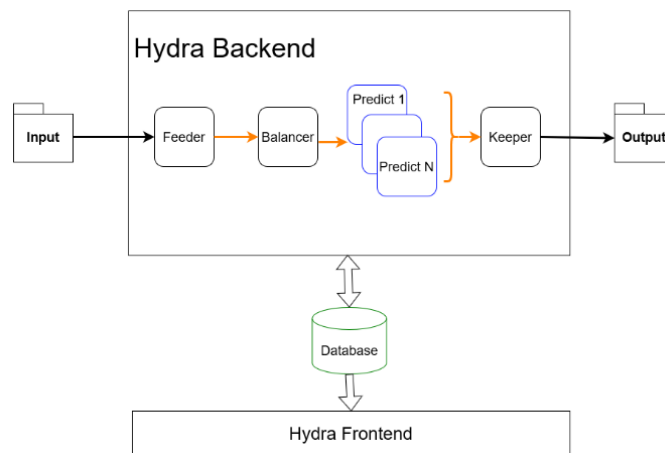
## Contents

<b>1</b>	<b>Introduction</b>	<b>1</b>
<b>2</b>	<b>The Hydra Back-end</b>	<b>2</b>
2.1	Database	2
2.2	Feeder	3
2.3	Load Balancing	3
2.4	Predict	3
2.5	Keeper	3
<b>3</b>	<b>The Hydra Front-End</b>	<b>4</b>
3.1	Labeler	4
3.2	Model Training Report Page	5
3.3	Library	5
3.4	Status	5
3.5	Run	6
3.6	Log	6
3.7	Grafana	6
<b>4</b>	<b>Deployments</b>	<b>7</b>
<b>5</b>	<b>Developments</b>	<b>7</b>
<b>6</b>	<b>Conclusion</b>	<b>8</b>

---

## 1 Introduction

Physics quality data is expensive and time-consuming to obtain. This expense underlies the importance of having good data quality monitoring (DQM). In GlueX, where Hydra was first developed and deployed, DQM consisted of an iterative series of checks and rechecks which takes data from its raw form, through calibration, to reconstruction, and finally when integrated into a physics analysis. This process is coordinated by the Online Monitoring Coordinator, the Offline Monitoring Coordinator, and the Physics Analysis Coordinator. The first and arguably most critical step of this process is the initial data collection, because data lost to problems with detectors (e.g. the failure of any electrical components) are unrecoverable. To protect the data acquisition in GlueX shifts of two people, responsible for managing the acquisition, are instructed to monitor Rootspy [1], a program which collects statistics from the current data taking run and displays a variety of plots to shift takers. Every day the Online Monitoring Coordinator looks over hundreds of plots generated based on the previous day of running and writes a short monitoring brief. This method, while useful for catching issues that might have gone unnoticed by shift crews, places more burden on people.



**Figure 1.** A simplified diagram of the Hydra system. The orange arrows indicate the path of inference orders through Hydra’s back end processes. The MySQL database is indicated in green.

Hydra was developed to alleviate this burden and free people up to work on things humans are naturally better at (e.g. making data taking decisions). Hydra aims to be an extensible framework for training and managing AI, which leverages the recent developments in computer vision, for near real-time monitoring. It is comprised of a Python back-end, supported by a MySQL database, and a Web-based front-end which allows for users to interact with and monitor the Hydra system(s). To shorten the runway for production Hydra was built primarily with computer vision in mind. This means that Hydra can, out of the box, be applied to a variety of image classification tasks.

## 2 The Hydra Back-end

Hydra runs images through a modular, multi-step workflow comprised of a set of Python scripts all of which interact with an underlying MySQL database. An overview of the system is shown in Fig. 1. Python was chosen to more easily support the use of Tensorflow [2] and Tensorflow-produced models, which formed the foundation for Google’s Inception v3 [3]. Although InceptionV3 is the model topology most used in Hydra, it is not a requirement and users can implement their own model so long as it is compatible with Tensorflow. The modular components of the Hydra Back-end are described in the following subsections.

### 2.1 Database

A comprehensive MySQL database supports both the back end and front end of Hydra. The database stores the location of the trained model files as well as the mapping that associates the various models to their corresponding plot type. This allows Hydra to run inference on all of the various plot types using the corresponding model. To support the front end, the database stores references to all available images from all available plot types, all valid labels to every plot type (different plot types need not have the same classifications), permissions lists for labeling each plot type, the labels to every plot, model classification for every plot (when a model’s performance is analyzed), the training set used to train every model, every in-situ inference performed by every

model, and the last few minutes of the current run. This coverage allows for extensive data mining, not only of the components of Hydra but also of overall data quality. For example, by recording all of this information Hydra has spotted electronic components in the process of failing, flickering on and off at time scales far shorter than what shift takers could detect using the cumulative plots. This depth of data tracking also allows for the pinpointing of the starting of detector problems to mere minutes (shorter if image rates are higher).

## **2.2 Feeder**

Hydra's Feeder is a light-weight script that watches an input directory for new images that need to be analyzed and ensures they are of the right shape to be fed into the corresponding model. If necessary, the image is resized to match the input shape of the model as recorded in the database. As long as this is done consistently, artifacts produced as a result of resizing have not proven to be an issue. Once the image is confirmed to be the right shape for model consumption Feeder sends an "Inference Order" to the load balancer via a ZeroMQ message.

## **2.3 Load Balancing**

The Load Balancer is responsible for distributing the Inference Orders it receives to a configurable number of Predict processes. It does this in Round Robin amongst the N Predict processes. It does not modify the Inference Order in any meaningful way (it only adds its processing time to the message metadata for monitoring) and merely passes the message on. Because of this simple pass through the Balancer takes about  $10\mu s$  to process an Inference Order.

## **2.4 Predict**

The Predict stage is where inference is run and a report is generated. Each copy of Hydra Predict has its own buffer to store Inference Orders and then processes them on a First-in-First-out (FIFO) basis. The script uses the Inference Order to identify which image needs to be processed and internally maps that image to the specific model (called a Hydra Head internally) trained to process it. Once processed a "Report" is created and transmitted via ZeroMQ to the Keeper process. This report contains meta data about the image, its processing, and the model's labels and normalized output weights, from which the classification for the image can be determined. In the event that a model classifies an image as "Bad" it automatically generates a Gradient weighted Class Activation Map (gradCAM) [4] to be included in the submitted report. It is important to note that this stage does not do anything other than manage the running of Hydra's various models and generating a Report. Actions (e.g. inference storage, RunTime displays, unbiased collection etc) are all taken by the Keeper, described in the next subsection.

## **2.5 Keeper**

The Keeper process takes various actions when it receives a Report from the Predict process(es). It records the inference in a RunHistory table and records the image, the gradCAM heatmap (if applicable), as well as a few key pieces of inference in a RunTime table. Based on the model's classification and the collect percentage, Keeper makes a determination of what images to keep for labeling. Keeper prioritizes the collections of examples where the image is classified as "Bad" or



the model's confidence is below threshold as configured in/read from the database on a per model basis. In addition, Keeper selects a random sampling, based on a configurable collect percentage, of images it sees. These images are used in future model training as well as in the monitoring of the model's in-situ performance. These examples provide very useful examples for future training to increase model robustness in problem classification and increase model confidence.

### 3 The Hydra Front-End

Hydra has a web-based front end which acts as the primary interface with the Hydra system. Various pages have been developed such that users can label images, evaluate model performance, view near real time classifications of incoming data, inspect data from the previous day, and monitor the Hydra systems status. A web based user interface enables users to perform data quality monitoring remotely further adding to the robustness of any DQM policies already in place. The various web pages that comprise the Hydra Front-end are described below.

#### 3.1 Labeler

All supervised learning techniques require labeled training data, which can be costly to obtain. For this reason, a substantial amount of time was devoted to reduce the cost (e.g. expert's time) of labeling. The Labeler, shown in Fig. 2 is based on a palette system whereby users who have permissions can select a label, referenced by a custom color, from a palette of labels and "paints" a set of images. To aid in the efficiency of labeling, shortcuts are provided to label blocks of images with the same label at the same time. After this the user may "Apply" the labels which stores the labels in the database and removes those images from the set of unlabeled images and replaces them with new to-be-labeled images (as applicable). An Editor mode is provided where users can change the label of a previously labeled image. In this mode labeled images can be filtered by both time and given label, allowing users to quickly filter through potentially hundreds of thousands of images to make the needed corrections. With the labeling web page experts are able to label images at a rate of about ten thousand images per hour.



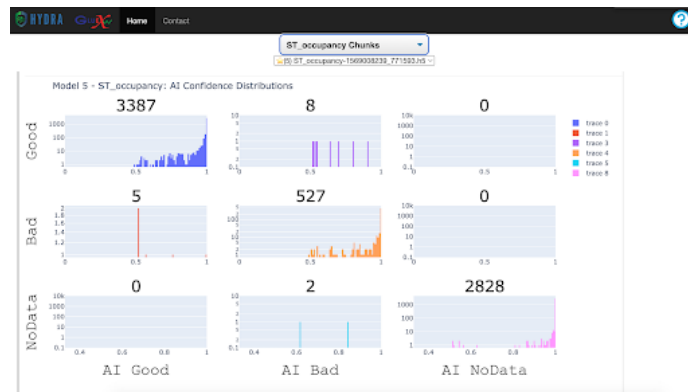
**Figure 2.** Snapshot of the online Labeler. Users can select the plot to label, select the appropriate label and label thousands of images quickly.

### 3.2 Model Training Report Page

Training is an iterative process; after training a new model an interactive report is produced which enumerates the differences between the model's classification and the human's classification. It is through analysis of these differences that potential training problems can be identified and corrected. Commonly, human errors in labeling (usually a few percent) can be found and corrected.

### 3.3 Library

The Library page, shown in Fig. 3, provides information regarding training for each of Hydra's models. It includes the sampling method used when generating the training set, training set size, and an enhanced confusion matrix. Active models, those used in production, are also indicated. The Enhanced Confusion Matrix (ECM) is the standard confusion matrix with a plot, per matrix cell, of the output weight of the model for each classification. With the ECM, a per label confirmation threshold can be applied. This threshold is a real valued number between 0 and 1 and acts to combat both false positives and false negatives. A model's classification is considered "confirmed" if and only if the output weight for the classification falls above the threshold. Each threshold can be modified, with valid permissions, via the web page. Default threshold settings are determined by the maximum effective F1 score in order to minimize false positives and false negatives. An image with an "unconfirmed" classification will be flagged by Keeper for labeling.



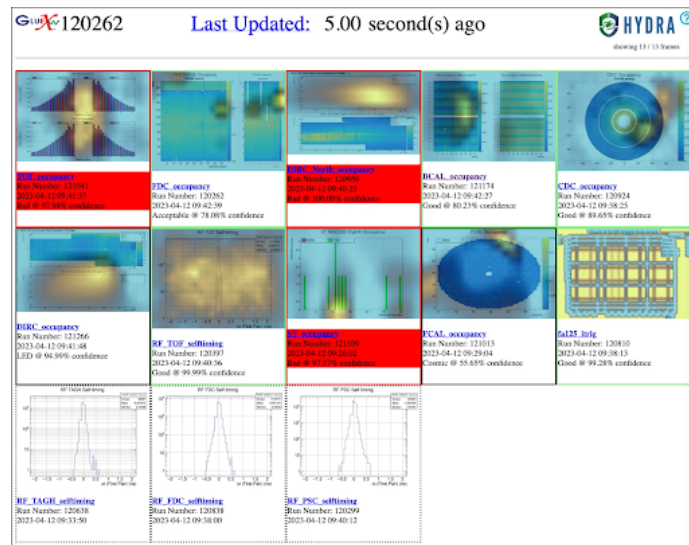
**Figure 3.** The library page displaying the enhanced confusion matrix for the active model (indicated with the star icon) is shown.

### 3.4 Status

The Status Page gives a near real time view of the computational health of Hydra. It does this by displaying histograms of the time each of the back end processes took to process individual images, or inference orders, over the last 24 hours. A scatter plot displays the average processing time for each back end process, where the average is taken over the set of images, as a function of the experiment's run number. Deviations in the individual distributions or average could indicate a technical fault with Hydra that includes, but is not limited to, a communication issue with the database server or issues with the underlying file system. These issues can inhibit Hydra and are, for the most part, easily corrected once identified.

### 3.5 Run

The Hydra Run page, shown in Fig. 4, is up in the various Counting Houses Hydra is deployed in. It provides a security camera style view of the images Hydra analyzes with Hydra’s sentiment in real time. The page auto-updates, styling the various frames according to the classification Hydra gives the image. Confirmed Bad and unconfirmed images are moved to the top left of the image grid and given visual indications of the model’s classification with an optional setting to display the gradCAM heatmap overlaid on the image. Custom alarms can be added depending on the preferences of each experimental hall. All of this helps guide shift takers to potential issues in an easy to digest, interpretable way. The Hydra run page also provide links to other Hydra web pages which may be of use to shift takers.



**Figure 4.** The Hydra Run page displaying near real time classifications along with gradCAM heatmaps overlaid on the images. These help indicate problematic areas of the images to aid the shift crew in diagnosis.

### 3.6 Log

The Hydra Log page provides an overview of all confirmed bad and any unconfirmed plots from the previous 24 hours. This page is often used as a daily brief during run coordination meetings to provide a quick snapshot of the prior day’s data quality. Any problems that Hydra observed in the previous day can be identified and discussed with the relevant detector experts.

### 3.7 Grafana

Each inference from Hydra is stored in the database. There are many different ways to visualize and interpret this data. While not a required part of Hydra, the deployments at Jefferson Laboratory (JLab) are supplied with a Grafana [5] server to visualize all of the inferences of Hydra. To accomplish this the inferences are viewed as a set of time series data, one set per plot type. Because every label and every output weight for those labels are recorded it is possible to query any time window and display the series of output weights for all labels in a scatter plot. Anecdotally, there



**Figure 5.** The Hydra Log page displaying confirmed bad plots from the previous day.

have been occasions where the the growth in Bad output weights and corresponding drop of Good output weights, even in a non-monotonic or sinusoidal manner, precedes certain detector failures. This behavior also signals that the model might need to be retrained with newly labeled images. While no conclusive robust study has been performed it is conceivable that this data may prove to have some predictive power when it comes to certain data acquisition problems.

## 4 Deployments

Currently, Hydra is deployed in all of JLab’s experimental halls, with Halls B and D seeing the most active use. When Hall-D was taking data Hydra was in its infancy and even still discovered many problems, some even subtle enough that they were missed or would have been missed by detector experts. After deployment in Hall-B, Hydra quickly set to work identifying many issues with super-human performance.

Deploying Hydra to all experimental halls came with a fair share of challenges. The first being making a system that can easily integrate with the existing, but distinct, monitoring systems already in place in each hall. To overcome this Hydra employs hall-agnostic technologies, such as using images in the place of underlying histograms values obtained from ROOT [6] trees where the layout of the trees would need to be known a priori. These images are trivially derived from ROOT based monitoring systems, allowing for quick deployments of the Hydra system. As Hydra does not seek to replace human based monitoring, it is deployed in as parasitic a way as possible. It does this by requiring only a standard naming convention for image files, an input directory, and a few directories for short and long term storage of images Hydra has selected to keep.

## 5 Developments

The goal of Hydra is to build a self sustaining system in as many ways as possible. It should intelligently suggest training, it should error correct whenever possible, and should be transparent and interpretable to humans. To accomplish this much of Hydra’s road map for development can be broken down into coming from one of three main tracks:

1. Features to expand on Hydra’s capabilities to detect and diagnose issues.
2. Features to enhance human control over the systems of Hydra and their operation.
3. developments to make Hydra more computationally efficient.

In order to expand Hydra’s capabilities related to detection and diagnosis, a multistage analysis pipeline is being developed. The first step of this pipeline includes generic anomaly detection, such as implementing a Siamese model [7], before further diagnostics. Additionally, the ability to mask regions of images that should be ignored would allow on Hydra to focus on important data and avoid red herrings. Hydra’s user interface is under continuous development to enhance user control and administration of the system without requiring knowledge of the back end processes or the MySQL database. Deployment to all experimental halls requires simultaneous monitoring of Hydra’s health, database monitoring, and the current running conditions in each hall to ensure consistent, stable operations. An administrative interface is being developed to provide interpretable and actionable information regarding Hydra’s health.

## 6 Conclusion

The Hydra system is a framework for managing the training and deployment of models for real time data quality monitoring. It is deployed in all of the experimental halls at Jefferson Laboratory and successfully detects data quality issues at a super-human level. It does this in a hall agnostic way with a robust web-based front end and back end, both of which are supported by a MySQL database. Real-time views of incoming data are viewable from anywhere in the world, but most importantly from the counting houses where shift crews can get an at-a-glance look into Hydra’s monitoring. Visual and, in some cases, audible alarms notify the shift crew when Hydra detects a problem. The visual indicators include a color determined by the classification and a gradCAM heatmap to aid the shift crew in determining the problematic regions of the image. Since Hydra looks at each image consistently and more frequently than the shift crews, corrective action(s) can be taken sooner. This is especially important while the shift crew is simultaneously responsible for the more complex tasks of running experiments in addition to data quality monitoring. Hydra is under very active development and looks to grow in robustness of detection, computational efficiency, and in human interface capabilities.

## Acknowledgments

Jefferson Science Associates, LLC operated Thomas Jefferson National Accelerator Facility for the United States Department of Energy under U.S. DOE Contract No. DE-AC05-06OR23177. after the paper has been written.

## References

- [1] D. Lawrence, “Rootspy.”
- [2] M. Abadi, A. Agarwal, P. Barham, E. Brevdo, Z. Chen, C. Citro et al., *TensorFlow: Large-scale machine learning on heterogeneous systems*, 2015.

- [3] C. Szegedy, V. Vanhoucke, S. Ioffe, J. Shlens and Z. Wojna, *Rethinking the inception architecture for computer vision*, 2015.
- [4] R.R. Selvaraju, M. Cogswell, A. Das, R. Vedantam, D. Parikh and D. Batra, *Grad-CAM: Visual explanations from deep networks via gradient-based localization*, *International Journal of Computer Vision* **128** (2019) 336.
- [5] Grafana Labs, *Grafana Documentation*, 2018.
- [6] R. Brun, F. Rademakers, P. Canal, A. Naumann, O. Couet, L. Moneta et al., *root-project/root: v6.18/02*, June, 2020. 10.5281/zenodo.3895860.
- [7] G. Koch, R. Zemel and R. Salakhutdinov, *Siamese neural networks for one-shot image recognition*, in *Proceedings of the ICML Deep Learning Workshop*, vol. 2, (Lille), 2015, <https://www.cs.cmu.edu/rsalakhu/papers/oneshot1.pdf>.

# Collective excitations and low-energy ionization signatures of relativistic particles in silicon detectors

---

Rouven Essig,<sup>a</sup> Ryan Plestid,<sup>b</sup> Aman Singal<sup>a,c</sup>

<sup>a</sup>*C. N. Yang Institute for Theoretical Physics, Stony Brook University, Stony Brook, NY 11794, USA*

<sup>b</sup>*Walter Burke Institute for Theoretical Physics, California Institute of Technology, Pasadena, CA 91125*

<sup>c</sup>*Institute for Advanced Computational Sciences, Stony Brook University, Stony Brook, NY 11794, USA*

*E-mail:* [rouven.essig@stonybrook.edu](mailto:rouven.essig@stonybrook.edu), [rplestid@caltech.edu](mailto:rplestid@caltech.edu),  
[aman.singal@stonybrook.edu](mailto:aman.singal@stonybrook.edu)

**ABSTRACT:** Solid-state detectors with a low energy threshold have several applications, including in direct-detection searches of non-relativistic halo dark-matter particles with sub-GeV masses. Moreover, when searching for relativistic or quasi-relativistic beyond-the-Standard-Model particles (i.e.,  $v/c \gtrsim 0.01$ ) that have an enhanced cross section for small energy transfers, a comparatively small detector with a low energy threshold may have better sensitivity than a larger detector with a higher energy threshold. In this paper, we provide accurate calculations of the low-energy ionization spectrum from high-velocity particles scattering in a dielectric material. We focus on silicon, although our results can be easily applied to other materials. We consider the full material response, in particular also the excitation of bulk plasmons. We generalize the energy-loss function to relativistic kinematics, and benchmark existing tools used for halo dark-matter scattering against publicly available electron energy-loss spectroscopy data. Compared to calculations of energy loss that are commonly used in the literature, such as the Photo-Absorption-Ionization model or the free-electron model, the inclusion of collective effects shifts the recoil ionization spectrum towards higher energies, typically peaking around 4–6 electron-hole pairs. We apply our results to the three benchmark examples: millicharged particles produced in a beam, neutrinos with a magnetic dipole moment produced in a reactor, and dark-matter particles that are upscattered by cosmic rays or in the Sun. Our results show that the proper inclusion of collective effects typically enhances a detector’s sensitivity to these particles, since detector backgrounds, such as dark counts, peak at lower energies.

---

## Contents

<b>1</b>	<b>Introduction</b>	<b>2</b>
<b>2</b>	<b>Low-energy excitations from relativistic particle scatters</b>	<b>3</b>
2.1	General formalism for energy loss of particles scattering with electrons	3
2.2	Comparison with average energy loss formalism	5
<b>3</b>	<b>Expressions for the dielectric function and comparison with EELS data</b>	<b>6</b>
<b>4</b>	<b>Phenomenology of relativistic particle scatters</b>	<b>10</b>
4.1	Millicharged particles	11
4.2	Neutrino dipole moments	13
4.3	Boosted dark matter	13
4.4	Systematic uncertainties on signal predictions	16
<b>5</b>	<b>Conclusions</b>	<b>16</b>
<b>A</b>	<b>Additional figures for momentum-weighted energy loss function</b>	<b>18</b>



# 1 Introduction

Several new direct-detection concepts to search for halo dark matter particles with mass below the proton have been proposed over the past decade [1]. Since dark-matter particles in our Milky-Way halo are non-relativistic, with  $\beta \equiv v/c \sim 10^{-3}$ , the resulting events have very little energy. Fortunately, the theoretical progress has been accompanied by a new generation of ever-improving low-threshold solid-state detectors capable of sensing the low-energy signals. In particular, some of the leading direct-detection bounds on halo dark matter with sub-GeV masses are from experiments that use semiconductors, usually silicon, that search for dark matter particles interacting with electrons [2], e.g., [3–11]. Their main advantage over larger detectors and noble-liquid or molecular targets [12–20] is their superior energy threshold, which translates into them having sensitivity to lower dark-matter masses. On the other hand, for semi-relativistic or relativistic dark-matter particles or other particles beyond the Standard Model (BSM), large-volume detectors often have an advantage over smaller solid-state detectors, as the low energy threshold of the small detectors does not compensate for the large volume of the bigger detectors. There are, however, several cases where a kinematic or dynamical enhancement occurs at low energies and for which a low-threshold solid-state detector could be superior. For this reason it is imperative to have accurate predictions for the low-energy signal of relativistic particles that scatter in solid-state detectors. The goal of this paper is to provide these accurate predictions.

The theoretical calculations for the scattering rates of *non-relativistic* halo dark matter in solid-state materials have become increasingly accurate and precise [2, 21–28], with Refs. [22–24] emphasizing the need to include the full material response, which is captured by the dielectric function or energy loss-function. Similarly, we here emphasize that accurate predictions for the low-energy signals from the scattering of *relativistic* particle must include the full material response (see also [29]). For example, a highly boosted particle will produce large transverse electromagnetic fields, as compared to a non-relativistic probe which will interact dominantly through Coulomb modes. We highlight in particular how relativistic particles can excite bulk plasmons (quasiparticles describing the collective excitation of electrons in, e.g., semiconductors), and how this drastically impacts the shape of the expected recoil spectrum when compared to calculations that do not include the plasmon.

Plasmons have previously received attention in the context of dark matter direct detection as a detection channel in e.g., [29–34], however primarily in the context of non-relativistic halo DM scattering.<sup>1</sup> However, plasmons are not dominantly excited in the scattering of non-relativistic halo dark matter. The situation changes qualitatively when one considers relativistic particles, in which case the plasmon is easily accessible, and low-energy events can be resonantly enhanced. This must be taken into account in order to predict the signal correctly and to derive accurate constraints.

In this paper, we focus on silicon as a representative material, but our results can be generalized to other dielectric materials including germanium, gallium arsenide, and silicon carbide. We consider in particular three types of particles and mediators: millicharged particles (produced in a beam), particles with a magnetic dipole moment (such as a neutrino with a magnetic dipole moment), and particles

---

<sup>1</sup>We note that [30] considered quasi-relativistic scattering in the context of boosted millicharged dark matter such that the plasmon is kinematically accessible; however, non-relativistic formulae were used to calculate the scattering rates.

(including dark matter) interacting with a massive (heavy or ultralight) dark photon that is kinetically mixed with the ordinary photon. Each of these can be relativistic when interacting with a detector material: they can be produced in accelerator-based experiments or accelerated due to scattering in “high-energy” environments; examples for the latter include “solar-reflected” dark matter [35–41] and dark matter boosted by cosmic-ray scattering [42–46].

The rest of the paper is organized as follows. In Section 2 we review the theory of non-radiative energy losses for relativistic charged particles with a particular emphasis on the role played by the longitudinal modes (which contain the plasmon). We provide scattering cross section formulae for our three representative examples (millicharged particles, neutrinos with a magnetic dipole moment, and particles interacting via a dark photon). All formulae require accurate knowledge of the dielectric function (or, equivalently, the material’s energy loss function) function, which also captures the plasmon. While plasmons are “well-known” physics, we will highlight it here for the particle physics community, especially as new applications of low-threshold detectors are being considered. In Section 3, we provide expressions for the dielectric function, comparing several codes that can calculate it with data from electron energy-loss spectroscopy (EELS). Next, in Section 4 we discuss the resulting spectra and phenomenology for our three particle examples. We summarize our findings and future directions in Section 5. An appendix provides additional details and figures describing the behavior of the dielectric function.

## 2 Low-energy excitations from relativistic particle scatters

### 2.1 General formalism for energy loss of particles scattering with electrons

A general formalism for energy loss by electrically charged particles was first given in [47]. The treatment assumes that the incident test charge, with four-momentum  $p$ , may be treated as a classical source of  $\mathbf{E}$  and  $\mathbf{B}$  fields. This is equivalent to the eikonal approximation [48] (valid for  $k \ll p$  with  $k$  the four-momentum transfer to the sample). As we have discussed above, small low-threshold detectors can only compete with large high-recoil detectors when their sensitivity is dominated by regions of low momentum transfer. Therefore, we will be interested in energy transfers no larger than 50 eV and momentum transfers less than the Fermi momentum  $k_F \sim 5$  keV, such that the classical electrodynamics treatment is an extremely good approximation over the full kinematic regime of interest.

We now give the scattering cross section for three different types of particles and mediators, before commenting on other cases. In all expressions, bulk material properties that differ from a free-electron cross section, i.e., “collective effects”, are captured using the dielectric function  $\epsilon(\omega, k)$ .

**1. Particles with an electric charge.** For an electrically charged particle, the resulting cross section (differential with respect to energy loss) is given by [47, 49]

$$\frac{d\sigma}{d\omega} = \frac{8\alpha\epsilon^2}{n\beta^2} \int_{k_{\min}}^{k_{\max}} \frac{dk}{k} \left\{ \text{Im} \left( -\frac{1}{\epsilon(\omega, k)} \right) + (\beta^2 k^2 - \omega^2) \text{Im} \left( \frac{1}{-k^2 + \epsilon(\omega, k)\omega^2} \right) \right\}. \quad (2.1)$$

Here  $k = |\mathbf{k}|$  is the three-momentum transfer to the sample,  $\varepsilon$  is the charge of the probe in units of  $e$ ,  $\omega$  is the energy transfer,  $\beta = |\mathbf{p}|/E$  is the three-velocity of the probe particle in the rest frame of the detector, and  $\epsilon(\omega, k)$  is the dielectric function of the material. The minimum momentum transfer is set by  $k_{\min} = \omega/\beta$ , while the maximum momentum transfer is  $k_{\max} = 2|\mathbf{p}| - k_{\min}$ ; in practice, since the integral has negligible support for  $k \gg k_F$ , the upper limit of the integral,  $k_{\max}$ , can simply be taken to infinity. This is justified for  $k_\mu k^\mu \ll 2p_\mu k^\mu$ , which is appropriate when  $|\mathbf{p}| \gg k_F \sim 5$  keV, since  $|\mathbf{k}| \lesssim k_F$  dominate the energy loss function. In Coulomb gauge, the two terms in the above equation may be identified with the exchange of Coulomb modes and transverse photons, respectively, and are related to density-density and current-current correlators in the rest frame of the material.

**2. Particles with a magnetic dipole moment.** The above formula can be generalized to other models beside a point-like electrically charged particle. The simplest generalization involves higher electromagnetic multipoles. For concreteness, we consider here a relativistic particle with a magnetic dipole moment  $\mu$ , which is described by  $\mathcal{L}_{\text{int}} \supset \frac{\mu}{2} \bar{\psi} \sigma_{\mu\nu} F^{\mu\nu} \psi$ . In this case, since the mediator is still a Standard Model photon, one may obtain the correct energy loss formula from Eq. (2.1) by comparing the lepton tensors for a magnetic dipole moment and a millicharge. In the limit of a highly-boosted incident particle, this ratio is simply  $-\mu^2 k_\nu k^\nu / e^2 = \mu^2 (\mathbf{k}^2 - \omega^2) / e^2$ . Therefore, for the case of a neutrino magnetic moment, we find

$$\frac{d\sigma}{d\omega} = \frac{2}{n\pi\beta^2} \int_{k_{\min}}^{k_{\max}} \frac{dk}{k} \mu_{\nu\alpha}^2 (k^2 - \omega^2) \times \left\{ \text{Im} \left( -\frac{1}{\epsilon(\omega, k)} \right) + (\beta^2 k^2 - \omega^2) \text{Im} \left( \frac{1}{-k^2 + \epsilon(\omega, k)\omega^2} \right) \right\}, \quad (2.2)$$

where we have allowed the neutrino magnetic moment to depend on the neutrino flavor.

**3. Particles interacting with a massive vector mediator (dark photon).** A similar procedure for a vector mediator with mass  $m_V$  (i.e., a dark photon) with coupling  $g_\chi$  to the relativistic probe with mass  $m_\chi$ , and coupling  $g_e$  to electrons<sup>2</sup> yields

$$\begin{aligned} \frac{d\sigma}{d\omega} &= \frac{8\alpha}{n\beta^2} [g_e g_\chi]^2 \int_{k_{\min}}^{k_{\max}} \frac{dk}{k} \left( \frac{k^2 - \omega^2}{k^2 + m_V^2 - \omega^2} \right)^2 \\ &\quad \times \left\{ \text{Im} \left( -\frac{1}{\epsilon(\omega, k)} \right) + (\beta^2 k^2 - \omega^2) \text{Im} \left( \frac{1}{-k^2 + \epsilon(\omega, k)\omega^2} \right) \right\}, \\ &= \frac{1}{\beta^2} \bar{\sigma}_e \int_{k_{\min}}^{k_{\max}} \frac{dk}{k} \left( \frac{k^2 - \omega^2}{k^2 + m_V^2 - \omega^2} \right)^2 \frac{2[(\alpha m_e)^2 + m_V^2 - \omega^2]^2}{(4\pi\alpha)\mu_{\chi e}^2 n} \\ &\quad \times \left\{ \text{Im} \left( -\frac{1}{\epsilon(\omega, k)} \right) + (\beta^2 k^2 - \omega^2) \text{Im} \left( \frac{1}{-k^2 + \epsilon(\omega, k)\omega^2} \right) \right\}, \end{aligned} \quad (2.3)$$

where  $\mu_{\chi e} = m_e m_\chi / (m_e + m_\chi)$  is the reduced mass. In the second equation, we have re-written the cross section in terms of a ‘‘reference cross section’’,  $\bar{\sigma}_e$ , as is common in the dark-matter literature.

<sup>2</sup>Strictly speaking we assume a vector coupling proportionally to the electric charge, i.e., such that the coupling to protons is  $g_p = -g_e$ . For practical purposes, if the interaction couples to electrons at all (which dominate material responses), the formulae can often still be applied, unless the coupling to nucleons is much larger than the coupling to electrons.

**4. Other particles and interactions.** More generally, one may consider different types of mediator particles, for instance a massive scalar, vector, pseudoscalar, or pseudovector. In this case one should be careful to treat in-medium effects properly, which can be accomplished using a thermal field theory formalism as discussed in Appendix A of [29]. Since the response of metals and semi-conductors are dominated by valence electrons, one may to a good approximation consider the charge and electron density as interchangeable and argue on these grounds that electromagnetic data usefully constrains any model of electrophilic interactions. This is especially true in the limit of small momentum transfers, where a non-relativistic approximation can be employed for the electrons and protons that dictate the detector response. In this limit, the longitudinal component of the electromagnetic response function is related to the scalar response function [29], and the same energy loss function characterizes both scalar- and vector-mediated scattering. This approximation is valid even for relativistic probes provided the momentum transfer satisfies  $\omega, k \ll m_e$ . These constraints are satisfied for all of the phenomenology we consider here, and so our results apply to both light scalar and vector mediators. Pseudoscalar and pseudovector interactions lead to spin-density-dependent response functions at low momentum transfers that cannot be extracted using EELS data. These could be obtained empirically using neutron magnetic scattering [50], however we do not pursue this idea further here. We focus instead on models whose required detector response can be obtained from standard EELS measurements. This is well motivated since light vector and scalar mediators naturally give cross sections that are enhanced in the low- $q^2$  limit where low-threshold detectors are most effective.

With the formulae in hand for the scattering cross section in semiconductors for various particles, Eqs. (2.1) to (2.3), we see that the problem reduces to finding accurate expressions or data for the dielectric function,  $\epsilon(\omega, k)$ . We discuss theoretical and experimental estimates for the dielectric function in Section 3. We will see that the plasmon peak plays a crucial role in determining the differential spectrum. Before doing so, however, we comment in Section 2.2 on how our formulae compare with the “average energy loss” formalism commonly used in the literature.

## 2.2 Comparison with average energy loss formalism

Equation (2.1) forms the basis of the theory of average energy loss for ultra-relativistic particles [51]. Indeed, weighting  $d\sigma/d\omega$  by the energy transfer  $\omega$ , and integrating over available energy losses one can derive expressions for  $\langle dE/dx \rangle$ . In many contexts involving Standard Model particles and relatively thick targets, the average energy loss is the relevant quantity. Exceptions to this rule exist even within the Standard Model. For example in the thin-target limit, it is well known that the most-probable, as opposed to the mean, energy loss is a better characterization of energy loss [51–53].<sup>3</sup> The inequivalence of these two quantities stems from the fact that Mott scattering is governed by a power-law with a long tail such that  $\langle dE/dx \rangle$  receives  $O(1)$  contributions from high-energy scatters that will rarely, if ever, occur for a fixed number of scatters against a thin target. As a result, the energy loss distribution in thin targets is better characterized in terms of its mode (i.e., its most likely energy loss) as opposed to its mean [51].

An analogous issue appears when one considers the detection of feebly interacting particles. For example, the cross section  $d\sigma/d\omega$  for a millicharged particle is obtained by re-scaling the Standard Model cross section by  $\epsilon^2$ , and so naively the statistical properties of the two distributions are identical. In

<sup>3</sup>More precisely, energy loss is probabilistic and characterized by the Vavilov distribution [53].

practice this is not the case, because the microscopic cross section for energy loss is a fat-tailed distribution. This makes the average energy loss, which determines the mean of the Gaussian distribution that emerges by the central limit theorem and characterizes energy loss for a particle with charge  $e$ , a poor characterization of the distribution that controls millicharged particle detection.

When considering the detection of feebly interacting particles, it is therefore essential to properly model the scattering cross section as a function of energy loss, and in particular the location of its peak. Approximations that model well the average energy loss  $\langle dE/dx \rangle$ , such as the photo-absorption ionization (PAI) model [49, 54, 55], are a poor choice for studies of detector sensitivity to feebly interacting particles. The PAI model makes crude assumptions that completely mismodel  $d\sigma/d\omega$ , and predicts a peak in the distribution at  $\sim 5$  eV rather than the correct value of  $\sim 16$  eV i.e., at the plasmon peak (see Fig. 3). The ultimate sensitivity of a detector to feebly interacting particles is governed by the locations in phase space in which the detection cross section is maximal. In a conventional large-volume detector, such as a liquid scintillator or a noble gas detector, which have a relatively high energy threshold (above the peak of  $d\sigma/d\omega$ ), the highest event rate will always occur at the lowest possible recoil energies (see e.g. [56–58] for a discussion). For low-threshold detectors, with sensitivity to energies at the plasmon peak and below, such as Skipper-CCDs [59], the greatest sensitivity is obtained close to the plasmon peak when it is kinematically accessible. This dictates the expected event spectrum and how to optimize the cuts for experimental searches. We will see several examples in Section 4.

### 3 Expressions for the dielectric function and comparison with EELS data

We saw in Section 2 that the differential scattering cross sections can be expressed in terms of the dielectric function of the material; in particular, Eq. (2.1) gives the expression for an electrically charged particle, Eq. (2.2) is applicable for particles interacting with a magnetic dipole moment, and Eq. (2.3) for particles with a dark-photon mediator. The dielectric function captures all relevant collective effects, and the formulae Eqs. (2.1) to (2.3) are valid for both relativistic and non-relativistic kinematics. We here discuss theoretical approximations for the dielectric function, and will show that we can use EELS data to validate our expressions, at least for electrically charged particles.

There are several publicly available tools for calculating dark-matter scattering off various materials and the resulting direct-detection signals, including QEDark [21, 60], DarkELF [23, 24], EXCEED-DM [25, 26], and QCDark [27, 61]. Due to the kinematics of virialized dark matter, the focus of the community has been to characterize correctly the region of phase space in which  $k \gtrsim \beta_{\text{vir}}^{-1}\omega$  where  $\beta_{\text{vir}} \sim 10^{-3}$ , such that the typical values for the recoil energy and momentum transfer are  $\omega \sim (\text{few})$  eV and  $k \sim (\text{few})$  keV, respectively.

The situation differs substantially for relativistic particles with  $\beta \sim 1$ . Then the natural scaling is  $\omega \sim k \sim (\text{few})$  eV. Often one encounters discussions of the so called “optical limit,” which refers to  $k \ll k_F$ , or tacitly  $k \rightarrow 0$  [62, 63]. Indeed, if one considers optical absorption measurements of on-shell photons then  $\omega = k \sim \text{few}$  eV. There is a crucial difference, however, between optical absorption and the scattering of relativistic particles. Photons are always transversely polarized, whereas a charged particle can interact with the sample via longitudinal Coulomb modes. In fact, it

is precisely these longitudinal modes, i.e., the longitudinally polarized bulk plasmon, which dominate the response function. Optical absorption data is therefore a *poor proxy* for relativistic scattering of charged particles [64].

We can write the dielectric function in terms of its real and imaginary part,

$$\epsilon(\omega, k) = \epsilon_1(\omega, k) + i\epsilon_2(\omega, k), \quad (3.1)$$

where  $\epsilon_{1,2}(\omega, k)$  are real, so that the energy loss function can be written as

$$\text{Im} \left( \frac{-1}{\epsilon_1(\omega, k) + i\epsilon_2(\omega, k)} \right) = \frac{\epsilon_2(\omega, k)}{|\epsilon_1(\omega, k)|^2 + |\epsilon_2(\omega, k)|^2}. \quad (3.2)$$

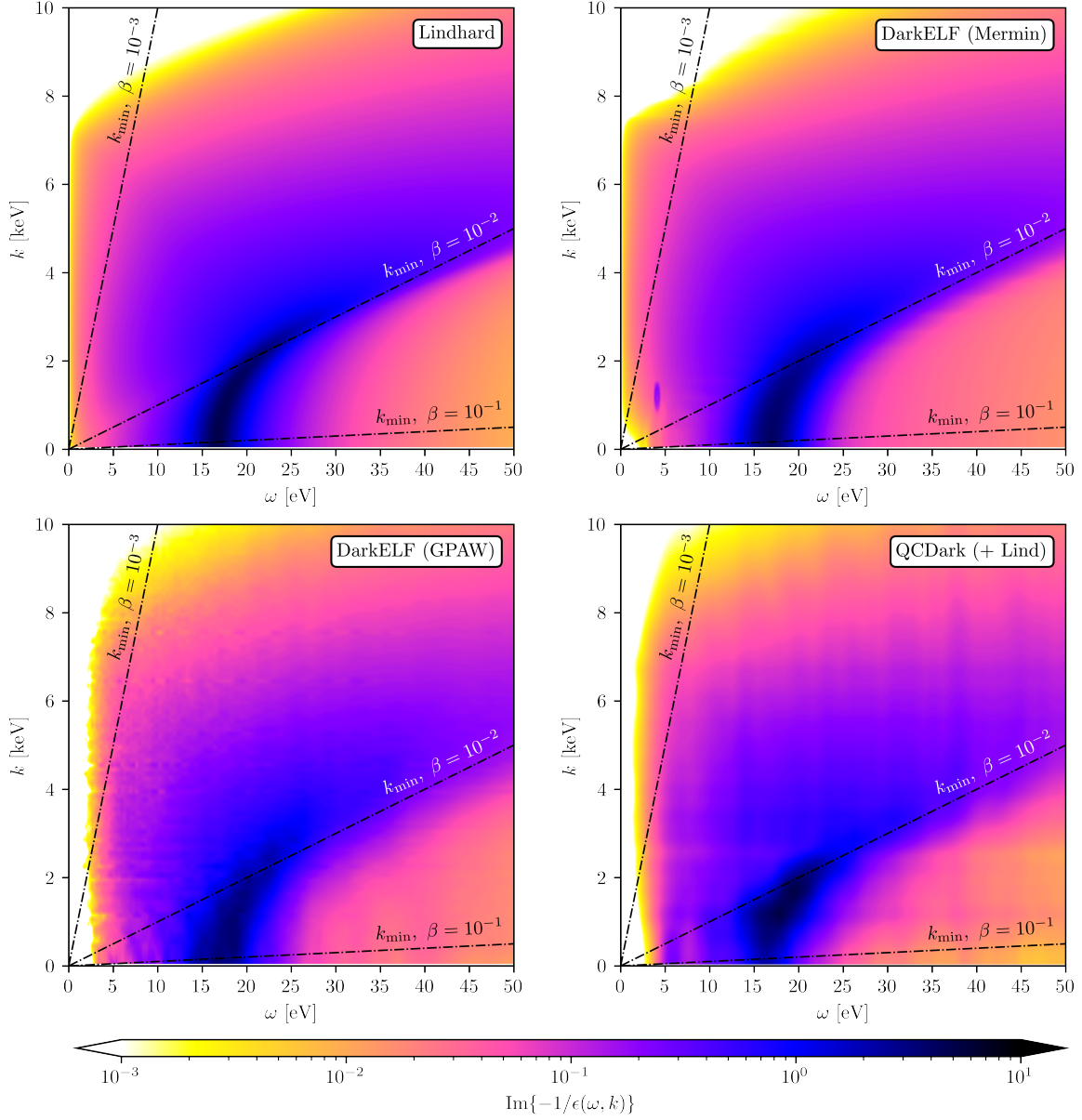
Many existing tools in the literature for dark matter scattering do not properly model the real part of the dielectric function at small momentum transfers. Fortunately, a good qualitative and reasonable quantitative description of  $\epsilon(\omega, k)$  for  $k \ll k_F$  is given by the Lindhard model [65], which provides a reasonable description for millicharged particle searches that are dominated by low momentum transfers. For massive mediators, or higher dimensional operators such as a magnetic dipole moment, larger momentum transfers can contribute  $O(1)$  fractions to the total cross section. Fortunately, in the limit  $k \gtrsim k_F$  where the Lindhard model is unreliable [66], the absolute value of the dielectric function is approximately unity (since  $\epsilon_1 \approx 1$  and  $\epsilon_2 \approx 0$ ) which is properly reproduced by the Lindhard model. The Lindhard model does not, however, properly model  $\epsilon_2$  at large values of  $k$ . Hence the Lindhard model is able to produce a reliable value for  $|\epsilon(\omega, k)|^2$  while being unable to calculate the electron loss function  $\{-1/\epsilon(\omega, k)\}$  at large  $k \gtrsim k_F$ .

More robust methods of calculating the dielectric function involve calculation of the electronic wavefunction using density functional theory (DFT) [66–68], and employing the random phase approximation (RPA) [69–72]. The open source tool `DarkELF` [23, 24] includes RPA calculations of both the real and imaginary parts of the dielectric function calculated using the DFT software `GPAW`. The `DarkELF` package also includes the option to fit a superposition of Lindhard dielectrics, which is referred to as the ‘Mermin’ model. The current implementation `DarkELF` does not, however, reconstruct the wavefunctions of core electrons. This causes the valence electron wavefunctions from `DarkELF` to mismodel large- $k$  modes. A reliable description of large- $k$  modes can be obtained using other tools, for example `QCDark` [27]. In its current state, however, `QCDark` only calculates the imaginary part of the RPA dielectric function. Therefore, when using `QCDark` to predict the energy loss function, one must supply the real part of the dielectric externally. More specifically, `QCDark` provides the crystal form factor as developed in [21], which is equivalently written as

$$|f_{\text{crystal}}(k, \omega)|^2 = \frac{k^5 V_{\text{cell}}}{8\pi^2 \alpha_{EM}^2 m_e^2} \epsilon_2^{\text{RPA}}(\omega, k), \quad (3.3)$$

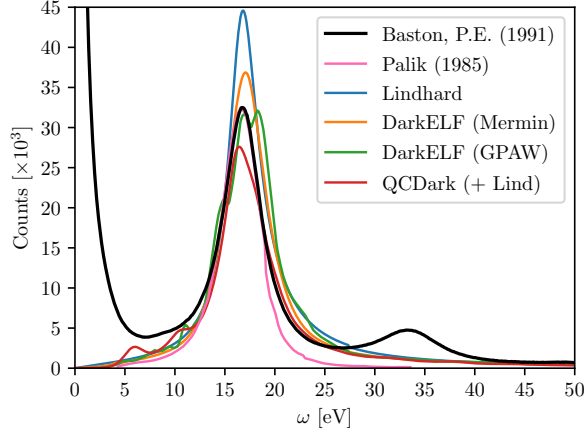
where  $V_{\text{cell}}$  is the volume of the unit cell,  $\alpha_{EM}$  is the electromagnetic fine structure constant, and  $m_e$  is the mass of the electron. We find that a reliable *global* approximation of the energy loss function can be obtained for silicon by taking the following model

$$\text{Im} \left[ \frac{-1}{\epsilon_1(\omega, k) + i\epsilon_2(\omega, k)} \right]_{\text{model}} = \frac{[\epsilon_2(\omega, k)]_{\text{QCDark}}}{[|\epsilon(\omega, k)|^2]_{\text{Lindhard}}}. \quad (3.4)$$



**Figure 1.** The electron loss function,  $\text{Im}\{-1/\epsilon(\omega, k)\}$  for silicon, plotted as a function of  $\omega$  and  $k$ . The top left panel shows the Lindhard approximation to the electron loss function; the top right panel shows the Mermin approximation built into the **DarkELF** program [23, 24]; the bottom left panel shows the GPAW DFT calculation of the dielectric function built into **DarkELF**; the bottom right panel shows the **QCDark** calculation of the imaginary part of the dielectric function [27] screened by the Lindhard  $1/|\epsilon(\omega, k)|^2$  as given by Eq. (3.4). The bottom right panel, due to the low  $\mathbf{k}$ -grid used in the calculation, is Gaussian smoothed with  $\sigma_\omega = 0.5$  eV and  $\sigma_k = 200$  eV. In all plots, the plasmon is visible for low  $k$  and  $\omega \sim 16.6$  eV. The lines indicate the minimum momentum,  $k_{\text{min}}$ , required to transfer energy  $\omega$  from an incoming particle with speed  $\beta$ . Note that the plasmon threshold occurs close to  $\beta \sim 10^{-2}$ .





**Figure 2.** Electron Energy-Loss Spectroscopy (EELS) data (**black line**) compared to our theoretical modeling (various **colored lines**) in a bulk silicon from [73, 74] with an incident electron beam kinetic energy of  $T = 100$  keV. We model the theoretical EELS rates by calculating the EELS cross section using Eq. (2.1) with various different approximations for the dielectric function  $\epsilon(\omega, k)$ . We normalize the rates to the plasmon peak,  $\omega = \omega_{pl}$  using experimental  $\epsilon(\omega, k \rightarrow 0)$  from [75], in conjunction with Eq. (3.5) and Eq. (3.6). The EELS data includes multiple scattering, with a secondary scattering peak visible at  $\omega = 2\omega_{pl}$ , which can be included by modeling multiple scatters (see [64] for a discussion). Note that the sharply rising peak in the experimental data towards low energies,  $\omega \lesssim 10$  eV is due to elastic scatters between incident electrons and the lattice, and is not captured in the models of the dielectric function  $\epsilon(\omega, k)$  considered here.

This model works in the low-energy region near the plasmon peak because the Lindhard model is reliable there and agrees reasonably with the more sophisticated calculation of  $\epsilon_2$  from QCDark [27]. In the high-energy region, the imaginary part of the dielectric function is small,  $\epsilon_2 \ll \epsilon_1 \approx 1$ , such that the denominator can effectively be replaced by unity in any model. We are then entirely insensitive to the mismodeling of  $\epsilon_2(\omega, k)$  at large values of  $k$  in the Lindhard model, while simultaneously benefiting from the Lindhard model’s realistic description of the bulk plasmon. However, note that the low  $k$  electron loss function is underestimated using this method, likely due to an overestimate of  $|\epsilon(\omega, k \ll k_F)|^2$  from the Lindhard model.

In Fig. 1, we show the electron loss function, which dominates energy loss in both the non-relativistic and relativistic regimes, computed in various approximations. This includes the Lindhard model [65], the Mermin model and density functional theory calculations from DarkELF [23, 24], and QCDark [27] screened by the Lindhard dielectric function as given in Eq. (3.4).

The response functions we make use of here are easily compared with existing EELS data. An EELS experiment involves quasi-relativistic electrons impinging on a thin sample (which precisely replicates the kinematics we are interested in) and allows for both Coulomb-mode and transverse-mode mediated scattering [64]. Any tool claiming to reliably predict low-energy event rates in a silicon (or other semiconductor) detector must necessarily reproduce EELS spectra. Previous comparisons with EELS (for URu<sub>2</sub>Si<sub>2</sub> specifically) and X-ray scattering data have focused on the kinematic regime relevant for halo dark matter direct detection i.e.,  $k \sim 5$  keV [22].

Figure 2 shows the EELS experimental data from Refs. [73, 74] for silicon. The incident electrons have



a kinetic energy of 100 keV. The peak at  $\omega \sim 0$  corresponds to elastic scattering of incident electrons with the lattice, and hence does not correspond to electron-hole pair excitations. The plasmon peak at  $\omega = \omega_{pl} \approx 16.6$  eV is visible. We further use experimental data available for the dielectric function at long wavelengths,  $\epsilon(\omega) \equiv \epsilon(\omega, k \rightarrow 0)$  from [75] to compute the differential EELS cross section [76],

$$\frac{d\sigma}{d\omega} \approx \frac{\alpha}{n_a \pi \beta^2} \text{Im} \left\{ \frac{-1}{\epsilon(\omega)} \right\} \log \left\{ 1 + \frac{\theta^2}{\theta_E^2} \right\}. \quad (3.5)$$

Here  $n_a$  is the number density of silicon atoms,  $\theta$  is the collection angle for the data (1.6 mrad), and  $\theta_E = \omega/\gamma m_e \beta^2$ . We then normalize the counts  $C(\omega)$  observed as

$$C(\omega) = \kappa \frac{d\sigma}{d\omega} \quad (3.6)$$

to fix the electron flux, where we obtain  $\kappa$  by fixing the value of  $C(\omega_{pl})$  to match experimental data at the plasmon peak.

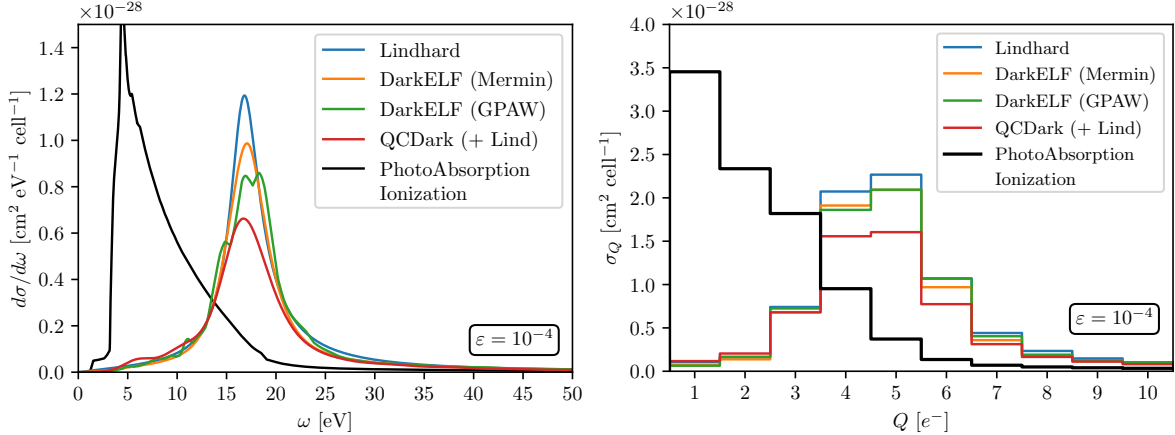
We compare the data to the cross section computed using the Lindhard model [65], Mermin and GPAW calculations from DarkELF [23, 24], and QCDark [27] screened with Lindhard as in Eq. (3.4). We normalize the counts using the flux obtained by fitting the semi-empirical differential cross section using Eq. (3.5) and Eq. (3.6). Any EELS measurement will have multiple scattering peaks whose amplitude grow with increased sample thickness [64]. In this work, we ignore multiple scatterings, though they can be included by assuming a Poisson process and normalizing the second peak to the corresponding peak in the experimental data. This would then fix the thickness of the sample.

The Lindhard and Mermin models [23, 24, 65] overestimate the cross section, while QCDark (with Lindhard screening Eq. (3.4)) [27] underestimates it. The latter is likely due to the Lindhard model overestimating the screening, causing the electron loss function to be underestimated at  $k \ll k_F$ . The DarkELF (GPAW) dielectric function [23, 24] correctly predicts the peak of the EELS data, which means the differential cross section agrees with the semi-empirical cross section that uses [75] and Eq. (3.5). However, it predicts a split plasmon with peaks at  $\omega \sim 16.9$  eV and  $\omega \sim 18.2$  eV, which seems unphysical, and a slightly broader plasmon peak than other approximations.

## 4 Phenomenology of relativistic particle scatters

In what follows we focus on three representative examples of BSM models for which low-threshold silicon detectors are well suited. We focus on the modification of the cross section due to collective effects. First, we consider millicharged particles produced in accelerator beams and/or cosmic rays [56, 57, 77–79]. Millicharged particles have a cross section that is enhanced at small momentum transfers, and, in the contexts we consider, are highly boosted. They are therefore a prime example where it is important to include plasmon excitations to correctly model the expected recoil spectrum. Moreover, searches for millicharged particles in the 100 MeV–100 GeV range is an active area of research, and SENSEI has recently demonstrated excellent sensitivity from data taken in the MINOS hall at Fermilab [80]; moreover, Oscura will have sensitivity to such particles [79].<sup>4</sup> Second, we consider a small silicon detector near a nuclear reactor as has recently been proposed, for example, in the

<sup>4</sup>The results of this paper were used in the analysis performed by SENSEI [80] and Oscura [79].



**Figure 3.** *Left panel:* the differential cross section of millicharged particle with charge  $\varepsilon = 10^{-4} e^-$  scattering in a silicon target, given in units of  $\text{cm}^2 e\text{V}^{-1}$  per unit cell. The various colored lines assume different methods for calculating the dielectric function of silicon. The black line assume the Photo Absorption Ionization (PAI) model [54, 55]. While PAI is frequently used for estimating the cross section, we see that it severely overestimates the cross section at low energies and underestimates it near the plasmon. The QCDark rates are calculated by screening the QCDark  $\text{Im}\{\epsilon(\omega, k)\}$  with a Lindhard  $|\epsilon(\omega, k)|^2$  (see Eq. (3.4)), and are Gaussian smoothed with  $\sigma_\omega = 0.5$  eV, while the DarkELF and Lindhard lines use a fully self-consistent  $\epsilon(\omega, k)$ . *Right panel:* the cross section calculated as a function of the number of electron-hole pairs created, where we use the secondary ionization model from [84] at 100 K. Note the peaks at  $Q = 4 e^-$  and  $Q = 5 e^-$ .

context of the vIOLETA collaboration [81–83]. As a representative example, we consider a search for a neutrino magnetic dipole moment, where scattering is moderately enhanced at low momenta, but not as strongly as for millicharged particles. The same set-up has promising sensitivity to light mediators that couple neutrinos to electrons and nucleons. Finally, we consider boosted dark matter as may be produced via solar reflection or by cosmic ray upscattering, e.g. [35–46]. We study, in particular, how the sensitivity changes as the mass of the mediator is varied.<sup>5</sup>

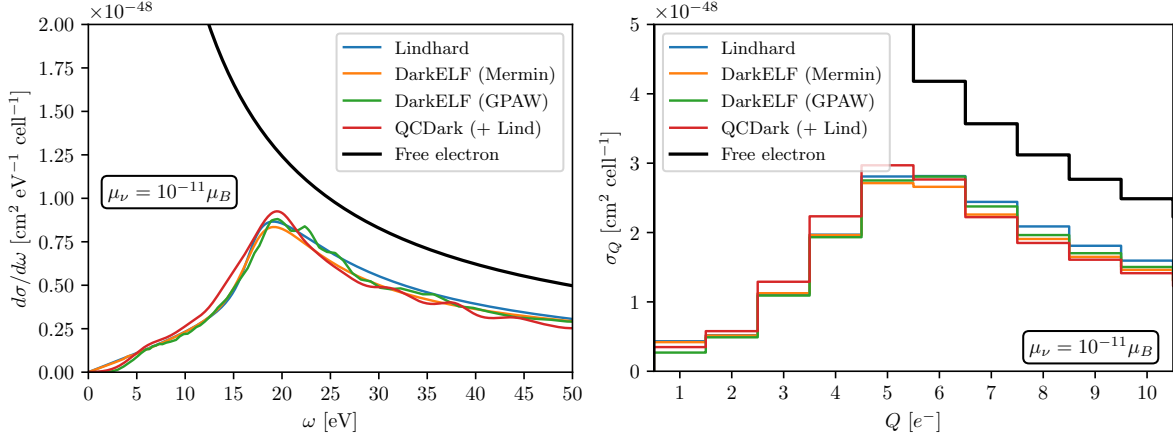
#### 4.1 Millicharged particles

Accelerator-based production of low-mass millicharged particles leads to a flux that is almost entirely relativistic, assuming the incoming proton-beam energy is sufficiently large [56, 57]. The cross section in this limit is nearly independent of the precise boost of the millicharged particle,  $\gamma_{\text{mcp}}$  and one may approximate the rate of millicharged particles that scatter downstream by

$$\frac{d\Gamma_{\text{det}}}{d\omega} = \Phi \times \frac{d\sigma_{\text{mcp}}}{d\omega}, \quad (4.1)$$

with  $d\sigma_{\text{mcp}}$  given by Eq. (2.1), and where  $\Phi$  is the flux of relativistic millicharged particles. The integration measure  $dk/k = d \log k$  is scale-independent such that small- $k$  regions are not phase-space suppressed. In  $\log(k)$ -space, the plasmon appears for  $k \lesssim 3$  keV (as can be seen in Fig. 1). Since  $k_{\text{min}} \geq \omega$  for  $\omega \sim 10$  eV, the plasmon contributes appreciably to the integral for roughly two-decades in  $k$ -space.

<sup>5</sup>The results of this paper will be used in [41] to improve predictions and bounds on solar-reflected dark matter.



**Figure 4.** *Left panel:* the differential cross section of neutrinos interacting with a silicon target through a magnetic dipole moment  $\mu_\nu = 10^{-11} \mu_B$ . The various colored lines assume different methods for calculating the dielectric function of silicon. The black line shows the results for a free electron. Note that the free electron approximation is a good estimate for the shape of the differential cross-section compared to modeling the same via a dielectric approximation at high recoil energies,  $\omega > 20$  eV, however it overestimates the rate by  $\sim 50\%$  in this region. The QCDark differential cross section is calculated in the same way as the left panel of Fig. 3. *Right panel:* the cross section versus the number of electron-hole pairs created, where we use the secondary ionization model from [84] at 100 K. The charge ionization spectrum is drastically different between the correct calculation and the free-electron calculation, and  $\sigma_Q$  first rises as a function of  $Q$ , until about  $Q \sim 5 e^-$ , then decreases again.

The left panel of Fig. 3 shows the differential cross section per primitive unit cell for a millicharged particle ( $\epsilon = 10^{-4}$ ) interacting with a silicon detector for various models (in 1 kg of silicon, there are  $\sim 1.07 \times 10^{25}$  primitive unit cells). The black line shows the results for the Photoionization Absorption (PAI) model, which is frequently used to model energy loss of fast charged particles in gases and other materials [49, 85]. The right panel of Fig. 3 shows the cross section as a function of the number of electron-hole pairs being created,  $Q$ , with the secondary ionization model taken from [84]. Compared to the PAI model, which peaks at  $Q = 1 e^-$ , the correct modeling, which includes the plasmon peak, shows that the cross section peaks at the  $Q = 4 e^-$  and  $5 e^-$  bins.

Our results can be immediately applied to set bounds on millicharged particles using existing data and to make sensitivity projections for future data. In particular, our cross sections were used by SENSEI to search for millicharged particles produced in the NuMI beam at Fermilab [80]. The search was consistent with a null signal, and the constraints on millicharged particles was found to be world leading for certain millicharged-particle masses. The SENSEI analysis was based on data taken in 2020, which had previously been used to constrain sub-GeV dark matter interactions in [8]. The analysis in 2020 only included the bins containing  $Q = 1 - 4 e^-$ . Given that the events peak at  $Q = 4 e^-$  and  $5 e^-$ , and also contain an appreciable number of events with  $Q = 6 e^-$ , SENSEI added the  $Q = 5 e^-$  and  $Q = 6 e^-$  bins. In addition, larger detectors are being planned. In particular, there is a plan to place a 1 kg Skipper-CCD detector in the NUMI beam line as part of the Oscura Integration Test before constructing the 10 kg Oscura dark matter detector. The cross sections discussed above are again needed for deriving accurate sensitivity projections [79].

## 4.2 Neutrino dipole moments

The magnetic dipole moments of the three neutrino species are predicted to either vanish, or be unobservably small, in the Standard Model [86, 87]. Searches for a non-zero neutrino dipole moment then represent a low-energy test of the Standard Model and, by proxy, an avenue for the discovery of BSM physics. Since a dipole operator is dimension-5, as compared to the standard dimension-6 contact interaction that governs neutrino scattering below the weak scale, it may be fruitfully pursued at low energies [87].

The recently proposed reactor neutrino experiment *vIOLETA* [81, 82], aims to place a low-threshold Skipper-CCD near an operating nuclear reactor. One proposed use-case for *vIOLETA* is to search for anomalous signatures of a neutrino dipole moment and of light mediators that allow neutrinos to interact with other Standard Model particles, such as electrons. Viable signatures include coherent scattering on nuclei and scattering on electrons. For dipole interactions and light mediators, the cross sections are comparable, and electron scattering is an attractive detection signature. Our results in Eq. (2.2) can be immediately applied to this detection channel.

Fig. 4 shows the differential cross section of neutrinos interacting with a silicon target for a magnetic dipole moment of  $\mu_\nu = 10^{-11} \mu_B$ . Using Eq. (2.2) as opposed to assuming scattering off a free electron (used in [82]). Collective effects alter both the overall rate, and the shape of the differential distribution with respect to energy transfer. The shift in the overall normalization has straightforward implications for detection prospects (they are slightly weakened), however the altered energy transfer spectrum has non-trivial effects. Shape discrimination is a powerful tool for distinguishing signal from background [82], and the notable peaked structure visible in the left panel of Fig. 4 offers a distinctive feature that may aid in future searches for neutrino dipole moments (or light mediators). This is to be compared with the free electron (at rest) recoil spectrum,

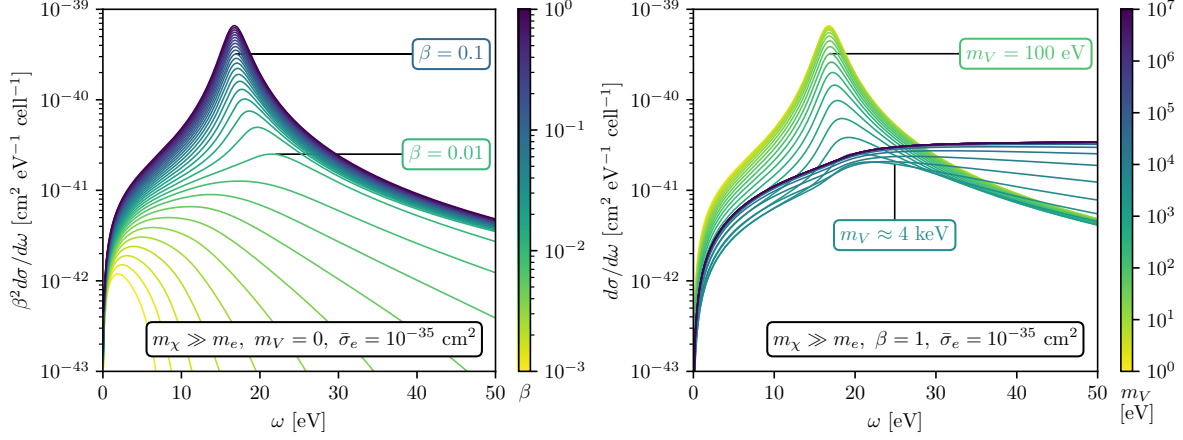
$$\left[ \frac{d\sigma}{dE_e} \right]_{\text{free electron}} = \alpha \mu_\nu^2 \left[ \frac{1}{E_e} - \frac{1}{E_\nu} \right], \quad (4.2)$$

which has no such feature and monotonically increases as  $E_e \rightarrow 0$ .

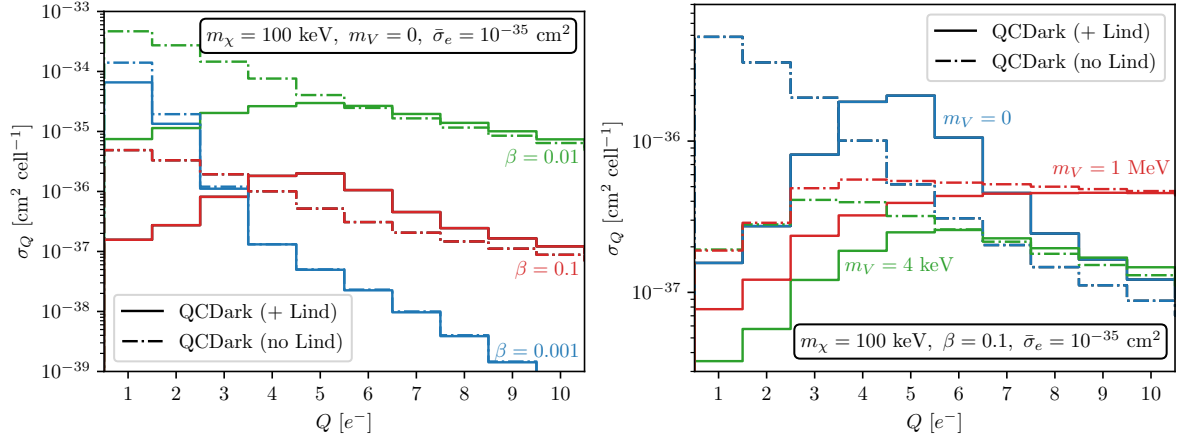
The right panel of Fig. 4 shows the cross section per unit cell of silicon as a function of electron-hole pairs ionized, using the secondary ionization model from [84] at a temperature of 100 K. Note that free-electron approximation dramatically overestimates the cross section for low charge ionization,  $Q \lesssim 5 e^-$ , while for larger  $Q \gtrsim 6 e^-$ , the cross section is overestimated in the free-electron model by roughly 50%.

## 4.3 Boosted dark matter

The assumptions of non-relativistic nature of dark matter are usually baked into the rate equations for dark matter–electron scattering in a lattice, especially because of the low speed of dark-matter particles in the galactic halo,  $\beta \lesssim 0.002$ . Recent developments in the treatment of dark matter particles boosted via solar reflection and cosmic rays [35–46] (see also [88–92]) have led to a need for a better understanding of dark matter–electron scattering without these underlying assumptions.

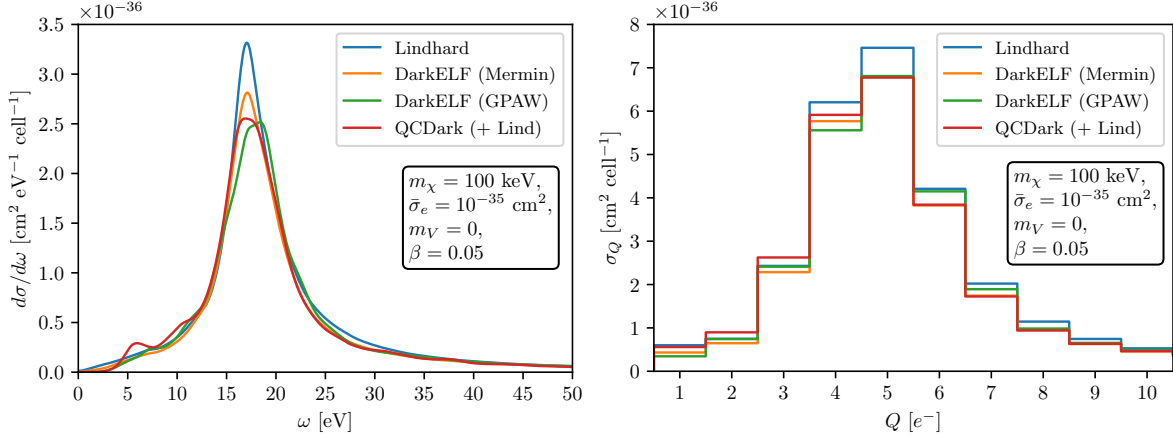


**Figure 5.** *Left panel:* the differential cross section per unit cell, weighted by  $\beta^2$ , for a dark matter particle with  $\bar{\sigma}_e = 10^{-35} \text{ cm}^2$  interacting with a silicon via a light mediator. Different colors indicate the speed of the incoming dark matter particle. The plasmon peak appears in the differential cross-section as the speed of the dark-matter particle is increased, and dominates the cross section for  $\beta \gtrsim 0.01$ . *Right panel:* the differential cross section per unit cell for a boosted dark matter particle with  $\beta = 1$  for various mediator masses,  $m_V$ . The dark matter particles interacting via lighter mediators have a cross section that is dominated by the plasmon whenever  $m_V \lesssim k_F$ . For  $m_V \rightarrow 0$ , the cross section agrees with that for millicharged-particle scattering shown in Fig. 3. These plots are made with the Lindhard approximation for the silicon dielectric function.



**Figure 6.** The dark matter–electron scattering cross section per unit cell, as a function of electron-hole pairs ionized,  $Q$ , following the ionization model from [84] for various incoming particle speeds,  $\beta$ . The solid lines show the effect of including collective effects, i.e., using  $\text{Im}\{-\epsilon(\omega, k)^{-1}\}$ , as compared to excluding them (dash-dotted lines), i.e., using only  $\text{Im}\{\epsilon(\omega, k)\}$ . The collective effects screen the cross section at low  $Q$ . The *left panel* shows the variation of the cross section with  $\beta$ ; for high  $\beta \gtrsim 0.01$ , the plasmon becomes accessible and enhances the cross section. The *right panel* shows the variation of the cross section with  $m_V$ , where the plasmon excitation becomes apparent for  $m_V \lesssim 4 \text{ keV}$ . These plots are made using the imaginary part of QCDark, where collective effects are modeled using Eq. (3.4).

Eq. (2.3) gives the differential cross section of dark matter–electron, including the case of relativistic dark matter.



**Figure 7.** *Left panel:* the differential cross section of a 100 keV boosted dark matter particle interacting with a silicon target with  $\beta = 0.05$  and a massless mediator. The various colored lines assume different methods for calculating the dielectric function of silicon. The **QCDark** differential cross section is calculated in the same way as the left panel of Fig. 3. *Right panel:* the cross section versus the number of electron-hole pairs created, where we use the secondary ionization model from [84] at 100 K.

Figure 5 shows the differential cross section of dark matter–electron scattering in a silicon target using Eq. (2.3) and assuming a Lindhard model for the silicon dielectric function [65]. The left panel shows the differential cross section for a dark matter particle with a light mediator,  $m_V \rightarrow 0$ , but with varying speeds  $\beta$  of the incoming dark matter particle. Note that since the minimum momentum transfer ( $k_{\min}$ ) scales as  $1/\beta$ , only fast dark matter particles are able to excite the plasmon. Hence plasmons are important for  $\beta \gtrsim 0.01$  and dominate the differential cross section for high-speed dark matter particles with  $\beta \gtrsim 0.1$ , but are largely irrelevant for halo dark matter (see also [30]).

The right panel of Fig. 5 shows the differential cross section per unit cell for boosted dark matter particles traveling at  $\beta = 1$  interacting with electrons in a silicon lattice, but for various vector-mediator masses,  $m_V$ . For higher mediator masses,  $m_V \gtrsim 1$  MeV, we can approximate  $k^4/(k^2 + m_V^2)^2 \sim k^4/m_V^4$ , which effectively causes the high  $k$  modes to be enhanced. For lighter mediator masses,  $m_V \lesssim 100$  eV, the plasmon dominates the differential cross section.

Fig. 6 shows the dark matter–electron scattering cross section per unit cell as a function of ionized charge,  $Q$ , using the secondary ionization model from [84], with and without collective effects. The collective effects ‘screen’ the cross section at low charge ionization  $Q$ , while the cross section in the high- $Q$  bins are enhanced for  $\beta \gtrsim 0.01$  as the plasmon becomes accessible. Similarly, the plasmon is accessible for lighter mediators,  $m_V \lesssim 4$  keV. We also note that the energy deposition peaks not at low  $Q$  as it would for halo-dark matter scatters, but at  $Q \gtrsim 5 e^-$ ; this means that the larger backgrounds towards lower values of  $Q$  typically seen in current dark-matter detectors do not much impact the sensitivity of such detectors to solar-reflected and otherwise boosted dark matter.

Fig. 7 compares dark matter–electron scattering cross section per unit cell calculated using various dielectric functions. The left (right) panel shows the differential cross section (binned with respect to ionized charge  $Q$ ) for a 100 keV dark matter particle of velocity  $\beta = 0.05$  interacting via a massless

mediator, with  $\bar{\sigma}_e = 10^{-35} \text{ cm}^2$ . Note that the Lindhard model overestimates the cross section for the  $Q = 5 e^-$  bin and there is  $\sim 5 - 10\%$  uncertainty in the  $3 e^- \leq Q \leq 7 e^-$  bins.

#### 4.4 Systematic uncertainties on signal predictions

In a counting experiment searching for hypothetical particles, the systematic uncertainties that must be understood are: 1) the uncertainty on the flux of feebly interacting particles, 2) the uncertainty on the cross section differential in energy transfer to the target, and 3) the uncertainty on the branching ratio of visible energy. The uncertainty on the flux is model dependent, and factorizes from the cross section and so we do not discuss it further.

As can be seen from Fig. 3, Fig. 4, and Fig. 7 the systematic uncertainty on the cross section is modest i.e., no larger than 20%. When comparing the curves in Fig. 3, Fig. 4, and Fig. 7 it is important to emphasize that we expect the Lindhard model to provide a good description of the lineshape, but not necessarily the normalization, in the vicinity of the plasmon. Since the `QCDark` curves use the Lindhard model to apply a screening correction to  $\epsilon_2(\omega, k)$  we expect their current implementation to *underpredict* the cross section. It is therefore reasonable to use the difference between the ‘Mermin’ and ‘GPAW’ `DarkELF` curves as a proxy for the systematic uncertainty. In the signal bins relevant for the SENSEI millicharged-particle analysis [80], the uncertainty is  $\lesssim 5\%$  in the relevant energy bins.

The cross section differential with respect to energy transfer gives an *upper bound* on the amount of energy deposited in the form of ionization. Energy transferred into phonons, or other vibrational modes, will likely transfer a substantial amount of their energy in the form of heat. We use the model from Ref. [84] in this work, which employs a Monte Carlo method to estimate the exclusive final states. Further work characterizing the exclusive final states as a function of the deposited energy and momentum transfer would help solidify the connection between  $d\sigma/d\omega$  and experimentally observable quantities such as the number of electron-hole pairs ionized. While we are currently unable to quantify this uncertainty, we do not expect any substantial changes to our qualitative findings: the plasmon peak provides helpful kinematic separation between signal and background, and serves to enhance the sensitivity of low-threshold detectors.

## 5 Conclusions

Semiconductors benefit from a small band gap, which allows sensitivity to small  $\sim \text{eV}$  energy depositions. Since the ionized electron-hole pairs are not free, collective effects play an important role at low energy and low momentum transfers. Of particular importance can be the role played by the bulk plasmon, a collective resonant mode that is well known to dominate EELS spectra.

When restricted to the non-relativistic limit, many of the collective effects become less pronounced. Scattering is dominated by regions of large momentum transfer and calculations largely reduce to the evaluation of a crystal form factor [21, 25–27, 60, 61]. Relativistic and quasi-relativistic particles are crucially different as emphasized in [30]. More recently, a plasmon-induced threshold effect in anisotropic “heavy electron” materials has recently been proposed for directional detection of light dark matter [34].



In this paper, we have focused on the scattering in silicon of particles that have larger velocities than those found for virialized dark matter particles in the Milky-Way halo, including relativistic particles with  $\beta \approx 1$ . This allows the plasmon to be kinematically accessible at almost all energies. Since the plasmon is a longitudinal excitation, it cannot be excited by the absorption of on-shell (and therefore transverse) photons. Optical data is then a poor proxy for the response of the material to incident relativistic particles. Moreover, the many tools that have been developed for non-relativistic scattering of dark matter perform poorly in the relativistic limit, in large part due to mismodelling of the plasmon.

We have made use of the proper, fully relativistic formalism for energy loss in materials using realistic models/calculations for the dielectric function of silicon (our formalism can be easily applied to other materials for which the dielectric function is known). We have validated our model calculation against publicly available EELS data and find good agreement. We have applied this formalism to three characteristic models: a millicharged particle, a neutrino dipole moment, and boosted dark matter with a light mediator. In particular, the differential cross sections for the scattering in materials of millicharged particles, of neutrinos with a magnetic dipole moment, and of boosted dark matter with a dark photon mediator are given in Eq. (2.1), Eq. (2.2), and Eq. (2.3), respectively. We find that the GPAW dielectric function in DarkELF [23, 24] produces reliable results when the incoming velocity of the probe particle is high,  $\beta \gtrsim 0.01$ . This is because even though the dielectric function does not include all-electron effects [25, 27], the target material response is dominated by low momentum transfers,  $k \lesssim k_F$ .

We have found important differences with existing implementations in the literature for the scattering of these particles. In particular, the plasmon dramatically impacts the shape of the  $d\sigma/d\omega$  for all three models, and can have important consequences for how experimental searches should be optimized. The plasmon effectively acts to screen the cross section at low energy transfers (below the plasmon energy) in analogy with a Thomas-Fermi form factor in atomic physics that screens the Rutherford cross section at low energy transfer. Moreover, it enhances the differential cross section near the plasmon energy. Our results show that the proper inclusion of collective effects typically enhances a detector's sensitivity to these particles, since detector backgrounds, such as dark counts, peak at lower energies.

**Note added:**

During the final stages of completing this paper, Ref. [93] appeared, which also considered the effects of the plasmon for relativistic dark-matter particles. They use the DarkELF-GPAW dielectric function and applied their formalism to cosmic-ray boosted dark matter to derive constraints using data from SENSEI at SNOLAB [94]. We provide additional expressions for the dielectric functions, and compare our results also to EELS data. Our calculations were also already used in [79, 80] for millicharged and boosted DM particles.

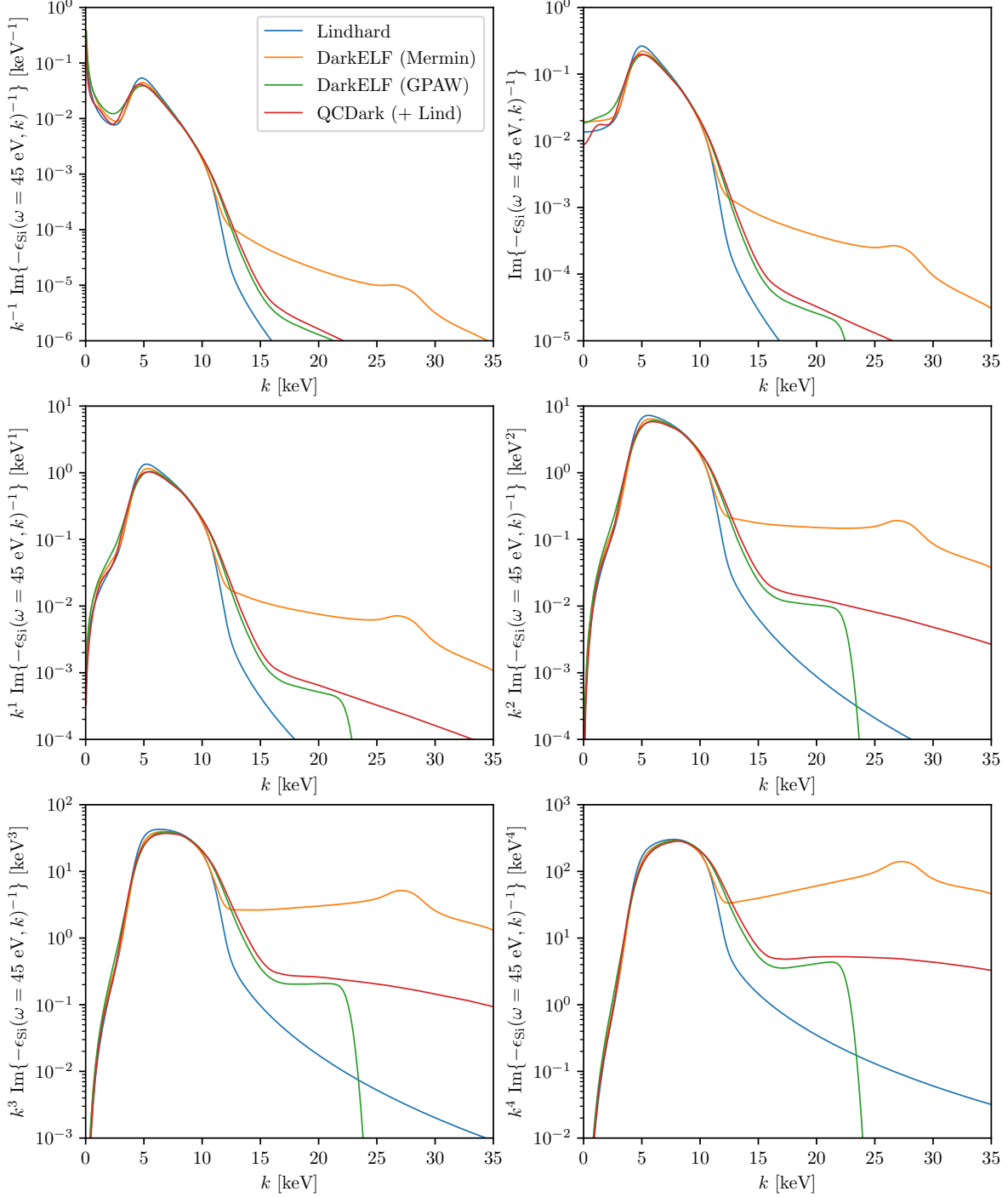


## Acknowledgments

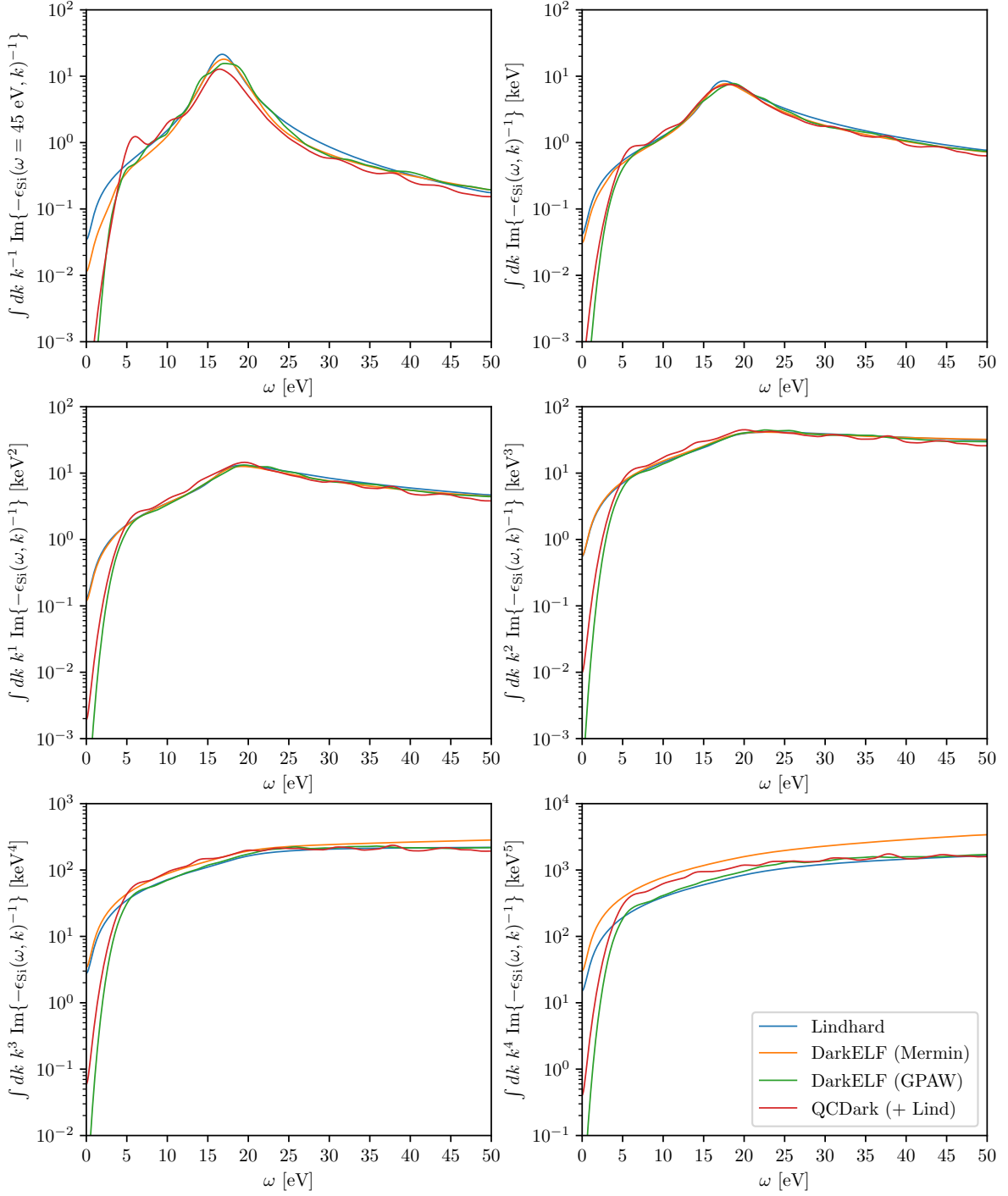
We thank Roni Harnik and Zhen Liu for early discussions, Santiago Perez for discussions on the photoionization absorption model, and the broader SENSEI group for their collaboration on the NuMI search for millicharged particles. R.E. acknowledges support from the US Department of Energy under Grant DE-SC0009854, from the Heising-Simons Foundation under Grant No. 79921, from the Simons Foundation under the Simons Investigator in Physics Award 623940, from the Binational Science Foundation under Grant No. 2020220, from Stony Brook IACS Seed Grant, and from Fermilab subcontract 664693 for the DoE DMNI award for Oscura. R.P. is supported by the Neutrino Theory Network under Award Number DEAC02-07CH11359, the U.S. Department of Energy, Office of Science, Office of High Energy Physics under Award Number DE-SC0011632, and by the Walter Burke Institute for Theoretical Physics. R.P. gratefully acknowledges support from the Simons Center for Geometry and Physics, Stony Brook University during the workshop *Lighting New Lampposts for Dark Matter and Beyond the Standard Model* where this project was initiated and a large portion of the research for this paper was performed. A.S. is supported in part by a Stony Brook IACS Seed Grant, from Fermilab subcontract 664693 for the DoE DMNI award for Oscura, from DoE Grant DE-SC0009854, and from the Simons Investigator in Physics Award 623940. We also thank Stony Brook Research Computing and Cyberinfrastructure, and the Institute for Advanced Computational Science at Stony Brook University for access to the high-performance SeaWulf computing system, which was made possible by a National Science Foundation grant No. 1531492.

## A Additional figures for momentum-weighted energy loss function

In this appendix, we provide additional figures, which we feel may be helpful in interpreting our results. In Fig. 8, we show a slice of the momentum-transfer-weighted energy loss function at a fixed energy transfer of  $\omega = 45$  eV. This is the integrand in Eqs. (2.1) to (2.3) for different interactions, ranging from a massless mediator ( $k^{-1}$ ), to a neutrino dipole moment ( $k^1$ ), to a contact operator ( $k^3$ ). In Fig. 9, we show the same momentum weightings, but at the level of the integral as a function of  $\omega$ . These curves dominate the relativistic energy loss formulae, Eqs. (2.1) to (2.3), although they receive additional corrections from the transverse modes for relativistic kinematics.



**Figure 8.** The wavenumber dependence of the silicon dielectric function calculated with various approximations and numerical techniques. The electron loss function,  $\text{Im}\{-\epsilon(\omega, k)^{-1}\}$  has been smoothed by averaging over the energy axis in a 2 eV bin centered at  $\omega = 45$  eV, and underwent Gaussian smoothing on the  $k$  axis with  $\sigma_k = 0.5$  keV. **QCDDark** shows the effect of *all-electron* inclusions at high  $k \gtrsim 23$  keV, while the Mermin function in **DarkELF** overestimates the imaginary part of  $\epsilon(\omega, k)$  for  $k \gtrsim 11$  keV.



**Figure 9.** The frequency dependence of  $\int dk k^n \text{Im}\{-1/\epsilon(\omega, k)\}$  for the silicon dielectric function calculated using various codes. The results have undergone a Gaussian smoothing with  $\sigma_\omega = 0.5\text{eV}$ .

## References

- [1] R. Essig et al., *Snowmass2021 Cosmic Frontier: The landscape of low-threshold dark matter direct detection in the next decade*, in *Snowmass 2021*, 3, 2022 [[2203.08297](#)].
- [2] R. Essig, J. Mardon and T. Volansky, *Direct Detection of Sub-GeV Dark Matter*, *Phys. Rev. D* **85** (2012) 076007 [[1108.5383](#)].
- [3] DAMIC collaboration, *Search for low-mass WIMPs in a 0.6 kg day exposure of the DAMIC experiment at SNOLAB*, *Phys. Rev. D* **94** (2016) 082006 [[1607.07410](#)].
- [4] SENSEI collaboration, *SENSEI: First Direct-Detection Constraints on sub-GeV Dark Matter from a Surface Run*, *Phys. Rev. Lett.* **121** (2018) 061803 [[1804.00088](#)].
- [5] SUPERCDMS collaboration, *First Dark Matter Constraints from a SuperCDMS Single-Charge Sensitive Detector*, *Phys. Rev. Lett.* **121** (2018) 051301 [[1804.10697](#)].
- [6] SENSEI collaboration, *SENSEI: Direct-Detection Constraints on Sub-GeV Dark Matter from a Shallow Underground Run Using a Prototype Skipper-CCD*, *Phys. Rev. Lett.* **122** (2019) 161801 [[1901.10478](#)].
- [7] DAMIC collaboration, *Constraints on Light Dark Matter Particles Interacting with Electrons from DAMIC at SNOLAB*, *Phys. Rev. Lett.* **123** (2019) 181802 [[1907.12628](#)].
- [8] SENSEI collaboration, *SENSEI: Direct-Detection Results on sub-GeV Dark Matter from a New Skipper-CCD*, *Phys. Rev. Lett.* **125** (2020) 171802 [[2004.11378](#)].
- [9] SUPERCDMS collaboration, *Constraints on low-mass, relic dark matter candidates from a surface-operated SuperCDMS single-charge sensitive detector*, *Phys. Rev. D* **102** (2020) 091101 [[2005.14067](#)].
- [10] EDELWEISS collaboration, *First germanium-based constraints on sub-MeV Dark Matter with the EDELWEISS experiment*, *Phys. Rev. Lett.* **125** (2020) 141301 [[2003.01046](#)].
- [11] DAMIC-M collaboration, *First Constraints from DAMIC-M on Sub-GeV Dark-Matter Particles Interacting with Electrons*, *Phys. Rev. Lett.* **130** (2023) 171003 [[2302.02372](#)].
- [12] DARKSIDE collaboration, *Constraints on Sub-GeV Dark-Matter–Electron Scattering from the DarkSide-50 Experiment*, *Phys. Rev. Lett.* **121** (2018) 111303 [[1802.06998](#)].
- [13] R. Essig, A. Manalaysay, J. Mardon, P. Sorensen and T. Volansky, *First Direct Detection Limits on sub-GeV Dark Matter from XENON10*, *Phys. Rev. Lett.* **109** (2012) 021301 [[1206.2644](#)].
- [14] R. Essig, T. Volansky and T.-T. Yu, *New Constraints and Prospects for sub-GeV Dark Matter Scattering off Electrons in Xenon*, *Phys. Rev. D* **96** (2017) 043017 [[1703.00910](#)].
- [15] XENON10 collaboration, *A Search for Light Dark Matter in Xenon10 Data*, *Phys. Rev. Lett.* **107** (2011) 051301 [[1104.3088](#)].
- [16] XENON collaboration, *Low-Mass Dark Matter Search Using Ionization Signals in Xenon100*, *Phys. Rev. D* **94** (2016) 092001 [[1605.06262](#)].
- [17] XENON collaboration, *Light Dark Matter Search with Ionization Signals in XENON1T*, *Phys. Rev. Lett.* **123** (2019) 251801 [[1907.11485](#)].
- [18] XENON collaboration, *Emission of single and few electrons in XENON1T and limits on light dark matter*, *Phys. Rev. D* **106** (2022) 022001 [[2112.12116](#)].
- [19] PANDAX-II collaboration, *Search for Light Dark Matter-Electron Scatterings in the PandaX-II Experiment*, *Phys. Rev. Lett.* **126** (2021) 211803 [[2101.07479](#)].

- [20] C. Blanco, J. Collar, Y. Kahn and B. Lillard, *Dark Matter-Electron Scattering from Aromatic Organic Targets*, *Phys. Rev. D* **101** (2020) 056001 [[1912.02822](#)].
- [21] R. Essig, M. Fernandez-Serra, J. Mardon, A. Soto, T. Volansky and T.-T. Yu, *Direct Detection of sub-GeV Dark Matter with Semiconductor Targets*, *JHEP* **05** (2016) 046 [[1509.01598](#)].
- [22] Y. Hochberg, Y. Kahn, N. Kurinsky, B.V. Lehmann, T.C. Yu and K.K. Berggren, *Determining Dark-Matter-Electron Scattering Rates from the Dielectric Function*, *Phys. Rev. Lett.* **127** (2021) 151802 [[2101.08263](#)].
- [23] S. Knapen, J. Kozaczuk and T. Lin, *Dark matter-electron scattering in dielectrics*, *Phys. Rev. D* **104** (2021) 015031 [[2101.08275](#)].
- [24] S. Knapen, J. Kozaczuk and T. Lin, *python package for dark matter scattering in dielectric targets*, *Phys. Rev. D* **105** (2022) 015014 [[2104.12786](#)].
- [25] S.M. Griffin, K. Inzani, T. Trickle, Z. Zhang and K.M. Zurek, *Extended calculation of dark matter-electron scattering in crystal targets*, *Physical Reviews D* **104** (2021) 095015 [[2105.05253](#)].
- [26] T. Trickle, *Extended calculation of electronic excitations for direct detection of dark matter*, *Phys. Rev. D* **107** (2023) 035035.
- [27] C.E. Dreyer, R. Essig, M. Fernandez-Serra, A. Singal and C. Zhen, *Fully ab-initio all-electron calculation of dark matter-electron scattering in crystals with evaluation of systematic uncertainties*, [2306.14944](#).
- [28] E.A. Peterson, S.L. Watkins, C. Lane and J.-X. Zhu, *Beyond-DFT ab initio Calculations for Accurate Prediction of Sub-GeV Dark Matter Experimental Reach*, [2310.00147](#).
- [29] R. Lasenby and A. Prabhu, *Dark matter-electron scattering in materials: Sum rules and heterostructures*, *Phys. Rev. D* **105** (2022) 095009 [[2110.01587](#)].
- [30] N. Kurinsky, D. Baxter, Y. Kahn and G. Krnjaic, *Dark matter interpretation of excesses in multiple direct detection experiments*, *Phys. Rev. D* **102** (2020) 015017 [[2002.06937](#)].
- [31] J. Kozaczuk and T. Lin, *Plasmon production from dark matter scattering*, *Phys. Rev. D* **101** (2020) 123012 [[2003.12077](#)].
- [32] S. Knapen, J. Kozaczuk and T. Lin, *Migdal Effect in Semiconductors*, *Phys. Rev. Lett.* **127** (2021) 081805 [[2011.09496](#)].
- [33] G.B. Gelmini, V. Takhistov and E. Vitagliano, *Scalar direct detection: In-medium effects*, *Phys. Lett. B* **809** (2020) 135779 [[2006.13909](#)].
- [34] C. Boyd, Y. Hochberg, Y. Kahn, E.D. Kramer, N. Kurinsky, B.V. Lehmann et al., *Directional detection of dark matter with anisotropic response functions*, *Phys. Rev. D* **108** (2023) 015015 [[2212.04505](#)].
- [35] H. An, M. Pospelov, J. Pradler and A. Ritz, *Directly Detecting MeV-scale Dark Matter via Solar Reflection*, *Phys. Rev. Lett.* **120** (2018) 141801 [[1708.03642](#)].
- [36] T. Emken, C. Kouvaris and N.G. Nielsen, *The Sun as a sub-GeV Dark Matter Accelerator*, *Phys. Rev. D* **97** (2018) 063007 [[1709.06573](#)].
- [37] T. Emken, *Dark Matter in the Earth and the Sun – Simulating Underground Scatterings for the Direct Detection of Low-Mass Dark Matter*, Ph.D. thesis, Southern Denmark U., CP3-Origins, 2019. [1906.07541](#).
- [38] T. Emken, *Solar reflection of light dark matter with heavy mediators*, *Phys. Rev. D* **105** (2022) 063020 [[2102.12483](#)].
- [39] H. An, H. Nie, M. Pospelov, J. Pradler and A. Ritz, *Solar reflection of dark matter*, *Phys. Rev. D* **104** (2021) 103026 [[2108.10332](#)].

- [40] Z.Y. Zhang et al., *Experimental Limits on Solar Reflected Dark Matter with a New Approach on Accelerated Dark Matter-Electron Analysis in Semiconductors*, [2309.14982](#).
- [41] T. Emken, R. Essig and H. Xu, *Solar reflection of dark matter with light mediators*, [to-appear](#).
- [42] T. Bringmann and M. Pospelov, *Novel direct detection constraints on light dark matter*, *Phys. Rev. Lett.* **122** (2019) 171801 [[1810.10543](#)].
- [43] C.V. Cappiello, K.C.Y. Ng and J.F. Beacom, *Reverse Direct Detection: Cosmic Ray Scattering With Light Dark Matter*, *Phys. Rev. D* **99** (2019) 063004 [[1810.07705](#)].
- [44] Y. Ema, F. Sala and R. Sato, *Light Dark Matter at Neutrino Experiments*, *Phys. Rev. Lett.* **122** (2019) 181802 [[1811.00520](#)].
- [45] J.B. Dent, B. Dutta, J.L. Newstead and I.M. Shoemaker, *Bounds on Cosmic Ray-Boosted Dark Matter in Simplified Models and its Corresponding Neutrino-Floor*, *Phys. Rev. D* **101** (2020) 116007 [[1907.03782](#)].
- [46] J.B. Dent, B. Dutta, J.L. Newstead, I.M. Shoemaker and N.T. Arellano, *Present and future status of light dark matter models from cosmic-ray electron upscattering*, *Phys. Rev. D* **103** (2021) 095015 [[2010.09749](#)].
- [47] E. Fermi, *The ionization loss of energy in gases and in condensed materials*, *Phys. Rev.* **57** (1940) 485.
- [48] S. Weinberg, *Lectures on Quantum Mechanics*, Cambridge University Press, 2 ed. (2015), [10.1017/CBO9781316276105](#).
- [49] W.W.M. Allison and J.H. Cobb, *Relativistic charged particle identification by energy loss*, *Annual Review of Nuclear and Particle Science* **30** (1980) 253 [<https://doi.org/10.1146/annurev.ns.30.120180.001345>].
- [50] S.W. Lovesey, *Theory of neutron scattering from condensed matter*, Clarendon Press, United Kingdom (1984).
- [51] PARTICLE DATA GROUP collaboration, *Review of Particle Physics*, *PTEP* **2022** (2022) 083C01.
- [52] L. Landau, *56 - on the energy loss of fast particles by ionisation*, in *Collected Papers of L.D. Landau*, D. TER HAAR, ed., pp. 417–424, Pergamon (1965), [DOI](#).
- [53] P.V. Vavilov, *Ionization losses of high-energy heavy particles*, *Sov. Phys. JETP* **5** (1957) 749.
- [54] H. Bichsel, *A method to improve tracking and particle identification in TPCs and silicon detectors*, *Nucl. Instrum. Meth. A* **562** (2006) 154.
- [55] TEXONO collaboration, *Constraints on millicharged particles with low threshold germanium detectors at Kuo-Sheng Reactor Neutrino Laboratory*, *Phys. Rev. D* **99** (2019) 032009 [[1808.02719](#)].
- [56] G. Magill, R. Plestid, M. Pospelov and Y.-D. Tsai, *Millicharged particles in neutrino experiments*, *Phys. Rev. Lett.* **122** (2019) 071801 [[1806.03310](#)].
- [57] R. Harnik, Z. Liu and O. Palamara, *Millicharged Particles in Liquid Argon Neutrino Experiments*, *JHEP* **07** (2019) 170 [[1902.03246](#)].
- [58] R. Harnik, R. Plestid, M. Pospelov and H. Ramani, *Millicharged cosmic rays and low recoil detectors*, *Phys. Rev. D* **103** (2021) 075029 [[2010.11190](#)].
- [59] SENSEI collaboration, *Single-electron and single-photon sensitivity with a silicon Skipper CCD*, *Phys. Rev. Lett.* **119** (2017) 131802 [[1706.00028](#)].
- [60] “QEDark.” <https://github.com/tientienyu/QEDark>.
- [61] “QCDark.” <https://github.com/asinalg14/QCDark>.

- [62] A. Bardasis and D. Hone, *Many-body effects in the optical properties of semiconductors*, *Phys. Rev.* **153** (1967) 849.
- [63] M.S. Hybertsen and S.G. Louie, *Ab initio static dielectric matrices from the density-functional approach. i. formulation and application to semiconductors and insulators*, *Phys. Rev. B* **35** (1987) 5585.
- [64] M.K. Kundmann, *Analysis of semiconductor EELS in the low-loss regime*, Ph.D. thesis, University of California Berkeley, 1986.
- [65] J. Lindhard, *On the properties of a gas of charged particles*, *Kgl. Danske Videnskab. Selskab Mat.-fys. Medd.* **28** (1954) .
- [66] M.L. Cohen and S.G. Louie, *Fundamentals of Condensed Matter Physics*, Cambridge University Press (2016).
- [67] W. Kohn and L.J. Sham, *Self-consistent equations including exchange and correlation effects*, *Phys. Rev.* **140** (1965) A1133.
- [68] P. Hohenberg and W. Kohn, *Inhomogeneous electron gas*, *Phys. Rev.* **136** (1964) B864.
- [69] D. Bohm and D. Pines, *A Collective Description of Electron Interactions. I. Magnetic Interactions*, *Physical Review* **82** (1951) 625.
- [70] D. Pines and D. Bohm, *A Collective Description of Electron Interactions: II. Collective vs Individual Particle Aspects of the Interactions*, *Physical Review* **85** (1952) 338.
- [71] D. Bohm and D. Pines, *A Collective Description of Electron Interactions: III. Coulomb Interactions in a Degenerate Electron Gas*, *Physical Review* **92** (1953) 609.
- [72] H. Ehrenreich and M.H. Cohen, *Self-Consistent Field Approach to the Many-Electron Problem*, *Physical Review* **115** (1959) 786.
- [73] Batson, Philip Edward, *Current trends for eels studies in physics*, *Microsc. Microanal. Microstruct.* **2** (1991) 395.
- [74] P. Ewels, T. Sikora, V. Serin, C.P. Ewels and L. Lajaunie, *A complete overhaul of the electron energy-loss spectroscopy and x-ray absorption spectroscopy database: eelsdb.eu*, *Microscopy and Microanalysis* **22** (2016) 717.
- [75] edited by Edward D. Palik, *Handbook of optical constants of solids*, Orlando : Academic Press, 1985. (1985).
- [76] R. Egerton, *Physics of electron scattering*, in *Electron Energy-Loss Spectroscopy in the Electron Microscope*, (Boston, MA), pp. 111–229, Springer US (2011), DOI.
- [77] ARGONEUT collaboration, *Improved Limits on Millicharged Particles Using the ArgoNeuT Experiment at Fermilab*, *Phys. Rev. Lett.* **124** (2020) 131801 [1911.07996].
- [78] R. Plestid, V. Takhistov, Y.-D. Tsai, T. Bringmann, A. Kusenko and M. Pospelov, *New Constraints on Millicharged Particles from Cosmic-ray Production*, *Phys. Rev. D* **102** (2020) 115032 [2002.11732].
- [79] OSCURA collaboration, *Searching for millicharged particles with 1 kg of Skipper-CCDs using the NuMI beam at Fermilab*, [2304.08625](#).
- [80] SENSEI collaboration, *SENSEI: Search for Millicharged Particles produced in the NuMI Beam*, [2305.04964](#).
- [81] G. Fernandez-Moroni, P.A.N. Machado, I. Martinez-Soler, Y.F. Perez-Gonzalez, D. Rodrigues and S. Rosauo-Alcaraz, *The physics potential of a reactor neutrino experiment with Skipper CCDs: Measuring the weak mixing angle*, *JHEP* **03** (2021) 186 [2009.10741].

- [82] G. Fernandez-Moroni, R. Harnik, P.A.N. Machado, I. Martinez-Soler, Y.F. Perez-Gonzalez, D. Rodrigues et al., *The physics potential of a reactor neutrino experiment with Skipper-CCDs: searching for new physics with light mediators*, *JHEP* **02** (2022) 127 [[2108.07310](#)].
- [83] CHANDLER, CONNIE, CONUS, DAYA BAY, JUNO, MTAS, NEOS, NuLAT, PROSPECT, RENO, RICOCHET, ROADSTR NEAR-FIELD WORKING GROUP, SOLID, STEREO, VALENCIA-NANTES TAGS, VIOLETA, WATCHMAN collaboration, *High Energy Physics Opportunities Using Reactor Antineutrinos*, [2203.07214](#).
- [84] K. Ramanathan and N. Kurinsky, *Ionization Yield in Silicon for eV-Scale Electron-Recoil Processes*, *Physical Review D* **102** (2020) 063026.
- [85] I. Smirnov, *Modeling of ionization produced by fast charged particles in gases*, *Nuclear Instruments and Methods in Physics Research Section A: Accelerators, Spectrometers, Detectors and Associated Equipment* **554** (2005) 474.
- [86] C. Giunti and A. Studenikin, *Neutrino electromagnetic properties*, *Phys. Atom. Nucl.* **72** (2009) 2089 [[0812.3646](#)].
- [87] C. Giunti and A. Studenikin, *Neutrino electromagnetic interactions: a window to new physics*, *Rev. Mod. Phys.* **87** (2015) 531 [[1403.6344](#)].
- [88] W. Wang, L. Wu, J.M. Yang, H. Zhou and B. Zhu, *Cosmic ray boosted sub-GeV gravitationally interacting dark matter in direct detection*, *JHEP* **12** (2020) 072 [[1912.09904](#)].
- [89] C. Xia, Y.-H. Xu and Y.-F. Zhou, *Constraining light dark matter upscattered by ultrahigh-energy cosmic rays*, *Nucl. Phys. B* **969** (2021) 115470 [[2009.00353](#)].
- [90] G. Guo, Y.-L.S. Tsai, M.-R. Wu and Q. Yuan, *Elastic and Inelastic Scattering of Cosmic-Rays on Sub-GeV Dark Matter*, *Phys. Rev. D* **102** (2020) 103004 [[2008.12137](#)].
- [91] Z.-L. Liang, C. Mo and P. Zhang, *In-medium screening effects for the Galactic halo and solar-reflected dark matter detection in semiconductor targets*, *Phys. Rev. D* **104** (2021) 096001 [[2107.01209](#)].
- [92] D. McKeen, M. Moore, D.E. Morrissey, M. Pospelov and H. Ramani, *Accelerating Earth-bound dark matter*, *Phys. Rev. D* **106** (2022) 035011 [[2202.08840](#)].
- [93] Z.-L. Liang, L. Su, L. Wu and B. Zhu, *Plasmon-enhanced Direct Detection of sub-MeV Dark Matter*, [2401.11971](#).
- [94] SENSEI collaboration, *SENSEI: First Direct-Detection Results on sub-GeV Dark Matter from SENSEI at SNOLAB*, [2312.13342](#).



PREPARED FOR SUBMISSION TO JINST

AI4EIC 2023 ANNUAL WORKSHOP  
CATHOLIC UNIVERSITY OF AMERICA, WASHINGTON D.C.

## Performance optimization for a scintillating glass electromagnetic calorimeter at the EIC

---

**J. Crafts<sup>b</sup> R. Fatemi<sup>a</sup> T. Horn<sup>b</sup> D. Kalinkin,<sup>a,1</sup>**

<sup>a</sup>*Department of Physics & Astronomy, University of Kentucky,  
177 Chem.-Phys. Building, 506 Library Drive, Lexington, 40506-0055, KY, USA*

<sup>b</sup>*Physics Department, American Christian University,  
620 Michigan Ave., N.E. Washington, 20064, DC, USA*

*E-mail:* [dkalinkin@uky.edu](mailto:dkalinkin@uky.edu)

**ABSTRACT:** The successful realization of the EIC scientific program requires the design and construction of high-performance particle detectors. Recent developments in the field of scientific computing and increased availability of high performance computing resources have made it possible to perform optimization of multi-parameter designs, even when the latter require longer computational times (for example simulations of particle interactions with matter). Procedures involving machine-assisted techniques used to inform the design decision have seen a considerable growth in popularity among the EIC detector community. Having already been realized for tracking and RICH PID detectors, it has a potential application in calorimetry designs. A SciGlass barrel calorimeter originally designed for EIC Detector-1 has a semi-projective geometry that allows for non-trivial performance gains, but also poses special challenges in the way of effective exploration of the design space while satisfying the available space and the cell dimension constraints together with the full detector acceptance requirement. This talk will cover specific approaches taken to perform this detector design optimization.

**KEYWORDS:** Analysis and statistical methods, Calorimeters, Particle detectors, Performance of High Energy Physics Detectors

---

<sup>1</sup>Corresponding author.

---

## Contents

<b>1</b>	<b>Introduction</b>	<b>1</b>
<b>2</b>	<b>Problem definition</b>	<b>1</b>
<b>3</b>	<b>Multi-objective Optimization using Genetic Algorithms</b>	<b>3</b>
<b>4</b>	<b>Constraints and dimensional reduction</b>	<b>3</b>
<b>5</b>	<b>Multi-objective Optimization using Bayesian Optimization</b>	<b>4</b>
<b>6</b>	<b>Software stack</b>	<b>6</b>
<b>7</b>	<b>Results</b>	<b>6</b>
<b>8</b>	<b>Conclusion</b>	<b>7</b>

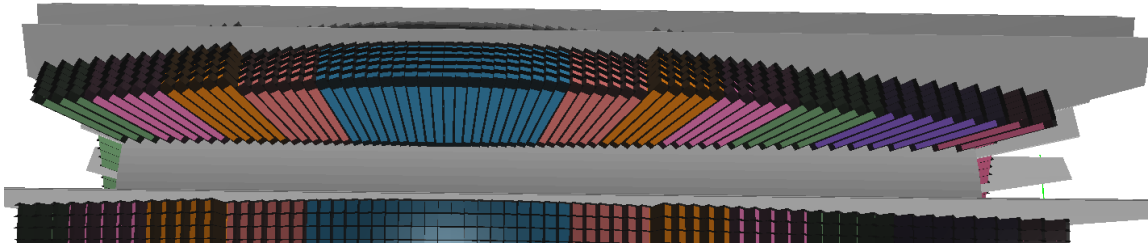
---

## 1 Introduction

The Electron-Ion Collider (EIC), a new accelerator facility that will be built in the next decade, provides the novel opportunity to utilize Machine Learning algorithms directly in the accelerator, detector and data acquisition design. Previous efforts at optimizing particle detector designs for EIC included a dual radiator RICH detector [1] and a tracker subsystem [2], both were aimed for the “Detector-I” concept. Generally a design optimization problem is a Multi-Objective Optimization (MOO) problem with metrics which are practically non-differentiable. Such problems were successfully addressed in simpler cases using Genetic Algorithms, and there were recent developments in advanced methods for Bayesian Optimization (e.g., [5]) showing promise for scaling to more complex tasks. The following paper summarizes findings in evaluation of the existing approaches for optimization of electromagnetic calorimeter detector to be used for EIC.

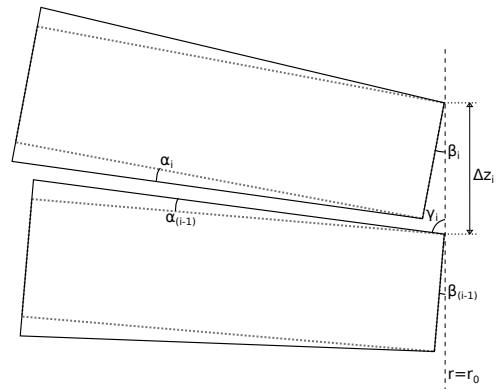
A projective homogeneous calorimeter with SciGlass radiator is envisioned for Detector-II at the EIC. This device will be used to measure the energy of electrons scattered at mid-rapidity (corresponding to interactions with high momentum transfer in deep-inelastic electron-proton scattering (DIS)). In this work, we attempt to solve the practical task of optimizing the geometrical shape of such a calorimeter. The reference design for this calorimeter is shown on (fig. 1).

## 2 Problem definition



**Figure 1:** Top-down view of one of the 12 sectors of the SciGlass projective geometry for Detector-II at EIC, with the sector in front of it removed for visibility. Seven different cell colors mark seven assumed shapes. Black denotes carbon fiber supports, and grey represent wall of the wedge box surrounding each sector.

The optimization procedure starts with defining a set of design parameters to be optimized and numerical objectives to quantify the detector performance. The focus of this work was on optimizing tower projectivity. To that end, the shapes of the towers were allowed to vary. The assumption was made that up to seven independent tower shapes can be manufactured, those are referred to as “families”. The difference in shape was encoded in terms of flaring angles for each trapezoid that corresponded to the angle between opposite faces of a cell. When looking at the cells from the middle towards the detector ends that flaring angle would accumulate towards the polar angle of each cell’s incline (fig. 2), since the adjacent sides of adjacent cells were coplanar with a 1 mm gap distance. An assumption was made that the towers from the same family would be stacked together, and families would go in the same order. That allowed to encode placements of the towers in an integer vector with 12 values: 7 for positive direction and 5 for the negative. Altogether, families flaring angles and numbers of towers used per family fit in a vector of 19 values.



**Figure 2:** Side-view schematic of longitudinal tower stacking with flaring angles  $\{\alpha_i\}$ .

The barrel SciGlass calorimeter subsystem serves several purposes: the measurement of electron and photon energy with excellent resolution, which is especially important for constraining kinematics of the scattered electron. It also needs to be able to help identify the scattered electron from the background of negatively charged hadrons, such as  $\pi^-$  that will be also present in DIS events. This is largely relying on shower profiling and discrimination based on the ratio of the deposited energy ( $E_{\text{dep}}$ ), as reconstructed from a  $3 \times 3$  tower cluster, and the momentum ( $p_{\text{trk}}$ ) of the particle as determined by an external tracking detector. In this work the true momentum of the particle ( $p_{\text{thrown}}$ ) will be used since a realistic tracking detector has not been included in this study. Initial evaluations of pion rejection had showed that this design could use a slight improvement for particles at lower values of  $p_T$  at which probabilities to encounter a pion are higher. Thus the focus of this work was on attempt at improving this quantity. Another responsibility of the subsystem is discrimination between  $\gamma$  from DVCS and  $\pi^0 \rightarrow \gamma\gamma$  signal from DVMP, which at high energies

relies on computationally expensive ML training, and is less optimal for including in an initial round of optimization.

### 3 Multi-objective Optimization using Genetic Algorithms

A direct approach using NSGA-II [3] implemented in pymoo [4] framework was applied to the present problem. The algorithm displayed decent performance for 1, 2 and 3 -objective problems when using default settings and population size of 100. One problem-specific consideration had to be made for the fact that implicit constraints placed by inherent possibility of overlaps occurring in the geometry, which prevent objective functions to be evaluated. The [4] framework does not allow for the user code to report such missing values, so instead values of 0 were reported when overlaps were detected, and non-overlapping minimized values were adjusted to always be negative.

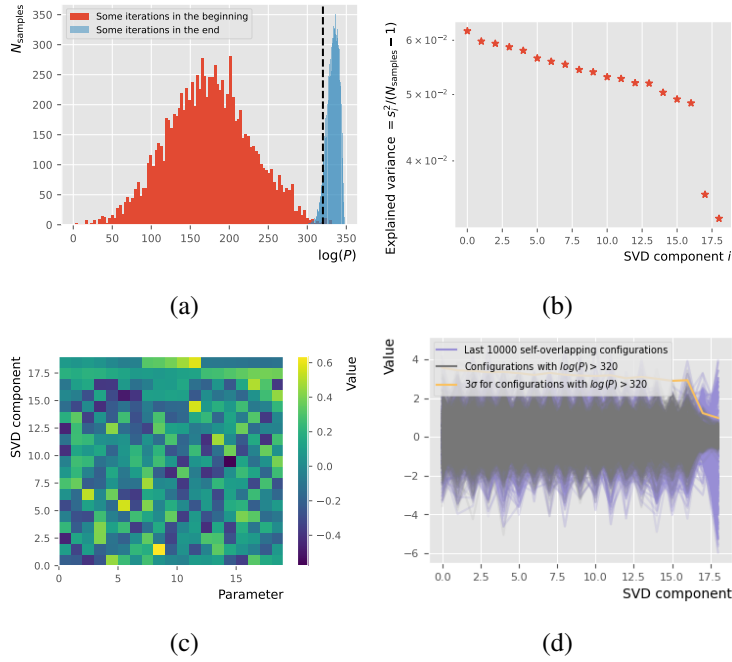
### 4 Constraints and dimensional reduction

The handling of constraints is particularly challenging for this problem. The cells of the calorimeter have to fit within the allocated volume, yet have a maximal possible acceptance within that limit. The resulting constraint on the parameters is non-linear due to complicated trigonometric relations arising for the angular parameters.

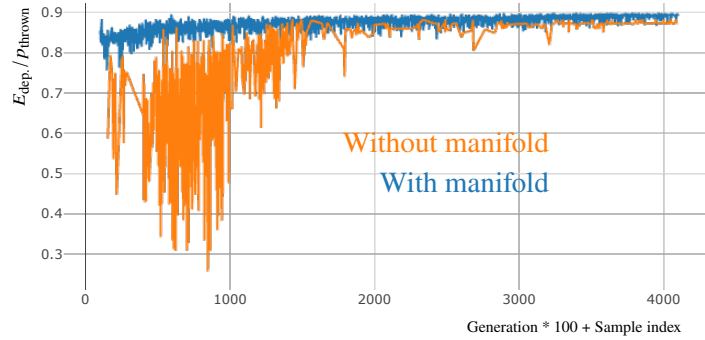
Another observation is that the time needed to evaluate the geometry for overlaps (via TGeo) is  $O(1 \text{ second})$ , much smaller than the time needed to evaluate the geometry for its performance which is at least  $O(1 \text{ minute})$ . One could ask then if it would be possible to pre-compute the manifold of parameters that correspond to valid geometries. The approach taken in this work is to use Markov Chain Monte Carlo (MCMC) walkers to explore the design space and approximately identify a subspace of valid geometries that occupy maximal acceptance within the detector envelope. The latter requirement is needed as we are not interested in valid geometries that don't use sufficient amount of towers. A value of the distance between the  $z$ -coordinates between the backward-most and forward-most towers is used as a proxy for acceptance that is easy to compute for a given geometry. In the end, the following probability distribution was given to the MCMC:

$$\log(P) = \begin{cases} -\infty, & \text{if parameter set doesn't pass the overlap check} \\ (z_{\text{rightmost tower}} - z_{\text{leftmost tower}})/(1 \text{ cm}), & \text{otherwise} \end{cases} \quad (4.1)$$

The MCMC was run until it converged to a concrete population effectively sampling a region of high  $\log(P)$ , as seen on fig. 3a. This population was then used to perform dimensional reduction. Generally, that would be achieved using a manifold learning method, but in this case, a simple Principal Component Analysis was applied. The main outcome was that two dimensions were highly constrained, as seen on fig. 3b. The eigenvectors corresponding to those directions, as seen on fig. 3c, had comparable components for variations in parameters of the same type. The PCA defines a transformation to a new parameter set. The limits for transformed parameters are not well-defined anymore, so instead a  $3\sigma$  variation across populations was used. Figure 3d shows how variations are different between initial population and converged population after MCMC. It makes sense that there were two components reduced, as when detector geometry is defined by stacking from the center in the  $\pm\hat{z}$  directions, there are two detector envelope boundaries to hit.



**Figure 3:** Results from MCMC, including analysis using PCA.



**Figure 4:** Values of energy deposition fraction at a given sample and generation for two-objective optimization using NSGA-II for raw parameterization vs parameterization in transformed coordinates.

The effect of dimensional reduction was evaluated for 2-objective MOO using NSGA-II implementation described in section 3. In comparison to optimization without dimensional reduction the convergence was achieved much faster with a slightly better outcome for the  $E_{\text{dep.}}/p_{\text{thrown}}$  objective as illustrated in fig. 4.

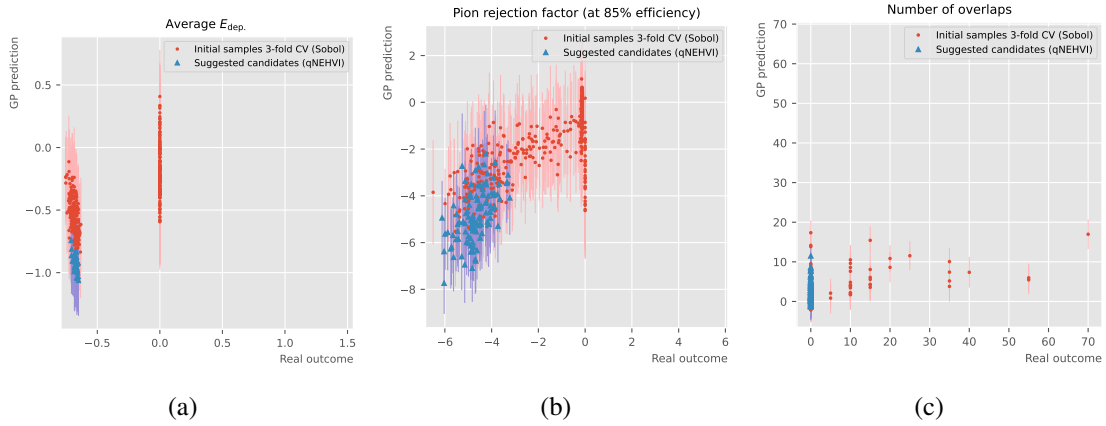
## 5 Multi-objective Optimization using Bayesian Optimization

Bayesian Optimization (BO) is another popular approach for doing MOO. It has the benefit of reducing a number of expensive objective evaluations compared to Genetic Algorithms by reducing

exploration and increasing exploitation. This approach however generally requires extra fine tuning to make it work.

The implementation of BO in the `Ax` framework with SAASBO [5] surrogate model in the qNEHVI [6] acquisition function was used in this study. The surrogate model was initialized by fitting it to evaluated designs with parameters from a Sobol quasi-random sequence of length 1000. That was followed by several hundred of BO iterations for which  $q = 3$  samples were evaluated at a time and the surrogate model was refitted at each iteration. Unlike for NSGA-II the computational overhead of the optimization algorithms was not negligible compared to the cost of evaluating the objective functions. Instead, it was a dominant cost in the time budget of the whole procedure.

The same overlap consideration from section 3 applies to implementation in `Ax`. However, in this case the missing values must also be ignored when determining a surrogate model fit model. The solution of returning a value of 0 with a large uncertainty appears to work sufficiently well for this purpose.



**Figure 5:** Cross-validation for Gaussian Process surrogate models. Red dots mark 3-fold cross validation of the Sobol-generated sample within the fit and blue triangles mark predicted and actual values for the points suggested by qNEHVI.

Another important consideration for BO lies within the surrogate model’s ability to adequately model the unknown objective function. To ensure that, a 3-fold cross validation has been performed for each of the objectives (shown on fig. 5) on points from a Sobol-generated sample. The cross validation shows decent correlation, especially for pion rejection factor<sup>1</sup>. Furthermore, correlation of predicted versus actual objective value can be visualized by the points suggested by qNEHVI. Those points, by construction, lie lower than typical predictions for the Sobol model, but they also often give lower actual outcomes, which indicates that qNEHVI with the given surrogate model is capable at picking improving points.

An attempt has been made at utilizing the OutcomeConstraint facility in `Ax` in hope of reducing chances of picking the invalid combinations of the parameters by requiring number of overlaps to be  $\leq 0$ . The way such constraint is handled in `Ax` is that it receives a surrogate model

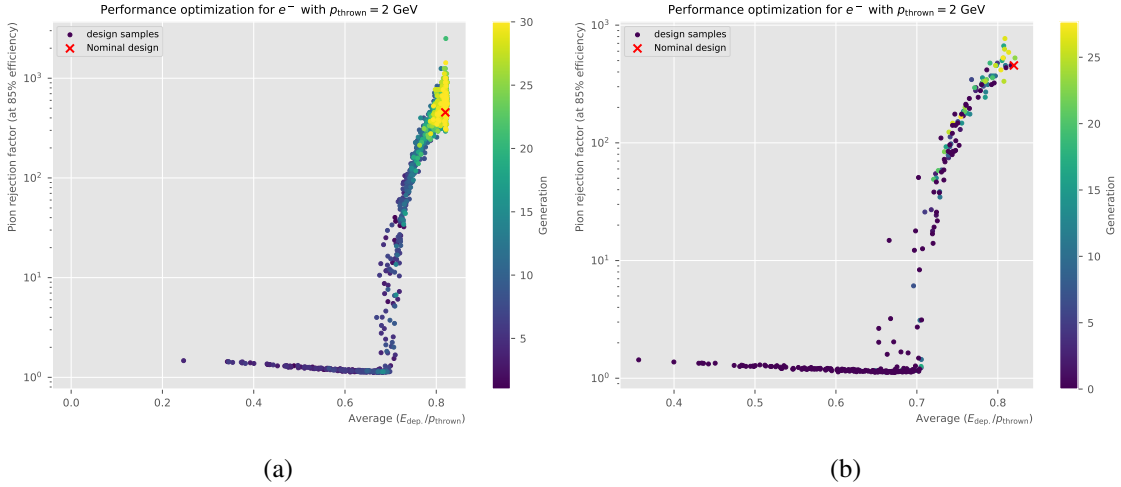
<sup>1</sup>In fact, the performance in cross validation can be improved slightly by tweaking the GP kernel. Unfortunately that one is hard-coded in the default implementation of the “FULLYBAYESIANMOO” model in the version of `Ax` available at the time of this writing.

of its own, however, as seen on fig. 5c, the cross validation for that is not satisfactory. In practice, running optimization without this constraint, like for GA, worked sufficiently well.

## 6 Software stack

As was explained earlier, `pymoo` and `Ax` frameworks were used for optimization. The detector geometry description was implemented for SciGlass calorimeter within `DD4hep` framework [7] in which the evaluation of different designs was achieved by automatically producing alternative “compact” XML file configurations with updated numerical parameters. The job scheduling was performed using `Dask.Distributed` cluster with workers running using a `Slurm` batch system. The development of the software was facilitated by caching evaluations using `joblib.Memory` memoization that performed well when accessing a common cache situated on network storage despite concurrent access from multiple nodes. The results of individual experiments were tracked using `MLflow`. The simulation output produced by `DD4hep`’s interface to the `Geant4` (`ddsims`) was analyzed using implementation of objective functions using `Awkward Array` [8] in-memory data representation loaded using `uiproot5` [9].

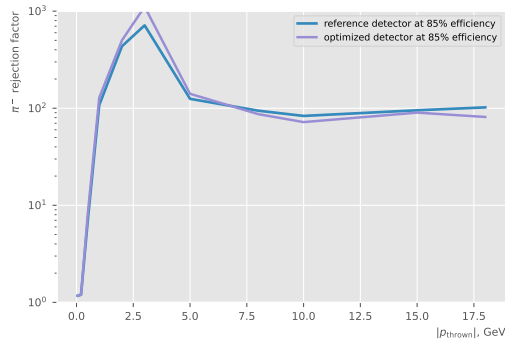
## 7 Results



**Figure 6:** Objective points from 40 iterations of NSGA-II (a) and Sobol and Bayesian Optimization (b). The red cross indicates the reference objective point corresponding to a detector configuration using hand-picked flaring angles and per-family tower counts.

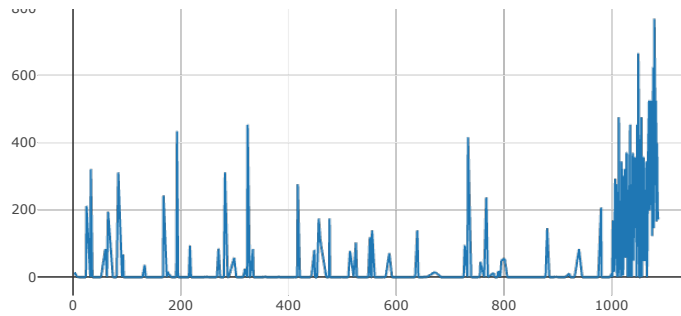
Optimization using both Genetic Algorithms (GA) and Bayesian Optimization (BO) approaches were performed for the SciGlass detector targeting two objectives:  $E_{\text{dep.}}/p_{\text{thrown}}$  (proxy for the detector acceptance and, partially, for the energy resolution) for 2 GeV electrons.

The result for GA is shown on fig. 6a. The narrow shape of the correlation suggests, in hindsight, that the optimization was close to being de-facto single-objective. The optimized detector was able to outperform the reference one in terms of pion rejection factor by a half of an order in magnitude. Full



**Figure 7:** Dependencies of pion rejection factors on thrown charged particle transverse momentum for the best NSGA-II result.

evaluation using a benchmarking software from Detector-I technology review [10] showed (fig. 7) how the optimal configuration trades diminished pion rejection at high transverse momentum for increase at low transverse momentum. This is a desirable trade as pion contamination is lesser for electron candidates with a high momentum.



**Figure 8:** Pion rejection as a function of iteration. Where first 1000 entries are the Sobol quasi-random sequence and what follows are the actual Bayesian Optimization iterations.

The result for BO shown on fig. 6b closely resembles the one obtained from the GA method, however shows that a potentially larger runtime, and, possibly, also additional setup, would be required to achieve benchmark performance of the GA method. Figure 8 shows real-time performance of the BO method, which picks up some local optimum after about  $\approx 100$  evaluations (corresponding to the iterations  $\approx 1100$  and further on the plot).

## 8 Conclusion

This work demonstrates an example of optimization of a real world projective calorimeter design for the future EIC Facility . The SciGlass detector has a potential application as a prominent design mid-rapidity electron measurement device in future Detector-II, and, as was demonstrated, can be further bettered using ML optimization techniques. The described suggested method for handling of implicit parameter constraints should be applicable for a wider range of problems, including to the problem of integrating dimensions of subsystems in full detector optimization tasks.



## Acknowledgments

We would thank the University of Kentucky Center for Computational Sciences and Information Technology Services Research Computing for their support and use of the Lipscomb Compute Cluster and associated research computing resources.

## References

- [1] E. Cisbani, A. Del Dotto, C. Fanelli, et al., *AI-optimized detector design for the future Electron-Ion Collider: the dual-radiator RICH case*, *JINST* **15** (2020) P05009.
- [2] C. Fanelli, Z. Papandreou, K. Suresh, et al., *AI-assisted optimization of the ECCE tracking system at the Electron Ion Collider*, *NIM A* **1047** (2023) 167748.
- [3] K. Deb, A. Pratap, S. Agarwal and T. Meyarivan, *A fast and elitist multiobjective genetic algorithm: NSGA-II*, *IEEE Transactions on Evolutionary Computation* **6** (2002) 2, pg. 182-197.
- [4] J. Blank and K. Deb, *pymoo: Multi-Objective Optimization in Python*, *IEEE Access* **8** (2020) pg. 89497-89509.
- [5] D. Eriksson, M. Jankowiak., *High-Dimensional Bayesian Optimization with Sparse Axis-Aligned Subspaces*, *Proceedings of the Thirty-Seventh Conference on Uncertainty in Artificial Intelligence* (2021).
- [6] S. Daulton, M. Balandat, E. Bakshy, *Parallel Bayesian Optimization of Multiple Noisy Objectives with Expected Hypervolume Improvement*, [arxiv:2105.08195](https://arxiv.org/abs/2105.08195).
- [7] Frank, M., Gaede, F., Petric, M., Sailer, A., *AIDAsoft/DD4hep*, *Zenodo* (2023) .
- [8] Pivarski, J., et al., *Awkward Array*, *Zenodo* (2024) [10.5281/zenodo.10498548](https://zenodo.org/record/10498548).
- [9] Pivarski, J., et al., *Uproot*, *Zenodo* (2024) [10.5281/zenodo.10573980](https://zenodo.org/record/10573980).
- [10] D. Kalinkin for the ePIC collaboration, *SciGlass: Performance Studies*, <https://indico.bnl.gov/event/18517/contributions/73620/> (2023).

# Considerations on the time resolution of single pixel irradiated 3D devices up to $10^{17}$ $n_{eq}/cm^2$ at 120 GeV SPS pion beams

Evangelos-Leonidas Gkougkousis<sup>(a)</sup>, Edgar Lemos Cid<sup>(b)</sup>, Viktor Coco<sup>(b)</sup>

<sup>(a)</sup> University of Zurich

<sup>(b)</sup> European Organization for Nuclear Research (CERN), Geneva, Switzerland

<sup>(c)</sup> Vienna University of Technology, Vienna, Austria

## Abstract

The proven radiation hardness of silicon 3D devices up to fluences of  $1 \times 10^{17}$   $n_{eq}/cm^2$  makes them an excellent choice for next generation trackers, providing  $< 10$   $\mu m$  position resolution at a high multiplicity environment. The anticipated pile-up increase at HL-LHC conditions and beyond, requires the addition of  $< 50$  ps per hit timing information to successfully resolve displaced and primary vertices. In this study, the timing performance, uniformity and efficiency of neutron and proton irradiated single pixel 3D devices is discussed. Fluences up to  $1 \times 10^{17}$   $n_{eq}/cm^2$  in three different geometrical implementations are evaluated using 120 GeV SPS pion beams. A MIMOSA-26 type telescope is used to provide detailed tracking information with a  $\sim 5$   $\mu m$  position resolution. Productions with single- and double-sided processes, yielding active thicknesses of 130 and 230  $\mu m$  respectively, are examined with varied pixel sizes from  $55 \times 55$   $\mu m^2$  to  $25 \times 100$   $\mu m^2$  and a comparative study of field uniformity is presented with respect to electrode geometry. The question of electronics bandwidth is extensively addressed with respect to achievable time resolution, efficiency and collected charge, forming a 3D phase space to which an appropriate operating point can be selected depending on the application requirements.

**Keywords:** 3D sensors; Radiation Hardness; Silicon Detectors; Bandwidth; Test Beam; Fast Timing; Readout Electronics

## 1. Introduction

Over the past decade, 3D pixel sensors have emerged as tracking devices in high-energy physics experiments, within environments of intense radiation fluxes, encountered in the  $|\eta| < 2$  regions of ATLAS Insertable B-Layer [1] and ATLAS Forward Proton (AFP) detector [2]. The sensor design, decoupling charge-generating volume from the drift distance, accommodates shorter electrode spacing, consequently decreasing the charge carrier trapping probability. Recent studies using the Transient Current Technique (TCT) [3, 4], have further substantiated the exceptional timing performance of such devices. For vertically incident events, the orthogonal relationship between drift direction and particle trajectory results in an absence of Landau fluctuations, key factor in extending theoretical timing performance of such devices, primarily constrained only by the signal's drift time.

This excellent performance is nevertheless impacted by field non-uniformities, intrinsic to the column geometry of the collection electrodes. The resulting radially expanding field within the pixel volume increases signal time-jitter, degrading

time resolution. Such a geometry, though detrimental under normal operation, can lead to high field densities near the collection electrode ( $> 30$  V/ $\mu m$ ) at higher bias voltages ( $> 500$  V) typically used after irradiation. In this operating mode, impact ionization and charge multiplication occur near the collection electrode in a similar way as in Multi-Wire Proportional Chambers (MWPCs) and can compensate for trapping induced charge collection efficiency issues.

In this study, three different geometries are examined after proton and neutron irradiation, using 120 GeV SPS pion beams [5]. Pixel sizes of  $55 \times 55$   $\mu m^2$  [6],  $25 \times 100$   $\mu m^2$  and  $50 \times 50$   $\mu m^2$  [7] in substrates of 230  $\mu m$  (190  $\mu m$  active depth) for the first geometry and 150  $\mu m$  (130  $\mu m$  active depth) for the second and third, are tested to establish the minimum active thickness and pixel size still yielding sufficient charge and low enough jitter to achieve a 30 ps time resolution. Questions of signal integrity, bandwidth and efficiency are treated.

## 2. Timing and Signal Integrity

Studies under a  $^{90}Sr$  source of the  $50 \times 50$   $\mu m$  variety single pixel structure (Figure 1 top), yield collected charge of  $1.73 \pm 0.02$  fq (10,830  $e^-$ ), in agreement with the theoretically predicted value of  $\sim 82$   $e/\mu m$  for a MIP in fully depleted Si [8] at a bias voltage of 20 V at  $-20$   $^\circ C$ . Signals are characterized by a fast rise time (10 % - 90 %) of  $175 \pm 4$  ps, but present a tail at the slower end, characteristic of field non-uniformities. Although charge per micrometer in the 3D device is reduced by a factor of 60 with respect to a typical LGAD<sup>1</sup> ( $34.3 \pm 0.4$  fq for 50  $\mu m$  thick HPK<sup>2</sup> device), an almost factor of 6 gain in rise time is noted ( $980 \pm 1.4$  ps for LGADs - Figure 1 bottom).

Analog time resolution of the LGAD-3D system can be approximated as the sum of a Landau fluctuations term, field related distortion effects and the noise-induced jitter [9]. Through a Constant Fraction Discriminator (CFD) time walk correction approach, a 2D time resolution map is established with respect to the CFD of each of the components (Figure 2). For LGADs, selecting higher CFDs to profit from increased

---

<sup>1</sup> Low Gain Avalanche Diode.

<sup>2</sup> Hamamatsu Photonics LTd.

signal to noise ratio incurs a penalty in slew rate, deteriorating time resolution, thus resulting in the characteristic S curve along the x-axis. The plateau at  $\sim 40\%$  of peak amplitude corresponds to a time when all primary charges have reached the gain layer. In the case of 3Ds, due to the decoupling of drift and charge generation volumes and reduced electrode distances, the slew rate remains practically constant. Absence of gain under normal operation can be partially addressed by selecting higher CFDs, without degradation on time resolution.

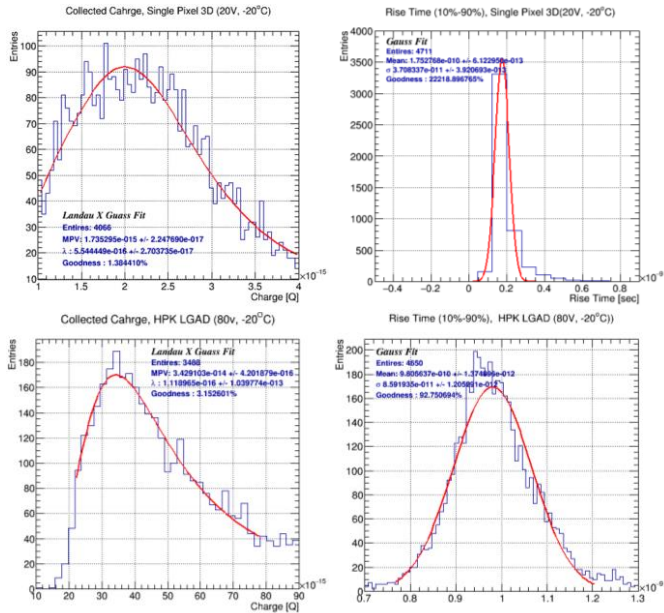


Fig. 1. Charge and rise time distributions of a  $150\ \mu\text{m}$ ,  $50 \times 50\ \mu\text{m}^2$  pitch, 3D single pixel device (top) and a  $50\ \mu\text{m}$  thick LGAD (bottom).

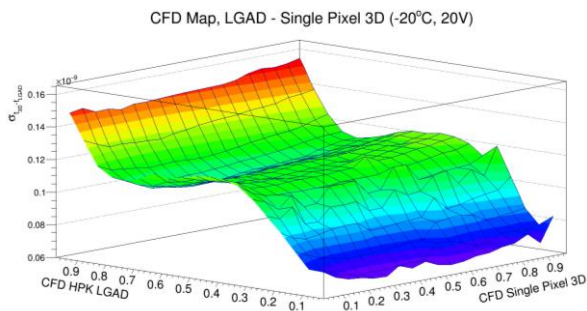


Fig. 2. Time resolution map of an LGAD - 3D ( $50 \times 50\ \mu\text{m}^2$  single pixel) system with respect to CFD thresholds. Constant slew-rate and absence of Landau fluctuations in the 3D case result in a flat dependence.

To mitigate statistical biases and efficiency issues at the dynamic range limit, a high bandwidth readout system ( $> 3\ \text{GHz}$ ) is crucial. Such effects can be studied by leveraging the Poissonian distribution of radioactive decays. Using a two-object coincidence system, a DUT bias scan is performed requesting identical number of events at each step. The reference device (LGAD) is set to a known bias, yielding 100% efficiency. An event frequency distribution is constructed at each step exploiting timestamp differences of

consecutive events. The per bias rate is determined through Bayesian inference of a Poisson fit, using the Gamma function as a conjugate prior [10]. The maximum achievable rate corresponds to the full efficiency point, assuming fixed source activity and geometrical acceptance. Relative efficiencies can subsequently be attributed for each bias, by comparing each point's corresponding rate with the one at the 100% efficiency point.

Figure 3 displays the relative efficiencies for varying bandwidth limits and analog-to-digital (ADC) scaling as a function of bias voltage. A typical S-curve is observed in the 2 GHz - 10 mV series, achieving 100% efficiency at  $\sim -36\ \text{V}$ . When the analog scaling is doubled, without other system changes, there's a noticeable efficiency improvement, peaking at  $\sim -30\ \text{V}$ . However, this configuration results in a 20% reduction in the per point event rate, compared to the 10-mV scenario. The requirement of a minimum 3 ADC bin threshold in the Time-over-Threshold (ToT) for the trigger circuit to latch, alters the signal distribution by eliminating its faster component when scaling is increased. The charge and amplitude to ToT proportionality of the used transimpedance amplifier, biases the charge distribution towards higher values, even though the actual trigger threshold remains the same.

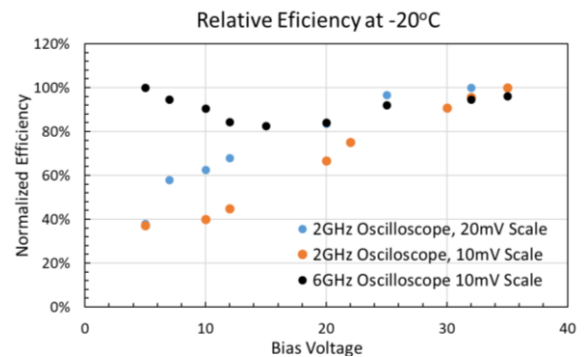


Fig. 3. Relative efficiency vs bias voltage for several ADC scaling values and bandwidth limits.

Increasing the ADC bandwidth from 2 to 6 GHz, while maintaining amplifier cut-off at 3 GHz, results to 100% relative efficiency at the lowest bias, but decreases as voltage rises. Using a square windowing function, the frequency of the highest harmonic is extracted from the Fast Fourier Transform (FFT) of the signal part of each waveform for biases of -5, -20, and -35 V (Figure 4). Bias noticeably affects signal composition, with the faster component dominating at higher fields. With decreasing bias, the signal fraction around 0.4 GHz increased from 20% to 80%. The convolution of a bandwidth cut, evolving signal population and normal efficiency S-curve expected as fields increase, account for the observed shape of the 6 GHz series in Figure 3. At lower biases, most signals fall below the bandwidth cut and are recorded. However, as the field intensifies, efficiency should increase, but part of the signal exceeds the bandwidth limit,

reducing event rate. At the highest bias, 80 % of the signal exceeds the frequency cut-off, yet the increased efficiency compensates, recovering the rate of the slower component to levels observed at lower fields.

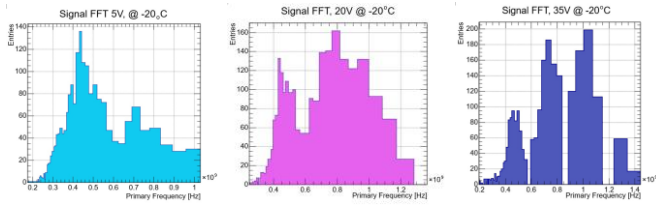


Fig. 4. Distributions of the frequency corresponding to the highest power harmonic for bias voltage of  $-5\text{ V}$ ,  $-20\text{ V}$  and  $-35\text{ V}$  at a 4000 events sample. A composition change is observed with respect to bias.

### 3. SPS pion Test beams

Properly addressing previously detailed issues and studying field non-uniformities require precise position resolution ( $\sim 5\ \mu\text{m}$ ) combined with high statistics and high bandwidth electronics. To that end, an intensive 16-week long test beam campaign using 120 GeV pions was undertaken at CERN SPS. A timing telescope consisting of 6 DUTs and 2 Reference planes in coincidence was placed within a temperature controlled XPS cold box. Plane alignment is achieved through micrometric piezo-electric actuators, while the entire system is positioned between the forward and backward arm of a EUDET-based MIMOSA-26 [11] telescope. An FE-I4 planar module, attached to the back end of cold box, is used as an ROI trigger and alignment plane (Figure 5).

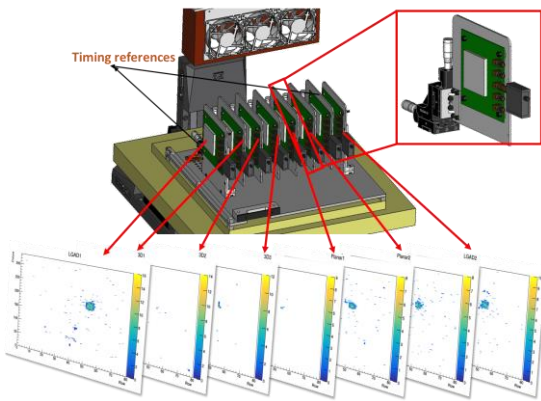


Fig. 5. CAD representation of the cold box with the DUT and timing reference planes. Occupancy distributions are used for plane alignment.

System read-out is achieved through 2 synchronized 6 GHz oscilloscopes [12], while a fast SiGe-based first stage transimpedance amplifier [13] in conjunction with a 6 GHz second stage voltage amplifier (ZX-60V3 [14]) is attached to each plane. Data, generated in two streams (tracking, timing) are synchronized using the SPS master clock in conjunction with a trigger VETO, while readout is performed during the synchrotron acceleration cycles to eliminate dead time. A timing diagram of the architecture can be seen in Figure 6.

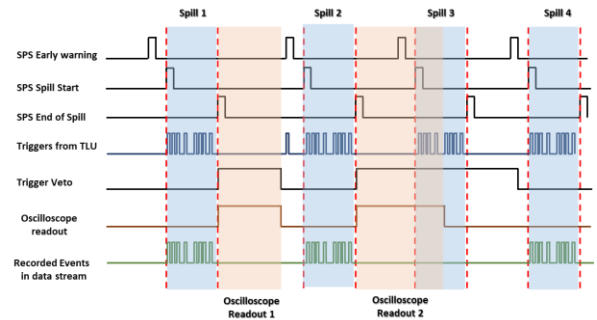


Fig. 6. Timing diagram of the trigger, readout and synchronisation system with respect to the VETO and SPS master clock signals.

Individual event waveforms are analyzed using a multi-factor weighted approach to address increased noise, inherent to the high bandwidth and capacitance of the DUTs. A low pass filter, comprised of a rectangular transfer function followed by a Gaussian decrease, with a  $\sigma$  of 0.5 GHz and the  $-10\text{ dB}$  point centered at 2.4 GHz, is applied at the analysis stage to improve SNR and allow for signal smoothing (Figure 7, 8). Although for the reference sensor (LGAD) such an operation dramatically improves signal quality and lowers noise (Figure 7), for the 3D structure, it results in a 60 % degradation of amplitude and 20 % increase of calculated collected charge, without any advantages on SNR. The lower capacitance of the DUT (20 – 80 fF depending on geometry) compared to that of the reference (2 pF for  $1\text{ x }1\text{ mm}^2$  LGADs) eliminates any potential gain from such an approach. In contrast, any low pass filtering will bias the signal statistics towards the high charge region, both due to the distorted signal shape and lower signal amplitudes, resulting to an enhanced rejection of the low amplitude tails, thus pushing the MPV of the Landau to a seemingly higher value.

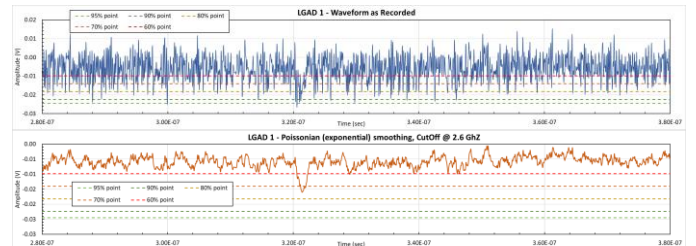


Fig. 7. As recorded and after a 2.4 GHz low-pass Gaussian filter LGAD signal. Dotted lines indicate percentages of the original signal amplitude.

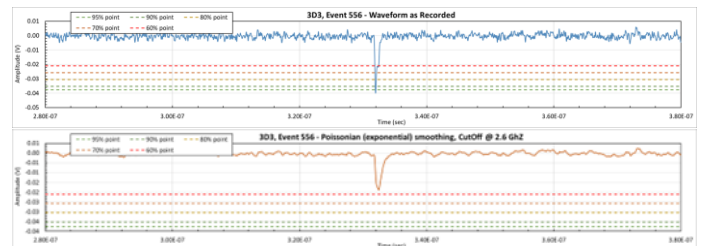


Fig. 8. As recorded and after a 2.4 GHz Gaussian filter 3D signal. Dotted lines indicate percentages of the original signal amplitude.



Using a Keizer window, the Fourier transform of the signal region of the Figure 7 & 9 event waveform is computed for the 3D and the LGAD sensors (Figure 9). While the unsmoothed 3D signal expands up to 5 GHz, the first harmonic of the LGAD signal debuts at 0.6 GHz. Applying the Gaussian low-pass filter with the 2.4 GHz cut-off frequency on the 3D signal, significantly reduces the higher frequency side of the spectrum. An appropriate readout electronics in this case would need to at least have a bandwidth of 5 GHz, whereas such an approach for an LGAD would be detrimental due to the higher induced noise without any gain on the signal side.

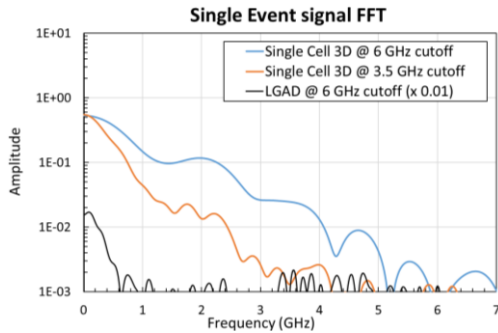


Fig. 9. Power Spectrum of an LGAD, 3D and Gaussian filtered 3D signal. A 40 % power loss is observed for the smoothed 3D signal.

#### 4. Fast front-end electronics

To adequately record high bandwidth signals, a discrete 16-channel read-out board based on a two-stage amplifier approach was designed (Figure 10). A two-stage single SiGe transistor amplifier geometry, with first stage configured as a transimpedance and the second as a voltage amplifier, was used. Provisions for individual channel shielding to further reduce noise are implemented, while a high frequency Rogers 3035 laminate is used in a five-layer PCB design with the signal plane encapsulated within isolated ground layers. Sensor bias is provided via a triaxial LEMO connector while keyed 8-fold coaxial high bandwidth mini-mcx connector arrays are placed unilaterally to the PCB.



Fig. 10. Prototype of the high bandwidth versatile multi-channel PCB.

The DUT is placed on a passive 300  $\mu\text{m}$  thick mezzanine board, populated with 18 coaxial mini-mcx connectors, to facilitate alignment and exchangeability. Peripheral components were optimized to ensure moderate gain fluctuation with frequency (Figure 11) through AWR simulations up to the 10 GHz limit. A mean noise ( $\sim$ RMS) of 1.2 mV for a gain of  $\sim$ 70 was achieved for the first iteration of

the board, with an observed undershoot due to mismatch in lower frequencies.

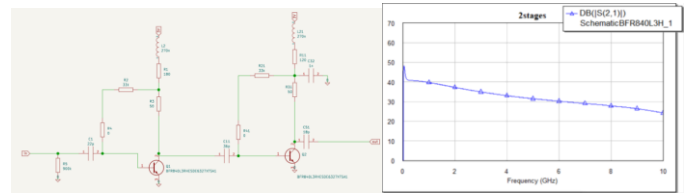


Fig. 11. Schematics of the circuit (left) and simulations (right) for up to 10 GHz of the amplification circuit of the two stage SiGe implementation.

#### 5. Conclusion

In this paper, the bandwidth dependent charge and time resolution of high-speed 3D signals was discussed. Signals extend up to a limit of 5 GHz and adapted read-out electronics are necessary for an unbiased charge and noise measurement. Through an SPS-Pion test beam, time resolution studies are performed using a high bandwidth system, synchronized to the accelerator clock. The issue of higher induced noise in the larger capacitance LGAD device used as time reference is treated through a Gaussian low pass filter. Finally, a dedicated discrete electronics readout-out board with a  $\sim$ 10 GHz bandwidth limit was designed where DUTs are placed on a detachable mezzanine to enable rapid exchange and testing.

#### References

- [1] B. Mandelli, *The Pixel Detector of the ATLAS Experiment for the Run 2 at the Large Hadron Collider*, Nuclear & Particle Physics Proceedings, Vol. 273–275, 2016, p. 1166-1172.
- [2] S. Grinstein, *The ATLAS Forward Proton Detector (AFP)*, Nuclear and Particle Physics Proceedings, Vol. 273–275, 2016, p. 1180-1184, ISSN 2405-6014.
- [3] G. Kramberger et al., *Timing performance of small cell 3D silicon detectors*, NIM A, Vol. 934, 2019, p. 26-32, ISSN 0168-9002.
- [4] Leena Diehl et al., *Comparison of the time resolution of unirradiated and irradiated LGADs and 3D sensors*, NIM A 1046 (2023) 167691.
- [5] G. Brianti, *The CERN Synchrotrons*, CERN-97-04; RAL-97-011.
- [6] S. Grinstein, *Beam Test Studies of 3D Pixel Sensors Irradiated Non-Uniformly for the ATLAS Forward Physics Detector*, NIMA Vol. 730, p. 28-32, ISSN 0168-9002.
- [7] G. Pellegrini et al., *3D-Si single sided sensors for the innermost layer of the ATLAS pixel upgrade*, NIMA, Vol. 924, p. 69-72, ISSN 0168-9002
- [8] W. Riegler, G. Aglieri Rinella, *Time resolution of silicon pixel sensors*, 2017, JINST 12, P11017.
- [9] Sadrozinski H.F.W., et al., *Ultra-fast silicon detectors (UFSD)*, NIM A, Vol. 831, 2016, p. 18-23, ISSN 0168-9002.
- [10] Misgiyati et al., *Bayesian Inference of Poisson Distribution using Conjugate and Non-Informative Priors*, Prosiding Seminar Nasional Metode Kuantitatif 2017, ISBN 978-602-98559-3-7.
- [11] J. Baudot et al., *First test results of MIMOSA-26, a fast CMOS sensor with integrated zero suppression and digitized output*, 2009 IEEE NSS/MIC Record, Orlando, FL, USA, 2009, pp. 1169-1173, doi: 10.1109/NSSMIC.2009.5402399.
- [12] Tektronix 6 Series B MSO Mixed Signal Oscilloscope Datasheet, <https://download.tek.com/datasheet/MSO6B-Datasheet-EN-US-48W-61716-10.pdf>
- [13] H.-M. Rein, M. Möller, *Design consideration for very-high-speed Si-bipolar IC's operating up to 50 Gb/s*, IEEE J Solid-State Circuits, 31 (8) (1996), pp. 1076-1090.
- [14] Mini-Circuits ZX60-V63+ Wideband Amplifier Datasheet, <https://www.minicircuits.com/pdfs/ZX60-V63+.pdf>

# **Classical and Bayesian statistical methods for low-level metrology**



---

---

# **Classical and Bayesian statistical methods for low-level metrology**

MANIFICAT Guillaume

---

---



#### MOTS-CLES

Métrologie ; Statistiques Bayésiennes ; limites de détection ; seuils de décision ; intervalles de confiance ; mesures de bas niveaux ; données censurées ; paramètres de nuisance

#### KEY-WORDS

Metrology; Bayesian statistics; detection limits; decision thresholds; confidence intervals; low level measurements; censored data; nuisance parameters

# Table des Matières

<b>ILLUSTRATIONS .....</b>	<b>4</b>
<b>1. INTRODUCTION .....</b>	<b>6</b>
<b>2. PRESENTATION OF THE PROBLEM.....</b>	<b>7</b>
<b>3. CLASSICAL FREQUENTIST APPROACH IN THE CASE OF HOMOSCEDASTIC GAUSSIAN.....</b>	<b>8</b>
<b>3.1. Statistical distribution of the variable N in the case of a signal and a noise that are both Gaussian.....</b>	<b>9</b>
<b>3.2. Decision thresholds .....</b>	<b>9</b>
3.2.1. Definition.....	9
3.2.2. Currie approach.....	9
<b>3.3. Detection limit.....</b>	<b>10</b>
<b>3.4. Confidence intervals and hypothesis testing.....</b>	<b>12</b>
<b>3.5. Relation between bounds of the confidence interval and decision threshold.....</b>	<b>14</b>
<b>4. BAYESIAN APPROACH FOR HOMOSCEDASTIC GAUSSIANS.....</b>	<b>16</b>
<b>4.1. Introduction to Bayesian methods .....</b>	<b>16</b>
4.1.1. Chosing a prior.....	18
<b>4.2. Presentation of the problem .....</b>	<b>18</b>
<b>4.3. Credibility interval and hypothesis testing.....</b>	<b>19</b>
4.3.1. Decision threshold.....	20
4.3.2. Detection limit.....	21
<b>5. SYNTHESIS.....</b>	<b>21</b>
<b>5.1. Frequentist point of view .....</b>	<b>21</b>
5.1.1. Calculation of the decision threshold and detection limit .....	21
5.1.2. Comparison with confidence interval .....	23
<b>5.2. Bayesian point of view.....</b>	<b>23</b>
<b>5.3. Verification by simulation .....</b>	<b>24</b>
<b>5.4. Conclusions on the homoscedastic case.....</b>	<b>24</b>

<b>6. POISSON DISTRIBUTIONS.....</b>	<b>24</b>
<b>6.1. frequentist approach .....</b>	<b>24</b>
<b>6.2. Conditional likelihood and hypothesis testing.....</b>	<b>26</b>
6.2.1. Uniformly most powerful test.....	27
6.2.2. Conditional likelihood in the presence of a signal.....	27
<b>6.3. Bayesian method .....</b>	<b>28</b>
6.3.1. Hypothesis testing .....	29
6.3.2. Marginal likelihood, binomial expansion and credibility intervals.....	30
6.3.3. Confidence intervals and detection limits.....	32
<b>6.4. Synthesis .....</b>	<b>32</b>
<b>7. HETEROSCEDASTIC GAUSSIANS AS A POISSON LAW LIMIT .....</b>	<b>33</b>
<b>7.1. Current method .....</b>	<b>33</b>
7.1.1. Decision thresholds and detection limits - the classic Currie approach.....	33
7.1.2. Bayesian approach in metrology .....	36
7.1.3. Pseudo Bayesian approach of the ISO 11929 standard.....	37
<b>7.2. Proposed approach using marginal and conditionnal likelihood .....</b>	<b>39</b>
7.2.1. Convolution of a Poisson distribution and a negative binomial distribution.....	39
<b>7.3. Asymptotic behavior .....</b>	<b>42</b>
7.3.1. Frequentist asymptotic behavior.....	42
7.3.2. Confidence intervals.....	42
7.3.3. Decision threshold obtained from the confidence interval .....	43
7.3.4. Decision threshold resulting from the conditional likelihood of Poisson laws .....	43
7.3.5. Detection limits.....	44
7.3.6. Optimal Test .....	45
7.3.7. Bayesian asymptotic behavior.....	45
<b>7.4. Detection limit divergence .....</b>	<b>46</b>
<b>7.5. Decision thresholds comparison .....</b>	<b>47</b>
<b>7.6. Influence of the prior .....</b>	<b>49</b>
<b>7.7. Coverage probability.....</b>	<b>50</b>
<b>7.8. Numerical Validation .....</b>	<b>50</b>
<b>7.9. Experimental validation .....</b>	<b>52</b>
<b>7.10. . Conclusions on the heteroskedastic case .....</b>	<b>53</b>
<b>8. DATA RENDERING.....</b>	<b>53</b>
<b>8.1. Current situation.....</b>	<b>54</b>

8.2.	Current normative requirements for data restitution in the field of radioactivity.....	56
8.3.	Public perception.....	56
9.	<b>CURRENT DISCUSSIONS ON STATISTICAL INFERENCE .....</b>	<b>57</b>
9.1.	An old discussion .....	57
9.2.	The current « revolt » .....	57
10.	<b>APPLICATION EXAMPLES.....</b>	<b>58</b>
10.1.	Giant Clams measurements as part of surveillance in Polynesia .....	58
10.2.	Tritium measurements in rainwater .....	61
10.3.	Astrophysics .....	63
10.4.	Particle physics .....	63
11.	<b>CONCLUSIONS.....</b>	<b>65</b>
12.	<b>THANKS .....</b>	<b>66</b>
ANNEXE 1	<b>PRODUCT AND CONVOLUTION OF GAUSSIAN DISTRIBUTIONS.....</b>	<b>72</b>
ANNEXE 2	<b>RAPPORTS D'ESSAI.....</b>	<b>73</b>
ANNEXE 3	<b>HYPERGEOMETRIC FUNCTION .....</b>	<b>74</b>
ANNEXE 4	<b>NEYMAN PEARSON LEMMA .....</b>	<b>76</b>

## Illustrations

Figure 1 - Frequentist principle diagram of the problem .....	7
Figure 2 - Schematic diagram (in 3D cavalier perspective) of the frequentist determination of the detection limit .....	11
Figure 3 - Representation of a 100-fold replication of measurement and determination of confidence intervals .....	13
Figure 4 - Representation of the different possible situations during a measurement process.....	15
Figure 5 - Bayesian schematic diagram of the problem .....	18
Figure 6 - Approximation of a Poisson law by a Gaussian for parameter values 2, 20 and 100 .....	40
Figure 7 - Decision thresholds calculated according to Currie (blue curve) and according to the proposed method (red curve) .....	48
Figure 8 - Detection limits calculated according to Currie (blue curve) and the proposed method (red curve).....	49
Figure 9 - Comparison of the ratio of real/theoretical false positives.....	51
Figure 10 – Picture of a giant clam in the Pacific .....	59
Figure 11 - measurement results (in fresh Bq/kg) with censoring of clam samples between 1989 and 2012 .....	60
Figure 12 - measurement results (in Bq/kg fresh) with censoring of giant clam samples between 1989 and 2004 and uncensored beyond.....	61
Figure 13 - comparison of the results of censored and uncensored measurements of the three devices.....	62
Figure 14 - Schematic diagram of the frequentist determination of the decision threshold.....	77

*"It ain't what you don't know that gets you into trouble. It's what you know for sure that just ain't so."*

**Mark Twain**

*"The greatest enemy of knowledge is not ignorance, it is the illusion of knowledge."*

**Stephen Hawking**

## Abstract

This document presents the statistical methods used to process low-level measurements in the presence of noise. These methods can be classical or Bayesian. The question is placed in the general framework of the problem of nuisance parameters, one of the canonical problems of statistical inference. By using a simple criterion proposed by Bolstad (2007), it is possible to define statistically significant results during a measurement process (act of measuring in the vocabulary of metrology). This result is similar for a classic paradigm (called "frequentist") or Bayesian: the presence of zero in the interval considered (confidence or credibility). It is shown that in the case of homoskedastic Gaussians, the commonly used results are found. The case of Poisson distributions is then considered. In the case of heteroscedastic Gaussians, which is that of radioactivity measurement, we can consider them as Poisson laws in the limit of large counts. The results are different from those commonly used, and in particular those from standards (ISO 11929). Their statistical performances, characterized by simulation, are better and are well verified experimentally. This is confirmed theoretically by the use of the Neyman-Pearson lemma which makes it possible to formally determine the statistical tests with the best performances. These results also make it possible to understand the paradox of the possible divergence of the detection limit. It is also formally shown that the confidence intervals thus calculated by getting rid of the nuisance parameter according to established methods result in the commonly used confidence interval. To our knowledge, this constitutes the first formal derivation of these confidence intervals.

This method is based on keeping the measurement results whether they are significant or not (not censoring them). This is recommended in several standards or documents, is compatible with the ISO 11929 standard and is in line with recent proposals in the field of statistics. On the other hand, all the information necessary to determine whether a measurement result is significant or not remains available. The conservation and restitution of all results is currently applied in the USA. The textbook case of the WIPP incident makes it possible to ensure favorable public perception.

The implications and applications of this method in different fields are finally discussed.

# 1. INTRODUCTION

The use of characteristic limits in radiation metrology (decision thresholds and detection limits) commonly leads to the consideration that results below these limits are unusable or meaningless. The situation considered is that of two measurements (measurements in metrology jargon):

- The first is that of a reference measurement in the absence of the desired signal.
- The second is that of a sample with the potential presence of a signal.

From the first reference measurement, characteristic limits are determined below which the signal is assumed to be absent. Below these limits, the measurement result is almost unused or to give an upper limit to the signal. In the last chapter of his book (Willink, 2013), Willink addresses measurement near a limit (noisy low-level signal for example) under the title "Measurement near a limit – an insoluble problem? ". He lists the difficulties encountered and is very pessimistic about the possibility of resolving the numerous paradoxes, inconsistencies and difficulties of this problem whatever the statistical paradigm used (Bayesian or frequentist).

Yet, in other domains, exploitation of data below characteristic limits is universally adopted (James & Roos, 1991). In a first report (MANIFICAT, 2015), we showed that the use of metrological data must include data below the characteristic limits. The question then arose about the best methods of using this data and what could be deduced from it. A brief paragraph of this report was dedicated to Bayesian methods and deserved to be developed towards the exploitation of the data.

As a continuation of this first work, this report presents the work carried out on the exploitation of low-level measurements in metrology, using the classical paradigm (known as frequentist) and the Bayesian paradigm.

This problem is placed in the more general framework of the elimination of nuisance parameters (Cox & Hinkley, 1974; Liseo, 2005) where the characteristic parameter of the noise (the reference) is not known precisely and is not intrinsically of interest. In fact, only the signal interests us.

After a presentation of the problem framework for each paradigm, we define the characteristic limits (decision threshold and detection limit) in each case. These notions are then applied in the case of homoscedastic Gaussians. The case of Poisson distributions is then presented. At the limit of large counts, these Poisson laws become heteroscedastic Gaussians. The method proposed here is based on the determination of confidence or credibility intervals using conditional and marginal likelihood, which makes it possible to eliminate the nuisance parameter. The presence of the zero value is sufficient to make the measurement non-significant, implicitly defining the characteristic limits. Providing the measurement result and its uncertainty is therefore necessary and sufficient. We will examine the compatibility with current standards and the impact of this method on them. Of course, an exact and numerical evaluation will be made of the statistical performance of this method. It is interesting to place this proposal within the framework of discussions on the concept of statistically significant result which animates the scientific world. The implications will then be examined before concluding.

## 2. PRESENTATION OF THE PROBLEM

We are in the presence of a sample whose measurements are represented by a random variable  $G$  associated with a parameter (the measurand which is denoted with a Greek letter  $\mu$ ).

We seek to determine the presence of a signal from one or more measurements carried out on this sample. This presence or absence of signal is determined in relation to a reference  $B$  also measured. This reference can be a sample, a measuring installation, etc. It is supposed not to contain a signal. In fact, everything is done physically to be as certain as possible to have a reference where any signal is assumed to be absent.

We seek to determine the difference between the sample and the reference by excess of the measurand compared to the reference. An example of this situation could be the measurement of an activity in a sample against a supposed reference (or not) devoid of any activity. The measurand of the possible signal  $S$  is assumed to be able to physically only take strictly positive values (for example mass or activity).

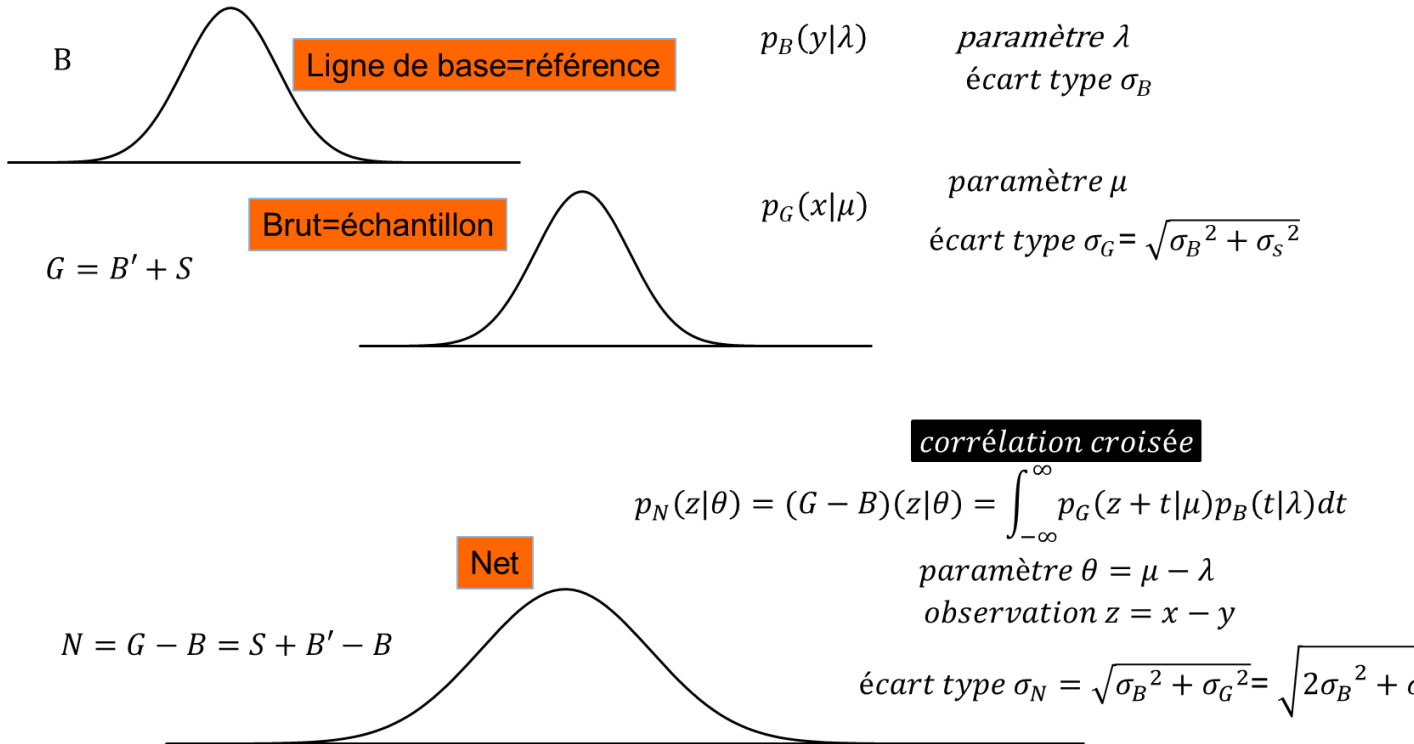


Figure 1 - Frequentist principle diagram of the problem

From the perspective of random variables, the sample is the result of the sum of the reference and the signal we are looking for:

$$G = B' + S$$

Note that in the random variable  $G$ , we do not know the contribution of  $B'$ .



In particular, this random variable has two components in its uncertainty: the measurement uncertainty and the possible intrinsic uncertainty of the desired signal. Thus, in the case of radioactivity measurement, the radioactive decay process is intrinsically random and has its own uncertainty independent of the measurement process.

Let us now consider the experimental context: by measuring the reference  $B$ , we obtain a value  $y$  while the measurement of the sample will give a value  $x$ , realization of the random variable  $G$ .

Metrology focuses on the net value  $z = x - y$ , by definition and with the notations above, it is a realization of the random variable  $N = G - B = S + B' - B$ .

This random variable  $N$  should not be confused with the random variable  $S$  even if  $B - B'$  is a random variable with zero expectation by definition.  $B$  and  $B'$  are in fact two independent and identically distributed random variables (iid in the jargon). Remembering that random variables  $S, B$  et  $B'$  are by definition independent (signal independent of noise), we have in terms of expectation::

$$E(N) = E(G - B) = E(S + B' - B) = E(S) + E(B) - E(B') = E(S)$$

**(1)**

But in terms of variances:

$$Var(N) = Var(G - B) = Var(S + B' - B) = Var(S) + Var(B) + Var(B') = Var(S) + 2.Var(B)$$

**(2)**

By measuring  $z$ , we therefore have access to the inference on the distribution of the random variable  $N$  which will have a greater uncertainty than that of  $S$ . By the convolution of  $S$  and  $B' - B$ , we obtain a more dispersed ("spread") random variable.

In particular, if the random variable  $S$  is necessarily positive (of positive support more precisely), the random variable  $N$  has no reason to be positive.

Thus, we can take for granted the fact that a measurement  $z$ , realization of the random variable  $N$ , can give a negative result (compared to the reference) simply because a subtraction is carried out which, due to intrinsic fluctuations, can lead to a negative value. This point is universally accepted by statisticians and measurement theorists (but not by all metrology practitioners)(Chambless et al., 1992; Ellison, 2014; ISO, 2010a; James & Roos, 1991) (IUPAC, 1998) (EURACHEM, 2012) (CETAMA, 2014) (ISO 11843, 2000) .

The following chapter will focus on the statistical characterization of the random variable  $N$  in the particular case of a Gaussian distribution of the signal and the noise, to the inference of its parameters as well as to the properties of associated quantities in particular the decision threshold and the detection limit.

### **3. CLASSICAL FREQUENTIST APPROACH IN THE CASE OF HOMOSCEDASTIC GAUSSIAN**

let's remember that  $N = S + B' - B$  and suppose that the random variables  $S$ ,  $B$  and  $B'$  are all Gaussians.

### 3.1. Statistical distribution of the variable $N$ in the case of a signal and a noise that are both Gaussian

$$p_S(x|\theta, \sigma_S) = \frac{e^{-\frac{(x-\theta)^2}{2\sigma_S^2}}}{\sqrt{2\pi}\sigma_S}, \quad p_B(x|\lambda) = \frac{e^{-\frac{(x-\lambda)^2}{2\sigma_B^2}}}{\sqrt{2\pi}\sigma_B} \text{ et } p_{B'}(x|\lambda) = \frac{e^{-\frac{(x-\lambda)^2}{2\sigma_B^2}}}{\sqrt{2\pi}\sigma_B}.$$

A linear combination of Gaussian variables being itself Gaussian, we deduce that (Bromiley, 2003) :

$$p_N(z|\theta) = \frac{e^{-\frac{(z-\theta)^2}{2(\sigma_S^2 + 2\sigma_B^2)}}}{\sqrt{2\pi(\sigma_S^2 + 2\sigma_B^2)}}$$

From this distribution, we can deduce two quantities of interest, important in metrology: the decision threshold and the detection limit.

## 3.2. Decision thresholds

### 3.2.1. Definition

In the frequentist paradigm, the decision threshold is the fixed value of the measurand such that, when the measurement result of a measurand quantifying the physical phenomenon is greater than it, we decide that the physical phenomenon is present (ISO, 2010a). Below this value, the measured value could therefore be reasonably explained by a simple fluctuation in the background noise. This threshold is generally determined by hypothesis tests using the Neyman-Pearson methodology (Neyman & Pearson, 1933) formalized in the case of metrology by Currie (Currie, 1968, 1999b, 2000, 2004).

This methodology is based on purely frequentist concepts (fixed parameter). We will therefore reason in the space of observations.

We want to know up to what measured value can we consider that the hypothesis of a zero parameter (no physical phenomenon due to the signal) is reasonable.

### 3.2.2. Currie approach

In this approach, we identify a hypothesis that we want to test, called the null hypothesis (which we will designate by  $H_0$ ).

It is generally an assertion about a distribution that we wish to test in the form of the absence of an effect (radioactivity for example).

Currie considers that only the case of a zero measurand (absence of effect,  $\theta=0$ ) should be used to establish the decision threshold (Currie, 1999a).

This means that he considers the situation where  $x$  comes from the background noise (the reference) AND the same for  $y$ .

$z = x - y$  is thus a realization of the random variable  $N = B' - B$  which has the probability distribution

$$p_N(z|0) = \frac{e^{-\frac{(z-0)^2}{4\sigma_B^2}}}{\sqrt{4\pi\sigma_B}} = \frac{e^{-\frac{z^2}{4\sigma_B^2}}}{\sqrt{4\pi\sigma_B}}$$

By setting a threshold of  $100\alpha_c\%$ , the decision threshold  $z_c$ , amounts to considering that if we were in the presence only of the reference, only  $100\alpha_c\%$  measurements would be higher than this threshold (and would therefore be false positives if we considered them as coming from a signal).

$$\alpha_c = p(N > z_c | H_0) = \int_{z_c}^{\infty} p_N(z|0) dz$$

$$\alpha_c = \int_{z_c}^{\infty} p_N(z|0) dz = \frac{1}{\sqrt{2\pi}\sigma_B} \int_{z_c}^{\infty} e^{-\frac{(z-0)^2}{2\sigma_B^2}} dz = 1 - \Phi\left(\frac{z_c}{\sqrt{2}\sigma_B}\right)$$

And thus :

$$z_c = \sqrt{2\sigma_B^2} \Phi^{-1}(1 - \alpha_c)$$

Where  $\Phi$  is the cumulative distribution of the standard normal distribution ( $\Phi^{-1}$  is its inverse function or quantile function).

Let us emphasize that for the moment this is one test among other possible ones. Authors have proposed a whole set of tests (Altshuler & Pasternack, 1963; Lehmann & Romano, 2005a; Strom & MacLellan, 2001). However, it is possible to prove that this test is in fact the best possible in the sense of the Neyman-Pearson approach.[Cf Annexe 4].

### 3.3. Detection limit

The detection limit  $\theta_d$  in its frequentist definition is the smallest true value of the measurand (parameter)  $\theta$  which guarantees the specified probability of being detectable by the measurement method (ISO, 2010a). This will coincide with the greatest true value which would have a non-negligible probability of being considered non significant by the measurement. It could give rise to observations equal to the decision threshold. In fact, the top of the range of  $\theta$  which would have a probability of at least  $1 - \beta_c$  to be detected by the measurement method coincides with the bottom of the range of  $\theta_d$  having a probability of at most  $\beta_c$  to be considered as non significant. The lowest reasonably detectable value coincides with the highest value likely to be classified as nonsignificant. In Currie's frequentist formulation (Currie, 1968), keeping the previous notations  $N$  and  $z$ , we get :

$$\beta_c = p(N < z_c | \theta_d) = \int_{-\infty}^{z_c} p_N(z|\theta_d) dz$$

(3)

And

$$1 - \beta_c = p(N < z_c | \theta_d) = \int_{z_c}^{\infty} p_N(z|\theta_d) dz$$

This corresponds to finding in the alternative hypothesis  $H_a$  the smallest value  $\theta_d$  of  $\theta$  for which we will have a probability  $\beta_c$  to have measurements below the decision threshold (false negative). We can rewrite this formula in the form:

$$\beta_c = \int_{-\infty}^{z_c} p_N(x|y, \theta_d) dz$$

We are looking for the value of the parameter  $\theta_d$  such that the dispersion of the measurements only very improbable gives measurements below the decision threshold. This supposes that we place ourselves in the case of an alternative hypothesis. ( $\theta_d \neq 0$ ) and therefore within the framework of the Neyman-Pearson approach. If there is no alternative hypothesis, there is no detection limit (Lehmann, 1993).

Setting  $\sigma_N = \sqrt{\sigma_S^2 + 2\sigma_B^2}$ , the detection limit is therefore calculated as follows for homoscedastic Gaussians

$$\beta_c = \int_{-\infty}^{z_c} p_N(z|\theta_d) dz = \frac{1}{\sqrt{2\pi}\sigma_N} \int_{-\infty}^{z_c} e^{-\frac{(z-\theta_d)^2}{2\sigma_N^2}} dz = \Phi\left(\frac{z_c - \theta_d}{\sigma_N}\right) = 1 - \Phi\left(\frac{\theta_d - z_c}{\sigma_N}\right)$$

$$\theta_d - z_c = \sigma_N \Phi^{-1}(1 - \beta_c)$$

$$\theta_d = z_c + \sigma_N \Phi^{-1}(1 - \beta_c)$$

It is common practice to assume that  $\beta_c = \alpha_c$ .

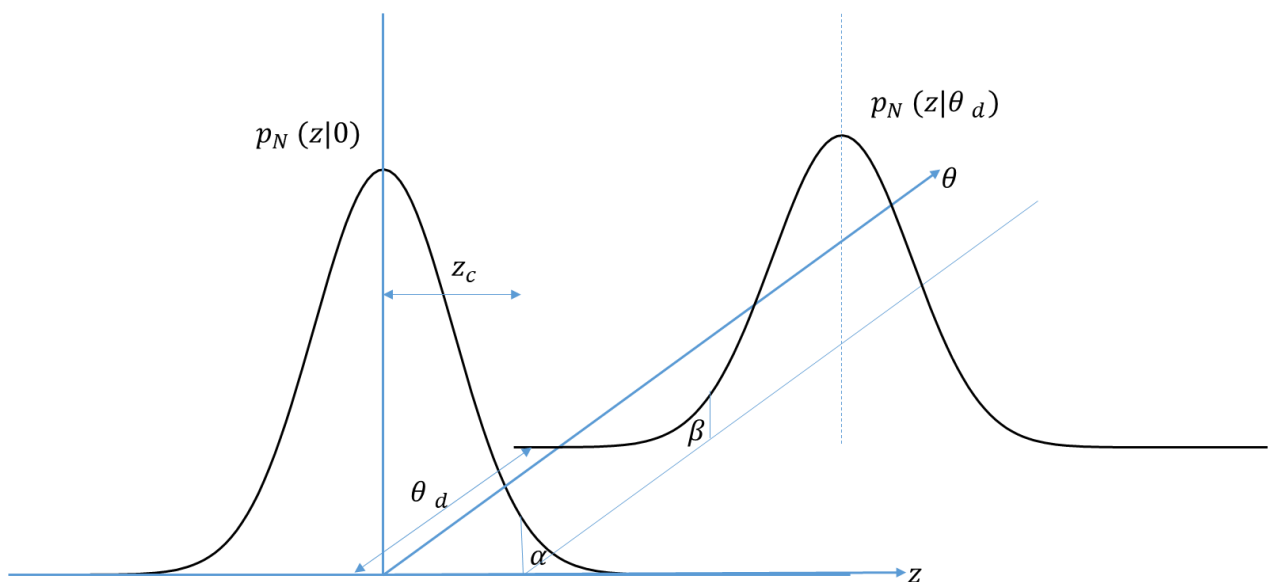


Figure 2 - Schematic diagram (in 3D cavalier perspective) of the frequentist determination of the detection limit

### 3.4. Confidence intervals and hypothesis testing

If we use homoskedastic Gaussian distributions for the baseline and sample, we have seen that the distribution of the difference (with the above notations for the random variable  $N$ ) will also be a Gaussian. Using the previous notations, we wish in this section to obtain a confidence interval of the mean  $\theta$  of the random variable  $N$  modeling the difference between the measurement  $G = S + B'$  and the reference  $B$ .

Consider a series of  $n$  measurements of differences between baseline and sample (realizations of the random variable  $N$ ). The average will be  $\bar{N}$  and its standard error  $\frac{\sigma_N}{\sqrt{n}}$ . If we define  $t = \sqrt{n} \frac{\bar{N} - \theta}{\sigma_N}$ , having a standard

normal distribution.  $p(t) = \frac{1}{\sqrt{2\pi}} e^{-\frac{t^2}{2}}$ .

Using the properties of this distribution, we can set a probability value  $\gamma$  such that there exists a  $k$  verifying :

$$P(-k \leq t \leq k) = \gamma$$

$$P\left(-k \leq \sqrt{n} \frac{\bar{N} - \theta}{\sigma_N} \leq k\right) = \gamma$$

$$P\left(-k \frac{\sigma_N}{\sqrt{n}} \leq \bar{N} - \theta \leq k \frac{\sigma_N}{\sqrt{n}}\right) = \gamma$$

$$P\left(\bar{N} - k \frac{\sigma_N}{\sqrt{n}} \leq \theta \leq \bar{N} + k \frac{\sigma_N}{\sqrt{n}}\right) = \gamma$$

We then call  $t$  a pivotal quantity

This therefore means that the probability that the interval  $\bar{N} \mp k \frac{\sigma_N}{\sqrt{n}}$  includes the parameter  $\theta$  (the true value sought) is  $\gamma$ .

It is important to remember that the value  $z$  is a realization of a random variable in the frequentist paradigm used here.  $\theta$  is set and must not be considered as a random quantity. It is therefore not possible to use the term probability to talk about  $\theta$ .

The fact that  $z$  (result of a measurement process) is a realization of a random variable is therefore expressed in the following form:

If I repeat my measurement 100 times, in  $100\gamma\%$  of the time, the true value of my parameter should be within the different interval calculated for each measurement.

This therefore absolutely does not say that for a particular interval calculated from a measurement  $z$ , we have  $100\gamma\%$  to have the parameter included in this particular interval. It rather specifies that  $100\gamma\%$  of my calculated intervals will include the true value  $\theta$ .

The figure below schematizes the idealized process of this virtual measurement repetition (virtual because these measurement replications are never done in reality). Each point represents a measurement of a sample whose true value is 0.15. The confidence interval would then be determined for each measurement, say with a

confidence index of 5%. Only 5 confidence intervals out of 100 will not include the true value. We speak of “coverage probability”. This probability is an essential frequentist parameter in statistics and constitutes an important evaluation criterion of the methods. This is also a justification by particle physicists for the use of confidence intervals including a negative part. An interval of the type  $[-a,b]$  will have a probability of  $\gamma\%$ . It can therefore include the value zero and cannot be considered as “unphysical”.

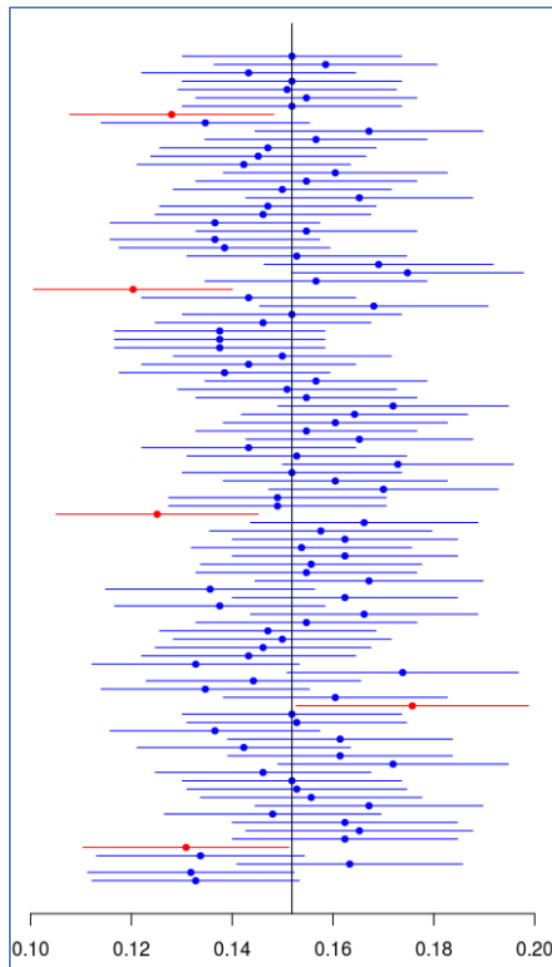


Figure 3 - Representation of a 100-fold replication of measurement and determination of confidence intervals

### 3.5. Relation between bounds of the confidence interval and decision threshold

In the case where we want to know whether a measurement is significant, it is enough to check that the zero value is not in the confidence interval calculated from this measurement (Willink, 2006).

**The decision threshold is therefore the smallest measurement for which the confidence interval contains the value zero.**

Let us consider the case of homoscedastic Gaussians.

$$P\left(z - k \frac{\sigma_N}{\sqrt{n}} \leq \theta \leq z + k \frac{\sigma_N}{\sqrt{n}}\right) = \gamma$$

With  $k = \Phi^{-1}\left(\frac{1-\gamma}{2}\right)$  and  $\gamma$  the coverage probability of the confidence interval.

For a realization  $z$  of the random variable  $N$ , the lower bound of the confidence interval of  $\theta$  is

$$z - \Phi^{-1}\left(\frac{1-\gamma}{2}\right) \frac{\sigma_N}{\sqrt{n}}$$

Thus :

$$z_c - \Phi^{-1}\left(\frac{1-\gamma}{2}\right) \frac{\sigma_N}{\sqrt{n}} = 0$$

$$z_c = \Phi^{-1}\left(\frac{1-\gamma}{2}\right) \frac{\sigma_N}{\sqrt{n}}$$

$$z_c = \sqrt{2\sigma_B^2} \Phi^{-1}\left(\frac{1-\gamma}{2}\right) \text{ in the hypothesis } H_0 = \{\theta = 0\}$$

where  $\Phi$  is the cumulative distribution function of the gaussian distribution. taking  $\frac{1-\gamma}{2} = \alpha_c$ , we obtain exactly the same result as with the direct hypothesis test.

$$z_c = \sqrt{2\sigma_B^2} \Phi^{-1}(\alpha_c)$$

We therefore find the Currie decision threshold.

**For the detection limit, the largest parameter value must be determined in the confidence interval compatible with a measurement  $z = z_c$ .**

We immediately recognize that the upper bound of the confidence interval of  $\theta$  for an observation  $z_c$  will give us back the expression of the detection limit.

More precisely :

$$\theta_d = z_c + \sqrt{2\sigma_B^2} \Phi^{-1}(\alpha_c) = 2z_c$$

Here again, we obviously find the result of Currie's approach.

Once we have made a measurement and determined a confidence interval, it is therefore not necessary to also carry out a hypothesis test. Just look if the confidence interval contains 0

In the case of a non significant result ( $z < z_c$ ), the upper bound of the confidence interval will be lower than the detection limit.

We can schematize everything we have just said as follows:

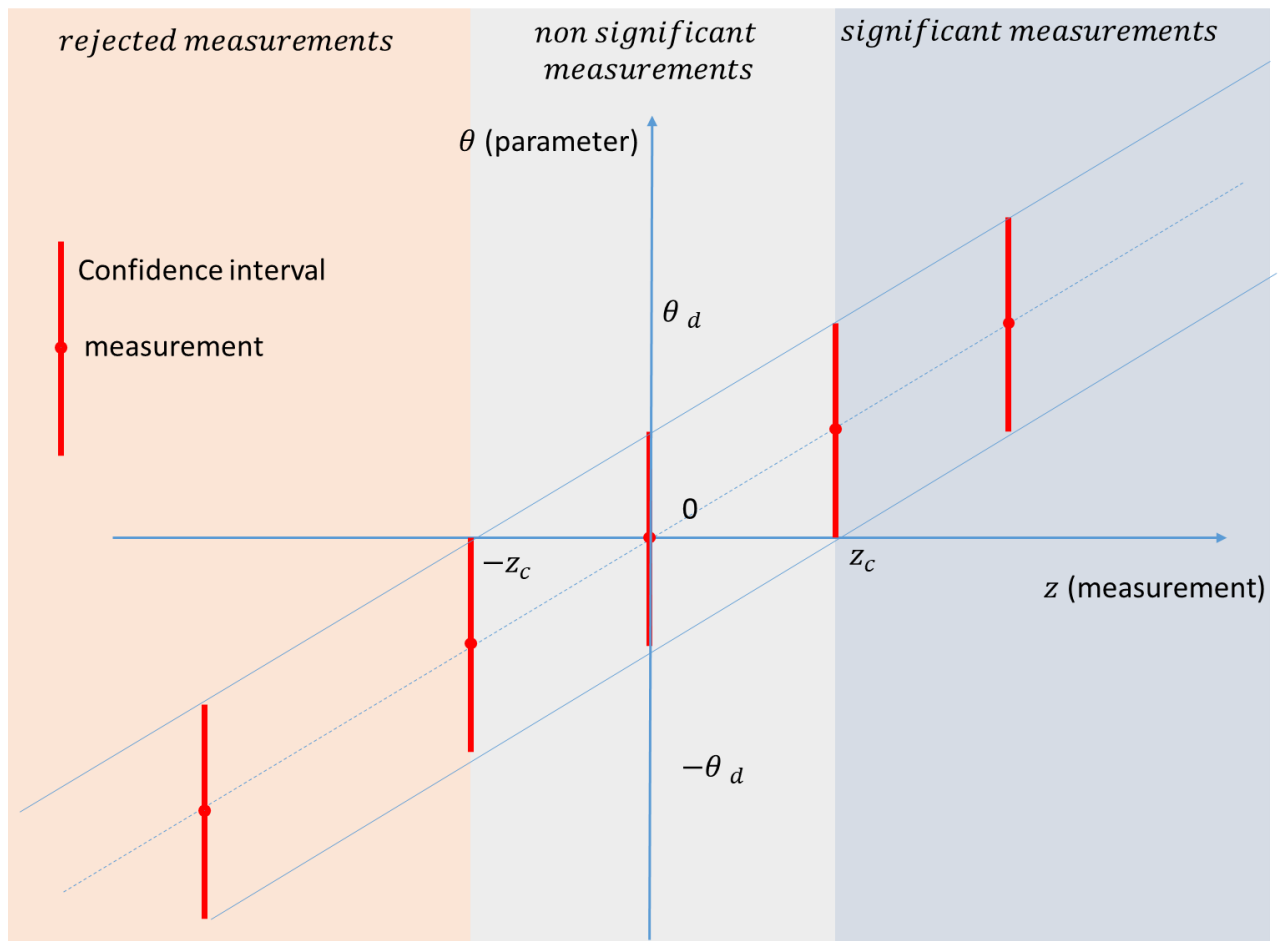


Figure 4 - Representation of the different possible situations during a measurement process



So if we know how to generate the confidence interval, we have all the information to determine the decision threshold and detection limit. If the interval “touches” the zero value of the parameter, the measurement will be equal to the decision threshold. The uncertainty will then be 100% and the upper limit of the interval will then be the detection limit. In addition, the hypothesis test used to determine it is that from Neyman Pearson's lemma, it is therefore the most efficient test.

**Uncertainty=100%  $\Leftrightarrow z = z_c \Leftrightarrow$  non significant results**

**$\Leftrightarrow$  lower bound of the confidence interval =0  $\Leftrightarrow$  upper bound=detection limit  $\theta_d$**

If the interval includes a negative part and a positive part then its uncertainty will be greater than 100%. The hypothesis test on the value 0 cannot be rejected.

**Uncertainty > 100%  $\Leftrightarrow$  measurement < decision threshold  $\Leftrightarrow$  non significance**

**$\Leftrightarrow$  lower bound of the confidence interval <0  $\Leftrightarrow$  upperbound<detection limit  $\theta_d$**

It is even possible to add another consideration. If the sample measurement is too low compared to the baseline, then it can be considered that it is no longer reasonably compatible with the baseline estimate. A measurement that is too negative can no longer be explained by measurement fluctuations. It will then be appropriate to carefully examine this measurement and this sample in order to rule out any possibility of error or bias.

**measurement < rejection threshold= $-z_c \Leftrightarrow$  suspicious results**

**$\Leftrightarrow$  upperbound<0**

We could therefore talk about a rejection threshold.

Let us emphasize once again that we are reasoning here on the variable  $N$  (net variable) and not on  $S$  (the variable sought). The first can absolutely have a confidence interval with a negative part. This confidence interval is determined using the probability distribution of  $N$ . We cannot determine the confidence interval for  $S$  because we do not have its probability distribution in the absence of the exact noise contribution within sample measurement.

## **4. BAYESIAN APPROACH FOR HOMOSCEDASTIC GAUSSIANS**

### **4.1. Introduction to Bayesian methods**

Bayesian statistics provide a way to infer desired physical parameters from observational data. The “classic” method (although subsequent to the birth of Bayesian methods), called frequentist, assumes that we are looking for an unknown but fixed parameter. The bayesian method (Gelman et al., 2013) assumes that the relationship between the observed quantities and the parameters is statistical. Mathematically, this amounts

to considering the parameters of interest as random variables with a probability density intended to completely describe our beliefs or knowledge about it.

The parameters are therefore modeled in terms of probability distributions: Starting from “a priori” distributions on these parameters, they are updated according to observations to produce so-called “a posteriori” distributions. Note that there are numerous mathematical-epistemological interpretations of Bayesian methods. Some authors have even counted 46,656 possible varieties of “Bayesianism”(Good, 1976).

Because we assign a distribution to the parameters, statistical inference is reduced to the application of probability theory.

If we consider a joint probabilistic distribution  $p_{X,U}(x, \mu)$  of observations and parameters,  $X$  and  $U$  respectively, it is possible to write  $p_{X,U}(x, \mu) = p_X(x|\mu)p_U(\mu)$ .

The first term  $p_X(x|\mu)$  (probability of having an observation  $x$  knowing the parameter  $\mu$ ) is called the likelihood. It will correspond to the chosen statistical model (Gaussian for example). This concept of likelihood also exists in frequentist methodologies and corresponds to the modeling of the distribution of observations as a function of parameters (Gaussian distribution of mean  $\mu$  for example).

The second term  $p_U(\mu)$  is the a priori or prior distribution of the parameter. It quantifies our prior beliefs about the distribution of parameters even before taking into account observations.

Likewise, we can write  $p_{X,U}(x, \mu) = p_U(\mu|x)p_X(x)$ . Bayes' theorem simply consists of writing :

$$p_U(\mu|x) = \frac{p_X(x|\mu)p_U(\mu)}{p_X(x)}$$

Where  $p_X(x)$  is the probability of the observation  $x$  integrated on all possible values of  $\mu$ , sometimes called marginal likelihood.  $p_U(\mu|x)$  is the a posteriori distribution (after the observations), the posterior. We will say that the posterior is equal to the product of the likelihood and the prior divided by the marginal likelihood.

Given that the posterior is a probability density which must be normalized to 1, we can consider  $p_X(x)$  as a simple normalization constant (because it does not depend on  $\mu$  i.e  $p_X(x) =$

$$\int_{-\infty}^{\infty} p_{X,U}(x, \mu)d\mu = \int_{-\infty}^{\infty} p_X(x|\mu)p_U(\mu)d\mu):$$

$$p_U(\mu|x) \sim p_U(x|\mu)p_U(\mu)$$

**(4)**

The posterior is proportional to the product of the prior and the likelihood. We carried out a Bayesian inversion:.

Subsequently, a prior of a parameter  $\mu$  will be denoted in the form  $\pi(\mu)$  to facilitate understanding. A crucial point of Bayesian methodology, which is also the cornerstone of the criticisms addressed to it, is its dependence on priors. There are many ways to choose them which are the subject of fierce and heated discussion.

### 4.1.1. Chosing a prior

A crucial point of Bayesian methodology is its dependence on priors. The choices of priors can be motivated by past experiences or by intuition, but also by computational aspects as in the case of conjugate priors.

Aware of this dependence on priors, in addition to the absence of a priori knowledge in a number of problems, numerous works have been interested in the definition of “non-informative” priors whose influence on the posterior probability is reduced to a minimum.

This type of prior respects the so-called Jeffreys rule in connection with invariances by transformation (translation in this case). With this prior, the confidence and credibility intervals often coincide (Jaynes, 1968; Karlen, 2002; Rosenkrantz, 1989; Severini, 1991) and it is therefore possible to use frequentist and Bayesian concepts interchangeably. In particular, the coverage probabilities will naturally apply to the credibility intervals and it will be possible to give a probability for a value of the parameter.

In the rest of the document, we will essentially use non-informative priors to investigate the questions asked in the Bayesian framework.

## 4.2. Presentation of the problem

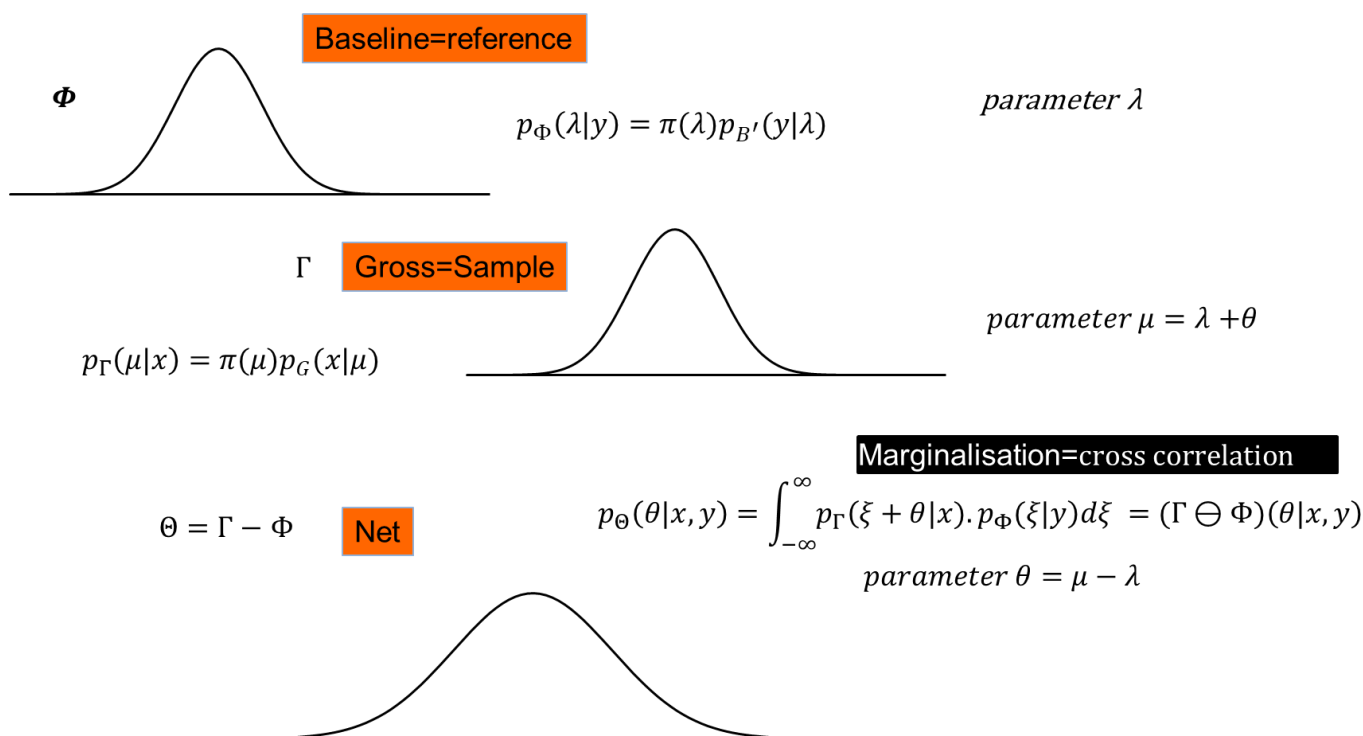


Figure 5 - Bayesian schematic diagram of the problem

As with the previous frequentist chapter, the variable of interest in this section is the random variable  $N$  (modeling the net measurement).

We wish to obtain its posterior distribution and exploit the credibility intervals.

As we have already mentioned, the frequentist point of view is to consider that observations are realizations of random variables whose probability distributions have fixed but unknown parameters.

In the Bayesian paradigm, models supposed to account for observations can incorporate constraints on the parameters (more precisely on the information available on the parameters), treated as random variables. In particular, for random variables  $\Gamma$  et  $\Phi$  modeling the sample measurement and the reference respectively, we can determine the following probability densities:

$$p_{\Gamma}(\mu|x) = \pi(\mu)p_G(x|\mu)$$

$$p_{\Phi}(\lambda|y) = \pi(\lambda)p_B(y|\lambda)$$

where  $\pi(\mu)$  et  $\pi(\lambda)$  are the corresponding priors.

Our choice in the present study is to consider non-informative priors  $\pi(\mu) = \pi(\lambda) = 1$  :

$$p_{\Gamma}(\mu|x) = \pi(\mu)p_G(x|\mu) = \frac{e^{-\frac{(x-\mu)^2}{2\sigma^2}}}{\sqrt{2\pi}\sigma}$$

$$p_{\Phi}(\lambda|y) = \pi(\lambda)p_B(y|\lambda) = \frac{e^{-\frac{(y-\lambda)^2}{2\sigma^2}}}{\sqrt{2\pi}\sigma}$$

The joint probability density is therefore :

$$p_{\Gamma\Phi}(\lambda, \mu|x, y) = \pi(\mu)\pi(\lambda)p_{\Gamma}(\mu|x)p_{\Phi}(\lambda|y) = \frac{e^{-\frac{(x-\mu)^2}{2\sigma^2}}}{\sqrt{2\pi}\sigma} \frac{e^{-\frac{(y-\lambda)^2}{2\sigma^2}}}{\sqrt{2\pi}\sigma}$$

We know that if  $G, B'$  are  $S$  gaussian densities of means  $\mu, \lambda$  and  $\theta$  respectively, then by construction of  $G = S + B'$  we have  $\mu = \lambda + \theta$  and by reparameterizing the equation above we find:

$$p_{\Gamma\Phi}(\lambda, \theta|x, y) = \pi(\lambda + \theta)\pi(\lambda)p_{\Gamma}(\lambda + \theta|x)p_{\Phi}(\lambda|y) = \frac{e^{-\frac{(x-\theta)^2}{2\sigma^2}}}{\sqrt{2\pi}\sigma} \frac{e^{-\frac{(y-\lambda)^2}{2\sigma^2}}}{\sqrt{2\pi}\sigma}$$

The Bayesian approach to getting rid of a nuisance parameter like  $\lambda$  est simply to integrate with respect to this parameter. This is called a marginalization.

$$p_{\Theta}(\theta|x, y) = \int p_{\Gamma\Phi}(\lambda, \theta|x, y)d\lambda = \int \frac{e^{-\frac{(x-\lambda-\theta)^2}{2\sigma^2}}}{\sqrt{2\pi}\sigma} \frac{e^{-\frac{(y-\lambda)^2}{2\sigma^2}}}{\sqrt{2\pi}\sigma} d\lambda = \frac{e^{-\frac{(z-\theta)^2}{4\sigma^2}}}{\sqrt{4\pi}\sigma}$$

With  $z = x - y$ . Given that we integrate over the entire domain of definition of  $\lambda$ ,  $\theta$  will take all possible values of  $]-\infty, +\infty[$ .

### 4.3. Credibility interval and hypothesis testing

In the Bayesian approach, the posterior distribution probabilistically contains all the information on the parameter. Given an observation  $z$ , the credibility interval  $[a, b]$  à  $(1 - \gamma)100\%$  is defined by :

$$p(a \leq \theta \leq b|z) = (1 - \gamma)$$

Unlike confidence intervals, it is therefore legitimate here to speak of a probability for the parameter to be found in this interval (Bolstad, 2007).

**There are several ways to perform hypothesis testing or their equivalent in the Bayesian approach.**

**We will use Bolstad's suggestion here (Bolstad, 2007). We will test the credibility of this null hypothesis by examining whether the null value is included in the credibility interval. If this is not the case, we will reject this hypothesis. Otherwise, we will consider this to be a credible value.**

The approach is essentially the same as examining whether the zero value is part of the confidence interval by replacing the latter with the credibility interval. The main advantage is to eliminate the one-off nature of the test. We do not test if the parameter is equal to a precise value (which from a mathematical point of view is a set of zero Lebesgues measure) but whether this parameter is included in an interval.

This agrees with the point of view of a certain number of statisticians who consider that the gap between hypothesis testing and estimation is not necessary. (Bolstad, 2007; Cumming, 2014; Cumming & Calin-Jageman, 2016; Kruschke & Liddell, 2018). It is enough to know the posterior distribution of the parameter of interest to both estimate the parameter and carry out hypothesis tests. Some of these authors even speak of “new statistics”. As we will see, knowledge of the posterior distribution is sufficient for both estimation and hypothesis testing corresponding to the decision threshold in the field of low-level metrology..

### 4.3.1. Decision threshold

In a similar way to 3.2, we propose to define a Bayesian decision threshold.

The decision threshold would be the smallest net measurement value  $z_c$  such that the zero value is the lower limit of the credibility interval:

$$\alpha_c = \int_{-\infty}^0 p_{\Omega}(\theta|z_c)d\theta = P(\Omega < 0|z_c)$$

In the case of members of the “location family” to which the Gaussians belong, we know that  $p_N(z|\theta) = f(\theta - z) = p_{\Omega}(\theta|z)$  because we then take a non-informative prior. This implies that, by change of variable  $t = \theta - z$ , we can write:

$$\alpha_c = \int_{z_c}^{\infty} p_N(z|0)dz = \int_{-\infty}^0 p_{\Theta}(t|z_c)dt$$

The frequentist and Bayesian decision thresholds therefore coincide.

Note that this definition of the decision threshold based on the inclusion of zero in the credibility interval corresponds exactly to that suggested by Jaynes (Jaynes, 1968, 2003). Indeed, Jaynes proposed using decision thresholds based on probability in this type of case.  $\alpha$  to have a given sign (Jaynes, 1968, 2003). Thus, we will determine a threshold  $z_c$  such that :

$$\alpha_c = p_{G,B}(\mu < \lambda | z_c)$$

By definition, given that  $\theta = \mu - \lambda$  where  $\lambda$  is the position parameter of the sample et  $\mu$  that of the reference :

$$p_{G,B}(\mu < \lambda | z_c) = p_{\theta}(\theta < 0 | z_c) = \int_{-\infty}^0 p_{\theta}(\theta | z_c) d\theta$$

(5)

We therefore seek to determine an observed value  $z_c$  which will ensure that the probability for  $\theta$  to be of negative sign is equal to a given  $\alpha_c\%$  (for example 2,5%). Remember that, by definition, this corresponds to a probability  $\alpha_c$  that the value of the sample parameter is lower than that of the reference. This corresponds to having a hypothesis  $H_0 : \theta < 0$  and an alternate hypothesis  $H_1 : \theta > 0$ . This is the exact Bayesian correspondence of the decision threshold defined in 3.2. To our knowledge, only Lemay has explicitly used this criterion in the field of metrology (Lemay, 2012, 2015). Others have done it in a somewhat concealed or unconscious way by firstly excluding the possibility of negative values of  $\theta$  then somewhat paradoxically considering despite everything that this represented the null hypothesis (Kirkpatrick & Young, 2009)

Another remark that can be made is that this definition based on a non-informative prior would not make sense if we had prohibited the existence of negative values (with a prior of the type for example  $\pi(\theta) = 1$  if  $(\theta > 0)$ ).

### 4.3.2. Detection limit

Similarly, we can determine a Bayesian detection limit. We are looking for the greatest possible value of the parameter compatible with the measurement of the decision threshold.

We look for the upper bound of the credibility interval such that:

$$\beta_c = P(\theta > \theta_d | z_c) = \int_{\theta_d}^{\infty} p_{\theta}(\theta | z_c) d\theta = \int_{-\infty}^{z_c} p_N(z | \theta_d) dz$$

The Bayesian detection limit will therefore coincide with the frequentist detection limit. It is therefore possible for us in this case to move indifferently from one point of view to another and to use the different insights provided.

## 5. SYNTHESIS

### 5.1. Frequentist point of view

#### 5.1.1. Calculation of the decision threshold and detection limit

As defined previously, homoscedasticity is the property of keeping a constant variance. In the case that concerns us, this means that the sample and the reference have the same variance. In other words, the signal has zero variance (adding a signal to the noise is done without increasing the uncertainty).

$$\sigma_s^2 = 0$$

$$\sigma_N = \sqrt{\sigma_B^2 + \sigma_G^2} = \sqrt{2\sigma_B^2 + \sigma_S^2} = \sqrt{2}\sigma_B$$

Apart from pathological cases, homoscedasticity can be modeled by the Dirac distribution.

$$p_S(z|\theta) = \delta(z - \theta)$$

In the absence of measurement uncertainty, there is no intrinsic variability of the signal

$$p_N(z|\theta) = \int_{-\infty}^{\infty} p_S(z - w|\theta) p_N(w|0, 2\sigma_B^2) dw = \int_{-\infty}^{\infty} \delta(z - w - \theta) \frac{e^{-\frac{w^2}{4\sigma_B^2}}}{\sqrt{4\pi\sigma_B}} dw = \frac{e^{-\frac{(z-\theta)^2}{2\sigma_N^2}}}{\sqrt{2\pi\sigma_N}}$$

We can thus calculate the decision threshold  $z_c$  in accordance with the method set out in 3.2. It must be such that, for a given  $\alpha_c$  :

$$\alpha_c = \int_{z_c}^{\infty} p_N^{H_0}(z|0) dz = \frac{1}{\sqrt{2\pi\sigma_N}} \int_{z_c}^{\infty} e^{-\frac{(z-0)^2}{2\sigma_N^2}} dz = 1 - \Phi\left(\frac{z_c}{\sigma_N}\right)$$

And so :

$$z_c = \sigma_N \Phi^{-1}(1 - \alpha_c) = \sqrt{2}\sigma_B \Phi^{-1}(1 - \alpha_c) = \sigma_N \Phi^{-1}(1 - \alpha_c)$$

**(6)**

The detection limit is calculated as explained in 3.3 :

$$\beta_c = \int_{-\infty}^{z_c} p_N(z|\theta_d) dz = \frac{1}{\sqrt{2\pi\sigma_N}} \int_{-\infty}^{z_c} e^{-\frac{(z-\theta_d)^2}{2\sigma_N^2}} dz = \Phi\left(\frac{z_c - \theta_d}{\sigma_N}\right) = 1 - \Phi\left(\frac{\theta_d - z_c}{\sigma_N}\right)$$

$$\theta_d - z_c = \sigma_N \Phi^{-1}(1 - \beta_c)$$

$$\theta_d = z_c + \sigma_N \Phi^{-1}(1 - \beta_c)$$

If we set  $\alpha_c = \beta_c$ , then :

$$\theta_d = 2z_c$$

**(7)**

This is the result of the classic Currie approach (Currie, 1968) for homoscedastic distributions.

In general, the results are returned as follows::

measurements	estimation
$z < z_c$ (non significant)	$< \theta_d$
$z > z_c$ (significant)	$\theta \pm \delta$

where  $\delta$  is the uncertainty.

### 5.1.2. Comparison with confidence interval

As we indicated in the paragraph 3.5, just knowing the confidence interval  $[a,b]$  is enough to know whether a result is significant or not:

$0 \in [a, b]$	Non significant results (0 is plausible value)
$0 \notin [a, b]$	Significant results (0 is not a plausible value)

It is therefore not even necessary to calculate the decision threshold. The detection limit can be useful, in the sense that, in the absence of measurement of the sample, it makes it possible to estimate the value of the parameter which would be the smallest possible while still being reasonably likely to be detected. It gives an idea of the performance of the measurement method.

On the other hand, determining the confidence interval gives for each specific measurement an upper limit to the set of parameter values compatible with this measurement. Instead of having a limit valid for all non-significant results, with the confidence interval we have a limit specific to each measurement (therefore more precise).

Thus, if from a measurement  $z$  we determine a confidence interval for the confidence index  $\alpha$ :

$$[\theta^-(z), \theta^+(z)]$$

If  $\theta^-(z) \leq 0$  the result is not significant and we can then estimate that the parameter (of the interval)  $\theta < \theta^+(z)$  avec  $\theta^+(z) \leq \theta_d$

## 5.2. Bayesian point of view

The Gaussian distribution is a member of the family location family. As mentioned previously, we will therefore choose a uniform prior for reasons of symmetry (so-called “non-informative” prior) as is customary (Box & Tiao, 1973). At this point, the credibility intervals exactly coincide with the confidence intervals (Jaynes, 2003; Jaynes & Kempthorne, 1976). We will therefore obtain exactly the same results as with the frequentist method.

If  $[a, b]$  is the credibility interval, we will deduce the same type of consideration as with the frequentist confidence interval.

$0 \in [a, b]$	Non significant results (0 credible value)
$0 \notin [a, b]$	Significant results (0 is not a credible value)

The confidence intervals here are strictly equal to the credibility intervals. So whether it is classic hypothesis testing, the confidence interval criterion or the credibility interval, the results will be the same for statistical significance, decision thresholds or detection limits. In particular, we will have the relationship:

$$\theta_d = 2z_c$$

**(8)**

This implies that the probability of recovery will also necessarily be adequate for the credibility interval. Indeed, the confidence interval is constructed from the principle of the probability of recovery. But the credibility



interval coincides with the confidence interval for the case of homoscedastic Gaussians (Karlen, 2002). Therefore the coverage probability of the Bayesian credibility interval will be the same as that of the confidence interval. Statistical performance should therefore be adequate.

### 5.3. Verification by simulation

Voigtman underlines the crucial importance of verifying the statistical properties of the quantities that we calculate (Voigtman, 2017) :

*« Finally, computer simulations are absolutely essential; no one who has seriously studied the fundamental aspects of detection limits has had infallible intuition, most certainly including the author. Indeed, in regard to detection limit theory and practice, it is fair to say that competently devised and performed computer simulations are the most effective way, by far, to avoid fooling oneself. »( page 197°*

He carried out simulations to check that the characteristic limits determined by Currie had the correct statistical properties. In this case, he verified for homoskedastic ideal systems that by setting the value of  $\alpha_c$  and deducing the decision thresholds and detection limits, we obtain 100.  $\alpha_c$ % false positives by simulations ( 5,005  $\pm$  0.033% compared to a theoretical rate of 5% for 1 million draws) (Voigtman, 2017). Let us specify that here we are indeed in the presence of false positives since the simulation will generate measurements for a zero parameter distribution. False negative rates were also checked (4,998  $\pm$  0.028% compared to a theoretical rate of 5% with 1 million draws). We can therefore consider that these limits have the desired statistical properties for homoscedastic systems. The confidence interval will by definition have the correct coverage probability since it is built to do so. It would be possible but unnecessary to check it.

### 5.4. Conclusions on the homoscedastic case

So whether for classic hypothesis tests, the confidence interval criterion or the credibility interval, the results will be the same for the statistical significance, the decision thresholds or the detection limits. The credible intervals being identical to the confidence intervals, it implies that the coverage probability will necessarily be adequate. It is therefore not necessary to carry out a specific hypothesis test in addition since the simple determination of the confidence interval is enough to give us all the necessary information. We are not adding extra work to ourselves by proceeding in this way, we save ourselves work

Furthermore, as mentioned before, the Neyman-Pearson lemma guarantees that this is the best possible test.

From the confidence interval, it is then possible to provide for non-significant results an upper limit to the desired parameter, more precise than the simple detection limit.

## 6. POISSON DISTRIBUTIONS

### 6.1. frequentist approach

The Poisson case corresponds to counting measurements of the reference and the sample, modeled respectively by random variables  $B$  et  $G = S + B'$  , Poisson distributions of parameters  $\lambda$  and  $\mu = \theta + \lambda$  :

$$p_B(y|\lambda) = \frac{\lambda^y e^{-\lambda}}{y!} \text{ et } p_G(x|\mu) = \frac{\mu^x e^{-\mu}}{x!}$$

The joint probability will then be

$$p_B(x, y|\lambda) = \frac{\lambda^y e^{-\lambda}}{y!} \frac{\mu^x e^{-\mu}}{x!} = \frac{\lambda^y e^{-\lambda} (\theta + \lambda)^x e^{-(\theta + \lambda)}}{y! x!}$$

As in the previous chapters, the objective is to carry out an inference on the parameter  $\theta$  and in particular test the hypothesis  $H_1 = \{ \theta > 0 \}$  against a null hypothesis  $H_0 = \{ \theta = 0 \}$  or  $H_0 = \{ \theta \leq 0 \}$

A first natural approach in the spirit of the Gaussian case presented in the previous chapters would be to consider the random variable of the difference  $N = G - B$ .

Let us mention, however, that the probability distribution of the difference between two Poisson distributions is not a Poisson distribution but a Skellam distribution. (Skellam, 1946) :

$$p_k(x - y|\lambda, \theta) = e^{-(\theta + 2\lambda)} \left( \frac{\lambda}{\lambda + \theta} \right)^{\frac{(x-y)}{2}} I_{|x-y|}(2\sqrt{\lambda(\lambda + \theta)})$$

where  $I_{|k|}$  is the modified Bessel Function of the First Kind.

We see that this probability density will depend both on  $\theta$  and  $\lambda$ . We will also note that intrinsically Skellam's law completely authorizes that  $\mu < \lambda$  and so  $\theta < 0$

Thus and contrary to the Gaussian laws previously studied, the probability density of the difference  $N = G - B$  depends on the parameter  $\lambda$  which we can consider here as a "nuisance" parameter as opposed to the parameter of interest  $\theta$  (Liseo, 2005; Pawitan, 2001).

We cannot therefore directly use the difference  $N$  to study  $\theta$  without knowing or previously estimating this nuisance parameter  $\lambda$ . What is done in the standards and reference texts is either to consider  $\lambda$  as known (in particle physics or astrophysics for example (Lista, 2016) or to resort to a Gaussian approximation of the Poisson law in order to try to reduce it to the Gaussian case (see previous chapters).

Is it possible in this case to find another joint probability density of  $G$  and  $B$  not depending on  $\lambda$  p for the case of Poisson laws?

Let us formulate the problem in the case of the decision threshold: in its traditional formulation, the decision threshold is the observation  $z_c$  of the random variable  $N$  such that :

$$P_{H_0}(N > z_c) = \alpha$$

As presented above, it is not possible in the Poissonian case (and more generally in the non-Gaussian case, we will come back to this) to determine directly  $z_c$  from this equation due to the presence of the nuisance parameter  $\lambda$ .

We see clearly that the reason for this difficulty is to immediately consider the random variable difference  $N$ .

We propose to get around this difficulty by considering conditional random variables, recognized as one of the methods for eliminating nuisance parameters. (Basu, 2011; Liseo, 2005; Sprott, 2008).

## 6.2. Conditional likelihood and hypothesis testing

The crucial point of our approach is to consider conditioning by sufficient statistics.

This is a very natural approach in statistics when faced with nuisance parameters. (Spratt, 2008) since, by definition, the conditional probability density of a random variable by its sufficient statistics is independent of the parameter of this law.

In the particular case of Poisson's laws which interest us here, the sufficient statistic is simply the sum of the random variables  $B + B'$  (more generally, the sum of random variables is the sufficient statistics of probability laws belonging to the family of natural exponentials).

Consequently, we can generalize in a very simple way the previous definition of the decision threshold by considering the conditional probability by  $B + B'$ :

$$\begin{aligned} p_{B'|B+B'}(B' = y' | B + B' = y + y') &= \frac{p_{B+B'|B'}(B + B' = y + y' | B' = y') p_{B'}(B' = y')}{p_{B+B'}(B + B' = y + y')} \\ &= \frac{p_B(B = y) p_{B'}(B' = y')}{p_{B+B'}(B + B' = y + y')} = \frac{\frac{\lambda^y e^{-\lambda}}{y!} \frac{\lambda^{y'} e^{-\lambda}}{y'!}}{\frac{(2\lambda)^{y+y'} e^{-2\lambda}}{(y+y')!}} \end{aligned}$$

$$p_{B'|B+B'}(B' = y' | B + B' = y + y') = \frac{(y+y')!}{y! y'!} \left(\frac{1}{2}\right)^{y+y'}$$

This expression is that of a negative binomial law for  $y'$  with parameters  $y$  and  $\frac{1}{2}$ .

We therefore have a probability density of  $y'$  containing no unknown parameters and, in particular, no  $\lambda$ . We have eliminated the nuisance parameter.

In our situation, assuming  $H_0 = \{\theta = 0\}$ , there is no signal ( $S = 0^\circ$  and  $G = B'$ ). If we make a measurement  $y$  for the reference ( $B$ ), then we will have as probability density of  $x$  in the sample :

$$p_{B'|B+B'}(G = x | B + B' = y + x) = \frac{(y+x)!}{y! x!} \left(\frac{1}{2}\right)^{y+x}$$

Let's lighten the notations by noting  $p_c(x; y) = p_{B'|B+B'}(G = x | B + B' = y + x) = \frac{(y+x)!}{y! x!} \left(\frac{1}{2}\right)^{y+x}$ .

$p_c(x; y)$  is indeed a probability density of  $x$  when we have a measurement of  $y$  and without any unknown parameters.

We know that the cumulative distribution function of the negative binomial distribution of parameters  $y$  and  $\frac{1}{2}$  is (JOHNSON et al., s. d.) the regularized incomplete beta function :

$$p(x < x_c; y) = I_{\frac{1}{2}}(y+1, x_c+1) = 1 - I_{\frac{1}{2}}(x_c+1, y+1)$$

where  $I_x(a, b) = \frac{B_x(a, b)}{B(a, b)}$  is the regularized incomplete beta function with  $B_x(a, b) = \int_0^x \omega^{a-1}(1 - \omega)^{b-1} d\omega$  the regularized incomplete beta function.

We then have :

$$p(x > x_c; y) = I_{\frac{1}{2}}(x_c + 1, y + 1)$$

For a given level of confidence  $\alpha_c$  ( $100 \cdot \alpha_c$  % is the fixed false positive rate that we do not wish to exceed), the decision threshold  $z_c = x_c - y$  can be defined by :

$$I_{\frac{1}{2}}(x_c + 1, y + 1) = \alpha_c$$

(9)

### 6.2.1. Uniformly most powerful test

We know that for the family of natural exponentials, there always exist uniformly more powerful hypothesis tests (UMP tests, -see corollaire 3.4.1 in (Lehmann & Romano, 2005b)). Consider the joint probability density

$$\begin{aligned} p_{G,B}(G = x, B = y) &= p_G(G = x|\mu)p_B(B = y|\lambda) = \frac{\mu^x}{x!} e^{-\mu} \frac{\lambda^y}{y!} e^{-\lambda} = \frac{e^{-\lambda-\mu}}{x! y!} e^{y \ln(\lambda) + x \ln(\mu)} \\ &= \frac{e^{-\lambda-\mu}}{x! y!} e^{(y+x) \ln(\lambda) + (x \ln(\mu) - x \ln(\lambda))} = \frac{e^{-\lambda-\mu}}{x! y!} e^{(x \ln(\frac{\mu}{\lambda}) + (y+x) \ln(\lambda))} \end{aligned}$$

Setting  $\theta = \ln(\frac{\mu}{\lambda})$ , we get :

$$p_{G,B}(G = x, B = y) = \frac{e^{-\lambda-\mu}}{x! y!} e^{(x\theta + (y+x) \ln(\lambda))}$$

From theorem 4.1.1 of Lehmann (Lehmann & Romano, 2005b) the UMP test to decide whether  $\theta > 0$  is based upon the test statistic  $p(G = B' = x | B' + B = x + y)$ .

The hypothesis test we used to define the decision threshold  $z_c = x_c - y$ , is the UMP test for this hypothesis. The decision threshold  $z_c$  is optimal. This therefore confirms the interest of conditional likelihoods in the presence of nuisance parameters.

### 6.2.2. Conditional likelihood in the presence of a signal

Now suppose the presence in the sample of a signal  $S$ , obeying a Poisson law of parameter  $\theta$ . After a measurement  $y$  of the reference, we will have a  $y'$  contribution of the noise in the sample. The probability density of  $y'$  will be

$$p_{B'|B+B'}(B' = y' | B + B' = y + y')$$

If we have a measurement of  $x$  for the sample, we have to subtract the contribution of the noise to know the contribution of the signal :

$$\begin{aligned}
P(S = x - y', B' = y' | \theta, B + B' = y + y') &= \frac{P(S = x - y', B' = y', B + B' = y + y' | \theta)}{P(B + B' = y + y')} = \\
&= \frac{P(S = x - y', B' = y', B = y | \theta)}{P(B + B' = y + y')} = \frac{P(S = x - y' | \theta) P(B' = y' | B + B' = y' + y) P(B + B' = y + y')}{P(B + B' = y + y')} \\
&= P(S = x - y' | \theta) P(B' = y' | B + B' = y' + y) = P(S = x - y' | \theta) p(y'; y)
\end{aligned}$$

If we do the sum over all possible  $y'$ , we get the following density

$$p_c(x, y | \theta) = \sum_{y'=0}^x P(S = x - y' | \theta) p(y'; y)$$

As a convolution of a negative binomial  $p_c(y'; y)$  and a Poisson distribution  $P(S = x - y' | \theta)$ . This simply expresses the idea that the probability of having a measurement  $x$  for the sample will be the sum of the probability of getting  $x - y'$  from the Poisson distribution times the probability of measuring  $y'$  knowing that we measured  $y$  for the reference.

This convolution of a Poisson distribution and a negative binomial distribution is what is called a Delaporte distribution. (JOHNSON et al., s. d.). This distribution has no simple expression but can be evaluated numerically (a R « package » exists). Note that  $p_{G|B}(x|y, \theta)$  will have a mean of  $\theta + y$  and a variance of  $\theta + 2y$ .

### 6.3. Bayesian method

Let us first recall that a gamma law  $\text{Gamma}(\alpha, \beta)$  can be expressed as :

$$\Gamma(x|\alpha, \beta) = \frac{x^{\alpha-1} e^{-\beta x} \beta^\alpha}{\Gamma(\alpha)}$$

To directly eliminate the nuisance parameter in a Bayesian approach, it would be necessary to proceed by marginalization (integrating on  $\lambda$  as we did for the homoscedastic gaussians). Before that, we will determine the posterior distribution of the parameter of interest. Using the notations from the previous paragraph, we know that the joint probability is:

$$p_{(G,B)}(x, y | \mu, \lambda) = \frac{\mu^x e^{-\mu} \lambda^y e^{-\lambda}}{x! y!}$$

Using the Bayesian formalism with a generalized Jeffreys prior (Jeffreys, 1946)  $\pi(\mu, \lambda) = \frac{1}{(\lambda\mu)^a}$ , where the hyperparameter  $a = 0$  for a uniform prior,  $a = 1/2$  a Jeffreys prior and  $a = 1$  for an inverse prior. This will allow us to evaluate the influence and adequacy of the prior at the end of the calculation. This is good practice in the application of Bayesian methodologies. We can obtain the joint probability density of the parameters:

$$p_{(\Gamma, \Phi)}(\mu, \lambda | x, y) \sim \frac{\mu^x e^{-\mu} \lambda^y e^{-\lambda}}{x! y!} \pi(\mu, \lambda) = \frac{\mu^{x-a} e^{-\mu} \lambda^{y-a} e^{-\lambda}}{x! y!}$$

Defining  $y_a = y - a$  and  $x_a = x - a$ , the joint probability density of the parameters (posterior distribution) would then be:

$$p_{(\Gamma, \Phi)}(\mu, \lambda | y_a) = C \pi(\lambda, \mu) \frac{\lambda^{y_a} e^{-\lambda} \mu^{x_a} e^{-\mu}}{y! x!} = C \frac{\lambda^{y_a} \mu^{x_a} e^{-(\lambda+\mu)}}{y! x!}$$

With C a normalization constant. We can also prove that this constant is  $C = \frac{x! y!}{\Gamma(x_a+1)\Gamma(y_a+1)}$ .

$$p_{(\Gamma, \Phi)}(\mu, \lambda | x_a, y_a) = \frac{\lambda^{y_a} \mu^{x_a} e^{-(\lambda+\mu)}}{\Gamma(y_a + 1)\Gamma(x_a + 1)} = \frac{\lambda^{y_a} (\lambda + \theta)^{x_a} e^{-(2\lambda+\theta)}}{\Gamma(y_a + 1)\Gamma(x_a + 1)}$$

(10)

To eliminate the nuisance parameter  $\lambda$ , in the Bayesian paradigm, we just need to integrate with respect to this parameter. We move from a likelihood with 2 parameters  $p_{(\Gamma, \Phi)}(\mu, \lambda | x, y)$  to a single-parameter likelihood  $p_{\theta}(\theta | x, y)$  (a marginal likelihood (Sprott, 2008)).

$$\begin{aligned} p_{\theta}(\theta | x_a, y_a) &= \int_0^{\infty} p_{(\Gamma, \Phi)}(\lambda + \theta, \lambda | x_a, y_a) d\lambda \\ &= \frac{1}{\Gamma(x_a + 1)\Gamma(y_a + 1)} \int_0^{\infty} (\lambda + \theta)^{x_a} e^{-(2\lambda+\theta)} \lambda^{y_a} d\lambda \end{aligned}$$

To our knowledge, there is no simple and general expression for this difference in gamma laws. (Johnson et al., 1994)

### 6.3.1. Hypothesis testing

By analogy with the frequentist case, the hypothesis test that we wish to carry out is to know if  $\lambda = \mu$ .

We could therefore be interested in the parameter  $\theta = \mu - \lambda$  and test the alternative hypothesis  $=\{H_1 = \{\theta > 0\}\}$ .

This is equivalent to being interested in  $\mu > \lambda$  and so  $\tau = \frac{\mu}{\lambda} > 1$ . The ratio of two gamma laws  $Gamma(x_a + 1, 1)$  et  $Gamma(y + 1, 1)$  is a Beta Prime distribution  $\beta'(x + 1, y + 1)$  whose cumulative distribution function is known (Bourguignon, 2021). The probability that  $\tau = \frac{\mu}{\lambda} > 1$  can be expressed as a regularized incomplete beta function:

$$I_{\frac{1}{2}}(x_a + 1, y_a + 1) = p_{\Gamma-\Phi}(\theta > 0) = 1 - p_{\Gamma-\Phi}(\theta < 0) = p_{\frac{\Gamma}{\Phi}}(\tau > 1)$$

It is therefore possible to define a decision threshold  $x_{ac}$ , for a given confidence index  $\alpha_c$  as :

$$I_{\frac{1}{2}}(x_{ac} + 1, y_a + 1) = \alpha_c$$

We find the same result for the decision threshold as in the frequentist approach of the previous paragraph with a small difference (the replacement of  $x$  by  $x_a$  and  $y$  by  $y_a$ ). This difference is linked to the choice of the

prior (which is logical and natural) and diminishes in influence if  $x$  and  $y$  are much larger than 1. It is therefore only significant for low counting values. Note also that for a uniform prior ( $a = 0$ ) the frequentist and Bayesian approach precisely coincide.

We can express the incomplete regularized beta function as a function of the sum of binomial coefficients (Kirkpatrick & Young, 2009; V. Vivier & Aupiais, 2007):

$$I_{1/2}(x_a + 1, y_a + 1) = \left(\frac{1}{2}\right)^{x_a + y_a + 1} \sum_{i=0}^{x_a} C_i^{x_a + y_a}$$

Where  $C_i^{x_a + y_a}$  is the binomial coefficient:

$$C_i^{x_a + y_a} = \frac{(x_a + y_a)!}{i! (x_a + y_a - i)!}$$

There are methods for inverting the incomplete beta function cumulative distribution function of the beta distribution. (Temme, 1992). In order to obtain the decision threshold, mathematical software also makes it possible to invert this function which is frequently found in the statistical literature.,

Approximations of the beta incomplete regularized function do exist (Abramowitz & Stegun, 1965) :

$$I_x(a + 1, b + 1) = \Phi \left[ 3 \frac{(bx)^{\frac{1}{3}} \left(1 - \frac{1}{9b}\right) - (a(1-x))^{\frac{1}{3}} \left(1 - \frac{1}{9a}\right)}{\sqrt{\frac{(a(1-x))^{2/3}}{a} + \frac{(bx)^{2/3}}{b}}} \right] + O\left(\frac{1}{\min(a, b)}\right)$$

**(11)**

Note that this approximation is considered valid at 0.5% for values of  $a$  and  $b$  such that  $a+b > 6$ .

### 6.3.2. Marginal likelihood, binomial expansion and credibility intervals

w  
e

w  
i  
l  
l

u  
s  
e

t  
h  
e

b  
i  
n  
o  
m

i  
a  
l

Probability Ratio Model for Simultaneous Source Detection and Count Rate Analysis:", "title-short": "A Simpler Alternative to the Probability Ratio Model for Simultaneous Source Detection and Count Rate Analysis", "volume": "109", "author": [{"family": "Lemay", "given": "Fran\u00e7ois"}], "issued": {"date-parts": [{"2015", 12}]}, {"id": "KB5StWU3/OSMwLrr4", "uris": ["http://zotero.org/users/5664173/items/ZAPVKJSV"], "itemData": {"id": "2653", "type": "article-journal", "abstract": "The analysis of low-level or background dominant radioactivity is complicated by the fact that sample net rate of activity above background may be negative, because of random fluctuations. The traditional large sample confidence intervals can contain negative values for the net rate, although we know the net rate is positive. This problem leads to statistically unsound practices such as the reporting of \u201cles than\u201c values when the net value lies below a certain \u201cdetectable limit\u201c. In this paper we present two Bayesian analyses of the data which take account of the fact that the net rate is positive, and thus always lead to positive estimates and probability intervals for the true underlying rate. The estimates and intervals are compared with classical results for twenty trial data sets.", "container-title": "Health Physics", "DOI": "10.1097/00004032-198211000-00007", "ISSN": "0017-9078", "issue": "5", "language": "en", "page": "693-703", "source": "Crossref", "title": "The Statistical Analysis of Low-level Radioactivity in the Presence of Background Counts:", "title-short": "The Statistical Analysis of Low-level Radioactivity in the Presence of Background Counts", "volume": "43", "author": [{"family": "Little", "given": "Roderick J. A."}], "issued": {"date-parts": [{"1982", 11}]}, "schema": "https://github.com/citation-style-language/schema/raw/master/csl-

(10) then marginalize in relation to  $\lambda$ .

$$p_{\Theta}(\theta | x_a, y_a) = \int_0^{\infty} p_{(\Gamma, B)}(\lambda, \mu = \lambda + \theta | x_a, y_a) d\lambda = \frac{1}{\Gamma(x_a + 1)\Gamma(y_a + 1)} \int_0^{\infty} (\lambda + \theta)^{x_a} e^{-(2\lambda + \theta)} \lambda^{y_a} d\lambda$$

If we restrict ourselves to  $x_a \in \mathbb{N}$  et  $b \in \mathbb{N}$ ,  $\Gamma(x_a + 1) = (x_a)!$  et  $\Gamma(y_a + 1) = (y_a)!$

We get :

$$p_{\Theta}(\theta | x_a, y_a) = \frac{1}{(x_a)!(y_a)!} \int_0^{\infty} (\lambda + \theta)^{x_a} e^{-(2\lambda + \theta)} \lambda^{y_a} d\lambda$$

But

$$(\lambda + \theta)^{x_a} = \sum_{i=0}^{x_a} C_g^i \theta^i \lambda^{x_a - i}$$

(Where  $C_i^g$  is the binomial coefficient

Therefore :

$$\begin{aligned} p_{\Theta}(\theta | x_a, y_a) &= \frac{1}{(x_a)!(y_a)!} \int_0^{\infty} \sum_{i=0}^{x_a} \frac{x_a!}{i!(x_a - i)!} \theta^i \lambda^{x_a + y_a - i} e^{-(2\lambda + \theta)} d\lambda \\ &= \frac{1}{y_a!} \sum_{i=0}^{x_a} \frac{\theta^i e^{-\theta}}{i!(x_a - i)!} \int_0^{\infty} \lambda^{x_a + y_a - i} e^{-(2\lambda)} d\lambda \end{aligned}$$



Knowing that  $\int_0^\infty x^\nu e^{-\mu x} dx = \frac{\Gamma(\nu)}{\mu^\nu}$ , we get for  $\theta > 0$

$$p_\Theta(\theta|x_a, y_a) = \frac{1}{y_a!} \sum_{i=0}^{x_a} \frac{\theta^i e^{-\theta}}{i! (x_a - i)!} \frac{(x_a + y_a - i)!}{2^{x_a + y_a - i + 1}}$$

**(12)**

We can recognize the product of two terms in this sum. One  $\frac{\theta^i e^{-\theta}}{i!}$ , is a Poisson distribution. The other is a negative binomial distribution  $\frac{(x_a + y_a - i)!}{y_a! 2^{x_a + y_a - i + 1}}$

In other words :

$$p_\Theta(\theta|x_a, y_a) = \sum_{i=0}^{x_a} p_S(i|\theta) p_V(x_a - i|y_a)$$

where :

$$p_S(i|\theta) = \frac{\theta^i e^{-\theta}}{i!}$$

Is a term from a Poisson law And

$$p_V(x_a - i|y_a) = \frac{(x_a + y_a - i)!}{y_a!}$$

Is a term from a negative binomial law of parameters  $(y_a, \frac{1}{2})$

This is the convolution of a Poisson distribution and a negative binomial distribution. We find again the frequentist expression of the paragraph 6.2.2 taking into account the effect of the chosen priors (which results in the transposition of  $x$  to  $x_a$  and  $y$  to  $y_a$ ). The influence of the priors will only be important for low count values.

We can see that the two methods recommended for getting rid of nuisance parameters (use of conditional likelihood in the frequentist case and marginal likelihood in the Bayesian case) lead to similar results (within the influence of priors).

### 6.3.3. Confidence intervals and detection limits

To obtain the detection limit, it would therefore be necessary, knowing the decision threshold  $x_{ac}$ , we must find  $\theta_d$  such that :

$$\beta_c = \frac{1}{(y_a)!} \sum_{i=0}^{x_{ac}} \frac{1}{i! (x_{ac} - i)!} \frac{(x_{ac} + y_a - i)!}{2^{x_{ac} + y_a - i + 1}} \int_{\theta_d}^{\infty} \theta^i e^{-\theta} d\theta$$

It should be noted that the integral is an incomplete gamma function (Gradshteyn et al., 2000) :

$$\int_{\theta_d}^{\infty} \theta^i e^{-\theta} d\theta = \Gamma(i, \theta_d) = (i)! e^{-\theta_d} \sum_{j=0}^i \frac{\theta_d^j}{j!}$$

And so,

$$\beta_c = \frac{1}{(y_a)!} \sum_{i=0}^{x_{ac}} \frac{1}{i! (x_a - i)!} \frac{(x_{ac} + y_a - i)!}{2^{x_{ac} + y_a - i + 1}} (i)! e^{-\theta_d} \sum_{j=0}^i \frac{\theta_d^j}{j!} = e^{-\theta_d} \sum_{i=0}^{x_{ac}} \frac{(x_{ac} + y_a - i)!}{(y_a)! (x_{ac} - i)!} \frac{1}{2^{x_{ac} + y_a - i + 1}} \sum_{j=0}^i \frac{\theta_d^j}{j!}$$

Knowing the decision threshold  $x_{ac}$ , the detection limit  $\theta_d$  must verify :

$$\beta_c = e^{-\theta_d} \sum_{i=0}^{y_a + k - a} \frac{(x_{ac} + y_a - i)!}{(y_a)! (y_a + x_{ac} - i)!} \frac{1}{2^{g_c + y_a - i + 1}} \sum_{j=0}^i \frac{\theta_d^j}{j!}$$

This formula could be evaluated numerically in particular for small values of  $y_a$ .

As we saw previously, the detection limit is nothing other than the upper limit of the confidence interval for a measurement equal to the decision threshold. To obtain the limits of a confidence interval, it is therefore more generally sufficient to set  $\alpha$  and  $\beta$  as lower and upper confidence indexes of the confidence interval. It is then necessary to find  $\theta_-$   $\theta_+$ , such that for measurements  $y$  of the reference and  $z + y$  of the sample we obtain

$$\alpha = \sum_{i=0}^{y_a + k - a} \frac{(2y_a + k - i)!}{(y_a)! (y_a + k - i)!} \frac{1}{2^{2y_a + k - i + 1}} \int_0^{\theta_-} \theta^i e^{-\theta} d\theta$$

And

$$\beta = \sum_{i=0}^{b + k - a} \frac{(2y_a + k - i)!}{(y_a)! (y_a + k - i)!} \frac{1}{2^{2y_a + k - i + 1}} \int_{\theta_+}^{\infty} \theta^i e^{-\theta} d\theta$$

## 6.4. Synthesis

For low-level metrology with Poisson laws, it is possible to determine a decision threshold from the frequentist point of view and from the Bayesian point of view and then to note their compatibility. Furthermore, we can prove using Neyman Pearson's lemma that this common threshold is the best possible. Likewise, the two approaches (conditional and marginal) lead to very similar results for the elimination of the nuisance parameter and the determination of the likelihood of the desired signal. In all these cases, only measurements with very low counting rates would lead to significant differences in results. It was not possible to define a simple expression detection limit even if it would be possible to determine it numerically.

We can now focus on the transition to the limit of Poisson's laws for large counting values. This will allow us to determine more explicit formulas which will apply for example to the case of measuring radioactivity. NOTE :

It is also possible to determine the distribution of  $\theta$  based on the measurements  $x_a, y_a$ :

$$p_{\Theta}(\theta | x_a, y_a) = \frac{1}{\Gamma(x_a + 1)\Gamma(y_a + 1)} \iint \lambda^{x_a} e^{-\lambda} \mu^{y_a} e^{-\mu} \delta(\theta + \mu - \lambda) d\mu d\lambda$$

It is then possible to express this probability distribution as hypergeometric functions (see Annexe 3).

## 7. HETEROSCEDASTIC GAUSSIANS AS A POISSON LAW LIMIT

### 7.1. Current method

#### 7.1.1. Decision thresholds and detection limits - the classic Currie approach

The current method is frequentist in its essence and was first developed by Currie (Currie, 1968). The standard in force for measuring radioactivity has colored this approach with considerations that are supposed to be Bayesian. (ISO, 2010a) drawing inspiration from the work of Weise (Weise, 1998; Weise et al., 2006, 2013). We will see what it is in a later paragraph..

In the case of radioactivity measurement, we naturally consider that the desired signal will behave according to Poisson's law. This has an intrinsic uncertainty (its variance is non-zero)

We thus get :

$$p_S(z|\theta) = \frac{\theta^z}{z!} e^{-\theta}$$

For large enough  $\theta$ , one can use the approximation (Barlow, 1993; Riley et al., 2006):

$$p_S(z|\theta) \sim \frac{e^{-\left(\frac{z-\theta}{2\theta}\right)^2}}{\sqrt{2\pi\theta}}$$

A Poisson distribution for large parameter values  $\theta$  behaves like a Gaussian with mean and variance  $\theta$ .

If the baseline also follows a Poisson distribution with a parameter  $\lambda$  much larger than 1, we can approximate a Gaussian law:

$$p_B(y|\lambda) = \frac{e^{-\left(\frac{y-\lambda}{2\lambda}\right)^2}}{\sqrt{2\pi\lambda}}$$

Setting :

$$\sigma_B^2 = \lambda$$

It is then possible to determine the distribution of the sample as a convolution product:

$$p_G(x|\mu) = (p_{B'} \oplus p_S)(x|\mu)$$

We can determine the convolution of two Gaussians (Bromiley, 2003) which will itself be a Gaussian:

$$p_G(x|\mu) \sim \frac{e^{-\left(\frac{x-\mu}{2(\lambda+\theta)}\right)^2}}{\sqrt{2\pi(\lambda+\theta)}}$$

Where the variance of the sample is the addition of the signal and the reference variances

$$\begin{aligned}\sigma_G^2 &= \lambda + \theta \\ \Rightarrow \sigma_G &= \sqrt{\lambda + \theta}\end{aligned}$$

To obtain the net distribution, we must subtract the noise included in the sample. In terms of distributions as we indicated in the introduction, this corresponds to making a cross-correlation of the distributions, which is itself a Gaussian:

$$p_N(z|\theta) \sim \frac{e^{-\frac{(z-\theta)^2}{2\sigma_N^2}}}{\sqrt{2\pi}\sigma_N}$$

**(13)**

Where  $\sigma_N^2 = \sigma_B^2 + \sigma_G^2 = \sigma_B^2 + \sigma_B^2 + \theta = 2\lambda + \theta$

Indeed, in a difference as in a sum of random variables, the resulting variance is the sum of the variances.

We seek to determine the result of a hypothesis test with the null hypothesis  $[\theta = 0]$ . It therefore seemed quite natural to consider that (Currie, 1968, 2008) :

$$\sigma_N(\theta = 0) = \sqrt{2\lambda + 0} = \sqrt{2\lambda}$$

Then estimate  $\lambda$  by replacing it with the measured value of the reference ( $y$ , which is the maximum likelihood estimator of the Poisson distribution for the reference). In fact, although this is not always explained in the scientific literature, the different authors find themselves confronted with the problem of an unknown nuisance parameter and assume it to be perfectly known as a solution to the problem (Currie, 1968; Lista, 2016). This is a profile likelihood process (Spratt, 2008) We then fall back on the homoskedastic hypothesis test (equations (5) et (6)) . The formula for the decision threshold is therefore exactly the same as for the homoscedastic case.:

$$z_c = \sigma_N \Phi^{-1}(1 - \alpha_c) = \sqrt{2}\sigma_B \Phi^{-1}(1 - \alpha_c) = \sqrt{2y}\Phi^{-1}(1 - \alpha_c)$$

**(14)**

with  $\Phi^{-1}(1 - \alpha_c) = k_{1-\alpha}$

$$z_c = \sigma_N \Phi^{-1}(1 - \alpha_c) = \sqrt{2}\sigma_B \Phi^{-1}(1 - \alpha_c) = \sqrt{2y}k_{1-\alpha}$$

**(15)**

While the detection limit is determined by the equation:

$$\beta_c = \int_{-\infty}^{z_c} p_N(z|\theta_d) dz = \frac{1}{\sqrt{2\pi}\sigma_N} \int_{-\infty}^{z_c} e^{-\frac{(z-\theta_d)^2}{2\sigma_N^2}} dz = 1 - \Phi\left(\frac{\theta_d - z_c}{\sigma_N}\right)$$

Which leads to the equation:

$$\Phi^{-1}(1 - \beta_c) = \frac{\theta_d - z_c}{\sigma_N}$$

As we have seen,  $\sigma_N$  is a function of  $\theta$ :

$$\Phi^{-1}(1 - \beta_c) = \frac{\theta_d - z_c}{\sqrt{2k_{1-\alpha}\sigma_B^2 + \theta_d}} = \frac{\theta_d - z_c}{\sqrt{z_c + \theta_d}}$$

$$(\Phi^{-1}(1 - \beta_c))^2 = \frac{(\theta_d - z_c)^2}{z_c + \theta_d}$$

If, as is customary, we take  $\beta_c = \alpha_c$

$$\theta_d = 2z_c + (k_{1-\alpha})^2$$

**(16)**

In Currie's approach, these are the formulas we obtain for the decision threshold and detection limit (Currie, 1999b, 2008; Strom & MacLellan, 2001). However, the Gaussian approximation for a Poisson distribution is only valid for large  $\theta$  (Barlow, 1993; Riley et al., 2006). It is therefore not possible to use it for  $\theta \approx 0$  ! Yet this is what is done in the classic Currie approach. Let us repeat that this also assumes perfect knowledge of the reference ( $\lambda$ ), which is in reality very rarely the case.

We also clearly see the conceptual problem; the hypothesis test will in no way depend on the variance of the signal. Whether or not the signal is tainted by significant "noise", the hypothesis test remains the same. In the limit considering zero dispersion for  $\theta = 0$  and infinite  $\theta > 0$ , the hypothesis test would remain the same, while under such conditions it is clear that it would be impossible to differentiate a signal from the baseline.

Several other points remain problematic in the classic approach. They will be addressed in the following paragraphs and we will see how the conditional or marginal likelihood approach provides solutions.

What is done in the standards and reference texts (FDA, 2004; IAEA, 2017) is to consider that the parameter  $\theta = \mu - \lambda$  will be expressed as a function  $z = x - y$  without further formal derivation ((FDA, 2004; IAEA, 2017; ISO, 2010a) and to assume that the Gaussian approximation of the Poisson law is valid. We therefore obtain the probability density of  $z$  in the form of the equation (13) :

$$p_N(z|\theta) \sim \frac{e^{-\frac{(z-\theta)^2}{2\sigma_N^2}}}{\sqrt{2\pi\sigma_N}} = \frac{e^{-\frac{(z-\theta)^2}{2(\lambda+\mu)}}}{\sqrt{2\pi(\lambda+\mu)}}$$

The variance is in fact assumed to be proportional to the count values:

$$\sigma_N^2 = \lambda + \mu \sim x + y$$

Which gives, in a Gaussian approximation, confidence intervals for  $\theta$  of the type:

$$[z \pm k\sigma_N] = [(x - y) \pm k(\sqrt{x + y})]$$

where  $k$  is the coverage factor.

As indicated previously, we assume that  $\lambda$  is known and can be approximated by  $y$  to get rid of the nuisance parameter. Furthermore, we assume that we can also approximate  $\mu \sim x$ . Note the inconsistency between the confidence interval where a measurement of  $z = x - y$  will lead to the possibility of having a confidence

interval containing 0 if  $z < k\sqrt{x+y}$  and the decision threshold of the previous paragraph which will reject this possibility if  $z > k\sqrt{2y}$ . This inconsistency is also that of assuming that  $\lambda \sim y$  because  $\lambda \gg 1$  but not that  $\mu = \lambda + \theta \sim x + y$ .

### 7.1.2. Bayesian approach in metrology

Some authors conclude that Bayesian statistics encounter too many difficulties to be used in metrology ((Willink, 2010a, 2010b, 2013). The criticisms relate in particular to the fact that the statistical performances are not adequate. As these statistical performances are often frequentist concepts, this type of discussion tends to focus on epistemological principles without it being easy to decide (Bergamaschi et al., 2013; Mana & Palmisano, 2014)

When we consider a parameter which by nature is strictly positive (such as mass or activity), almost unanimous usage dictates that we use a positive support prior.. That is to say, if  $\theta$  is the parameter of the desired signal, the prior  $\pi(\theta)$  will be defined so that  $\pi(\theta) = 0$  if  $\theta < 0$ . Usually, we use a prior that we will call Heavyside prior defined byr

$$\begin{aligned} \pi(\theta) &= 0 \text{ si } \theta < 0 \\ \pi(\theta) &= C \text{ si } \theta \geq 0 \end{aligned} \tag{17}$$

where  $C$  is a positive constant. This is the case of the overwhelming majority of publications and standards that use Bayesian methodologies in the field of metrology. (Analytical Method Committee, The Royal Society of Chemistry, 2010; Analytical Methods Committee, The Royal Society of Chemistry, 2008; Bergamaschi et al., 2013; Bochud et al., 2007; Heisel et al., 2009; IAEA, 2017; Kirkpatrick et al., 2013, 2015; Korun et al., 2014, 2016; Laedermann et al., 2005; Lira, 2009; Michel, 2016; Miller et al., 2002; Nosek & Nosková, 2016; Rivals et al., 2012; A. Vivier et al., 2009; Weise et al., 2006; Zähringer & Kirchner, 2008). Some authors have identified difficulties with this prior but attributing these to Bayesian methodology in general. (Willink, 2010b, 2010c, 2013).

This amounts in our formulation presented in paragraph 4.2, to consider that the variable  $\theta$  must be positive because the desired signal must be positive. Let us insist on the fact that we are taking our desires for realities.. What we want to achieve is the true value, but what we have access to through measurement is an inference on the parameter of the variable  $\Omega = \Gamma - \Phi$ , the difference between  $\mu$  and  $\lambda$ .

An attempt has nevertheless been made to introduce Bayesian concepts into the definition of characteristic limits (decision thresholds and detection limits): The measurement of ionizing radiation.

### 7.1.3. Pseudo Bayesian approach of the ISO 11929 standard

In the field of radioactivity measurement, the ISO 11929 standard is the reference (ISO, 2010a). It uses the principle of maximum entropy (Jaynes, 2003; Weise et al., 2006) to establish that the probability density is expressed as follows (annex F of (ISO, 2010a)):

$$p_{\Omega}(\theta|y) = C\pi(\theta)e^{-\frac{(\theta-y)^2}{2u_{\theta}^2(\theta)}}$$

Where  $\pi(\theta)$  is the Heavyside prior :  $\pi(\theta) = 0$  if  $\theta \in ]-\infty, 0]$  and  $\pi(\theta) = 1$  if  $\theta \in [0, +\infty]$ .  $C$  is a normalization constant and  $u_{\theta}(\theta)$  is the uncertainty for the variable  $\theta$ .

The principle of maximum entropy determines the type of distribution in the least arbitrary way possible, taking into account all constraints. It actually states that the least arbitrary distribution possible on  $[-\infty, +\infty]$  given a mean and a standard error is a gaussian distribution. On the other hand, on  $[0, +\infty]$ , it is possible to show that the distributions are truncated Gaussian distributions (Dowson & Wragg, 1973). Since the standard deviation is not known since it depends on  $\theta$  and  $\lambda$ , the authors are forced to assume that  $u_{\theta}(\theta) \sim u_y(y)$  where  $u_y(y)$  is the uncertainty of the variable  $y$ . By normalizing the probability density, we obtain :

$$p_{\Delta}(\theta|y) = \frac{e^{-\frac{(\theta-y)^2}{2u_y^2(y)}}}{\sqrt{2\pi} u_y(y) \Phi\left(\frac{y}{u_y(y)}\right)} \text{ avec } \theta \in [0, +\infty]$$

This probability density is used to determine an estimator and a credibility interval. Regarding the estimator ( $\hat{\theta} = \hat{y}$  in ISO notations) :

$$\hat{\theta} = \int_0^{+\infty} \theta \frac{e^{-\frac{(\theta-y)^2}{2u_y^2(y)}}}{\sqrt{2\pi} u_y(y) \Phi\left(\frac{y}{u_y(y)}\right)} d\theta = y + \frac{u_y(y)}{\sqrt{2\pi}} \frac{e^{-\frac{y^2}{2u_y^2(y)}}}{\Phi\left(\frac{y}{u_y(y)}\right)}$$

The authors of the standard also calculate a credibility interval  $[\theta^{\triangleleft}, \theta^{\triangleright}]$ .

$$p_{\Delta}(\theta < \theta^{\triangleleft}|y) = \int_0^{\theta^{\triangleleft}} \frac{e^{-\frac{(\theta-y)^2}{2u_y^2(y)}}}{\sqrt{2\pi} u_y(y) \Phi\left(\frac{y}{u_y(y)}\right)} d\theta = \alpha/2$$

$$\Phi\left(\frac{\theta^{\triangleleft} - y}{u_y(y)}\right) = \Phi\left(\frac{y}{u_y(y)}\right) \left(1 - \frac{\alpha}{2}\right)$$

$$\theta^{\triangleleft} = y - u_y(y) \Phi^{-1}\left(\Phi\left(\frac{y}{u_y(y)}\right) \left(1 - \frac{\alpha}{2}\right)\right)$$

And

$$\theta^{\triangleright} = y + u_y(y) \Phi^{-1}\left(1 - \Phi\left(\frac{y}{u_y(y)}\right) \frac{\alpha}{2}\right)$$

This interval only contains positive terms because, due to the chosen prior, we must have  $\theta^{\triangleleft} > 0 \forall y$ . The case of credibility intervals for  $y < 0$  is evacuated by specifying that this interval must only be calculated for a measurement greater than the decision threshold.

In the ISO 11929 standard, the decision threshold is calculated using a frequentist mode. And for a good reason ! Indeed, the choice of the Heavyside prior, by definition prohibits the possibility that the parameter is not greater than zero and therefore that the credibility interval contains 0. The value  $\theta = 0$  having a null Lebesgues

measure, no integral equation will be able to tell us that this is possible unless we use not functions but distributions in the sense of Schwarz (Dirac delta function). This is verified in the calculation we have just performed. If we assume that  $\theta > 0$ , we cannot show that  $\theta = 0$  has a non-zero probability. Faced with this impasse, the only solution was to use a frequentist method.

By applying the inverse Bayes' theorem:

$$p_{G-B}(y|\theta) = \frac{e^{-\frac{(\theta-y)^2}{2u_\theta^2(\theta)}}}{\sqrt{2\pi}u(y)}$$

(ISO, 2010a)

From there, it is possible to calculate the decision threshold as  $\alpha_c = p_N(y > y_c | \theta = 0) = \int_{y_c}^{\infty} p_N(y|0) dy = \int_{y_c}^{\infty} \frac{1}{\sqrt{2\pi}u(y)} e^{-\frac{(0-y)^2}{2u_\theta^2(0)}} dy = 1 - \Phi\left(\frac{y_c}{u(\theta=0)}\right) \theta = 0 \quad y_c = u(\theta = 0) \Phi^{-1}(1 - \alpha_c) = \sqrt{2y} \Phi^{-1}(1 - \alpha_c)$

As we have seen, this is the application of the frequentist method.

This is not reprehensible in itself and it is inevitable due to the Heavyside prior, but one might wonder the benefit of using a Bayesian formalism to ultimately use frequentist methods. Note that this amounts to making the Currie approximation which leads to the equation (14).

This underestimates the decision threshold and does not give good statistical performances as we will see in numerical experiments.

The detection limit is also determined in a frequentist manner with the same approximation used by Currie.

We can therefore list the errors or problems as follows:

:

- By using the principle of maximum entropy, the standard is limited to the use of truncated Gaussian distributions and only those.
- Furthermore, the probability distribution of maximum entropy is only Gaussian (truncated or not) if the variance and the mean are known
- • It was therefore necessary to assume the known variance, which implies estimating the nuisance parameter (replacing the nuisance parameter with an estimate)
- The prior used is a Heavyside prior which implies that the desired parameter  $\theta > 0$ . This prior excludes the possibility of using Bayesian methods to determine decision threshold and detection limit.
- The characteristic limits determined are in fact determined by the Currie method. We will see later what are their statistical performances.

## 7.2. Proposed approach using marginal and conditionnal likelihood

We have already seen that in an estimation interval approach, it is not necessary to calculate the decision threshold since the simple view of the confidence or credibility interval is enough to know the significant nature or not of the measurement. .



For comparison with the classical method, we will nevertheless calculate the characteristic limits.

The decision threshold is the smallest measure from which the confidence or credibility interval will include the value zero. As we saw in the paragraph 4.3.1, we want to get a  $z_c$  such that for a given confidence index  $\alpha_c$ , the credibility interval of the net signal barely includes zero:

$$\alpha_c = \int_{-\infty}^0 p_{\theta}(\theta|z_c) d\theta$$

### 7.2.1. Convolution of a Poisson distribution and a negative binomial distribution

We have seen in the case of Poisson distributions that the conditional and marginal likelihoods are convolutions of a negative binomial distribution and a Poisson distribution (Delaporte's law). This convolution has no simple expression. However, the negative binomial distribution converges quite quickly to the normal distribution. This is due to the fact that the negative binomial law  $NB(y, p)$  for  $p = 1/2$  can be seen as a sum of geometric laws, which, through the central limit theorem, ensures rapid convergence towards a Gaussian distribution (S. Bagui & Mehra, 2019, 2019). (JOHNSON et al., s. d.) gives as a benchmark a value of approximately  $y \sim 10$ .

$$p_c(y; y') = \frac{(y + y')!}{y! y'!} \left(\frac{1}{2}\right)^{y+y'+1} \sim \frac{e^{-\frac{(y'-y)^2}{4y}}}{\sqrt{2\pi 2y}}$$

The convolution product of a negative binomial distribution and a Poisson distribution can then be considered as the convolution product of a Gaussian distribution with mean  $y$  and variance  $2y$  with a Poisson distribution  $S$ .

$$p_S(u) = \frac{\theta^u}{u!} e^{-\theta}$$

A Poisson distribution with parameter  $\theta$  can be approximated by a Gaussian with mean  $\theta$  and variance  $\theta$  (Barlow, 1993) only if  $\theta$  is large:

$$\frac{\theta^z}{z!} e^{-\theta} \sim \frac{e^{-\frac{(z-\theta)^2}{2\theta}}}{\sqrt{2\pi\theta}}$$

for  $\theta \gg 1$

Here, nothing allows us to say that  $\theta$  is large. Quite the contrary!

On the other hand, if a Gaussian distribution has a sufficiently large variance, we can consider that it can be equivalent to a Poisson distribution. (Figure 6)

Indeed if  $y \gg 1$ :

$$p_c(y; y') \sim \frac{e^{-\frac{(y'-y)^2}{4y}}}{\sqrt{2\pi 2y}} = \frac{e^{-\frac{((y'+y)-2y)^2}{4y}}}{\sqrt{2\pi 2y}} \sim \frac{(2y)^{y+y'} e^{-2y}}{(y + y')!}$$

We will therefore consider that the Gaussian  $p_c$  is the limit of a Poisson distribution of parameter  $2y$ , for a large  $y$ .

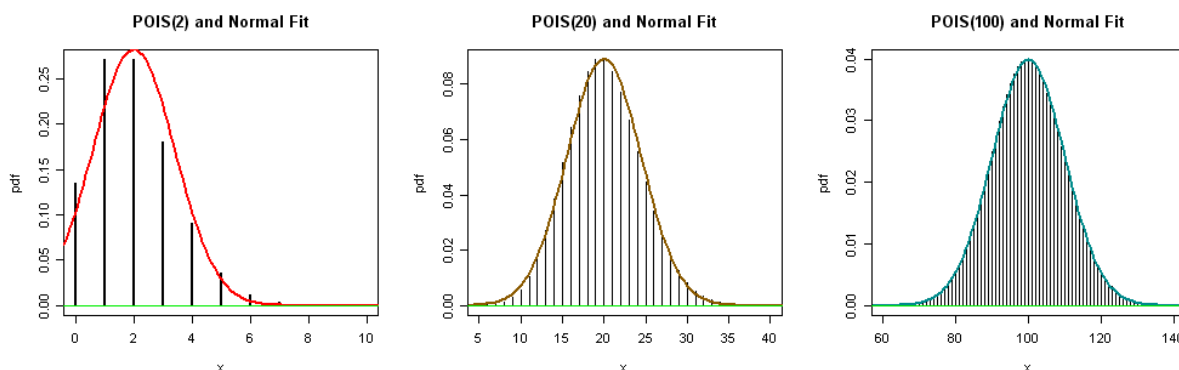


Figure 6 - Approximation of a Poisson law by a Gaussian for parameter values 2, 20 and 100

Rather than considering that a Poisson distribution of the signal, poorly measured and of low parameter, can be approximated by a Gaussian distribution, it is more appropriate to consider the Gaussian distribution as the limit of a Poisson distribution. From then on, it becomes easier to make the convolution product of this Gaussian with a Poisson distribution. The convolution of two Poisson laws is itself a Poisson law, with parameter the sum of the parameters (Papoulis, 2002). We therefore obtain the following expression for the conditional likelihood:

$$p_{S+v}(z|\theta) \sim \frac{(\theta + 2y)^{z+2y}}{(z + 2y)!} e^{-\theta-2y}, \text{ si } y \gg 1$$

**(18)**

This is consistent with a result of (Kruglov, 2012) which characterizes the convolution of a Poisson distribution and a Gaussian as having the characteristic function of a left-shifted Poisson distribution. In a similar way (Koudou & Pommeret, 2002) showed the stability of the Poisson-Gauss family by convolution.

If we use Bayes' theorem with a conjugate prior (Gelman et al., 2013)  $\pi(\theta + 2y) = (\theta + 2y)^{u-1} e^{-v(\theta+2y)}$ , we then obtain the marginal likelihood of  $\theta + 2y$  (pour  $v = 0$ ):

$$p_{\theta}(\theta|z, y) = \frac{(\theta + 2y)^{z+2y+u-1}}{(z + 2y + u - 1)!} e^{-\theta-2y}$$

**(19)**

Which is a gamma law of parameters 1 and  $z + 2y + u - 1$  for the variable  $\theta + 2y$ .

And the decision threshold  $z_c$  is determined analogously to the equation (5):

$$\alpha = \int_{-2y}^0 \frac{(\theta + 2y)^{z_c+2y+u-1}}{(z_c + 2y + u - 1)!} e^{-\theta-2y} d\theta$$

Note that the lower bound is  $-2y$  and not  $-\infty$  because by construction the variable of a gamma law must be positive.

setting  $\vartheta = \theta + 2y$ , we get

$$\alpha = \int_0^{2y} \frac{(\vartheta)^{z_c+2y+\alpha-1}}{(z_c+2y+u-1)!} e^{-\vartheta} d\vartheta$$

Which can be expressed as a regularized incomplete gamma function:

$$\alpha = \frac{\int_0^{2\sigma^2} (\mu)^{z_c+2y+\alpha-1} e^{-\mu} d\mu}{\Gamma(z_c+2y+u-1)} = \frac{\gamma(z_c+2y+\alpha-1, 2\sigma^2)}{\Gamma(z_c+2y+u-1)} = P(z_c+2y+\alpha-1, 2\sigma^2)$$

Likewise, the detection limit  $\theta_d$  will be determined by the equation :

$$\begin{aligned} \beta &= \int_{\theta_d}^{\infty} \frac{(\theta+2y)^{z_c+2y+\alpha-1}}{(z_c+2y+u-1)!} e^{-\theta-2y} d\theta = \int_{\mu_d-2y}^{\infty} \frac{(\mu)^{z_c+2y}}{(z_c+2y+u-1)!} e^{-\mu} d\mu = \frac{\Gamma(z_c+2y+\alpha-1, \mu_d-2y)}{\Gamma(z_c+2y+u-1)} \\ &= 1 - P(z_c+2y+u-1, \mu_d-2y) \end{aligned}$$

From a frequentist point of view, we can from (18) determine a confidence interval in the form (Johnson et al., 1994) :

$$\begin{aligned} F^{-1}\left(\frac{\alpha}{2}; z+2y, 1\right) < \theta+2y < F^{-1}\left(1-\frac{\alpha}{2}; z+2y+1, 1\right) \\ F^{-1}\left(\frac{\alpha}{2}; z+2y, 1\right) - 2y < \theta < F^{-1}\left(1-\frac{\alpha}{2}; z+2y+1, 1\right) - 2y \end{aligned}$$

where  $F^{-1}$  is the inverse cumulative distribution function of the gamma distribution. Which gives the Bayesian result up to the factor  $\alpha - 1$ . In particular, there is a coincidence between Bayesian and frequentist results for  $\alpha = 1$  (uniform prior) as expected. This result would make it possible to obtain more precise estimation intervals than by considering the Gaussian approximation of the Poisson distribution.

## 7.3. Asymptotic behavior

### 7.3.1. Frequentist asymptotic behavior

From what we have just seen, knowing that  $z = x - y$ , from the frequentist point of view we have for the equation (18):

$$p_{S+V}(x, y|\theta) \sim \frac{(\theta+2y)^{x+y}}{(x+y)!} e^{-\theta+2y} \sim \frac{e^{-\frac{1}{2}\frac{(\theta+2y-(x-y)-2y)^2}{(x+y)}}}{\sqrt{2\pi(x+y)}} = \frac{e^{-\frac{1}{2}\frac{(\theta-(x-y))^2}{(x+y)}}}{\sqrt{2\pi(x+y)}}, \text{ si } y \gg 1$$

**(20)**

While from a Bayesian point of view, the equation (19) becomes

$$p_{\theta}(\theta|z, y) = \frac{(\theta+2y)^{x+y+\alpha-1}}{(x+y+\alpha-1)!} e^{-\theta-2y}$$

Which is a shape parameter gamma law  $x+y+\alpha-1$  and scale parameter 1. When  $2y \gg 1$ , this distribution tends towards a Gaussian (Johnson et al., 1994) with equal mean and variance:

$$p_{\theta}(\theta|x, y) \sim \frac{e^{-\frac{1}{2}\frac{(\theta+2y-(x-y)-2y)^2}{(x+y)}}}{\sqrt{2\pi(x+y)}} \sim \frac{e^{-\frac{1}{2}\frac{(\theta-(x-y))^2}{(x+y)}}}{\sqrt{2\pi(x+y)}} \quad (21)$$

### 7.3.2. Confidence intervals

From equation (20) we can identify a pivotal quantity  $t = \frac{\theta-(x-y)}{\sqrt{(x+y)}}$  which will have a Gaussian probability density with mean 0 and variance 1:

$$p(t) \sim e^{-\frac{t^2}{2}}$$

Using the properties of this distribution, as in paragraph 3.4, we can set a statistical risk  $\gamma$  such that there exists a real  $k$  with the constraint :

$$P(-k \leq t \leq k) = \gamma$$

By performing the calculation, we obtain  $k = \Phi^{-1}(\gamma)$  where  $\Phi^{-1}$  is the inverse of the distribution function of the standard Gaussian distribution (quantile function).  $P\left(-k \leq \frac{\theta-(x-y)}{\sqrt{(x+y)}} \leq k\right) = \gamma$

$$P\left(-k\sqrt{(x+y)} \leq \theta - (x-y) \leq k\sqrt{(x+y)}\right) = \gamma$$

$$P\left((x-y) - k\sqrt{(x+y)} \leq \theta \leq (x-y) + k\sqrt{(x+y)}\right) = \gamma$$

For a reference measurement  $y$  and a sample measurement  $x$ , we therefore obtain a confidence interval for  $\theta$  :  $[z - k\sqrt{(x+y)}, z + k\sqrt{(x+y)}]$  with coverage probability  $\gamma$  and  $z = x - y$ .

If we compare with the expression recommended by the standards (ISO, 2010b), we see that it is precisely this type of confidence interval that is used for radioactivity measurements. The counting difference  $(x - y)$  is used as an estimator of  $\theta$  and  $\sqrt{(x+y)}$  is used as the uncertainty of this difference.

### 7.3.3. Decision threshold obtained from the confidence interval

To determine the decision threshold, we need to determine what would be the smallest value of  $z$  (or equivalently,  $x$  because  $y$  is known) authorizing  $\theta = 0$  to belong to the confidence interval.

This corresponds to the lower bound of the confidence interval being zero:

$$x_c - y - k\sqrt{(x_c + y)} = 0$$

thus :

$$z_c = k\sqrt{(z_c + 2y)}$$

(22)

And so :

$$z_c^2 = k_{1-\alpha_c}^2(2y + z_c)$$

with  $k_{1-\alpha_c} = \Phi^{-1}(1 - \alpha_c)$ .

The solution to this quadratic equation is :

$$z_c = \frac{k_{1-\alpha_c}^2 + \sqrt{k_{1-\alpha_c}^4 + 8k_{1-\alpha_c}^2 y}}{2}$$

**(23)**

We find the expression of equation (22) by different authors (Altshuler & Pasternack, 1963; Alvarez, 2007; Turner, 2007). These authors take heteroscedasticity into account in a somewhat ad hoc manner by postulating that the uncertainty of  $p_N(z|\theta)$ , the probability density of  $z$ , is  $\sigma_N = \sqrt{2\sigma_B^2 + z}$ . They start from the expression  $\sigma_N^2 = 2\sigma_B^2 + \theta$  where  $\sigma_B$  is the uncertainty of the reference and do the only thing possible without knowing  $\theta$  : approximate it by  $z$  (the parameter of the  $z$  distribution is replaced by the measurement  $z$ ).

### 7.3.4. Decision threshold resulting from the conditional likelihood of Poisson laws

We have seen (equation (9) from paragraph 6.2) that the decision threshold can be obtained from the conditional likelihood in the case of Poisson distributions in the form:

$$I_{\frac{1}{2}}(x_c + 1, y + 1) = \alpha_c$$

Where  $I_{1/2}(x_c + 1, y + 1)$  is the regularized incomplete beta function,  $x_c$  is the decision threshold for  $x$  and  $\alpha_c$  is the confidence index of the hypothesis test. Furthermore we saw that it was possible to obtain an approximation of the regularized incomplete beta function (equation (11))

Using this approximation, and using Taylor expansions in  $\frac{z_c}{y}$ , we get :

$$1 - \alpha_c \sim \Phi\left(\frac{z_c}{\sqrt{2y}}\right)$$

thus :

$$z_c = \sqrt{2y}\Phi^{-1}(1 - \alpha_c)$$

We therefore find in this approximation for large values of  $x$  and  $y$ , equation (6) (homoscedastic) if  $(\sigma_C^2 + \sigma_B^2) \sim 2(\sigma_B^2) = 2y$ . Cela correspond au seuil de décision de Currie (14) qui n'est donc qu'une approximation au premier ordre en  $\frac{z_c}{y}$

If we continue the expansion to the next order we find:

$$1 - \alpha_c \sim \Phi\left(\frac{z_c}{\sqrt{2y + z_c}}\right)$$

And :

$$z_c = \sqrt{2y + z_c} \Phi^{-1}(1 - \alpha_c)$$

**(24)**

We find the expression (22), knowing that  $z_c = x_c - y$ .

We can note that the decision threshold thus determined indicates that the Currie-11929 decision threshold underestimates false positives and will therefore declare results that are not significant to be significant. In fact, this Currie decision threshold is lower than the one we determined and will therefore consider more measurements significant..

### 7.3.5. Detection limits

We know that under present conditions:

$$\theta_d = 2z_c = k_{1-\alpha_c}^2 + \sqrt{k_{1-\alpha_c}^4 + 8k_{1-\alpha_c}^2 y}$$

**(25)**

Indeed, the confidence and credibility intervals of a Gaussian distribution used here are symmetrical. So an interval with zero lower bound, of estimator  $z = z_c$  will have an upper bound  $2z_c$ .

### 7.3.6. Optimal Test

The approach presented in the previous paragraph amounts to considering a Gaussian probability density with an expectation  $\lambda$  and a variance  $y$  as well as an alternative probability density of expectation  $\mu$  and variance  $y + z$  as a first approximation. The Neyman-Pearson lemma (see annex 4) insures that the best test of the hypothesis  $\lambda = \mu$  is the z-test of different variances (Moore et al., 2009). This test will give (22) ensuring that it is the best hypothesis test. This will therefore be valid to the extent that the second order approximation in  $z/\sigma$  is valid.

This ensures that the decision thresholds and detection limits previously determined by (23) and (25) are optimal.

This also allows us to say that the best test to know whether we should reject a hypothesis of the type  $\theta = \theta_o$  will be the inclusion of  $\theta_o$  in the confidence interval calculated from paragraph 7.3.2. No other test will perform better. Indeed, this confidence interval is based on the probability density  $p_W(x|y, \theta)$ . The best test to know if a result is significant is therefore to check that 0 is not included in the confidence interval. No other test can have better performance. In particular, normative decision thresholds will have worse statistical performances.

### 7.3.7. Bayesian asymptotic behavior

For large  $k$ , the gamma functions  $f(\lambda|k) = \frac{\lambda^k}{k!} e^{-\lambda}$  tend towards Gaussians of average  $k$  and variance  $k$  (S. C. Bagui & Mehra, 2016; Barlow, 1993). So for large  $x$  and  $y$  :

$$p_{\Gamma}(\mu|x) = \frac{\mu^x e^{-\mu}}{x!} \sim \frac{1}{\sqrt{2\pi(x)}} e^{-\frac{(\mu-x)^2}{2(x)}} \text{ et } p_{\Phi}(\lambda|y) = \frac{\lambda^y e^{-\lambda}}{y!} \sim \frac{1}{\sqrt{2\pi(y)}} e^{-\frac{(\lambda-y)^2}{2(y)}}$$

By calculating the cross correlation, we therefore obtain the formula:

$$p_{\Theta}(\theta|x, y) = \frac{1}{\sqrt{2\pi(x+y)}} e^{-\frac{(\theta-x+y)^2}{2(x+y)}}$$

Lemay had already observed that this formula was a very good approximation of  $p_{\Theta}(\theta|x, y)$  (Lemay, 2012, 2015).

Using equation (5) to determine the decision threshold, it is therefore necessary to find  $z_c$  with  $x = y + z_c$  such that

$$z_c = \sqrt{(2y + z_c)k_{\alpha_c}} \quad (26)$$

If we note, as it is traditionally done:

$$k_{\alpha_c} = \Phi^{-1}(1 - \alpha_c)$$

Then,  $z_c^2 = k_{\alpha_c}(2y + z_c)$ .

By solving the quadratic equation, we have:

$$z_c = \frac{k_{\alpha_c}^2 + \sqrt{k_{\alpha_c}^4 + 8k_{\alpha_c}^2 y}}{2} \quad (27)$$

This expression is equivalent to those of (Altshuler & Pasternack, 1963; Alvarez, 2007; Turner, 2007) with one essential difference already mentioned. The decision threshold here only depends on observation  $y$  while, in the mentioned references, it depends on an unknown parameter value which is approximated by observations.

The detection limit expression is given by :

$$\theta_d = z_c + \sqrt{(2y + z_c)}\Phi^{-1}(1 - \beta_c) \quad (28)$$

If we chose  $\beta_c = \alpha_c$ , we get :

$$\theta_d = k_{\alpha_c}^2 + \sqrt{k_{\alpha_c}^4 + 8k_{1-\alpha_c}^2 y} = 2 z_c$$

(29)

While traditional approaches are forced to use formulas including unknown parameters that can only be estimated, this is not the case here.. We are therefore in the presence of exact formulas,for large  $y$ .

It is now useful to see how these proposed characteristic limits differ from established limits (Currie-11929) from the point of view of the consequences but also of their statistical performance or in practice.

## 7.4. Detection limit divergence

Several authors have noted that, under certain conditions, the detection limit could diverge (Kirkpatrick et al., 2013, 2015).

It is common in usual metrological situations to assume that the desired parameter depends on the quantity measured up to a multiplicative calibration variable. Si, par exemple, des comptages sont effectués, le paramètre final recherché est l'activité  $a$  qui va s'exprimer en fonction du nombre de coups net mesurés  $z$  sous la forme :

$$av = z$$

where  $v$  is a calibration coefficient.

It is then possible to determine the detection limit in terms of activity and no longer counting. However, the uncertainty in the calibration coefficient must be taken into account.

This is commonly done by adding to the uncertainty (Dietrich, 1991; Kirkpatrick et al., 2013) a term of the form  $\sigma_v^2 a^2$ . Determination of the detection limit in terms of activity  $a_d$  is then done in the form of the solution of the quadratic equation (following the Currie approach used to determine the equation (16)) :

$$\theta_d = a_d v = z_c + \sqrt{(\sigma_o^2 + a_d v + \sigma_v^2 a_d^2) k_{1-\beta_c}}$$

$$\text{where } z_c = k_{\alpha_c} \sigma_0 = k_{\alpha_c} \sqrt{2b}$$

We then get the solution

$$a_d = \frac{\frac{2 k_{\alpha_c} \sigma_0 + k_{\beta_c}^2}{v} + \sqrt{\left(\frac{2 k_{\alpha_c} \sigma_0 + k_{\beta_c}^2}{v}\right)^2 - 4\left(1 - k_{\beta_c}^2 \frac{\sigma_v^2}{v^2}\right)(k_{\beta_c}^2 - k_{\beta_c}^2) \frac{\sigma_o^2}{v^2}}}{2\left(1 - k_{\beta_c}^2 \frac{\sigma_v^2}{v^2}\right)}$$

The problem appears because the term  $\left(1 - k_{\beta_c}^2 \frac{\sigma_v^2}{v^2}\right)$  in the denominator can be zero when  $1/k_{\beta_c}^2 = \frac{\sigma_v^2}{v^2}$ , causing the detection limit expressed in terms of activity to diverge. The decision threshold can then be calculated ( $a_c = \frac{k_{\alpha_c} \sigma_0}{v}$ ) but not the detection limit. This situation is considered non-physical and attempts have been made to overcome this difficulty (Kirkpatrick et al., 2015). In fact, the decision threshold calculated in this



way does not take into account the uncertainty of the calibration coefficient. If this is taken into account, we can determine a decision threshold on the activities.

The uncertainty of the activity  $\sigma_a$  can be expressed using relative uncertainties (Dietrich, 1991):

$$\frac{\sigma_a^2}{a^2} = \frac{\sigma_v^2}{v^2} + \frac{2\sigma_N^2}{z^2}$$

The decision threshold on the activity is then such that:

$$a_c = k_{\alpha_c} \sigma_a$$

And thus :

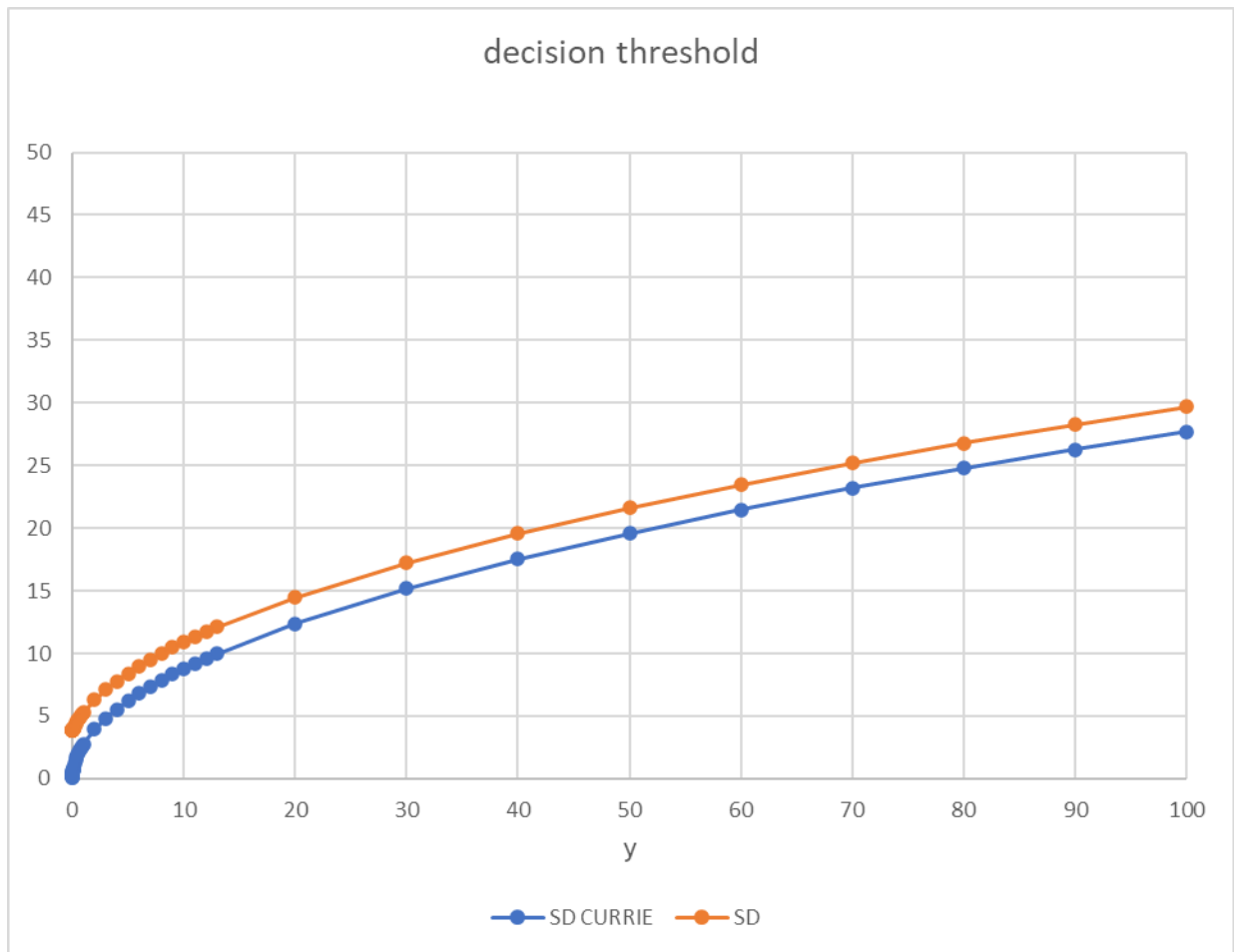
$$\frac{1}{k_{\alpha_c}^2} = \frac{\sigma_v^2}{v^2} + \frac{2\sigma_N^2}{z^2}$$

**(30)**

We can see that when  $\frac{1}{k_{\alpha_c} z} = \frac{\sigma_v^2}{v^2}$  no value of  $z$  will be able to verify (30). In this case the relative uncertainty is greater than 100%! No measurement of the activity will ever be significant. The decision threshold diverges and it is therefore perfectly logical that the same applies to the detection limit. No theoretical value will be able to give a significant measured activity. Under such conditions of uncertainty, all measurements are insignificant because we can never be certain that they stand out from the background noise. On the other hand, for each measurement it is possible to give a confidence interval and therefore an upper limit.

## 7.5. Decision thresholds comparison

Figure 7 illustrates the differences between the decision thresholds calculated by the formula (14) due to Currie and that given by the interval method (27) which coincides with Althulser's formula (Althulser & Pasternack, 1963; Strom & MacLellan, 2001)). They were calculated for  $k_{1-\alpha_c} = 2$ . We observe that the Currie decision threshold tends towards zero for  $y$  tending towards zero. Currie's calculation is based on the fact that  $y$  is large and is therefore no longer valid within this limit. It is therefore not surprising that it predicts that the decision threshold disappears for  $y = 0$ . The Currie decision threshold is also always smaller than the threshold from the intervals. It is underestimated.



**Figure 7 - Decision thresholds calculated according to Currie (blue curve) and according to the proposed method (red curve)**

Figure 8 illustrates the detection limits calculated using the different methods. It appears that the detection limits according to Currie is very slightly underestimated. Remember that quantitative differences are not the main thing. The important thing is that all the necessary information is contained within the confidence interval. There is no need to calculate a decision threshold or detection limit. The non-significant nature of a measurement is determined by the inclusion of zero in the confidence interval and this is the optimal way to do it. While the upper limit of the interval will give us a smaller upper bound for the estimation of the desired parameter  $\theta$ .

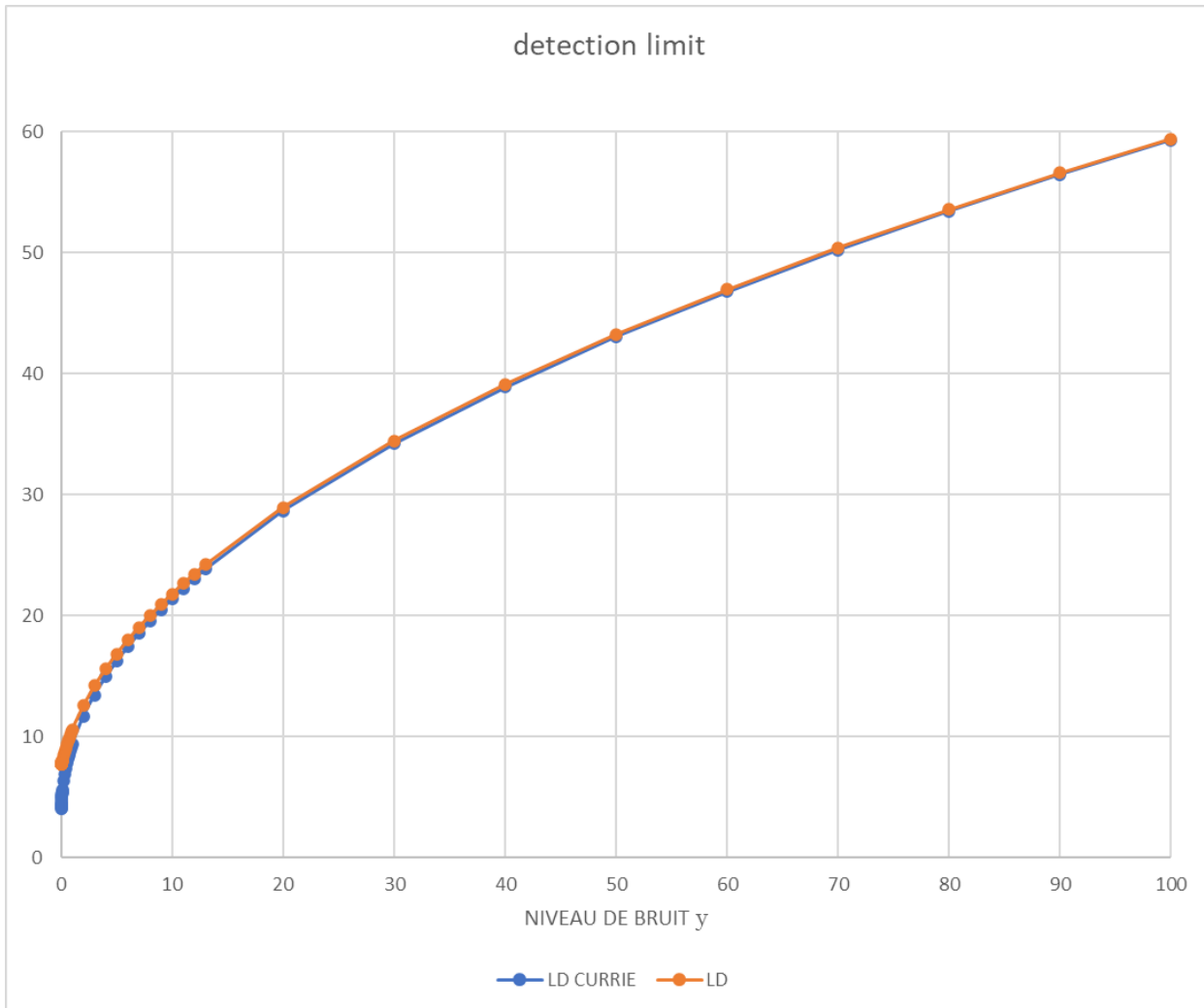


Figure 8 - Detection limits calculated according to Currie (blue curve) and the proposed method (red curve)

## 7.6. Influence of the prior

The commonly used priors for a Poisson distribution are the uniform prior, the Jeffreys prior and the inverse prior corresponding respectively to  $a = 0$ ,  $a = 1/2$  and  $a = 1$  for a prior  $\pi(\lambda, \mu) = \frac{1}{(\lambda\mu)^a}$ . The calculations carried out show that for these priors, their influence on the decision thresholds and detection limits consists of adding  $a$  to count values  $(y, x)$ . This has an influence on low count values but very quickly this influence becomes negligible as  $y$  increases.

The choice of the prior is therefore not decisive apart from low count values. This is consistent with what is encountered for a simple measurement of a single Poisson distribution (Bolstad, 2007).

Note that it would be possible to take into account possible different experiment times for the measurement of the reference and the sample. To do this, it is enough to extrapolate the counts proportionally to the same

measurement of time. If we measure  $x$  et  $y$  during  $t_G$  and  $t_B$ , then simply choose a reference time and calculate the counts for this value.

## 7.7. Coverage probability

Willink studied the probability of recovery of Bayesian credibility intervals obtained with a Heavyside prior for Gaussian or Student distributions. (Willink, 2010b). Recall that by construction the frequentist confidence intervals for a probability  $\alpha$ , if the experiments were repeated multiple times, should include the true value  $100(1 - \alpha)\%$  on average. Through Monte Carlo simulations, Willink observed that this is not the case for credibility intervals when the sample measurement approaches that of the reference. He even showed that when the difference tends towards zero, the credibility intervals have an overlap probability which tends towards zero! These intervals therefore no longer have any chance of containing the true value in the frequentist sense of the term. As with his other observations, Willink attributed this inconsistency to Bayesian methodologies in general (particularly those employing so-called "objective" priors). Other authors have been interested in the question. Some explain this inconsistency by the fact that the confidence and credibility intervals do not answer quite the same question. (Mana & Palmisano, 2014). They were interested in Gaussian distributions. Others, conversely, draw inspiration from methods developed in particle physics in a frequentist framework to modify the credibility intervals and thus ensure a satisfactory coverage probability. (Lee et al., 2016). The elements we provided on the Heavyside prior explain the problem.

In fact, we have seen for the case of Gaussians, that the confidence and credibility intervals coincide if we use a uniform prior (including negative values). By construction, the coverage probability of confidence intervals will be  $100(1 - \alpha)\%$ . Credibility intervals being identical to confidence intervals in this case, we are therefore certain, without even having to carry out simulations, that the coverage probability of these credibility intervals is correct! The inconsistency is therefore lifted for the case of Gaussians. We did not perform the calculation for Student distributions, but the credibility and confidence intervals of Student distributions coincide for a uniform prior. It is when a Heavyside prior is used that coverage inconsistencies appear for the credibility intervals. The conclusion is therefore identical: the Heavyside prior is the source of the problem.

Coverage probabilities are therefore perfectly adequate for the credibility intervals of the Gaussian and Student distributions if we reject the Heavyside priors and use priors including a negative part.

It is the case for the credibility intervals of the random variable  $\Theta$  and the confidence intervals of the random variable de la variable aléatoire  $N$ . On the other hand, if we consider fish laws, this is not the case. Their supports must be positive. They will be included in the support materials  $\Theta$  and  $N$ . This implies that the respective intervals will have a greater coverage. If  $[\alpha, \beta]$  is the 95% credibility interval for  $\Theta$  with  $\alpha < 0$ , we can say that the positive values will be in an interval of  $[0, \beta]$  but without being able to guarantee that exactly 95% values will be included in this interval. On the other hand, at least 95% of the values will be there. We say that the confidence interval « overcovers ». In the absence of data on the contribution of noise to the sample measurement, it is not possible to deconvolve  $\Gamma$  ou  $\Theta$

## 7.8. Numerical Validation

It is possible to carry out simulation tests to validate the results obtained. Here we adopt Strom's approach (Strom & MacLellan, 2001). This involves starting from a given background noise distribution and determining

the decision threshold after drawing from this distribution. Secondly, a new draw is carried out and this draw is compared to the decision threshold previously determined with the same distribution. We are therefore in the presence of background noise. Logically, a result deemed to be significant is therefore a false positive. The use of decision thresholds should therefore give a false positive rate equal to  $\alpha$ , the chosen confidence index.

For homoskedastic distributions, this is indeed the case (Voigtman, 2017). If we are interested in heteroskedastic distributions (which is the case for radioactivity), it is possible to consider Poisson distributions. First of all, a pure radioactive source can be considered as having an activity following a Poisson distribution. On the other hand, for high activities, its distribution can be approximated by a Poisson Gauss distribution (Gaussian distribution with a heteroscedastic standard deviation). We therefore tested the Currie decision thresholds (which are those of ISO 11929) and those determined by our method. We will limit ourselves here to testing the Poisson-Gaussian approximations of the decision thresholds (equation(27)). We will determine the ratio of the false positive rate between the observed value and the theoretical value for a given value of the background noise parameter. This rate should be as close as possible to 1. We have made a million draws of the background noise. For each draw, we determine the decision threshold, then we make a new draw which we compare to the previously calculated decision threshold.

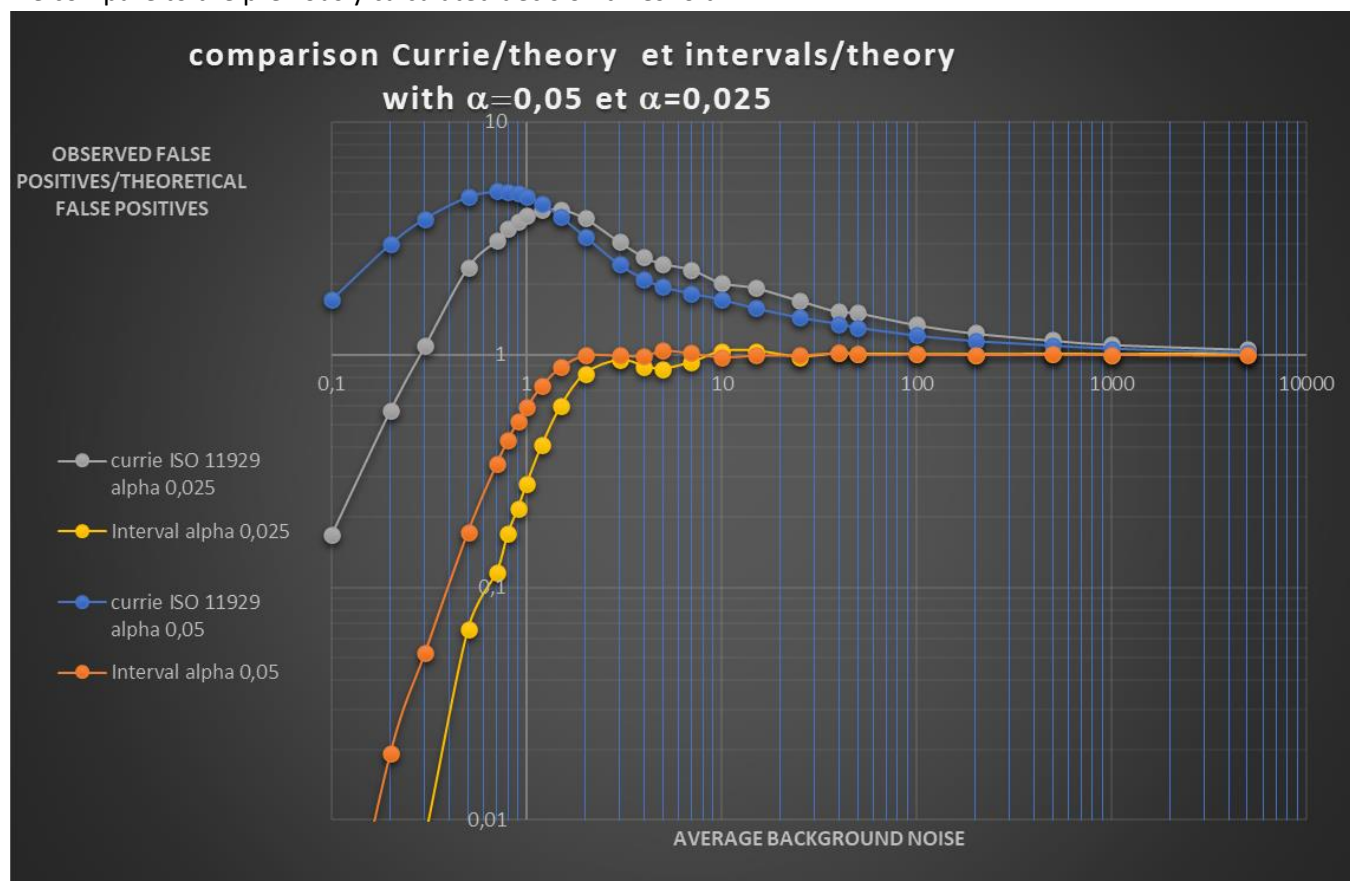


Figure 9 - Comparison of the ratio of real/theoretical false positives

We observe that Currie decision thresholds are only effective from very high counts of background noise. (larger than 1000). For such values the influence of heteroscedasticity becomes weak compared to the value of the background noise. The distribution becomes almost homoscedastic. It is therefore logical that the Currie

thresholds determined with a homoscedastic hypothesis become more efficient. The thresholds derived from the confidence intervals are just as efficient for these high values of the background noise. Below these values, we notice, as expected, that the false positive rate observed in the case of Currie is significantly higher than the theoretical rate  $\alpha$ . This corresponds to an underestimation of the decision threshold since there are more measurements from the background noise which are considered significant. This therefore confirms the calculations carried out previously, in particular the fact that the Currie decision threshold is an underestimate of the decision threshold.

This is not the case for the decision thresholds that we determined from the confidence intervals which remain efficient up to low values of the background noise.. It is interesting to note that the false positive rate remains consistent with the theoretical value up to values of the background noise in the domain of validity of the Stirling approximation and the approximation of the equation (11). For very low background noise values, the observed background noise counting statistic becomes low and the decision thresholds are impacted.. Indeed, it becomes more and more likely that the observed background noise is zero. At this point, for the Currie formula, the decision threshold is zero (any non-zero measurement becomes significant). This leads to an excess number of false positives (up to 25 times the theoretical value). In (27), terms including  $k_{1-\alpha_c}$  become predominant when the background noise is low and thus lead to decision thresholds higher than those of Currie guaranteeing that the decision thresholds are not too low for zero count. However, for very low background noise values, this threshold becomes too high. It would be possible to use the results of paragraph 6 to determine decision thresholds valid for low background noise values. The equations would need to be solved numerically for each background count value. We didn't do it here. We can therefore confidently consider that the statistical performance of the decision thresholds calculated with our method is much better than that of Currie and ISO 11929, which validates the approach.

This has implications for biological dosimetry. Indeed, for the determination of decision thresholds in the measurement of chromosomal aberrations, it is customary to consider possibly expanded Poisson distributions. We measure the number of chromosomal aberrations in an unexposed population and compare it to that of an exposed population. The simulation carried out therefore makes it possible to establish that up to low average values ( $\sim 3$ ) of chromosomal aberrations in the unexposed population, the decision thresholds calculated using Bayesian methods with Gaussian Poisson approximation are efficient.

## 7.9. Experimental validation

IRSN carries out a very large number of radioactivity measurements in the environment with very low activities..

For example, in 2019 an environmental sample (S19EEA21-98B1) was measured in the laboratory using liquid scintillation. The goal was to determine the activity of the tritium present in it. The decision threshold was determined according to the ISO 11929 standard as being worth 0.289 counts per minute (cpm) for the test portion. Measurement by liquid scintillation gives 0.300 cpm. It was therefore concluded in accordance with existing standards that the activity of the sample was significant. The confidence interval was therefore always calculated according to existing standards. It is  $0.300 \pm 0.305$  cpm or  $[-0.005; 0.605]$ . 0 is included in this confidence interval. The result is therefore not significant since zero is a value compatible with the measurements. We cannot reject the null hypothesis (no activity in the sample). The relative uncertainty is 102%. In fact there is conflict and inconsistency between Currie's hypothesis test and the confidence interval which, let us remember, is nothing other than the set of values of the parameter which verifies a hypothesis

test with complete uncertainty. The measuring laboratory, considering that this result was not presentable, decided, as is usual in these cases, to remeasure the sample. This second measurement confirmed that the activity was not significant. This inconsistency between confidence interval and decision threshold was highlighted in the paragraph 7.1. We therefore note experimentally that indeed the decision thresholds calculated according to standard 11929 (and which are those of Currie) are underestimated and give false positives that the confidence interval criterion would consider to be insignificant. In addition, it is clear that measurement laboratories then take into consideration the confidence interval criterion by rejecting results whose uncertainty is greater than 100%. It would therefore be much simpler and faster to simply calculate the confidence interval directly. It makes it possible to determine the significant nature or not of the measurement, gives an estimate of the activity, avoids making a second measurement and can be used subsequently whether it is significant or not..

**0 included in the confidence interval = uncertainty > 100% = non significant sample.**

The sample result sheet is attached to this document

## **7.10. . Conclusions on the heteroskedastic case**

Let's summarize:

- Traditionally used hypothesis tests (Currie-ISO 11929) do not have the expected statistical performance.
- The use of credibility or confidence intervals, formed from conditional or marginal likelihood, makes it possible to extract the characteristic limits (decision thresholds and detection limits) but this time with correct statistical performance.
- Neyman Pearson's lemma ensures that this is the best possible test.
- The simple observation of the estimation interval (Bayesian or frequentist since they almost coincide except for very low counting values) makes it possible in any case to determine the significant nature or not of the measurement.
- These same intervals make it possible to give an upper limit to our parameter which depends on the measurement and which is more precise than a detection limit.
- In practice, the use of Currie's decision threshold, which is in fact optimal only for the homoskedastic case, can lead to experimental inconsistencies in a heteroscedastic case. These are resolved in practice by remeasurements. This inconsistency obviously does not exist when we use confidence intervals as hypothesis tests or, equivalently, when the intervals are based on hypothesis tests. To the extent that the proposed test coincides with that resulting from the Neyman-Pearson lemma, it must logically have better statistical performances. Experience therefore confirms this conclusion.
- Theory, experiment and simulations therefore converge towards the fact that the hypothesis test proposed here is the best.
- Cases where the detection limit diverges. exist The use of conditional or marginal likelihoods makes it possible to eliminate the nuisance parameters, to explain the origin of this difficulty and to resolve it while always making it possible to give an upper limit to the parameter.

## **8. DATA RENDERING**

## 8.1. Current situation

Currently, in metrology, a measurement result  $z$  not statistically significant ( $z < z_c$ ) is returned in the form  $< \theta_d$  (where  $\theta_d$  is the detection limit). In mathematics, we call this type of result censored data.. To be precise, this is left-censored data. The logic behind is to consider that if a measurement is lower than the decision threshold, then only parameters larger than  $\theta_d$  will have a probability of at least  $100 \cdot \beta_c \%$  to give this measurement. The difficulties of dealing with mixtures of significant and non-significant data have been widely discussed elsewhere (Helsel & Helsel, 2012). Their principle is to try to reconstruct the missing data based on hypotheses about the distribution of the underlying parameter. The performance of these methods strongly depends on the percentage of censored data and even the type of methods depends on this percentage. This makes automating data processing extremely difficult. Indeed, the simple addition of a single result can modify the processing method. There is an extensive literature on processing censored data and a large number of methods. Let us repeat that they were originally developed as a stopgap when it was impossible to have uncensored data. In particular, the most used method - substitution - is the one which is unanimously considered the worst by statisticians (Helsel, 2006; Helsel & Helsel, 2012). It consists of a censored result  $< \theta_d$  to replace it with  $\theta_d$ . Any statistician questioned on the subject would be stunned to learn that measurement data is thus censored and not used. He would retort that, in all cases, it is preferable to use basic data to carry out statistical processing.

The first remark that can be made is that the hypothesis test in no way invalidates the measurement result. This one is what it is. The measurement results remain perfectly usable for data processing (average, spatial trend, temporal trend, limit, etc.). It is completely rigorous and scientifically accurate to return a measurement result below the decision threshold. An uncertainty must always be given with a measurement result, including this one.

This is also what is done in the field of particle physics. The established practice is to always return the measurement results independently of the inference made from them. (Anselmann et al., 1995; James & Roos, 1991). This even if the measurement result is negative. This is how, for example, the squared experimental mass of the neutrino is currently recorded in the community of particle physicists as being  $-0,6 \pm 1,9 eV^2$  (Beringer et al., 2012). The fact that a squared mass cannot be negative is not unknown to particle physicists... Simply, the confidence interval covers the zero value and therefore experimentally, taking into account the uncertainties, the zero value is compatible with the experimental results..

We can find several recommendations not to censor the data. The ironic thing is that the very creator of the detection limits and decision thresholds (Lloyd Currie) also strongly recommended returning the results without censoring them! It is worth mentioning this because some are convinced that uncensored restitution is incompatible with the concepts of characteristic limits (decision thresholds and detection limits). This is explained without any ambiguity by Currie in an article (Currie, 2008) on nuclear measurements for radioactivity in the environment.

We reproduce below the main passage on this subject:



### 8.2.1. Statement of the problem; values and non-values

Quantifying measurement uncertainty for low-level results—i.e., those that are close to detection limits—deserves very careful attention: (a) because of the impact of the blank and its variability, and (b) because of the tendency of some to report such data simply as “non-detects” (Lambert et al., 1991) or “zeroes” or “less than” (upper limits). The recommendations of IUPAC (1995, 1998) in such cases are unambiguous: experimental results should not be censored, and they should *always* include quantitative estimates of uncertainty, following the guidelines of ISO-GUM (ISO, 1995). When a result is indistinguishable from the blank, based on comparison of the result ( $\hat{L}$ ) with the critical level ( $L_C$ ), then it is important also to indicate that fact, perhaps with an asterisk or “ND” for not detected. But “ND” should never be used alone. Otherwise there will be information loss, and possibly bias if “ND” is interpreted as “zero”.

Many scientific organizations recommend reporting measurement results in full with their uncertainty. First of all the IUPAC-International Union of Pure and Applied Chemistry- in its “Orange book” which brings together all its recommendations in terms of chemical analysis (Incedy et al., 1998). Here again, it is useful to reproduce the passage from 18.4.3.7 devoted to the restitution of non-significant results :

- (2) A result falling below  $L_C$ , triggering the decision "not detected" should not be construed as demonstrating analyte absence. (See section 18.4.3.6.) Reporting such a result as "zero" or as " $<L_D$ " is *not* recommended; the estimated value (net signal, concentration) and its uncertainty should *always* be reported.

In a similar way, but less explicitly, the ISO guide allows no exception in its recommendation to always give a measurement result with its uncertainty. (JCGM, 2008). For radioactivity measurements, as mentioned, the ISO 11929 standard requires the determination of the confidence interval in all cases. On the other hand, it is not very explicit on the restitution of data, simply mentioning that the customer must be provided with any requested information.

Despite all this and in a scientifically incomprehensible way, this recommendation (or even this normative requirement) is not generally followed in Europe..

This is not the case in the USA in the field of radioactivity. There is an interagency document in the USA, the MARLAP-Multi-Agency Radiological Laboratory Analytical Protocols Manual (FDA, 2004). This applies to the DOE (Department of Energy), the USGS (United States Geological Survey), the DOD (Department of Defense), the FDA (Food and Drug Administration), the NRC (Nuclear Regulatory Commission) , to the EPA (Environmental Protection Agency) and to NIST (National Institute of Standards and Technology equivalent of LNE), in short to any federal scientific institution that measures radioactivity in the USA. Any laboratory or organization carrying out field or laboratory measurements on behalf of one of these government organizations should comply with this principle of full restitution. ((FDA, 2004) paragraph 19.3.9 recommendations) :

- The laboratory should report all results, whether positive, negative, or zero, as obtained, together with their uncertainties.

Additional guidance is added in paragraph 20.3 (where MDC is the notation adopted for the detection limit): *The laboratory should report each measurement result and its uncertainty as obtained (as recommended in Chapter 19) even if the result is less than zero. The laboratory should never report a result as "less than MDC"*

It can not be any clearer.

## 8.2. Current normative requirements for data restitution in the field of radioactivity

Even if the scientific basis of the ISO 11929 standard is incorrect, does it accept the fact of restoring the measurement results in full?

Based on the current standard (ISO 11929 :2010 (ISO, 2010a)), it can be observed that it is mentioned in clause 7: *"The content of the test report depends on the specific application as well as on demands of the customer or regulator"*

As long as there is agreement from the client (which is easy for an internal client), it is therefore possible to mention the desired information. In the same clause 7, it is written that one must always determine and keep in a document:

*"d) the primary measurement result,  $y$ , and the standard uncertainty,  $u(y)$ , associated with  $y$ "*

So determining the measurement and its uncertainty is in any case a normative requirement. If we continue reading this clause, we find that we must also mention:

*"h) a statement as to whether or not the physical effect is recognized as being present;  
NOTE If the physical effect is not recognized as being present, i.e. if  $y < y^*$  [ce qui correspond au seuil de decision  $z_c$ ], it is occasionally demanded by the regulator to document  $< y\#$  [correspondant à la limite de detection  $\theta_d$ ] instead of the measured result,  $y$ . Such documentation can be meaningful since it allows, by comparison with the guideline value, to demonstrate that the measurement procedure is suitable for the intended measurement purpose."*

This means that the only thing that is required at the level of the standard for a non-significant result in addition to the results and the uncertainty, is a mention of this non-significant character. If the authority requires it, it is possible to return in the form  $< \theta_d$  but this is just an additional option. There is therefore no normative obstacle to returning the results in an uncensored manner. It is even rather the opposite, the censored restitution is a tolerance compared to what should ideally be restored.

There is therefore no need to wait for a change in the standard to return uncensored results.

## 8.3. Public perception

Although, to our knowledge, there is no study on public perception regarding the restitution of non-significant measurement results, several observations of principle can be made and a textbook case exists.

Studies have been done on scientists' understanding of the concept of statistically significant. They conclude that the overwhelming majority of researchers and engineers have an approximate or even completely

erroneous conception of this idea (Belia et al., 2005; Greenland et al., 2016). There is little chance that the general public will correctly understand what the experts themselves struggle to explain.

## 9. CURRENT DISCUSSIONS ON STATISTICAL INFERENCE

“Statistically significant- don’t use it, don’t say it”- American statistician

### 9.1. An old discussion

Even if critics of the concept of “statistically significant” have raised objections from its inception, it has become almost universally accepted. Voices are regularly raised to recall or explain the faults and problems of this approach. (Giere, 1972; Harlow et al., 1997; Rozeboom, 1960). The first criticisms mainly concerned the difference in approach between Neyman and Pearson on the one hand and Fisher on the other. The two approaches are often grouped under the term Null Hypothesis Significance Testing (NHST) as we have mentioned. With the resurrection of the Bayesian paradigm, the philosophical and interpretative differences between it and frequentism have been the main front of criticism. Other criticisms have regularly been made of the totally arbitrary nature of the threshold used to declare a result as significant. The p-value is traditionally set at 0.05. There is no objective justification for this specific threshold (Cowles & Davis, 1982). The designer (Fisher) of the p-value never really gave an explanation on the origin of the threshold at 0.05. As we mentioned, this threshold is not the same in the field of radioactivity (0.025) or in particle physics. The interested reader can refer to Nickerson for an overview of the controversies before 2000 (Nickerson, 2000). Of course, the criticisms varied as the concept became more hegemonic in publications (for example, it established itself in the field of psychology until reaching a presence in 95% of publications). (Hubbard & Ryan, 2000)) More recently these criticisms of principle have intensified by focusing more on the consequences of the methodology.

### 9.2. The current « revolt »

In 2005, in a resounding publication (more than 8,300 citations), Ioannidis showed that a significant percentage of scientific publications are likely false. (Ioannidis, 2005). We will not explain the details of the reasoning here but you can find an educational explanation in the video. The problem is partly linked to statistical considerations and in particular to statistical “significance”. As a result, this publication led to what we call the reproducibility crisis. Attempts to replicate results have been made, sometimes with astonishing results (out of 53 studies chosen as important on cancer, only 6 could be successfully reproduced). In 2006, the book “the cult of statistical significance” was published (Ziliak & McCloskey, 2008). Written by economists, it focuses its criticism on the fact that a statistically significant difference can correspond to a tiny effect, differentiating between what is statistically significant and what is practically significant. Under certain conditions, an effect can indeed be tiny but statistically significant and therefore of no real importance. It is clear that the term significant is not very happy for this reason. In 2016, the American Statistical Association took up the subject. This professional association has 18,000 members, historically the second oldest existing professional society in the United States. For the first time in its history, it published recommendations in the form of a declaration (Wasserstein & Lazar, 2016). We reproduce below the 6 recommendations:

1. ***P-values can indicate how incompatible the data are with a specified statistical model.***

2. *P-values do not measure the probability that the studied hypothesis is true, or the probability that the data were produced by random chance alone.*
3. *Scientific conclusions and business or policy decisions should not be based only on whether a p-value passes a specific threshold.*
4. *Proper inference requires full reporting and transparency.*
5. *A p-value, or statistical significance, does not measure the size of an effect or the importance of a result.*
6. *By itself, a p-value does not provide a good measure of evidence regarding a model or hypothesis.*

Initially, this crisis focused on scientific studies aimed at proving the existence of an effect or the effectiveness of treatment. She therefore focused on the concept of p-value. We saw previously that there is a close link between the p-value and the hypothesis testing approach in metrology. Through its use of the concept of “statistically significant”, metrology is also fully concerned. If we translate these recommendations into the metrological context, the main points would be as follows::

- The significant nature of a measurement does not alone prove the presence of a signal.
- • Conversely, a non-significant result does not by itself prove the absence of a signal.
- No scientific conclusion should be based solely on the fact that a measurement exceeds the decision threshold.

Correct inference requires full restitution and total transparency of results.

The conclusion is immediate. In the context of metrology, a significant and non-significant result should not be treated differently! **The measurements must therefore always be reproduced in the same way, providing a result with its uncertainty.**

In a March 2019 issue of Nature, an article co-authored by more than 800 scientists from all disciplines (Amrhein et al., 2019) calls for the concept of “statistically significant” to be abandoned. The same month, the journal “American Statistician” published a special 400-page special issue with around fifty contributions (including big names in statistics) devoted solely to the subject of statistically significant. It is impossible to summarize all of these contributions and suggestions here, but the consensus seems to be on abandoning a differentiated treatment of significant and non-significant results. This arbitrary “dichotomization” is rejected in favor of a full restitution of the results and a mention of the p-value with possible comments.

This revolt, since this is how it has been described, has not yet reached the field of metrology but it seems inevitable to the author (and profitable for all) that this will come in the short or medium term.

## 10. APPLICATION EXAMPLES

### 10.1. Giant Clams measurements as part of surveillance in Polynesia

Nous allons reprendre ici, un exemple utilisé dans un précédent rapport. Pour plus de détail, il conviendra de s’y référer (Manificat, 2015).

Carried out since 1962 in Polynesia, radiological monitoring of the French environment, which currently concerns seven islands (Tahiti, Maupiti, Hao, Rangiroa, Hiva Oa, Mangareva and Tubuai) representative of the five archipelagos, consists of regularly taking samples of varied nature in the different environments (air, water, soil) with which the population may be in contact, as well as foodstuffs (Bouisset 2011, Bouisset 2014).

Regarding foodstuffs, the samples analyzed are representative of the food ration of Polynesians living in the five archipelagos of this territory, and come from the open sea marine environment, the lagoon marine environment and the terrestrial environment..

Among the marine samples, the giant clam (*Tridacna maxima*) is a filter-feeding organism collected and measured for many years as part of the IRSN monitoring program..

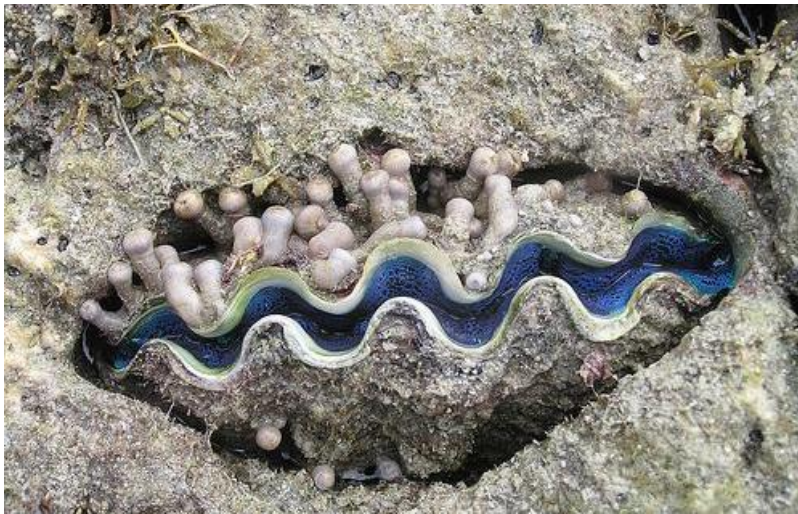


Figure 10 - Picture of a giant clam in the Pacific

Cesium 137 has obviously been monitored for many years.

Here is what the chronicle of the measurement results of cesium 137 in Bq/kg in the giant clams gives, adopting the standard restitution and therefore censoring the non-significant results..

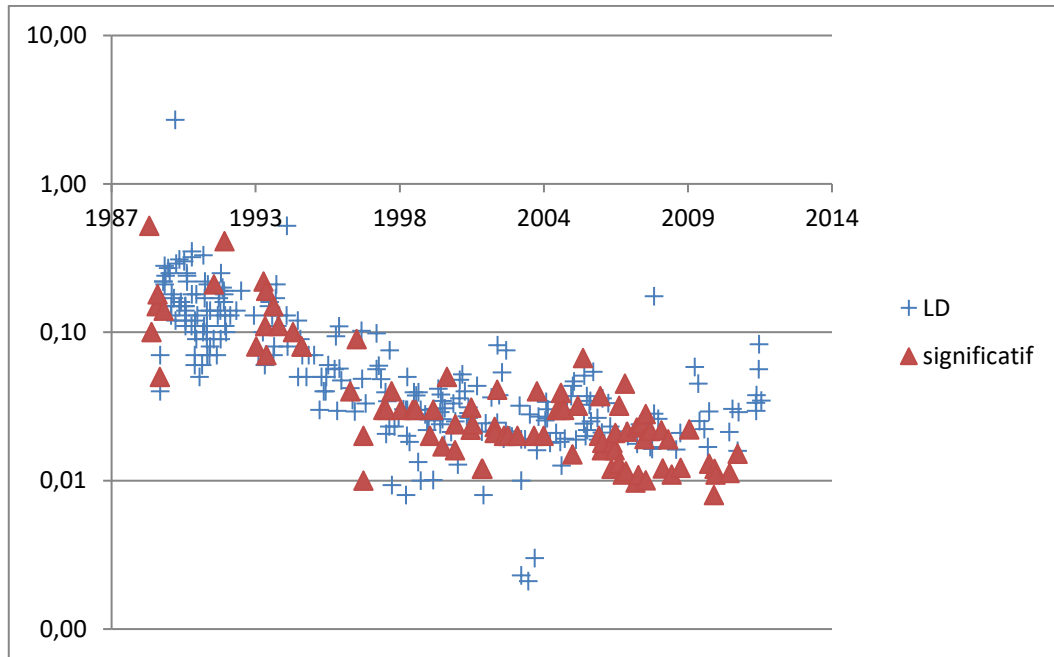


Figure 11 - measurement results (in fresh Bq/kg) with censoring of clam samples between 1989 and 2012

We can clearly discern a plateau in the results from the 2000s. However, the existence of this plateau does not correspond to a physical reality. There is no contribution of cesium 137 to Polynesia as shown by the water and air samples taken elsewhere. Cesium 137 must therefore decrease.

If we reanalyze the spectra to extract the non-significant results, we obtain the following curve:

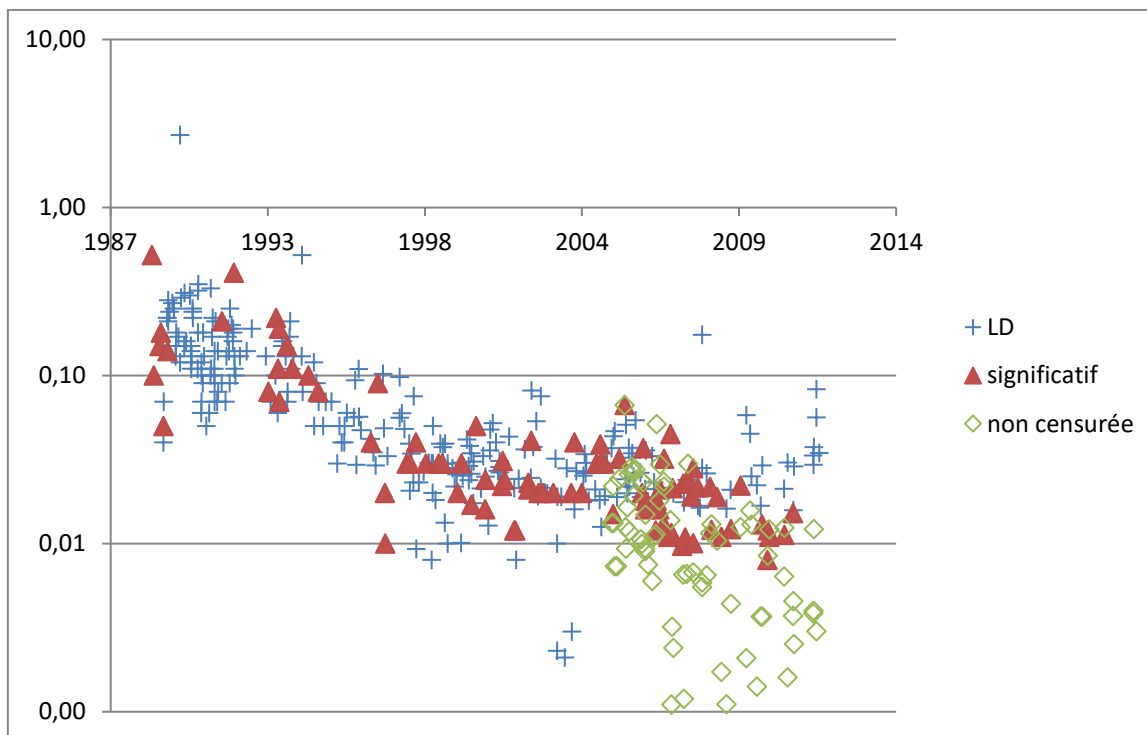


Figure 12 - measurement results (in Bq/kg fresh) with censoring of giant clam samples between 1989 and 2004 and uncensored beyond

We can clearly see the disappearance of this plateau and the continuation of the decline, which match physical reality. The uncensored results therefore make it possible to study long-term trends. On the other hand, the measurement of cesium 137 is done by gamma spectrometry which involves analyzing spectra. Even for these complex measurements, it is perfectly possible to extract uncensored results.

## 10.2. Tritium measurements in rainwater

Around forty rainwater samples were studied using three tritium measuring devices with detection capabilities ranging from the most efficient to the least efficient.

Measurement devices	Number of measurements	Censorship rate	Non censored data provided	Comments
ALOKA	46	4 %	no	These measurements will be considered as « true values »
TriCarb	45	31 %	yes	
TriCarb « classical »	38	85 %	yes	

Aloka is a very efficient detector and the vast majority of tritium measurement results have been declared statistically significant according to the ISO standard. We can therefore consider these results to be a very good approximation of the true values. On the other hand, for the other two devices, the rates of censored values (not significant) are respectively 31% for tricarb and 85% for “classic” Tricarb. Work was done to extract the uncensored values from these two devices. A comparison is therefore possible between the “true” values of the Aloka and the censored and uncensored values of the two other measuring devices. The figure below summarizes the results.

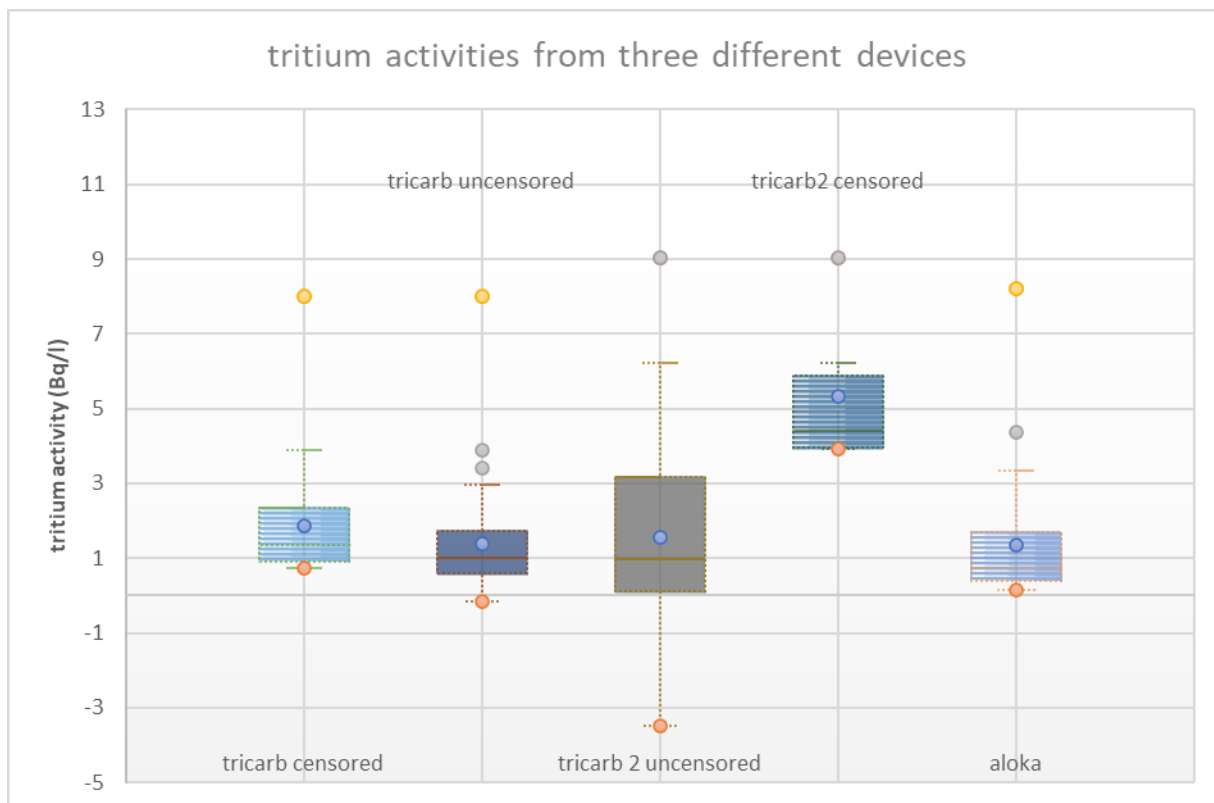


Figure 13 - comparison of the results of censored and uncensored measurements of the three devices.

We see that the censored values (first and fourth “box-plots”) are biased compared to the true values. This is all the more true with a non performing detector where the censorship rate is close to 80%.

On the other hand, as soon as we integrate the non-significant values (second and third “box-plots”) we find results comparable with the true values, provided that the negative values are included. These Tricarb values are logically more dispersed (greater uncertainty). Indeed, the performance of the detector is linked to the uncertainty in the reference, which will directly reflect when we subtract from the values measured for the sample. It is possible to statistically compare the distributions of uncensored values of the three devices. Tests indicate that the three detectors give completely compatible values. A comparison with mathematical methods for exploiting censored results was also made. It unambiguously concludes that the uncensored results perform better.



This physical experiment ensures that the method presented in this report is not a mathematical artifice. We find the true values with consistent statistical performances.

### 10.3. Astrophysics

It should also be noted that the determination of these decision thresholds and detection limits corresponds exactly to that of the so-called « on-off » astrophysics problem. (or Li-ma problem) (Gillesen & Harney, 2005; Gregory, 2005; Li & Ma, 1983). This involves determining whether during an observation of an area of space, something was detected as significantly deviating from the background noise. The latter is generally determined by observing an area known to be free of the desired phenomenon. This problem is commonly encountered in gamma-ray burst research. The resolution method is generally to consider that the background noise parameter is known both from a frequentist and Bayesian point of view. This amounts to considering that in our notation  $\mu = \lambda + \theta$ , where  $\lambda$  is known. To our knowledge, the method presented in this document is the first not to use this approximation. Let us also mention that the application of Bayesian methodology is done for this problem using a prior with positive support under the pretext of the non-physical nature of the negative parameters..

A detector points to a region (called « On ») suspected of containing a gamma ray source. For a time  $t_{On}$ , it is counting  $N_{On}$  gamma photons. The detector is then pointed towards a region (called « Off ») where it is assumed that no gamma sources are present. during a time  $t_{Off}$ ,  $N_{Off}$  gamma photons are counted. Setting  $\alpha = t_{On}/t_{Off}$ , it is then possible to assume that the background noise in the « On » region possess the same distribution as in the « Off » region. This amounts to considering that in the « On » region the background noise is  $\alpha N_{Off}$ . We will assume that we are in a Poissonian model, which is natural for rare events. It is then possible to say from equation (9) that the decision threshold  $k$  vérify :

$$\alpha_c = I_{1/2}(\alpha N_{Off} + k + 1 - a, \alpha N_{Off} + 1 - a)$$

In the field of astrophysics, it is customary to use the significance  $S$  defined as the ratio between the signal and the standard deviation.

We therefore have, passing to the limit of large counts:

$$S = \frac{N_{On} - \alpha N_{Off}}{N_{On} + \alpha N_{Off}}$$

### 10.4. Particle physics

The problem of determining whether a signal deviates from the background noise for background distributions is also ubiquitous in particle physics. Events are counted in different configurations and the aim is to determine whether during experiments these counts deviate from the basic signal. This was particularly the case for the discovery of the Higgs boson. (van Dyk, 2014) where the equivalent of the probability  $\alpha_c$  was chosen as worth approximately  $10^{-6}$ . The methodologies used are generally frequentist but also reject negative parameters considered as non-physical. Some researchers use Bayesian methods with of course strictly positive supported priors. (Gregory, 2005; James, 2006; Lista, 2016). Whether for Bayesian or frequentist methods, the background noise parameter is generally assumed to be known. For example, to deal with a counting problem

(Lista, 2016), we assume that the background noise parameter is perfectly known  $\lambda$ , we are interested in the signal parameter  $s$  et on a une distribution du comptage brut (signal+bruit de fond) :

$$p_G(n|s, \lambda) = \frac{(s + \lambda)^n}{n!} e^{-(s+\lambda)}$$

This approach has been modified to take into account the fact that the background noise is not always perfectly known (Lista, 2016).

In the work presented here, the background noise parameter is not assumed to be known and only observations are taken into account beyond the mathematical model used (likelihood function). If we assume that the background noise is Gaussian with a mean  $y$  and a variance  $2\sigma_B^2$ , we therefore show using the results of this document that the level of “significance” will in fact be:

$$Z = \frac{n - y}{\sqrt{2\sigma_B^2 + n - y}}$$

The significance level is defined as the equivalent number of standard deviations for the measurement ((Lista, 2016). A Confidence index of à 5% will correspond to  $Z=1,6$ , 2,5% for  $Z\sim 2$  and it is customary to declare a discovery in particle physics for  $Z=5$  ( $\alpha_c=3,7 \cdot 10^{-5}\%$ ).

Another point of view would be to consider the Skellam distribution in its Gaussian limit. If we have a measurement  $y$  for the reference and  $x$  for the sample, the level of significance will then be:

$$Z = \frac{x - y}{\sqrt{x + y}}$$

This is perfectly consistent with the fact that the difference between a Poisson distribution of parameter  $\mu$  and a Poisson distribution of parameter  $\lambda$  is a Skellam distribution with mean  $\mu - \lambda$  and variance  $\lambda + \mu$  (Skellam, 1946). Using maximum likelihood estimators, we obtain the previous result.

It is also possible from the results of 7.2.1, 7.3.2 to determine the confidence interval for the parameter  $\theta$ . On the other hand, it is not possible to guarantee both the coverage probability and the positivity of a sample position parameter. We can give a confidence interval for a parameter  $\theta$  which will have the right coverage properties but it will potentially include negative values because it is the parameter of the net random variable. The alternative is to give an interval containing only positive values but it will then not have the good coverage properties.

# 11. CONCLUSIONS

The low-level measurement problem can be approached in at least two different ways. Classical statistics allows the use of the Neyman-Pearson lemma. This allows us to obtain the optimal hypothesis test. The other approach is that of Bayesian statistics. With very few exceptions, the application of Bayesian methodology to metrology issues is inevitably done with strictly positive support priors for measurands which are ideally positive. ((Bergamaschi et al., 2013; Bochud et al., 2007; IAEA, 2017; ISO, 2010a; Korun et al., 2014, 2016; Laedermann et al., 2005; Lira, 2009; Little, 1982; Michel, 2016; Miller et al., 2002; Rivals et al., 2012; A. Vivier et al., 2009; Weise et al., 2006; Zähringer & Kirchner, 2008; Zorko et al., 2016)). It seemed natural to limit ourselves to a domain where the desired parameter is positive. As we have seen, this confuses the true signal with the net signal and biases the results with inadequate statistical performance. Using a simple criterion very similar to that of classical statistics, we were able to formulate a way to determine the significant nature of a measurement. This direct use of confidence or credibility intervals makes it possible to obtain an optimal test according to the Neyman-Pearson methodology and largely reconciles classical and Bayesian approaches. Numerical simulations confirm the statistical performance of these criteria.

The recommendations and conclusions deduced from this document are therefore as follows::

- • Measurements below the decision threshold should not be censored.
- The difficulties encountered fall within the framework of the difficult problem of nuisance parameters (how to find  $\theta$  without knowing  $\lambda$ ). We propose a conditional approach for the frequentist approach and a marginal approach for the Bayesian approach. The two approaches converge for sufficient count values. This method works with members of the family of natural exponentials with quadratic variance (NEF-QVF) which bring together a large part of the probability densities commonly used in metrology. The use of a prior with positive support such as the Heavyside prior should be avoided in the case where we admit the possibility of fluctuating measurements around the reference (negative measurements).
- • Rejecting the negative part of the confidence interval like  $[-a,b]$  under the pretext of its non-physical character is nonsense. The parameter accessible to measurement by inference is not the “true” signal but the “net” signal which differs from it by its greater dispersion. This “net” signal has no physical reason to be positive and under no circumstances should the intervals be truncated by excluding the negative part.
- Obtaining the probability density of the parameter  $\theta$  based on observations  $z$ ,  $p(\theta|z)$  is sufficient to define an estimation interval for the parameter and determine the significant nature or not of the measurement. This also provides an upper bound for the parameter which will depend on the measurement and will be more precise than the detection limit. The hypothesis tests which make it possible to define the characteristic limits of the model (decision thresholds, detection limits) are intrinsic to the construction of the estimation intervals. Mere knowledge of this interval is sufficient. This also makes it possible to avoid several paradoxes (inconsistency between the estimation intervals and the hypothesis tests as mentioned in paragraph 7.9, divergence of the detection limit as mentioned in 7.3.6). It is therefore necessary and sufficient to provide a result with its uncertainty. This is in line with current concerns in the field of statistics on the use of the significant nature or not of a result. No other test can have better statistical performance.

- For Gaussian distributions and more generally for position parameters, the equality between the confidence intervals and the credibility intervals ensures that these intervals and the associated characteristic limits have the right statistical properties (coverage probability). For the case of radioactivity, numerical experiments show that the decision threshold determined from the estimation intervals is better than that of Currie and ISO11929. In fact, Neyman Pearson's lemma guarantees that this is the case.
- The confidence intervals contain all the necessary information and there is no need to censor the data
- The ISO 11929 standard is inadequate and its theoretical foundation is erroneous through the use of a Heavyside prior and the use of frequentist characteristic limits on Bayesian distributions. It leads to underestimated decision thresholds.
- The method proposed here gives substantially the same results for a frequentist or Bayesian approach. The (small) differences at low count values can be explained by the choice of the prior. These differences reflect the epistemic uncertainty of the lack of measurement data.
- The method can easily be used to determine characteristic limits on other metrological techniques such as biological dosimetry, electron paramagnetic resonance, particle physics or astrophysics.

Many avenues of work exist. Applying these methodologies to cases where both location and dispersion are unknown would lead to Student distributions and it would be useful to calculate their characteristic limits. The extension of this methodology to techniques requiring calibration curves is another avenue. Furthermore, certain paradoxes identified in the use of Bayesian methods in metrology (Attivissimo et al., 2012) would perhaps see avenues of resolution open up.

## 12. THANKS

I thank Alain Vivier for introducing me to this problem and for the fierce discussions which forced me to clarify my ideas. I also thank the strange fate that gave me the opportunity and time to think about this question. Finally I thank a disciple of Basu who will recognize himself.

## References

- [1] Abramowitz, M., & Stegun, I. A. (Éds.). (1965). *Handbook of Mathematical Functions : With Formulas, Graphs, and Mathematical Tables* (0009-Revised edition éd.). Dover Publications.
- [2] Altshuler, B., & Pasternack, B. (1963). Statistical Measures of the Lower Limit of Detection of a Radioactivity Counter: *Health Physics*, 9(3), 293-298. <https://doi.org/10.1097/00004032-196303000-00005>
- [3] Alvarez, J. L. (2007). Poisson-based detection limit and signal confidence intervals for few total counts. *Health Physics*, 93(2), 120-126. <https://doi.org/10.1097/01.HP.0000261331.73389.bd>
- [4] Amrhein, V., Greenland, S., & McShane, B. (2019). Retire statistical significance. *Nature*, 567, 305-307.
- [5] Analytical Method Committee, The Royal Society of Chemistry. (2010). Response from the Analytical Methods Committee (AMC) to the paper "Uncertainty in repeated measurement of a small non-negative quantity : Explanation and discussion of Bayesian methodology". *Accreditation and Quality Assurance*, 15(3), 189-191. <https://doi.org/10.1007/s00769-010-0643-3>
- [6] Analytical Methods Committee, The Royal Society of Chemistry. (2008). Measurement uncertainty evaluation for a non-negative measurand : An alternative to limit of detection. *Accreditation and Quality Assurance*, 13(1), 29-32. <https://doi.org/10.1007/s00769-007-0339-5>
- [7] Anselmann, P., Hampel, W., Heusser, G., Kiko, J., Kirsten, T., Laubenstein, M., Pernicka, E., Pezzoni, S., Rönn, U., & Sann, M. (1995). GALLEX solar neutrino observations : Complete results for GALLEX II. *Physics Letters B*, 357(1-2), 237-247.
- [8] Attivissimo, F., Giaquinto, N., & Savino, M. (2012). A Bayesian paradox and its impact on the GUM approach to uncertainty. *Measurement*, 45(9), Article 9. <https://doi.org/10.1016/j.measurement.2012.01.022>
- [9] Bagui, S. C., & Mehra, K. L. (2016). Convergence of Binomial, Poisson, Negative-Binomial, and Gamma to Normal Distribution : Moment Generating Functions Technique. *American Journal of Mathematics and Statistics*, 6(3), Article 3.
- [10] Bagui, S., & Mehra, K. (2019). On the Convergence of Negative Binomial Distribution. *American Journal of Mathematics and Statistics*, 9, 44-50.
- [11] Barlow, R. J. (1993). *Statistics : A Guide to the Use of Statistical Methods in the Physical Sciences*. Wiley.
- [12] Basu, D. (2011). On the Elimination of Nuisance Parameters. In A. DasGupta (Éd.), *Selected Works of Debabrata Basu* (p. 279-290). Springer New York. [https://doi.org/10.1007/978-1-4419-5825-9\\_26](https://doi.org/10.1007/978-1-4419-5825-9_26)
- [13] Belia, S., Fidler, F., Williams, J., & Cumming, G. (2005). Researchers Misunderstand Confidence Intervals and Standard Error Bars. *Psychological Methods*, 10(4), Article 4. <https://doi.org/10.1037/1082-989X.10.4.389>
- [14] Bergamaschi, L., D'Agostino, G., Giordani, L., Mana, G., & Oddone, M. (2013). The detection of signals hidden in noise. *Metrologia*, 50(3), Article 3. <https://doi.org/10.1088/0026-1394/50/3/269>
- [15] Beringer, J., Arguin, J.-F., Barnett, R. M., Copic, K., Dahl, O., Groom, D. E., Lin, C.-J., Lys, J., Murayama, H., Wohl, C. G., Yao, W.-M., Zyla, P. A., Amsler, C., Antonelli, M., Asner, D. M., Baer, H., Band, H. R., Basaglia, T., Bauer, C. W., ... Schaffner, P. (2012). Review of Particle Physics. *Physical Review D*, 86(1), Article 1. <https://doi.org/10.1103/PhysRevD.86.010001>
- [16] Bochud, F. O., Bailat, C. J., & Laedermann, J.-P. (2007). Bayesian statistics in radionuclide metrology : Measurement of a decaying source. *Metrologia*, 44(4), Article 4. <https://doi.org/10.1088/0026-1394/44/4/S13>
- [17] Bolstad, W. M. (2007). *Introduction to Bayesian statistics* (2nd ed). John Wiley.
- [18] Bourguignon, M. (2021). A new regression model for positive random variables with skewed and long tail. *METRON*, 79, 33-55.
- [19] Box, G. E. P., & Tiao, G. C. (1973). *Bayesian inference in statistical analysis*. Addison-Wesley.
- [20] Bromiley, P. A. (2003). *Products and Convolutions of Gaussian Probability Density Functions* (Tina-Vision Memo, p. 13).
- [21] Chambless, D. A., Dubose, S. S., & Sensintaffar, E. L. (1992). Detection Limit Concepts : Foundations, Myths, and Utilization. *Health Physics*, 63(3), 338-340. <https://doi.org/10.1097/00004032-199209000-00010>
- [22] Cowles, M., & Davis, C. (1982). On the Origins of the .05 Level of Statistical Significance. *American Psychologist*, 37(5), 553.
- [23] Cumming, G. (2014). The new statistics : Why and how. *Psychological Science*, 25(1), 7-29. <https://doi.org/10.1177/0956797613504966>

- [24] Cumming, G., & Calin-Jageman, R. (2016). *Introduction to the New Statistics : Estimation, Open Science, and Beyond*. Routledge.
- [25] Currie, L. A. (1968). Limits for qualitative detection and quantitative determination. Application to radiochemistry. *Analytical Chemistry*, 40(3), 586-593. <https://doi.org/10.1021/ac60259a007>
- [26] Currie, L. A. (2008). Detection and quantification capabilities in nuclear analytical measurements. In *Radioactivity in the Environment* (Vol. 11, p. 49-135). Elsevier. [https://doi.org/10.1016/S1569-4860\(07\)11003-2](https://doi.org/10.1016/S1569-4860(07)11003-2)
- [27] Dietrich, C. F. (1991). *Uncertainty, calibration, and probability : The statistics of scientific and industrial measurement* (2nd ed). A. Hilger.
- [28] Dowson, D., & Wragg, A. (1973). Maximum-entropy distributions having prescribed first and second moments (Corresp.). *IEEE Transactions on Information Theory*, 19(5), 689-693. <https://doi.org/10.1109/TIT.1973.1055060>
- [29] Ellison, S. L. R. (2014). Implementing measurement uncertainty for analytical chemistry : The *Eurachem Guide* for measurement uncertainty. *Metrologia*, 51(4), S199-S205. <https://doi.org/10.1088/0026-1394/51/4/S199>
- [30] FDA, U. (2004). *NIST: Multi-Agency Radiological Laboratory Analytical Protocols Manual (MARLAP), FDA, USGS, NUREG-1576*. EPA 402-B-04-001C, NTIS PB2004-105421, Alexandria, VA, USA.
- [31] Gelman, A., Carlin, J. B., Stern, H. S., Dunson, D. B., Vehtari, A., & Rubin, D. B. (2013). *Bayesian Data Analysis, Third Edition* (3 edition). Chapman and Hall/CRC.
- [32] Giere, R. N. (1972). *The significance test controversy*.
- [33] Gillissen, S., & Harney, H. L. (2005). Significance in gamma-ray astronomy – the Li & Ma problem in Bayesian statistics. *Astronomy & Astrophysics*, 430(1), 355-362. <https://doi.org/10.1051/0004-6361:20035839>
- [34] Good, I. J. (1976). The Bayesian Influence, or How to Sweep Subjectivism under the Carpet. In W. L. Harper & C. A. Hooker (Éds.), *Foundations of Probability Theory, Statistical Inference, and Statistical Theories of Science* (p. 125-174). Springer Netherlands. [https://doi.org/10.1007/978-94-010-1436-6\\_5](https://doi.org/10.1007/978-94-010-1436-6_5)
- [35] Gradshteyn, I. S., Ryzhik, I. M., & Jeffrey, A. (2000). *Table of Integrals, Series, and Products* (6th Revised edition). Academic Press Inc.
- [36] Greenland, S., Senn, S. J., Rothman, K. J., Carlin, J. B., Poole, C., Goodman, S. N., & Altman, D. G. (2016). Statistical tests, P values, confidence intervals, and power : A guide to misinterpretations. *European Journal of Epidemiology*, 31(4), 337-350. <https://doi.org/10.1007/s10654-016-0149-3>
- [37] Gregory, P. (2005). *Bayesian Logical Data Analysis for the Physical Sciences : A Comparative Approach with Mathematica® Support*. Cambridge University Press.
- [38] Harlow, L. L., Mulaik, S. A., & Steiger, J. H. (Éds.). (1997). *What if there were no significance tests?* Lawrence Erlbaum Associates Publishers.
- [39] Heisel, M., Kaether, F., & Simgen, H. (2009). Statistical analysis of low-level material screening measurements via gamma-spectroscopy. *Applied Radiation and Isotopes*, 67(5), 741-745. <https://doi.org/10.1016/j.apradiso.2009.01.028>
- [40] Helsel, D. R. (2006). Fabricating data : How substituting values for nondetects can ruin results, and what can be done about it. *Chemosphere*, 65(11), 2434-2439. <https://doi.org/10.1016/j.chemosphere.2006.04.051>
- [41] Helsel, D. R., & Helsel, D. R. (2012). *Statistics for censored environmental data using Minitab and R* (2nd ed). Wiley.
- [42] Hubbard, R., & Ryan, P. A. (2000). The Historical Growth of Statistical Significance Testing in Psychology—and Its Future Prospects. *Educational and Psychological Measurement*, 60(5), 661-681. <https://doi.org/10.1177/00131640021970808>
- [43] IAEA. (2017). *Determination and Interpretation of Characteristic Limits for Radioactivity Measurements*. <https://www-pub.iaea.org/books/iaeabooks/12203/Determination-and-Interpretation-of-Characteristic-Limits-for-Radioactivity-Measurements>
- [44] Inczedy, J., Lengyel, T., Ure, A. M., Gelencsér, A., & Hulanicki, A. (1998). Compendium of analytical nomenclature. *The Orange Book, 3rd Edn*.
- [45] Ioannidis, J. P. (2005). Why most published research findings are false. *PLoS med*, 2(8), e124.

- [46] ISO. (2010a). *ISO 11929:2010(en), Determination of the characteristic limits (decision threshold, detection limit and limits of the confidence interval) for measurements of ionizing radiation—Fundamentals and application*. <https://www.iso.org/obp/ui/#iso:std:iso:11929:ed-1:v1:en>
- [47] ISO. (2010b). *ISO 11929:2010(en), Determination of the characteristic limits (decision threshold, detection limit and limits of the confidence interval) for measurements of ionizing radiation—Fundamentals and application*. <https://www.iso.org/obp/ui/#iso:std:iso:11929:ed-1:v1:en>
- [48] James, F. (2006). *Statistical Methods in Experimental Physics : 2nd Edition* (2nd edition). World Scientific Publishing Company.
- [49] James, F., & Roos, M. (1991). Statistical notes on the problem of experimental observations near an unphysical region. *Physical Review D*, 44(1), 299-301. <https://doi.org/10.1103/PhysRevD.44.299>
- [50] Jaynes, E. T. (1968). Prior Probabilities. *IEEE Transactions on Systems Science and Cybernetics*, 4(3), 227-241. <https://doi.org/10.1109/TSSC.1968.300117>
- [51] Jaynes, E. T. (2003). *Probability Theory : The Logic of Science*. Cambridge University Press.
- [52] Jaynes, E. T., & Kempthorne, O. (1976). Confidence Intervals vs Bayesian Intervals. In W. L. Harper & C. A. Hooker (Éds.), *Foundations of Probability Theory, Statistical Inference, and Statistical Theories of Science : Proceedings of an International Research Colloquium held at the University of Western Ontario, London, Canada, 10–13 May 1973 Volume II Foundations and Philosophy of Statistical Inference* (p. 175-257). Springer Netherlands. [https://doi.org/10.1007/978-94-010-1436-6\\_6](https://doi.org/10.1007/978-94-010-1436-6_6)
- [53] JCGM, J. (2008). Evaluation of measurement data—Guide to the expression of uncertainty in measurement. *Int. Organ. Stand. Geneva ISBN, 50*, 134.
- [54] Jeffreys, H. (1946). An Invariant Form for the Prior Probability in Estimation Problems. *Proceedings of the Royal Society of London. Series A, Mathematical and Physical Sciences*, 186(1007), 453-461.
- [55] JOHNSON, N. L., KEMP, A. W., & KOTZ, S. (s. d.). *Univariate Discrete Distributions*.
- [56] Johnson, N. L., Kotz, S., & Balakrishnan, N. (1994). *Continuous univariate distributions vol 2* (2nd ed). Wiley.
- [57] Karlen, D. (2002). Credibility of confidence intervals. *Advanced Statistical Techniques in Particle Physics, Proceedings*, 53-57.
- [58] Karlin, S., & Rubin, H. (1956). The theory of decision procedures for distributions with monotone likelihood ratio. *The Annals of Mathematical Statistics*, 272-299.
- [59] Kirkpatrick, J. M., Russ, W., Venkataraman, R., & Young, B. M. (2015). Calculation of the detection limit in radiation measurements with systematic uncertainties. *Nuclear Instruments and Methods in Physics Research Section A: Accelerators, Spectrometers, Detectors and Associated Equipment*, 784, 306-310. <https://doi.org/10.1016/j.nima.2015.01.005>
- [60] Kirkpatrick, J. M., Venkataraman, R., & Young, B. M. (2013). Minimum detectable activity, systematic uncertainties, and the ISO 11929 standard. *Journal of Radioanalytical and Nuclear Chemistry*, 296(2), 1005-1010. <https://doi.org/10.1007/s10967-012-2083-5>
- [61] Kirkpatrick, J. M., & Young, B. M. (2009). Poisson Statistical Methods for the Analysis of Low-Count Gamma Spectra. *IEEE Transactions on Nuclear Science*, 56(3), 1278-1282. <https://doi.org/10.1109/TNS.2009.2020516>
- [62] Korun, M., Vodenik, B., & Zorko, B. (2014). Reporting gamma-ray spectrometric measurement results near the natural limit : Primary measurement results, best estimates calculated with the Bayesian posterior and best estimates calculated with the probability density distribution resembling shifting. *Journal of Radioanalytical and Nuclear Chemistry*, 299(3), 1839-1846. <https://doi.org/10.1007/s10967-014-2970-z>
- [63] Korun, M., Vodenik, B., & Zorko, B. (2016). Calculation of the decision thresholds for radionuclides identified in gamma-ray spectra by post-processing peak analysis results. *Nuclear Instruments and Methods in Physics Research Section A: Accelerators, Spectrometers, Detectors and Associated Equipment*, 813, 102-110. <https://doi.org/10.1016/j.nima.2016.01.020>
- [64] Koudou, A. E., & Pommeret, D. (2002). A Characterization of Poisson–Gaussian Families by Convolution-Stability. *Journal of Multivariate Analysis*, 81(1), 120-127. <https://doi.org/10.1006/jmva.2001.1995>

- [65] Kruglov, V. M. (2012). A characterization of the convolution of Gaussian and Poisson distributions. *Sankhya A*, 74(1), Article 1. <https://doi.org/10.1007/s13171-012-0005-9>
- [66] Kruschke, J. K., & Liddell, T. M. (2018). The Bayesian New Statistics : Hypothesis testing, estimation, meta-analysis, and power analysis from a Bayesian perspective. *Psychonomic Bulletin & Review*, 25(1), 178-206. <https://doi.org/10.3758/s13423-016-1221-4>
- [67] Laedermann, J.-P., Valley, J.-F., & Bochud, F. O. (2005). Measurement of radioactive samples : Application of the Bayesian statistical decision theory. *Metrologia*, 42(5), 442-448. <https://doi.org/10.1088/0026-1394/42/5/015>
- [68] Lee, K. B., Lee, J. M., Park, T. S., Lee, S. H., Jeong, M., & Lee, M.-K. (2016). Clarification of the calculation of minimum detectable activity in low-level radioactivity measurements. *Applied Radiation and Isotopes*, 109, 449-451. <https://doi.org/10.1016/j.apradiso.2015.11.043>
- [69] Lehmann, E. L. (1993). The Fisher, Neyman-Pearson Theories of Testing Hypotheses : One Theory or Two? *Journal of the American Statistical Association*, 88(424), 1242-1249. <https://doi.org/10.1080/01621459.1993.10476404>
- [70] Lehmann, E. L., & Romano, J. P. (2005a). *Testing statistical hypotheses* (3rd ed). Springer.
- [71] Lehmann, E. L., & Romano, J. P. (2005b). *Testing statistical hypotheses* (3rd ed). Springer.
- [72] Lemay, F. (2012). Multichannel Statistical Analysis of Low-level Radioactivity in the Presence of Background Counts: *Health Physics*, 103(6), 770-779. <https://doi.org/10.1097/HP.0b013e31825ff079>
- [73] Lemay, F. (2015). A Simpler Alternative to the Probability Ratio Model for Simultaneous Source Detection and Count Rate Analysis: *Health Physics*, 109(6), 608-609. <https://doi.org/10.1097/HP.0000000000000367>
- [74] Li, T.-P., & Ma, Y.-Q. (1983). Analysis methods for results in gamma-ray astronomy. *The Astrophysical Journal*, 272, 317-324.
- [75] Lira, I. (2009). On the meaning of coverage probabilities. *Metrologia*, 46(6), 616-618. <https://doi.org/10.1088/0026-1394/46/6/002>
- [76] Liseo, B. (2005). The Elimination of Nuisance Parameters. In D. K. Dey & C. R. Rao (Éds.), *Handbook of Statistics* (Vol. 25, p. 193-219). Elsevier. [https://doi.org/10.1016/S0169-7161\(05\)25007-1](https://doi.org/10.1016/S0169-7161(05)25007-1)
- [77] Lista, L. (2016). *Statistical methods for data analysis in particle physics*. Springer.
- [78] Little, R. J. A. (1982). The Statistical Analysis of Low-level Radioactivity in the Presence of Background Counts: *Health Physics*, 43(5), 693-703. <https://doi.org/10.1097/00004032-198211000-00007>
- [79] Mana, G., & Palmisano, Ca. (2014). Interval estimations in metrology. *Metrologia*, 51(3), 191-196. <https://doi.org/10.1088/0026-1394/51/3/191>
- [80] Manificat, guillaume. (2015). *Utilisation résultats de mesures non censurées pour les estimations de radioactivité* (SESURE 2015-20). IRSN.
- [81] Michel, R. (2016). Measuring, Estimating, and Deciding under Uncertainty. *Applied Radiation and Isotopes*, 109, 6-11. <https://doi.org/10.1016/j.apradiso.2015.12.013>
- [82] Miller, G., Martz, H. F., Little, T. T., & Guilmette, R. (2002). Using exact poisson likelihood functions in bayesian interpretation of counting measurements. *Health Physics*, 83(4), 512-518. <https://doi.org/10.1097/00004032-200210000-00009>
- [83] Moore, D. S., McCabe, G. P., & Craig, B. A. (2009). *Introduction to the practice of statistics* (6th ed). W.H. Freeman.
- [84] Nickerson, R. S. (2000). Null hypothesis significance testing : A review of an old and continuing controversy. *Psychological methods*, 5(2), 241.
- [85] Nosek, D., & Nosková, J. (2016). On Bayesian analysis of on-off measurements. *Nuclear Instruments and Methods in Physics Research Section A: Accelerators, Spectrometers, Detectors and Associated Equipment*, 820, 23-33. <https://doi.org/10.1016/j.nima.2016.02.094>
- [86] Papoulis, A. (2002). *PROBABILITY, RANDOM VARIABLES, AND STOCHASTIC PROCESSES*.
- [87] Pawitan, Y. (2001). *In all likelihood : Statistical modelling and inference using likelihood*. Clarendon Press ; Oxford University Press.



- [88] Riley, K. F., Hobson, M. P., & Bence, S. J. (2006). *Mathematical methods for physics and engineering : A comprehensive guide*. Cambridge university press.
- [89] Rivals, I., Fabbri, C., Euvrard, G., & Blanchard, X. (2012). A Bayesian method with empirically fitted priors for the evaluation of environmental radioactivity : Application to low-level radioxenon measurements. *Journal of Radioanalytical and Nuclear Chemistry*, 292(1), 141-153. <https://doi.org/10.1007/s10967-011-1390-6>
- [90] Rosenkrantz, R. D. (1989). Marginalization and Prior Probabilities (1980). In *E. T. Jaynes : Papers on Probability, Statistics and Statistical Physics* (p. 337-375). Springer, Dordrecht. [https://doi.org/10.1007/978-94-009-6581-2\\_12](https://doi.org/10.1007/978-94-009-6581-2_12)
- [91] Rozeboom, W. W. (1960). The fallacy of the null-hypothesis significance test. *Psychological bulletin*, 57(5), 416.
- [92] Severini, T. A. (1991). On the Relationship Between Bayesian and Non-Bayesian Interval Estimates. *Journal of the Royal Statistical Society. Series B (Methodological)*, 53(3), 611-618.
- [93] Skellam, J. G. (1946). The Frequency Distribution of the Difference Between Two Poisson Variates Belonging to Different Populations. *Journal of the Royal Statistical Society*, 109(3), 296. <https://doi.org/10.2307/2981372>
- [94] Sprott, D. A. (2008). *Statistical inference in science*. Springer Science & Business Media.
- [95] Strom, D. J., & MacLellan, J. A. (2001). EVALUATION OF EIGHT DECISION RULES FOR LOW-LEVEL RADIOACTIVITY COUNTING: *Health Physics*, 81(1), 27-34. <https://doi.org/10.1097/00004032-200107000-00005>
- [96] Temme, N. M. (1992). Asymptotic inversion of incomplete gamma functions. *Mathematics of Computation*, 58(198), 755-764. <https://doi.org/10.1090/S0025-5718-1992-1122079-8>
- [97] Turner, J. E. (2007). *Atoms, radiation, and radiation protection* (3rd completely rev. and enl. ed). Wiley-VCH.
- [98] van Dyk, D. A. (2014). The Role of Statistics in the Discovery of a Higgs Boson. *Annual Review of Statistics and Its Application*, 1(1), 41-59. <https://doi.org/10.1146/annurev-statistics-062713-085841>
- [99] Vivier, A., Le Petit, G., Pigeon, B., & Blanchard, X. (2009). Probabilistic assessment for a sample to be radioactive or not : Application to radioxenon analysis. *Journal of Radioanalytical and Nuclear Chemistry*, 282(3), 743-748. <https://doi.org/10.1007/s10967-009-0315-0>
- [100] Vivier, V., & Aupiais, J. (2007). Optimization of the decision threshold for single radioactive counting. *Radiochimica Acta*, 95(8). <https://doi.org/10.1524/ract.2007.95.8.477>
- [101] Voigtman, E. (2017). *Limits of detection in chemical analysis*. Wiley.
- [102] Wasserstein, R. L., & Lazar, N. A. (2016). The ASA's Statement on p-Values : Context, Process, and Purpose. *The American Statistician*, 70(2), 129-133. <https://doi.org/10.1080/00031305.2016.1154108>
- [103] Weise, K. (1998). Bayesian-statistical decision threshold, detection limit, and confidence interval in nuclear radiation measurement. *Kerntechnik*, 63, 214-224.
- [104] Weise, K., Hübel, K., Rose, E., Schläger, M., Schrammel, D., Täschner, M., & Michel, R. (2006). Bayesian decision threshold, detection limit and confidence limits in ionising-radiation measurement. *Radiation Protection Dosimetry*, 121(1), 52-63. <https://doi.org/10.1093/rpd/ncl095>
- [105] Weise, K., Kanisch, G., Michel, R., Schläger, M., Schrammel, D., Täschner, M., & Fachverband für Strahlenschutz (Éds.). (2013). *Characteristic values in measurement of ionizing radiation—Material for a critical discussion on fundamentals and alternatives*. TÜV Media.
- [106] Willink, R. (2006). Principles of probability and statistics for metrology. *Metrologia*, 43(4), S211-S219. <https://doi.org/10.1088/0026-1394/43/4/S07>
- [107] Willink, R. (2010a). Difficulties arising from the representation of the measurand by a probability distribution. *Measurement Science and Technology*, 21(1), 015110. <https://doi.org/10.1088/0957-0233/21/1/015110>
- [108] Willink, R. (2010b). Measurement of small quantities : Further observations on Bayesian methodology. *Accreditation and Quality Assurance*, 15(9), 521-527. <https://doi.org/10.1007/s00769-010-0664-y>
- [109] Willink, R. (2010c). Uncertainty in repeated measurement of a small non-negative quantity : Explanation and discussion of Bayesian methodology. *Accreditation and Quality Assurance*, 15(3), 181-188. <https://doi.org/10.1007/s00769-009-0595-7>
- [110] Willink, R. (2013). *Measurement Uncertainty and Probability*. Cambridge University Press. <https://doi.org/10.1017/CBO9781139135085>

- [111] Zähringer, M., & Kirchner, G. (2008). Nuclide ratios and source identification from high-resolution gamma-ray spectra with Bayesian decision methods. *Nuclear Instruments and Methods in Physics Research Section A: Accelerators, Spectrometers, Detectors and Associated Equipment*, 594(3), 400-406. <https://doi.org/10.1016/j.nima.2008.06.044>
- [112] Ziliak, S. T., & McCloskey, D. N. (2008). *The cult of statistical significance : How the standard error costs us jobs, justice, and lives*. University of Michigan Press.
- [113] Zorko, B., Korun, M., Mora Canadas, J. C., Nicoulaud-Gouin, V., Chyly, P., Blixt Buhr, A. M., Lager, C., Aquilonius, K., & Krajewski, P. (2016). Systematic influences of gamma-ray spectrometry data near the decision threshold for radioactivity measurements in the environment. *Journal of Environmental Radioactivity*, 158-159, 119-128. <https://doi.org/10.1016/j.jenvrad.2016.04.009>

## ANNEXE 1 PRODUCT AND CONVOLUTION OF GAUSSIAN DISTRIBUTIONS

### 1.1 Product

If  $f$  and  $g$  are both gaussian distributions :

$$f(x) = \frac{1}{\sqrt{2\pi}\sigma_f} e^{-\frac{(x-\mu_f)^2}{2\sigma_f^2}} \text{ et } g(x) = \frac{1}{\sqrt{2\pi}\sigma_g} e^{-\frac{(x-\mu_g)^2}{2\sigma_g^2}}$$

$$\text{with } \sigma_{fg} = \sqrt{\frac{\sigma_f^2\sigma_g^2}{\sigma_f^2+\sigma_g^2}} \text{ and } \mu_{fg} = \frac{\mu_f\sigma_f^2+\mu_g\sigma_g^2}{\sigma_f^2+\sigma_g^2}$$

the product will be :

$$f(x)g(x) = \frac{1}{\sqrt{2\pi}\sigma_{fg}} e^{-\frac{(x-\mu_{fg})^2}{2\sigma_{fg}^2}} \frac{1}{\sqrt{2\pi(\sigma_f^2 + \sigma_g^2)}} e^{-\frac{(\mu_f-\mu_g)^2}{2(\sigma_f^2+\sigma_g^2)}}$$

### 1.2 Convolution

If  $f$  and  $g$  are both gaussian distributions :

$$f(x) = \frac{1}{\sqrt{2\pi}\sigma_f} e^{-\frac{(x-\mu_f)^2}{2\sigma_f^2}} \text{ et } g(x) = \frac{1}{\sqrt{2\pi}\sigma_g} e^{-\frac{(x-\mu_g)^2}{2\sigma_g^2}}$$

Then their convolution will be (Bromiley, 2003) :

$$f \oplus g(x) = \int f(t-x)g(t)dx = \frac{1}{\sqrt{2\pi(\sigma_f^2+\sigma_g^2)}} e^{-\frac{(x-(\mu_f+\mu_g))^2}{2(\sigma_f^2+\sigma_g^2)}}$$

## ANNEXE 2 RAPPORTS D'ESSAI

SL 31 **3H Combustion Environnement** Monophase : 15,00 ml  
 P# 3HCombEnv Prise d'essai : 1,00 ml  
**1+MPLIQ** U(Pe) : 0,04 ml (k=2)  
 Ech. N° 1 Fact. correctif : 1,00  
 Essai N° 1 **Recomptage** Rdt comb : 100,00 %  
 3.8.b U(Rdt comb) : 7,00 % (k=2)

LUM	N <sub>brut</sub> (cpm) 0 à 8 KeV		N <sub>brut</sub> (cpm) 15 à 80 keV		N <sub>brut</sub> (cpm) 80 à 2000 keV		Temps (min)	Tsie	Date de comptage
4	1,960	bon	3,020	bon	4,040	bon	50	521,17	24/07/2019 13:12:09
4	2,540	bon	3,200	bon	4,280	bon	50	522,39	25/07/2019 09:26:28
4	1,980	bon	3,160	bon	3,420	douteux	50	519,07	26/07/2019 05:40:45
4	2,240	bon	3,380	bon	4,640	bon	50	521,15	27/07/2019 01:55:05
<b>Nbrut</b>	<b>2,180</b>	<b>cpm</b>	<b>3,190</b>	<b>cpm</b>	<b>4,095</b>	<b>cpm</b>	<b>200</b>	<b>520,95</b>	<b>25/07/2019 19:33:37</b>
MP	2,172	cpm	3,008	cpm	4,305	cpm			
<b>Nnet</b>	<b>0,008</b>	<b>cpm</b>	<b>0,183</b>	<b>cpm</b>	<b>-0,210</b>	<b>cpm</b>			
Sigma	0,289	cpm	0,340	cpm	0,407	cpm			

SL 31 **3H Combustion Environnement** Monophase : 15,00 ml  
 P# 3HCombEnv Prise d'essai : 2,00 ml  
**15+S19EEA21-98B1** U(Pe) : 0,08 ml (k=2)  
 Ech. N° 15 Fact. correctif : 1,00  
 Essai N° 1 **Recomptage alcool** Rdt comb : 100,00 %  
 3.8.b U(Rdt comb) : 7,00 % (k=2)

LUM	N <sub>brut</sub> (cpm) 0 à 8 KeV		N <sub>brut</sub> (cpm) 15 à 80 keV		N <sub>brut</sub> (cpm) 80 à 2000 keV		Temps (min)	Tsie	Date de comptage
4	2,140	bon	2,720	douteux	3,860	bon	50	450,27	25/07/2019 03:17:28
3	2,540	bon	3,340	bon	4,280	bon	50	444,74	25/07/2019 23:32:06
3	2,760	bon	3,480	bon	4,200	bon	50	450,40	26/07/2019 19:46:30
3	2,480	bon	3,600	bon	4,160	bon	50	454,92	27/07/2019 16:00:45
<b>Nbrut</b>	<b>2,480</b>	<b>cpm</b>	<b>3,285</b>	<b>cpm</b>	<b>4,125</b>	<b>cpm</b>	<b>200</b>	<b>450,08</b>	<b>26/07/2019 09:39:12</b>
MP	2,180	cpm	3,190	cpm	4,095	cpm			
<b>Nnet</b>	<b>0,300</b>	<b>cpm</b>	<b>0,095</b>	<b>cpm</b>	<b>0,030</b>	<b>cpm</b>	46,27	841,00	Tsie de 0 à 8 KeV
SD	0,289	cpm	0,350	cpm	0,397	cpm			
LD	0,599	cpm	0,000	cpm					

**CALCUL FENÊTRE : 0 à 8 KeV**

Radionucléide : 3H *Tsie OK*  
 Période(j) : 4,50E+03

Rdt (3H) = 42,94 ± 3,90 % (k=2) le 25/08/2017

Nnet (3H) = 0,300 ± 0,305 cpm (k=2)

Activité brute = 0,012 Bq/pe U(A)/A = 102,48 % (k=2)

SD = 5,616 Bq/l A = 0,012 Bq/pe  
 LD = 11,622 Bq/l A = **5,822E+00 Bq/l**

### ANNEXE 3 HYPERGEOMETRIC FUNCTION

We saw that we could express  $p_{\theta}(\theta|x, y) = \frac{1}{\Gamma(x+1)\Gamma(y+1)} \iint \lambda^y e^{-\lambda} \mu^x e^{-\mu} \delta(\theta + \mu - \lambda) d\mu d\lambda$

It is then necessary to differentiate the case  $\theta > 0$  from  $\theta < 0$  (Papoulis, 2002).

$$p_{\theta}(\theta|x, y) = \frac{1}{\Gamma(x+1)\Gamma(y+1)} \int_0^{\infty} (\mu + \theta)^x e^{-(2\mu+\theta)} \mu^y d\mu \text{ pour } \theta > 0$$

$$p_{\theta}(\theta|g, b) = \frac{1}{\Gamma(x+1)\Gamma(y+1)} \int_0^{\infty} \lambda^x e^{-(2\lambda-\theta)} (\lambda - \theta)^y d\lambda \text{ pour } \theta < 0$$

The above integrals can be expressed in the form of a confluent hypergeometric Tricomi function (Bergamaschi et al., 2013):

$$U(a, b, z) = \frac{1}{\Gamma(a)} \int_0^{\infty} e^{-zt} t^{a-1} (1+t)^{b-a-1} dt$$

For  $\theta > 0$

$$\begin{aligned} p_{\theta}(\theta|x, y) &= \frac{1}{\Gamma(x+1)\Gamma(y+1)} e^{-\theta} \int_0^{\infty} (\mu + \theta)^x e^{-2\mu} \mu^y d\mu \\ &= \frac{1}{\Gamma(x+1)\Gamma(y+1)} e^{-\theta} \theta^{x+y} \int_0^{\infty} \left(\frac{\mu}{\theta} + 1\right)^x e^{-2\theta \frac{\mu}{\theta}} \left(\frac{\mu}{\theta}\right)^y \theta d\left(\frac{\mu}{\theta}\right) \\ &= \frac{1}{\Gamma(x+1)\Gamma(y+1)} e^{-\theta} \theta^{x+y+1} \int_0^{\infty} (t+1)^x e^{-2\theta t} (t)^y dt \\ &= \frac{1}{\Gamma(x+1)} e^{-\theta} \theta^{x+y+1} U(y, x+y+2, 2\theta) \end{aligned}$$

In the same way, for  $\theta < 0$  :

$$p_{\theta}(\theta|x, y) = \frac{1}{\Gamma(x+1)} e^{\theta} \theta^{x+y+1} U(x, x+y+2, -2\theta)$$

Tables or mathematical software then make it possible to calculate this expression for all the values of  $\theta, x$  and  $y$ .

It is possible to calculate the decision threshold from this expression:

$$p_{\theta}(\theta > 0|x, y) = 1 - p_{\theta}(\theta < 0|x, y) = 1 - \alpha_c = \frac{1}{\Gamma(y+1)} \int_0^{\infty} e^{-\theta} \theta^{x+y+1} U(y, x+y+2, 2\theta) d\theta$$

Mathematics tables (Gradshteyn et al., 2000) give us :

$$\int_0^{\infty} e^{-s\theta} \theta^{b-1} U(a, c, \theta) d\theta = \frac{\Gamma(b)\Gamma(b-c+1)}{\Gamma(a+b-c+1)} F(b, b-c+1; a+b-c+1; 1-s)$$

Where  $F(a, b; c; x)$  is the hypergeometric function.

By changing the variable  $v = 2\theta$ , we get :

$$\alpha_c = \frac{1}{\Gamma(x+1)} \int_0^{\infty} e^{-v/2} (v/2)^{x+y+1} U(y, x+y+2, v) dv$$

Using the previously mentioned formula, we obtain:

$$\alpha_c = \frac{1}{2^{x+y+1}} \frac{1}{\Gamma(x+1)} \frac{\Gamma(x+y+2)}{\Gamma(y+1)} F(x+y+2, 1; y+1; 1/2)$$

If we know  $y$ , this amounts to finding  $k$  such that:

$$\alpha_c = \frac{1}{2^{2y+k+1}} \frac{1}{\Gamma(y+k+1)} \frac{\Gamma(2y+k+2)}{\Gamma(y+1)} F(2y+k+2, 1; y+1; 1/2)$$

The advantage of this type of formula is that it does not require any knowledge other than  $y$  to obtain an expression for  $k$ .

## ANNEXE 4 NEYMAN PEARSON LEMMA

Consider a null hypothesis  $H_0$ . This is an assertion about a statistical distribution that we wish to test, generally in the form of the absence of an effect.

We then consider the alternative hypothesis  $H_a$ . Our goal is then to determine, using a test on observations, which hypothesis is most compatible with the data. Let us insist on the fact that Neyman Pearson's approach, which the metrological criteria are based on, necessarily requires the definition of this alternative hypothesis.

In the null hypothesis, we assume that it is the noise ( $B'$ ) which will generate the measurement  $x$  (we therefore have in this hypothesis  $\theta=0$ ). We know that if we obtained  $y$  during a first measurement then a second measurement is distributed according to  $p_N$  :

$$p_{G|B}^{H_0}(x|y) = p_N(x|y) = \frac{e^{-\frac{(x-y)^2}{4\sigma_B^2}}}{\sqrt{4\pi\sigma_B}} = \frac{e^{-\frac{z^2}{4\sigma_B^2}}}{\sqrt{4\pi\sigma_B}} = p_N(z|0, 2\sigma_B^2)$$

For the alternative hypothesis ( $\theta > 0$ ),

$$p_{G|B}^{H_a}(x|y) = p_N(z|\theta, 2\sigma_B^2) = \int_{-\infty}^{\infty} p_S(z-w|\theta)p_N(w|\varepsilon, 2\sigma_B^2)dw = \int_{-\infty}^{\infty} p_S(x-y'|\theta)p_N(y'|y, 2\sigma_B^2)dw$$

The Neyman-Pearson approach will seek to determine whether it is likely that  $\theta=0$  through the use of likelihood ratios (Lehmann & Romano, 2005a) :

$$\Lambda(z|\theta) = \frac{p_{H_0}(z)}{p_{H_a}(z|\theta)} = \frac{\frac{e^{-\frac{z^2}{4\sigma^2}}}{\sqrt{4\pi\sigma}}}{\frac{e^{-\frac{(z-\theta)^2}{4\sigma^2}}}{\sqrt{4\pi\sigma}}} = e^{-\frac{(2z\theta-\theta^2)}{4\sigma^2}}$$

(31)

Neyman Pearson's lemma proves that the most powerful test is the one that rejects  $H_0$  for the benefit of  $H_a$  when  $\Lambda(z|\theta) \leq c_\alpha$ , with  $c_\alpha$  such that:

$$p_{H_0}(\Lambda(z|\theta) \leq c_\alpha) = \alpha$$

This means that the set of  $z$  such that  $\Lambda(z|\theta) \leq c_\alpha$  is equivalent to the set of  $z$  such that  $z > z_c$ , with  $z_c$  determined by :

$$p_{G-B}^{H_0}(z > z_c) = \alpha$$

By the most powerful test, we mean the test that will minimize the false negative rate for a fixed false positive rate. Note that the ratio of the equation (31) is decreasing as  $z$  increases, if  $\theta$  is positive. This condition is met in the present case since we are interested in a positive physical quantity. We can even add that this ratio decreases monotonically. The Karlin-Rubin theorem (Karlin & Rubin, 1956) which is an extension of the

Neyman-Pearson lemma, then assures us that it is the uniformly most powerful test. That is to say, if we want to test whether  $\theta > 0$ , the criterion  $z > z_c$  with  $z_c$  such that

$$\alpha_c = \int_{z_c}^{\infty} p_{H_0}(z) dz = \int_{z_c}^{\infty} p_N(z|0) dz$$

**(32)**

Will lead to the test minimizing the false negative rate, while fixing the false positive rate. Note that we are in fact testing whether  $\theta > 0$  which corresponds to testing whether  $\mu > \lambda$ .

The proportion of false negatives for a given value of the parameter  $\theta$  will then be:

$$\beta_c = \int_0^{z_c} p_N(z|\theta) dz$$

**(33)**

No other statistical test of the same level  $\alpha_c$  will be able to give a smaller  $\beta_c$  (the power of the test).

Note that such a definition is perfectly compatible with that of the ISO (ISO, 2010a) which does not specify the type of hypothesis test to be carried out.

Under the null hypothesis, the proportion of measures exceeding this desired level  $z_c$  must therefore reach a value  $\alpha$  that we set a priori. If the measurement exceeds this threshold thus determined, we can reject this hypothesis. Only  $100\alpha\%$  The measures would statistically exceed this level  $z_c$  if the parameter was null. This amounts to having  $100\alpha\%$  probability of false positive if the parameter was zero.

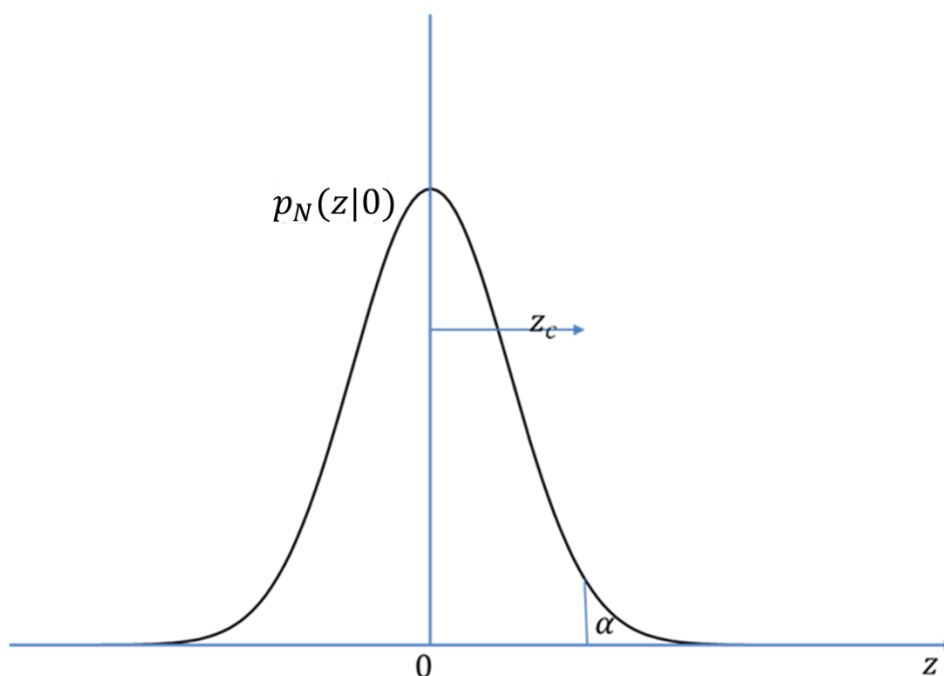


Figure 14 - Schematic diagram of the frequentist determination of the decision threshold





# Nonperturbative Collins-Soper Kernel from Chiral Quarks with Physical Masses

Dennis Bollweg,<sup>1</sup> Xiang Gao,<sup>2,\*</sup> Swagato Mukherjee,<sup>1</sup> and Yong Zhao<sup>2</sup>

<sup>1</sup>*Physics Department, Brookhaven National Laboratory, Upton, New York 11973, USA*

<sup>2</sup>*Physics Division, Argonne National Laboratory, Lemont, Illinois 60439, USA*

(Dated: March 4, 2024)

## Abstract

We present a lattice QCD calculation of the rapidity anomalous dimension of quark transverse-momentum-dependent distributions, i.e., the Collins-Soper (CS) kernel, up to transverse separations of about 1 fm. This unitary lattice calculation is conducted, for the first time, employing the chiral-symmetry-preserving domain wall fermion discretization and physical values of light and strange quark masses. The CS kernel is extracted from the ratios of pion quasi-transverse-momentum-dependent wave functions (quasi-TMDWFs) at next-to-leading logarithmic perturbative accuracy. Also for the first time, we utilize the recently proposed Coulomb-gauge-fixed quasi-TMDWF correlator without a Wilson line. We observe significantly slower signal decay with increasing quark separations compared to the established gauge-invariant method with a staple-shaped Wilson line. This enables us to determine the CS kernel at large nonperturbative transverse separations and find its near-linear dependence on the latter. Our result is consistent with the recent lattice calculation using gauge-invariant quasi-TMDWFs, and agrees with various recent phenomenological parametrizations of experimental data.

---

\* [gaox@anl.gov](mailto:gaox@anl.gov)

## I. INTRODUCTION

The parton transverse-momentum-dependent distributions (TMDs) are crucial for a three-dimensional understanding of parton motions within a hadron, offering a more comprehensive view than traditional one-dimensional parton distribution functions (PDFs). It sheds light not only on the intrinsic motion of partons in transverse directions but also on the interplay between the transverse momentum of quarks and the spin of nucleons or quarks themselves. This comprehensive perspective is crucial for a deep understanding of the dynamic and complex nature of nucleons. The accurate characterization of TMDs is also critical for interpreting experimental data from high-energy collisions, particularly in relation to the transverse momentum distributions of electroweak and Higgs bosons [1, 2]. They are fundamental to precision measurements, such as determining the mass and width of the W boson [3, 4]. As high-energy physics experiments continue to advance, the measurement of TMDs will become increasingly important. The ongoing and future experiments at facilities such as the Large Hadron Collider [5, 6] and Electron-Ion Collider [7–10] are expected to profoundly enrich our knowledge of TMDs. This will not only enhance our grasp of hadron structure and nucleon spin but also contribute significantly to the broader field of particle physics.

Central to the study and practical application of TMDs is the Collins-Soper (CS) kernel, which is responsible for the (rapidity) scale evolution of TMDs [11, 12], enabling the consistent interpretation of experimental data across different energy scales. It is instrumental in connecting theoretical predictions with experimental observations. The TMDs and CS kernel can be extracted through the global analysis of experimental data including the semi-inclusive deep inelastic scattering (SIDIS) and Drell-Yan processes [13–29]. However, the nonperturbative nature of Quantum Chromodynamics (QCD) at low transverse momenta necessitates certain parametrizations and introduces model dependence. As a result, there is an increasing interest for these intrinsically nonperturbative quantities to be calculated directly from first-principles lattice QCD.

Although direct simulation of TMDs on the Euclidean lattice is impractical, as TMDs are defined on the light-cone, it has been demonstrated that they can be accessed through quasi-TMDs within the framework of Large-Momentum Effective Theory (LaMET) [30–32].

The quasi-TMDs involve the matrix elements of equal-time gauge-invariant (GI) operators:

$$O_{\Gamma}^{\text{GI}}(\mathbf{b}; \eta) = \bar{\psi}\left(\frac{\mathbf{b}}{2}\right)\Gamma W_{\square}\left(\frac{\mathbf{b}}{2}, -\frac{\mathbf{b}}{2}, \eta\right)\psi\left(-\frac{\mathbf{b}}{2}\right), \quad (1)$$

with  $\mathbf{b} = (b_{\perp}, b_z)$  covering both longitudinal ( $b_z$ ) and transverse ( $b_{\perp}$ ) directions, linked by a staple-shaped Wilson line  $W_{\square}$  whose length is characterized by  $\eta$ . In the large momentum and  $\eta \rightarrow \infty$  limit, the quasi-TMDs can be related to the light-cone TMDs through the perturbative factorization [33–46]. Building on this, significant advancements have been achieved over the past few years. The CS kernel has been extracted from either quasi-TMD parton distribution functions (TMDPDFs) [47–49], quasi-TMD wave functions (TMDWFs) [49–55], or the moments of the quasi-TMDs [56]. Lattice QCD calculations of soft functions [50, 51, 53], along with the first results of nucleon TMD PDFs [57] and pion TMDWFs [58] also have been reported. Additionally, progress has also been made in the systematical control of these calculations, including improved matching up to two loops [59, 60], addressing the operator mixing and working at physical quark masses [54, 55, 61–67].

Despite notable progress, the lattice calculation of TMDs remains challenging. To suppress power corrections, a large momentum  $P_z$  is required, which incurs a significant computational cost. In addition, the signal-to-noise ratio of the quasi-TMD matrix elements is adversely affected by exponential decay as the total length of the space-like Wilson line increases. This decay makes it particularly difficult to investigate quasi-TMDs at large  $b_{\perp}$ , where the results are desired to complement the phenomenological analysis. What’s more, the linear divergence and pinch-pole singularity in the Wilson lines also complicate the renormalization procedure, although they could be cancelled by the Wilson loop [68] or held fixed by keeping a constant length of the Wilson line for given  $b_{\perp}$  [54]. Besides, the operator mixings of Wilson-line operators [62–66] also need to be subtracted systematically [54]. Recently, a novel approach has been proposed for computing parton physics in the Coulomb gauge (CG)[69], notably without the use of Wilson lines. Thereby, the complexity induced by the Wilson line can be avoided. It has been demonstrated that, in the large momentum limit, the CG quasi-PDF falls into the same universality class as the GI case under the LaMET framework. Further progress has been made in the realm of quasi-TMDs [70], involving the matrix elements of equal-time operators,

$$O_{\Gamma}^{\text{CG}}(\mathbf{b}) = \bar{\psi}\left(\frac{\mathbf{b}}{2}\right)\Gamma\psi\left(-\frac{\mathbf{b}}{2}\right)|_{\nabla \cdot \mathbf{A}=0}, \quad (2)$$

with the CG condition  $\nabla \cdot \mathbf{A} = 0$  but without a Wilson line. The factorization of quasi-TMDs in the CG has been derived from the soft collinear effective theory (SCET) [70] and verified at one loop in perturbation theory [70, 71]. In this study, we have, for the first time, computed the quasi-TMDWFs of the pion in the CG and extracted the CS kernel from these measurements. Without Wilson lines, the CG correlators are multiplicatively renormalizable and free from the linear divergence [69] and pinch singularity, as well as the operator mixings originating from the Wilson line geometry. Through our calculation, we show that, the CG approach leads to consistent CS kernel with the conventional GI approach. Moreover, the CG approach can significantly reduce the signal-to-noise ratio and extend the prediction power of lattice computation in the nonperturbative regime of interest to TMD physics.

## II. THEORETICAL FRAMEWORK

The pion quasi-TMDWF in the CG is defined as the Fourier transform of the matrix elements:

$$\tilde{\phi}_\Gamma^{\text{CG}}(b_\perp, b_z, P_z, \mu) = \langle \Omega | O_\Gamma^{\text{CG}}(\mathbf{b}) | \pi^+; P_z \rangle, \quad (3)$$

where the pion is boosted with momentum  $\mathbf{P} = (0, 0, P_z)$ . By selecting  $\Gamma = \gamma_t \gamma_5$  or  $\gamma_z \gamma_5$ , the quasi-TMDWF  $\tilde{\phi}_\Gamma(x, b_\perp, P_z, \mu)$  can be related to the light-cone TMDWF  $\phi(x, b_\perp, \zeta, \mu)$  (under the principle-value prescription of the light-cone Wilson lines [72]) in the large  $P_z$  limit through perturbative factorization, which can be expressed as [37, 42, 70],

$$\begin{aligned} \frac{\tilde{\phi}_\Gamma(x, b_\perp, P_z, \mu)}{\sqrt{S_r(b_\perp, \mu)}} &= H(x, \bar{x}, P_z, \mu) \phi(x, b_\perp, \zeta, \mu) \exp \left[ \frac{1}{4} \left( \ln \frac{(2xP_z)^2}{\zeta} + \ln \frac{(2\bar{x}P_z)^2}{\zeta} \right) \gamma^{\overline{\text{MS}}}(b_\perp, \mu) \right] \\ &+ \mathcal{O} \left( \frac{\Lambda_{\text{QCD}}^2}{(xP_z)^2}, \frac{1}{(b_\perp(xP_z))^2}, \frac{\Lambda_{\text{QCD}}^2}{(\bar{x}P_z)^2}, \frac{1}{(b_\perp(\bar{x}P_z))^2} \right), \end{aligned} \quad (4)$$

with  $\bar{x} = 1 - x$ .  $\gamma^{\overline{\text{MS}}}(b_\perp, \mu)$  is the CS kernel that governs the rapidity scale evolution from  $\zeta$  to  $(2xP_z)^2$  (or  $(2\bar{x}P_z)^2$ ).  $H(x, \bar{x}, P_z, \mu)$  is a hard matching kernel that has been computed from one-loop perturbation theory [70, 71].  $S_r(b_\perp, \mu)$  represents the reduced soft functions, extractable from the form factors of fast-moving color-charged states [37, 42, 70]. Consequently, the  $x$ -dependent light-cone TMDWF can be derived, subject to power corrections that are suppressed by large  $P_z$  and  $b_\perp$ . Alternatively, the CS kernel can be

extracted through the ratios of the quasi-TMDWFs with different momenta  $P_1$  and  $P_2$ ,

$$\gamma^{\overline{\text{MS}}}(b_\perp, \mu) = \frac{1}{\ln(P_2/P_1)} \ln \left[ \frac{\tilde{\phi}(x, b_\perp, P_2, \mu)}{\tilde{\phi}(x, b_\perp, P_1, \mu)} \right] + \delta\gamma^{\overline{\text{MS}}}(x, \mu, P_1, P_2) + \text{p.c.}, \quad (5)$$

with perturbative corrections  $\delta\gamma^{\overline{\text{MS}}}$  inferred from  $H(x, \bar{x}, P_z, \mu)$  and power corrections (p.c.).

### III. LATTICE SETUP

The bare matrix elements of the pion quasi-TMDWF can be extracted from the two-point correlation functions in the lattice simulations. For CG quasi-TMDWFs, we compute,

$$C_{\pi O}^{\text{CG}}(t_s; b_\perp, b_z, P_z) = \langle O_\Gamma^{\text{CG}}(\mathbf{b}, \mathbf{P}, t_s) \pi^\dagger(\mathbf{y}_0, 0) \rangle, \quad (6)$$

with,

$$O_\Gamma^{\text{CG}}(\mathbf{b}, \mathbf{P}, t_s) = \sum_{\mathbf{y}} \bar{d}(\mathbf{y} + \frac{\mathbf{b}}{2}, t_s) \Gamma u(\mathbf{y} - \frac{\mathbf{b}}{2}, t_s) |_{\nabla \cdot \mathbf{A}=0} e^{-i\mathbf{P} \cdot (\mathbf{y} - \mathbf{y}_0)}. \quad (7)$$

Here  $\mathbf{y}_0$  is the source position, and  $t_s$  is the time separation. We chose  $\Gamma = \gamma_t \gamma_5$ , as it should be free from the operator mixings caused by chiral symmetry breaking [62, 64, 65] under our lattice setup.

To improve the signal-to-noise ratio and increase the overlap with the pion ground state, we used extended pion source after boosted Gaussian smearing [73],

$$\pi^\dagger(\mathbf{y}, t_s) = \bar{u}_s(\mathbf{y}, t_s) \gamma_5 d_s(\mathbf{y}, t_s), \quad (8)$$

with the  $s$  denoting the smeared fields. We also compute the pion-pion two-point functions,

$$C_{\pi\pi}(t_s, P_z) = \langle \pi(\mathbf{P}, t_s) \pi^\dagger(\mathbf{y}_0, 0) \rangle, \quad (9)$$

with smeared source and sink to extract the energy spectrum created by  $\pi^\dagger$  as well as the overlap amplitudes.

For the lattice simulation, we utilized a 2+1-flavor Domain-wall gauge ensemble generated by RBC and UKQCD Collaborations of size  $N_s^3 \times N_t \times N_5 = 64^3 \times 128 \times 12$ , denoted by 64I [74]. The quark masses are at the physical point and the lattice spacing is  $a^{-1} = 2.3549(49)$  GeV ( $a = 0.0836$  fm). For the boosted Gaussian smearing, the Gaussian radius was chosen to be  $r_G = 0.58$  fm, and we chose the quark boost parameter  $j_z$  to be 0 and

6 [75, 76] which are optimal to hadron momentum  $P_z = 2\pi n_z/(N_s a)$  with  $n_z = 0$  and 8, so that the largest momentum in our calculation is  $P_z = 1.85$  GeV. Since only two-point functions are involved in this calculation, measurements at other momenta ( $n_z \in [0, 8]$ ) were also computed through contractions using the same profiled quark propagator.

To increase the statistics, we used 64 configurations coupled with All Mode Averaging (AMA) technique [77]. We computed 2 exact and 128 sloppy solutions for the quasi-TMDWFs with momenta  $n_z \in [4, 8]$ , while 1 exact and 32 sloppy solutions for the cases with  $n_z = [0, 3]$ . The quark propagators are evaluated from CG-fixed configurations using deflation based solver with 2000 eigen vectors.

After fixing the CG, the GI quasi-TMDWF defined from Eq. (1) shares the same quark propagators as the CG case but needs an additional staple-shaped Wilson line to maintain the gauge invariance. Therefore, we also computed the GI quasi-TMDWF correlators  $C_{\pi O}^{\text{GI}}(t_s; b_\perp, b_z, P_z, \eta)$  during the contraction. We chose  $\eta = 12a$  in this case using the same setup of the staple-shaped Wilson line as Ref. [54]. We employed Wilson flow [78], with a flow time  $t_F = 1.0$  (roughly smears the gauge fields over the radius  $\sqrt{8a^2}$ ), to suppress the ultraviolet (UV) fluctuations and enhance the signal-to-noise ratio.

#### IV. QUASI-TMDWF

The pion-pion and quasi-TMDWF correlators have the following spectral decompositions,

$$C_{\pi\pi}(t_s; P_z) = \sum_{n=0}^{N_{\text{st}}-1} \frac{|Z_n|^2}{2E_n} (e^{-E_n t_s} + e^{-E_n(L_t - t_s)}), \quad (10)$$

and,

$$C_{\pi O}^{\text{CG}}(t_s; b_\perp, b_z, P_z) = \sum_{n=0}^{N_{\text{st}}-1} \frac{Z_n}{2E_n} \langle \Omega | O_{\gamma_t \gamma_5}^{\text{CG}} | n \rangle (e^{-E_n t_s} + e^{-E_n(L_t - t_s)}), \quad (11)$$

where  $E_n(P_z)$  is the energy level, and  $Z_n = \langle n | \pi^\dagger(P_z) | \Omega \rangle$  is the overlap amplitude created by the pion interpolator (real and positive [54]).  $|\Omega\rangle$  represents the vacuum state, while  $|n\rangle = |0\rangle, |1\rangle, \dots$  represents the ground state as well as the excited states.

To take the advantage of high correlations between the pion-pion and quasi-TMDWF two-point functions, we construct their ratio as,

$$R(t_s; b_\perp, b_z, P_z) = \frac{-i C_{\pi O}^{\text{CG}}(t_s; b_\perp, b_z, P_z)}{C_{\pi\pi}(t_s; P_z)}. \quad (12)$$

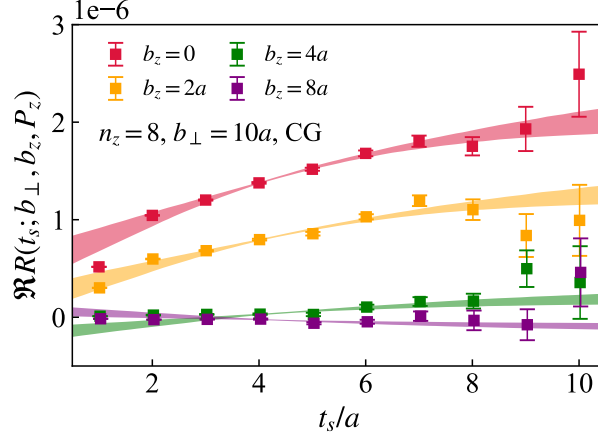


FIG. 1.  $R(t_s; b_\perp, b_z, P_z)$  as a function of  $t_s$  for  $n_z = 8$  and  $b_\perp = 10a$ . The bands are results from the two-state fits.

In Fig. 1, the ratios of our largest momentum  $n_z = 8$  at  $b_\perp = 10a$  are shown as an example. In the  $t_s \rightarrow \infty$  limit, this ratio will reduce to  $\langle \Omega | O_{\gamma_t \gamma_5} | 0 \rangle / Z_0 = E_0 \tilde{\phi}^B / Z_0$  and gives the bare quasi-TMDWF matrix elements  $\tilde{\phi}^B(b_\perp, b_z, P_z, a)$ . In practice, with finite  $t_s$  we truncate Eq. (10) and Eq. (11) up to  $N_{st} = 2$  and extract the bare matrix elements through the two-state fit. The fit results are shown as the bands in Fig. 1 which can nicely describe the data point.

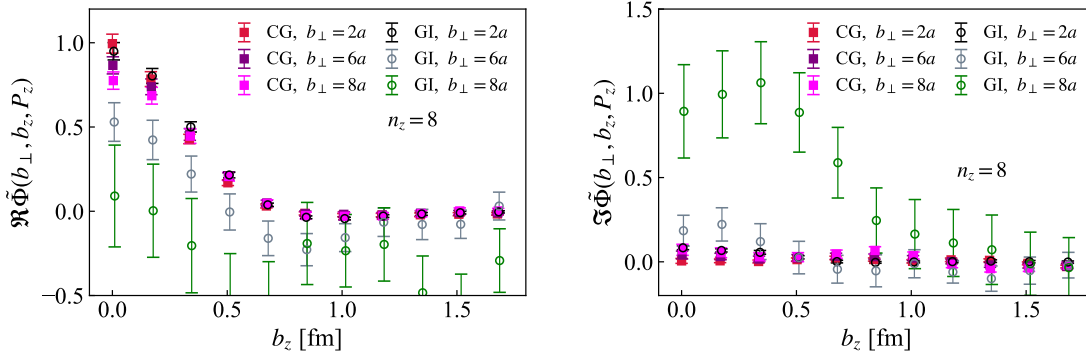


FIG. 2. The real (left) and imaginary (right) parts of the renormalized quasi-TMDWF matrix elements at  $n_z = 8$  with  $b_\perp = 2a, 6a, 8a$  for the CG (filled squared symbols) and GI cases (open circled symbols).

The renormalization of CG quasi-TMD operator is straightforward. It involves only the CG quark wave function renormalization, which is an overall multiplicative constant and does not depend on the spatial separations  $b_\perp$  and  $b_z$  [69].

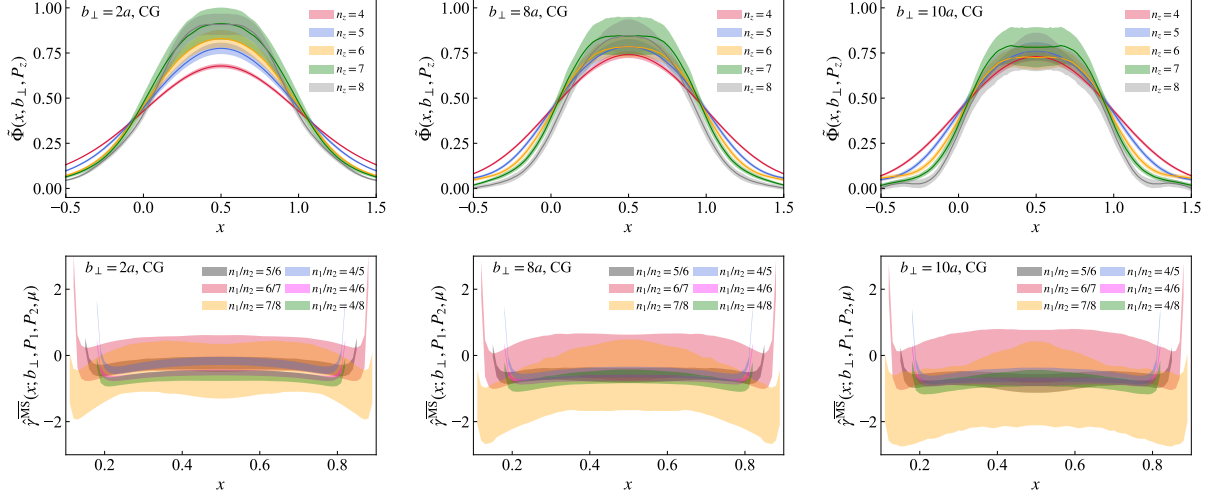


FIG. 3. Upper panels: CG quasi-TMDWFs at momentum  $n_z \in [4, 8]$  and  $b_\perp = 2a, 8a, 10a$ . Lower panels: CS kernel estimator  $\hat{\gamma}^{\overline{\text{MS}}}(x, b_\perp, P_1, P_2, \mu)$  derived from the ratio of the quasi-TMDWFs..

In contrast, the GI quasi-TMD operator defined in Eq. (1), though also subject to multiplicative renormalization, requires the removal of pinch pole singularities, cusp divergences, and linear divergences associated with the Wilson line [61, 68, 79, 80]. This renormalization is proportional to the total link length. In our implementation, the total length of the staple-shape Wilson line is  $2\eta + b_\perp$ , independent of  $b_z$ .

Since the renormalization process solely involves the UV properties of operators and is independent of the external hadron states, we use the renormalization group invariant ratios [54]

$$\tilde{\Phi}(b_\perp, b_z, P_z) = \frac{\tilde{\phi}^B(b_\perp, b_z, P_z, \eta, a)}{\tilde{\phi}^B(b_\perp, 0, 0, \eta, a)}, \quad (13)$$

without affecting the  $x$ - and  $P_z$ -dependences of the quasi-TMDWF after Fourier transform. The above ratio also may reduce some correlated uncertainties and eliminate some power corrections. Thus, we also adopt the same procedure for the CG matrix elements, whose renormalization is  $b_\perp$  and  $\eta$  independent.

In Fig. 2, we show the renormalized matrix elements for our largest momentum,  $P_z = 1.85$  GeV, and for  $b_\perp = 2a, 6a$  and  $8a$ , as a function of  $b_z$ , for both CG (filled squared symbols) and GI (open circled symbols) cases. The left panel and right panel show the real and imaginary parts, respectively. It is evident that reasonable signal remains for the CG case even when  $b_\perp$  become large. In contrast, the signal-to-noise ratio of the GI matrix elements rapidly



deteriorates as  $b_\perp$  increases, primarily due to the long Wilson line and its UV fluctuations. In addition, it is shown that the imaginary parts of the CG case are consistently zero, while they have non-zero values for GI case. This is expected as the imaginary part depends on the longitudinal orientation of the Wilson line in the GI case [72], whereas the CG condition does not favor any direction [70].

One can also observe that the matrix elements decrease as a function of  $b_z$ , diminishing to zero within the errors when  $b_z \gtrsim 1$  fm. This behavior facilitates the numerical Fourier transform to  $x$ -space with a simple truncation at the maximum value of  $b_z$ , which is expressed as,

$$\tilde{\Phi}(x, b_\perp, P_z) = \frac{P_z}{\pi} \int_0^{b_z^{\max}} e^{i(x-\frac{1}{2})P_z b_z} \tilde{\Phi}(b_\perp, b_z, P_z) \quad (14)$$

where we apply a first-order spline interpolation to smooth the data points. Since the CG quasi-TMDWF correlator is real and symmetric in  $b^z$ , the distribution must be real in the  $x$ -space.

In the upper panel of Fig. 3, we show selected results of the CG quasi-TMDWFs with momentum  $n_z \in [4, 8]$  and  $b_\perp = 2a, 8a, 10a$ . Encouragingly, reasonable signal persists even when  $b_\perp$  is as large as  $10a$ . However, the signal-to-noise ratio decreases as the momentum increases. In addition, it is evident that the quasi-TMDWFs, though appearing to be non-zero outside the physical region, have a trend to shrink into  $x \in [0, 1]$  as the momentum increases. This observation is consistent with the power expansion of the LaMET, suggesting the quasi-TMDWF is approaching the light-cone TMDWF in the large momentum limit.

## V. THE COLLINS-SOPER KERNEL

According to Eq. (5), we define the following estimator of the CS kernel utilizing the quasi-TMDWFs at finite momenta,

$$\hat{\gamma}^{\overline{\text{MS}}}(x, b_\perp, P_1, P_2, \mu) = \frac{1}{\ln(P_2/P_1)} \ln \left[ \frac{\tilde{\Phi}(x, b_\perp, P_2)}{\tilde{\Phi}(x, b_\perp, P_1)} \right] + \delta\gamma^{\overline{\text{MS}}}(x, \mu, P_1, P_2). \quad (15)$$

In this work, we applied the perturbative corrections  $\delta\gamma^{\overline{\text{MS}}}$  derived from the next-to-leading logarithm (NLL) matching kernels for the CG case [38, 43, 54, 70] as only one-loop non-cusp anomalous dimension is available. The  $\overline{\text{MS}}$  scale has been set to be  $\mu = 2$  GeV. If the power corrections and higher-order corrections are small,  $\hat{\gamma}^{\overline{\text{MS}}}$  should be independent of  $P_z$  and  $x$ .

In the lower panels of Fig. 3, we show the CS kernel estimators for the CG case with various combination of momenta,  $n_1$  and  $n_2$ , as a function of  $x$ . The  $x$ -independent plateaus can be found in the moderate  $x$  region within the errors, which is robust even at the largest  $b_\perp$ . This indicates the effectiveness of the factorization formula in (4). In the end-point regions of both small and large  $x$ , the results appear to diverge, signaling a breakdown of the factorization in these areas. However, the length of plateaus extend as the momentum increases, which is consistent with the power corrections suggested in Eq. (4).

As for the momentum dependence, it is absent even for the case of large  $b_\perp$  due, which indicates well suppressed power corrections by  $1/(P_z b_\perp)$ , despite their slightly larger errors. However, results at small  $b_\perp$  (e.g., for  $2a$ ) and with small momentum (e.g., for  $n_1 = 4$ ) deviated from the ones derived from larger momenta. This momentum dependence is reduced when  $n_1$  and  $n_2$  gets close, and disappear when  $n_1$  and  $n_2$  are close enough (e.g., for  $n_1/n_2 = 4/5$ ). This observation suggests that the power corrections and higher-order perturbative corrections are not well suppressed in the cases of small  $b_\perp$  and large differences in  $P_z$ .

To estimate the CS kernel, we averaged over the estimator  $\hat{\gamma}^{\overline{\text{MS}}}(x, b_\perp, \mu, P_1, P_2)$  within  $x \in [x_0, 1 - x_0]$  across various  $n_1$  and  $n_2$ . Only the cases of  $n_2 - n_1 = 1$  are considered. The value of  $x_0$  is determined by requiring  $2x_0 P_z b_\perp > 1$  and  $2x_0 P_z > 0.7$  GeV, suggested by the power correction. As a result,  $b_\perp = a$  is always excluded in this work. The averages over  $x$  and different values  $n_1/n_2$  are carried out for each bootstrap sample of gauge configurations. The results are quoted from the median and 68% confidence limit of the distribution of all bootstrap samples. Thus, our quoted errors include the correlated statistical and systematic errors arising from  $x$  and  $P_z$  averaging.

Our results for the CS kernel are shown as the black points in Fig. 4. The error bars indicate errors when  $n_1/n_2 = 6/7$  and  $7/8$  are excluded from the average. The averages including  $n_1/n_2 = 6/7$  and  $7/8$  are depicted as black patches under the data points.

The CS kernel extracted from the GI quasi-TMDWFs calculated in this work is also shown as the blue points and patches, which is consistent with the CG case at smaller  $b_\perp$ . We do not show the CS kernel from the GI quasi-TMDWFs at  $b_\perp > 4a$  because the results are too noisy for comparison as already indicated in Fig. 2. It has been demonstrated in Ref. [55] that after the matching correction, which takes into account of the power corrections at small  $b_\perp$  [54] and the so-called linear renormalon subtraction at large  $b_\perp$  [71], the imaginary part of the CS kernel in the GI case is consistent with zero, so we only take the real part of

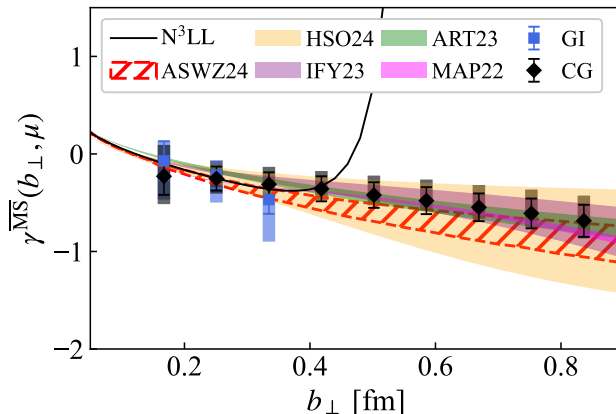


FIG. 4. The CS kernel determined from the CG quasi-TMDWFs are shown as the black points and patches, which represent the exclusion and inclusion of momentum pairs  $n_1/n_2 = 6/7$  and  $7/8$ , respectively. The results from GI quasi-TMDWFs calculated in this work are shown as the blue points and patches. For comparison, the CS kernels from recent phenomenological parameterizations of experimental data are shown from MAP22 [26], ART23 [27], IFY23 [28] and HSO24 (E605) [29]. We also show the perturbative results ( $N^3\text{LL}$ ) from Ref. [81, 82], as well as a recent lattice calculation (ASWZ24) from GI quasi-TMDWFs in the continuum limit with high statistics [55].

the final result.

Our results agree with the  $N^3\text{LL}$  perturbative prediction [81, 82] at the short distances ( $b_{\perp} \lesssim 0.4$  fm). Beyond this point, the perturbative prediction becomes sensitive to the Landau pole and, thereby, loses reliability.

Although our CS kernel from GI the case loses signal for  $b_{\perp} \gtrsim 0.4$  fm, our CG results continue to show very good signals at  $b_{\perp}$  up to about 1 fm.

For comparisons, we show the most recent lattice QCD calculation (ASWZ24) from GI quasi-TMDWFs in the continuum limit with high statistics [55]. Evidently, the results from CG and GI case are consistent with each other, suggesting they fall into the same universality class in the large  $P_z$  limit under the framework of LaMET.

Furthermore, our nonperturbative theoretical predictions of the CS kernel are in agreement with the recent phenomenological parameterizations of experimental data, MAP22 [26], ART23 [27], IFY23 [28], and HSO24 (E605) [29], which shows a near-linear  $b_{\perp}$  dependence in the nonperturbative regime as proposed in Ref. [83].

## VI. CONCLUSION

We conducted the first lattice QCD calculation of the CS kernel utilizing the recently proposed CG quasi-TMD approach as well as employing unitary domain wall fermion discretization with physical quark masses and a fine lattice spacing.

The CG approach shows significantly lower signal decay, allowing the CS kernel to be determined for extended transverse separations. At the same time, we show that our results are well compatible with the widely used gauge-invariant method. Notably, our results agree with the recent phenomenological parameterizations of experimental data and suggest a near-linear dependence of the CS kernel on large  $b_{\perp}$ .

This work lays a solid foundation for future research into the CS kernel at larger values of  $b_{\perp}$ , and advances the QCD computations in the nonperturbative regime of TMD physics.

## ACKNOWLEDGEMENTS

We thank Rui Zhang and Jinchen He for valuable discussions, and Artur Avkhadiev for helpful comments on the manuscript. We also thank Ted Rogers and J. Osvaldo Gonzalez for communications on the HSO parameterization.

This material is based upon work supported by The U.S. Department of Energy, Office of Science, Office of Nuclear Physics through Contract No. DE-SC0012704, Contract No. DE-AC02-06CH11357, and within the frameworks of Scientific Discovery through Advanced Computing (SciDAC) award Fundamental Nuclear Physics at the Exascale and Beyond and the Topical Collaboration in Nuclear Theory 3D quark-gluon structure of hadrons: mass, spin, and tomography. YZ is partially supported by the 2023 Physical Sciences and Engineering (PSE) Early Investigator Named Award program at Argonne National Laboratory.

This research used awards of computer time provided by: The INCITE program at Argonne Leadership Computing Facility, a DOE Office of Science User Facility operated under Contract DE-AC02-06CH11357; the ALCC program at the Oak Ridge Leadership Computing Facility, which is a DOE Office of Science User Facility supported under Contract DE-AC05-00OR22725; the National Energy Research Scientific Computing Center, a DOE Office of Science User Facility supported by the Office of Science of the U.S. Department of Energy under Contract DE-AC02-05CH11231 using NERSC award NP-ERCAP0028137.

Part of the data analysis is carried out on Swing, a high-performance computing cluster operated by the Laboratory Computing Resource Center at Argonne National Laboratory.

- 
- [1] J. C. Collins, D. E. Soper, and G. F. Sterman, *Nucl. Phys. B* **250**, 199 (1985).
- [2] M. Grewal, Z.-B. Kang, J.-W. Qiu, and A. Signori, *Phys. Rev. D* **101**, 114023 (2020), [arXiv:2003.07453 \[hep-ph\]](#).
- [3] G. Bozzi and A. Signori, *Adv. High Energy Phys.* **2019**, 2526897 (2019), [arXiv:1901.01162 \[hep-ph\]](#).
- [4] T. Aaltonen *et al.* (CDF), *Science* **376**, 170 (2022).
- [5] D. Kikoła, M. G. Echevarria, C. Hadjidakis, J.-P. Lansberg, C. Lorcé, L. Massacrier, C. M. Quintans, A. Signori, and B. Trzeciak, *Few Body Syst.* **58**, 139 (2017), [arXiv:1702.01546 \[hep-ex\]](#).
- [6] J. L. Feng *et al.*, *J. Phys. G* **50**, 030501 (2023), [arXiv:2203.05090 \[hep-ex\]](#).
- [7] D. Boer *et al.*, (2011), [arXiv:1108.1713 \[nucl-th\]](#).
- [8] A. Accardi *et al.*, *Eur. Phys. J. A* **52**, 268 (2016), [arXiv:1212.1701 \[nucl-ex\]](#).
- [9] R. Abdul Khalek *et al.*, (2022), [arXiv:2203.13199 \[hep-ph\]](#).
- [10] R. Abir *et al.*, (2023), [arXiv:2305.14572 \[hep-ph\]](#).
- [11] J. C. Collins and D. E. Soper, *Nucl. Phys. B* **193**, 381 (1981), [Erratum: *Nucl.Phys.B* 213, 545 (1983)].
- [12] J. C. Collins and D. E. Soper, *Nucl. Phys. B* **197**, 446 (1982).
- [13] C. T. H. Davies, B. R. Webber, and W. J. Stirling, **1**, I.95 (1984).
- [14] G. A. Ladinsky and C. P. Yuan, *Phys. Rev. D* **50**, R4239 (1994), [arXiv:hep-ph/9311341](#).
- [15] F. Landry, R. Brock, P. M. Nadolsky, and C. P. Yuan, *Phys. Rev. D* **67**, 073016 (2003), [arXiv:hep-ph/0212159](#).
- [16] A. V. Konychev and P. M. Nadolsky, *Phys. Lett. B* **633**, 710 (2006), [arXiv:hep-ph/0506225](#).
- [17] P. Sun, J. Isaacson, C. P. Yuan, and F. Yuan, *Int. J. Mod. Phys. A* **33**, 1841006 (2018), [arXiv:1406.3073 \[hep-ph\]](#).
- [18] U. D'Alesio, M. G. Echevarria, S. Melis, and I. Scimemi, *JHEP* **11**, 098 (2014), [arXiv:1407.3311 \[hep-ph\]](#).
- [19] A. Bacchetta, F. Delcarro, C. Pisano, M. Radici, and A. Signori, *JHEP* **06**, 081 (2017), [Erratum: *JHEP* 06, 051 (2019)], [arXiv:1703.10157 \[hep-ph\]](#).
- [20] I. Scimemi and A. Vladimirov, *Eur. Phys. J. C* **78**, 89 (2018), [arXiv:1706.01473 \[hep-ph\]](#).

- [21] V. Bertone, I. Scimemi, and A. Vladimirov, *JHEP* **06**, 028 (2019), [arXiv:1902.08474 \[hep-ph\]](#).
- [22] I. Scimemi and A. Vladimirov, *JHEP* **06**, 137 (2020), [arXiv:1912.06532 \[hep-ph\]](#).
- [23] A. Bacchetta, V. Bertone, C. Bissolotti, G. Bozzi, F. Delcarro, F. Piacenza, and M. Radici, *JHEP* **07**, 117 (2020), [arXiv:1912.07550 \[hep-ph\]](#).
- [24] F. Hautmann, I. Scimemi, and A. Vladimirov, *Phys. Lett. B* **806**, 135478 (2020), [arXiv:2002.12810 \[hep-ph\]](#).
- [25] M. Bury, F. Hautmann, S. Leal-Gomez, I. Scimemi, A. Vladimirov, and P. Zurita, *JHEP* **10**, 118 (2022), [arXiv:2201.07114 \[hep-ph\]](#).
- [26] A. Bacchetta, V. Bertone, C. Bissolotti, G. Bozzi, M. Cerutti, F. Piacenza, M. Radici, and A. Signori (MAP (Multi-dimensional Analyses of Partonic distributions)), *JHEP* **10**, 127 (2022), [arXiv:2206.07598 \[hep-ph\]](#).
- [27] V. Moos, I. Scimemi, A. Vladimirov, and P. Zurita, (2023), [arXiv:2305.07473 \[hep-ph\]](#).
- [28] J. Isaacson, Y. Fu, and C. P. Yuan, (2023), [arXiv:2311.09916 \[hep-ph\]](#).
- [29] F. Aslan, M. Boglione, J. O. Gonzalez-Hernandez, T. Rainaldi, T. C. Rogers, and A. Simonelli, (2024), [arXiv:2401.14266 \[hep-ph\]](#).
- [30] X. Ji, *Phys. Rev. Lett.* **110**, 262002 (2013), [arXiv:1305.1539 \[hep-ph\]](#).
- [31] X. Ji, *Sci. China Phys. Mech. Astron.* **57**, 1407 (2014), [arXiv:1404.6680 \[hep-ph\]](#).
- [32] X. Ji, Y.-S. Liu, Y. Liu, J.-H. Zhang, and Y. Zhao, *Rev. Mod. Phys.* **93**, 035005 (2021), [arXiv:2004.03543 \[hep-ph\]](#).
- [33] X. Ji, P. Sun, X. Xiong, and F. Yuan, *Phys. Rev. D* **91**, 074009 (2015), [arXiv:1405.7640 \[hep-ph\]](#).
- [34] X. Ji, L.-C. Jin, F. Yuan, J.-H. Zhang, and Y. Zhao, *Phys. Rev. D* **99**, 114006 (2019), [arXiv:1801.05930 \[hep-ph\]](#).
- [35] M. A. Ebert, I. W. Stewart, and Y. Zhao, *Phys. Rev. D* **99**, 034505 (2019), [arXiv:1811.00026 \[hep-ph\]](#).
- [36] M. A. Ebert, I. W. Stewart, and Y. Zhao, *JHEP* **09**, 037 (2019), [arXiv:1901.03685 \[hep-ph\]](#).
- [37] X. Ji, Y. Liu, and Y.-S. Liu, *Nucl. Phys. B* **955**, 115054 (2020), [arXiv:1910.11415 \[hep-ph\]](#).
- [38] X. Ji, Y. Liu, and Y.-S. Liu, *Phys. Lett. B* **811**, 135946 (2020), [arXiv:1911.03840 \[hep-ph\]](#).
- [39] M. A. Ebert, S. T. Schindler, I. W. Stewart, and Y. Zhao, *JHEP* **09**, 099 (2020), [arXiv:2004.14831 \[hep-ph\]](#).
- [40] A. A. Vladimirov and A. Schäfer, *Phys. Rev. D* **101**, 074517 (2020), [arXiv:2002.07527 \[hep-ph\]](#).

- [41] X. Ji, Y. Liu, A. Schäfer, and F. Yuan, *Phys. Rev. D* **103**, 074005 (2021), [arXiv:2011.13397 \[hep-ph\]](#).
- [42] X. Ji and Y. Liu, *Phys. Rev. D* **105**, 076014 (2022), [arXiv:2106.05310 \[hep-ph\]](#).
- [43] M. A. Ebert, S. T. Schindler, I. W. Stewart, and Y. Zhao, *JHEP* **04**, 178 (2022), [arXiv:2201.08401 \[hep-ph\]](#).
- [44] S. T. Schindler, I. W. Stewart, and Y. Zhao, *JHEP* **08**, 084 (2022), [arXiv:2205.12369 \[hep-ph\]](#).
- [45] R. Zhu, Y. Ji, J.-H. Zhang, and S. Zhao, *JHEP* **02**, 114 (2023), [arXiv:2209.05443 \[hep-ph\]](#).
- [46] S. Rodini and A. Vladimirov, *JHEP* **09**, 117 (2023), [arXiv:2211.04494 \[hep-ph\]](#).
- [47] P. Shanahan, M. Wagman, and Y. Zhao, *Phys. Rev. D* **102**, 014511 (2020), [arXiv:2003.06063 \[hep-lat\]](#).
- [48] P. Shanahan, M. Wagman, and Y. Zhao, *Phys. Rev. D* **104**, 114502 (2021), [arXiv:2107.11930 \[hep-lat\]](#).
- [49] H.-T. Shu, M. Schlemmer, T. Sizmann, A. Vladimirov, L. Walter, M. Engelhardt, A. Schäfer, and Y.-B. Yang, *Phys. Rev. D* **108**, 074519 (2023), [arXiv:2302.06502 \[hep-lat\]](#).
- [50] Q.-A. Zhang et al. (Lattice Parton), *Phys. Rev. Lett.* **125**, 192001 (2020), [arXiv:2005.14572 \[hep-lat\]](#).
- [51] Y. Li et al., *Phys. Rev. Lett.* **128**, 062002 (2022), [arXiv:2106.13027 \[hep-lat\]](#).
- [52] M.-H. Chu et al. (LPC), *Phys. Rev. D* **106**, 034509 (2022), [arXiv:2204.00200 \[hep-lat\]](#).
- [53] M.-H. Chu et al. (Lattice Parton (LPC)), *JHEP* **08**, 172 (2023), [arXiv:2306.06488 \[hep-lat\]](#).
- [54] A. Avkhadiev, P. E. Shanahan, M. L. Wagman, and Y. Zhao, *Phys. Rev. D* **108**, 114505 (2023), [arXiv:2307.12359 \[hep-lat\]](#).
- [55] A. Avkhadiev, P. E. Shanahan, M. L. Wagman, and Y. Zhao, (2024), [arXiv:2402.06725 \[hep-lat\]](#).
- [56] M. Schlemmer, A. Vladimirov, C. Zimmermann, M. Engelhardt, and A. Schäfer, *JHEP* **08**, 004 (2021), [arXiv:2103.16991 \[hep-lat\]](#).
- [57] J.-C. He, M.-H. Chu, J. Hua, X. Ji, A. Schäfer, Y. Su, W. Wang, Y. Yang, J.-H. Zhang, and Q.-A. Zhang (LPC), (2022), [arXiv:2211.02340 \[hep-lat\]](#).
- [58] M.-H. Chu et al., (2023), [arXiv:2302.09961 \[hep-lat\]](#).
- [59] O. del Río and A. Vladimirov, *Phys. Rev. D* **108**, 114009 (2023), [arXiv:2304.14440 \[hep-ph\]](#).
- [60] X. Ji, Y. Liu, and Y. Su, *JHEP* **08**, 037 (2023), [arXiv:2305.04416 \[hep-ph\]](#).
- [61] X. Ji, J.-H. Zhang, and Y. Zhao, *Phys. Rev. Lett.* **120**, 112001 (2018), [arXiv:1706.08962](#)



- [hep-ph].
- [62] M. Constantinou, H. Panagopoulos, and G. Spanoudes, *Phys. Rev. D* **99**, 074508 (2019), [arXiv:1901.03862 \[hep-lat\]](#).
- [63] P. Shanahan, M. L. Wagman, and Y. Zhao, *Phys. Rev. D* **101**, 074505 (2020), [arXiv:1911.00800 \[hep-lat\]](#).
- [64] J. R. Green, K. Jansen, and F. Steffens, *Phys. Rev. D* **101**, 074509 (2020), [arXiv:2002.09408 \[hep-lat\]](#).
- [65] Y. Ji, J.-H. Zhang, S. Zhao, and R. Zhu, *Phys. Rev. D* **104**, 094510 (2021), [arXiv:2104.13345 \[hep-ph\]](#).
- [66] C. Alexandrou *et al.*, *Phys. Rev. D* **108**, 114503 (2023), [arXiv:2305.11824 \[hep-lat\]](#).
- [67] G. Spanoudes, M. Constantinou, and H. Panagopoulos, (2024), [arXiv:2401.01182 \[hep-lat\]](#).
- [68] K. Zhang, X. Ji, Y.-B. Yang, F. Yao, and J.-H. Zhang ([Lattice Parton Collaboration (LPC)]), *Phys. Rev. Lett.* **129**, 082002 (2022), [arXiv:2205.13402 \[hep-lat\]](#).
- [69] X. Gao, W.-Y. Liu, and Y. Zhao, (2023), [arXiv:2306.14960 \[hep-ph\]](#).
- [70] Y. Zhao, (2023), [arXiv:2311.01391 \[hep-ph\]](#).
- [71] Y. Liu and Y. Su, (2023), [arXiv:2311.06907 \[hep-ph\]](#).
- [72] A. V. Belitsky, X. Ji, and F. Yuan, *Nucl. Phys. B* **656**, 165 (2003), [arXiv:hep-ph/0208038](#).
- [73] G. S. Bali, B. Lang, B. U. Musch, and A. Schäfer, *Phys. Rev. D* **93**, 094515 (2016), [arXiv:1602.05525 \[hep-lat\]](#).
- [74] T. Blum *et al.* (RBC, UKQCD), *Phys. Rev. D* **108**, 054507 (2023), [arXiv:2301.08696 \[hep-lat\]](#).
- [75] X. Gao, N. Karthik, S. Mukherjee, P. Petreczky, S. Syritsyn, and Y. Zhao, *Phys. Rev. D* **104**, 114515 (2021), [arXiv:2102.06047 \[hep-lat\]](#).
- [76] X. Gao, L. Jin, C. Kallidonis, N. Karthik, S. Mukherjee, P. Petreczky, C. Shugert, S. Syritsyn, and Y. Zhao, *Phys. Rev. D* **102**, 094513 (2020), [arXiv:2007.06590 \[hep-lat\]](#).
- [77] E. Shintani, R. Arthur, T. Blum, T. Izubuchi, C. Jung, and C. Lehner, *Phys. Rev. D* **91**, 114511 (2015), [arXiv:1402.0244 \[hep-lat\]](#).
- [78] M. Lüscher, *JHEP* **08**, 071 (2010), [Erratum: *JHEP* 03, 092 (2014)], [arXiv:1006.4518 \[hep-lat\]](#).
- [79] J. Green, K. Jansen, and F. Steffens, *Phys. Rev. Lett.* **121**, 022004 (2018), [arXiv:1707.07152 \[hep-lat\]](#).
- [80] T. Ishikawa, Y.-Q. Ma, J.-W. Qiu, and S. Yoshida, *Phys. Rev. D* **96**, 094019 (2017), [arXiv:1707.03107 \[hep-ph\]](#).

- [81] A. A. Vladimirov, [Phys. Rev. Lett. \*\*118\*\*, 062001 \(2017\)](#), [arXiv:1610.05791 \[hep-ph\]](#).
- [82] Y. Li and H. X. Zhu, [Phys. Rev. Lett. \*\*118\*\*, 022004 \(2017\)](#), [arXiv:1604.01404 \[hep-ph\]](#).
- [83] J. Collins and T. Rogers, [Phys. Rev. D \*\*91\*\*, 074020 \(2015\)](#), [arXiv:1412.3820 \[hep-ph\]](#).

## $J/\psi$ –pair production at NLL in TMD factorisation at the LHC

Alice Colpani Serri,<sup>a,\*</sup> Jelle Bor,<sup>b,c</sup> Daniël Boer<sup>b</sup> and Jean-Philippe Lansberg<sup>c</sup>

<sup>a</sup>*Faculty of Physics, Warsaw University of Technology,  
plac Politechniki 1, 00-661, Warszawa, Poland*

<sup>b</sup>*Van Swinderen Institute for Particle Physics and Gravity, University of Groningen,  
Nijenborgh 4, 9747 AG Groningen, The Netherlands*

<sup>c</sup>*Université Paris-Saclay, CNRS, IJCLab,*

*rue Georges Clémenceau 15, 91405 Orsay, France*

*E-mail: [alice.colpani\\_serri.dokt@pw.edu.pl](mailto:alice.colpani_serri.dokt@pw.edu.pl), [j.bor@rug.nl](mailto:j.bor@rug.nl), [d.boer@rug.nl](mailto:d.boer@rug.nl),  
[jean-philippe.lansberg@in2p3.fr](mailto:jean-philippe.lansberg@in2p3.fr)*

$J/\psi$ –pair production at the LHC is currently one of the few tools available to probe gluon transverse momentum distributions (TMDs). In this context, data from LHCb in the collider mode have the potential to probe the evolution of the unpolarised-gluon TMDs and to measure the distribution of the linearly-polarised gluon in unpolarised protons for the first time. In this proceedings contribution, improved predictions obtained for the LHC (at  $\sqrt{s} = 13$  TeV) up to next-to-leading logarithm (NLL) in TMD factorisation are presented. We show the obtained predictions of transverse-momentum distributions at different invariant masses and rapidities computed in the LHCb acceptance along with PDF uncertainty. We predict the azimuthal modulations of the cross section that arise from linearly-polarised gluons.

*The European Physical Society Conference on High Energy Physics (EPS-HEP2023)  
21-25 August 2023  
Hamburg, Germany*

---

\*Speaker

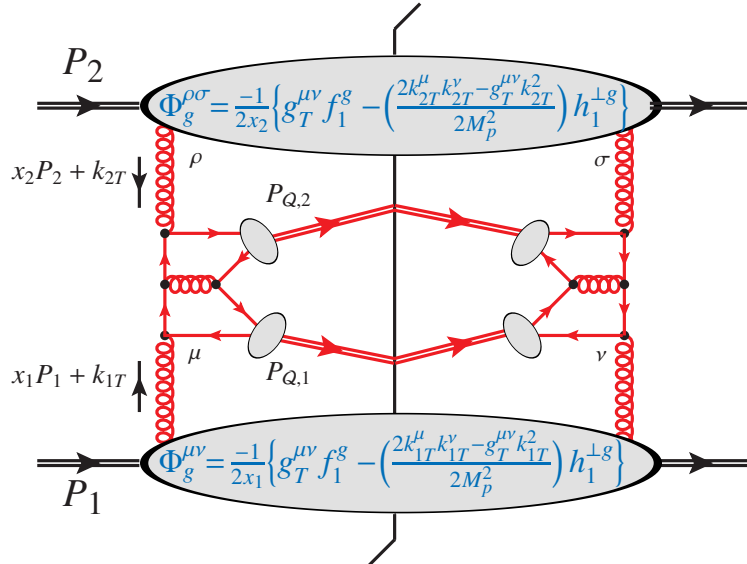
## 1. Introduction

Inclusive  $J/\psi$ -pair production in proton-proton collisions represents a great tool to allow for extractions of the poorly known gluon Transverse Momentum Dependent Parton Distribution Functions (TMD-PDFs or TMDs) [1, 2]. Indeed, this process is mainly generated by gluon-gluon fusion and Color Singlet (CS) transitions are the main source of  $J/\psi$  pairs, for which TMD-factorisation-breaking effects are absent [3–5]. For this reason  $J/\psi$ -pair production is considered a great candidate for probing gluon TMDs at the LHC. Moreover, the invariant mass of the  $J/\psi$ -pair in the final state can be tuned with the individual momenta of the two  $J/\psi$ , allowing for the investigation of the scale evolution of the TMDs.

## 2. Overview of the process and formalism

The process considered in our study is the simultaneous production of two  $J/\psi$  in a single parton scattering from unpolarised proton-proton collisions. The  $J/\psi$  is relatively easy to produce and to detect, allowing for the collection of a large number of experimental data. From a theoretical point of view, though, it is still not clear how to treat quarkonium production: many models have been proposed in an attempt to describe quarkonium-production mechanisms. However, the consensus is that the *Colour-Singlet Model* (CSM) works for the particular case where a  $J/\psi$ -pair is generated [6].

A leading-order Feynman diagram of the process is shown in Figure 1. The protons have momentum  $P_1$  and  $P_2$  and the partons take a momentum fraction  $x_i$  from them (collinear contribution), besides having a transverse component  $k_{iT}$ . Considering the TMD factorisation [8], the non-perturbative gluon TMDs are defined through the hadron correlator  $\Phi(x_i, k_{iT})$ . For an



**Figure 1:** Schematic overview of the inclusive scattering for  $p + p \rightarrow J/\psi + J/\psi$  in TMD factorisation. From [7].

unpolarised proton in particular,  $\Phi(x_i, k_{iT})$  is parameterised in terms of two independent TMDs at leading twist [9]: the unpolarised gluon distribution,  $f_1^g$ , and the linearly-polarised gluon distribution,  $h_1^{\perp g}$  (see Figure 1). The hadronic cross section for a gluon-fusion process, considering the production of a quarkonium pair, is given by the following equation [2]:

$$\begin{aligned} \frac{d\sigma}{dM_{QQ} dy_{QQ} d^2 q_T d\Omega} &= \frac{\sqrt{M_{QQ}^2 - 4M_Q^2}}{(2\pi)^2 8s M_{QQ}^2} \times \left\{ F_1 C[f_1^g f_1^g] + F_2 C[w_2 h_1^{\perp g} h_1^{\perp g}] \right. \\ &\quad + \left( F_3 C[w_3 f_1^g h_1^{\perp g}] + F_3' C[w_3' h_1^{\perp g} f_1^g] \right) \cos(2\phi_{CS}) \\ &\quad \left. + F_4 C[w_4 h_1^{\perp g} h_1^{\perp g}] \cos(4\phi_{CS}) \right\}, \end{aligned} \quad (1)$$

where  $d\Omega = d \cos(\theta_{CS}) d\phi_{CS}$ , with  $\theta_{CS}$  and  $\phi_{CS}$  the polar and azimuthal Collins-Soper angles respectively.  $M_Q$  is the quarkonium mass (in our calculations for  $\psi + \psi$ , we took  $M_Q = 3.1$  GeV), while  $M_{QQ}$  indicates the invariant mass of the quarkonium pair, which we set as the hard scale of the process.  $y_{QQ}$  represents the rapidity of the quarkonium pair defined in the proton center-of-mass frame, i.e.:

$$x_{1,2} = \frac{e^{\pm y} M_{QQ}}{\sqrt{s}}, \quad (2)$$

with  $s = (P_1 + P_2)^2$ . The coefficients  $F_i$  are the hard-scattering coefficients. They contain the explicit dependence on  $M_{QQ}$  and the angle  $\theta_{CS}$ . The  $C[fg]$  are convolutions containing different combinations of  $f_1^g$  and  $h_1^{\perp g}$ , in general:

$$C[wfg] = \int d^2 k_{1T} \int d^2 k_{2T} \delta^2(k_{1T} + k_{2T} - q_T) w(k_{1T}, k_{2T}) f(x_1, k_{1T}^2) g(x_2, k_{2T}^2), \quad (3)$$

where  $k_{iT}$  are the transverse momenta of the gluons,  $q_T$  is the transverse momentum of the quarkonium-pair and  $w(k_{1T}, k_{2T})$  are transverse weights [10]. The azimuthal angle defined by the quarkonium pair in the final state is directly related to gluon TMDs [1]:

$$\langle \cos(2\phi_{CS}) \rangle = \frac{1}{2} \frac{F_3 (C[w_3 f_1^g h_1^{\perp g}] + C[w_3' h_1^{\perp g} f_1^g])}{F_1 C[f_1^g f_1^g] + F_2 C[w_2 h_1^{\perp g} h_1^{\perp g}]}, \quad (4)$$

$$\langle \cos(4\phi_{CS}) \rangle = \frac{1}{2} \frac{F_4 C[w_4 h_1^{\perp g} h_1^{\perp g}]}{F_1 C[f_1^g f_1^g] + F_2 C[w_2 h_1^{\perp g} h_1^{\perp g}]}. \quad (5)$$

These are the expressions of the azimuthal modulations normalised to the azimuthally-independent part of the cross section. We note that such modulations are non-vanishing only if  $h_1^{\perp g}$  is not zero.

### 3. Switching on TMD evolution and results

TMD-evolution studies are commonly implemented in impact-parameter space [8],  $b_T$ , in which the convolutions can be written as simple products [11]:

$$\begin{aligned} C[wfg](x_1, x_2, q_T; Q) &= \int_0^\infty \frac{db_T}{2\pi} b_T^n J_m(b_T q_T) e^{-S_A(b_T^*; Q^2, Q)} e^{-S_{NP}(b_T; Q)} \\ &\quad \times \hat{f}(x_1, b_T^*; \mu_b^2, \mu_b) \hat{g}(x_2, b_T^*; \mu_b^2, \mu_b), \end{aligned} \quad (6)$$

where  $Q$  is the hard scale of the process (which we choose to be  $M_{QQ}$ ) and  $J_m(b_T q_T)$  is the Bessel function of order  $m$ .  $S_A$  is the perturbative Sudakov factor at next-to-leading-logarithmic (NLL) accuracy [12, 13] and  $S_{NP}$  the non-perturbative one, chosen to be a Gaussian [2]:

$$S_{NP}(b_T; Q) = A \ln \frac{Q}{Q_{NP}} b_T^2 \quad \text{with} \quad Q_{NP} = 1 \text{ GeV}. \quad (7)$$

$\hat{f}$  and  $\hat{g}$  are the Fourier-transformed gluon TMDs:

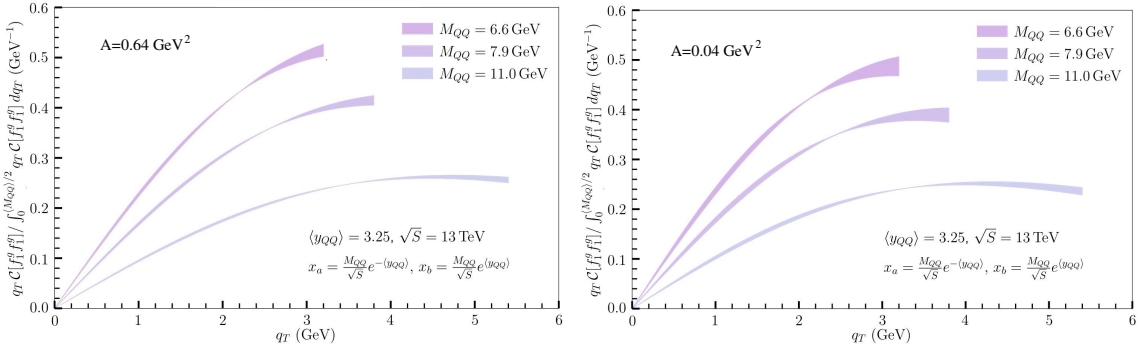
$$\hat{f}_1^g(x, b_T^2) \equiv \int d^2 q_T e^{i b_T \cdot q_T} f_1^g(x, q_T^2), \quad (8)$$

$$\hat{h}_1^{\perp g}(x, b_T^2) \equiv \int d^2 q_T \frac{(b_T \cdot q_T)^2 - \frac{1}{2} b_T^2 q_T^2}{b_T^2 M_p^2} e^{i b_T \cdot q_T} h_1^{\perp g}(x, q_T^2). \quad (9)$$

The expressions above are valid for  $b_0/Q \leq b_T \leq b_{T,\max}$  (with  $b_{T,\max}$  estimated to be around  $1.5 \text{ GeV}^{-1}$  and with  $b_0 = 2e^{-\gamma_E}$ ): when  $\mu_b = b_0/b_T$  becomes larger than  $Q$ , the evolution should stop ( $S_A = 0$ ), while for values larger than  $b_{T,\max}$  perturbation theory starts to become less reliable. To force the Fourier transform of these perturbative objects to remain in the range where they make sense, one changes [11, 14]  $b_T$  into two variants in Equation (6) as :

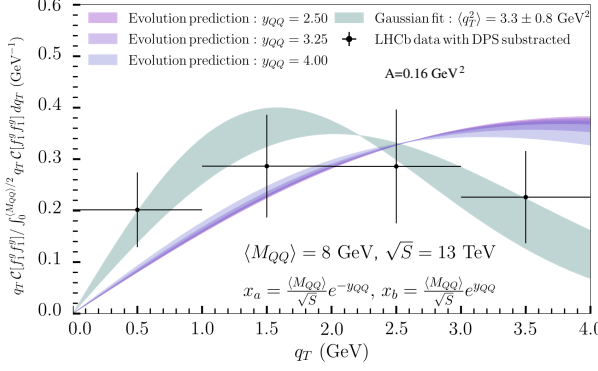
$$b_c(b_T^*) = \sqrt{(b_T^*)^2 + \left(\frac{b_0}{Q}\right)^2} \quad \text{and} \quad b_T^*(b_T) = \frac{b_T}{\sqrt{1 + \left(b_T/b_{T,\max}\right)^2}}. \quad (10)$$

Such a formalism has been implemented for quarkonium-pair production for the first time in [7], where TMD evolution effects have been shown to be measurable. We present updated results, taking into account also the  $x$  and  $y_{QQ}$  dependence and PDF (mstw2008lo [15]) uncertainty.



**Figure 2:** Normalised  $q_T$  spectrum at fixed rapidity ( $y_{QQ} = 3.25$ ) with three different values of the mass  $M_{QQ} = 6.6, 7.9$  and  $11.0 \text{ GeV}$  and  $A = 0.64 \text{ GeV}^2$  (left) and  $0.04 \text{ GeV}^2$  (right).

The plots in Figure 2 show the normalised  $q_T$  spectrum for  $J/\psi$ -pair production using the evolved TMDs at  $M_{QQ} = 6.6, 7.9$  and  $11.0 \text{ GeV}$ . These values are chosen according to the bins of the recent preliminary LHCb measurements [16] of this process. The width of each band represents the PDF uncertainty. The difference between left and right plots is given by the different chosen value of  $A$  (Equation (7)): changing this quantity gives an estimate of the non-perturbative TMD



**Figure 3:** Normalised  $q_T$  spectrum for 3 values of rapidity ( $y = 2.50, 3.25, 4.00$ ) at fixed  $M_{QQ}$  (8 GeV) and  $A = 0.16 \text{ GeV}^2$ . The gray band represents the uncertainty of the gaussian fit made in [2] and the black crosses are the experimental data from LHCb published in 2017 [17] from which DPS had been subtracted [2].

uncertainty. The plots suggest that the peak is moving towards larger  $q_T$  values when the scale increases, while the PDF uncertainty tends to decrease. In Figure 3, the  $q_T$  spectrum is plotted with fixed invariant mass ( $M_{QQ} = 8 \text{ GeV}$ ) and varying the rapidity ( $y = 2.50, 3.25$  and  $4.00$ ). Changing the rapidity slightly affects the  $q_T$ -spectrum behaviour. Again, the band widths correspond to the PDF uncertainty.

From Equations (4) and (5), we have computed the azimuthal modulations  $\langle \cos(2\phi_{CS}) \rangle$  and  $\langle \cos(4\phi_{CS}) \rangle$ . We have performed a study in different  $\cos(\theta_{CS})$  bins, namely  $[0, 0.25]$ ,  $[0.25, 0.50]$ ,  $[0.50, 0.75]$ ,  $[0.75, 1]$  and  $[0, 1]$  for  $M_{QQ} = 8$  and  $11 \text{ GeV}$ . Both modulations show a mass dependence at fixed  $q_T$  and they become larger for a larger value of the mass (they increase of a factor  $\sim 2$ ). We have found that  $\langle \cos(2\phi_{CS}) \rangle$  is positive in all bins and that it increases while increasing  $q_T$  and has higher contribution for  $\cos(\theta_{CS}) \in [0.50, 0.75]$  (expectation of  $\mathcal{O}(\text{few}\%)$ ).  $\langle \cos(4\phi_{CS}) \rangle$  has higher positive contribution for  $\cos(\theta_{CS}) \in [0, 0.25]$ , then it becomes negative at  $\cos(\theta_{CS}) \sim 0.3$  after which it reaches the highest contribution (in absolute value) for  $\cos(\theta_{CS}) \in [0.50, 0.75]$  (expectation of  $\mathcal{O}(1\%)$ ). In both cases, we have large non-perturbative uncertainties. Such preliminary results are compatible with the latest experimental data from LHCb [16], presented at this conference, from which  $\langle \cos(2\phi) \rangle = -0.029 \pm 0.050 \pm 0.009$  and  $\langle \cos(4\phi) \rangle = -0.087 \pm 0.052 \pm 0.013$  have been found considering the overall  $\cos(\theta_{CS})$  region.

#### 4. Conclusions and outlook

Quarkonium production has the potential to probe the internal structure of the nucleon. Double- $J/\psi$  production in particular gives the possibility to investigate gluon TMD-induced effects and  $\Upsilon$  predictions could be studied soon. TMD evolution effects are measurable and we have shown the obtained predictions considering  $x$  and rapidity dependencies and PDF uncertainty for the first time.

We are currently working on a novel method to determine the non-perturbative Sudakov factor because certain issues with a simple Gaussian Ansatz have been identified, which improve our predictions for double- $J/\psi$  production. In the future, studies could be performed considering polarised protons (like in the fixed-target experiments at the LHC) in order to access more gluon TMDs. In particular, double- $J/\psi$  production is the most promising process for accessing the gluon Sivvers function [18].

## Acknowledgements

This work was supported in part by the European Union’s Horizon 2020 research and innovation program under Grant Agreements No. 824093 (Strong2020) in order to contribute to the EU Virtual Access “NLOAccess”. This project has also received funding from the French Agence Nationale de la Recherche (ANR) via the grant ANR-20-CE31-0015 (“PrecisOnium”) and was also partly supported by the French CNRS via the COPIN-IN2P3 bilateral agreement.

## References

- [1] J.-P. Lansberg, C. Pisano, F. Scarpa and M. Schlegel, *Pinning down the linearly-polarised gluons inside unpolarised protons using quarkonium-pair production at the LHC*, *Phys. Lett. B* **784** (2018) 217 [1710.01684].
- [2] F. Scarpa, D. Boer, M.G. Echevarria, J.-P. Lansberg, C. Pisano and M. Schlegel, *Studies of gluon TMDs and their evolution using quarkonium-pair production at the LHC*, *Eur. Phys. J. C* **80** (2020) 87 [1909.05769].
- [3] J. Collins and J.-W. Qiu,  *$k_T$  factorization is violated in production of high-transverse-momentum particles in hadron-hadron collisions*, *Phys. Rev. D* **75** (2007) 114014 [0705.2141].
- [4] J. Collins, *2-soft-gluon exchange and factorization breaking*, 0708.4410.
- [5] T.C. Rogers and P.J. Mulders, *No Generalized TMD-Factorization in Hadro-Production of High Transverse Momentum Hadrons*, *Phys. Rev. D* **81** (2010) 094006 [1001.2977].
- [6] J.-P. Lansberg, *New Observables in Inclusive Production of Quarkonia*, *Phys. Rept.* **889** (2020) 1 [1903.09185].
- [7] F. Scarpa, *Probing the gluon Transverse Momentum-Dependent distributions inside the proton through quarkonium-pair production at the LHC*, Ph.D. thesis, High-Energy Frontier, Groningen U., Groningen U., U. Paris-Saclay, 2020. 10.33612/diss.128346301.
- [8] J. Collins, *Foundations of perturbative QCD*, vol. 32, Cambridge University Press (11, 2013).
- [9] P.J. Mulders and J. Rodrigues, *Transverse momentum dependence in gluon distribution and fragmentation functions*, *Phys. Rev. D* **63** (2001) 094021 [hep-ph/0009343].
- [10] J.-P. Lansberg, C. Pisano and M. Schlegel, *Associated production of a dilepton and a  $\Upsilon(J/\psi)$  at the LHC as a probe of gluon transverse momentum dependent distributions*, *Nucl. Phys. B* **920** (2017) 192 [1702.00305].
- [11] J.C. Collins, D.E. Soper and G.F. Sterman, *Transverse Momentum Distribution in Drell-Yan Pair and  $W$  and  $Z$  Boson Production*, *Nucl. Phys. B* **250** (1985) 199.
- [12] J.C. Collins and D.E. Soper, *Back-To-Back Jets: Fourier Transform from  $B$  to  $K$ -Transverse*, *Nucl. Phys. B* **197** (1982) 446.
- [13] MAP (MULTI-DIMENSIONAL ANALYSES OF PARTONIC DISTRIBUTIONS) collaboration, *Unpolarized transverse momentum distributions from a global fit of Drell-Yan and semi-inclusive deep-inelastic scattering data*, *JHEP* **10** (2022) 127 [2206.07598].
- [14] J. Collins, L. Gamberg, A. Prokudin, T.C. Rogers, N. Sato and B. Wang, *Relating Transverse Momentum Dependent and Collinear Factorization Theorems in a Generalized Formalism*, *Phys. Rev. D* **94** (2016) 034014 [1605.00671].
- [15] A.D. Martin, W.J. Stirling, R.S. Thorne and G. Watt, *Parton distributions for the LHC*, *Eur. Phys. J. C* **63** (2009) 189 [0901.0002].
- [16] L. An, *Study of associated quarkonium production in pp collisions at LHCb*, in *EPS-HEP2023 Conference, Hamburg, 2023*, <https://indico.desy.de/event/34916/contributions/146987/>.
- [17] LHCb collaboration, *Measurement of the  $J/\psi$  pair production cross-section in pp collisions at  $\sqrt{s} = 13$  TeV*, *JHEP* **06** (2017) 047 [1612.07451].
- [18] C. Hadjidakis, D. Kikoła, J. Lansberg, L. Massacrier, M. Echevarria, A. Kusina et al., *A fixed-target programme at the LHC: Physics case and projected performances for heavy-ion, hadron, spin and astroparticle studies*, *Physics Reports* **911** (2021) 1.



# A new Wolfenstein-like expansion of lepton flavor mixing towards understanding its fine structure

Zhi-zhong Xing<sup>1,2</sup> \*

<sup>1</sup>Institute of High Energy Physics and School of Physical Sciences,  
University of Chinese Academy of Sciences, Beijing 100049, China

<sup>2</sup>Center of High Energy Physics, Peking University, Beijing 100871, China

## Abstract

Taking the tri-bimaximal flavor mixing pattern as a particular basis, we propose a new way to expand the  $3 \times 3$  unitary Pontecorvo-Maki-Nakagawa-Sakata (PMNS) lepton flavor mixing matrix  $U$  in powers of the magnitude of its smallest element  $\xi \equiv |U_{e3}| \simeq 0.149$ . Such a Wolfenstein-like parametrization of  $U$  allows us to easily describe the salient features and fine structures of flavor mixing and CP violation, both in vacuum and in matter.

arXiv:2403.00559v1 [hep-ph] 1 Mar 2024

---

\*E-mail: xingzz@ihep.ac.cn

# 1 Motivation

Among the three Euler-like rotation angles of the Cabibbo-Kobayashi-Maskawa (CKM) quark flavor mixing matrix  $V$  [1, 2], it is the largest one — the Cabibbo angle  $\theta_C \simeq 13^\circ$  that was most accurately measured from the very beginning [3]. That is why Wolfenstein proposed a remarkable parametrization of the CKM matrix  $V$  in 1983 by expanding its nine matrix elements in powers of a small parameter  $\lambda \equiv \sin \theta_C \simeq 0.225$  [4], from which the hierarchical structure of quark flavor mixing can be well understood. For example, one may easily arrive at the four-layered ordering

$$|V_{tb}| > |V_{ud}| > |V_{cs}| \gg |V_{us}| > |V_{cd}| \gg |V_{cb}| > |V_{ts}| \gg |V_{td}| > |V_{ub}| \quad (1)$$

of respective  $\mathcal{O}(1)$ ,  $\mathcal{O}(\lambda)$ ,  $\mathcal{O}(\lambda^2)$  and  $\mathcal{O}(\lambda^3)$  as a natural consequence of the unitarity of  $V$  [5]. In particular, the CKM matrix  $V$  approaches the unique identity matrix  $I$  in the  $\lambda \rightarrow 0$  limit, implying that the up- and down-type quark sectors should have an underlying parallelism between their flavor textures. Such a conceptually interesting limit is quite suggestive, and it has widely been considered for explicit model building [6].

In comparison, two of the three Euler-like rotation angles of the Pontecorvo-Maki-Nakagawa-Sakata (PMNS) lepton flavor mixing matrix  $U$  (i.e.,  $\theta_{12} \simeq 33.4^\circ$  and  $\theta_{23} \sim 45^\circ$  [3]) are so large that a naive Wolfenstein-like parametrization of  $U$  seems quite unlikely<sup>1</sup>. A very real possibility is that the leading-order term of the PMNS matrix  $U$  is a constant flavor mixing pattern  $U_0$  consisting of two large angles and originating from a kind of discrete flavor symmetry, while the smallest flavor mixing angle  $\theta_{13} \simeq 8.6^\circ$  and CP-violating effects arise after small perturbations or quantum corrections to  $U_0$  are taken into account [10, 11]. From the point of view of model building [6, 12, 13, 14], the most popular choice of  $U_0$  has been the tri-bimaximal flavor mixing pattern  $U_{\text{TBM}}$  [15, 16, 17] which predicts  $\theta_{12}^{(0)} = \cot \sqrt{2} \simeq 35.26^\circ$ ,  $\theta_{13}^{(0)} = 0^\circ$  and  $\theta_{23}^{(0)} = 45^\circ$ . Given the smallness of  $\theta_{13}$ , several attempts have been made along the above line of thought to expand the  $U_{\text{TBM}}$ -based PMNS matrix  $U$  in powers of the small Wolfenstein parameter  $\lambda$  that is borrowed from quark flavor mixing (see, e.g., Refs. [18, 19, 20, 21, 22]).

Guided by the best-fit values and  $1\sigma$  intervals of three lepton flavor mixing angles extracted from a global analysis of the currently available experimental data on neutrino oscillations [23, 24],

$$\text{NMO} : \quad \theta_{12} = 0.583_{-0.013}^{+0.013}, \quad \theta_{13} = 0.150_{-0.002}^{+0.002}, \quad \theta_{23} = 0.736_{-0.015}^{+0.019} \quad (2)$$

for the normal mass ordering (NMO) of three active neutrinos, or

$$\text{IMO} : \quad \theta_{12} = 0.583_{-0.013}^{+0.013}, \quad \theta_{13} = 0.150_{-0.002}^{+0.002}, \quad \theta_{23} = 0.855_{-0.020}^{+0.018} \quad (3)$$

in the inverted mass ordering (IMO) case, we find that the smallest angles  $\theta_{13}$  is most accurately determined and thus suitable for serving as an optimal expansion parameter<sup>2</sup>. So we are going

<sup>1</sup>But see, e.g., Refs. [7, 8, 9], for the early attempts in this regard.

<sup>2</sup>It is worth pointing out that the previous phenomenological conjecture  $|U_{e3}| = \lambda/\sqrt{2} \simeq 0.159$  [25] is no more favored by the Daya Bay precision measurements (i.e.,  $\sin \theta_{13} \simeq 0.149$ ) [26].

to study an expansion of the  $U_{\text{TBM}}$ -based PMNS matrix  $U$  in powers of the small parameter  $\xi \equiv |U_{e3}| = \sin \theta_{13} \simeq 0.149 \simeq 0.662\lambda$ . Moreover, the best-fit values of  $\theta_{12}$  and  $\theta_{23}$  lead us to

$$\begin{aligned} \text{NMO : } \quad \theta_{12} - \theta_{12}^{(0)} &\simeq -0.032 \simeq -1.463\xi^2, \\ \theta_{23} - \theta_{23}^{(0)} &\simeq -0.049 \simeq -2.225\xi^2; \end{aligned} \quad (4)$$

as well as

$$\begin{aligned} \text{IMO : } \quad \theta_{12} - \theta_{12}^{(0)} &\simeq -0.032 \simeq -1.463\xi^2, \\ \theta_{23} - \theta_{23}^{(0)} &\simeq +0.070 \simeq +3.135\xi^2. \end{aligned} \quad (5)$$

Eqs. (4) and (5) imply that the observed values of  $\theta_{12}$  and  $\theta_{23}$  are most likely to deviate from their respective tri-bimaximal flavor mixing limits at the level of  $\mathcal{O}(\xi^2)$ . This observation provides us with a new angle of view, which is quite different from those in the previous attempts, to expand  $U$  in the basis of  $U_{\text{TBM}}$ .

In what follows we shall propose a new expansion of the PMNS matrix  $U$  by starting from the standard Euler-like parametrization of  $U$  and taking account of

- $\sin \theta_{13} \equiv \xi \simeq 0.149$  as the lepton flavor mixing expansion parameter;
- $\theta_{12} = \theta_{12}^{(0)} - A\xi^2$  with  $\theta_{12}^{(0)} = \cot \sqrt{2} \simeq 35.26^\circ$  and  $A \sim \mathcal{O}(1)$ ;
- $\theta_{23} = \theta_{23}^{(0)} - B\xi^2$  with  $\theta_{23}^{(0)} = 45^\circ$  and  $|B| \sim \mathcal{O}(1)$ .

It is obvious that  $B \neq 0$  characterizes the effect of  $\mu$ - $\tau$  permutation symmetry breaking of  $U$ , and the sign of  $B$  determines the octant of  $\theta_{23}$  [27, 28]. In this case the PMNS matrix will be expressed in terms of the tri-bimaximal flavor mixing pattern  $U_{\text{TBM}}$ , the three real parameters  $\xi$ ,  $A$  and  $B$ , and the poorly known CP-violating phase  $\delta$ . Here we leave aside the two possible extra CP phases associated with the Majorana nature of massive neutrinos, as they are completely unknown and have no effect on the fine structure of  $U$ .

## 2 The expansion of $U$

As advocated by the Particle Data Group (PDG), the standard Euler-like parametrization of the unitary  $3 \times 3$  PMNS matrix  $U$  is explicitly of the form [3]

$$U = \begin{pmatrix} c_{12}c_{13} & s_{12}c_{13} & s_{13}e^{-i\delta} \\ -s_{12}c_{23} - c_{12}s_{13}s_{23}e^{i\delta} & c_{12}c_{23} - s_{12}s_{13}s_{23}e^{i\delta} & c_{13}s_{23} \\ s_{12}s_{23} - c_{12}s_{13}c_{23}e^{i\delta} & -c_{12}s_{23} - s_{12}s_{13}c_{23}e^{i\delta} & c_{13}c_{23} \end{pmatrix}, \quad (6)$$

in which  $c_{ij} \equiv \cos \theta_{ij}$  and  $s_{ij} \equiv \sin \theta_{ij}$  (for  $ij = 12, 13, 23$ ) with  $\theta_{ij}$  lying in the first quadrant,  $\delta$  denotes the irreducible CP-violating phase responsible for CP violation in neutrino oscillations, and possible additional CP phases of the Majorana nature can always be factored out on the

right-hand side of  $U$  and thus have been omitted. Following the strategy outlined above for a Wolfenstein-like expansion of the  $U_{\text{TBM}}$ -based PMNS matrix  $U$ , we have

$$\begin{aligned}
s_{13} &\equiv \xi, \\
c_{13} &= 1 - \frac{1}{2}\xi^2 - \frac{1}{8}\xi^4 + \mathcal{O}(\xi^6), \\
s_{12} &= \frac{1}{\sqrt{3}} \left[ 1 - \sqrt{2}A\xi^2 - \frac{1}{2}A^2\xi^4 \right] + \mathcal{O}(\xi^6), \\
c_{12} &= \frac{2}{\sqrt{6}} \left[ 1 + \frac{1}{\sqrt{2}}A\xi^2 - \frac{1}{2}A^2\xi^4 \right] + \mathcal{O}(\xi^6), \\
s_{23} &= \frac{1}{\sqrt{2}} \left[ 1 - B\xi^2 - \frac{1}{2}B^2\xi^4 \right] + \mathcal{O}(\xi^6), \\
c_{23} &= \frac{1}{\sqrt{2}} \left[ 1 + B\xi^2 - \frac{1}{2}B^2\xi^4 \right] + \mathcal{O}(\xi^6). \tag{7}
\end{aligned}$$

Substituting Eq. (7) into Eq. (6), we immediately arrive at the nine elements of  $U$  in the PDG-advocated phase convention as follows:

$$\begin{aligned}
U_{e1} &= \frac{2}{\sqrt{6}} - \frac{1 - \sqrt{2}A}{\sqrt{6}}\xi^2 - \frac{1 + 2\sqrt{2}A + 4A^2}{4\sqrt{6}}\xi^4, \\
U_{e2} &= \frac{1}{\sqrt{3}} - \frac{1 + 2\sqrt{2}A}{2\sqrt{3}}\xi^2 - \frac{1 - 4\sqrt{2}A + 4A^2}{8\sqrt{3}}\xi^4, \\
U_{e3} &= \xi e^{-i\delta}, \\
U_{\mu 1} &= -\frac{1}{\sqrt{6}} - \frac{1}{\sqrt{3}}\xi e^{i\delta} + \frac{\sqrt{2}A - B}{\sqrt{6}}\xi^2 - \frac{A - \sqrt{2}B}{\sqrt{6}}\xi^3 e^{i\delta} + \frac{A^2 + B^2 + 2\sqrt{2}AB}{2\sqrt{6}}\xi^4 \\
&\quad + \frac{A^2 + B^2 + \sqrt{2}AB}{2\sqrt{3}}\xi^5 e^{i\delta}, \\
U_{\mu 2} &= \frac{1}{\sqrt{3}} - \frac{1}{\sqrt{6}}\xi e^{i\delta} + \frac{A + \sqrt{2}B}{\sqrt{6}}\xi^2 + \frac{\sqrt{2}A + B}{\sqrt{6}}\xi^3 e^{i\delta} - \frac{A^2 + B^2 - \sqrt{2}AB}{2\sqrt{3}}\xi^4 \\
&\quad + \frac{A^2 + B^2 + 2\sqrt{2}AB}{2\sqrt{6}}\xi^5 e^{i\delta}, \\
U_{\mu 3} &= \frac{1}{\sqrt{2}} - \frac{1 + 2B}{2\sqrt{2}}\xi^2 - \frac{(1 - 2B)^2}{8\sqrt{2}}\xi^4, \\
U_{\tau 1} &= \frac{1}{\sqrt{6}} - \frac{1}{\sqrt{3}}\xi e^{i\delta} - \frac{\sqrt{2}A + B}{\sqrt{6}}\xi^2 - \frac{A + \sqrt{2}B}{\sqrt{6}}\xi^3 e^{i\delta} - \frac{A^2 + B^2 - 2\sqrt{2}AB}{2\sqrt{6}}\xi^4 \\
&\quad + \frac{A^2 + B^2 - \sqrt{2}AB}{2\sqrt{3}}\xi^5 e^{i\delta}, \\
U_{\tau 2} &= -\frac{1}{\sqrt{3}} - \frac{1}{\sqrt{6}}\xi e^{i\delta} - \frac{A - \sqrt{2}B}{\sqrt{6}}\xi^2 + \frac{\sqrt{2}A - B}{\sqrt{6}}\xi^3 e^{i\delta} + \frac{A^2 + B^2 + \sqrt{2}AB}{2\sqrt{3}}\xi^4 \\
&\quad + \frac{A^2 + B^2 + 2\sqrt{2}AB}{2\sqrt{6}}\xi^5 e^{i\delta}, \\
U_{\tau 3} &= \frac{1}{\sqrt{2}} - \frac{1 - 2B}{2\sqrt{2}}\xi^2 - \frac{(1 + 2B)^2}{8\sqrt{2}}\xi^4, \tag{8}
\end{aligned}$$

up to  $\mathcal{O}(\xi^6)$  or equivalently  $\mathcal{O}(10^{-5})$ . This degree of precision and accuracy for the elements of  $U$  should be good enough to confront the present and future precision measurements of various

neutrino oscillation channels. Some comments and discussions are in order.

- The two off-diagonal asymmetries of the unitary PMNS matrix  $U$ , which largely characterize its geometrical structure about the  $U_{e1}$ - $U_{\mu 2}$ - $U_{\tau 3}$  and  $U_{e3}$ - $U_{\mu 2}$ - $U_{\tau 1}$  axes, are given by

$$\begin{aligned}
\mathcal{A}_1 &\equiv |U_{e2}|^2 - |U_{\mu 1}|^2 = |U_{\mu 3}|^2 - |U_{\tau 2}|^2 = |U_{\tau 1}|^2 - |U_{e3}|^2 \\
&\simeq +\frac{1}{6} - \frac{\sqrt{2}}{3}\xi \cos \delta - \frac{1}{3} \left( 2 + 2A^2 + B^2 + 2\sqrt{2}AB \right) \xi^2, \\
\mathcal{A}_2 &\equiv |U_{e2}|^2 - |U_{\mu 3}|^2 = |U_{\mu 1}|^2 - |U_{\tau 2}|^2 = |U_{\tau 3}|^2 - |U_{e1}|^2 \\
&\simeq -\frac{1}{6} + \frac{1}{6} \left( 1 - 4\sqrt{2}A + 6B \right) \xi^2.
\end{aligned} \tag{9}$$

In comparison, the corresponding off-diagonal asymmetries of the CKM quark flavor mixing matrix  $V$  are respectively of  $\mathcal{O}(\lambda^6)$  and  $\mathcal{O}(\lambda^2)$  [5]. So the PMNS matrix  $U$  is geometrically not so symmetrical as the CKM matrix  $V$ . Given the fact that either  $\mathcal{A}_1 = 0$  or  $\mathcal{A}_2 = 0$  would imply the congruence of three pairs of the PMNS unitarity triangles in the complex plane [29], we find that the relatively large off-diagonal asymmetries of  $U$  means that its six unitarity triangles are not very similar to one another in shape.

- The three  $\mu$ - $\tau$  interchange asymmetries of the PMNS matrix  $U$ , which describe small effects of the  $\mu$ - $\tau$  flavor symmetry breaking, are found to be

$$\begin{aligned}
\Delta_1 &\equiv |U_{\tau 1}|^2 - |U_{\mu 1}|^2 \simeq -\frac{2}{3}B\xi^2 \left[ 1 - 2 \left( 1 + \sqrt{2}A \right) \xi^2 \right] - \frac{2}{3}\xi \left( \sqrt{2} - A\xi^2 \right) \cos \delta, \\
\Delta_2 &\equiv |U_{\tau 2}|^2 - |U_{\mu 2}|^2 \simeq -\frac{2}{3}B\xi^2 \left[ 2 - \left( 1 - 2\sqrt{2}A \right) \xi^2 \right] + \frac{2}{3}\xi \left( \sqrt{2} - A\xi^2 \right) \cos \delta, \\
\Delta_3 &\equiv |U_{\tau 3}|^2 - |U_{\mu 3}|^2 \simeq 2B\xi^2 \left( 1 - \xi^2 \right).
\end{aligned} \tag{10}$$

Of course,  $\Delta_1 + \Delta_2 + \Delta_3 = 0$  holds, as assured by the unitarity of  $U$ . One can simply see that  $\Delta_1 = \Delta_2 = \Delta_3 = 0$  requires both  $B = 0$  and  $\delta = \pm\pi/2$ , the conditions that allow  $U$  to have the exact  $\mu$ - $\tau$  reflection symmetry [30]. The preliminary T2K measurement hints at  $\delta \sim -\pi/2$  [31], and thus  $\Delta_1$ ,  $\Delta_2$  and  $\Delta_3$  are all expected to be of  $\mathcal{O}(10^{-2})$ . It is therefore expected that the  $\mu$ - $\tau$  permutation or reflection symmetry may serve as a minimal lepton flavor symmetry which is greatly helpful for explicit model building [27, 28].

- The well-known Jarlskog invariant of leptonic CP violation [32, 33], which measures the universal strength of CP-violating effects in neutrino oscillations, is given as

$$\mathcal{J}_\nu \equiv \text{Im} \left( U_{e2}U_{\mu 3}U_{e3}^*U_{\mu 2}^* \right) \simeq \frac{1}{6}\xi \left[ \sqrt{2} - \left( \sqrt{2} + A \right) \xi^2 \right] \sin \delta. \tag{11}$$

So  $\mathcal{J}_\nu \simeq 3.5 \times 10^{-2} \sin \delta$  holds in the leading-order approximation. Given  $\delta \sim -\pi/2$ , for instance, the size of the leptonic Jarlskog invariant will be about a thousand times larger than that of its counterpart in the quark sector [3].

Note that one may only keep the leading-order terms of  $\mathcal{A}_1$ ,  $\mathcal{A}_2$ ,  $\Delta_1$ ,  $\Delta_2$ ,  $\Delta_3$  and  $\mathcal{J}_\nu$  in most cases, as they are analytically simple enough and numerically accurate enough.

### 3 The ordering of $|U_{\alpha i}|$

Taking account of the  $U_{\text{TBM}}$ -based expansion of the PMNS matrix  $U$  in powers of  $\xi \simeq 0.149$  in Eq. (8), we find that the analytical approximation

$$U \simeq \begin{pmatrix} \frac{2}{\sqrt{6}} - \frac{1 - \sqrt{2}A}{\sqrt{6}}\xi^2 & \frac{1}{\sqrt{3}} - \frac{1 + 2\sqrt{2}A}{2\sqrt{3}}\xi^2 & \xi e^{-i\delta} \\ -\frac{1}{\sqrt{6}} - \frac{1}{\sqrt{3}}\xi e^{i\delta} + \frac{\sqrt{2}A - B}{\sqrt{6}}\xi^2 & \frac{1}{\sqrt{3}} - \frac{1}{\sqrt{6}}\xi e^{i\delta} + \frac{A + \sqrt{2}B}{\sqrt{6}}\xi^2 & \frac{1}{\sqrt{2}} - \frac{1 + 2B}{2\sqrt{2}}\xi^2 \\ \frac{1}{\sqrt{6}} - \frac{1}{\sqrt{3}}\xi e^{i\delta} - \frac{\sqrt{2}A + B}{\sqrt{6}}\xi^2 & -\frac{1}{\sqrt{3}} - \frac{1}{\sqrt{6}}\xi e^{i\delta} - \frac{A - \sqrt{2}B}{\sqrt{6}}\xi^2 & \frac{1}{\sqrt{2}} - \frac{1 - 2B}{2\sqrt{2}}\xi^2 \end{pmatrix} \quad (12)$$

is actually good enough to fit current neutrino oscillation data. Let us examine to what extent one may identify the ordering of  $|U_{\alpha i}|$  (for  $\alpha = e, \mu, \tau$  and  $i = 1, 2, 3$ ).

- For the matrix elements in the first row of  $U$ , it is easy to identify  $|U_{e1}| > |U_{e2}| > |U_{e3}|$ . In fact,  $|U_{e1}|$  and  $|U_{e3}|$  are the largest and smallest moduli among the nine elements of  $U$ .
- For the matrix elements in the third column of  $U$ , the sign of  $B$  is crucial as it determines whether  $|U_{\mu 3}|$  is larger or smaller than its counterpart  $|U_{\tau 3}|$ . This point is obviously supported by  $|U_{\tau 3}|^2 - |U_{\mu 3}|^2 \simeq 2B\xi^2$  obtained from Eq. (10). We are therefore left with  $|U_{\tau 3}| \geq |U_{\mu 3}| > |U_{e3}|$  for  $B \geq 0$ , or  $|U_{\mu 3}| \geq |U_{\tau 3}| > |U_{e3}|$  for  $B \leq 0$ .
- For the matrix elements in the second and third rows of  $U$ , the smallness of  $\xi$  assures that  $|U_{\mu 1}| < |U_{\mu 2}| < |U_{\mu 3}|$  and  $|U_{\tau 1}| < |U_{\tau 2}| < |U_{\tau 3}|$  hold. This observation is independent of the values of  $A$ ,  $B$  and  $\delta$  in the Wolfenstein-like expansion of  $U$  proposed above.
- To compare between the magnitudes of  $U_{\tau i}$  and  $U_{\mu i}$  (for  $i = 1, 2$ ), we may simplify the expressions of  $\Delta_1$  and  $\Delta_2$  in Eq. (10) as follows:

$$\begin{aligned} |U_{\tau 1}|^2 - |U_{\mu 1}|^2 &\simeq -\frac{2}{3}\xi \left( \sqrt{2} \cos \delta + B\xi \right), \\ |U_{\tau 2}|^2 - |U_{\mu 2}|^2 &\simeq +\frac{2}{3}\xi \left( \sqrt{2} \cos \delta - 2B\xi \right). \end{aligned} \quad (13)$$

It becomes clear that  $|U_{\tau 1}| \leq |U_{\mu 1}|$  will hold if  $\sqrt{2} \cos \delta + B\xi \geq 0$  is satisfied; and  $|U_{\tau 1}| \geq |U_{\mu 1}|$  will hold if  $\sqrt{2} \cos \delta + B\xi$  flips its sign. On the other hand,  $|U_{\tau 2}| \geq |U_{\mu 2}|$  will hold if  $\cos \delta \geq \sqrt{2}B\xi$  is satisfied; and  $|U_{\tau 2}| \leq |U_{\mu 2}|$  will hold if  $\cos \delta \leq \sqrt{2}B\xi$  is satisfied.

- Whether  $|U_{e2}|$  can be larger or smaller than  $|U_{\mu 2}|$  or  $|U_{\tau 2}|$  is another open question before the quadrant of the CP-violating phase  $\delta$  is surely determined. The reason is simply that

$$\begin{aligned} |U_{e2}|^2 &\simeq |U_{\mu 2}|^2 - \frac{1}{2} \left( 1 + 2\sqrt{2}A \right) \xi^2 + \frac{\sqrt{2}}{3}\xi \left( \cos \delta - \sqrt{2}B\xi \right) \\ &\simeq |U_{\tau 2}|^2 - \frac{1}{2} \left( 1 + 2\sqrt{2}A \right) \xi^2 - \frac{\sqrt{2}}{3}\xi \left( \cos \delta - \sqrt{2}B\xi \right) \end{aligned} \quad (14)$$

holds to the accuracy of  $\mathcal{O}(\xi^2)$ . In case of  $\cos \delta = 0$ , however, the sign of  $B$  will play a part.

A summary of the above discussions leads us to the following most likely ordering of the nine matrix elements of  $U$  in magnitude:

$$|U_{e1}| > \{|U_{\mu3}|, |U_{\tau3}|\} > \{|U_{e2}|, |U_{\mu2}|, |U_{\tau2}|\} > \{|U_{\mu1}|, |U_{\tau1}|\} > |U_{e3}|, \quad (15)$$

where the ordering of the *bracketed* moduli remains unidentifiable from the present neutrino oscillation data. That is why the next-generation long-baseline neutrino oscillation experiments aim to pin down the octant of  $\theta_{23}$  (or equivalently, the sign of  $B$ ) and the quadrant of  $\delta$ .

To be more specific, let us simply take the best-fit value of  $\delta$  to illustrate the ordering of the nine PMNS moduli  $|U_{\alpha i}|$  (for  $\alpha = e, \mu, \tau$  and  $i = 1, 2, 3$ ). Given [23, 24]

$$\text{NMO} : \quad \delta \simeq -0.711\pi, \quad A \simeq 1.463, \quad B \simeq 2.225, \quad (16)$$

where the values of  $A$  and  $B$  are directly extracted from Eq. (4), we obtain  $|U_{\tau1}| > |U_{\mu1}|$  from Eq. (13),  $|U_{\tau2}| < |U_{e2}| < |U_{\mu2}|$  from Eq. (14) and  $|U_{\tau3}| > |U_{\mu3}|$  from Eq. (10). As a result,

$$\text{NMO} : \quad |U_{e1}| > |U_{\tau3}| > |U_{\mu3}| > |U_{\mu2}| > |U_{e2}| > |U_{\tau2}| > |U_{\tau1}| > |U_{\mu1}| > |U_{e3}|. \quad (17)$$

In the IMO case, we input [23, 24]

$$\text{IMO} : \quad \delta \simeq -0.467\pi, \quad A \simeq 1.463, \quad B \simeq -3.135, \quad (18)$$

where the values of  $A$  and  $B$  are directly extracted from Eq. (5), and then find  $|U_{\tau1}| > |U_{\mu1}|$  and  $|U_{e2}| < |U_{\mu2}| < |U_{\tau2}|$  from Eq. (14) and  $|U_{\tau3}| < |U_{\mu3}|$  from Eq. (10). As a consequence,

$$\text{IMO} : \quad |U_{e1}| > |U_{\mu3}| > |U_{\tau3}| > |U_{\tau2}| > |U_{\mu2}| > |U_{e2}| > |U_{\tau1}| > |U_{\mu1}| > |U_{e3}|. \quad (19)$$

We see that the nine PMNS matrix elements do not have a clearly layered hierarchy in magnitude, as compared with the four-layered ordering of the nine CKM moduli shown in Eq. (1). The reason behind this difference should be closely related to the underlying mechanism responsible for the origin of tiny neutrino masses, although it remains vague and unclear at present.

## 4 The unitarity triangle

The ‘‘appearance’’ neutrino oscillation  $\nu_\mu \rightarrow \nu_e$  and its CP-conjugated process  $\bar{\nu}_\mu \rightarrow \bar{\nu}_e$  are the only realistic channels to measure leptonic CP violation in a long-baseline oscillation experiment like T2K [31]. It is the so-called unitarity triangle  $\Delta_\tau$  [34] defined by the orthogonality relation  $U_{e1}U_{\mu1}^* + U_{e2}U_{\mu2}^* + U_{e3}U_{\mu3}^* = 0$  in the complex plane that is directly related to  $\nu_\mu \rightarrow \nu_e$  and  $\bar{\nu}_\mu \rightarrow \bar{\nu}_e$  oscillations. In view of the PDG-advocated phase convention of  $U$  taken in Eq. (6) or (8), we find that it is more convenient to use the side  $U_{e3}U_{\mu3}^*$  to rescale the three sides of  $\Delta_\tau$  [35]. In this case, we simply arrive at

$$\Delta'_\tau : \quad \frac{U_{e1}U_{\mu1}^*}{U_{e3}U_{\mu3}^*} + \frac{U_{e2}U_{\mu2}^*}{U_{e3}U_{\mu3}^*} + 1 = 0, \quad (20)$$

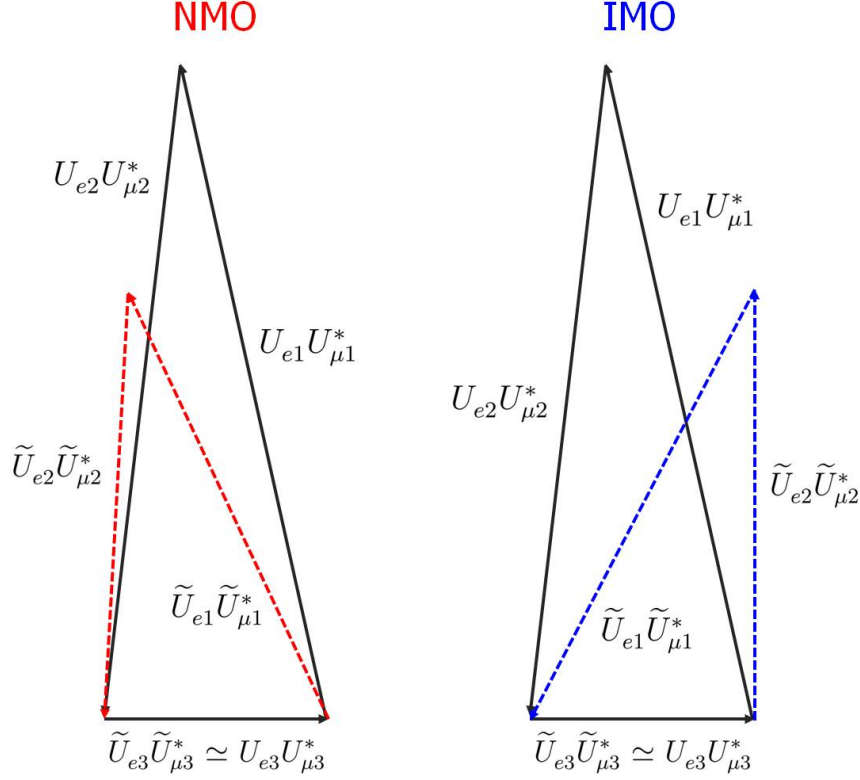


Figure 1: An illustration of the geometrical shapes of the rescaled unitarity triangle  $\Delta'_\tau$  (solid black) and its effective matter-corrected counterpart  $\tilde{\Delta}'_\tau$  (dashed red for the NMO case and dashed blue for the IMO case) in the complex plane, where  $\delta \simeq -\pi/2$  has typically been input.

where the two sloping sides are given by

$$\begin{aligned} \frac{U_{e1}U_{\mu1}^*}{U_{e3}U_{\mu3}^*} &\simeq -\frac{\sqrt{2}}{3\xi}e^{i\delta} - \frac{2}{3}, \\ \frac{U_{e2}U_{\mu2}^*}{U_{e3}U_{\mu3}^*} &\simeq +\frac{\sqrt{2}}{3\xi}e^{i\delta} - \frac{1}{3}, \end{aligned} \quad (21)$$

to a good degree of accuracy. Just taking  $\delta \simeq -\pi/2$  and  $\xi \simeq 0.149$  for example, we obtain the numerical results  $|U_{e1}U_{\mu1}^*|/|U_{e3}U_{\mu3}^*| \simeq 3.23$  and  $|U_{e2}U_{\mu2}^*|/|U_{e3}U_{\mu3}^*| \simeq 3.18$ . Namely, two of the three sides of  $\Delta'_\tau$  are about three times longer than the shortest one in magnitude, as illustrated by the solid black triangle in Fig. 1. Note that the height of  $\Delta'_\tau$ , denoted as  $\mathcal{J}'_\nu$ , is correlated with the Jarlskog invariant  $\mathcal{J}_\nu$  as follows:

$$\mathcal{J}'_\nu = \frac{\mathcal{J}_\nu}{|U_{e3}U_{\mu3}^*|^2} \simeq \frac{1}{3\xi} \left[ \sqrt{2} - (A - 2\sqrt{2}B) \xi^2 \right] \sin \delta, \quad (22)$$

where the expression of  $\mathcal{J}_\nu$  obtained in Eq. (11) has been used. We are then left with the result  $\mathcal{J}'_\nu \simeq \sqrt{2} \sin \delta / (3\xi)$  in the leading-order approximation, as clearly indicated by the imaginary parts of the two sloping sides of  $\Delta'_\tau$  in Eq. (21).

It is well known that the terrestrial matter effects on  $\nu_\mu \rightarrow \nu_e$  and  $\bar{\nu}_\mu \rightarrow \bar{\nu}_e$  oscillations are not very significant in the T2K and Hyper-Kamiokande experiments with the baseline length  $L \simeq 295$  km and the typical beam energy  $E \simeq 0.6$  GeV [3], but such effects can modify the shape



of the above unitarity triangle and thus modify the Jarlskog invariant of CP violation to some extent. To see this point more clearly, let us consider the *effective* rescaled unitarity triangle

$$\tilde{\Delta}'_{\tau} : \frac{\tilde{U}_{e1}\tilde{U}_{\mu1}^*}{\tilde{U}_{e3}\tilde{U}_{\mu3}^*} + \frac{\tilde{U}_{e2}\tilde{U}_{\mu2}^*}{\tilde{U}_{e3}\tilde{U}_{\mu3}^*} + 1 = 0, \quad (23)$$

where  $\tilde{U}_{ei}$  and  $\tilde{U}_{\mu i}$  (for  $i = 1, 2, 3$ ) denote the effective PMNS matrix elements in matter. Following the analytical approximations made in Ref. [36], we obtain  $\tilde{U}_{e3}\tilde{U}_{\mu3}^* \simeq U_{e3}U_{\mu3}^*$  and

$$\begin{aligned} \frac{\tilde{U}_{e1}\tilde{U}_{\mu1}^*}{\tilde{U}_{e3}\tilde{U}_{\mu3}^*} &\simeq \frac{\alpha}{\epsilon} \cdot \frac{U_{e1}U_{\mu1}^*}{U_{e3}U_{\mu3}^*} - \frac{\epsilon - \alpha - \beta}{2\epsilon}, \\ \frac{\tilde{U}_{e2}\tilde{U}_{\mu2}^*}{\tilde{U}_{e3}\tilde{U}_{\mu3}^*} &\simeq \frac{\alpha}{\epsilon} \cdot \frac{U_{e2}U_{\mu2}^*}{U_{e3}U_{\mu3}^*} - \frac{\epsilon - \alpha + \beta}{2\epsilon}, \end{aligned} \quad (24)$$

to a good degree of accuracy, where  $\alpha \equiv \Delta m_{21}^2/\Delta m_{31}^2$ ,  $\beta \equiv \mathbb{A}/\Delta m_{31}^2$ ,  $\mathbb{A} \equiv 2\sqrt{2}G_{\text{F}}N_e E$ , and

$$\epsilon \equiv \sqrt{\alpha^2 - 2(|U_{e1}|^2 - |U_{e2}|^2)\alpha\beta + (1 - |U_{e3}|^2)^2\beta^2} \quad (25)$$

with  $\Delta m_{ij}^2$  (for  $i, j = 1, 2, 3$ ) being the neutrino mass-squared differences,  $G_{\text{F}}$  being the Fermi constant,  $N_e$  being the terrestrial background density of electrons, and  $E$  being the neutrino beam energy [37, 38]. Substituting Eq. (21) into Eq. (24), we arrive at

$$\begin{aligned} \frac{\tilde{U}_{e1}\tilde{U}_{\mu1}^*}{\tilde{U}_{e3}\tilde{U}_{\mu3}^*} &\simeq - \left( \frac{\sqrt{2}}{3\xi} e^{i\delta} + \frac{1}{6} \right) \frac{\alpha}{\epsilon} - \frac{1}{2} \left( 1 - \frac{\beta}{\epsilon} \right), \\ \frac{\tilde{U}_{e2}\tilde{U}_{\mu2}^*}{\tilde{U}_{e3}\tilde{U}_{\mu3}^*} &\simeq + \left( \frac{\sqrt{2}}{3\xi} e^{i\delta} + \frac{1}{6} \right) \frac{\alpha}{\epsilon} - \frac{1}{2} \left( 1 + \frac{\beta}{\epsilon} \right). \end{aligned} \quad (26)$$

This result shows that the terrestrial matter effects can obviously modify the rescaled unitarity triangle  $\tilde{\Delta}'_{\tau}$  in vacuum. Taking account of  $\tilde{\mathcal{J}}_{\nu}/\mathcal{J}_{\nu} \simeq |\alpha|/\epsilon$  obtained in Ref. [36], where  $\tilde{\mathcal{J}}_{\nu}$  denotes the effective Jarlskog invariant in matter, we may similarly achieve the height of  $\tilde{\Delta}'_{\tau}$ :

$$\tilde{\mathcal{J}}'_{\nu} = \frac{\tilde{\mathcal{J}}_{\nu}}{|\tilde{U}_{e3}\tilde{U}_{\mu3}^*|^2} \simeq \frac{\alpha}{3\epsilon\xi} \left[ \sqrt{2} - \left( A - 2\sqrt{2}B \right) \xi^2 \right] \sin \delta, \quad (27)$$

whose leading term is certainly consistent with the imaginary parts of the two sloping sides of  $\tilde{\Delta}'_{\tau}$  that can directly be seen from Eq. (26).

To illustrate, one may typically take  $\mathbb{A} \simeq 2.28 \times 10^{-4} \text{ eV}^2 (E/\text{GeV})$  for a neutrino trajectory through the Earth's crust [39], which is suitable for the realistic ongoing and upcoming long-baseline neutrino oscillation experiments. Of course, the matter parameter  $\mathbb{A}$  should flip its sign for an antineutrino beam, and both  $\alpha$  and  $\beta$  are sensitive to the neutrino mass ordering (i.e., the sign of  $\Delta m_{31}^2$ ). Given the best-fit values  $\Delta m_{21}^2 \simeq 7.41 \times 10^{-5} \text{ eV}^2$ ,  $\Delta m_{31}^2 \simeq 2.51 \times 10^{-3} \text{ eV}^2$  (NMO) or  $\Delta m_{31}^2 \simeq -2.41 \times 10^{-3} \text{ eV}^2$  (IMO) [23, 24], we have  $\alpha \simeq 2.95 \times 10^{-2}$  (NMO) or  $\alpha \simeq -3.07 \times 10^{-2}$  (IMO), together with  $\beta \simeq 5.45 \times 10^{-2}$  (NMO) or  $\beta \simeq -5.68 \times 10^{-2}$  (IMO) for the T2K and Hyper-Kamiokande neutrino oscillation experiments with  $E \simeq 0.6 \text{ GeV}$ . In this

case we obtain  $\epsilon \simeq 4.97 \times 10^{-2}$  (NMO) or  $\epsilon \simeq 5.18 \times 10^{-2}$  (IMO) after taking into account the best-fit values of  $\theta_{12}$  and  $\theta_{13}$  given in Eqs. (2) and (3). Fig. 1 illustrates how the geometrical shape of  $\Delta'_\tau$  changes as a consequence of the terrestrial matter effects on neutrino oscillations in the NMO and IMO cases. It becomes clear that the area of  $\tilde{\Delta}'_\tau$  is remarkably smaller than that of  $\Delta'_\tau$ , and their ratio is simply governed by  $\tilde{\mathcal{J}}_\nu/\mathcal{J}_\nu \simeq |\alpha|/\epsilon$  as discussed above.

It is finally worth pointing out that  $\theta_{12}$ ,  $\theta_{23}$  and  $\delta$  are essentially insensitive to terrestrial matter effects in the  $E \lesssim 1$  GeV region [40, 41, 42], and  $\sin 2\tilde{\theta}_{12}/\sin 2\theta_{12} \simeq \tilde{\mathcal{J}}_\nu/\mathcal{J}_\nu \simeq |\alpha|/\epsilon$  holds as a good approximation [36]. These observations imply that  $\xi$ ,  $B$  and  $\delta$  in our Wolfenstein-like expansion of the PMNS matrix  $U$  are also expected to be insensitive to terrestrial matter effects in an accelerator-based neutrino oscillation experiment with  $E \lesssim 1$  GeV, and only  $A$  is an exception. To be specific, we take  $\tilde{\theta}_{12} \simeq \theta_{12}^{(0)} - \tilde{A}\xi^2$  and then obtain

$$\tilde{A}\xi^2 \simeq A\xi^2 \frac{|\alpha|}{\epsilon} + \sqrt{2} \left( 1 - \frac{|\alpha|}{\epsilon} \right). \quad (28)$$

The second term on the right-hand side of Eq. (28) is in general unsuppressed as it arises from  $\theta_{12}^{(0)} \simeq 35.26^\circ$ . Although  $\tilde{A}$  itself may be far above  $\mathcal{O}(1)$ , it does not really point to a significant matter effect simply because it is not directly related to any observable of neutrino oscillations.

## 5 Summary

Motivated by the fact that the fine structure of quark flavor mixing can well be understood in the Wolfenstein expansion of the CKM matrix  $V$ , we have proposed a similar expansion of the PMNS matrix  $U$  in the basis of the tri-bimaximal mixing pattern  $U_{\text{TBM}}$  towards understanding the fine structure of lepton flavor mixing. The corresponding expansion parameters are  $\lambda$  for  $V$  and  $\xi$  for  $U$ , and thus we can easily arrive at

$$\lim_{\lambda \rightarrow 0} V = I, \quad \lim_{\xi \rightarrow 0} U = U_{\text{TBM}}, \quad (29)$$

in the limits of vanishing or vanishingly small  $\lambda$  and  $\xi$ . While  $I$  is unique in the quark sector,  $U_{\text{TBM}}$  is just our choice in the lepton sector. However, we have argued that it is rather reasonable to choose  $U_{\text{TBM}}$  as an expansion basis of  $U$  since this constant pattern is particularly favored from the point of view of model building with the help of an underlying discrete flavor symmetry.

We have discussed the ordering of the nine PMNS moduli, the leptonic unitarity triangle  $\Delta_\tau$  and its effective counterpart in terrestrial matter by using the Wolfenstein-like expansion of  $U$  proposed in this paper. Our approach proves to be very useful and instructive. More applications of this new parametrization of  $U$  in neutrino physics will be explored elsewhere.

## Acknowledgements

This work was supported in part by the National Natural Science Foundation of China under grant No. 12075254 and grant No. 11835013.

## References

- [1] N. Cabibbo, Unitary Symmetry and Leptonic Decays, *Phys. Rev. Lett.* **10** (1963) 531.
- [2] M. Kobayashi and T. Maskawa, CP Violation in the Renormalizable Theory of Weak Interaction, *Prog. Theor. Phys.* **49** (1973) 652.
- [3] R. L. Workman *et al.* [Particle Data Group], “Review of Particle Physics,” *PTEP* **2022** (2022), 083C01
- [4] L. Wolfenstein, Parametrization of the Kobayashi-Maskawa Matrix, *Phys. Rev. Lett.* **51** (1983) 1945.
- [5] Z. Z. Xing, “On the hierarchy of quark mixings,” *Nuovo Cim. A* **109** (1996), 115-118
- [6] Z. z. Xing, “Flavor structures of charged fermions and massive neutrinos,” *Phys. Rept.* **854** (2020), 1-147 [arXiv:1909.09610 [hep-ph]].
- [7] Z. z. Xing, Wolfenstein - like parametrization of the neutrino mixing matrix, *J. Phys. G* **29** (2003) 2227 [hep-ph/0211465].
- [8] P. Kaus and S. Meshkov, “Neutrino mass matrix and hierarchy,” *AIP Conf. Proc.* **672** (2003) no.1, 117-125 [arXiv:hep-ph/0211338 [hep-ph]].
- [9] V. Gupta, G. Sánchez-Colón, S. Rajpoot and H. C. Wang, “Lepton flavor mixing in the Wolfenstein scheme,” *Phys. Rev. D* **87** (2013), 073009 [arXiv:1304.1065 [hep-ph]].
- [10] H. Fritzsch and Z. Z. Xing, “Lepton mass hierarchy and neutrino oscillations,” *Phys. Lett. B* **372** (1996), 265-270 [arXiv:hep-ph/9509389 [hep-ph]].
- [11] H. Fritzsch and Z. z. Xing, “Large leptonic flavor mixing and the mass spectrum of leptons,” *Phys. Lett. B* **440** (1998), 313-318 [arXiv:hep-ph/9808272 [hep-ph]].
- [12] F. Feruglio and A. Romanino, “Lepton flavor symmetries,” *Rev. Mod. Phys.* **93** (2021) no.1, 015007 [arXiv:1912.06028 [hep-ph]].
- [13] S. F. King, “Unified Models of Neutrinos, Flavour and CP Violation,” *Prog. Part. Nucl. Phys.* **94** (2017), 217-256 [arXiv:1701.04413 [hep-ph]].
- [14] G. J. Ding and J. W. F. Valle, “The symmetry approach to quark and lepton masses and mixing,” [arXiv:2402.16963 [hep-ph]].
- [15] P. F. Harrison, D. H. Perkins and W. G. Scott, “Tri-bimaximal mixing and the neutrino oscillation data,” *Phys. Lett. B* **530** (2002), 167 [arXiv:hep-ph/0202074 [hep-ph]].
- [16] Z. z. Xing, “Nearly tri-bimaximal neutrino mixing and CP violation,” *Phys. Lett. B* **533** (2002), 85-93 [arXiv:hep-ph/0204049 [hep-ph]].
- [17] X. G. He and A. Zee, “Some simple mixing and mass matrices for neutrinos,” *Phys. Lett. B* **560** (2003), 87-90 [arXiv:hep-ph/0301092 [hep-ph]].
- [18] N. Li and B. Q. Ma, “Parametrization of neutrino mixing matrix in tri-bimaximal mixing pattern,” *Phys. Rev. D* **71** (2005), 017302 [arXiv:hep-ph/0412126 [hep-ph]].

- [19] S. F. King, “Parametrizing the lepton mixing matrix in terms of deviations from tri-bimaximal mixing,” *Phys. Lett. B* **659** (2008), 244-251 [arXiv:0710.0530 [hep-ph]].
- [20] S. F. King, “Tri-bimaximal Neutrino Mixing and  $\theta_{13}$ ,” *Phys. Lett. B* **675** (2009), 347-351 [arXiv:0903.3199 [hep-ph]].
- [21] S. F. King, “Tri-bimaximal-Cabibbo Mixing,” *Phys. Lett. B* **718** (2012), 136-142 [arXiv:1205.0506 [hep-ph]].
- [22] Z. Liu and Y. L. Wu, “Leptonic CP Violation and Wolfenstein Parametrization for Lepton Mixing,” *Phys. Lett. B* **733** (2014), 226-232 [arXiv:1403.2440 [hep-ph]].
- [23] M. C. Gonzalez-Garcia, M. Maltoni and T. Schwetz, “NuFIT: Three-Flavour Global Analyses of Neutrino Oscillation Experiments,” *Universe* **7** (2021) no.12, 459 [arXiv:2111.03086 [hep-ph]]; NuFit webpage, <http://www.nu-fit.org>.
- [24] F. Capozzi, E. Di Valentino, E. Lisi, A. Marrone, A. Melchiorri and A. Palazzo, “Unfinished fabric of the three neutrino paradigm,” *Phys. Rev. D* **104** (2021) no.8, 083031 [arXiv:2107.00532 [hep-ph]].
- [25] C. Giunti and M. Tanimoto, “Deviation of neutrino mixing from bimaximal,” *Phys. Rev. D* **66** (2002), 053013 [arXiv:hep-ph/0207096 [hep-ph]].
- [26] D. Adey *et al.* [Daya Bay], “Measurement of the Electron Antineutrino Oscillation with 1958 Days of Operation at Daya Bay,” *Phys. Rev. Lett.* **121** (2018) no.24, 241805 [arXiv:1809.02261 [hep-ex]].
- [27] Z. z. Xing and Z. h. Zhao, “A review of  $\mu$ - $\tau$  flavor symmetry in neutrino physics,” *Rept. Prog. Phys.* **79** (2016) no.7, 076201 [arXiv:1512.04207 [hep-ph]].
- [28] Z. z. Xing, “The  $\mu$ - $\tau$  reflection symmetry of Majorana neutrinos,” *Rept. Prog. Phys.* **86** (2023) no.7, 076201 [arXiv:2210.11922 [hep-ph]].
- [29] Z. z. Xing, “Can the lepton flavor mixing matrix be symmetric?,” *Phys. Rev. D* **65** (2002), 113010 [arXiv:hep-ph/0204050 [hep-ph]].
- [30] P. F. Harrison and W. G. Scott, “ $\mu$ - $\tau$  reflection symmetry in lepton mixing and neutrino oscillations,” *Phys. Lett. B* **547** (2002), 219-228 [arXiv:hep-ph/0210197 [hep-ph]].
- [31] K. Abe *et al.* [T2K], “Measurements of neutrino oscillation parameters from the T2K experiment using  $3.6 \times 10^{21}$  protons on target,” *Eur. Phys. J. C* **83** (2023) no.9, 782 [arXiv:2303.03222 [hep-ex]].
- [32] C. Jarlskog, “Commutator of the Quark Mass Matrices in the Standard Electroweak Model and a Measure of Maximal CP Nonconservation,” *Phys. Rev. Lett.* **55** (1985), 1039
- [33] D. d. Wu, “The Rephasing Invariants and CP,” *Phys. Rev. D* **33** (1986), 860
- [34] H. Fritzsch and Z. z. Xing, Mass and flavor mixing schemes of quarks and leptons, *Prog. Part. Nucl. Phys.* **45** (2000) 1 [hep-ph/9912358].
- [35] Z. Z. Xing and D. Zhang, “Distinguishing between the twin  $b$ -flavored unitarity triangles on a circular arc,” *Phys. Lett. B* **803** (2020), 135302 [arXiv:1911.03292 [hep-ph]].

- [36] Z. z. Xing and J. y. Zhu, “Analytical approximations for matter effects on CP violation in the accelerator-based neutrino oscillations with  $E \lesssim 1$  GeV,” *JHEP* **07** (2016), 011 [arXiv:1603.02002 [hep-ph]].
- [37] L. Wolfenstein, “Neutrino Oscillations in Matter,” *Phys. Rev. D* **17** (1978), 2369-2374
- [38] S. P. Mikheyev and A. Y. Smirnov, “Resonance Amplification of Oscillations in Matter and Spectroscopy of Solar Neutrinos,” *Sov. J. Nucl. Phys.* **42** (1985), 913-917
- [39] I. Mocioiu and R. Shrock, “Matter effects on neutrino oscillations in long baseline experiments,” *Phys. Rev. D* **62** (2000), 053017 [arXiv:hep-ph/0002149 [hep-ph]].
- [40] H. Minakata and H. Nunokawa, “Measuring leptonic CP violation by low-energy neutrino oscillation experiments,” *Phys. Lett. B* **495** (2000), 369-377 [arXiv:hep-ph/0004114 [hep-ph]].
- [41] E. K. Akhmedov, P. Huber, M. Lindner and T. Ohlsson, “T violation in neutrino oscillations in matter,” *Nucl. Phys. B* **608** (2001), 394-422 [arXiv:hep-ph/0105029 [hep-ph]].
- [42] Z. z. Xing, “Flavor mixing and CP violation of massive neutrinos,” *Int. J. Mod. Phys. A* **19** (2004), 1-80 [arXiv:hep-ph/0307359 [hep-ph]].

# Ground water retention correlation to atmospheric muon rates

T. Avgitas<sup>a</sup>, J.-C. Ianigro<sup>a</sup>, J. Marteau<sup>a</sup>

<sup>a</sup>Univ Lyon, Univ Claude Bernard Lyon 1, CNRS/IN2P3, IP2I Lyon, UMR 5822, , F-69622, Villeurbanne, France

---

## Abstract

Muography is an investigation technique based on the detection of the atmospheric muon flux' modification through matter. It has found lately multiple applications in geosciences, archaeology, and non invasive industrial controls. Mostly known for its imaging capabilities, muography may be exploited as well for monitoring purposes since the atmospheric muon flux is available permanently. In this paper we present an interesting measurement performed in the context of an archaeological project called Archémuons, on the archaeological site of "Palais du Miroir" in Vienne, South of Lyon, France. We installed a muon detector in an underground gallery within the foundations of the building for the second half of 2023. The primary goal is to measure details of those foundations which are largely not excavated yet. Meanwhile we observed over more than 6 months long-term and short-term variations of the muon rates since the start of the experiment, which seem to exhibit a correlation with the rain accumulating on the free field just above the gallery. We propose as an explanation for this behavior the retention of water by the soil above the detector site.

*Keywords:* muography, Archémuons, hydrology, precipitation, soil porosity

---

## 1. Introduction

Muon imaging or muography has emerged as a powerful non-invasive method to complement standard tools in Earth Sciences and is nowadays applied to a growing number of fields such as industrial controls, homeland security, civil engineering. This technique relies on the detection of modifications - absorption or scattering - in the atmospheric muon flux when these particles cross a target. Atmospheric muons are secondary products of primary cosmic-rays, essentially protons and helium nuclei expelled by stars, interacting with nuclei encountered on the top of the atmosphere.

The rather low interaction cross-section of muons with matter ensures that most of them reach the Earth's ground level and that furthermore they may significantly penetrate large and dense structures. As suggested originally by Alvarez in 1970 for the Chephren pyramid (Alvarez et al., 1970), this property may be exploited to perform density contrasts analysis of the interior of the target like X-rays do in medical imaging. As suggested by previous works in volcanology (Jourde et al., 2016), geology (Tramontini et al., 2019) or atmosphere surveys (Di Renzo et al., 2021), the permanence of the muons flux may find applications in monitoring the changes in the inner

---

*Email addresses:* avgitas@ip2i.in2p3.fr (T. Avgitas), ianigro@ip2i.in2p3.fr (J.-C. Ianigro),  
marteau@ip2i.in2p3.fr (J. Marteau)

*Preprint submitted to Arxiv*

*March 4, 2024*

part of targets under study. This is one of the goal of the Archémuons project running since 2023 in Vienne, South of Lyon, France. The primary objective of the project is the characterization of underground galleries in a barely excavated archaeological site. To this end Archémuons collaboration consists of three institutes, IP2I of Lyon, Archéorient<sup>1</sup> and LGL-TPE<sup>2</sup> with the latter two being in charge of the geophysics surveys related to the properties of the soil that covers the galleries.

Given the particular topology of the site (fig. 1), where the galleries are covered by a few meters wide flat field, it has been possible to record the changes in the muon flux crossing this piece of standard soil from Summer to Winter and study the correlations with the cumulative rain. Worth mentioning that the full project also foresees comparison of the muographic measurements with other geophysics measurements to assess the performance of this method with respect to more traditional surveys for shallow soil depths of the order of a few meters. The main result of the present study is that we observe an overall decrease with time of the recorded muon rates crossing the soil overburden and the increase of the total precipitation received by the soil during the same period. We propose as an explanation for this behavior the retention of water by the soil above the detector site.

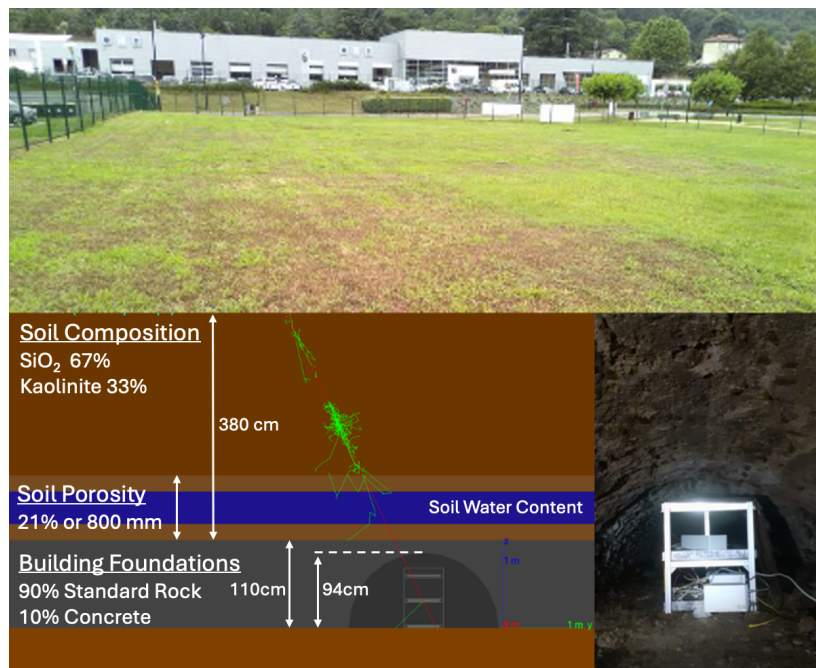


Figure 1: top - The field above the foundations of the archaeological site of Palais du Miroir. Bottom (left) - The simulated version of our experimental setup, the details are discussed inside the text. Bottom (right) - Photograph of the muon tracker installed inside the foundations' gallery.

<sup>1</sup>French National Centre for Scientific Research CNRS, UMR 5133, Archéorient, Lyon, France

<sup>2</sup>Laboratoire de Géologie de Lyon: Terre, Planètes, Environnement, Université de Lyon, Université Lyon 1 and Ecole Normale Supérieure de Lyon, UMR CNRS 5276, F-69622 Villeurbanne, France

## 2. Experimental setup

The detector we installed inside the gallery was a three scintillation-planes tracker. Particles that traverse all three planes are registered as a sequence of three  $(x,y,z)$  coordinates points where  $z$  is the distance between planes, 63 cm between the extreme planes and 32.5 cm between the bottom detector and the middle one (fig. 1 – Bottom (right)). A linear regression fit is then applied for these points to determine whether they belong on the trace of a linear trajectory or not. Based on the chi-square value, along with other event selection criteria, we apply a cut to sample only tracks with high degree of linearity, since these are most likely to be muons. The dimensions of the planes (40 cm x 40 cm) define a maximum zenithal angle for the incoming muons,  $\theta_{max} = 42^\circ$ .

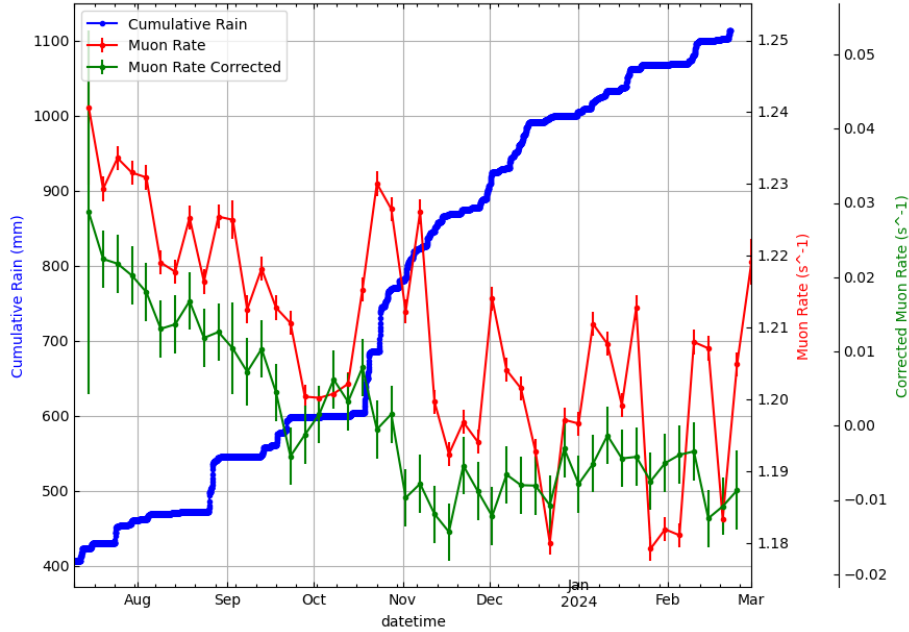


Figure 2: Time series for the hourly cumulative precipitation (blue), the detected muon rates (red) and the residual muon rates (green) after accounting for the atmospheric pressure contribution (both aggregated over a period of 5 days).

We used environmental data taken from the Climate Data Store<sup>3</sup>, specifically the “Re-analysis” atmospheric parameters dataset for the closest coordinate grid point to our site (N 45.53°, E 4.86°) (Hersbach et al., 2017). Weather data are provided in hourly values, and we aggregated the muon data with the same time step. It has been established in the past that there is a linear dependence of the muon rates to the local atmospheric pressure (Jourde et al., 2016). To account for the impact of the pressure changes on the measured muon counts we fit the respective scatter plot (fig. 3a) with a linear regression model, that we then use to correct the hourly muon rates. The mean value for the hourly rate during the DAQ was  $r_0 = 1.20764 \pm 0.00025 \text{ s}^{-1}$  which corresponds to the  $0.00 \text{ s}^{-1}$  rate value for the corrected flux (green y axis - fig. 2). This

<sup>3</sup><https://cds.climate.copernicus.eu/>



information becomes relevant when one needs to calculate the relative change of the corrected muon rates.

Both the corrected daily muon rates (green points with error bars) and the experimental daily muon rate values (red points with error bars) show a decreasing trend which correlates with an increase of the cumulative precipitation (fig. 2). We see that the muon rates from mid November 2023 until the end of February 2024 have stopped their downward trend and have stabilized. This could mean that the additional precipitation does not remain inside the soil overburden, and we can hypothesize that at this point the soil porosity is saturated with water, so that the additional water passes through. Under the assumption (see next paragraph) of 380 cm of soil that withholds a maximum precipitation of 800 mm we calculated a porosity of 21%. The cumulative precipitation is measured from the start of the year and shows that by the initialization of our measurements the ground had already received  $\sim 430$  mm of water which at the end of the year had reached  $\sim 1000$  mm. This behavior is shown clearly when plotting the corrected daily muon rates as a function of the cumulative precipitation (fig. 3b).

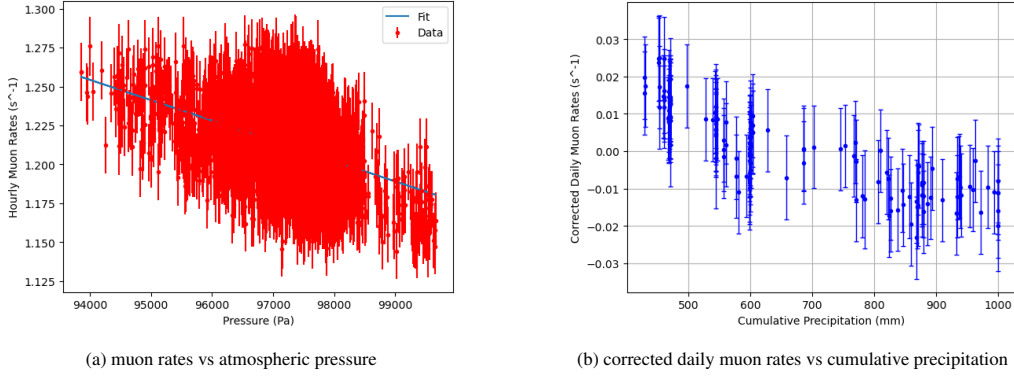


Figure 3: Scatter Plots: (a) Hourly muon rates vs atmospheric pressure. Linear Fit Results - Intercept =  $2.48 \pm 0.04 s^{-1}$ , Slope =  $-131 \pm 4 \times 10^{-7} s^{-1} Pa^{-1}$ . (b) the corrected muon rates plotted against the cumulative precipitation shows clearly the correlation between the two variables (pearson: -0.84), the error bars give an indication of the large uncertainties for the relevant calculations in sections 3 & 4.

### Overburden Opacity

The value for the soil height above the gallery shown in figure 1 is retrieved by a series of calculation based on the experimental data acquired during the first 96 days that returned an experimental muon rate value<sup>4</sup> of  $0.3326 \pm 0.0005 s^{-1}$ . The overburden was hypothesized to comprise of standard rock (table 8 - Groom et al. (2001)). The efficiency of the detector was evaluated based on measurements done at the last floor and the basement of the Dirac building, where IP2I of Lyon is operating. The materials of the building between the two positions amount to 3 m.w.e and with this prior we retrieved an overall efficiency for the detector equal to  $0.1524 \pm 0.0004$ . With this efficiency accounted for, the theoretical muon rate is  $2.182 \pm 0.003 s^{-1}$  that corresponds to  $360.7 \pm 0.6$  cm of standard rock overburden. Opacity is defined as the material

<sup>4</sup>The selection cuts used for the muon tagging at the time of this evaluation were stricter than the ones mentioned previously.

density ( $\rho$ ) times the length ( $\ell$ ) of the muon trajectory within it. The overburden opacity for vertical muons is in this case  $956 \text{ g/cm}^2$ . In terms of opacity we subtract 400 mm of water and 16 cm of stone/cement mixture (sec. 3) for the gallery arch and we retrieve 380 cm of soil.

### 3. Simulation

The simulation we used is based on Geant4 libraries (Agostinelli et al. (2003), Allison et al. (2006), Allison et al. (2016)) and uses randomly generated muon tracks that follow the parametrisation described in Shukla & Sankrith (2018) for the particle energy and the zenithal track distribution while the azimuthal distribution is considered isotropic. The simulated detector follows the actual detector geometry. The sensitive material used for the scintillation parts is polyvinyl-toluene (Luxium Solutions, BC-416) for the extreme panels and polyethylene for the middle one. The information returned from the simulation is the position, energy, energy deposition, momentum direction and the type of particle for each interaction with the detector’s scintillation parts.

A valid muon event in this context is an event where the muon deposits energy on every detector volumes even for those that are accompanied by other particles (mainly electrons and gammas) which may also interact with the detector. In this sense the simulation will always tend to overestimate the signal since it doesn’t take into account the detection efficiency and the event selection algorithm for the experimental data analysis.

The implementation of the different structures surrounding the detector is based on the visual inspection and measurements performed at the site but the materials used are arbitrarily selected since there is no sample catalog of the exact properties so much for the building blocks of the foundations as much for the composition of the soil above them. We assumed a mixture of cement (10%) and rock (90%) for the building foundations and a “Clay Loam” (33% Clay, 33% Silt, 34% Sand) type of soil for the overburden. Silt and Sand for simplification purposes are considered to be both  $\text{SiO}_2$  while the Clay is presumed to be pure Kaolinite ( $\text{Al}_2\text{Si}_2\text{O}_5(\text{OH})_4$ ), giving rise to a soil with  $2.3 \text{ g/cm}^3$  density.

The porosity in this context is represented as a void volume, placed beneath the soil, which can be filled with different ratios of air and water. The water saturation of this volume at 100% corresponds to 800 mm of water retention. In fig. 1 (bottom left) the water saturation drawn (blue strip) is 50% (400 mm), that is similar to the value it should have at the initialization of the measurements.

### 4. Data-Monte Carlo comparison

With the mean hourly muon rate (section 2) as a reference value and by consulting fig. 3b we calculate that the relative change of the muon rates from the start of the experiment until their stabilization in mid November is  $2.3\% \pm 0.14\%$ <sup>5</sup>.

To study the response of the detector to the water retention effect we simulated 3.8M muons that would be detected under open sky conditions, which in terms of experimental DAQ time corresponds to  $\sim 10$  days. We then run the simulation two times, the first for 50% water saturation

---

<sup>5</sup>The initial rate is calculated by the data collected the first three days as  $r_0 = 1.2362 \pm 0.0017 \text{ s}^{-1}$  and the change in the muon rates until the stabilization is  $\Delta r = 0.0286 \pm 0.0017 \text{ s}^{-1}$ , with the final corrected muon rate calculated for the entire period after mid November at  $-0.0074 \pm 0.0005 \text{ s}^{-1}$ .

(or 400mm cumulative precipitation) which resulted in 714816 detected muons. The second run was for 100% water saturation (or 800mm cumulative precipitation) for which 704269 muons were detected. The relative change for the detected muons between the two water configurations is 1.47%.

This result is of the same order of magnitude with the experimental value which is encouraging given the simplicity of our hypotheses and the way that the environmental parameters have been acquired. It is clear that the experimental results and the simulation will be better constraint once the information from the geophysics surveys become available to us.

## **5. Conclusions & Outlook**

In this note we present preliminary results on an hydrological survey performed with the muography technique, by placing a detector in an underground gallery topped with a few meters of soil. This study takes place in a more general study of an archaeological site, more precisely designed to characterize the shapes and depths of underground galleries not completely excavated. The site is located in Vienne, close to Lyon, France. The detector located underground recorded almost continuously atmospheric muons under a 3.8 meters overburden from June 2023 to February 2024. The changes in the measured atmospheric muon flux have been studied in correlation with the accumulated rain in the overburden soil. Given the very simple topology of the experimental setup, the number of parameters to be tuned in this analysis is relatively limited, which makes this configuration very powerful to further study the muography performance for hydrological surveys. Here we present a simplified model adjusting the porosity of the soil to reproduce the observed data. A Monte-Carlo simulation has been developed to allow for data-MC comparison and the model proves to be satisfactorily reproducing the data. The project will be continued in 2024 and the analysis improved by additional information from other geophysical surveys (ERT, georadar and distributed acoustic sensing) conducted recently and at present under analysis. The adjunction of a meteorological weather station would facilitate the method by giving more accurate insights for the local conditions, since the 0.5% difference between the experiment and the simulation could be easily explained by the divergence of local precipitation to the values presented here.

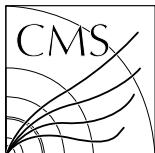
## **Acknowledgements**

We would like to thank Laurence Brissaud, Jean-Luc Prisset for their initiative to include Archémuons collaboration into their archaeological activities at Palais de Miroir, the direction of the Saint-Roman-en-Gal museum and specifically Giulia Ciucci for the support and the facilitation of the experimental activities. Finally we should acknowledge Christophe Benech (Archéorient) and Benoît Tauzin (LGL-TPE) contributions for setting up and performing the geophysics surveys.

This work has been carried out with the support of the LabEx LIO of the Université Claude Bernard Lyon 1, which has been created as part of a program for future development (reference number ANR-10-LABEX-066) initiated by the French government and overseen by the Agence Nationale de la Recherche (ANR). This study is also part of the ANR-19-CE05-0033 MEGAMU project.

## References

- L.W. Alvarez et al., Search for Hidden Chambers in the Pyramids. *Science*, 167:832–839, 1970.
- K. Jourde et al., Monitoring temporal opacity fluctuations of large structures with muon radiography: a calibration experiment using a water tower, *Nature Scientific Reports*, 14 March 2016, DOI:10.1038/srep23054
- M. Tramontini et al., Middle-atmosphere dynamics observed with a portable muon detector. *Earth and Space Science* 6, 1865–1876, 2019 <https://doi.org/10.1029/2019EA000655>
- F. Di Renzo et al., Study of the cosmic muon rate nearby the advanced Virgo detector at the end of the O3 run, *Proceedings of Science, PoS, EPS-HEP2021*, 059, 2022, DOI:10.22323/1.398.0059
- H. Hersbach et al., Complete ERA5 from 1940: Fifth generation of ECMWF atmospheric reanalyses of the global climate. Copernicus Climate Change Service (C3S) Data Store (CDS). DOI: 10.24381/cds.143582cf (Accessed on 27-02-2024)
- D. E. Groom, N. V. Mokhov, S. I. Striganov, Muon stopping power and range tables 10 MeV - 100 TeV, *Atomic Data and Nuclear Tables*, Vol. 76, No. 2, July 2001
- S. Agostinelli et al., Geant4 - A Simulation Toolkit, *Nucl. Instrum. Meth. A* 506 (2003) 250-303
- J. Allison et al., Geant4 Developments and Applications, *IEEE Trans. Nucl. Sci.* 53 (2006) 270-278
- J. Allison et al., Recent Developments in Geant4, *Nucl. Instrum. Meth. A* 835 (2016) 186-225
- P. Shukla and S. Sankrith, Energy and angular distributions of atmospheric muons at the Earth, *International Journal of Modern Physics A* Vol. 33, No. 30, 1850175 (2018)



# Constraints on anomalous Higgs boson couplings from its production and decay using the $WW$ channel in proton-proton collisions at $\sqrt{s} = 13$ TeV

The CMS Collaboration\*

## Abstract

A study of the anomalous couplings of the Higgs boson to vector bosons, including  $CP$ -violation effects, has been conducted using its production and decay in the  $WW$  channel. This analysis is performed on proton-proton collision data collected with the CMS detector at the CERN LHC during 2016–2018 at a center-of-mass energy of 13 TeV, and corresponds to an integrated luminosity of  $138 \text{ fb}^{-1}$ . The different-flavor dilepton ( $e\mu$ ) final state is analyzed, with dedicated categories targeting gluon fusion, electroweak vector boson fusion, and associated production with a  $W$  or  $Z$  boson. Kinematic information from associated jets is combined using matrix element techniques to increase the sensitivity to anomalous effects at the production vertex. A simultaneous measurement of four Higgs boson couplings to electroweak vector bosons is performed in the framework of a standard model effective field theory. All measurements are consistent with the expectations for the standard model Higgs boson and constraints are set on the fractional contribution of the anomalous couplings to the Higgs boson production cross section.

*Submitted to the European Physical Journal C*



# 1 Introduction

After the discovery of the Higgs boson (H) by the ATLAS and CMS Collaborations in 2012 [1–3], the CMS [4–11] and ATLAS [12–18] experiments set constraints on the spin-parity properties of the Higgs boson and its couplings with gluons and electroweak (EW) gauge bosons, denoted here as Hgg and HVV, respectively. The Higgs boson quantum numbers are consistent with the standard model (SM) expectation  $J^{PC} = 0^{++}$ , but the possibility of small, anomalous couplings is not yet ruled out. In beyond-the-SM (BSM) theories, interactions with the Higgs boson may occur through several anomalous couplings, which lead to new tensor structures in the interaction terms that can be both  $CP$ -even or  $CP$ -odd. The  $CP$ -odd anomalous couplings between the Higgs boson and BSM particles may generate  $CP$  violation in the interactions of the Higgs boson.

In this paper, we study the tensor structure of the Hgg and HVV couplings, and we search for several anomalous effects, including  $CP$  violation, using the different-flavor dilepton ( $e\mu$ ) final state from  $H \rightarrow WW$  decays. The Higgs boson production processes include gluon fusion (ggH), EW vector boson fusion (VBF), and associated production with a  $W$  or  $Z$  boson (VH). Higgs boson production and decay processes are sensitive to certain anomalous contributions, which can be described by higher-dimensional operators in an effective field theory (EFT) [19] that can modify the kinematic distributions of the Higgs boson decay products and the particles from associated production.

Each production process of the Higgs boson is identified using its kinematic features, and events are assigned to corresponding production categories. The matrix element likelihood approach (MELA) [20–24] is employed to construct observables that are optimal for the measurement of anomalous couplings, or EFT operators, at the production vertex. These and other decay-based variables are used to explore all kinematic features of the events, giving the analysis sensitivity to simultaneous anomalous effects at the Higgs boson production and decay vertices. Fully simulated signal samples that include anomalous couplings incorporate the detector response into the analysis.

The analysis is based on the proton-proton (pp) collision data collected at the CERN LHC from 2016 to 2018, at a center-of-mass energy of 13 TeV, corresponding to an integrated luminosity of  $138 \text{ fb}^{-1}$ . This paper builds on a previous analysis conducted by the CMS Collaboration in the  $H \rightarrow WW$  channel [25], which focused on measuring the Higgs boson production cross sections and coupling parameters in the so-called  $\kappa$  framework [26]. We follow a formalism used in previous CMS analyses of anomalous couplings in Run 1 and Run 2 [4–11, 27, 28], focusing on the case where the Higgs boson is produced on-shell. The coupling parameters are extracted using the signal strength and the fractional contributions of the couplings to the cross section. A general study of the HVV interaction is performed with four anomalous couplings analyzed individually. Through  $SU(2) \times U(1)$  symmetry considerations, the anomalous HVV couplings are reduced in number to three and analyzed simultaneously. The primary HVV coupling measurements are performed in terms of cross section fractions with additional interpretations in terms of EFT couplings included. A study of the Hgg interaction is also performed in terms of a  $CP$ -odd anomalous coupling cross section fraction.

This paper is organized as follows. The phenomenology of anomalous couplings is discussed in Section 2. Section 3 gives a brief overview of the CMS apparatus. Data sets and Monte Carlo (MC) simulation samples are discussed in Section 4. The event reconstruction and selection are outlined in Sections 5 and 6, respectively. Methods to estimate backgrounds are given in Section 7. In Section 8, we discuss the kinematic variables associated with Higgs boson production and decay. Sources of systematic uncertainties are presented in Section 9. The

results are presented and discussed in Section 10. Finally, a summary is given in Section 11. Tabulated results are provided in the HEPData record for this analysis [29].

## 2 Phenomenology

In this analysis, we investigate anomalous coupling effects in gluon fusion or electroweak Higgs boson production, as well as in its decay to  $WW$  pairs. A detailed discussion of the theoretical considerations can be found in Refs. [22, 24, 28]. The interaction of the spin-zero Higgs boson with two spin-one gauge bosons  $V_1 V_2$ , such as  $WW$ ,  $ZZ$ ,  $Z\gamma$ ,  $\gamma\gamma$ , or  $gg$ , can be parametrized by the scattering amplitude

$$A(\text{H}V_1 V_2) \sim \left[ a_1^{\text{VV}} + \frac{\kappa_1^{\text{VV}} q_{V_1}^2 + \kappa_2^{\text{VV}} q_{V_2}^2}{(\Lambda_1^{\text{VV}})^2} \right] m_{V_1}^2 \epsilon_{V_1}^* \epsilon_{V_2}^* \quad (1)$$

$$+ \frac{1}{v} a_2^{\text{VV}} f_{\mu\nu}^{*(1)} f^{*(2),\mu\nu} + \frac{1}{v} a_3^{\text{VV}} f_{\mu\nu}^{*(1)} \tilde{f}^{*(2),\mu\nu},$$

where  $q_{V_i}$  and  $\epsilon_{V_i}$  are the spin-one gauge boson four-momentum and polarization vectors,  $m_{V_1}$  is the pole mass of the boson,  $f^{(i),\mu\nu} = \epsilon_{V_i}^\mu q_{V_i}^\nu - \epsilon_{V_i}^\nu q_{V_i}^\mu$  and  $\tilde{f}_{\mu\nu}^{(i)} = \frac{1}{2} \epsilon_{\mu\nu\rho\sigma} f^{(i),\rho\sigma}$  (with  $\epsilon_{\mu\nu\rho\sigma}$  the Levi-Civita symbol),  $\Lambda_1^{\text{VV}}$  is the scale of BSM physics, and  $v$  is the Higgs field vacuum expectation value.

The only leading tree-level contributions in the scattering amplitude are  $a_1^{\text{ZZ}} \neq 0$  and  $a_1^{\text{WW}} \neq 0$ ; other  $a_1$  coupling parameters ( $Z\gamma$ ,  $\gamma\gamma$ ,  $gg$ ) do not contribute because the pole mass vanishes. Additional  $ZZ$  and  $WW$  couplings are considered anomalous contributions. Anomalous terms arising in the SM via loop effects are typically small and are not yet accessible experimentally. The BSM contributions, however, could yield larger coupling parameters. Among the anomalous contributions, considerations of symmetry and gauge invariance require  $\kappa_1^{\text{ZZ}} = \kappa_2^{\text{ZZ}}$ ,  $\kappa_1^{\gamma\gamma} = \kappa_2^{\gamma\gamma} = 0$ ,  $\kappa_1^{\text{gg}} = \kappa_2^{\text{gg}} = 0$ , and  $\kappa_1^{\text{Z}\gamma} = 0$  [24]. The presence of  $CP$ -odd  $a_3^{\text{VV}}$  couplings together with any of the other couplings (all of them  $CP$ -even), will result in  $CP$  violation. We reduce the number of independent parameters by assuming that  $a_2^{\gamma\gamma}$ ,  $a_3^{\gamma\gamma}$ ,  $a_2^{\text{Z}\gamma}$  and  $a_3^{\text{Z}\gamma}$  are constrained in direct decays of  $\text{H} \rightarrow \gamma\gamma$  and  $Z\gamma$ , therefore fixing them to be zero. The  $a_2^{\text{gg}}$  term results from loop effects in the SM.

The relationship between the  $ZZ$  and  $WW$  couplings is mostly relevant for VBF production. There are no kinematic differences between the  $ZZ$  and  $WW$  fusion processes; therefore, it is not possible to disentangle the couplings. One possibility is to set the  $ZZ$  and  $WW$  couplings to be equal,  $a_i = a_i^{\text{ZZ}} = a_i^{\text{WW}}$ , leaving four HVV anomalous couplings to be measured:  $a_2$ ,  $a_3$ ,  $\kappa_1 / (\Lambda_1)^2$ , and  $\kappa_2^{\text{Z}\gamma} / (\Lambda_1^{\text{Z}\gamma})^2$ . The  $a_1^{\text{ZZ}} = a_1^{\text{WW}}$  relationship also appears under custodial symmetry. This approach provides a general test of the Higgs boson Lagrangian tensor structure and a search for  $CP$  violation in HVV interactions. In an alternative approach, the  $\text{SU}(2) \times \text{U}(1)$  symmetry reduces the number of independent HVV anomalous couplings to three ( $a_2$ ,  $a_3$ , and



$\kappa_1/(\Lambda_1)^2$ ) through the introduction of the following coupling parameter relationships [19] :

$$a_1^{WW} = a_1^{ZZ}, \quad (2)$$

$$a_2^{WW} = c_w^2 a_2^{ZZ}, \quad (3)$$

$$a_3^{WW} = c_w^2 a_3^{ZZ}, \quad (4)$$

$$\frac{\kappa_1^{WW}}{(\Lambda_1^{WW})^2} = \frac{1}{c_w^2 - s_w^2} \left( \frac{\kappa_1^{ZZ}}{(\Lambda_1^{ZZ})^2} - 2s_w^2 \frac{a_2^{ZZ}}{m_Z^2} \right), \quad (5)$$

$$\frac{\kappa_2^{Z\gamma}}{(\Lambda_1^{Z\gamma})^2} = \frac{2s_w c_w}{c_w^2 - s_w^2} \left( \frac{\kappa_1^{ZZ}}{(\Lambda_1^{ZZ})^2} - \frac{a_2^{ZZ}}{m_Z^2} \right), \quad (6)$$

where  $c_w$  and  $s_w$  are the cosine and sine of the weak mixing angle, respectively, and  $m_Z$  is the Z boson mass. With this approach, there is a linear relationship between the scattering amplitude couplings and the SM EFT (SMEFT) couplings in the Higgs basis [19] :

$$\delta c_z = \frac{1}{2} a_1^{ZZ} - 1, \quad (7)$$

$$c_{zz} = -\frac{2s_w^2 c_w^2}{e^2} a_2^{ZZ}, \quad (8)$$

$$\tilde{c}_{zz} = -\frac{2s_w^2 c_w^2}{e^2} a_3^{ZZ}, \quad (9)$$

$$c_{z\Box} = \frac{m_Z^2 s_w^2}{e^2} \frac{\kappa_1^{ZZ}}{(\Lambda_1^{ZZ})^2}, \quad (10)$$

where  $e$  is the electron charge. The amplitude couplings may also be related to the SMEFT Warsaw basis [19, 30] couplings through the following translation [28, 31] :

$$\delta a_1^{ZZ} = \frac{v^2}{\Lambda^2} \left( 2c_{H\Box} + \frac{6e^2}{s_w^2} c_{HWB} + \left( \frac{3c_w^2}{2s_w^2} - \frac{1}{2} \right) c_{HD} \right), \quad (11)$$

$$\kappa_1^{ZZ} = \frac{v^2}{\Lambda^2} \left( -\frac{2e^2}{s_w^2} c_{HWB} + \left( 1 - \frac{1}{2s_w^2} \right) c_{HD} \right), \quad (12)$$

$$a_2^{ZZ} = -2 \frac{v^2}{\Lambda^2} (s_w^2 c_{HB} + c_w^2 c_{HW} + s_w c_w c_{HWB}), \quad (13)$$

$$a_3^{ZZ} = -2 \frac{v^2}{\Lambda^2} (s_w^2 c_{HB} + c_w^2 c_{H\bar{W}} + s_w c_w c_{H\bar{W}B}), \quad (14)$$

where  $\Lambda$  is the UV cutoff of the theory (set to 1 TeV), and  $\delta a_1^{ZZ}$  is a correction to the SM value of  $a_1^{ZZ}$ . Further discussion on the EFT operators corresponding to the couplings considered here may be found in Chapter 2.2 of Ref. [19]. The assumed constraints on  $a_2^{\gamma\gamma}$ ,  $a_3^{\gamma\gamma}$ ,  $a_2^{Z\gamma}$  and  $a_3^{Z\gamma}$  imply that only one of the three coupling parameters  $c_{HW}$ ,  $c_{HWB}$ , and  $c_{HB}$  is independent; the same is also true for their  $CP$ -odd counterparts  $c_{H\bar{W}}$ ,  $c_{H\bar{W}B}$ , and  $c_{H\bar{B}}$ . Therefore, we have four independent HVV couplings in both the Higgs and Warsaw basis. All the EFT couplings are expected to be zero in the SM.

We thus adopt two approaches to the HVV coupling study. In Approach 1, we use the  $a_i^{ZZ} = a_i^{WW}$  relationship and individually analyze each of the four anomalous couplings. In Approach 2, we enforce the  $SU(2) \times U(1)$  relationships from Eqs. (2–6) and analyze the three independent anomalous couplings both individually and simultaneously. Approach 1 may be considered to follow the relationships from Eqs. (2–5) in the limiting case  $c_w = 1$ .

Table 1: The cross sections ( $\sigma_i$ ) of the anomalous contributions ( $a_i$ ) relative to the SM value ( $\sigma_1$ ) used to define the fractional cross sections  $f_{ai}$  for the Approach 1 and 2 coupling relationships. For the  $\kappa_1$  and  $\kappa_2^{Z\gamma}$  couplings, the numerical values  $\Lambda_1 = \Lambda_1^{Z\gamma} = 100$  GeV are chosen to keep all coefficients of similar order of magnitude.

$f_{ai}$	$a_i$	Approach 1 $\sigma_i/\sigma_1$	Approach 2 $\sigma_i/\sigma_1$
$f_{a2}$	$a_2$	0.361	6.376
$f_{a3}$	$a_3$	0.153	0.153
$f_{\Lambda 1}$	$\kappa_1$	0.682	5.241
$f_{\Lambda 1}^{Z\gamma}$	$\kappa_2^{Z\gamma}$	1.746	—

It is convenient to measure the fractional contribution of the anomalous couplings to the Higgs boson cross section rather than the anomalous couplings themselves. For the anomalous HVV couplings, the effective fractional cross sections  $f_{ai}$  are defined as

$$f_{ai} = \frac{|a_i|^2 \sigma_i}{\sum_j |a_j|^2 \sigma_j} \text{sign} \left( \frac{a_i}{a_1} \right), \quad (15)$$

where  $\sum_j$  sums over all the coupling parameters considered, including  $a_1$ , and  $\sigma_i$  is the cross section for the process corresponding to  $a_i = 1$  and  $a_{j \neq i} = 0$ . Many systematic uncertainties cancel out in the ratio, and the physical range is conveniently bounded between  $-1$  and  $+1$ . Our primary measurements are performed in terms of cross section fractions, with additional interpretations in terms of the SMEFT Higgs and Warsaw basis couplings also included. For consistency with previous CMS measurements, the  $\sigma_i$  coefficients used to define the fractional cross sections correspond to the  $gg \rightarrow H \rightarrow VV \rightarrow 2e2\mu$  process [28]. The numerical values are given in Table 1 as calculated using the JHUGEN simulation [20–23]. Two sets of values are shown corresponding to the different coupling relationships adopted in Approach 1 and 2.

It has been shown that the angular correlations of the associated jets in the  $ggH + 2$  jets process are sensitive to anomalous Hgg coupling effects at the production vertex [32]. The quark-quark initiated process,  $qq \rightarrow qqH$ , corresponds to the gluon scattering topology sensitive to anomalous effects. For the anomalous Hgg coupling, the effective fractional cross section can be defined as

$$f_{a3}^{ggH} = \frac{|a_3^{gg}|^2 \sigma_3^{gg}}{|a_2^{gg}|^2 \sigma_2^{gg} + |a_3^{gg}|^2 \sigma_3^{gg}} \text{sign} \left( \frac{a_3^{gg}}{a_2^{gg}} \right). \quad (16)$$

The  $\sigma_3^{gg}$  and  $\sigma_2^{gg}$  cross sections correspond to  $a_3^{gg} = 1, a_2^{gg} = 0$  and  $a_2^{gg} = 1, a_3^{gg} = 0$ , respectively, and are equal. With this analysis it is not possible to distinguish the top quark, bottom quark, and heavy BSM particle contributions in the gluon fusion loop. As such, the Hgg coupling is treated as an effective coupling with heavy degrees of freedom integrated out.

### 3 The CMS detector

The CMS apparatus [33] is a multipurpose, nearly hermetic detector, designed to identify electrons, muons, photons, and (charged and neutral) hadrons [34–37]. A global reconstruction “particle-flow” (PF) algorithm [38] combines the information provided by the all-silicon inner tracker and by the crystal electromagnetic and brass-scintillator hadron calorimeters, operating inside a 3.8 T superconducting solenoid, with data from gas-ionization muon detectors interleaved with the solenoid return yoke, to build  $\tau$  leptons, jets, missing transverse momentum, and other physics objects [39–41].

Events of interest are selected using a two-tiered trigger system [42, 43]. The first level (L1), composed of custom hardware processors, uses information from the calorimeters and muon detectors to select events at a rate of around 100 kHz within a fixed latency of about  $4 \mu\text{s}$  [42]. The second level, known as the high-level trigger (HLT), consists of a farm of processors running a version of the full event reconstruction software optimized for fast processing, and reduces the event rate to around 1 kHz before data storage [43]. A more detailed description of the CMS detector, together with a definition of the coordinate system and kinematic variables, can be found in Ref. [33].

## 4 Data sets and simulation

The data sets included in this analysis were recorded with the CMS detector in 2016, 2017, and 2018, and correspond to integrated luminosities of 36.3, 41.5, and  $59.7 \text{ fb}^{-1}$ , respectively [44–46]. The collision events must fulfill HLT selection criteria that require the presence of one or two leptons satisfying isolation and identification requirements. For the 2016 data set, the single-electron trigger has a transverse momentum ( $p_T$ ) threshold of 25 GeV for electrons with pseudorapidity  $|\eta| < 2.1$  and 27 GeV for  $2.1 < |\eta| < 2.5$ , whereas the single-muon trigger has a  $p_T$  threshold of 24 GeV for  $|\eta| < 2.4$ . For the 2017 (2018) data set, the  $p_T$  threshold is 35 (32) GeV for the single-electron trigger (covering  $|\eta| < 2.5$ ) and 27 (24) GeV for the single-muon trigger ( $|\eta| < 2.4$ ). The dilepton  $e\mu$  trigger has  $p_T$  thresholds of 23 and 12 GeV for the leading and subleading leptons, respectively, with the same coverage in pseudorapidity for electrons and muons as above. During the first part of data taking in 2016, a lower  $p_T$  threshold of 8 GeV for the subleading muon was used.

Monte Carlo event generators are used to model the signal and background processes. For each process, three independent sets of simulated events, corresponding to the three years of data taking, are used. This approach includes year-dependent effects in the CMS detector, data taking, and event reconstruction. All simulated events corresponding to a given data set share the same set of parton distribution functions (PDFs), underlying event (UE) tune, and parton shower (PS) configuration. The PDF sets used are NNPDF 3.0 [47, 48] for 2016 and NNPDF 3.1 [49] for 2017 and 2018. The CUETP8M1 [50] tune is used to describe the UE in 2016 simulations, whereas the CP5 [51] tune is adopted in 2017 and 2018 simulated events. The MC samples are interfaced with PYTHIA 8.226 [52] in 2016, and 8.230 in 2017 and 2018, for the modeling of UE, PS, and hadronization. Standard Model Higgs boson production through ggH, VBF, and VH is simulated at next-to-leading order (NLO) accuracy in quantum chromodynamics (QCD), including finite quark mass effects, using POWHEG v2 [53–59]. The MINLO HVJ [58] extension of POWHEG v2 is used for the simulation of WH and quark-induced ZH production, providing NLO accuracy for the VH + 0- and 1-jet processes. For ggH production, the simulated events are weighted to match the NNLOPS [60, 61] prediction in the hadronic jet multiplicity ( $N_{\text{jet}}$ ) and Higgs boson  $p_T$  distributions. The weighting is based on  $p_T$  and  $N_{\text{jet}}$  as computed in the simplified template cross section scheme 1.0 [62]. The MINLO HJJ [63] generator, which provides NLO accuracy for  $N_{\text{jet}} \geq 2$ , is also used for ggH production. The associated production processes with top quarks ( $t\bar{t}H$ ) and bottom quarks ( $b\bar{b}H$ ) are simulated with POWHEG v2 and MADGRAPH5\_aMC@NLO v2.2.2 [64], respectively, and have a negligible contribution in the analysis phase space. All SM Higgs boson samples are normalized to the cross sections recommended in Ref. [19]. The Higgs boson mass in the event generation is assumed to be 125 GeV, while a value of 125.38 GeV [65] is used for the calculation of cross sections and branching fractions. The decay to a pair of W bosons and subsequently to leptons or hadrons is performed using the JHUGEN v5.2.5 generator in 2016, and v7.1.4 in 2017 and 2018, for ggH, VBF, and quark-

induced ZH samples. The Higgs boson and W boson decays are performed using PYTHIA 8.212 for the other signal simulations.

The ggH, VBF, and VH Higgs boson events with HVV anomalous couplings are generated with JHUGEN at LO accuracy. With respect to the  $\kappa_2^{Z\gamma}/(\Lambda_1^{Z\gamma})^2$  coupling parameter discussed in Section 2, the sign convention of the photon field is determined by the sign in front of the gauge fields in the covariant derivative. In this analysis, we define the covariant derivative  $D_\mu = \partial_\mu - ie\sigma^i W_\mu^i/(2s_w) + ieB_\mu/(2c_w)$  following the convention in JHUGEN [31]. The JHUGEN and POWHEG SM Higgs boson simulations were compared after parton showering and no significant differences in the distributions of kinematic observables were found. We adopt the JHUGEN simulation to describe the kinematic features in all production modes with HVV anomalous couplings. The expected yields are scaled to match the SM theoretical predictions [19] for inclusive cross sections and the POWHEG SM prediction of relative event yields in the event categorization based on associated particles. Simulation of the ggH + 2 jets process with Hgg anomalous couplings is done using MINLO X0JJ [66] at NLO in QCD. A large number of signal samples with various anomalous couplings were generated. The MELA package [20–24] contains a library of matrix elements from JHUGEN for different Higgs boson signal hypotheses. The ratio of matrix elements allows reweighting of generated signal events to any coupling signal hypothesis with the same production mechanism. This procedure is used in the construction of the predictions for the different coupling components and their interference, allowing us to cover all points in the signal model phase space with sufficient statistical precision.

Background events are produced using several simulations. The quark-initiated nonresonant WW process is simulated with POWHEG v2 [67] at NLO accuracy for inclusive production. A reweighting is performed to match the diboson  $p_T$  spectrum computed at NNLO+NNLL QCD accuracy [68, 69]. The MCFM v7.0 [70–72] generator is used to simulate gluon-induced WW production at LO accuracy, with the normalization chosen to match the NLO cross section [73]. Nonresonant EW production of WW pairs with two additional jets is simulated at LO accuracy with MADGRAPH5\_aMC@NLO v2.4.2 using the MLM matching and merging scheme [74]. Top quark pair production ( $t\bar{t}$ ) and single top quark processes, including tW, s- and t-channel contributions, are simulated with POWHEG v2 [75–77]. A reweighting of the top quark and antiquark  $p_T$  spectrum at parton level is performed for the  $t\bar{t}$  simulation in order to match the NNLO and next-to-next-to-leading logarithm (NNLL) QCD predictions, including also the NLO EW contribution [78].

The Drell–Yan (DY) production of a charged-lepton pair is simulated with MADGRAPH5\_aMC@NLO v2.4.2 at NLO accuracy with up to two additional partons, using the FxFx matching and merging scheme [79]. Production of a W boson associated with an initial state radiation photon ( $W\gamma$ ) is simulated with MADGRAPH5\_aMC@NLO v2.4.2 at NLO accuracy with up to 1 additional parton, using the FxFx jet merging. Diboson processes containing at least one Z boson or a virtual photon ( $\gamma^*$ ) with a mass as low as 100 MeV are generated with POWHEG v2 [67] at NLO accuracy. Production of a W boson in association with a  $\gamma^*$  ( $W\gamma^*$ ) for masses below 100 MeV is simulated by PYTHIA 8.212 in the parton showering of  $W\gamma$  events. Triboson processes with inclusive decays are also simulated at NLO accuracy with MADGRAPH5\_aMC@NLO v2.4.2.

For all processes, the detector response is simulated using a detailed description of the CMS detector, based on the GEANT4 toolkit [80]. The distribution of additional pp interactions within the same or nearby bunch crossings (pileup) in the simulation is reweighted to match that observed in data. The efficiency of the trigger system is evaluated in data on a per lepton

basis using dilepton events consistent with the Z boson decay. The overall efficiencies of the trigger selections used in the analysis are obtained as the average of the per-lepton efficiencies weighted by their probability. The resulting efficiencies are applied directly on simulated events.

## 5 Event reconstruction

The identification and measurement of the properties of individual particles (PF candidates) in an event is achieved in the PF algorithm by combining information from various subdetectors. Electrons are identified and their momenta are measured in the pseudorapidity interval  $|\eta| < 2.5$  by combining tracks in the silicon tracker with spatially compatible energy deposits in the electromagnetic calorimeter. Muons are identified and their momenta are measured in the pseudorapidity range  $|\eta| < 2.4$  by matching tracks in the muon system and the silicon tracker. For better rejection of nonprompt leptons, increasing the sensitivity of the analysis, leptons are required to be isolated and well reconstructed using a set of criteria based on the quality of the track reconstruction, shape of calorimetric deposits, and energy flux in the vicinity of the particle's trajectory [34, 35]. In addition, a selection based on a dedicated multivariate analysis (MVA) tagger developed for the CMS  $t\bar{t}H$  analysis [81] is added in all channels for muon candidates.

Multiple pp interaction vertices are identified from tracking information by use of the adaptive vertex fitting algorithm [82]. The primary pp interaction vertex is taken to be the vertex corresponding to the hardest scattering in the event, evaluated using tracking information alone, as described in Section 9.4.1 of Ref. [83]. Leptons are required to be associated to the primary vertex using transverse and longitudinal impact parameter criteria [34, 35].

Hadronic jets are clustered from PF candidates using the infrared- and collinear-safe anti- $k_T$  algorithm with distance parameters of 0.4 (AK4) and 0.8 (AK8). The jet momentum is determined as the vectorial sum of all particle momenta in the jet. The AK8 jets considered are required to be reconstructed within the silicon tracker acceptance ( $|\eta| < 2.4$ ), whereas AK4 jets are reconstructed in the range  $|\eta| < 4.7$ . For AK4 jets, contamination from pileup is suppressed using charged-hadron subtraction which removes charged PF candidates originating from vertices other than the primary interaction vertex. The residual contribution from neutral particles originating from pileup vertices is removed by means of an event-by-event jet-area-based correction to the jet four-momentum [84]. For AK8 jets, the pileup-per-particle identification algorithm (PUPPI) [85] is used to mitigate the effect of pileup at the reconstructed-particle level, making use of local shape information, event pileup properties, and tracking information. Additional selection criteria are applied to remove jets potentially dominated by instrumental effects or reconstruction failures [84].

The AK8 jets are used to reconstruct hadronic V boson decays in a single merged jet when the decay products are highly collimated. This approach targets boosted W or Z bosons originating from the VH production mode. Such Lorentz-boosted V decays are identified using the ratio of the 2- to 1-subjettiness [86],  $\tau_2/\tau_1$ , and the groomed jet mass  $m_j$ . The groomed mass is calculated after applying a modified mass drop algorithm [87, 88], known as the soft-drop algorithm [89], with parameters  $\beta = 0$ ,  $z_{\text{cut}} = 0.1$ , and  $R_0 = 0.8$ . The algorithm also identifies two hard subjects within the AK8 jet.

We refer to the identification of jets likely originating from bottom quarks as b tagging [90, 91]. For each AK4 jet in the event, a score is calculated through a multivariate combination of different jet properties, making use of boosted decision trees and deep neural networks. A jet

is considered b-tagged if its associated score exceeds a threshold, tuned to achieve a certain tagging efficiency as measured in  $t\bar{t}$  events. The chosen working point corresponds to about 90% efficiency for bottom quark jets and to a mistagging rate of about 10% for light-flavor or gluon jets and of about 50% for charm quark jets.

The missing transverse momentum vector  $\vec{p}_T^{\text{miss}}$  is computed as the negative vector sum of the transverse momenta of all the PF candidates in an event, and its magnitude is denoted as  $p_T^{\text{miss}}$  [41]. The PUPPI algorithm is applied to reduce the pileup dependence of the  $\vec{p}_T^{\text{miss}}$  observable by computing the  $\vec{p}_T^{\text{miss}}$  from the PF candidates weighted by their probability to originate from the primary interaction vertex [41].

## 6 Event selection

The analysis is performed using  $H \rightarrow WW$  candidate events in the  $e\mu$  final state. For an event to be selected, the transverse momenta of the leading lepton  $p_T^{\ell 1}$  and the subleading lepton  $p_T^{\ell 2}$  must be greater than 25 and 13 GeV, respectively. The  $p_T^{\ell 2}$  threshold in the case of a muon is lowered to 10 GeV for the 2016 data set because of the lower threshold in the corresponding HLT algorithm. Events containing additional leptons with  $p_T > 10$  GeV are discarded. The dilepton system is required to have an invariant mass  $m_{\ell\ell}$  greater than 12 GeV and transverse momentum  $p_T^{\ell\ell}$  above 30 GeV. A requirement on the missing transverse momentum of  $p_T^{\text{miss}} > 20$  GeV is implemented. We define transverse mass discriminating variables  $m_T^H$  and  $m_T^{\ell 2}$  as

$$m_T^H = \sqrt{2p_T^{\ell\ell} p_T^{\text{miss}} [1 - \cos \Delta\Phi(\vec{p}_T^{\ell\ell}, \vec{p}_T^{\text{miss}})]}, \quad (17)$$

$$m_T^{\ell 2} = \sqrt{2p_T^{\ell 2} p_T^{\text{miss}} [1 - \cos \Delta\Phi(\vec{p}_T^{\ell 2}, \vec{p}_T^{\text{miss}})]}, \quad (18)$$

and select events with  $m_T^H > 60$  GeV and  $m_T^{\ell 2} > 30$  GeV. The  $m_T^H$  requirement suppresses the  $DY \rightarrow \tau\tau$  background process and avoids overlap with the  $H \rightarrow \tau\tau$  analysis [11]. To ensure orthogonality with a future off-shell  $H \rightarrow WW$  analysis we require  $m_T^H < 125$  GeV. In addition, the region  $76.2 < m_{\ell\ell} < 106.2$  GeV is excluded to avoid overlap with the off-shell  $H \rightarrow ZZ \rightarrow 2\ell 2\nu$  analysis [10]. These requirements will simplify a future combination of Higgs boson decay final states. Finally, events with any b-tagged jets with  $p_T > 20$  GeV are vetoed. These base selection criteria are summarized in Table 2.

Table 2: Summary of the base selection criteria.

Variable	Selection
Number of leptons	2 ( $e\mu$ of opposite charge)
$p_T^{\ell 1}$	>25 GeV
$p_T^{\ell 2}$	>13 GeV (10 GeV for 2016 data)
$m_{\ell\ell}$	12–76.2 GeV or >106.2 GeV
$p_T^{\ell\ell}$	>30 GeV
$p_T^{\text{miss}}$	>20 GeV
$m_T^{\ell 2}$	>30 GeV
$m_T^H$	60–125 GeV
$N_{\text{jet}}$ (b jets)	0

For the HVV coupling analysis, exclusive selection criteria, which are based on the associated jet activity in the event, are applied that target the ggH, VBF, and VH production processes.

The AK4 (AK8) jets considered are required to have  $p_T > 30$  (200) GeV. In the ggH channel, zero or one AK4 jet is required in the event. For the VBF and Resolved VH channels, we require two AK4 jets with dijet masses of  $m_{jj} > 120$  GeV and  $60 < m_{jj} < 120$  GeV, respectively. The Boosted VH channel requires the presence of a V-tagged AK8 jet (V jet); such jets have a groomed mass in the region  $65 < m_j < 105$  GeV and satisfy the requirement  $\tau_2/\tau_1 < 0.4$ . In the other channels, a V jet veto is implemented to ensure orthogonality. These production channels for the HVV coupling study are summarized in Table 3.

Table 3: Summary of the ggH, VBF, and VH production channels used for the HVV coupling study.

Variable	ggH	VBF	Resolved VH	Boosted VH
$N_{\text{jet}}$ (V jets)	0	0	0	$>0$
$N_{\text{jet}}$ (AK4 jets)	0 & 1	2	2	—
$m_{jj}$	—	$>120$ GeV	60–120 GeV	—

As the production vertex of the ggH + 2 jets process is sensitive to anomalous Hgg coupling effects, we use a 2-jet ggH channel that follows the VBF selection described above for the Hgg coupling analysis. The HWW decay vertex is not sensitive to anomalous Hgg effects, and so decay-based variables are not studied in this channel. This permits a relatively tight selection of  $m_{\ell\ell} < 55$  GeV which is beneficial for background suppression. The 0- and 1-jet ggH channels are also included to constrain the ggH signal strength. All channels included for the Hgg coupling study are summarized in Table 4.

Table 4: Summary of ggH channel selections used for the Hgg coupling study.

Variable	ggH	2-jet ggH
$N_{\text{jet}}$ (AK4 jets)	0 & 1	2
$m_{jj}$	—	$>120$ GeV
$m_{\ell\ell}$	—	$<55$ GeV

Control regions (CRs) are defined using the base selection criteria together with a set of alternative requirements summarized in Table 5. They are used to validate the background description and to estimate the number of background events in the signal region (SR). A dedicated  $\tau\tau$  CR targets events from the DY process  $Z \rightarrow \tau\tau$  with  $\tau$  leptons decaying leptonically to produce the  $e\mu$  final state. Also a top quark CR is defined to enhance events with one or more top quarks decaying to a W boson and bottom quark. Splitting events according to the number of associated jets, separate  $\tau\tau$  and top quark CRs are defined for the 0-, 1- and 2-jet SRs. An additional CR with an enhanced contribution from the nonresonant WW background is used in the 2-jet SR. All CRs are used in the final data fit to constrain the DY, top quark, and WW background normalizations.

Table 5: Summary of the  $\tau\tau$ , top quark, and WW control region requirements.

Variable	$\tau\tau$	top quark	WW
$m_{\ell\ell}$	40–80 GeV	$>50$ GeV	$>106.2$ GeV
$m_T^H$	$<60$ GeV	—	60–125 GeV
$m_T^{\ell 2}$	—	$>30$ GeV	$>30$ GeV
$N_{\text{jet}}$ (b jets)	0	$>0$	0

Additional  $\tau\tau$ , top quark, and WW CRs are defined requiring a V jet. These CRs are used to validate the background description in the Boosted VH channel. However, they generally do

not have a sufficient number of events to significantly constrain the background normalizations in the final fit to the data. As such, we rely on the 2-jet CRs to determine the normalizations to be used in the Boosted VH channel. Agreement between data and the background prediction in the V jet CRs is observed when using normalizations determined in the 2-jet CRs.

## 7 Background estimation

The nonprompt-lepton backgrounds originating from leptonic decays of heavy quarks, hadrons misidentified as leptons, and electrons from photon conversions are suppressed by identification and isolation requirements imposed on electrons and muons. In this analysis, the nonprompt-lepton background primarily originates from  $W$ +jets events and is estimated from data, as described in detail in Ref. [92]. The procedure involves measuring the rate at which a nonprompt lepton passing a loose selection further passes a tight selection (misidentification rate) and the corresponding rate for a prompt lepton to pass this selection (prompt rate). The misidentification rate is measured in a data sample enriched in multijet events, whereas the prompt rate is measured using a tag-and-probe method [93] in a data sample enriched in  $DY$  events. The nonprompt-lepton background estimation is validated with data in a CR enriched with  $W$ +jets events, in which a pair of same-sign leptons is required.

The backgrounds from top quark processes and nonresonant  $WW$  production are estimated using a combination of MC simulations and the dedicated CRs described in the previous section. The normalisations of these backgrounds are left as free parameters in the fit, keeping different parameters for each jet multiplicity region. The top quark background normalization is measured from the observed data in the top quark enriched CRs. A separate normalization parameter is included for the quark-induced and gluon-induced  $WW$  backgrounds. For the 2-jet regions, the  $WW$  enriched CR is used to constrain the  $WW$  background normalisation parameters. In the 0- and 1-jet channels, these parameters are constrained directly in the signal regions, which span the high  $m_{\ell\ell}$  phase space enriched in  $WW$  events.

The  $DY \rightarrow \tau\tau$  background process is estimated with a data-embedding technique [94]. As for the top quark and  $WW$  backgrounds, the  $DY$  normalization is left unconstrained in the data fit. The  $DY \rightarrow \tau\tau$  enriched CR described in Section 6 is used to constrain the free normalization parameters in the 0-, 1-, 2-jet regions. The data-embedded samples cover the events that pass the  $e\mu$  triggers, which represent the vast majority of the selected events. The remaining  $DY \rightarrow \tau\tau$  events, which enter the analysis through the single-lepton triggers ( $\approx 5\%$  of the total), are estimated using MC simulation.

The  $WZ$  and  $W\gamma^*$  background contributions are simulated as described in Section 4, and a data-to-simulation scale factor is derived in a three-lepton CR, as described in Ref. [92]. The contribution of the  $W\gamma$  process may also be a background because of photon conversions in the detector material. This process is estimated using MC simulation and validated using data in a CR requiring events with a leading  $\mu$  and a trailing  $e$  with same sign and a separation in  $\Delta R = \sqrt{\Delta\phi^2 + \Delta\eta^2}$  (where  $\phi$  is the azimuthal angle in radians) smaller than 0.5. Triple vector boson production is a minor background in all channels and is estimated using MC simulation.

## 8 Observables and kinematic discriminants

In this paper, we search for anomalous  $HVV$  and  $Hgg$  coupling effects by studying:

1. the two quark jets from VBF and VH production ( $HVV$  coupling);



2. the  $H \rightarrow WW$  decay products (HVV coupling); and
3. the two quark jets from  $ggH + 2$  jets production (Hgg coupling).

The VBF, VH, and  $ggH$  production and decay topologies relevant for the HVV coupling are illustrated in Fig. 1.

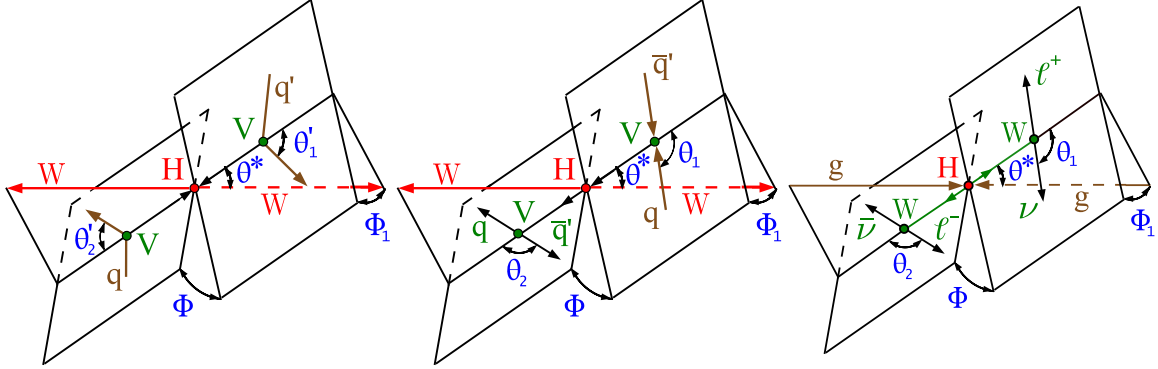


Figure 1: Topologies of the Higgs boson production and decay for vector boson fusion  $qq' \rightarrow qq'H$  (left),  $q\bar{q}' \rightarrow VH$  (center), and gluon fusion with decay  $gg \rightarrow H \rightarrow 2\ell 2\nu$  (right). For the electroweak production topologies, the intermediate vector bosons and their decays are shown in green and the  $H \rightarrow WW$  decay is marked in red. For the  $gg \rightarrow H \rightarrow 2\ell 2\nu$  topology, the  $W$  boson leptonic decays are shown in green. In all cases, the incoming particles are depicted in brown and the angles characterizing kinematic distributions are marked in blue. Five angles fully characterize the orientation of the production and decay chain and are defined in the suitable rest frames.

When combined with the momentum transfer of the vector bosons, the five angles illustrated for VBF/VH production provide complete kinematic information for production and decay of the Higgs boson. The illustration for Higgs boson production via  $ggH$  in association with two jets is identical to the VBF diagram, except for replacing the intermediate vector bosons by gluons. Full production kinematic information is extracted for VBF, VH, and  $ggH + 2$  jets candidate events using discriminants built from the matrix element calculations of the MELA package. The MELA approach is designed to reduce the number of observables to a minimum, while retaining all essential information. To form the production-based MELA kinematic discriminants, we use jets to reconstruct the four-momentum of the associated production particles. The presence of two neutrinos in the final state means it is not possible to reconstruct the four-momentum of all the Higgs boson decay products. Therefore, decay-based kinematic discriminants built from matrix elements are not used in this analysis. Instead, we rely on kinematic variables related to the measured final state of the Higgs boson decay. The strategies used for each of the topologies listed above are now discussed in more detail.

## 8.1 Kinematic features of two quark jets in VBF and VH channels

Kinematic distributions of associated particles in VBF and VH production are sensitive to the anomalous HVV couplings of the Higgs boson. As illustrated in Fig. 1, a set of seven observables can be defined for the VBF and VH production topologies:  $\Omega = \{\theta_1^{(l)}, \theta_2^{(l)}, \theta^*, \Phi, \Phi_1, q_1^2, q_2^2\}$ , with  $q_1^2$  and  $q_2^2$  the squared four-momenta of the vector bosons [22]. Three types of discriminants are defined using the full kinematic description characterized by  $\Omega$ . The first type of discriminant is designed to separate signal and background Higgs boson production processes:

$$\mathcal{D}_{\text{sig}} = \frac{\mathcal{P}_{\text{sig}}(\Omega)}{\mathcal{P}_{\text{sig}}(\Omega) + \mathcal{P}_{\text{bkg}}(\Omega)}, \quad (19)$$

where the probability density  $\mathcal{P}$  for a specific process is calculated from the matrix elements provided by the MELA package. The second type of discriminant separates the anomalous coupling BSM process from that of the SM:

$$\mathcal{D}_{\text{BSM}} = \frac{\mathcal{P}_{\text{BSM}}(\Omega)}{\mathcal{P}_{\text{BSM}}(\Omega) + \mathcal{P}_{\text{SM}}(\Omega)}. \quad (20)$$

Throughout this document the generic BSM label is generally replaced by the specific anomalous coupling state targeted. For the  $a_3$   $CP$ -odd and  $a_2$   $CP$ -even coupling parameters, we use, respectively,  $\mathcal{D}_{0-}$  and  $\mathcal{D}_{0+}$ , whereas for the  $\Lambda_1$  coupling parameters we use  $\mathcal{D}_{\Lambda_1}$  and  $\mathcal{D}_{\Lambda_1}^{Z\gamma}$ . The third type of discriminant isolates the interference contribution:

$$\mathcal{D}_{\text{int}} = \frac{\mathcal{P}_{\text{SM-BSM}}^{\text{int}}(\Omega)}{\mathcal{P}_{\text{SM}}(\Omega) + \mathcal{P}_{\text{BSM}}(\Omega)}, \quad (21)$$

where  $\mathcal{P}_{\text{SM-BSM}}^{\text{int}}$  is the interference part of the probability distribution for a process with a mixture of the SM and BSM contributions. The  $CP$  label is generally used for the  $a_3$  coupling parameter, as the BSM signal in this case is a pseudoscalar and the interference discriminant is a  $CP$ -sensitive observable. The  $\mathcal{P}$  values are normalized to give the same integrated cross sections in the relevant phase space of each process. Such normalization leads to a balanced distribution of events in the range between 0 and 1 for  $\mathcal{D}_{\text{sig}}$  and  $\mathcal{D}_{\text{BSM}}$ , and between  $-1$  and  $+1$  for  $\mathcal{D}_{\text{int}}$ .

The selected events are split into three main production channels: VBF, Resolved VH, and Boosted VH. In the first two channels, the four-momenta of the two AK4 jets assigned as the associated particles are used in the MELA probability calculation. For the Boosted VH category, we use the four-momentum of the two subjects of the V-tagged AK8 jet. An estimate of the Higgs boson four-momentum is also required for the probability calculation. This can not be measured directly since the final state contains two neutrinos. As such, we construct a proxy Higgs boson four-momentum in the following manner. The  $p_x$  and  $p_y$  of the dineutrino system are estimated from the  $\vec{p}_T^{\text{miss}}$  in a given event. The corresponding  $p_z$  is then set to equal that of the dilepton system, which is based on the observed correlation between these variables at the generator level for simulated signals. Finally, the mass of the dineutrino system is set equal to the mean value of the generator-level dineutrino mass. The resulting four-momentum can then be combined with that of the measured dilepton system to create a proxy Higgs boson four-momentum. We note that the MELA probability calculation for the production vertices is largely based on the kinematic features of the associated particles, so the reconstruction of the proxy Higgs boson has a relatively small effect on the final discriminants. As an illustrative example of the MELA based discriminants used in this analysis, Fig. 2 shows the  $\mathcal{D}_{0-}$  discriminant in the VBF and Resolved VH production channels for a number of different signal hypotheses. The discriminants are designed to target the dominant signal production process in a given channel.

In the VBF channel, a  $\mathcal{D}_{\text{VBF}}$  discriminant is constructed, following Eq. (19), where  $\mathcal{P}_{\text{sig}}$  corresponds to the probability for the VBF production hypothesis, and  $\mathcal{P}_{\text{bkg}}$  corresponds to that of gluon fusion production in association with two jets. The discriminant is also suitable for separating SM backgrounds from the VBF signal process. In the Resolved and Boosted VH channels, the corresponding discriminants do not give a significant level of separation with

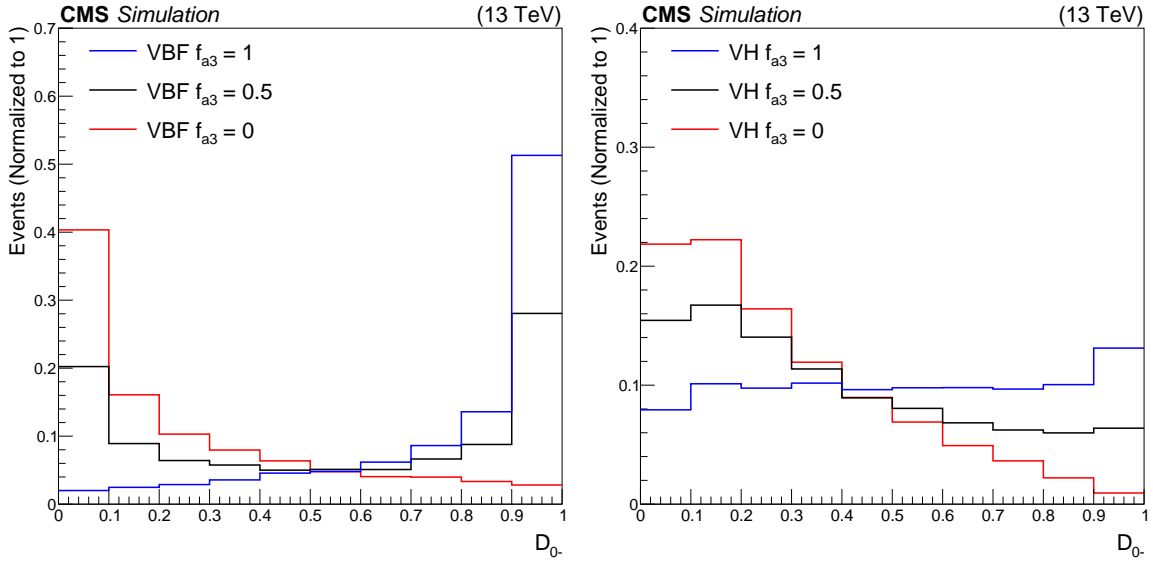


Figure 2: The  $\mathcal{D}_{0-}$  discriminant in the VBF (left) and Resolved VH (right) production channels for a number of VBF (left) and VH (right) signal hypotheses. Pure  $a_1$  ( $f_{a3} = 0$ ) and  $a_3$  ( $f_{a3} = 1$ ) HVV signal hypotheses are shown along with a mixed coupling hypothesis ( $f_{a3} = 0.5$ ). All distributions are normalized to unity.

respect to ggH production or SM backgrounds. This is due to the relatively tight selection criteria, which limit the phase space to VH-like events. Hence, these discriminants are not included in the VH channels.

The  $\mathcal{D}_{CP}$  discriminant is sensitive to the sign of the interference between the  $CP$ -even SM and  $CP$ -odd BSM states. An asymmetry between the number of events detected with positive and negative  $\mathcal{D}_{CP}$  values is expected for mixed  $CP$  states. Therefore, a forward-backward categorization (forward defined as  $\mathcal{D}_{CP} > 0$  and backward as  $\mathcal{D}_{CP} < 0$ ) is used to analyze the  $CP$ -odd couplings. Similarly,  $\mathcal{D}_{\text{int}}$  gives sensitivity to the sign of the interference between the SM and  $a_2$  HVV BSM states. A forward-backward  $\mathcal{D}_{\text{int}}$  categorization is also included. The value of  $\mathcal{D}_{\text{int}}$  used to define the categories is chosen to symmetrize the SM Higgs boson expectation. In the case of the  $\Lambda_1$  measurements, the interference discriminants were shown to be highly correlated with the  $\mathcal{D}_{\text{BSM}}$  discriminants and so are not considered.

We now discuss the categorization and construction of the final multidimensional discriminants used for the two HVV coupling approaches defined in Section 2. The binning of the final discriminants was optimized to ensure sufficient statistical precision in the predictions of all bins, while retaining the kinematic information required to discriminate between the SM and anomalous coupling signal hypotheses.

### 8.1.1 VBF/VH analysis strategy for Approach 1

In Approach 1, each of the four anomalous HVV coupling parameters ( $a_2$ ,  $a_3$ ,  $\kappa_1/(\Lambda_1)^2$ , and  $\kappa_2^{Z\gamma}/(\Lambda_1^{Z\gamma})^2$ ) are analyzed separately. For this purpose, we construct a multidimensional discriminant for each of the four anomalous couplings in the VBF, Resolved VH, and Boosted VH channels.

In the VBF channel, we use two bins of the production discriminant  $\mathcal{D}_{\text{VBF}}$ , corresponding to low and high purity, using a bin boundary of 0.75. The  $m_{\ell\ell}$  variable, which is sensitive to anomalous effects at the  $H \rightarrow WW$  decay vertex, is included with two bins in the range 12–

76.2 GeV. A bin boundary of 45 GeV is chosen based on the expected signal shape changes induced by anomalous effects. Finally, one of the  $\mathcal{D}_{\text{BSM}}$  discriminants is included with ten equally sized bins. Depending on the anomalous coupling under study this discriminant may be  $\mathcal{D}_{0+}$ ,  $\mathcal{D}_{0-}$ ,  $\mathcal{D}_{\Lambda_1}$  or  $\mathcal{D}_{\Lambda_1}^{Z\gamma}$ .

For the VH channels, the  $m_{\ell\ell}$  and  $\mathcal{D}_{\text{BSM}}$  observables are used to build 2D kinematic discriminants. The  $m_{\ell\ell}$  bins are the same as for the VBF channel. In the Resolved VH channel, we use four  $\mathcal{D}_{\text{BSM}}$  bins of equal size. For the Boosted VH case, three variable bins with boundaries of 0.6 and 0.8 are used, a large first bin is chosen because relatively little signal is expected at low values of  $\mathcal{D}_{\text{BSM}}$ . A distinct multidimensional discriminant is constructed for each anomalous coupling hypothesis in the VH channels.

For the  $a_3$  coupling parameter, a forward-backward categorization of events based on  $\mathcal{D}_{CP}$  is implemented. In the case of the  $a_2$  coupling parameter,  $\mathcal{D}_{\text{int}}$  is largely correlated with  $\mathcal{D}_{0+}$  in the VH channels. Therefore, a forward-backward  $\mathcal{D}_{\text{int}}$  categorization is implemented only in the VBF channel. Figures 3–5 show the discriminants used in the final fit to the data for the  $a_2$ ,  $a_3$ ,  $\kappa_1/(\Lambda_1)^2$ , and  $\kappa_2^{Z\gamma}/(\Lambda_1^{Z\gamma})^2$  Approach 1 coupling studies in the VBF and VH channels. A summary of the observables used in the HVV Approach 1 analysis may be found in Table 6.

### 8.1.2 VBF/VH analysis strategy for Approach 2

In Approach 2, we use one categorization strategy and build one multidimensional discriminant in each channel to target all the HVV coupling parameters ( $a_2$ ,  $a_3$ ,  $\kappa_1/(\Lambda_1)^2$ ) simultaneously. In the VBF channel, the  $\mathcal{D}_{CP}$  and  $\mathcal{D}_{\text{int}}$  discriminants are used to create four interference categories. Both  $\mathcal{D}_{\text{VBF}}$  and  $m_{\ell\ell}$  are used as for Approach 1. All three  $\mathcal{D}_{\text{BSM}}$  discriminants that target the  $a_2$ ,  $a_3$  and  $\kappa_1/(\Lambda_1)^2$  coupling parameters are included. However, the number of bins we implement is limited by the number of simulated events. Also the  $\mathcal{D}_{\text{BSM}}$  discriminants are significantly correlated and so have similar performance for all couplings. Therefore, we use the  $CP$ -odd discriminant  $\mathcal{D}_{0-}$  and just one of the  $CP$ -even discriminants,  $\mathcal{D}_{0+}$ , both with three bins and bin boundaries of 0.1 and 0.9. A dedicated rebinning strategy is applied to the  $[\mathcal{D}_{0-}, \mathcal{D}_{0+}]$  distribution merging bins dominated by the SM Higgs boson prediction or with low precision in the background prediction. In the VH channels, just two categories using  $\mathcal{D}_{CP}$  are defined and the discriminant is built using  $m_{\ell\ell}$  as for Approach 1. Again, both  $\mathcal{D}_{0-}$  and  $\mathcal{D}_{0+}$  are chosen for the final discriminant. For the Resolved VH channel, we use three bins with boundaries of 0.25 and 0.75, whereas for the Boosted VH case we use two bins with a boundary of 0.8. The same rebinning strategy described for the VBF channel is applied to both Resolved and Boosted VH multidimensional discriminants. Table 6 includes a summary of the observables used in the HVV Approach 2 analysis.

## 8.2 Kinematic features of $H \rightarrow WW$ decay products in 0- and 1-jet ggH channels

Similar to the SM  $H \rightarrow WW$  analysis [25], we use  $m_{\ell\ell}$  and  $m_T$  to build 2D discriminants in the 0- and 1-jet ggH channels. The distributions have nine bins for  $m_{\ell\ell}$  in the range 12–200 GeV and six bins for  $m_T$  in the range 60–125 GeV. The bin widths vary and are optimized to achieve good separation between the SM Higgs boson signal and backgrounds, as well as between the different anomalous coupling signal hypotheses. In particular, a finer binning with respect to the SM  $H \rightarrow WW$  analysis is implemented in regions where anomalous effects are most significant. Figure 6 shows the  $[m_T, m_{\ell\ell}]$  distributions in the 0- and 1-jet ggH channels. The same  $[m_T, m_{\ell\ell}]$  discriminant is used to study all HVV anomalous couplings for both Approach 1 and 2.

### 8.3 Kinematic features of two quark jets in 2-jet ggH channel

For the Hgg coupling, we adopt a similar approach to the VBF  $CP$  study, where the  $CP$ -odd  $a_3$  HVV coupling parameter is included. In this case, the optimal observables are  $\mathcal{D}_{0-}^{\text{ggH}}$  and  $\mathcal{D}_{CP}^{\text{ggH}}$ , targeting the  $CP$ -odd  $a_3$  Hgg coupling parameter. A forward-backward categorization is implemented using  $\mathcal{D}_{CP}^{\text{ggH}}$ , and the  $\mathcal{D}_{\text{VBF}}$  and  $\mathcal{D}_{0-}^{\text{ggH}}$  observables are used to build 2D discriminants. The  $m_{\ell\ell}$  variable is not considered in this case because it is not sensitive to anomalous Hgg effects. For  $\mathcal{D}_{\text{VBF}}$ , the bin boundary is relaxed to 0.5 to ensure sufficient ggH events are accepted in the more VBF-like bin. For  $\mathcal{D}_{0-}$ , eight (five) bins are used in the more (less) VBF-like bin with larger bin sizes at the extremes of the distribution to ensure sufficient precision in the background and signal predictions. The 0- and 1-jet channels discussed previously are also included in this study to constrain the ggH signal strength. The  $[\mathcal{D}_{\text{VBF}}, \mathcal{D}_{0-}^{\text{ggH}}]$  distributions used to analyze the Hgg  $a_3$  anomalous coupling in the 2-jet ggH channel are shown in Fig. 7. A summary of the observables used in the Hgg analysis is given in Table 6.

Table 6: The kinematic observables used for the interference based categorization and for the final discriminants used in the fits to data to study the HVV and Hgg couplings. For each of the anomalous HVV couplings in Approach 1, we have a dedicated analysis in the VBF and VH channels. In Approach 2, we use one analysis to target all anomalous HVV couplings simultaneously.

Analysis	Channel	Categorization	Final discriminant
HVV Approach 1	VBF ( $a_2$ )	$\mathcal{D}_{\text{int}}$	$[\mathcal{D}_{\text{VBF}}, m_{\ell\ell}, \mathcal{D}_{0+}]$
	VBF ( $a_3$ )	$\mathcal{D}_{CP}$	$[\mathcal{D}_{\text{VBF}}, m_{\ell\ell}, \mathcal{D}_{0-}]$
	VBF ( $\kappa_1$ )	—	$[\mathcal{D}_{\text{VBF}}, m_{\ell\ell}, \mathcal{D}_{\Delta 1}]$
	VBF ( $\kappa_2^{Z\gamma}$ )	—	$[\mathcal{D}_{\text{VBF}}, m_{\ell\ell}, \mathcal{D}_{\Delta 1}^{Z\gamma}]$
	VH ( $a_2$ )	—	$[m_{\ell\ell}, \mathcal{D}_{0+}]$
	VH ( $a_3$ )	$\mathcal{D}_{CP}$	$[m_{\ell\ell}, \mathcal{D}_{0-}]$
	VH ( $\kappa_1$ )	—	$[m_{\ell\ell}, \mathcal{D}_{\Delta 1}]$
	VH ( $\kappa_2^{Z\gamma}$ )	—	$[m_{\ell\ell}, \mathcal{D}_{\Delta 1}^{Z\gamma}]$
HVV Approach 2	0- & 1-jet ggH	—	$[m_{\text{T}}, m_{\ell\ell}]$
	VBF	$\mathcal{D}_{CP}, \mathcal{D}_{\text{int}}$	$[\mathcal{D}_{\text{VBF}}, m_{\ell\ell}, \mathcal{D}_{0-}, \mathcal{D}_{0+}]$
	VH	$\mathcal{D}_{CP}$	$[m_{\ell\ell}, \mathcal{D}_{0-}, \mathcal{D}_{0+}]$
Hgg	0- & 1-jet ggH	—	$[m_{\text{T}}, m_{\ell\ell}]$
	2-jet ggH	$\mathcal{D}_{CP}^{\text{ggH}}$	$[\mathcal{D}_{\text{VBF}}, \mathcal{D}_{0-}^{\text{ggH}}]$

## 9 Systematic uncertainties

The signal extraction is performed using binned templates to describe the various signal and background processes. Systematic uncertainties that change the normalization or shape of the templates are included. All the uncertainties are modeled as nuisance parameters that are profiled in the maximum likelihood fit described in Section 10. The systematic uncertainties arise from both experimental or theoretical sources.

### 9.1 Experimental uncertainties

The following experimental systematic uncertainties are included in the final fit to data:

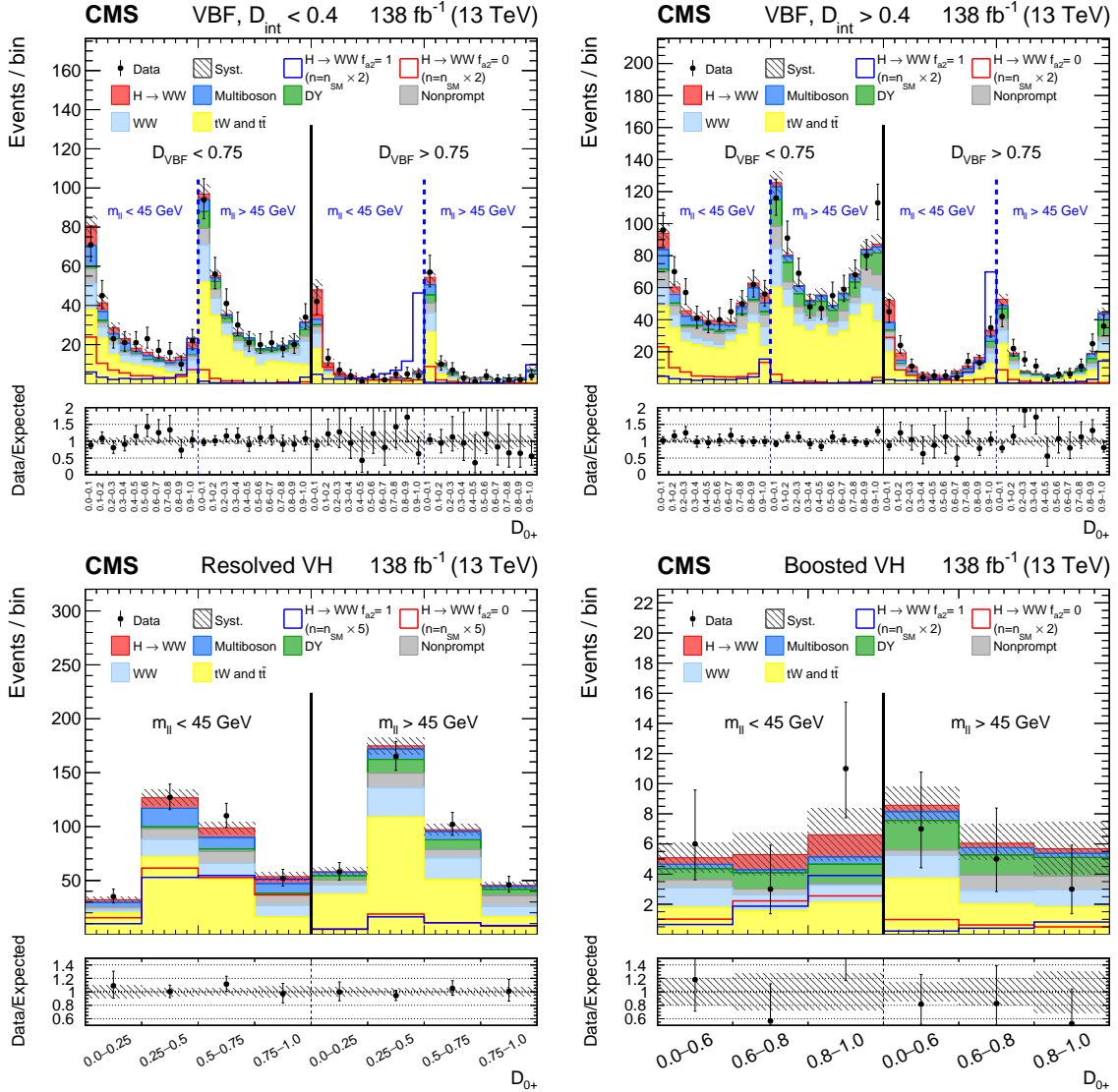


Figure 3: Observed and predicted distributions after fitting the data for  $[D_{\text{VBF}}, m_{\ell\ell}, D_{0+}]$  in the VBF channel (upper), and for  $[m_{\ell\ell}, D_{0+}]$  in the Resolved VH (lower left) and Boosted VH (lower right) channels. For the VBF channel, the  $D_{\text{int}} < 0.4$  (left) and  $D_{\text{int}} > 0.4$  (right) categories are shown. The predicted Higgs boson signal is shown stacked on top of the background distributions. For the fit, the  $a_1$  and  $a_2$  HVV coupling contributions are included. The corresponding pure  $a_1$  ( $f_{a_2} = 0$ ) and  $a_2$  ( $f_{a_2} = 1$ ) signal hypotheses are also shown superimposed, their yields correspond to the predicted number of SM signal events scaled by an arbitrary factor to improve visibility. The uncertainty band corresponds to the total systematic uncertainty. The lower panel in each figure shows the ratio of the number of events observed to the total prediction.

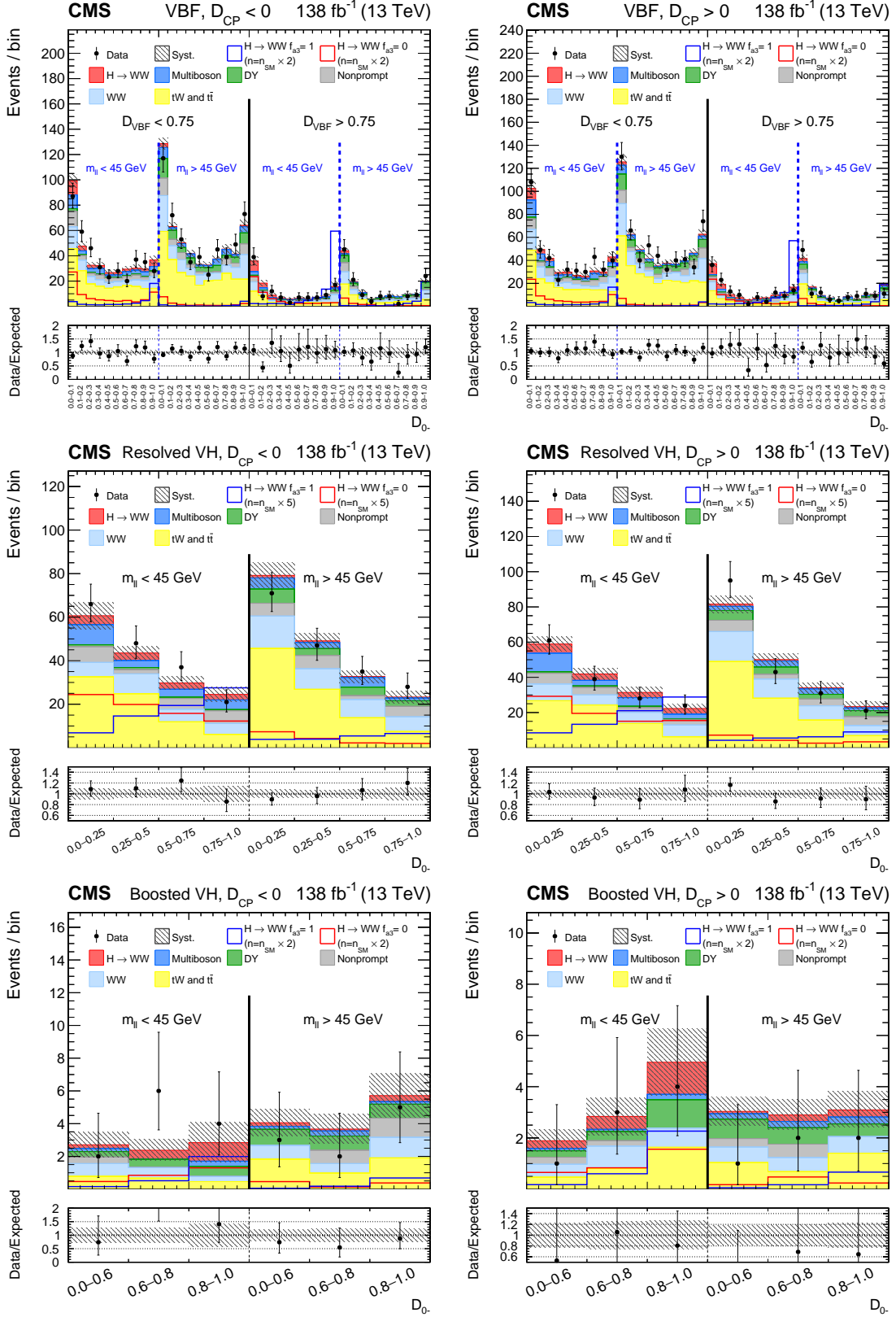


Figure 4: Observed and predicted distributions after fitting the data for  $[D_{\text{VBF}}, m_{\ell\ell}, D_{0-}]$  in the VBF channel (upper), and for  $[m_{\ell\ell}, D_{0-}]$  in the Resolved VH (middle) and Boosted VH (lower) channels. For each channel, the  $\mathcal{D}_{CP} < 0$  (left) and  $\mathcal{D}_{CP} > 0$  (right) categories are shown. For the fit, the  $a_1$  and  $a_3$  HVV coupling contributions are included. More details are given in the caption of Fig. 3.

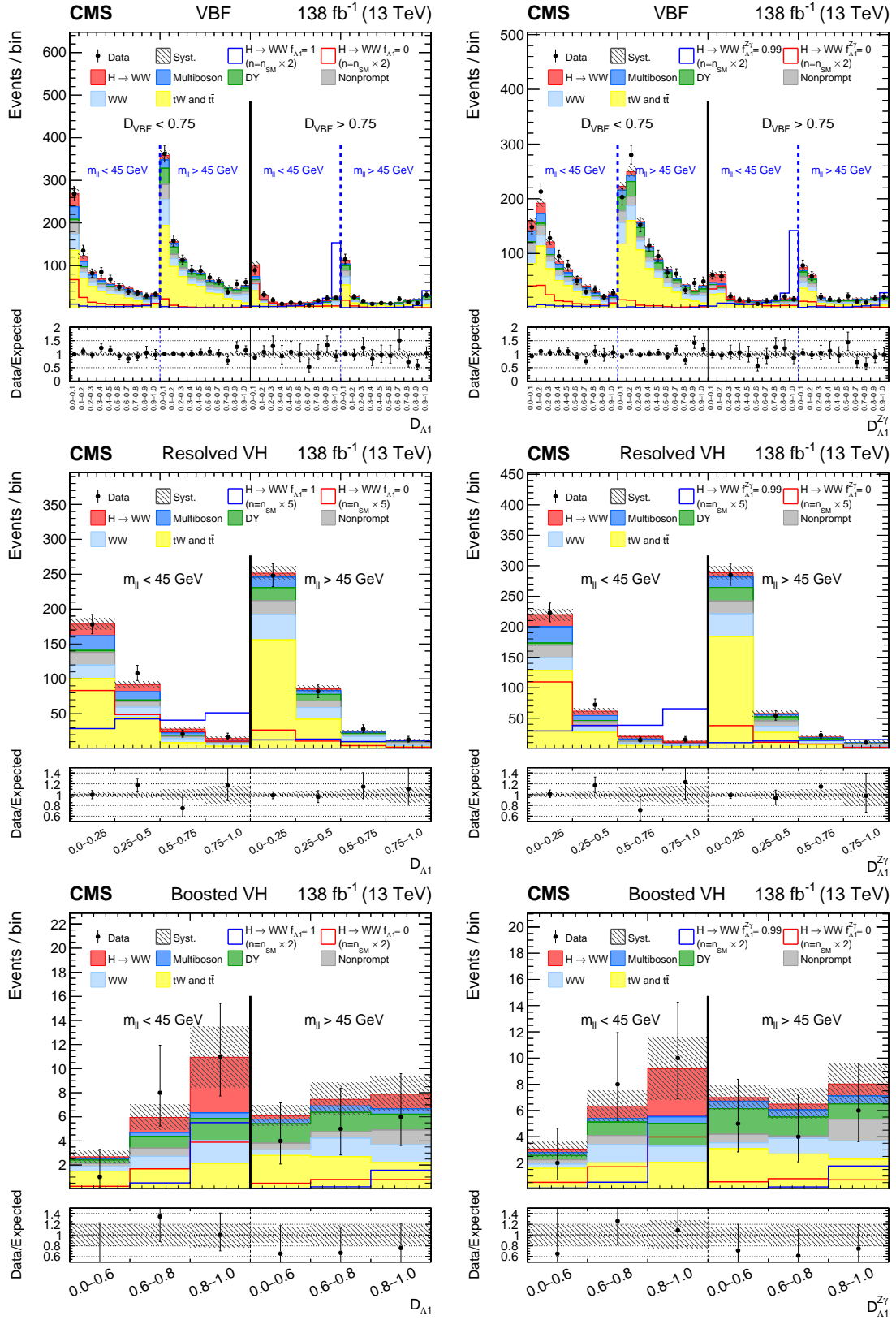


Figure 5: Observed and predicted distributions after fitting the data for  $[D_{VBF}, m_{\ell\ell}, D_{\Delta 1}]$  (upper left) and  $[D_{VBF}, m_{\ell\ell}, D_{\Delta 1}^{Z\gamma}]$  (upper right) in the VBF channel, and for  $[m_{\ell\ell}, D_{\Delta 1}]$  (left) and  $[m_{\ell\ell}, D_{\Delta 1}^{Z\gamma}]$  (right) in the Resolved VH (middle) and Boosted VH (lower) channels. For the fits, the  $a_1$  and  $\kappa_1/(\Lambda_1)^2$  (left) or  $a_1$  and  $\kappa_2^{Z\gamma}/(\Lambda_1^{Z\gamma})^2$  (right) HVV coupling contributions are included. More details are given in the caption of Fig. 3.



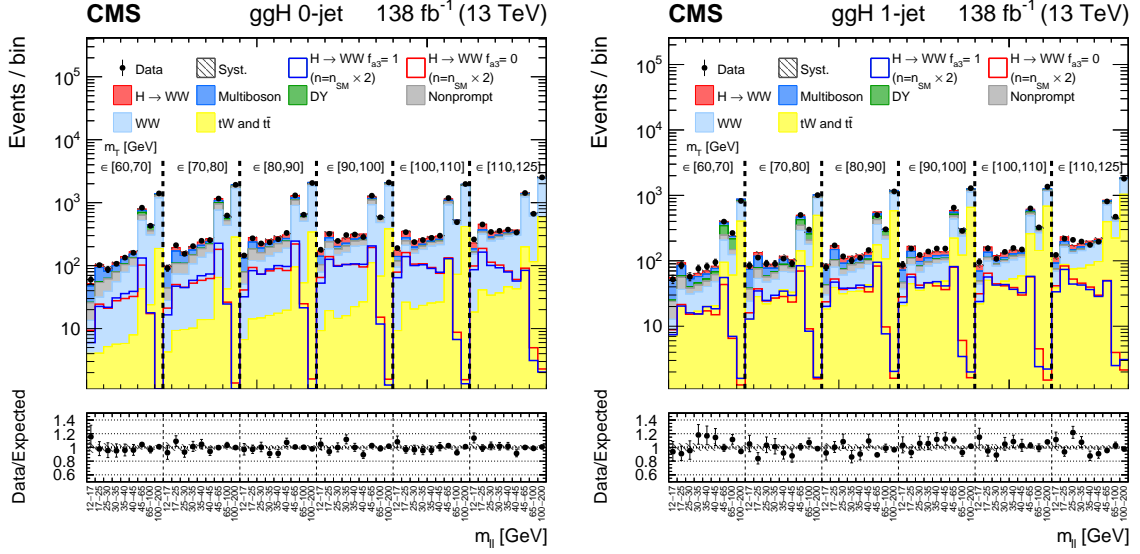


Figure 6: Observed and predicted distributions after fitting the data for  $[m_T, m_{\ell\ell}]$  in the 0- (left) and 1-jet (right) ggH channels. For the fit, the  $a_1$  and  $a_3$  HVV coupling contributions are included. More details are given in the caption of Fig. 3.

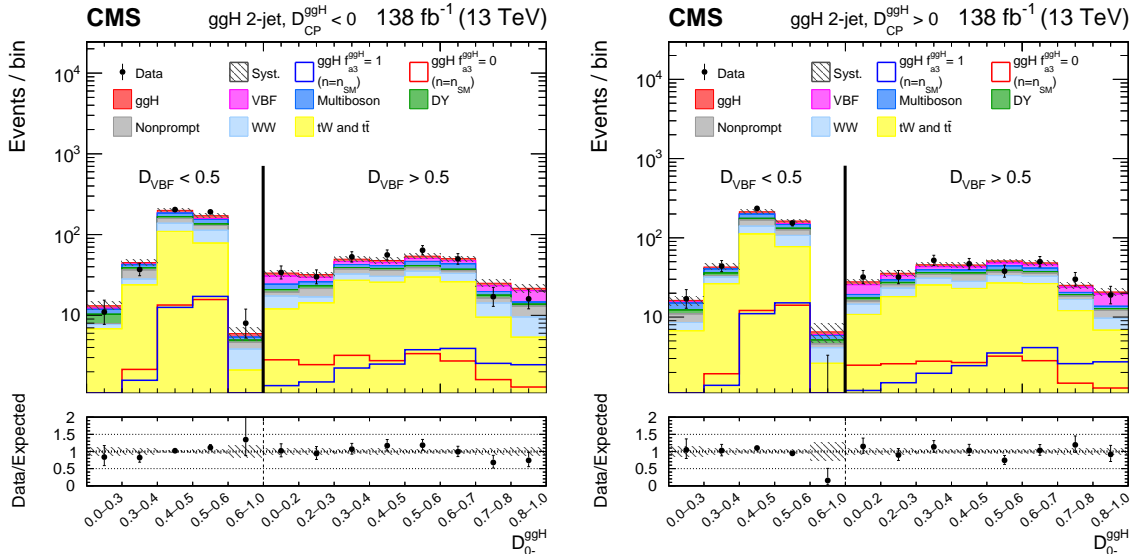


Figure 7: Observed and predicted distributions after fitting the data for  $[D_{VBF}, D_0^{ggH}]$  in the 2-jet ggH channel. Both the  $D_{CP}^{ggH} < 0$  (left) and  $D_{CP}^{ggH} > 0$  (right) categories are shown. In this case, the VBF and ggH signals are shown separately. For the fit, the  $a_2^{gg}$  and  $a_3^{gg}$  coupling contributions are included. The corresponding pure  $a_2^{gg}$  ( $f_{a3}^{ggH} = 0$ ) and  $a_3^{gg}$  ( $f_{a3}^{ggH} = 1$ ) signal hypotheses are also shown superimposed, their yields correspond to the predicted number of SM signal events. More details are given in the caption of Fig. 3.

- The total uncertainty associated with the measurement of the integrated luminosity for 2016, 2017, and 2018 is 1.2% [44], 2.3% [45], and 2.5% [46], respectively. This uncertainty is partially correlated among the three data sets, resulting in an overall uncertainty of 1.6%.
- The systematic uncertainty in the trigger efficiency is determined by varying the tag lepton selection criteria and the Z boson mass window used in the tag-and-probe

method. It affects both the normalization and the shape of the signal and background distributions, and is kept uncorrelated among data sets. The total normalization uncertainty is less than 1%.

- The tag-and-probe method is also used to determine the lepton identification and isolation efficiency. Corrections are applied to account for any discrepancy in the efficiencies measured in data and simulation. The corresponding systematic uncertainty is about 1% for electrons and 2% for muons.
- The uncertainties in the determination of the lepton momentum scale mainly arise from the limited data sample used for their estimation. The impact on the normalization of the signal and background templates ranges between 0.6–1.0% for the electron momentum scale and is about 0.2% for the muon momentum scale. They are treated as uncorrelated among the three data-taking years.
- The jet energy scale uncertainty is modeled by implementing eleven independent nuisance parameters corresponding to different jet energy correction sources, six of which are correlated among the three data sets. Their effects vary in the range of 1–10%, mainly depending on the jet multiplicity in the analysis phase space. Another source of uncertainty arises from the jet energy resolution smearing applied to simulated samples to match the  $p_T$  resolution measured in data. The effect varies in a range of 1–5%, depending on the jet multiplicity and is uncorrelated among the data sets. These uncertainties are included for both AK4 and AK8 jets. In addition, the  $m_J$  scale and resolution, and V tagging corrections with their corresponding uncertainties are included for V-tagged AK8 jets. These variables are calibrated in a top quark-antiquark sample enriched in hadronically decaying W bosons [95].
- The effects of the unclustered energy scale, jet energy scale, and lepton  $p_T$  scales are included for the calculation of the missing transverse momentum. The resulting normalization systematic uncertainty is 1–10% and is treated as uncorrelated among the years.
- Both the normalization and shape of the signal and background templates are affected by the jet pileup identification uncertainty. The effect is below 1%.
- The uncertainty associated with the b tagging efficiency is modeled by seventeen nuisance parameters out of which five are of a theoretical origin and are correlated among the three data sets. The remaining set of four parameters per data set are treated as uncorrelated as they arise from the statistical accuracy of the efficiency measurement [90].
- Estimation of the nonprompt-lepton background is affected by the limited size of the data sets used for the misidentification rate measurements. It is also affected by the difference in the flavor composition of jets misidentified as leptons between the misidentification rate measurement region (enriched in multijet events) and the signal phase space. The effects on the nonprompt-lepton background estimation range between a few percent to about 10% depending on the SR and are treated as nuisance parameters uncorrelated between electrons and muons and among the three data sets. A normalization uncertainty of 30% [92] is assigned to fully cover for any discrepancies with respect to data in a  $W$ +jets CR and is treated as uncorrelated among data sets.
- The statistical uncertainties due to the limited number of simulated events are also included for all bins of the background distributions used to extract the results [96].

## 9.2 Theoretical uncertainties

Multiple theoretical uncertainties are considered and are correlated among data sets, unless stated otherwise:

- The uncertainties related to the choice of PDF and  $\alpha_S$  have a minor effect on the shape of the distributions. Therefore, only normalization effects related to the event acceptance and to the cross section are included. However, these uncertainties are not considered for the backgrounds that have their normalization constrained through data in dedicated CRs. For the Higgs boson signal processes, these uncertainties are calculated by the LHC Higgs cross section working group [19].
- The theoretical uncertainties arising from missing higher-order corrections in the cross section calculations are also included. Background simulations are reweighted to the alternative scenarios corresponding to renormalization  $\mu_R$  and factorization  $\mu_F$  scales varied by factors 0.5 or 2 and the envelopes of the varied templates are taken as the one standard deviations. For background processes that have their normalization constrained through data in dedicated CRs, we consider only the shape effect of the uncertainties coming from the missing higher-order corrections. The WW nonresonant background has the uncertainties derived by varying  $\mu_R$ ,  $\mu_F$ , and the resummation scale. For the ggH and VBF signal processes, the effects of the missing higher-order corrections on the overall cross section are decoupled into multiple sources according to the recipes described in Ref. [19].
- The uncertainty due to the pileup modeling was included for the main simulated background processes (DY, WW, top quark) as well as the ggH and VBF signals. The effect is determined by varying the total inelastic pp cross section (69.2 mb [97, 98]) within the assigned 5% uncertainty.
- The PS modeling mainly affects the jet multiplicity, causing migration of events between categories that results in template shape changes. Associated uncertainties are evaluated by reweighting events with varied PS weights computed with PYTHIA 8.212. The effect on the signal strength is found to be below 1%.
- Uncertainties associated with UE modeling are evaluated by varying the UE tune parameters used in the MC sample generation. Systematic uncertainties are correlated between the 2017 and 2018 data sets since they share the same UE tunes, whereas for 2016 the uncertainty is considered uncorrelated. The UE uncertainty has a minimal effect on the template shapes and affects the normalization by about 1.5%.
- A 15% uncertainty is applied to the relative fraction of the gg-induced component in nonresonant WW production [99]. The relative fraction between single top quark and  $t\bar{t}$  processes is assigned a systematic uncertainty of 8% [100]. Additional process-specific (DY, VZ,  $V\gamma$ ,  $V\gamma^*$ ) uncertainties, related to corrections to account for possible discrepancies between data and simulation, are assigned and are correlated among data sets.

## 10 Results

The optimization and validation of the analysis were performed using simulation and data in CRs. The data in the SRs were examined once all details of the analysis were finalized. For the final results, we perform a binned maximum likelihood fit to the data combining all channels and data-taking periods. The statistical approach was developed by the ATLAS and CMS Collaborations in the context of the LHC Higgs Combination Group [101]. The likelihood

function is defined for candidate events as:

$$\mathcal{L}(\text{data}|\mu_{\text{ggH}}, \mu_{\text{EW}}, f_{ai}, \theta) = \prod_j \text{Poisson}(n_j | s_j(\mu_{\text{ggH}}, \mu_{\text{EW}}, f_{ai}, \theta) + b_j(\theta)) p(\tilde{\theta}|\theta), \quad (22)$$

where  $j$  runs over all bins and  $n_j$  is the observed number of data events in each bin. Total signal and background expectations in each bin are represented by  $s_j$  and  $b_j$ , respectively. The individual signal and background processes considered in each category are described using binned templates of multidimensional discriminants as described in Section 8. Each signal process is parametrized as a linear combination of terms originating from the SM, and anomalous couplings and their interference. The signal expectation depends on the parameters  $\mu_{\text{ggH}}$ ,  $\mu_{\text{EW}}$ , and  $f_{ai}$ , and is constrained by the data fit. Both the signal and background expectations are functions of  $\theta$ , which represents the full set of nuisance parameters corresponding to the systematic uncertainties. The CRs described in Section 6 are included in the fit in the form of single bins, representing the number of events in each CR.

The  $\mu_{\text{ggH}}$  and  $\mu_{\text{EW}}$  parameters correspond to the Higgs boson signal strength modifiers for the ggH and VBF/VH signals, respectively. Signal yields for the VBF and VH processes are related to each other because the same HVV couplings enter both in production and decay of the Higgs boson. The ggH signal is initiated predominantly by the top fermion couplings and is unrelated to the VBF and VH production mechanisms. As the signal strength modifiers are free parameters in the fit, the overall signal event yield is not used to discriminate between alternative signal hypotheses. The  $f_{ai}$  parameter corresponds to the anomalous coupling cross section fraction and determines the shape of the signal expectation. The cross section fraction for the SM coupling is simply taken as  $1 - |f_{ai}|$ . In Approach 1, the SM and just one anomalous HVV coupling are included, and each  $f_{ai}$  is thus studied independently. Depending on the particular anomalous coupling under investigation,  $f_{ai}$  may represent  $f_{a2}$ ,  $f_{a3}$ ,  $f_{\Lambda 1}$ , or  $f_{\Lambda 1}^{Z\gamma}$ . For Approach 2, the SM and three anomalous HVV couplings are included. In this case,  $f_{ai}$  represents  $f_{a2}$ ,  $f_{a3}$  and  $f_{\Lambda 1}$ , which are studied simultaneously. It is explicitly required that  $|f_{a2}| + |f_{a3}| + |f_{\Lambda 1}| \leq 1$  to avoid probing an unphysical parameter space. Finally, there is just one anomalous coupling corresponding to  $f_{a3}^{\text{ggH}}$  to consider for the Hgg vertex. For this study, we also include the effect of the CP-odd HVV anomalous coupling on the VBF process. This is achieved by including  $f_{a3}$  as a free parameter in the fit. The  $p(\tilde{\theta}|\theta)$  are the probability density functions (PDFs) for the observed values of the nuisance parameters,  $\tilde{\theta}$ , obtained from calibration measurements. The systematic uncertainties that affect only the normalizations of the signal and background processes are treated as PDFs following a log-normal distribution, whereas shape-altering systematic uncertainties are treated as Gaussian PDFs [101].

Additional interpretations in terms of the SMEFT Higgs and Warsaw basis coupling parameters are also considered using Eqs. (7–10) and Eqs. (11–14), respectively. In each case, four independent couplings are studied simultaneously and the effect of the couplings on the total width of the Higgs boson is taken into account. For the  $f_{ai}$  measurements, this effect is absorbed by the signal strength modifiers. A parameterization of the partial widths of the main Higgs boson decay modes as a function of the couplings is used to determine the effect on the Higgs boson width [24, 28].

The likelihood is maximized with respect to the signal modifier parameters and with respect to the nuisance parameters. Confidence level (CL) intervals are determined from profile likelihood scans of the respective parameters. The allowed 68% and 95% CL intervals are defined using the set of parameter values at which the profile likelihood function  $-2\Delta \ln \mathcal{L} = 1.00$  and 3.84 [102], respectively, for which exact coverage is expected in the asymptotic limit [103]. The likelihood value at a given  $f_{ai}$  is determined by the shape of the signal hypothesis and the rel-

ative signal event yields between categories. Expected results are obtained using the Asimov data set [104] constructed using the SM values of the signal modifier parameters.

For Approach 1, where we assume  $a_i^{ZZ} = a_i^{WW}$ , the expected and observed  $f_{a2}$ ,  $f_{a3}$ ,  $f_{\Lambda 1}$ , and  $f_{\Lambda 1}^{Z\gamma}$  likelihood scans are shown in Fig. 8. Significant interference effects for negative values of  $f_{a2}$ , around  $-0.25$ , and positive values of  $f_{\Lambda 1}$ , around  $0.5$ , are evident. Relatively large changes in the signal shape with respect to the SM are predicted at these values. Also evident are narrow minima around  $f_{ai} = 0$ . The anomalous coupling terms in Eq. (1) have a  $q_i^2$  dependence, which can be larger at the VBF/VH production vertex than at the Higgs decay vertex. This causes the shape of the VBF/VH signal hypothesis to change quickly with  $f_{ai}$ . The axis scales are varied to improve the visibility of important features for  $f_{a2}$  and  $f_{\Lambda 1}$ . For Approach 2, where the SU(2)  $\times$  U(1) coupling relationships from Eqs. (2–6) are adopted, the expected and observed  $f_{a2}$ ,  $f_{a3}$  and  $f_{\Lambda 1}$  likelihood scans are shown in Fig. 9. The results are shown for each  $f_{ai}$  separately with the other two  $f_{ai}$  either fixed to zero or left floating in the fit. The measured values of the signal strength parameters correspond to  $\mu_{EW} = 0.9_{-0.24}^{+0.19}$  and  $\mu_{ggH} = 0.9_{-0.20}^{+0.38}$  when all parameters float simultaneously. It is notable that the observed  $-2\Delta \ln \mathcal{L}$  profile values are generally lower than expected. This is consistent with a downward statistical fluctuation in the number of VBF and VH events. The lowest  $\mu_{EW}$  value measured is  $0.82$  for the Approach 1  $f_{a3}$  fit which can be compared with the highest value of  $0.97$  for the corresponding  $f_{\Lambda 1}$  fit. In each case, the uncertainty in  $\mu_{EW}$  is about 20% and as such all fitted values are consistent with both the SM and each other. More generally, all anomalous HVV coupling parameter measurements are consistent with the expectations for the SM Higgs boson. The p-value compatibility of the full Approach 2 fit, where all signal parameters float simultaneously, with the SM is 91%. A summary of constraints on the anomalous HVV coupling parameters with the best fit values and allowed 68% and 95% CL intervals are shown in Table 7. The most stringent constraints on the HVV anomalous coupling cross section fractions are at the per mille level. Some constraints are less stringent than expected due to the fitted values of  $\mu_{EW}$  being lower than the SM expectation. The observed correlation coefficients between HVV anomalous coupling cross section fractions and signal strength modifiers are displayed in Fig. 10.

For the SMEFT Higgs basis interpretation, the expected and observed constraints on the  $\delta c_z$ ,  $c_{z\Box}$ ,  $c_{zz}$ , and  $\tilde{c}_{zz}$  coupling parameters are shown in Fig. 11. Table 8 presents a summary of the constraints on the couplings whereas Fig. 10 reports the observed correlation coefficients between them. For the Warsaw basis interpretation, the expected and observed constraints on the  $c_{H\Box}$ ,  $c_{HD}$ ,  $c_{HW}$ ,  $c_{HWB}$ ,  $c_{HB}$ ,  $c_{H\bar{W}}$ ,  $c_{H\bar{W}B}$ , and  $c_{H\bar{B}}$  coupling parameters are presented in Table 9. To cover all the Warsaw basis coupling parameters, three independent fits to the data were performed with a different choice of four independent couplings in each. A summary of the constraints on the SMEFT Higgs and Warsaw basis coupling parameters is presented in Fig. 12.

Finally, the expected and observed  $f_{a3}^{ggH}$  likelihood scans are shown in Fig. 13. The result is consistent with the expectation for a SM Higgs boson. Excluding the effect of the CP-odd HVV anomalous coupling, by fixing  $f_{a3}$  to zero, has a negligible effect. For  $|f_{a3}^{ggH}|$  approaching unity, the observed  $-2\Delta \ln \mathcal{L}$  profile values are larger than expected. This is consistent with downward statistical fluctuations in the data for a couple of bins where sensitivity to the  $a_3$  Hgg coupling contribution is enhanced (Fig. 7 left). The constraint on the anomalous Hgg coupling parameter with the best fit value and allowed 68% CL interval is shown in Table 7.

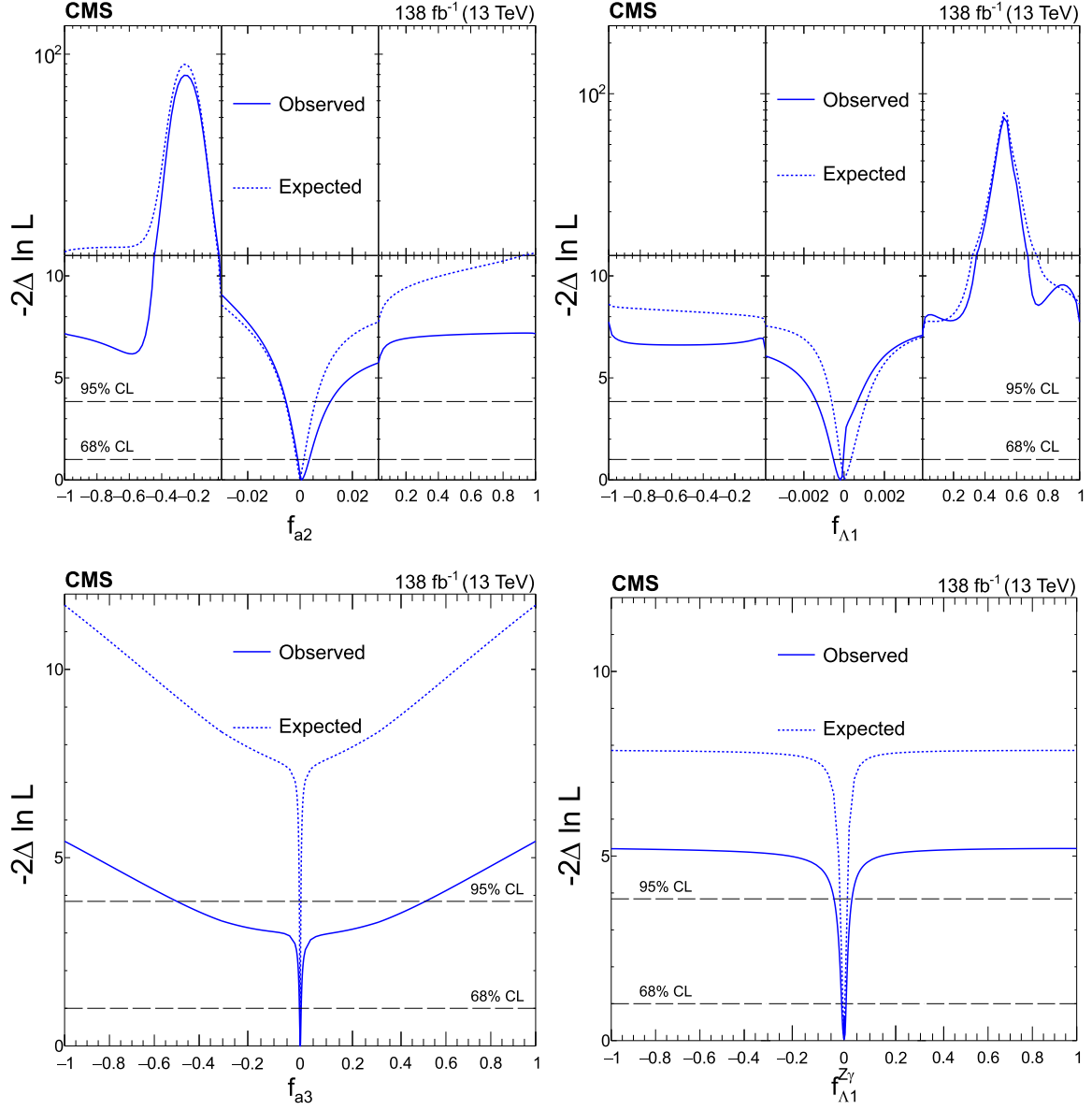


Figure 8: Expected (dashed) and observed (solid) profiled likelihood on  $f_{a2}$  (upper left),  $f_{\Lambda 1}$  (upper right),  $f_{a3}$  (lower left), and  $f_{\Lambda 1}^{Z\gamma}$  (lower right) using Approach 1. In each case, the signal strength modifiers are treated as free parameters. The dashed horizontal lines show the 68 and 95% CL regions. Axis scales are varied for  $f_{a2}$  and  $f_{\Lambda 1}$  to improve the visibility of important features.

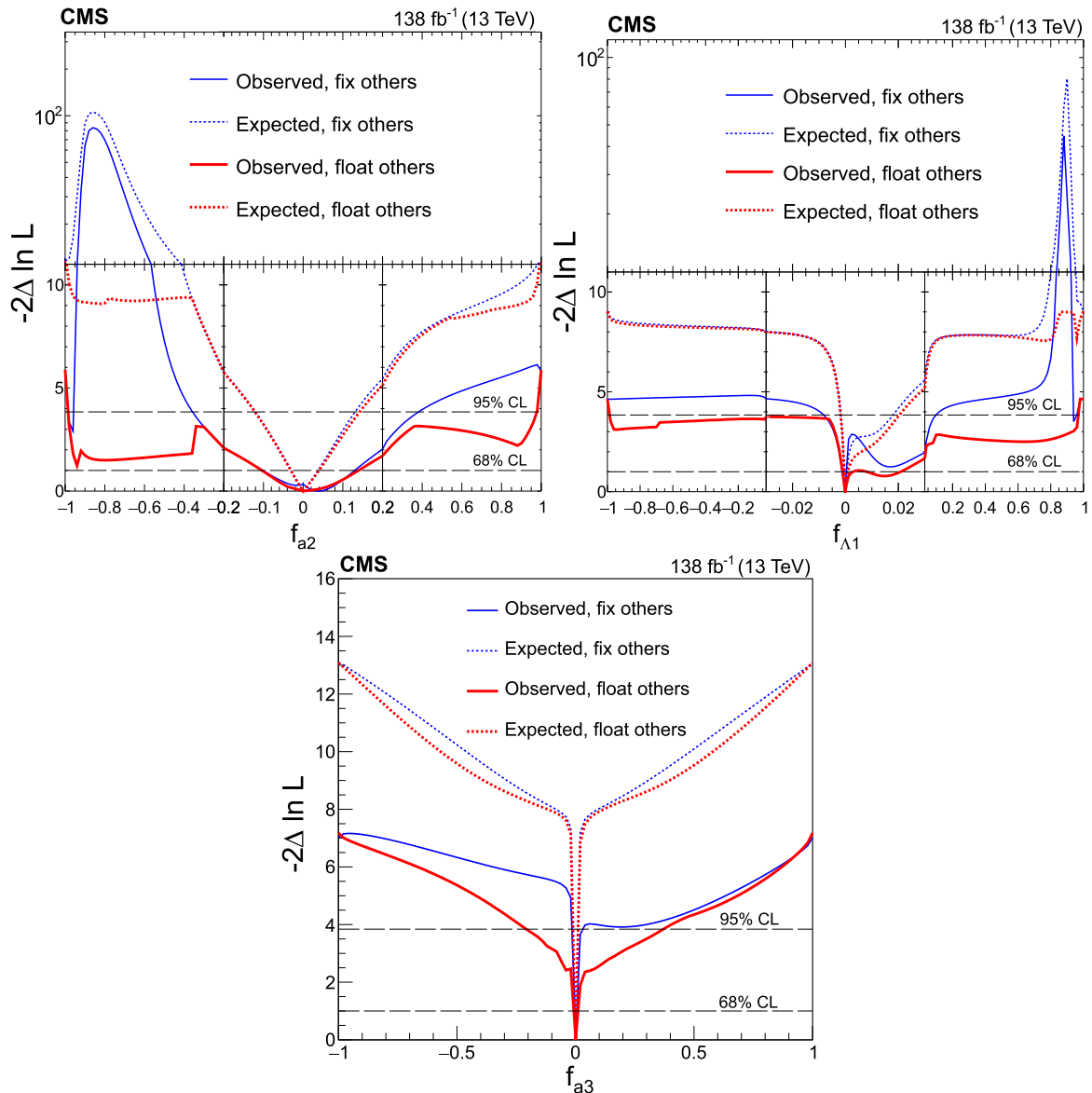


Figure 9: Expected (dashed) and observed (solid) profiled likelihood on  $f_{a2}$  (upper left),  $f_{\Lambda 1}$  (upper right) and  $f_{a3}$  (bottom) using Approach 2. The other two anomalous coupling cross section fractions are either fixed to zero (blue) or left floating in the fit (red). In each case, the signal strength modifiers are treated as free parameters. The dashed horizontal lines show the 68 and 95% CL regions. Axis scales are varied for  $f_{a2}$  and  $f_{\Lambda 1}$  to improve the visibility of important features.

## 11 Summary

This paper presents a study of the anomalous couplings of the Higgs boson (H) with vector bosons, including  $CP$  violating effects, using its associated production with hadronic jets in gluon fusion, electroweak vector boson fusion, and associated production with a W or Z boson, and its subsequent decay to a pair of W bosons. The results are based on the proton-proton collision data set collected by the CMS detector at the LHC during 2016–2018, corresponding to an integrated luminosity of  $138 \text{ fb}^{-1}$  at a center-of-mass energy of 13 TeV. The analysis targets the different-flavor dilepton ( $e\mu$ ) final state, with kinematic information from associated jets

Table 7: Summary of constraints on the anomalous HVV and Hgg coupling parameters with the best fit values and allowed 68 and 95% CL (in square brackets) intervals. For Approach 1, each  $f_{ai}$  is studied independently. For Approach 2, each  $f_{ai}$  is shown separately with the other two cross section fractions either fixed to zero or left floating in the fit. In each case, the signal strength modifiers are treated as free parameters.

Analysis	$f_{ai}$		Observed ( $\times 10^{-3}$ )	Expected ( $\times 10^{-3}$ )
HVV Approach 1	$f_{a2}$	best fit	0.5	0.0
		68% CL	[−0.8, 3.5]	[−1.4, 1.3]
		95% CL	[−5.7, 12.0]	[−5.2, 6.1]
	$f_{a3}$	best fit	0.9	0.0
		68% CL	[−2.7, 4.1]	[−0.7, 0.7]
		95% CL	[−553.0, 561.0]	[−2.8, 2.9]
	$f_{\Lambda 1}$	best fit	−0.2	0.0
		68% CL	[−0.5, 0.0]	[−0.2, 0.5]
		95% CL	[−1.4, 0.7]	[−0.6, 1.4]
	$f_{\Lambda 1}^{Z\gamma}$	best fit	3.0	0.0
		68% CL	[−11.0, 9.1]	[−5.0, 3.8]
		95% CL	[−55.0, 42.0]	[−14.0, 11.0]
HVV Approach 2 (Fix others)	$f_{a2}$	best fit	38.0	0.0
		68% CL	[−112.2, 129.3]	[−30.9, 37.5]
		95% CL	[−376.6, 430.0] $\cup$ [−989.2, −826.3]	[−126.1, 136.8]
	$f_{a3}$	best fit	0.8	0.0
		68% CL	[−0.8, 3.5]	[−0.8, 1.1]
		95% CL	[−7.6, 58.8]	[−3.4, 4.3]
$f_{\Lambda 1}$	best fit	−0.15	0.0	
	68% CL	[−1.21, 0.16]	[−0.4, 0.4]	
	95% CL	[−19.5, 118.5] $\cup$ [909.9, 964.1]	[−1.7, 18.9]	
HVV Approach 2 (Float others)	$f_{a2}$	best fit	−1.0	0.0
		68% CL	[−104.1, 139.9]	[−31.1, 39.8]
		95% CL	[−986.4, 981.2]	[−127.5, 148.7]
	$f_{a3}$	best fit	0.34	0.0
		68% CL	[−0.69, 3.4]	[−1.0, 1.2]
		95% CL	[−8.0, 361.5]	[−4.3, 5.3]
$f_{\Lambda 1}$	best fit	−0.1	0.0	
	68% CL	[−1.08, 3.78] $\cup$ [7.2, 20.7]	[−0.4, 0.9]	
	95% CL	[−994.8, 993.9]	[−1.9, 21.4]	
Hgg	$f_{a3}^{ggH}$	best fit	−34	0
		68% CL	[−721, 383]	[−1000, 1000]
		95% CL	[−1000, 1000]	[−1000, 1000]



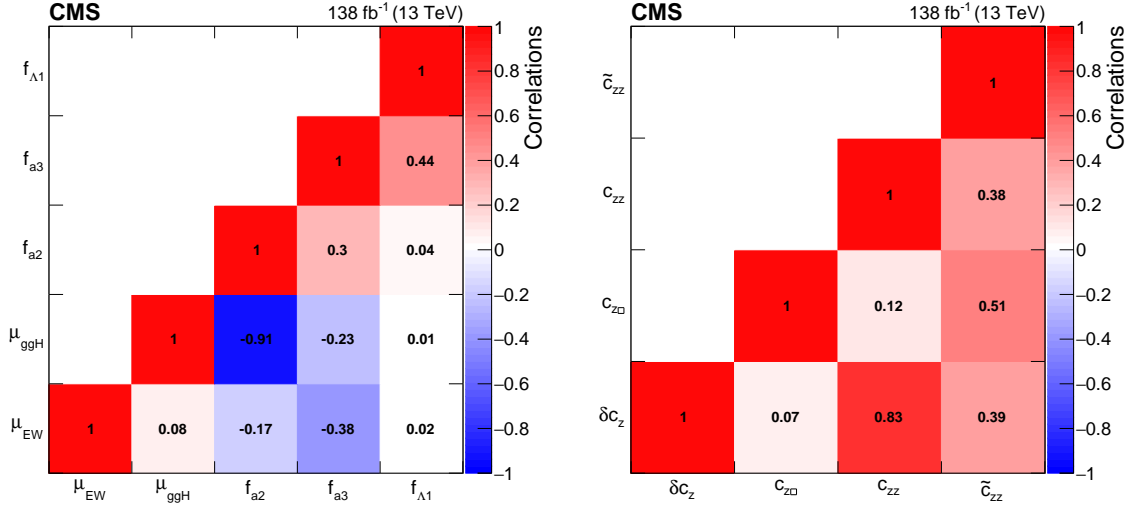


Figure 10: The observed correlation coefficients between HVV anomalous coupling cross section fractions and signal strength modifiers (left) and between SMEFT Higgs basis coupling parameters (right).

Table 8: Summary of constraints on the SMEFT Higgs basis coupling parameters with the best fit values and 68% CL uncertainties. All four couplings are studied simultaneously.

Coupling	Observed	Expected
$\delta c_z$	$-0.06^{+0.09}_{-0.16}$	$0.00^{+0.08}_{-0.10}$
$c_{z\Box}$	$0.01^{+0.02}_{-0.06}$	$0.00^{+0.02}_{-0.02}$
$c_{zz}$	$0.03^{+0.30}_{-0.52}$	$0.00^{+0.23}_{-0.29}$
$\tilde{c}_{zz}$	$-0.17^{+0.42}_{-0.30}$	$0.00^{+0.29}_{-0.32}$

Table 9: Summary of constraints on the SMEFT Warsaw basis coupling parameters with the best fit values and 68% CL uncertainties. Only one of  $c_{HW}$ ,  $c_{HWB}$ , and  $c_{HB}$  is independent, the same is also true for  $c_{H\bar{W}}$ ,  $c_{H\bar{W}B}$ , and  $c_{H\bar{B}}$ . Three independent fits to the data were performed with a different choice of four independent couplings in each.

Coupling	Observed	Expected
$c_{H\Box}$	$-0.76^{+1.43}_{-3.43}$	$0.00^{+1.37}_{-1.84}$
$c_{HD}$	$-0.12^{+0.93}_{-0.32}$	$0.00^{+0.43}_{-0.30}$
$c_{HW}$	$0.08^{+0.43}_{-0.87}$	$0.00^{+0.37}_{-0.48}$
$c_{HWB}$	$0.17^{+0.88}_{-1.79}$	$0.00^{+0.77}_{-0.96}$
$c_{HB}$	$0.03^{+0.13}_{-0.26}$	$0.00^{+0.11}_{-0.14}$
$c_{H\bar{W}}$	$-0.26^{+0.67}_{-0.50}$	$0.00^{+0.48}_{-0.52}$
$c_{H\bar{W}B}$	$-0.54^{+1.37}_{-1.03}$	$0.00^{+0.99}_{-1.07}$
$c_{H\bar{B}}$	$-0.08^{+0.20}_{-0.15}$	$0.00^{+0.15}_{-0.16}$

combined using matrix element techniques to increase sensitivity to anomalous effects at the production vertex. Dedicated Monte Carlo simulation and matrix element reweighting provide modeling of all kinematic features in the production and decay of the Higgs boson with

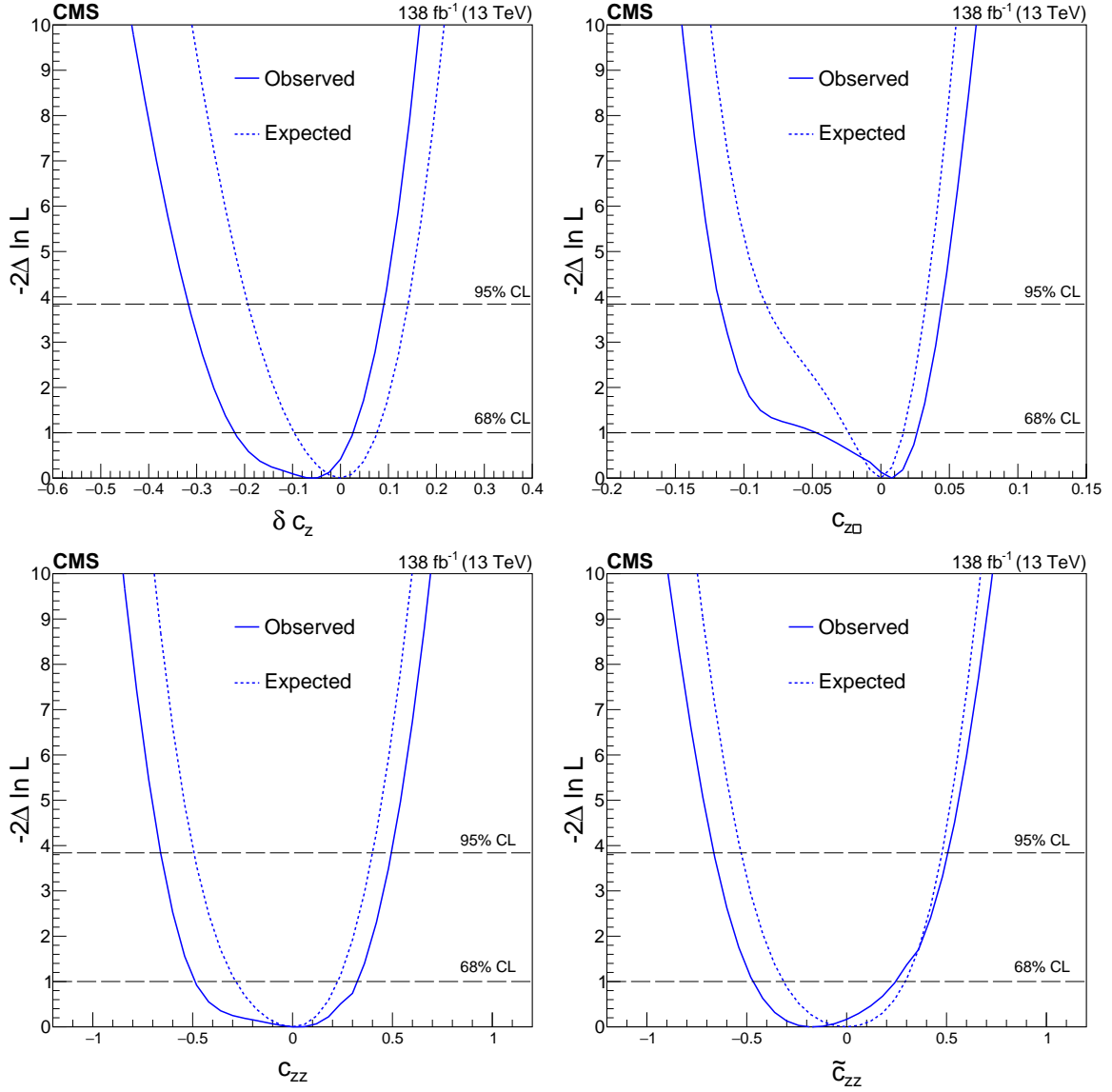


Figure 11: Expected (dashed) and observed (solid) profiled likelihood on the  $\delta c_z$  (upper left),  $c_{zD}$  (upper right),  $c_{zz}$  (lower left), and  $\tilde{c}_{zz}$  (lower right) couplings of the SMEFT Higgs basis. All four couplings are studied simultaneously. The dashed horizontal lines show the 68 and 95% CL regions.

full simulation of detector effects. A simultaneous measurement of four Higgs boson couplings to electroweak vector bosons has been performed in the framework of a standard model effective field theory. All measurements are consistent with the expectations for the standard model Higgs boson and constraints are set on the fractional contribution of the anomalous couplings to the Higgs boson cross section. The most stringent constraints on the HVV anomalous coupling cross section fractions are at the per mille level. These results are in agreement with those obtained in the  $H \rightarrow ZZ$  and  $H \rightarrow \tau\tau$  channels, and also significantly surpass those of the previous  $H \rightarrow WW$  anomalous coupling analysis from the CMS experiment in both scope and precision.

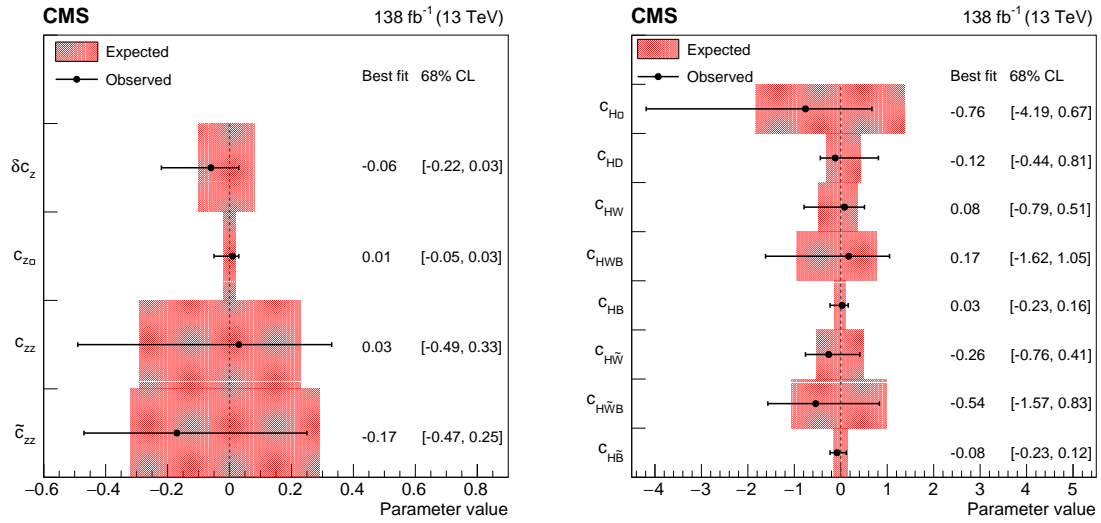


Figure 12: Summary of constraints on the SMEFT Higgs (left) and Warsaw (right) basis coupling parameters with the best fit values and 68% CL uncertainties. For the Warsaw basis, only one of  $c_{HW}$ ,  $c_{HWB}$ , and  $c_{HB}$  is independent, the same is also true for  $c_{H\tilde{W}}$ ,  $c_{H\tilde{W}B}$ , and  $c_{H\tilde{B}}$ .

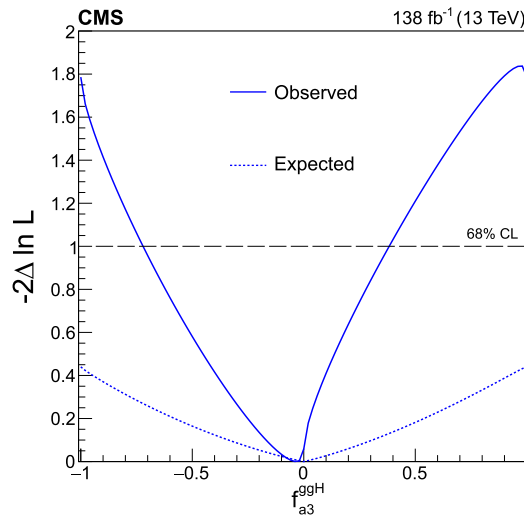


Figure 13: Expected (dashed) and observed (solid) profiled likelihood on  $f_{a3}^{ggH}$ . The signal strength modifiers and the  $CP$ -odd HVV anomalous coupling cross section fraction are treated as free parameters. The crossing of the observed likelihood with the dashed horizontal line shows the observed 68% CL region.

## Acknowledgments

We congratulate our colleagues in the CERN accelerator departments for the excellent performance of the LHC and thank the technical and administrative staffs at CERN and at other CMS institutes for their contributions to the success of the CMS effort. In addition, we gratefully acknowledge the computing centers and personnel of the Worldwide LHC Computing Grid and other centers for delivering so effectively the computing infrastructure essential to our analyses. Finally, we acknowledge the enduring support for the construction and operation of the LHC, the CMS detector, and the supporting computing infrastructure provided by the following funding agencies: SC (Armenia), BMBWF and FWF (Austria); FNRS and

FWO (Belgium); CNPq, CAPES, FAPERJ, FAPERGS, and FAPESP (Brazil); MES and BNSF (Bulgaria); CERN; CAS, MoST, and NSFC (China); MINCIENCIAS (Colombia); MSES and CSF (Croatia); RIF (Cyprus); SENESCYT (Ecuador); ERC PRG, RVTT3 and MoER TK202 (Estonia); Academy of Finland, MEC, and HIP (Finland); CEA and CNRS/IN2P3 (France); SRNSF (Georgia); BMBF, DFG, and HGF (Germany); GSRI (Greece); NKFIH (Hungary); DAE and DST (India); IPM (Iran); SFI (Ireland); INFN (Italy); MSIP and NRF (Republic of Korea); MES (Latvia); LMTLT (Lithuania); MOE and UM (Malaysia); BUAP, CINVESTAV, CONACYT, LNS, SEP, and UASLP-FAI (Mexico); MOS (Montenegro); MBIE (New Zealand); PAEC (Pakistan); MES and NSC (Poland); FCT (Portugal); MESTD (Serbia); MCIN/AEI and PCTI (Spain); MOSTR (Sri Lanka); Swiss Funding Agencies (Switzerland); MST (Taipei); MHESI and NSTDA (Thailand); TUBITAK and TENMAK (Turkey); NASU (Ukraine); STFC (United Kingdom); DOE and NSF (USA).

Individuals have received support from the Marie-Curie program and the European Research Council and Horizon 2020 Grant, contract Nos. 675440, 724704, 752730, 758316, 765710, 824093, 101115353, and COST Action CA16108 (European Union); the Leventis Foundation; the Alfred P. Sloan Foundation; the Alexander von Humboldt Foundation; the Science Committee, project no. 22rl-037 (Armenia); the Belgian Federal Science Policy Office; the Fonds pour la Formation à la Recherche dans l'Industrie et dans l'Agriculture (FRIA-Belgium); the Agentschap voor Innovatie door Wetenschap en Technologie (IWT-Belgium); the F.R.S.-FNRS and FWO (Belgium) under the "Excellence of Science – EOS" – be.h project n. 30820817; the Beijing Municipal Science & Technology Commission, No. Z191100007219010 and Fundamental Research Funds for the Central Universities (China); the Ministry of Education, Youth and Sports (MEYS) of the Czech Republic; the Shota Rustaveli National Science Foundation, grant FR-22-985 (Georgia); the Deutsche Forschungsgemeinschaft (DFG), under Germany's Excellence Strategy – EXC 2121 "Quantum Universe" – 390833306, and under project number 400140256 – GRK2497; the Hellenic Foundation for Research and Innovation (HFRI), Project Number 2288 (Greece); the Hungarian Academy of Sciences, the New National Excellence Program – ÚNKP, the NKFIH research grants K 124845, K 124850, K 128713, K 128786, K 129058, K 131991, K 133046, K 138136, K 143460, K 143477, 2020-2.2.1-ED-2021-00181, and TKP2021-NKTA-64 (Hungary); the Council of Science and Industrial Research, India; ICSC – National Research Center for High Performance Computing, Big Data and Quantum Computing, funded by the EU NexGeneration program (Italy); the Latvian Council of Science; the Ministry of Education and Science, project no. 2022/WK/14, and the National Science Center, contracts Opus 2021/41/B/ST2/01369 and 2021/43/B/ST2/01552 (Poland); the Fundação para a Ciência e a Tecnologia, grant CEECIND/01334/2018 (Portugal); the National Priorities Research Program by Qatar National Research Fund; MCIN/AEI/10.13039/501100011033, ERDF "a way of making Europe", and the Programa Estatal de Fomento de la Investigación Científica y Técnica de Excelencia María de Maeztu, grant MDM-2017-0765 and Programa Severo Ochoa del Principado de Asturias (Spain); the Chulalongkorn Academic into Its 2nd Century Project Advancement Project, and the National Science, Research and Innovation Fund via the Program Management Unit for Human Resources & Institutional Development, Research and Innovation, grant B37G660013 (Thailand); the Kavli Foundation; the Nvidia Corporation; the SuperMicro Corporation; the Welch Foundation, contract C-1845; and the Weston Havens Foundation (USA).

## References

- [1] ATLAS Collaboration, "Observation of a new particle in the search for the standard model Higgs boson with the ATLAS detector at the LHC", *Phys. Lett. B* **716** (2012) 1,

- doi:10.1016/j.physletb.2012.08.020, arXiv:1207.7214.
- [2] CMS Collaboration, "Observation of a new boson at a mass of 125 GeV with the CMS experiment at the LHC", *Phys. Lett. B* **716** (2012) 30, doi:10.1016/j.physletb.2012.08.021, arXiv:1207.7235.
- [3] CMS Collaboration, "Observation of a new boson with mass near 125 GeV in pp collisions at  $\sqrt{s} = 7$  and 8 TeV", *JHEP* **06** (2013) 081, doi:10.1007/JHEP06(2013)081, arXiv:1303.4571.
- [4] CMS Collaboration, "On the mass and spin-parity of the Higgs boson candidate via its decays to Z boson pairs", *Phys. Rev. Lett.* **110** (2013) 081803, doi:10.1103/PhysRevLett.110.081803, arXiv:1212.6639.
- [5] CMS Collaboration, "Measurement of the properties of a Higgs boson in the four-lepton final state", *Phys. Rev. D* **89** (2014) 092007, doi:10.1103/PhysRevD.89.092007, arXiv:1312.5353.
- [6] CMS Collaboration, "Constraints on the spin-parity and anomalous HVV couplings of the Higgs boson in proton collisions at 7 and 8 TeV", *Phys. Rev. D* **92** (2015) 012004, doi:10.1103/PhysRevD.92.012004, arXiv:1411.3441.
- [7] CMS Collaboration, "Limits on the Higgs boson lifetime and width from its decay to four charged leptons", *Phys. Rev. D* **92** (2015) 072010, doi:10.1103/PhysRevD.92.072010, arXiv:1507.06656.
- [8] CMS Collaboration, "Combined search for anomalous pseudoscalar HVV couplings in VH production and  $H \rightarrow VV$  decay", *Phys. Lett. B* **759** (2016) 672, doi:10.1016/j.physletb.2016.06.004, arXiv:1602.04305.
- [9] CMS Collaboration, "Constraints on anomalous Higgs boson couplings using production and decay information in the four-lepton final state", *Phys. Lett. B* **775** (2017) 1, doi:10.1016/j.physletb.2017.10.021, arXiv:1707.00541.
- [10] CMS Collaboration, "Measurements of the Higgs boson width and anomalous HVV couplings from on-shell and off-shell production in the four-lepton final state", *Phys. Rev. D* **99** (2019) 112003, doi:10.1103/PhysRevD.99.112003, arXiv:1901.00174.
- [11] CMS Collaboration, "Constraints on anomalous HVV couplings from the production of Higgs bosons decaying to  $\tau$  lepton pairs", *Phys. Rev. D* **100** (2019) 112002, doi:10.1103/PhysRevD.100.112002, arXiv:1903.06973.
- [12] ATLAS Collaboration, "Evidence for the spin-0 nature of the Higgs boson using ATLAS data", *Phys. Lett. B* **726** (2013) 120, doi:10.1016/j.physletb.2013.08.026, arXiv:1307.1432.
- [13] ATLAS Collaboration, "Study of the spin and parity of the Higgs boson in diboson decays with the ATLAS detector", *Eur. Phys. J. C* **75** (2015) 476, doi:10.1140/epjc/s10052-015-3685-1, arXiv:1506.05669.
- [14] ATLAS Collaboration, "Test of CP invariance in vector-boson fusion production of the Higgs boson using the Optimal Observable method in the ditau decay channel with the ATLAS detector", *Eur. Phys. J. C* **76** (2016) 658, doi:10.1140/epjc/s10052-016-4499-5, arXiv:1602.04516.

- 
- [15] ATLAS Collaboration, “Measurement of inclusive and differential cross sections in the  $H \rightarrow ZZ^* \rightarrow 4\ell$  decay channel in pp collisions at  $\sqrt{s} = 13$  TeV with the ATLAS detector”, *JHEP* **10** (2017) 132, doi:10.1007/JHEP10(2017)132, arXiv:1708.02810.
- [16] ATLAS Collaboration, “Measurement of the Higgs boson coupling properties in the  $H \rightarrow ZZ^* \rightarrow 4\ell$  decay channel at  $\sqrt{s} = 13$  TeV with the ATLAS detector”, *JHEP* **03** (2018) 095, doi:10.1007/JHEP03(2018)095, arXiv:1712.02304.
- [17] ATLAS Collaboration, “Measurements of Higgs boson properties in the diphoton decay channel with  $36 \text{ fb}^{-1}$  of pp collision data at  $\sqrt{s} = 13$  TeV with the ATLAS detector”, *Phys. Rev. D* **98** (2018) 052005, doi:10.1103/PhysRevD.98.052005, arXiv:1802.04146.
- [18] ATLAS Collaboration, “Test of CP invariance in vector-boson fusion production of the Higgs boson in the  $H \rightarrow \tau\tau$  channel in proton–proton collisions at  $\sqrt{s} = 13$  TeV with the ATLAS detector”, *Phys. Lett. B* **805** (2020) 135426, doi:10.1016/j.physletb.2020.135426, arXiv:2002.05315.
- [19] LHC Higgs Cross Section Working Group, “Handbook of LHC Higgs cross sections: 4. Deciphering the nature of the Higgs sector”, CERN Report CERN-2017-002-M, 2016. doi:10.23731/CYRM-2017-002, arXiv:1610.07922.
- [20] Y. Gao et al., “Spin determination of single-produced resonances at hadron colliders”, *Phys. Rev. D* **81** (2010) 075022, doi:10.1103/PhysRevD.81.075022, arXiv:1001.3396.
- [21] S. Bolognesi et al., “On the spin and parity of a single-produced resonance at the LHC”, *Phys. Rev. D* **86** (2012) 095031, doi:10.1103/PhysRevD.86.095031, arXiv:1208.4018.
- [22] I. Anderson et al., “Constraining anomalous HVV interactions at proton and lepton colliders”, *Phys. Rev. D* **89** (2014) 035007, doi:10.1103/PhysRevD.89.035007, arXiv:1309.4819.
- [23] A. V. Gritsan, R. Rötsch, M. Schulze, and M. Xiao, “Constraining anomalous Higgs boson couplings to the heavy flavor fermions using matrix element techniques”, *Phys. Rev. D* **94** (2016) 055023, doi:10.1103/PhysRevD.94.055023, arXiv:1606.03107.
- [24] A. V. Gritsan et al., “New features in the JHU generator framework: constraining Higgs boson properties from on-shell and off-shell production”, *Phys. Rev. D* **102** (2020) 056022, doi:10.1103/PhysRevD.102.056022, arXiv:2002.09888.
- [25] CMS Collaboration, “Measurements of the Higgs boson production cross section and couplings in the W boson pair decay channel in proton-proton collisions at  $\sqrt{s} = 13$  TeV”, *Eur. Phys. J. C* **83** (2023) 667, doi:10.1140/epjc/s10052-023-11632-6, arXiv:2206.09466.
- [26] LHC Higgs Cross Section Working Group, “Handbook of LHC Higgs cross sections: 3. Higgs Properties: Report of the LHC Higgs Cross Section Working Group”, CERN Report CERN-2013-004, 2013. doi:10.5170/CERN-2013-004, arXiv:1307.1347.

- [27] CMS Collaboration, “Measurements of  $t\bar{t}H$  production and the  $CP$  structure of the Yukawa interaction between the Higgs boson and top quark in the diphoton decay channel”, *Phys. Rev. Lett.* **125** (2020) 061801, doi:10.1103/PhysRevLett.125.061801, arXiv:2003.10866.
- [28] CMS Collaboration, “Constraints on anomalous Higgs boson couplings to vector bosons and fermions in its production and decay using the four-lepton final state”, *Phys. Rev. D* **104** (2021) 052004, doi:10.1103/physrevd.104.052004, arXiv:2104.12152.
- [29] HEPData record for this analysis, 2024. doi:x/hepdata.x.
- [30] B. Grzadkowski, M. Iskrzyński, M. Misiak, and J. Rosiek, “Dimension-six terms in the standard model lagrangian”, *JHEP* **10** (2010) 085, doi:10.1007/jhep10(2010)085, arXiv:1008.4884.
- [31] J. Davis et al., “Constraining anomalous Higgs boson couplings to virtual photons”, *Phys. Rev. D* **105** (2022) 096027, doi:10.1103/PhysRevD.105.096027, arXiv:2109.13363.
- [32] A. V. Gritsan et al., “New features in the JHU generator framework: Constraining Higgs boson properties from on-shell and off-shell production”, *Phys. Rev. D* **102** (2020) doi:10.1103/physrevd.102.056022.
- [33] CMS Collaboration, “The CMS experiment at the CERN LHC”, *JINST* **3** (2008) S08004, doi:10.1088/1748-0221/3/08/S08004.
- [34] CMS Collaboration, “Performance of electron reconstruction and selection with the CMS detector in proton-proton collisions at  $\sqrt{s} = 8$  TeV”, *JINST* **10** (2015) P06005, doi:10.1088/1748-0221/10/06/P06005, arXiv:1502.02701.
- [35] CMS Collaboration, “Performance of the CMS muon detector and muon reconstruction with proton-proton collisions at  $\sqrt{s} = 13$  TeV”, *JINST* **13** (2018) P06015, doi:10.1088/1748-0221/13/06/P06015, arXiv:1804.04528.
- [36] CMS Collaboration, “Performance of photon reconstruction and identification with the CMS detector in proton-proton collisions at  $\sqrt{s} = 8$  TeV”, *JINST* **10** (2015) P08010, doi:10.1088/1748-0221/10/08/P08010, arXiv:1502.02702.
- [37] CMS Collaboration, “Description and performance of track and primary-vertex reconstruction with the CMS tracker”, *JINST* **9** (2014) P10009, doi:10.1088/1748-0221/9/10/P10009, arXiv:1405.6569.
- [38] CMS Collaboration, “Particle-flow reconstruction and global event description with the CMS detector”, *JINST* **12** (2017) P10003, doi:10.1088/1748-0221/12/10/P10003, arXiv:1706.04965.
- [39] CMS Collaboration, “Performance of reconstruction and identification of  $\tau$  leptons decaying to hadrons and  $\nu_\tau$  in pp collisions at  $\sqrt{s} = 13$  TeV”, *JINST* **13** (2018) P10005, doi:10.1088/1748-0221/13/10/P10005, arXiv:1809.02816.
- [40] CMS Collaboration, “Jet energy scale and resolution in the CMS experiment in pp collisions at 8 TeV”, *JINST* **12** (2017) P02014, doi:10.1088/1748-0221/12/02/P02014, arXiv:1607.03663.

- 
- [41] CMS Collaboration, “Performance of missing transverse momentum reconstruction in proton-proton collisions at  $\sqrt{s} = 13$  TeV using the CMS detector”, *JINST* **14** (2019) P07004, doi:10.1088/1748-0221/14/07/P07004, arXiv:1903.06078.
- [42] CMS Collaboration, “Performance of the CMS Level-1 trigger in proton-proton collisions at  $\sqrt{s} = 13$  TeV”, *JINST* **15** (2020) P10017, doi:10.1088/1748-0221/15/10/P10017, arXiv:2006.10165.
- [43] CMS Collaboration, “The CMS trigger system”, *JINST* **12** (2017) P01020, doi:10.1088/1748-0221/12/01/P01020, arXiv:1609.02366.
- [44] CMS Collaboration, “Precision luminosity measurement in proton-proton collisions at  $\sqrt{s} = 13$  TeV in 2015 and 2016 at CMS”, *Eur. Phys. J. C* **800** (2021) 81, doi:10.1140/epjc/s10052-021-09538-2, arXiv:2104.01927.
- [45] CMS Collaboration, “CMS luminosity measurement for the 2017 data-taking period at  $\sqrt{s} = 13$  TeV”, CMS Physics Analysis Summary CMS-PAS-LUM-17-004, 2017.
- [46] CMS Collaboration, “CMS luminosity measurement for the 2018 data-taking period at  $\sqrt{s} = 13$  TeV”, CMS Physics Analysis Summary CMS-PAS-LUM-18-002, 2019.
- [47] NNPDF Collaboration, “Parton distributions with QED corrections”, *Nucl. Phys. B* **877** (2013) 290, doi:10.1016/j.nuclphysb.2013.10.010, arXiv:1308.0598.
- [48] NNPDF Collaboration, “Unbiased global determination of parton distributions and their uncertainties at NNLO and at LO”, *Nucl. Phys. B* **855** (2012) 153, doi:10.1016/j.nuclphysb.2011.09.024, arXiv:1107.2652.
- [49] NNPDF Collaboration, “Parton distributions from high-precision collider data”, *Eur. Phys. J. C* **77** (2017) 663, doi:10.1140/epjc/s10052-017-5199-5, arXiv:1706.00428.
- [50] CMS Collaboration, “Event generator tunes obtained from underlying event and multiparton scattering measurements”, *Eur. Phys. J. C* **76** (2016) 155, doi:10.1140/epjc/s10052-016-3988-x, arXiv:1512.00815.
- [51] CMS Collaboration, “Extraction and validation of a new set of CMS PYTHIA8 tunes from underlying-event measurements”, *Eur. Phys. J. C* **80** (2020) 4, doi:10.1140/epjc/s10052-019-7499-4, arXiv:1903.12179.
- [52] T. Sjöstrand et al., “An introduction to PYTHIA 8.2”, *Comput. Phys. Commun.* **191** (2015) 159, doi:10.1016/j.cpc.2015.01.024, arXiv:1410.3012.
- [53] P. Nason, “A new method for combining NLO QCD with shower Monte Carlo algorithms”, *JHEP* **11** (2004) 040, doi:10.1088/1126-6708/2004/11/040, arXiv:hep-ph/0409146.
- [54] S. Frixione, P. Nason, and C. Oleari, “Matching NLO QCD computations with parton shower simulations: the POWHEG method”, *JHEP* **11** (2007) 070, doi:10.1088/1126-6708/2007/11/070, arXiv:0709.2092.
- [55] S. Alioli, P. Nason, C. Oleari, and E. Re, “A general framework for implementing NLO calculations in shower Monte Carlo programs: the POWHEG BOX”, *JHEP* **06** (2010) 043, doi:10.1007/JHEP06(2010)043, arXiv:1002.2581.



- [56] E. Bagnaschi, G. Degrandi, P. Slavich, and A. Vicini, “Higgs production via gluon fusion in the POWHEG approach in the SM and in the MSSM”, *JHEP* **02** (2012) 088, doi:10.1007/JHEP02(2012)088, arXiv:1111.2854.
- [57] P. Nason and C. Oleari, “NLO Higgs boson production via vector-boson fusion matched with shower in POWHEG”, *JHEP* **02** (2010) 037, doi:10.1007/JHEP02(2010)037, arXiv:0911.5299.
- [58] G. Luisoni, P. Nason, C. Oleari, and F. Tramontano, “ $HW^\pm/HZ + 0$  and 1 jet at NLO with the POWHEG BOX interfaced to GoSam and their merging within MiNLO”, *JHEP* **10** (2013) 083, doi:10.1007/JHEP10(2013)083, arXiv:1306.2542.
- [59] H. B. Hartanto, B. Jager, L. Reina, and D. Wackerth, “Higgs boson production in association with top quarks in the POWHEG BOX”, *Phys. Rev. D* **91** (2015) 094003, doi:10.1103/PhysRevD.91.094003, arXiv:1501.04498.
- [60] K. Hamilton, P. Nason, E. Re, and G. Zanderighi, “NNLOPS simulation of Higgs boson production”, *JHEP* **10** (2013) 222, doi:10.1007/JHEP10(2013)222, arXiv:1309.0017.
- [61] K. Hamilton, P. Nason, and G. Zanderighi, “Finite quark-mass effects in the NNLOPS POWHEG+MiNLO Higgs generator”, *JHEP* **05** (2015) 140, doi:10.1007/JHEP05(2015)140, arXiv:1501.04637.
- [62] N. Berger et al., “Simplified template cross sections — stage 1.1”, 2019. arXiv:1906.02754.
- [63] R. Frederix and K. Hamilton, “Extending the MINLO method”, *JHEP* **05** (2016) 042, doi:10.1007/JHEP05(2016)042, arXiv:1512.02663.
- [64] J. Alwall et al., “The automated computation of tree-level and next-to-leading order differential cross sections, and their matching to parton shower simulations”, *JHEP* **07** (2014) 079, doi:10.1007/JHEP07(2014)079, arXiv:1405.0301.
- [65] CMS Collaboration, “A measurement of the Higgs boson mass in the diphoton decay channel”, *Phys. Lett. B* **805** (2020) 135425, doi:10.1016/j.physletb.2020.135425, arXiv:2002.06398.
- [66] P. Nason, C. Oleari, M. Rocco, and M. Zaro, “An interface between the POWHEG BOX and MadGraph5\_aMC@NLO”, *Eur. Phys. J. C* **80** (2020) 10, doi:10.1140/epjc/s10052-020-08559-7, arXiv:2008.06364.
- [67] P. Nason and G. Zanderighi, “ $W^+W^-$ ,  $WZ$  and  $ZZ$  production in the POWHEG-BOX-V2”, *Eur. Phys. J. C* **74** (2014) 2702, doi:10.1140/epjc/s10052-013-2702-5, arXiv:1311.1365.
- [68] P. Meade, H. Ramani, and M. Zeng, “Transverse momentum resummation effects in  $W^+W^-$  measurements”, *Phys. Rev. D* **90** (2014) 114006, doi:10.1103/PhysRevD.90.114006, arXiv:1407.4481.
- [69] P. Jaiswal and T. Okui, “Explanation of the  $WW$  excess at the LHC by jet-veto resummation”, *Phys. Rev. D* **90** (2014) 073009, doi:10.1103/PhysRevD.90.073009, arXiv:1407.4537.


- [70] J. M. Campbell and R. K. Ellis, “An update on vector boson pair production at hadron colliders”, *Phys. Rev. D* **60** (1999) 113006, doi:10.1103/PhysRevD.60.113006, arXiv:hep-ph/9905386.
- [71] J. M. Campbell, R. K. Ellis, and C. Williams, “Vector boson pair production at the LHC”, *JHEP* **07** (2011) 018, doi:10.1007/JHEP07(2011)018, arXiv:1105.0020.
- [72] J. M. Campbell, R. K. Ellis, and W. T. Giele, “A multi-threaded version of MCFM”, *Eur. Phys. J. C* **75** (2015) 246, doi:10.1140/epjc/s10052-015-3461-2, arXiv:1503.06182.
- [73] F. Caola et al., “QCD corrections to vector boson pair production in gluon fusion including interference effects with off-shell Higgs at the LHC”, *JHEP* **07** (2016) 087, doi:10.1007/JHEP07(2016)087, arXiv:1605.04610.
- [74] Alwall, J. and others, “Comparative study of various algorithms for the merging of parton showers and matrix elements in hadronic collisions”, *Eur. Phys. J. C* **53** (2008) 473, doi:10.1140/epjc/s10052-007-0490-5, arXiv:0706.2569.
- [75] S. Frixione, P. Nason, and G. Ridolfi, “A positive-weight next-to-leading-order Monte Carlo for heavy flavour hadroproduction”, *JHEP* **09** (2007) 126, doi:10.1088/1126-6708/2007/09/126, arXiv:0707.3088.
- [76] S. Alioli, P. Nason, C. Oleari, and E. Re, “NLO single-top production matched with shower in POWHEG:  $s$ - and  $t$ -channel contributions”, *JHEP* **09** (2009) 111, doi:10.1088/1126-6708/2009/09/111, arXiv:0907.4076. [Erratum: doi:10.1007/JHEP02(2010)011].
- [77] E. Re, “Single-top  $Wt$ -channel production matched with parton showers using the POWHEG method”, *Eur. Phys. J. C* **71** (2011) 1547, doi:10.1140/epjc/s10052-011-1547-z, arXiv:1009.2450.
- [78] M. Czakon et al., “Top-pair production at the LHC through NNLO QCD and NLO EW”, *JHEP* **10** (2017) 186, doi:10.1007/JHEP10(2017)186, arXiv:1705.04105.
- [79] R. Frederix and S. Frixione, “Merging meets matching in MC@NLO”, *JHEP* **12** (2012) 061, doi:10.1007/JHEP12(2012)061, arXiv:1209.6215.
- [80] GEANT4 Collaboration, “GEANT4 — a simulation toolkit”, *Nucl. Instrum. Meth. A* **506** (2003) 250, doi:10.1016/S0168-9002(03)01368-8.
- [81] CMS Collaboration, “Muon identification using multivariate techniques in the CMS experiment in proton-proton collisions at  $\sqrt{s} = 13$  TeV”, 2023. arXiv:2310.03844. Submitted to *JINST*.
- [82] W. Waltenberger, R. Frühwirth, and P. Vanlaer, “Adaptive vertex fitting”, *J. Phys. G* **34** (2007) N343, doi:10.1088/0954-3899/34/12/N01.
- [83] CMS Collaboration, “Technical proposal for the Phase-II upgrade of the Compact Muon Solenoid”, CMS Technical Proposal CERN-LHCC-2015-010, CMS-TDR-15-02, 2015.
- [84] CMS Collaboration, “Pileup mitigation at CMS in 13 TeV data”, *JINST* **15** (2020) P09018, doi:10.1088/1748-0221/15/09/p09018, arXiv:2003.00503.

- [85] D. Bertolini, P. Harris, M. Low, and N. Tran, “Pileup per particle identification”, *JHEP* **10** (2014) 059, doi:10.1007/JHEP10(2014)059, arXiv:1407.6013.
- [86] J. Thaler and K. Van Tilburg, “Identifying boosted objects with  $N$ -subjettiness”, *JHEP* **03** (2011) 015, doi:10.1007/JHEP03(2011)015, arXiv:1011.2268.
- [87] M. Dasgupta, A. Fregoso, S. Marzani, and G. P. Salam, “Towards an understanding of jet substructure”, *JHEP* **09** (2013) 029, doi:10.1007/JHEP09(2013)029, arXiv:1307.0007.
- [88] J. M. Butterworth, A. R. Davison, M. Rubin, and G. P. Salam, “Jet substructure as a new Higgs search channel at the LHC”, *Phys. Rev. Lett.* **100** (2008) 242001, doi:10.1103/PhysRevLett.100.242001, arXiv:0802.2470.
- [89] A. J. Larkoski, S. Marzani, G. Soyez, and J. Thaler, “Soft Drop”, *JHEP* **05** (2014) 146, doi:10.1007/JHEP05(2014)146, arXiv:1402.2657.
- [90] CMS Collaboration, “Identification of heavy-flavour jets with the CMS detector in pp collisions at 13 TeV”, *JINST* **13** (2018) P05011, doi:10.1088/1748-0221/13/05/P05011, arXiv:1712.07158.
- [91] CMS Collaboration, “CMS Phase 1 heavy flavour identification performance and developments”, CMS Detector Performance Summary CMS-DP-2020-019, 2017.
- [92] CMS Collaboration, “Measurements of properties of the Higgs boson decaying to a  $W$  boson pair in pp collisions at  $\sqrt{s} = 13$  TeV”, *Phys. Lett. B* **791** (2019) 96, doi:10.1016/j.physletb.2018.12.073, arXiv:1806.05246.
- [93] CMS Collaboration, “Measurements of inclusive  $W$  and  $Z$  cross sections in pp collisions at  $\sqrt{s} = 7$  TeV”, *JHEP* **01** (2011) 080, doi:10.1007/JHEP01(2011)080, arXiv:1012.2466.
- [94] CMS Collaboration, “An embedding technique to determine  $\tau\tau$  backgrounds in proton-proton collision data”, *JINST* **14** (2019) P06032, doi:10.1088/1748-0221/14/06/P06032, arXiv:1903.01216.
- [95] CMS Collaboration, “Identification techniques for highly boosted  $W$  bosons that decay into hadrons”, *JHEP* **12** (2014) 017, doi:10.1007/JHEP12(2014)017, arXiv:1410.4227.
- [96] R. Barlow and C. Beeston, “Fitting using finite Monte Carlo samples”, *Comput. Phys. Commun.* **77** (1993) 219, doi:10.1016/0010-4655(93)90005-w.
- [97] ATLAS Collaboration, “Measurement of the inelastic proton-proton cross section at  $\sqrt{s} = 13$  TeV with the ATLAS detector at the LHC”, *Phys. Rev. Lett.* **117** (2016) 182002, doi:10.1103/PhysRevLett.117.182002, arXiv:1606.02625.
- [98] CMS Collaboration, “Measurement of the inelastic proton-proton cross section at  $\sqrt{s} = 13$  TeV”, *JHEP* **07** (2018) 161, doi:10.1007/JHEP07(2018)161, arXiv:1802.02613.
- [99] G. Passarino, “Higgs CAT”, *Eur. Phys. J. C* **74** (2014) 2866, doi:10.1140/epjc/s10052-014-2866-7, arXiv:1312.2397.









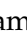


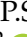


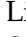
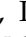


- [100] CMS Collaboration, “Measurement of Higgs boson production and properties in the WW decay channel with leptonic final states”, *JHEP* **01** (2014) 096, doi:10.1007/JHEP01(2014)096, arXiv:1312.1129.
- [101] The ATLAS Collaboration, The CMS Collaboration, The LHC Higgs Combination Group, “Procedure for the LHC Higgs boson search combination in Summer 2011”, Technical Report ATL-PHYS-PUB 2011-11, CMS NOTE 2011/005, 2011.
- [102] CMS Collaboration, “Combined measurements of Higgs boson couplings in proton-proton collisions at  $\sqrt{s} = 13$  TeV”, *Eur. Phys. J. C* **79** (2019) 421, doi:10.1140/epjc/s10052-019-6909-y, arXiv:1809.10733.
- [103] S. S. Wilks, “The large-sample distribution of the likelihood ratio for testing composite hypotheses”, *Annals Math. Statist.* **9** (1938) 60, doi:10.1214/aoms/1177732360.
- [104] G. Cowan, K. Cranmer, E. Gross, and O. Vitells, “Asymptotic formulae for likelihood-based tests of new physics”, *Eur. Phys. J. C* **71** (2011) 1554, doi:10.1140/epjc/s10052-011-1554-0, arXiv:1007.1727.

## A The CMS Collaboration




### Yerevan Physics Institute, Yerevan, Armenia

A. Hayrapetyan, A. Tumasyan<sup>1</sup> 

### Institut für Hochenergiephysik, Vienna, Austria

W. Adam , J.W. Andrejkovic, T. Bergauer , S. Chatterjee , K. Damanakis , M. Dragicevic , P.S. Hussain , M. Jeitler<sup>2</sup> , N. Krammer , A. Li , D. Liko , I. Mikulec , J. Schieck<sup>2</sup> , R. Schöfbeck , D. Schwarz , M. Sonawane , S. Templ , W. Waltenberger , C.-E. Wulz<sup>2</sup> 














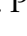
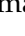
### Universiteit Antwerpen, Antwerpen, Belgium

M.R. Darwish<sup>3</sup> , T. Janssen , P. Van Mechelen 











### Vrije Universiteit Brussel, Brussel, Belgium

E.S. Bols , J. D'Hondt , S. Dansana , A. De Moor , M. Delcourt , H. El Faham , S. Lowette , I. Makarenko , D. Müller , A.R. Sahasransu , S. Tavernier , M. Tytgat<sup>4</sup> , G.P. Van Onsem , S. Van Putte , D. Vannerom 

### Université Libre de Bruxelles, Bruxelles, Belgium

B. Clerbaux , A.K. Das, G. De Lentdecker , L. Favart , P. Gianneios , D. Hohov , J. Jaramillo , A. Khalilzadeh, K. Lee , M. Mahdavikhorrani , A. Malara , S. Paredes , L. Pétré , N. Postiau, L. Thomas , M. Vanden Bemden , C. Vander Velde , P. Vanlaer 




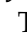


### Ghent University, Ghent, Belgium

M. De Coen , D. Dobur , Y. Hong , J. Knolle , L. Lambrecht , G. Mestdach, K. Mota Amarilo , C. Rendón, A. Samalan, K. Skovpen , N. Van Den Bossche , J. van der Linden , L. Wezenbeek 







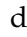











### Université Catholique de Louvain, Louvain-la-Neuve, Belgium

A. Benecke , A. Bethani , G. Bruno , C. Caputo , C. Delaere , I.S. Donertas , A. Giammanco , K. Jaffel , Sa. Jain , V. Lemaitre, J. Lidrych , P. Mastrapasqua , K. Mondal , T.T. Tran , S. Wertz 

### Centro Brasileiro de Pesquisas Físicas, Rio de Janeiro, Brazil

G.A. Alves , E. Coelho , C. Hensel , T. Menezes De Oliveira , A. Moraes , P. Rebello Teles , M. Soeiro

### Universidade do Estado do Rio de Janeiro, Rio de Janeiro, Brazil

W.L. Aldá Júnior , M. Alves Gallo Pereira , M. Barroso Ferreira Filho , H. Brandao Malbouisson , W. Carvalho , J. Chinellato<sup>5</sup>, E.M. Da Costa , G.G. Da Silveira<sup>6</sup> , D. De Jesus Damiao , S. Fonseca De Souza , R. Gomes De Souza, J. Martins<sup>7</sup> , C. Mora Herrera , L. Mundim , H. Nogima , J.P. Pinheiro , A. Santoro , A. Sznajder , M. Thiel , A. Vilela Pereira 

### Universidade Estadual Paulista, Universidade Federal do ABC, São Paulo, Brazil

C.A. Bernardes<sup>6</sup> , L. Calligaris , T.R. Fernandez Perez Tomei , E.M. Gregores , P.G. Mercadante , S.F. Novaes , B. Orzari , Sandra S. Padula 

### Institute for Nuclear Research and Nuclear Energy, Bulgarian Academy of Sciences, Sofia, Bulgaria

A. Aleksandrov , G. Antchev , R. Hadjiiska , P. Iaydjiev , M. Misheva , M. Shopova , G. Sultanov 




### University of Sofia, Sofia, Bulgaria

A. Dimitrov , L. Litov , B. Pavlov , P. Petkov , A. Petrov , E. Shumka 

**Instituto De Alta Investigación, Universidad de Tarapacá, Casilla 7 D, Arica, Chile**

S. Keshri , S. Thakur 





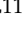




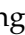

**Beihang University, Beijing, China**

T. Cheng , T. Javaid , L. Yuan 

**Department of Physics, Tsinghua University, Beijing, China**

Z. Hu , J. Liu, K. Yi<sup>8,9</sup> 


**Institute of High Energy Physics, Beijing, China**

G.M. Chen<sup>10</sup> , H.S. Chen<sup>10</sup> , M. Chen<sup>10</sup> , F. Iemmi , C.H. Jiang, A. Kapoor<sup>11</sup> , H. Liao , Z.-A. Liu<sup>12</sup> , R. Sharma<sup>13</sup> , J.N. Song<sup>12</sup>, J. Tao , C. Wang<sup>10</sup>, J. Wang , Z. Wang<sup>10</sup>, H. Zhang 


**State Key Laboratory of Nuclear Physics and Technology, Peking University, Beijing, China**

A. Agapitos , Y. Ban , A. Levin , C. Li , Q. Li , Y. Mao, S.J. Qian , X. Sun , D. Wang , H. Yang, L. Zhang , C. Zhou 

**Sun Yat-Sen University, Guangzhou, China**

Z. You 

**University of Science and Technology of China, Hefei, China**

N. Lu 

**Nanjing Normal University, Nanjing, China**

G. Bauer<sup>14</sup>

**Institute of Modern Physics and Key Laboratory of Nuclear Physics and Ion-beam Application (MOE) - Fudan University, Shanghai, China**

X. Gao<sup>15</sup> , D. Leggat, H. Okawa 





**Zhejiang University, Hangzhou, Zhejiang, China**

Z. Lin , C. Lu , M. Xiao 





**Universidad de Los Andes, Bogota, Colombia**

C. Avila , D.A. Barbosa Trujillo, A. Cabrera , C. Florez , J. Fraga , J.A. Reyes Vega

**Universidad de Antioquia, Medellin, Colombia**

J. Mejia Guisao , F. Ramirez , M. Rodriguez , J.D. Ruiz Alvarez 

**University of Split, Faculty of Electrical Engineering, Mechanical Engineering and Naval Architecture, Split, Croatia**

D. Giljanovic , N. Godinovic , D. Lelas , A. Sculac 









**University of Split, Faculty of Science, Split, Croatia**

M. Kovac , T. Sculac 

**Institute Rudjer Boskovic, Zagreb, Croatia**

P. Bargassa , V. Brigljevic , B.K. Chitroda , D. Ferencek , S. Mishra , A. Starodumov<sup>16</sup> , T. Susa 

**University of Cyprus, Nicosia, Cyprus**

A. Attikis , K. Christoforou , S. Konstantinou , J. Mousa , C. Nicolaou, F. Ptochos , P.A. Razis , H. Rykaczewski, H. Saka , A. Stepennov 

**Charles University, Prague, Czech Republic**

M. Finger , M. Finger Jr. , A. Kveton 

**Escuela Politecnica Nacional, Quito, Ecuador**

E. Ayala 

**Universidad San Francisco de Quito, Quito, Ecuador**

E. Carrera Jarrin 









**Academy of Scientific Research and Technology of the Arab Republic of Egypt, Egyptian Network of High Energy Physics, Cairo, Egypt**

S. Elgammal<sup>17</sup>, A. Ellithi Kamel<sup>18</sup>

**Center for High Energy Physics (CHEP-FU), Fayoum University, El-Fayoum, Egypt**

M.A. Mahmoud , Y. Mohammed 











**National Institute of Chemical Physics and Biophysics, Tallinn, Estonia**

K. Ehataht , M. Kadastik, T. Lange , S. Nandan , C. Nielsen , J. Pata , M. Raidal ,  
L. Tani , C. Veelken 

**Department of Physics, University of Helsinki, Helsinki, Finland**

H. Kirschenmann , K. Osterberg , M. Voutilainen 
















**Helsinki Institute of Physics, Helsinki, Finland**

S. Bharthuar , E. Brücken , F. Garcia , K.T.S. Kallonen , R. Kinnunen, T. Lampén ,  
K. Lassila-Perini , S. Lehti , T. Lindén , L. Martikainen , M. Myllymäki , M.m. Rantanen ,  
H. Siikonen , E. Tuominen , J. Tuominiemi 








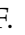
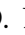




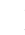








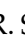
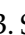





**Lappeenranta-Lahti University of Technology, Lappeenranta, Finland**

P. Luukka , H. Petrow 


**IRFU, CEA, Université Paris-Saclay, Gif-sur-Yvette, France**

M. Besancon , F. Couderc , M. Dejardin , D. Denegri, J.L. Faure, F. Ferri , S. Ganjour ,  
P. Gras , G. Hamel de Monchenault , V. Lohezic , J. Malcles , J. Rander, A. Rosowsky ,  
M.Ö. Sahin , A. Savoy-Navarro<sup>19</sup> , P. Simkina , M. Titov , M. Tornago 





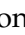













**Laboratoire Leprince-Ringuet, CNRS/IN2P3, Ecole Polytechnique, Institut Polytechnique de Paris, Palaiseau, France**

C. Baldenegro Barrera , F. Beaudette , A. Buchot Perraguin , P. Busson , A. Cappati ,  
C. Charlot , M. Chiusi , F. Damas , O. Davignon , A. De Wit , B.A. Fontana Santos Alves ,  
S. Ghosh , A. Gilbert , R. Granier de Cassagnac , A. Hakimi ,  
B. Harikrishnan , L. Kalipoliti , G. Liu , J. Motta , M. Nguyen , C. Ochando ,  
L. Portales , R. Salerno , J.B. Sauvan , Y. Sirois , A. Tarabini , E. Vernazza , A. Zabi ,  
A. Zghiche 

**Université de Strasbourg, CNRS, IPHC UMR 7178, Strasbourg, France**

J.-L. Agram<sup>20</sup> , J. Andrea , D. Apparú , D. Bloch , J.-M. Brom , E.C. Chabert ,  
C. Collard , S. Falke , U. Goerlach , C. Grimault, R. Haeberle , A.-C. Le Bihan ,  
M. Meena , G. Saha , M.A. Sessini , P. Van Hove 

**Institut de Physique des 2 Infinis de Lyon (IP2I), Villeurbanne, France**

S. Beauceron , B. Blancon , G. Boudoul , N. Chanon , J. Choi , D. Contardo ,  
P. Depasse , C. Dozen<sup>21</sup> , H. El Mamouni, J. Fay , S. Gascon , M. Gouzevitch ,  
C. Greenberg, G. Grenier , B. Ille , I.B. Laktineh, M. Lethuillier , L. Mirabito, S. Perries,  
A. Purohit , M. Vander Donckt , P. Verdier , J. Xiao 


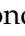



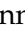

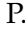







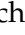

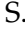



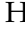


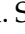
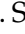
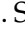
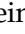


**Georgian Technical University, Tbilisi, Georgia**

G. Adamov, I. Lomidze , Z. Tsamalaidze<sup>16</sup> 

**RWTH Aachen University, I. Physikalisches Institut, Aachen, Germany**

V. Botta , L. Feld , K. Klein , M. Lipinski , D. Meuser , A. Pauls , N. Rówert ,  
M. Teroerde 


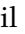



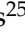
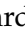

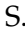






















**RWTH Aachen University, III. Physikalisches Institut A, Aachen, Germany**

S. Diekmann , A. Dodonova , N. Eich , D. Eliseev , F. Engelke , J. Erdmann ,  
M. Erdmann , P. Fackeldey , B. Fischer , T. Hebbeker , K. Hoepfner , F. Ivone ,  
A. Jung , M.y. Lee , L. Mastrolorenzo, F. Mausolf , M. Merschmeyer , A. Meyer ,  
S. Mukherjee , D. Noll , F. Nowotny, A. Pozdnyakov , Y. Rath, W. Redjeb , F. Rehm,  
H. Reithler , U. Sarkar , V. Sarkisovi , A. Schmidt , A. Sharma , J.L. Spah , A. Stein ,  
F. Torres Da Silva De Araujo<sup>22</sup> , L. Vigilante, S. Wiedenbeck , S. Zaleski




















**RWTH Aachen University, III. Physikalisches Institut B, Aachen, Germany**

C. Dziwok , G. Flügge , W. Haj Ahmad<sup>23</sup> , T. Kress , A. Nowack , O. Pooth ,  
A. Stahl , T. Ziemons , A. Zotz 




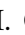










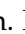












**Deutsches Elektronen-Synchrotron, Hamburg, Germany**

H. Aarup Petersen , M. Aldaya Martin , J. Alimena , S. Amoroso, Y. An , S. Baxter ,  
M. Bayatmakou , H. Becerril Gonzalez , O. Behnke , A. Belvedere , S. Bhattacharya ,  
F. Blekman<sup>24</sup> , K. Borras<sup>25</sup> , A. Campbell , A. Cardini , C. Cheng, F. Colombina ,  
S. Consuegra Rodríguez , G. Correia Silva , M. De Silva , G. Eckerlin, D. Eckstein ,  
L.I. Estevez Banos , O. Filatov , E. Gallo<sup>24</sup> , A. Geiser , A. Giraldi , G. Greau,  
V. Guglielmi , M. Guthoff , A. Hinzmann , A. Jafari<sup>26</sup> , L. Jeppe , N.Z. Jomhari ,  
B. Kaech , M. Kasemann , C. Kleinwort , R. Kogler , M. Komm , D. Krücker ,  
W. Lange, D. Leyva Pernia , K. Lipka<sup>27</sup> , W. Lohmann<sup>28</sup> , R. Mankel , I.-A. Melzer-  
Pellmann , M. Mendizabal Morentin , A.B. Meyer , G. Milella , A. Mussgiller ,  
L.P. Nair , A. Nürnberg , Y. Otariid, J. Park , D. Pérez Adán , E. Ranken ,  
A. Raspereza , B. Ribeiro Lopes , J. Rübenach, A. Saggio , M. Scham<sup>29,25</sup> ,  
S. Schnake<sup>25</sup> , P. Schütze , C. Schwanenberger<sup>24</sup> , D. Selivanova , K. Sharko ,  
M. Shchedrolosiev , R.E. Sosa Ricardo , D. Stafford, F. Vazzoler , A. Ventura Barroso ,  
R. Walsh , Q. Wang , Y. Wen , K. Wichmann, L. Wiens<sup>25</sup> , C. Wissing , Y. Yang ,  
A. Zimmermann Castro Santos 




**University of Hamburg, Hamburg, Germany**

A. Albrecht , S. Albrecht , M. Antonello , S. Bein , L. Benato , S. Bollweg,  
M. Bonanomi , P. Connor , M. Eich, K. El Morabit , Y. Fischer , A. Fröhlich, C. Garbers ,  
E. Garutti , A. Grohsjean , M. Hajheidari, J. Haller , H.R. Jabusch , G. Kasieczka ,  
P. Keicher, R. Klanner , W. Korcari , T. Kramer , V. Kutzner , F. Labe , J. Lange ,  
A. Lobanov , C. Matthies , A. Mehta , L. Moureaux , M. Mrowietz, A. Nigamova ,  
Y. Nissan, A. Paasch , K.J. Pena Rodriguez , T. Quadfasel , B. Raciti , M. Rieger ,  
D. Savoie , J. Schindler , P. Schleper , M. Schröder , J. Schwandt , M. Sommerhalder ,  
H. Stadie , G. Steinbrück , A. Tews, M. Wolf 

**Karlsruher Institut fuer Technologie, Karlsruhe, Germany**

S. Brommer , M. Burkart, E. Butz , T. Chwalek , A. Dierlamm , A. Droll, N. Fal-  
termann , M. Giffels , A. Gottmann , F. Hartmann<sup>30</sup> , R. Hofsaess , M. Horzela ,  
U. Husemann , J. Kieseler , M. Klute , R. Koppenhöfer , J.M. Lawhorn , M. Link,  
A. Lintuluoto , S. Maier , S. Mitra , M. Mormile , Th. Müller , M. Neukum, M. Oh ,  
M. Presilla , G. Quast , K. Rabbertz , B. Regnery , N. Shadskiy , I. Shvetsov ,  
H.J. Simonis , M. Toms , N. Trevisani , R. Ulrich , R.F. Von Cube , M. Wassmer 



S. Wieland , F. Wittig, R. Wolf , X. Zuo 





**Institute of Nuclear and Particle Physics (INPP), NCSR Demokritos, Aghia Paraskevi, Greece**

G. Anagnostou, G. Daskalakis , A. Kyriakis, A. Papadopoulos<sup>30</sup>, A. Stakia 

**National and Kapodistrian University of Athens, Athens, Greece**

P. Kontaxakis , G. Melachroinos, A. Panagiotou, I. Papavergou , I. Paraskevas , N. Saoulidou , K. Theofilatos , E. Tziaferi , K. Vellidis , I. Zisopoulos 

**National Technical University of Athens, Athens, Greece**

G. Bakas , T. Chatzistavrou, G. Karapostoli , K. Kousouris , I. Papakrivopoulos , E. Siamarkou, G. Tsipolitis, A. Zacharopoulou




**University of Ioánnina, Ioánnina, Greece**

K. Adamidis, I. Bestintzanos, I. Evangelou , C. Foudas, C. Kamtsikis, P. Katsoulis, P. Kokkas , P.G. Kosmoglou Kioseoglou , N. Manthos , I. Papadopoulos , J. Strogas 



**HUN-REN Wigner Research Centre for Physics, Budapest, Hungary**

M. Bartók<sup>31</sup> , C. Hajdu , D. Horvath<sup>32,33</sup> , K. Márton, F. Sikler , V. Veszpremi 

**MTA-ELTE Lendület CMS Particle and Nuclear Physics Group, Eötvös Loránd University, Budapest, Hungary**

M. Csanád , K. Farkas , M.M.A. Gadallah<sup>34</sup> , Á. Kadlecik , P. Major , K. Mandal , G. Pásztor , A.J. Rádl<sup>35</sup> , G.I. Veres 




**Faculty of Informatics, University of Debrecen, Debrecen, Hungary**

P. Raics, B. Ujvari , G. Zilizi 















**Institute of Nuclear Research ATOMKI, Debrecen, Hungary**

G. Bencze, S. Czellar, J. Molnar, Z. Szillasi

**Karoly Robert Campus, MATE Institute of Technology, Gyongyos, Hungary**

T. Csorgo<sup>35</sup> , F. Nemes<sup>35</sup> , T. Novak 

**Panjab University, Chandigarh, India**

J. Babbar , S. Bansal , S.B. Beri, V. Bhatnagar , G. Chaudhary , S. Chauhan , N. Dhingra<sup>36</sup> , A. Kaur , A. Kaur , H. Kaur , M. Kaur , S. Kumar , K. Sandeep , T. Sheokand, J.B. Singh , A. Singla 















**University of Delhi, Delhi, India**

A. Ahmed , A. Bhardwaj , A. Chhetri , B.C. Choudhary , A. Kumar , A. Kumar , M. Naimuddin , K. Ranjan , S. Saumya 


**Saha Institute of Nuclear Physics, HBNI, Kolkata, India**

S. Baradia , S. Barman<sup>37</sup> , S. Bhattacharya , S. Dutta , S. Dutta, S. Sarkar

**Indian Institute of Technology Madras, Madras, India**


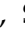
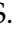

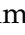
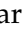

M.M. Ameen , P.K. Behera , S.C. Behera , S. Chatterjee , P. Jana , P. Kalbhor , J.R. Komaragiri<sup>38</sup> , D. Kumar<sup>38</sup> , L. Panwar<sup>38</sup> , P.R. Pujahari , N.R. Saha , A. Sharma , A.K. Sikdar , S. Verma 

**Tata Institute of Fundamental Research-A, Mumbai, India**




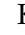





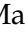


S. Dugad, M. Kumar , G.B. Mohanty , P. Suryadevara

**Tata Institute of Fundamental Research-B, Mumbai, India**








A. Bala , S. Banerjee , R.M. Chatterjee, R.K. Dewanjee<sup>39</sup> , M. Guchait , Sh. Jain 

A. Jaiswal , S. Karmakar , S. Kumar , G. Majumder , K. Mazumdar , S. Parolia ,  
A. Thachayath 

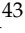


**National Institute of Science Education and Research, An OCC of Homi Bhabha National Institute, Bhubaneswar, Odisha, India**

S. Bahinipati<sup>40</sup> , C. Kar , D. Maity<sup>41</sup> , P. Mal , T. Mishra , V.K. Muraleedharan Nair Bindhu<sup>41</sup> , K. Naskar<sup>41</sup> , A. Nayak<sup>41</sup> , P. Sadangi, P. Saha , S.K. Swain ,  
S. Varghese<sup>41</sup> , D. Vats<sup>41</sup> 

**Indian Institute of Science Education and Research (IISER), Pune, India**

S. Acharya<sup>42</sup> , A. Alpana , S. Dube , B. Gomber<sup>42</sup> , B. Kansal , A. Laha , B. Sahu<sup>42</sup> ,  
S. Sharma , K.Y. Vaish

**Isfahan University of Technology, Isfahan, Iran**

H. Bakhshiansohi<sup>43</sup> , E. Khazaie<sup>44</sup> , M. Zeinali<sup>45</sup> 




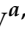

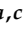




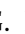


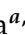

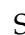

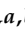





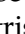



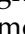
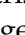

**Institute for Research in Fundamental Sciences (IPM), Tehran, Iran**

S. Chenarani<sup>46</sup> , S.M. Etesami , M. Khakzad , M. Mohammadi Najafabadi 











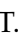

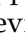

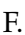


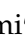



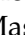
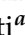


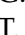

**University College Dublin, Dublin, Ireland**

M. Grunewald 

**INFN Sezione di Bari<sup>a</sup>, Università di Bari<sup>b</sup>, Politecnico di Bari<sup>c</sup>, Bari, Italy**

M. Abbrescia<sup>a,b</sup> , R. Aly<sup>a,c,47</sup> , A. Colaleo<sup>a,b</sup> , D. Creanza<sup>a,c</sup> , B. D'Anzi<sup>a,b</sup> ,  
N. De Filippis<sup>a,c</sup> , M. De Palma<sup>a,b</sup> , A. Di Florio<sup>a,c</sup> , W. Elmetenawee<sup>a,b,47</sup> ,  
L. Fiore<sup>a</sup> , G. Iaselli<sup>a,c</sup> , M. Louka<sup>a,b</sup>, G. Maggi<sup>a,c</sup> , M. Maggi<sup>a</sup>, I. Margjeka<sup>a,b</sup> ,  
V. Mastrapasqua<sup>a,b</sup> , S. My<sup>a,b</sup> , S. Nuzzo<sup>a,b</sup> , A. Pellicchia<sup>a,b</sup> , A. Pompili<sup>a,b</sup> ,  
G. Pugliese<sup>a,c</sup> , R. Radogna<sup>a</sup> , G. Ramirez-Sanchez<sup>a,c</sup> , D. Ramos<sup>a</sup> , A. Ranieri<sup>a</sup> ,  
L. Silvestris<sup>a</sup> , F.M. Simone<sup>a,b</sup> , Ü. Sözbilir<sup>a</sup> , A. Stamerra<sup>a</sup> , R. Venditti<sup>a</sup> ,  
P. Verwilligen<sup>a</sup> , A. Zaza<sup>a,b</sup> 


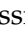
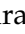






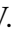
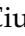
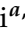



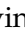
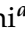
**INFN Sezione di Bologna<sup>a</sup>, Università di Bologna<sup>b</sup>, Bologna, Italy**

G. Abbiendi<sup>a</sup> , C. Battilana<sup>a,b</sup> , D. Bonacorsi<sup>a,b</sup> , L. Borgonovi<sup>a</sup> , R. Campanini<sup>a,b</sup> ,  
P. Capiluppi<sup>a,b</sup> , A. Castro<sup>a,b</sup> , F.R. Cavallo<sup>a</sup> , M. Cuffiani<sup>a,b</sup> , G.M. Dallavalle<sup>a</sup> ,  
T. Diotallevi<sup>a,b</sup> , F. Fabbri<sup>a</sup> , A. Fanfani<sup>a,b</sup> , D. Fasanella<sup>a,b</sup> , P. Giacomelli<sup>a</sup> ,  
L. Giommi<sup>a,b</sup> , C. Grandi<sup>a</sup> , L. Guiducci<sup>a,b</sup> , S. Lo Meo<sup>a,48</sup> , L. Lunerti<sup>a,b</sup> ,  
G. Masetti<sup>a</sup> , F.L. Navarria<sup>a,b</sup> , A. Perrotta<sup>a</sup> , F. Primavera<sup>a,b</sup> , A.M. Rossi<sup>a,b</sup> ,  
T. Rovelli<sup>a,b</sup> , G.P. Siroli<sup>a,b</sup> 

**INFN Sezione di Catania<sup>a</sup>, Università di Catania<sup>b</sup>, Catania, Italy**

S. Costa<sup>a,b,49</sup> , A. Di Mattia<sup>a</sup> , R. Potenza<sup>a,b</sup>, A. Tricomi<sup>a,b,49</sup> , C. Tuve<sup>a,b</sup> 

**INFN Sezione di Firenze<sup>a</sup>, Università di Firenze<sup>b</sup>, Firenze, Italy**

P. Assiouras<sup>a</sup> , G. Barbagli<sup>a</sup> , G. Bardelli<sup>a,b</sup> , B. Camaiani<sup>a,b</sup> , A. Cassese<sup>a</sup> ,  
R. Ceccarelli<sup>a</sup> , V. Ciulli<sup>a,b</sup> , C. Civinini<sup>a</sup> , R. D'Alessandro<sup>a,b</sup> , E. Focardi<sup>a,b</sup> ,  
T. Kello<sup>a</sup>, G. Latino<sup>a,b</sup> , P. Lenzi<sup>a,b</sup> , M. Lizzo<sup>a</sup> , M. Meschini<sup>a</sup> , S. Paoletti<sup>a</sup> ,  
A. Papanastassiou<sup>a,b</sup>, G. Sguazzoni<sup>a</sup> , L. Viliani<sup>a</sup> 

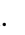






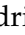
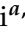






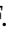

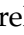


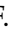


**INFN Laboratori Nazionali di Frascati, Frascati, Italy**

L. Benussi , S. Bianco , S. Meola<sup>50</sup> , D. Piccolo 

**INFN Sezione di Genova<sup>a</sup>, Università di Genova<sup>b</sup>, Genova, Italy**

P. Chatagnon<sup>a</sup> , F. Ferro<sup>a</sup> , E. Robutti<sup>a</sup> , S. Tosi<sup>a,b</sup> 


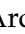


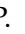






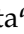

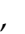



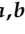



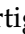






**INFN Sezione di Milano-Bicocca<sup>a</sup>, Università di Milano-Bicocca<sup>b</sup>, Milano, Italy**

A. Benaglia<sup>a</sup> , G. Boldrini<sup>a,b</sup> , F. Brivio<sup>a</sup> , F. Cetorelli<sup>a</sup> , F. De Guio<sup>a,b</sup> , M.E. Dinardo<sup>a,b</sup> , P. Dini<sup>a</sup> , S. Gennai<sup>a</sup> , R. Gerosa<sup>a,b</sup> , A. Ghezzi<sup>a,b</sup> , P. Govoni<sup>a,b</sup> , L. Guzzi<sup>a</sup> , M.T. Lucchini<sup>a,b</sup> , M. Malberti<sup>a</sup> , S. Malvezzi<sup>a</sup> , A. Massironi<sup>a</sup> , D. Menasce<sup>a</sup> , L. Moroni<sup>a</sup> , M. Paganoni<sup>a,b</sup> , D. Pedrini<sup>a</sup> , B.S. Pinolini<sup>a</sup>, S. Ragazzi<sup>a,b</sup> , T. Tabarelli de Fatis<sup>a,b</sup> , D. Zuolo<sup>a</sup> 




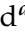


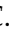

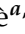


**INFN Sezione di Napoli<sup>a</sup>, Università di Napoli 'Federico II'<sup>b</sup>, Napoli, Italy; Università della Basilicata<sup>c</sup>, Potenza, Italy; Scuola Superiore Meridionale (SSM)<sup>d</sup>, Napoli, Italy**

S. Buontempo<sup>a</sup> , A. Cagnotta<sup>a,b</sup> , F. Carnevali<sup>a,b</sup>, N. Cavallo<sup>a,c</sup> , F. Fabozzi<sup>a,c</sup> , A.O.M. Iorio<sup>a,b</sup> , L. Lista<sup>a,b,51</sup> , P. Paolucci<sup>a,30</sup> , B. Rossi<sup>a</sup> , C. Sciacca<sup>a,b</sup> 







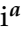



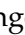

**INFN Sezione di Padova<sup>a</sup>, Università di Padova<sup>b</sup>, Padova, Italy; Università di Trento<sup>c</sup>, Trento, Italy**

R. Ardino<sup>a</sup> , P. Azzi<sup>a</sup> , N. Bacchetta<sup>a,52</sup> , D. Bisello<sup>a,b</sup> , P. Bortignon<sup>a</sup> , A. Bragagnolo<sup>a,b</sup> , R. Carlin<sup>a,b</sup> , P. Checchia<sup>a</sup> , T. Dorigo<sup>a</sup> , F. Gasparini<sup>a,b</sup> , U. Gasparini<sup>a,b</sup> , F. Gonella<sup>a</sup> , E. Lusiani<sup>a</sup> , M. Margoni<sup>a,b</sup> , F. Marini<sup>a</sup> , M. Migliorini<sup>a,b</sup> , J. Pazzini<sup>a,b</sup> , P. Ronchese<sup>a,b</sup> , R. Rossin<sup>a,b</sup> , F. Simonetto<sup>a,b</sup> , G. Strong<sup>a</sup> , M. Tosi<sup>a,b</sup> , A. Triossi<sup>a,b</sup> , S. Ventura<sup>a</sup> , H. Yarar<sup>a,b</sup>, M. Zanetti<sup>a,b</sup> , P. Zotto<sup>a,b</sup> , A. Zucchetta<sup>a,b</sup> , G. Zumerle<sup>a,b</sup> 

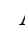



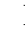


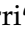




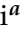





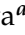

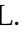

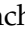
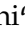






**INFN Sezione di Pavia<sup>a</sup>, Università di Pavia<sup>b</sup>, Pavia, Italy**

S. Abu Zeid<sup>a,53</sup> , C. Aimè<sup>a,b</sup> , A. Braghieri<sup>a</sup> , S. Calzaferri<sup>a</sup> , D. Fiorina<sup>a</sup> , P. Montagna<sup>a,b</sup> , V. Re<sup>a</sup> , C. Riccardi<sup>a,b</sup> , P. Salvini<sup>a</sup> , I. Vai<sup>a,b</sup> , P. Vitulo<sup>a,b</sup> 


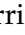



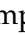
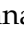
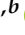


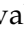
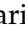

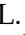
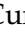
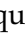
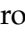


**INFN Sezione di Perugia<sup>a</sup>, Università di Perugia<sup>b</sup>, Perugia, Italy**

S. Ajmal<sup>a,b</sup> , G.M. Bilei<sup>a</sup> , D. Ciangottini<sup>a,b</sup> , L. Fanò<sup>a,b</sup> , M. Magherini<sup>a,b</sup> , G. Mantovani<sup>a,b</sup>, V. Mariani<sup>a,b</sup> , M. Menichelli<sup>a</sup> , F. Moscatelli<sup>a,54</sup> , A. Rossi<sup>a,b</sup> , A. Santocchia<sup>a,b</sup> , D. Spiga<sup>a</sup> , T. Tedeschi<sup>a,b</sup> 


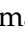

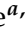





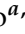



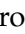


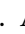
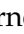

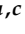


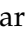
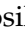






**INFN Sezione di Pisa<sup>a</sup>, Università di Pisa<sup>b</sup>, Scuola Normale Superiore di Pisa<sup>c</sup>, Pisa, Italy; Università di Siena<sup>d</sup>, Siena, Italy**

P. Asenov<sup>a,b</sup> , P. Azzurri<sup>a</sup> , G. Bagliesi<sup>a</sup> , R. Bhattacharya<sup>a</sup> , L. Bianchini<sup>a,b</sup> , T. Boccali<sup>a</sup> , E. Bossini<sup>a</sup> , D. Bruschini<sup>a,c</sup> , R. Castaldi<sup>a</sup> , M.A. Ciocci<sup>a,b</sup> , M. Cipriani<sup>a,b</sup> , V. D'Amante<sup>a,d</sup> , R. Dell'Orso<sup>a</sup> , S. Donato<sup>a</sup> , A. Giassi<sup>a</sup> , F. Ligabue<sup>a,c</sup> , D. Matos Figueiredo<sup>a</sup> , A. Messineo<sup>a,b</sup> , M. Musich<sup>a,b</sup> , F. Palla<sup>a</sup> , A. Rizzi<sup>a,b</sup> , G. Rolandi<sup>a,c</sup> , S. Roy Chowdhury<sup>a</sup> , T. Sarkar<sup>a</sup> , A. Scribano<sup>a</sup> , P. Spagnolo<sup>a</sup> , R. Tenchini<sup>a</sup> , G. Tonelli<sup>a,b</sup> , N. Turini<sup>a,d</sup> , A. Venturi<sup>a</sup> , P.G. Verdini<sup>a</sup> 

**INFN Sezione di Roma<sup>a</sup>, Sapienza Università di Roma<sup>b</sup>, Roma, Italy**







P. Barria<sup>a</sup> , M. Campana<sup>a,b</sup> , F. Cavallari<sup>a</sup> , L. Cunqueiro Mendez<sup>a,b</sup> , D. Del Re<sup>a,b</sup> , E. Di Marco<sup>a</sup> , M. Diemoz<sup>a</sup> , F. Errico<sup>a,b</sup> , E. Longo<sup>a,b</sup> , P. Meridiani<sup>a</sup> , J. Mijuskovic<sup>a,b</sup> , G. Organtini<sup>a,b</sup> , F. Pandolfi<sup>a</sup> , R. Paramatti<sup>a,b</sup> , C. Quaranta<sup>a,b</sup> , S. Rahatlou<sup>a,b</sup> , C. Rovelli<sup>a</sup> , F. Santanastasio<sup>a,b</sup> , L. Soffi<sup>a</sup> 

**INFN Sezione di Torino<sup>a</sup>, Università di Torino<sup>b</sup>, Torino, Italy; Università del Piemonte Orientale<sup>c</sup>, Novara, Italy**











N. Amapane<sup>a,b</sup> , R. Arcidiacono<sup>a,c</sup> , S. Argiro<sup>a,b</sup> , M. Arneodo<sup>a,c</sup> , N. Bartosik<sup>a</sup> , R. Bellan<sup>a,b</sup> , A. Bellora<sup>a,b</sup> , C. Biino<sup>a</sup> , C. Borca<sup>a,b</sup> , N. Cartiglia<sup>a</sup> , M. Costa<sup>a,b</sup> , R. Covarelli<sup>a,b</sup> , N. Demaria<sup>a</sup> , L. Finco<sup>a</sup> , M. Grippo<sup>a,b</sup> , B. Kiani<sup>a,b</sup> , F. Legger<sup>a</sup> , F. Luongo<sup>a,b</sup> , C. Mariotti<sup>a</sup> , L. Markovic<sup>a,b</sup> , S. Maselli<sup>a</sup> , A. Mecca<sup>a,b</sup> , E. Migliore<sup>a,b</sup> , M. Monteno<sup>a</sup> , R. Mulargia<sup>a</sup> , M.M. Obertino<sup>a,b</sup> , G. Ortona<sup>a</sup> , L. Pacher<sup>a,b</sup> , N. Pastrone<sup>a</sup> , M. Pelliccioni<sup>a</sup> , M. Ruspa<sup>a,c</sup> , F. Siviero<sup>a,b</sup> , V. Sola<sup>a,b</sup> , A. Solano<sup>a,b</sup> , A. Staiano<sup>a</sup> , C. Tarricone<sup>a,b</sup> , D. Trocino<sup>a</sup> , G. Umoret<sup>a,b</sup> 

E. Vlasov<sup>a,b</sup> 

**INFN Sezione di Trieste<sup>a</sup>, Università di Trieste<sup>b</sup>, Trieste, Italy**

S. Belforte<sup>a</sup> , V. Candelise<sup>a,b</sup> , M. Casarsa<sup>a</sup> , F. Cossutti<sup>a</sup> , K. De Leo<sup>a,b</sup> ,  
G. Della Ricca<sup>a,b</sup> 



**Kyungpook National University, Daegu, Korea**

S. Dogra , J. Hong , C. Huh , B. Kim , D.H. Kim , J. Kim, H. Lee, S.W. Lee ,  
C.S. Moon , Y.D. Oh , M.S. Ryu , S. Sekmen , Y.C. Yang 

**Department of Mathematics and Physics - GWNNU, Gangneung, Korea**

M.S. Kim 

**Chonnam National University, Institute for Universe and Elementary Particles, Kwangju, Korea**

G. Bak , P. Gwak , H. Kim , D.H. Moon 

**Hanyang University, Seoul, Korea**

E. Asilar , D. Kim , T.J. Kim , J.A. Merlin

**Korea University, Seoul, Korea**

S. Choi , S. Han, B. Hong , K. Lee, K.S. Lee , S. Lee , J. Park, S.K. Park, J. Yoo 






**Kyung Hee University, Department of Physics, Seoul, Korea**

J. Goh , S. Yang 


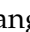





**Sejong University, Seoul, Korea**

H. S. Kim , Y. Kim, S. Lee

**Seoul National University, Seoul, Korea**

J. Almond, J.H. Bhyun, J. Choi , W. Jun , J. Kim , S. Ko , H. Kwon , H. Lee , J. Lee ,  
J. Lee , B.H. Oh , S.B. Oh , H. Seo , U.K. Yang, I. Yoon 

**University of Seoul, Seoul, Korea**

W. Jang , D.Y. Kang, Y. Kang , S. Kim , B. Ko, J.S.H. Lee , Y. Lee , I.C. Park , Y. Roh,  
I.J. Watson 


**Yonsei University, Department of Physics, Seoul, Korea**

S. Ha , H.D. Yoo 

**Sungkyunkwan University, Suwon, Korea**

M. Choi , M.R. Kim , H. Lee, Y. Lee , I. Yu 


**College of Engineering and Technology, American University of the Middle East (AUM),  
Dasman, Kuwait**

T. Beyrouthy, Y. Maghrbi 

**Riga Technical University, Riga, Latvia**

K. Dreimanis , A. Gaile , G. Pikurs, A. Potrebko , M. Seidel , V. Veckalns<sup>55</sup> 

**University of Latvia (LU), Riga, Latvia**

N.R. Strautnieks 

**Vilnius University, Vilnius, Lithuania**

M. Ambrozas , A. Juodagalvis , A. Rinkevicius , G. Tamulaitis 

**National Centre for Particle Physics, Universiti Malaya, Kuala Lumpur, Malaysia**

N. Bin Norjoharuddeen , I. Yusuff<sup>56</sup> , Z. Zolkapli

**Universidad de Sonora (UNISON), Hermosillo, Mexico**

J.F. Benitez , A. Castaneda Hernandez , H.A. Encinas Acosta, L.G. Gallegos Maríñez, M. León Coello , J.A. Murillo Quijada , A. Sehrawat , L. Valencia Palomo 

**Centro de Investigacion y de Estudios Avanzados del IPN, Mexico City, Mexico**

G. Ayala , H. Castilla-Valdez , H. Crotte Ledesma, E. De La Cruz-Burelo , I. Heredia-De La Cruz<sup>57</sup> , R. Lopez-Fernandez , C.A. Mondragon Herrera, A. Sánchez Hernández 


**Universidad Iberoamericana, Mexico City, Mexico**

C. Oropeza Barrera , M. Ramírez García 

**Benemerita Universidad Autonoma de Puebla, Puebla, Mexico**

I. Bautista , I. Pedraza , H.A. Salazar Ibarguen , C. Uribe Estrada 

**University of Montenegro, Podgorica, Montenegro**

I. Bubanja, N. Raicevic 

**University of Canterbury, Christchurch, New Zealand**

P.H. Butler 







**National Centre for Physics, Quaid-I-Azam University, Islamabad, Pakistan**

A. Ahmad , M.I. Asghar, A. Awais , M.I.M. Awan, H.R. Hoorani , W.A. Khan 







**AGH University of Krakow, Faculty of Computer Science, Electronics and Telecommunications, Krakow, Poland**

V. Avati, L. Grzanka , M. Malawski 

**National Centre for Nuclear Research, Swierk, Poland**

H. Bialkowska , M. Bluj , B. Boimska , M. Górski , M. Kazana , M. Szeleper , P. Zalewski 

















**Institute of Experimental Physics, Faculty of Physics, University of Warsaw, Warsaw, Poland**

K. Bunkowski , K. Doroba , A. Kalinowski , M. Konecki , J. Krolikowski , A. Muhammad 

**Warsaw University of Technology, Warsaw, Poland**

K. Pozniak , W. Zabolotny 



**Laboratório de Instrumentação e Física Experimental de Partículas, Lisboa, Portugal**

M. Araujo , D. Bastos , C. Beirão Da Cruz E Silva , A. Boletti , M. Bozzo , T. Camporesi , G. Da Molin , P. Faccioli , M. Gallinaro , J. Hollar , N. Leonardo , T. Niknejad , A. Petrilli , M. Pisano , J. Seixas , J. Varela , J.W. Wulff




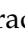


















**Faculty of Physics, University of Belgrade, Belgrade, Serbia**

P. Adzic , P. Milenovic 

**VINCA Institute of Nuclear Sciences, University of Belgrade, Belgrade, Serbia**

M. Dordevic , J. Milosevic , V. Rekovic

**Centro de Investigaciones Energéticas Medioambientales y Tecnológicas (CIEMAT), Madrid, Spain**

M. Aguilar-Benitez, J. Alcaraz Maestre , Cristina F. Bedoya , M. Cepeda , M. Cerrada , N. Colino , B. De La Cruz , A. Delgado Peris , A. Escalante Del Valle , D. Fernández Del Val , J.P. Fernández Ramos , J. Flix , M.C. Fouz , O. Gonzalez Lopez , S. Goy Lopez , J.M. Hernandez , M.I. Josa , D. Moran , C. M. Morcillo Perez , Á. Navarro Tobar , C. Perez Dengra , A. Pérez-Calero Yzquierdo , J. Puerta Pelayo 
















I. Redondo , D.D. Redondo Ferrero , L. Romero, S. Sánchez Navas , L. Urda Gómez , J. Vazquez Escobar , C. Willmott














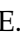




**Universidad Autónoma de Madrid, Madrid, Spain**

J.F. de Trocóniz 

**Universidad de Oviedo, Instituto Universitario de Ciencias y Tecnologías Espaciales de Asturias (ICTEA), Oviedo, Spain**

B. Alvarez Gonzalez , J. Cuevas , J. Fernandez Menendez , S. Folgueras , I. Gonzalez Caballero , J.R. González Fernández , E. Palencia Cortezon , C. Ramón Álvarez , V. Rodríguez Bouza , A. Soto Rodríguez , A. Trapote , C. Vico Villalba , P. Vischia 

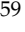



**Instituto de Física de Cantabria (IFCA), CSIC-Universidad de Cantabria, Santander, Spain**

S. Bhowmik , S. Blanco Fernández , J.A. Brochero Cifuentes , I.J. Cabrillo , A. Calderon , J. Duarte Campderros , M. Fernandez , G. Gomez , C. Lasaosa García , C. Martinez Rivero , P. Martinez Ruiz del Arbol , F. Matorras , P. Matorras Cuevas , E. Navarrete Ramos , J. Piedra Gomez , L. Scodellaro , I. Vila , J.M. Vizan Garcia 

**University of Colombo, Colombo, Sri Lanka**

M.K. Jayananda , B. Kailasapathy<sup>58</sup> , D.U.J. Sonnadara , D.D.C. Wickramarathna 

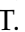
**University of Ruhuna, Department of Physics, Matara, Sri Lanka**

W.G.D. Dharmaratna<sup>59</sup> , K. Liyanage , N. Perera , N. Wickramage 







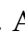
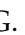








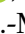





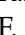
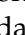


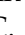







**CERN, European Organization for Nuclear Research, Geneva, Switzerland**

D. Abbaneo , C. Amendola , E. Auffray , G. Auzinger , J. Baechler, D. Barney , A. Bermúdez Martínez , M. Bianco , B. Bilin , A.A. Bin Anuar , A. Bocci , C. Botta , E. Brondolin , C. Caillol , G. Cerminara , N. Chernyavskaya , D. d'Enterria , A. Dabrowski , A. David , A. De Roeck , M.M. Defranchis , M. Deile , M. Dobson , L. Forthomme , G. Franzoni , W. Funk , S. Giani, D. Gigi, K. Gill , F. Glege , L. Gouskos , M. Haranko , J. Hegeman , B. Huber, V. Innocente , T. James , P. Janot , S. Laurila , P. Lecoq , E. Leutgeb , C. Lourenço , B. Maier , L. Malgeri , M. Mannelli , A.C. Marini , M. Matthewman, F. Meijers , S. Mersi , E. Meschi , V. Milosevic , F. Monti , F. Moortgat , M. Mulders , I. Neutelings , S. Orfanelli, F. Pantaleo , G. Petrucciani , A. Pfeiffer , M. Pierini , D. Piparo , H. Qu , D. Rabady , G. Reales Gutiérrez, M. Rovere , H. Sakulin , S. Scarfi , C. Schwick, M. Selvaggi , A. Sharma , K. Shchelina , P. Silva , P. Sphicas<sup>60</sup> , A.G. Stahl Leitner , A. Steen , S. Summers , D. Treille , P. Tropea , A. Tsirou, D. Walter , J. Wanczyk<sup>61</sup> , J. Wang, S. Wuchterl , P. Zehetner , P. Zejdl , W.D. Zeuner






















**Paul Scherrer Institut, Villigen, Switzerland**

T. Bevilacqua<sup>62</sup> , L. Caminada<sup>62</sup> , A. Ebrahimi , W. Erdmann , R. Horisberger , Q. Ingram , H.C. Kaestli , D. Kotlinski , C. Lange , M. Missiroli<sup>62</sup> , L. Noehte<sup>62</sup> , T. Rohe 





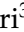


**ETH Zurich - Institute for Particle Physics and Astrophysics (IPA), Zurich, Switzerland**

T.K. Aarrestad , K. Androsova<sup>61</sup> , M. Backhaus , A. Calandri , C. Cazzaniga , K. Datta , A. De Cosa , G. Dissertori , M. Dittmar, M. Donegà , F. Eble , M. Galli , K. Gedia , F. Glessgen , C. Grab , D. Hits , W. Lustermann , A.-M. Lyon , R.A. Manzoni , M. Marchegiani , L. Marchese , C. Martin Perez , A. Mascellani<sup>61</sup> , F. Nessi-Tedaldi , F. Pauss , V. Perovic , S. Pigazzini , C. Reissel , T. Reitenspiess , B. Ristic , F. Riti , D. Ruini, R. Seidita , J. Steggemann<sup>61</sup> , D. Valsecchi , R. Wallny 





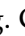














**Universität Zürich, Zurich, Switzerland**

C. Amsler<sup>63</sup> , P. Bäertschi , D. Brzhechko , M.F. Canelli , K. Cormier , J.K. Heikkilä , M. Huwiler , W. Jin , A. Jofrehei , B. Kilminster , S. Leontsinis , S.P. Liechti , A. Macchiolo , P. Meiring , U. Molinatti , A. Reimers , P. Robmann , S. Sanchez Cruz , M. Senger , Y. Takahashi , R. Tramontano 

#### National Central University, Chung-Li, Taiwan

C. Adloff<sup>64</sup> , D. Bhowmik , C.M. Kuo , W. Lin , P.K. Rout , P.C. Tiwari<sup>38</sup> , S.S. Yu 


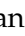
















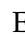

#### National Taiwan University (NTU), Taipei, Taiwan

L. Ceard , Y. Chao , K.F. Chen , P.s. Chen , Z.g. Chen , A. De Iorio , W.-S. Hou , T.h. Hsu , Y.w. Kao , R. Khurana , G. Kole , Y.y. Li , R.-S. Lu , E. Paganis , X.f. Su , J. Thomas-Wilsker , L.s. Tsai , H.y. Wu , E. Yazgan 

#### High Energy Physics Research Unit, Department of Physics, Faculty of Science, Chulalongkorn University, Bangkok, Thailand

C. Asawatrangkuldee , N. Srimanobhas , V. Wachirapusanand 

#### Çukurova University, Physics Department, Science and Art Faculty, Adana, Turkey

D. Agyel , F. Boran , Z.S. Demiroglu , F. Dolek , I. Dumanoglu<sup>65</sup> , E. Eskut , Y. Guler<sup>66</sup> , E. Gurpinar Guler<sup>66</sup> , C. Isik , O. Kara , A. Kayis Topaksu , U. Kiminsu , G. Onengut , K. Ozdemir<sup>67</sup> , A. Polatoz , B. Tali<sup>68</sup> , U.G. Tok , S. Turkcapar , E. Uslan , I.S. Zorbakir 

#### Middle East Technical University, Physics Department, Ankara, Turkey

M. Yalvac<sup>69</sup> 


#### Bogazici University, Istanbul, Turkey

B. Akgun , I.O. Atakisi , E. Gülmez , M. Kaya<sup>70</sup> , O. Kaya<sup>71</sup> , S. Tekten<sup>72</sup> 

#### Istanbul Technical University, Istanbul, Turkey

A. Cakir , K. Cankocak<sup>65,73</sup> , Y. Komurcu , S. Sen<sup>74</sup> 

#### Istanbul University, Istanbul, Turkey

O. Aydilek , S. Cerci<sup>68</sup> , V. Epshteyn , B. Hacisahinoglu , I. Hos<sup>75</sup> , B. Kaynak , S. Ozkorucuklu , O. Potok , H. Sert , C. Simsek , C. Zorbilmez 

#### Yildiz Technical University, Istanbul, Turkey

B. Isildak<sup>76</sup> , D. Sunar Cerci<sup>68</sup> 



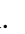





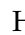








#### Institute for Scintillation Materials of National Academy of Science of Ukraine, Kharkiv, Ukraine

A. Boyaryntsev , B. Grynyov 











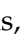










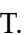
#### National Science Centre, Kharkiv Institute of Physics and Technology, Kharkiv, Ukraine

L. Levchuk 







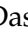







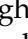


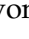
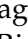
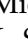



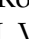
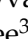









#### University of Bristol, Bristol, United Kingdom

D. Anthony , J.J. Brooke , A. Bundock , F. Bury , E. Clement , D. Cussans , H. Flacher , M. Glowacki , J. Goldstein , H.F. Heath , L. Kreczko , S. Paramesvaran , S. Seif El Nasr-Storey , V.J. Smith , N. Stylianou<sup>77</sup> , K. Walkingshaw Pass , R. White 




#### Rutherford Appleton Laboratory, Didcot, United Kingdom

A.H. Ball , K.W. Bell , A. Belyaev<sup>78</sup> , C. Brew , R.M. Brown , D.J.A. Cockerill , C. Cooke , K.V. Ellis , K. Harder , S. Harper , M.-L. Holmberg<sup>79</sup> , J. Linacre , K. Manolopoulos , D.M. Newbold , E. Olaiya , D. Petyt , T. Reis , G. Salvi , T. Schuh , C.H. Shepherd-Themistocleous , I.R. Tomalin , T. Williams 


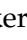








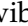
**Imperial College, London, United Kingdom**

R. Bainbridge , P. Bloch , C.E. Brown , O. Buchmuller, V. Cacchio, C.A. Carrillo Montoya , G.S. Chahal<sup>80</sup> , D. Colling , J.S. Dancu, I. Das , P. Dauncey , G. Davies , J. Davies, M. Della Negra , S. Fayer, G. Fedi , G. Hall , M.H. Hassanshahi , A. Howard, G. Iles , M. Knight , J. Langford , J. León Holgado , L. Lyons , A.-M. Magnan , S. Malik, M. Mieskolainen , J. Nash<sup>81</sup> , M. Pesaresi , B.C. Radburn-Smith , A. Richards, A. Rose , K. Savva , C. Seez , R. Shukla , A. Tapper , K. Uchida , G.P. Uttley , L.H. Vage, T. Virdee<sup>30</sup> , M. Vojinovic , N. Wardle , D. Winterbottom 

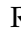




**Brunel University, Uxbridge, United Kingdom**

K. Coldham, J.E. Cole , A. Khan, P. Kyberd , I.D. Reid 

**Baylor University, Waco, Texas, USA**

S. Abdullin , A. Brinkerhoff , B. Caraway , J. Dittmann , K. Hatakeyama , J. Hiltbrand , B. McMaster , M. Saunders , S. Sawant , C. Sutantawibul , J. Wilson 

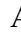






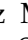
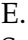


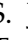

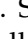




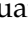

**Catholic University of America, Washington, DC, USA**

R. Bartek , A. Dominguez , C. Huerta Escamilla, A.E. Simsek , R. Uniyal , A.M. Vargas Hernandez 





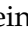




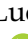
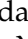
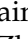
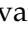

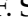
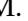

**The University of Alabama, Tuscaloosa, Alabama, USA**

B. Bam , R. Chudasama , S.I. Cooper , S.V. Gleyzer , C.U. Perez , P. Rumerio<sup>82</sup> , E. Usai , R. Yi 





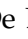





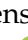

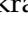





**Boston University, Boston, Massachusetts, USA**

A. Akpinar , D. Arcaro , C. Cosby , Z. Demiralgi , C. Erice , C. Fangmeier , C. Fernandez Madrazo , E. Fontanesi , D. Gastler , F. Golf , S. Jeon , I. Reed , J. Rohlf , K. Salyer , D. Sperka , D. Spitzbart , I. Suarez , A. Tsatsos , S. Yuan , A.G. Zecchinelli 

**Brown University, Providence, Rhode Island, USA**

G. Benelli , X. Coubez<sup>25</sup>, D. Cutts , M. Hadley , U. Heintz , J.M. Hogan<sup>83</sup> , T. Kwon , G. Landsberg , K.T. Lau , D. Li , J. Luo , S. Mondal , M. Narain<sup>†</sup> , N. Pervan , S. Sagir<sup>84</sup> , F. Simpson , M. Stamenkovic , W.Y. Wong, X. Yan , W. Zhang

**University of California, Davis, Davis, California, USA**

S. Abbott , J. Bonilla , C. Brainerd , R. Breedon , M. Calderon De La Barca Sanchez , M. Chertok , M. Citron , J. Conway , P.T. Cox , R. Erbacher , F. Jensen , O. Kukral , G. Mocellin , M. Mulhearn , D. Pellett , W. Wei , Y. Yao , F. Zhang 




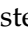
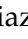


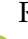


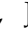

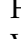





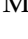
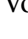
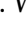

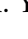
**University of California, Los Angeles, California, USA**

M. Bachtis , R. Cousins , A. Datta , G. Flores Avila, J. Hauser , M. Ignatenko , M.A. Iqbal , T. Lam , E. Manca , A. Nunez Del Prado, D. Saltzberg , V. Valuev 

**University of California, Riverside, Riverside, California, USA**




R. Clare , J.W. Gary , M. Gordon, G. Hanson , W. Si , S. Wimpenny<sup>†</sup> 

**University of California, San Diego, La Jolla, California, USA**











J.G. Branson , S. Cittolin , S. Cooperstein , D. Diaz , J. Duarte , L. Giannini , J. Guiang , R. Kansal , V. Krutelyov , R. Lee , J. Letts , M. Masciovecchio , F. Mokhtar , S. Mukherjee , M. Pieri , M. Quinnan , B.V. Sathia Narayanan , V. Sharma , M. Tadel , E. Vourliotis , F. Würthwein , Y. Xiang , A. Yagil 

**University of California, Santa Barbara - Department of Physics, Santa Barbara, California, USA**





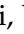













A. Barzdukas , L. Brennan , C. Campagnari , A. Dorsett , J. Incandela , J. Kim , A.J. Li , P. Masterson , H. Mei , J. Richman , U. Sarica , R. Schmitz , F. Setti , J. Sheplock , D. Stuart , T.Á. Vami , S. Wang 















#### California Institute of Technology, Pasadena, California, USA

A. Bornheim , O. Cerri , A. Latorre , J. Mao , H.B. Newman , M. Spiropulu , J.R. Vlimant , C. Wang , S. Xie , R.Y. Zhu 
















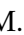


#### Carnegie Mellon University, Pittsburgh, Pennsylvania, USA

J. Alison , S. An , M.B. Andrews , P. Bryant , M. Cremonesi , V. Dutta , T. Ferguson , A. Harilal , C. Liu , T. Mudholkar , S. Murthy , P. Palit , M. Paulini , A. Roberts , A. Sanchez , W. Terrill 



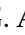













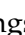















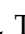








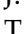

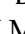




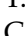
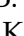





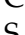
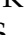





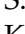
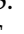
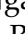
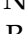
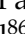


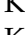
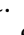
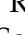

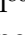
#### University of Colorado Boulder, Boulder, Colorado, USA

J.P. Cumalat , W.T. Ford , A. Hart , A. Hassani , G. Karathanasis , E. MacDonald , N. Manganelli , A. Perloff , C. Savard , N. Schonbeck , K. Stenson , K.A. Ulmer , S.R. Wagner , N. Zipper 


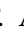



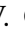
















#### Cornell University, Ithaca, New York, USA

J. Alexander , S. Bright-Thonney , X. Chen , D.J. Cranshaw , J. Fan , X. Fan , D. Gadkari , S. Hogan , P. Kotamnives , J. Monroy , M. Oshiro , J.R. Patterson , J. Reichert , M. Reid , A. Ryd , J. Thom , P. Wittich , R. Zou 

















#### Fermi National Accelerator Laboratory, Batavia, Illinois, USA

M. Albrow , M. Alyari , O. Amram , G. Apollinari , A. Apresyan , L.A.T. Bauerdick , D. Berry , J. Berryhill , P.C. Bhat , K. Burkett , J.N. Butler , A. Canepa , G.B. Cerati , H.W.K. Cheung , F. Chlebana , G. Cummings , J. Dickinson , I. Dutta , V.D. Elvira , Y. Feng , J. Freeman , A. Gandrakota , Z. Gecse , L. Gray , D. Green , A. Grummer , S. Grünendahl , D. Guerrero , O. Gutsche , R.M. Harris , R. Heller , T.C. Herwig , J. Hirschauer , L. Horyn , B. Jayatilaka , S. Jindariani , M. Johnson , U. Joshi , T. Klijnsma , B. Klima , K.H.M. Kwok , S. Lammel , D. Lincoln , R. Lipton , T. Liu , C. Madrid , K. Maeshima , C. Mantilla , D. Mason , P. McBride , P. Merkel , S. Mrenna , S. Nahn , J. Ngadiuba , D. Noonan , V. Papadimitriou , N. Pastika , K. Pedro , C. Pena<sup>85</sup> , F. Ravera , A. Reinsvold Hall<sup>86</sup> , L. Ristori , E. Sexton-Kennedy , N. Smith , A. Soha , L. Spiegel , S. Stoynev , J. Strait , L. Taylor , S. Tkaczyk , N.V. Tran , L. Uplegger , E.W. Vaandering , I. Zoi 

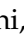
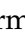






#### University of Florida, Gainesville, Florida, USA

C. Aruta , P. Avery , D. Bourilkov , L. Cadamuro , P. Chang , V. Cherepanov , R.D. Field , E. Koenig , M. Kolosova , J. Konigsberg , A. Korytov , K.H. Lo , K. Matchev , N. Menendez , G. Mitselmakher , K. Mohrman , A. Muthirakalayil Madhu , N. Rawal , D. Rosenzweig , S. Rosenzweig , K. Shi , J. Wang 

















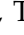





#### Florida State University, Tallahassee, Florida, USA

T. Adams , A. Al Kadhimi , A. Askew , S. Bower , R. Habibullah , V. Hagopian , R. Hashmi , R.S. Kim , S. Kim , T. Kolberg , G. Martinez , H. Prosper , P.R. Prova , M. Wulansatiti , R. Yohay , J. Zhang 








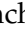


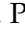
#### Florida Institute of Technology, Melbourne, Florida, USA

B. Alsufyani , M.M. Baarmand , S. Butalla , T. Elkafrawy<sup>53</sup> , M. Hohlmann , R. Kumar Verma , M. Rahmani , E. Yanes 





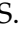





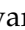
#### University of Illinois Chicago, Chicago, USA, Chicago, USA

M.R. Adams , A. Baty , C. Bennett, R. Cavanaugh , R. Escobar Franco , O. Evdokimov , C.E. Gerber , D.J. Hofman , J.h. Lee , D. S. Lemos , A.H. Merrit , C. Mills , S. Nanda , G. Oh , B. Ozek , D. Pilipovic , R. Pradhan , T. Roy , S. Rudrabhatla , M.B. Tonjes , N. Varelas , Z. Ye , J. Yoo 


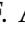



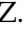




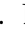











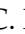

#### **The University of Iowa, Iowa City, Iowa, USA**

M. Alhousseini , D. Blend, K. Dilsiz<sup>87</sup> , L. Emediato , G. Karaman , O.K. Köseyan , J.-P. Merlo, A. Mestvirishvili<sup>88</sup> , J. Nachtman , O. Neogi, H. Ogul<sup>89</sup> , Y. Onel , A. Penzo , C. Snyder, E. Tiras<sup>90</sup> 



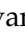
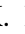
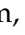


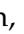
#### **Johns Hopkins University, Baltimore, Maryland, USA**

B. Blumenfeld , L. Corcodilos , J. Davis , A.V. Gritsan , L. Kang , S. Kyriacou , P. Maksimovic , M. Roguljic , J. Roskes , S. Sekhar , M. Swartz 

#### **The University of Kansas, Lawrence, Kansas, USA**

A. Abreu , L.F. Alcerro Alcerro , J. Anguiano , P. Baringer , A. Bean , Z. Flowers , D. Grove , J. King , G. Krintiras , M. Lazarovits , C. Le Mahieu , C. Lindsey, J. Marquez , N. Minafra , M. Murray , M. Nickel , M. Pitt , S. Popescu<sup>91</sup> , C. Rogan , C. Royon , R. Salvatico , S. Sanders , C. Smith , Q. Wang , G. Wilson 





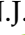
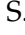









#### **Kansas State University, Manhattan, Kansas, USA**

B. Allmond , A. Ivanov , K. Kaadze , A. Kalogeropoulos , D. Kim, Y. Maravin , K. Nam, J. Natoli , D. Roy , G. Sorrentino 






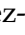

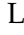


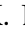
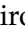



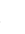






#### **Lawrence Livermore National Laboratory, Livermore, California, USA**

F. Rebassoo , D. Wright 













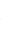

#### **University of Maryland, College Park, Maryland, USA**

A. Baden , A. Belloni , Y.M. Chen , S.C. Eno , N.J. Hadley , S. Jabeen , R.G. Kellogg , T. Koeth , Y. Lai , S. Lascio , A.C. Mignerey , S. Nabili , C. Palmer , C. Papageorgakis , M.M. Paranipe, L. Wang 

#### **Massachusetts Institute of Technology, Cambridge, Massachusetts, USA**

J. Bendavid , I.A. Cali , M. D'Alfonso , J. Eysermans , C. Freer , G. Gomez-Ceballos , M. Goncharov, G. Grosso, P. Harris, D. Hoang, D. Kovalskyi , J. Krupa , L. Lavezzo , Y.-J. Lee , K. Long , C. Mironov , A. Novak , C. Paus , D. Rankin , C. Roland , G. Roland , S. Rothman , G.S.F. Stephans , Z. Wang , B. Wyslouch , T. J. Yang 



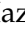

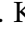
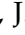




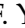

#### **University of Minnesota, Minneapolis, Minnesota, USA**

B. Crossman , B.M. Joshi , C. Kapsiak , M. Krohn , D. Mahon , J. Mans , B. Marzocchi , S. Pandey , M. Revering , R. Rusack , R. Saradhy , N. Schroeder , N. Strobbe , M.A. Wadud 

#### **University of Mississippi, Oxford, Mississippi, USA**

L.M. Cremaldi 














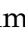



#### **University of Nebraska-Lincoln, Lincoln, Nebraska, USA**

K. Bloom , D.R. Claes , G. Haza , J. Hossain , C. Joo , I. Kravchenko , J.E. Siado , W. Tabb , A. Vagnerini , A. Wightman , F. Yan , D. Yu 



#### **State University of New York at Buffalo, Buffalo, New York, USA**

H. Bandyopadhyay , L. Hay , I. Iashvili , A. Kharchilava , M. Morris , D. Nguyen , S. Rappoccio , H. Rejeb Sfar, A. Williams 





















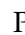





#### **Northeastern University, Boston, Massachusetts, USA**

G. Alverson , E. Barberis , J. Dervan, Y. Haddad , Y. Han , A. Krishna , J. Li , M. Lu , G. Madigan , R. McCarthy , D.M. Morse , V. Nguyen , T. Orimoto , A. Parker , L. Skinnari , A. Tishelman-Charny , B. Wang , D. Wood 






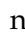


#### **Northwestern University, Evanston, Illinois, USA**

S. Bhattacharya , J. Bueghly, Z. Chen , S. Dittmer , K.A. Hahn , Y. Liu , Y. Miao , D.G. Monk , M.H. Schmitt , A. Taliercio , M. Velasco



















#### **University of Notre Dame, Notre Dame, Indiana, USA**

G. Agarwal , R. Band , R. Bucci, S. Castells , A. Das , R. Goldouzian , M. Hildreth , K.W. Ho , K. Hurtado Anampa , T. Ivanov , C. Jessop , K. Lannon , J. Lawrence , N. Loukas , L. Lutton , J. Mariano, N. Marinelli, I. Mcalister, T. McCauley , C. Mcgrady , C. Moore , Y. Musienko<sup>16</sup> , H. Nelson , M. Osherson , A. Piccinelli , R. Ruchti , A. Townsend , Y. Wan, M. Wayne , H. Yockey, M. Zarucki , L. Zygala 

#### **The Ohio State University, Columbus, Ohio, USA**

A. Basnet , B. Bylsma, M. Carrigan , L.S. Durkin , C. Hill , M. Joyce , M. Nunez Ornelas , K. Wei, B.L. Winer , B. R. Yates 



















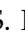

#### **Princeton University, Princeton, New Jersey, USA**

F.M. Addesa , H. Bouchamaoui , P. Das , G. Dezoort , P. Elmer , A. Frankenthal , B. Greenberg , N. Haubrich , G. Kopp , S. Kwan , D. Lange , A. Loeliger , D. Marlow , I. Ojalvo , J. Olsen , A. Shevelev , D. Stickland , C. Tully 




#### **University of Puerto Rico, Mayaguez, Puerto Rico, USA**

S. Malik 












#### **Purdue University, West Lafayette, Indiana, USA**

A.S. Bakshi , V.E. Barnes , S. Chandra , R. Chawla , S. Das , A. Gu , L. Gutay, M. Jones , A.W. Jung , D. Kondratyev , A.M. Koshy, M. Liu , G. Negro , N. Neumeister , G. Paspalaki , S. Piperov , V. Scheurer, J.F. Schulte , M. Stojanovic , J. Thieman , A. K. Viridi , F. Wang , W. Xie 

#### **Purdue University Northwest, Hammond, Indiana, USA**

J. Dolen , N. Parashar , A. Pathak 

#### **Rice University, Houston, Texas, USA**

D. Acosta , T. Carnahan , K.M. Ecklund , P.J. Fernández Manteca , S. Freed, P. Gardner, F.J.M. Geurts , W. Li , O. Miguel Colin , B.P. Padley , R. Redjimi, J. Rotter , E. Yigitbasi , Y. Zhang 















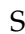
#### **University of Rochester, Rochester, New York, USA**

A. Bodek , P. de Barbaro , R. Demina , J.L. Dulemba , A. Garcia-Bellido , O. Hindrichs , A. Khukhunaishvili , N. Parmar, P. Parygin<sup>92</sup> , E. Popova<sup>92</sup> , R. Taus 




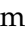

#### **The Rockefeller University, New York, New York, USA**

K. Goulianos 

#### **Rutgers, The State University of New Jersey, Piscataway, New Jersey, USA**

B. Chiarito, J.P. Chou , Y. Gershtein , E. Halkiadakis , M. Heindl , D. Jaroslowski , O. Karacheban<sup>28</sup> , I. Laflotte , A. Lath , R. Montalvo, K. Nash, H. Routray , S. Salur , S. Schnetzer, S. Somalwar , R. Stone , S.A. Thayil , S. Thomas, J. Vora , H. Wang 

#### **University of Tennessee, Knoxville, Tennessee, USA**






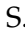




H. Acharya, D. Ally , A.G. Delannoy , S. Fiorendi , S. Higginbotham , T. Holmes 

A.R. Kanuganti , N. Karunarathna , L. Lee , E. Nibigira , S. Spanier 












**Texas A&M University, College Station, Texas, USA**

D. Aebi , M. Ahmad , O. Bouhali<sup>93</sup> , R. Eusebi , J. Gilmore , T. Huang , T. Kamon<sup>94</sup> , H. Kim , S. Luo , R. Mueller , D. Overton , D. Rathjens , A. Safonov 








**Texas Tech University, Lubbock, Texas, USA**

N. Akchurin , J. Damgov , V. Hegde , A. Hussain , Y. Kazhykarim, K. Lamichhane , S.W. Lee , A. Mankel , T. Peltola , I. Volobouev , A. Whitbeck 

**Vanderbilt University, Nashville, Tennessee, USA**

E. Appelt , Y. Chen , S. Greene, A. Gurrola , W. Johns , R. Kunnawalkam Elayavalli , A. Melo , F. Romeo , P. Sheldon , S. Tuo , J. Velkovska , J. Viinikainen 




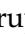
















**University of Virginia, Charlottesville, Virginia, USA**

B. Cardwell , B. Cox , J. Hakala , R. Hirosky , A. Ledovskoy , C. Neu , C.E. Perez Lara 






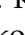




**Wayne State University, Detroit, Michigan, USA**

P.E. Karchin 

**University of Wisconsin - Madison, Madison, Wisconsin, USA**

A. Aravind, S. Banerjee , K. Black , T. Bose , S. Dasu , I. De Bruyn , P. Everaerts , C. Galloni, H. He , M. Herndon , A. Herve , C.K. Koraka , A. Lanaro, R. Loveless , J. Madhusudanan Sreekala , A. Mallampalli , A. Mohammadi , S. Mondal, G. Parida , D. Pinna, A. Savin, V. Shang , V. Sharma , W.H. Smith , D. Teague, H.F. Tsoi , W. Vetens , A. Warden 

**Authors affiliated with an institute or an international laboratory covered by a cooperation agreement with CERN**

S. Afanasiev , V. Andreev , Yu. Andreev , T. Aushev , M. Azarkin , A. Babaev , A. Belyaev , V. Blinov<sup>95</sup>, E. Boos , V. Borshch , D. Budkouski , V. Chekhovsky, R. Chistov<sup>95</sup> , M. Danilov<sup>95</sup> , A. Dermenev , T. Dimova<sup>95</sup> , D. Druzhkin<sup>96</sup> , M. Dubinin<sup>85</sup> , L. Dudko , A. Ershov , G. Gavrilo , V. Gavrilo , S. Gninenko , V. Golovtsov , N. Golubev , I. Golutvin , I. Gorbunov , A. Gribushin , Y. Ivanov , V. Kachanov , V. Karjavine , A. Karneyev , V. Kim<sup>95</sup> , M. Kirakosyan, D. Kirpichnikov , M. Kirsanov , V. Klyukhin , O. Kodolova<sup>97</sup> , V. Korenkov , A. Kozyrev<sup>95</sup> , N. Krasnikov , A. Lanev , P. Levchenko<sup>98</sup> , N. Lychkovskaya , V. Makarenko , A. Malakhov , V. Matveev<sup>95</sup> , V. Murzin , A. Nikitenko<sup>99,97</sup> , S. Obraztsov , V. Oreshkin , V. Palichik , V. Perelygin , S. Petrushanko , S. Polikarpov<sup>95</sup> , V. Popov , O. Radchenko<sup>95</sup> , M. Savina , V. Savrin , V. Shalaev , S. Shmatov , S. Shulha , Y. Skovpen<sup>95</sup> , S. Slabospitskii , V. Smirnov , A. Snigirev , D. Sosnov , V. Sulimov , E. Tcherniaev , A. Terkulov , O. Teryaev , I. Tlisova , A. Toropin , L. Uvarov , A. Uzunian , A. Vorobyev<sup>†</sup>, N. Voytishin , B.S. Yuldashev<sup>100</sup>, A. Zarubin , I. Zhizhin , A. Zhokin 

†: Deceased

<sup>1</sup>Also at Yerevan State University, Yerevan, Armenia

<sup>2</sup>Also at TU Wien, Vienna, Austria

<sup>3</sup>Also at Institute of Basic and Applied Sciences, Faculty of Engineering, Arab Academy for Science, Technology and Maritime Transport, Alexandria, Egypt

<sup>4</sup>Also at Ghent University, Ghent, Belgium

<sup>5</sup>Also at Universidade Estadual de Campinas, Campinas, Brazil

- 
- <sup>6</sup>Also at Federal University of Rio Grande do Sul, Porto Alegre, Brazil
- <sup>7</sup>Also at UFMS, Nova Andradina, Brazil
- <sup>8</sup>Also at Nanjing Normal University, Nanjing, China
- <sup>9</sup>Now at The University of Iowa, Iowa City, Iowa, USA
- <sup>10</sup>Also at University of Chinese Academy of Sciences, Beijing, China
- <sup>11</sup>Also at China Center of Advanced Science and Technology, Beijing, China
- <sup>12</sup>Also at University of Chinese Academy of Sciences, Beijing, China
- <sup>13</sup>Also at China Spallation Neutron Source, Guangdong, China
- <sup>14</sup>Now at Henan Normal University, Xinxiang, China
- <sup>15</sup>Also at Université Libre de Bruxelles, Bruxelles, Belgium
- <sup>16</sup>Also at an institute or an international laboratory covered by a cooperation agreement with CERN
- <sup>17</sup>Now at British University in Egypt, Cairo, Egypt
- <sup>18</sup>Now at Cairo University, Cairo, Egypt
- <sup>19</sup>Also at Purdue University, West Lafayette, Indiana, USA
- <sup>20</sup>Also at Université de Haute Alsace, Mulhouse, France
- <sup>21</sup>Also at Department of Physics, Tsinghua University, Beijing, China
- <sup>22</sup>Also at The University of the State of Amazonas, Manaus, Brazil
- <sup>23</sup>Also at Erzincan Binali Yildirim University, Erzincan, Turkey
- <sup>24</sup>Also at University of Hamburg, Hamburg, Germany
- <sup>25</sup>Also at RWTH Aachen University, III. Physikalisches Institut A, Aachen, Germany
- <sup>26</sup>Also at Isfahan University of Technology, Isfahan, Iran
- <sup>27</sup>Also at Bergische University Wuppertal (BUW), Wuppertal, Germany
- <sup>28</sup>Also at Brandenburg University of Technology, Cottbus, Germany
- <sup>29</sup>Also at Forschungszentrum Jülich, Juelich, Germany
- <sup>30</sup>Also at CERN, European Organization for Nuclear Research, Geneva, Switzerland
- <sup>31</sup>Also at Institute of Physics, University of Debrecen, Debrecen, Hungary
- <sup>32</sup>Also at Institute of Nuclear Research ATOMKI, Debrecen, Hungary
- <sup>33</sup>Now at Universitatea Babeş-Bolyai - Facultatea de Fizica, Cluj-Napoca, Romania
- <sup>34</sup>Also at Physics Department, Faculty of Science, Assiut University, Assiut, Egypt
- <sup>35</sup>Also at HUN-REN Wigner Research Centre for Physics, Budapest, Hungary
- <sup>36</sup>Also at Punjab Agricultural University, Ludhiana, India
- <sup>37</sup>Also at University of Visva-Bharati, Santiniketan, India
- <sup>38</sup>Also at Indian Institute of Science (IISc), Bangalore, India
- <sup>39</sup>Also at Birla Institute of Technology, Mesra, Mesra, India
- <sup>40</sup>Also at IIT Bhubaneswar, Bhubaneswar, India
- <sup>41</sup>Also at Institute of Physics, Bhubaneswar, India
- <sup>42</sup>Also at University of Hyderabad, Hyderabad, India
- <sup>43</sup>Also at Deutsches Elektronen-Synchrotron, Hamburg, Germany
- <sup>44</sup>Also at Department of Physics, Isfahan University of Technology, Isfahan, Iran
- <sup>45</sup>Also at Sharif University of Technology, Tehran, Iran
- <sup>46</sup>Also at Department of Physics, University of Science and Technology of Mazandaran, Behshahr, Iran
- <sup>47</sup>Also at Helwan University, Cairo, Egypt
- <sup>48</sup>Also at Italian National Agency for New Technologies, Energy and Sustainable Economic Development, Bologna, Italy
- <sup>49</sup>Also at Centro Siciliano di Fisica Nucleare e di Struttura Della Materia, Catania, Italy
- <sup>50</sup>Also at Università degli Studi Guglielmo Marconi, Roma, Italy
- <sup>51</sup>Also at Scuola Superiore Meridionale, Università di Napoli 'Federico II', Napoli, Italy

- <sup>52</sup>Also at Fermi National Accelerator Laboratory, Batavia, Illinois, USA
- <sup>53</sup>Also at Ain Shams University, Cairo, Egypt
- <sup>54</sup>Also at Consiglio Nazionale delle Ricerche - Istituto Officina dei Materiali, Perugia, Italy
- <sup>55</sup>Also at Riga Technical University, Riga, Latvia
- <sup>56</sup>Also at Department of Applied Physics, Faculty of Science and Technology, Universiti Kebangsaan Malaysia, Bangi, Malaysia
- <sup>57</sup>Also at Consejo Nacional de Ciencia y Tecnología, Mexico City, Mexico
- <sup>58</sup>Also at Trincomalee Campus, Eastern University, Sri Lanka, Nilaveli, Sri Lanka
- <sup>59</sup>Also at Saegis Campus, Nugegoda, Sri Lanka
- <sup>60</sup>Also at National and Kapodistrian University of Athens, Athens, Greece
- <sup>61</sup>Also at Ecole Polytechnique Fédérale Lausanne, Lausanne, Switzerland
- <sup>62</sup>Also at Universität Zürich, Zurich, Switzerland
- <sup>63</sup>Also at Stefan Meyer Institute for Subatomic Physics, Vienna, Austria
- <sup>64</sup>Also at Laboratoire d'Annecy-le-Vieux de Physique des Particules, IN2P3-CNRS, Annecy-le-Vieux, France
- <sup>65</sup>Also at Near East University, Research Center of Experimental Health Science, Mersin, Turkey
- <sup>66</sup>Also at Konya Technical University, Konya, Turkey
- <sup>67</sup>Also at Izmir Bakircay University, Izmir, Turkey
- <sup>68</sup>Also at Adiyaman University, Adiyaman, Turkey
- <sup>69</sup>Also at Bozok Universiteleri Rektörlüğü, Yozgat, Turkey
- <sup>70</sup>Also at Marmara University, Istanbul, Turkey
- <sup>71</sup>Also at Milli Savunma University, Istanbul, Turkey
- <sup>72</sup>Also at Kafkas University, Kars, Turkey
- <sup>73</sup>Now at Istanbul Okan University, Istanbul, Turkey
- <sup>74</sup>Also at Hacettepe University, Ankara, Turkey
- <sup>75</sup>Also at Istanbul University - Cerrahpasa, Faculty of Engineering, Istanbul, Turkey
- <sup>76</sup>Also at Yildiz Technical University, Istanbul, Turkey
- <sup>77</sup>Also at Vrije Universiteit Brussel, Brussel, Belgium
- <sup>78</sup>Also at School of Physics and Astronomy, University of Southampton, Southampton, United Kingdom
- <sup>79</sup>Also at University of Bristol, Bristol, United Kingdom
- <sup>80</sup>Also at IPPP Durham University, Durham, United Kingdom
- <sup>81</sup>Also at Monash University, Faculty of Science, Clayton, Australia
- <sup>82</sup>Also at Università di Torino, Torino, Italy
- <sup>83</sup>Also at Bethel University, St. Paul, Minnesota, USA
- <sup>84</sup>Also at Karamanoğlu Mehmetbey University, Karaman, Turkey
- <sup>85</sup>Also at California Institute of Technology, Pasadena, California, USA
- <sup>86</sup>Also at United States Naval Academy, Annapolis, Maryland, USA
- <sup>87</sup>Also at Bingöl University, Bingöl, Turkey
- <sup>88</sup>Also at Georgian Technical University, Tbilisi, Georgia
- <sup>89</sup>Also at Sinop University, Sinop, Turkey
- <sup>90</sup>Also at Erciyes University, Kayseri, Turkey
- <sup>91</sup>Also at Horia Hulubei National Institute of Physics and Nuclear Engineering (IFIN-HH), Bucharest, Romania
- <sup>92</sup>Now at an institute or an international laboratory covered by a cooperation agreement with CERN
- <sup>93</sup>Also at Texas A&M University at Qatar, Doha, Qatar
- <sup>94</sup>Also at Kyungpook National University, Daegu, Korea

<sup>95</sup>Also at another institute or international laboratory covered by a cooperation agreement with CERN

<sup>96</sup>Also at Universiteit Antwerpen, Antwerpen, Belgium

<sup>97</sup>Also at Yerevan Physics Institute, Yerevan, Armenia

<sup>98</sup>Also at Northeastern University, Boston, Massachusetts, USA

<sup>99</sup>Also at Imperial College, London, United Kingdom

<sup>100</sup>Also at Institute of Nuclear Physics of the Uzbekistan Academy of Sciences, Tashkent, Uzbekistan





# Search for heavy neutral leptons in final states with electrons, muons, and hadronically decaying tau leptons in proton-proton collisions at $\sqrt{s} = 13$ TeV

The CMS Collaboration\*

## Abstract

A search for heavy neutral leptons (HNLs) of Majorana or Dirac type using proton-proton collision data at  $\sqrt{s} = 13$  TeV is presented. The data were collected by the CMS experiment at the CERN LHC and correspond to an integrated luminosity of  $138 \text{ fb}^{-1}$ . Events with three charged leptons (electrons, muons, and hadronically decaying tau leptons) are selected, corresponding to HNL production in association with a charged lepton and decay of the HNL to two charged leptons and a standard model (SM) neutrino. The search is performed for HNL masses between 10 GeV and 1.5 TeV. No evidence for an HNL signal is observed in data. Upper limits at 95% confidence level are found for the squared coupling strength of the HNL to SM neutrinos, considering exclusive coupling of the HNL to a single SM neutrino generation, for both Majorana and Dirac HNLs. The limits exceed previously achieved experimental constraints for a wide range of HNL masses, and the limits on tau neutrino coupling scenarios with HNL masses above the W boson mass are presented for the first time.

*Submitted to the Journal of High Energy Physics*





# 1 Introduction

The observation of neutrino oscillations [1–3] implies that neutrinos have a nonzero mass [4]. Direct neutrino mass measurements [5, 6], as well as constraints from cosmological observations [7–9], indicate that the neutrino masses are much smaller than those of the other fermions in the standard model (SM) of particle physics. A possible mechanism for the generation of gauge-invariant neutrino mass terms and an explanation of their small scale is the see-saw mechanism [10–17], which introduces new heavy neutral leptons (HNLs) with right-handed chirality that are singlets under all SM gauge groups, but mix with the SM neutrinos. In addition, HNL models can provide a viable dark matter candidate [18, 19], and a mechanism to generate the matter-antimatter asymmetry of the universe [20–22].

We consider a simplified model with a single HNL (labelled  $N$  in diagrams and formulas) of Majorana or Dirac type that couples through the neutrino mixing matrix exclusively to a single generation of SM neutrinos [23, 24]. The signatures of such models in proton-proton (pp) collisions have been studied extensively [17, 25–31]. We focus on the production in association with a charged lepton  $\ell^\pm$ , which proceeds via the charged-current Drell–Yan (DY) process  $q\bar{q}' \rightarrow W^\pm \rightarrow N\ell^\pm$  [32, 33] or via the vector boson fusion (VBF) process  $q\gamma \rightarrow N\ell^\pm q'$  [34–37]. Several searches for this production mode have been performed by the ATLAS, CMS, and LHCb experiments at the CERN LHC [38–48]. The fully leptonic decay channel  $N \rightarrow \ell\ell\nu$  results in final states with three charged leptons, as illustrated in Fig. 1. Due to the assumption of an exclusive coupling to a single SM generation, the charged lepton originating from the HNL production and the one from the first decay vertex in the case of  $W$ -boson-mediated decays are necessarily of the same flavour and from the generation to which the HNL couples. In the case of an HNL of Majorana type, both lepton number violating (LNV) and lepton number

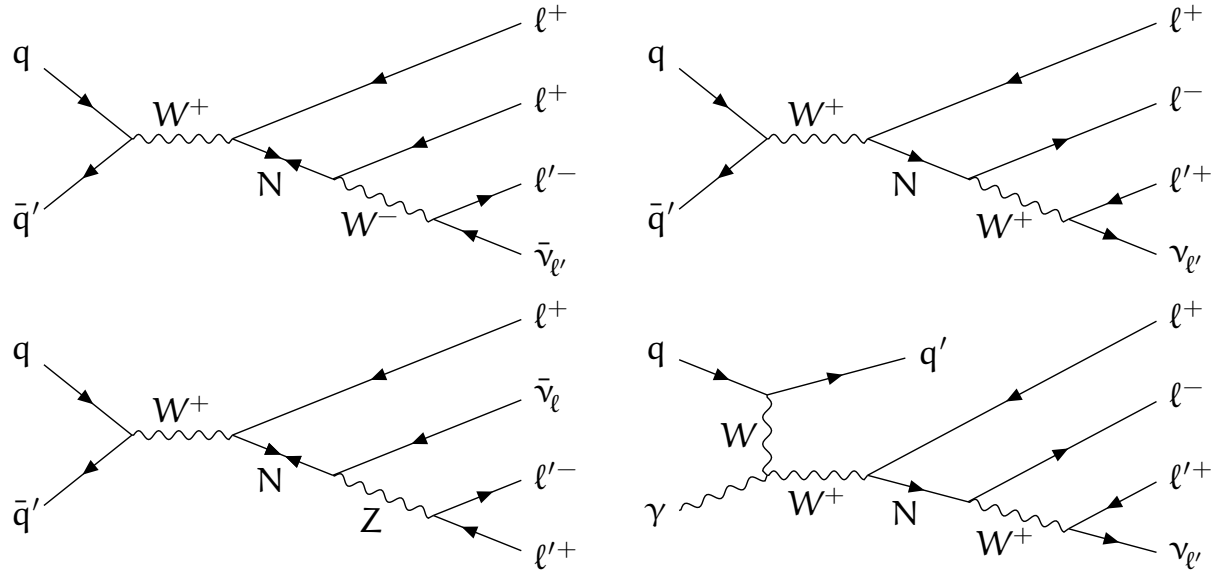


Figure 1: Examples of Feynman diagrams for production and decay of an HNL (indicated with the symbol  $N$ ) resulting in final states with three charged leptons. The production processes DY (upper row and lower left) and VBF (lower right) are shown, with decays mediated by a  $W$  boson (upper row and lower right) or a  $Z$  boson (lower left). In the left column, HNLs of Majorana type with an LNV decay are shown, whereas the right column has HNLs of Dirac type with an LNC decay. The leptons that couple directly to the HNL (indicated with the symbol  $\ell$ ) are restricted to the SM generation that couples with the HNL, whereas the leptons from the  $W$  and  $Z$  boson decays (indicated with the symbol  $\ell'$ ) can be from any SM generation.

conserving (LNC) decays are possible, and as a result these two charged leptons can be of the same or opposite charge. For an HNL of Dirac type, only LNC decays are possible and these two charged leptons thus always have opposite charge.

In this article, we present a search for HNLs in events with three charged leptons (electrons  $e$ , muons  $\mu$ , and hadronically decaying tau leptons  $\tau_h$ , in the following referred to as “leptons”), using pp collision data collected in 2016–2018 at  $\sqrt{s} = 13$  TeV and corresponding to an integrated luminosity of  $138 \text{ fb}^{-1}$ . We select events with all possible combinations of three light leptons (electrons and muons), resulting in the  $eee$ ,  $ee\mu$ ,  $e\mu\mu$ , and  $\mu\mu\mu$  flavour channels, as well as events with one  $\tau_h$  and any combination of two light leptons, resulting in the  $ee\tau_h$ ,  $e\mu\tau_h$ , and  $\mu\mu\tau_h$  flavour channels. Events with an HNL decay mediated by a Z boson or with an LNC decay mediated by a W boson result in events with an opposite-sign same-flavour (OSSF) lepton pair, whereas events without such a pair are only possible for an LNV decay. The HNL scenarios with exclusive electron (muon) neutrino coupling are only probed in the  $eee$  and  $ee\mu$  ( $\mu\mu\mu$  and  $e\mu\mu$ ) channels. In the scenario of exclusive tau neutrino couplings, the two tau leptons can decay leptonically or hadronically, and thus the  $eee$ ,  $ee\mu$ ,  $e\mu\mu$ , and  $\mu\mu\mu$  channels provide sensitivity to HNL events where both tau leptons decay leptonically, whereas the  $ee\tau_h$ ,  $e\mu\tau_h$ , and  $\mu\mu\tau_h$  channels provide sensitivity where one tau lepton each decays leptonically and hadronically. Two strategies based on event categorization or on machine-learning discriminants are employed to separate the HNL signal from the SM background, where diboson production is the most important contribution. Our results are interpreted for HNL masses  $m_N$  between 10 GeV and 1.5 TeV. To facilitate reinterpretations within more general HNL models [49, 50], we provide tabulated results in the HEPData record for this analysis [51].

The CMS Collaboration presented in Ref. [42] a search in events with three light leptons using pp collision data collected in 2016 at  $\sqrt{s} = 13$  TeV and corresponding to an integrated luminosity of  $35.9 \text{ fb}^{-1}$ , constraining the mixing parameter  $|V_{\ell N}|^2$  between the HNL and the SM neutrino generation for  $m_N$  between 1 GeV and 1.2 TeV. This article supersedes those results, and improves them not only because of the larger data set, but also from refined light-lepton identification (ID) criteria, improved background estimation techniques, and signal-to-background discrimination based on machine learning. Additionally, we include for the first time in HNL searches at the LHC events with  $\tau_h$  and use state-of-the-art  $\tau_h$  ID techniques.

The mean lifetime of an HNL is proportional to  $m_N^{-5} V_{\ell N}^{-2}$  [52]. The HNL events that have a large decay length compared with the impact parameter resolution of the CMS tracker have a reduced selection efficiency in this analysis because we require that leptons originate from the primary interaction vertex (PV). Two dedicated HNL searches presented by the CMS Collaboration, based on the same pp collision data set used in this analysis, reconstruct the secondary HNL decay vertex in events with three light leptons [46] or apply a displaced jet tagger to events with two light leptons [48], and constrain long-lived HNL scenarios for  $1 < m_N < 20$  GeV. The results of this analysis are complementary since they probe short-lived HNL scenarios with  $m_N > 10$  GeV not excluded by the dedicated searches for long-lived HNLs.

## 2 The CMS detector and event reconstruction

The central feature of the CMS apparatus is a superconducting solenoid of 6 m internal diameter, providing a magnetic field of 3.8 T. Within the solenoid volume are a silicon pixel and strip tracker, a lead tungstate crystal electromagnetic calorimeter (ECAL), and a brass and scintillator hadron calorimeter (HCAL), each composed of a barrel and two endcap sections. Forward calorimeters extend the pseudorapidity ( $\eta$ ) coverage provided by the barrel and endcap de-

tectors. Muons are measured in gas-ionization detectors embedded in the steel flux-return yoke outside the solenoid. A more detailed description of the CMS detector, together with a definition of the coordinate system used and the relevant kinematic variables, is reported in Refs. [53, 54].

Events of interest are selected using a two-tiered trigger system. The first level, composed of custom hardware processors, uses information from the calorimeters and muon detectors to select events at a rate of around 100 kHz within a fixed latency of about  $4 \mu\text{s}$  [55]. The second level, known as the high-level trigger, consists of a farm of processors running a version of the full event reconstruction software optimized for fast processing, and reduces the event rate to around 1 kHz before data storage [56].

The global event reconstruction with the particle-flow (PF) algorithm [57] reconstructs and identifies each individual particle in an event, with an optimized combination of all subdetector information. In this process, the identification of the particle type (photon, electron, muon, charged or neutral hadron) plays an important role in the determination of the particle direction and energy. Photons are identified as ECAL energy clusters not linked to the extrapolation of any charged-particle trajectory to the ECAL. Electrons are identified as a charged-particle track and potentially many ECAL energy clusters corresponding to the extrapolation of this track to the ECAL and to possible bremsstrahlung photons emitted along the way through the tracker material. Muons are identified as tracks in the central tracker consistent with either a track or several hits in the muon system, and associated with calorimeter deposits compatible with the muon hypothesis. Charged hadrons are identified as charged-particle tracks neither identified as electrons, nor as muons. Finally, neutral hadrons are identified as HCAL energy clusters not linked to any charged-hadron trajectory, or as a combined ECAL and HCAL energy excess with respect to the expected charged-hadron energy deposit. The PV is taken to be the vertex corresponding to the hardest scattering in the event, evaluated using tracking information alone, as described in Section 9.4.1 of Ref. [58].

For each event, hadronic jets are clustered from these reconstructed particles using the infrared and collinear safe anti- $k_T$  algorithm [59, 60] with a distance parameter of 0.4. Jet momentum is determined as the vectorial sum of all particle momenta in the jet, and is found from simulation to be, on average, within 5–10% of the true momentum over the entire transverse momentum ( $p_T$ ) spectrum and detector acceptance. Additional pp interactions within the same or nearby bunch crossings (pileup) can contribute additional tracks and calorimetric energy depositions to the jet momentum. To mitigate this effect, charged particles identified to be originating from pileup vertices are discarded and an offset correction is applied to correct for remaining contributions. Jet energy corrections are derived from simulation to bring the measured response of jets to that of particle-level jets on average. In situ measurements of the momentum balance in dijet, photon+jet, Z+jet, and multijet events are used to correct for any residual differences in the jet energy scale between data and simulation [61]. Only jets with  $p_T > 25 \text{ GeV}$  and  $|\eta| < 2.4$  are considered in this analysis. Additional selection criteria are applied to each jet to remove jets potentially dominated by anomalous contributions from various subdetector components or reconstruction failures [62].

The missing transverse momentum vector  $\vec{p}_T^{\text{miss}}$  is computed as the negative  $\vec{p}_T$  sum of all PF candidates in an event, and its magnitude is denoted as  $p_T^{\text{miss}}$  [63]. The  $\vec{p}_T^{\text{miss}}$  is modified to account for corrections to the energy scale of the reconstructed jets in the event. Anomalous high- $p_T^{\text{miss}}$  events can arise from a variety of reconstruction failures, detector malfunctions, or noncollisional backgrounds. Such events are rejected by event filters that identify more than 85% of the spurious high- $p_T^{\text{miss}}$  events with a mistagging rate of less than 0.1% [63].

The DEEPIET algorithm [64–66] is applied to identify jets arising from the hadronization of b hadrons. We use a loose working point to tag jets as “b jets” with a selection efficiency for b quark jets of more than 90%, and a misidentification rate for c quark jets (light quark and gluon jets) of 50 (20)%.

### 3 Event simulation

Event samples simulated with Monte Carlo event generators are used to evaluate the signal selection efficiency, to predict background contributions, to train machine learning discriminators, and to validate background estimation techniques based on control samples in data. The simulated event samples are processed with a full simulation of the CMS detector based on the GEANT4 toolkit [67], and are reconstructed with the same software as the data samples. Additional simulated pileup interactions are added to the simulated events to match the observed pileup distribution as well, with a mean pileup of 23 (32) in 2016 (2017–2018) [68]. Separate event samples are generated for each data-taking year, reflecting the differences in the LHC running conditions and the CMS detector performance.

For the signal process, event samples are generated with the MADGRAPH5\_aMC@NLO v2.6.5 program [69, 70], using a model that extends the SM particle content by up to three right-handed neutrinos [26, 29, 36, 37]. The DY production process is simulated for  $m_N < 80$  GeV at leading order (LO) in the strong coupling  $\alpha_s$ , whereas the simulation is performed at next-to-LO (NLO) in all other cases. In the matrix element calculation, the NNPDF3.1 [71] parton distribution functions (PDFs) are used for the DY production process, and the NNPDF3.1\_luxQED [72–74] PDFs for the VBF production process. Separate samples are generated for HNLs that couple to electron, muon, or tau neutrinos, and for different  $m_N$  values between 10 GeV and 1.5 TeV. The VBF samples are generated only for masses of at least 600 GeV, since the contribution from VBF production is only relevant at high masses. For  $m_N > 30$  GeV, no HNL lifetime effects are included in the simulation and a fixed value of  $|V_{\ell N}|^2 = 10^{-4}$  is used. The HNL production cross section is proportional to  $|V_{\ell N}|^2$  [37], and thus the generated samples can be used to emulate any  $|V_{\ell N}|^2$  value by applying a corresponding normalization factor. At 30 GeV and lower, we calculate the HNL mean lifetime analytically [75] and include it in the simulation of the HNL decay. Samples are generated with one fixed  $|V_{\ell N}|^2$  value between  $10^{-6}$  and  $10^{-3}$  for each mass point, and we emulate other  $|V_{\ell N}|^2$  values by reweighting the HNL decay length distribution as described in Ref. [46]. In all cases, the samples are generated assuming an HNL of Majorana nature, i.e. including both LNV and LNC decays, and samples for a Dirac HNL are obtained by selecting only the subset of simulated events with LNC decays and applying appropriate event weights.

Furthermore, the MADGRAPH5\_aMC@NLO generator is used to simulate background samples at NLO for WZ and  $Z\gamma$  diboson production, for Higgs boson (H) production in association with a vector boson or a top quark pair ( $t\bar{t}$ ), for triboson production, for  $t\bar{t}$  production in association with a W or Z boson, for s-channel and tZ single top quark production, and for four top quark production. It is also used at LO for DY vector boson production in association with jets (Z+jets and W+jets), H production in association with a single top quark,  $t\bar{t}$  production in association with two bosons, and three top quark production. Background samples for  $q\bar{q}$ -initiated WW and ZZ diboson production, gluon fusion and VBF H production,  $t\bar{t}$  production, and t-channel and tW single-t production are generated with the POWHEG 2 program [76–84] at NLO. The gluon-gluon-initiated ZZ diboson production is simulated with the MCFM v7.0.1 generator [85–87] at LO. In all cases, the NNPDF3.1 PDFs are used.

The generators are interfaced with the PYTHIA v8.230 program [88] for the underlying event description with the CP5 tune [89], the parton shower simulation, and hadronization. For MADGRAPH5\_aMC@NLO samples simulated at LO (NLO), jets from matrix element calculations are merged with those from the parton shower using the MLM [90] (FxFx [91]) matching scheme. In POWHEG samples for H production, the decay to four leptons is simulated with the JHUGEN v5.2.5 program [92].

## 4 Lepton selection

Electrons are measured in the range  $|\eta| < 2.5$ , and their momentum is estimated by combining the energy measurement in the ECAL with the momentum measurement in the tracker [93, 94]. Electrons with  $1.44 < |\eta| < 1.57$  in the transition region between the barrel and endcap are not considered in the analysis because of performance limitations of the electron reconstruction in this region. Muons are measured in the range  $|\eta| < 2.4$ , with detection planes made using three technologies: drift tubes, cathode strip chambers, and resistive plate chambers [95].

We select reconstructed electrons and muons with  $p_T > 10$  GeV that are compatible with originating from the PV and isolated from other particles in the event. The relative isolation variable  $I_{\text{rel}}$  is defined as the scalar  $p_T$  sum of all PF particles reconstructed within a cone around the lepton direction divided by the lepton  $p_T$ , with the cone size defined in terms of  $\Delta R = \sqrt{(\Delta\eta)^2 + (\Delta\phi)^2}$ , where  $\Delta\eta$  and  $\Delta\phi$  are the  $\eta$  and azimuthal angle difference between the particle and the lepton. We use a variable cone size of 0.2 for leptons with  $p_T < 50$  GeV, of  $10 \text{ GeV}/p_T$  for  $50 < p_T < 200$  GeV, and of 0.05 for  $p_T > 200$  GeV, which improves the efficiency for high- $p_T$  leptons by removing the accidental overlap with other particles [96]. Additionally, corrections for pileup contributions to  $I_{\text{rel}}$  are applied. All reconstructed electrons and muons are required to have  $I_{\text{rel}} < 0.4$ . For electrons, we additionally require that there be at most one tracker layer that contributes no hit on the track, to reduce contributions from photon conversions [93]. For muons, we additionally apply the “medium” set of ID criteria defined in Ref. [95].

Electrons and muons produced directly from the prompt decay of HNLs, W and Z bosons, or tau leptons are referred to as “prompt” leptons. Background contributions with “nonprompt” leptons arise from events with genuine leptons produced in hadron decays and photon conversions, as well as from events with jet constituents misidentified as leptons. To distinguish between prompt and nonprompt electrons and muons, the two additional sets of ID criteria defined in Ref. [97] are applied, labelled “loose” and “tight”. The tight ID is based on a multivariate analysis (MVA) discriminant using the methods developed for various CMS measurements and searches with multilepton signatures [98–103], described in more detail for the case of muons in Ref. [104]. Tight electrons and muons are required to have the MVA discriminant exceed certain thresholds, resulting in a prompt electron (muon) selection efficiency of about 85 (92)%. The misidentification rate for nonprompt electrons (muons) is less than 0.6% (about 1%). The loose ID is defined by requiring that electrons and muons either pass the tight ID, or pass selection requirements on some properties that are also used as inputs to the MVA discriminant.

Jets are used to reconstruct  $\tau_h$  candidates with the hadrons-plus-strips algorithm [105], which combines one or three tracks with energy deposits in the calorimeters, to identify the  $\tau_h$  decay modes. Neutral pions are reconstructed as ECAL energy deposition “strips” with dynamic size in  $\eta$ - $\phi$  from reconstructed electrons and photons, where the strip size varies as a function of the  $p_T$  of the electron or photon candidate. The  $\tau_h$  decay mode is then obtained by combining the

charged hadrons with the strips. We consider decay modes with one or three charged hadrons, with or without neutral pions, and require the  $\tau_h$  candidate to have  $p_T > 20$  GeV and  $|\eta| < 2.3$ .

To distinguish genuine  $\tau_h$  decays from jets originating from the hadronization of quarks or gluons, and from electrons and muons, the DEEPTAU algorithm is used [106]. Information from all individual reconstructed particles near the  $\tau_h$  axis is combined with properties of the  $\tau_h$  candidate and the event to provide a multiclassification output equivalent to a Bayesian probability of the  $\tau_h$  to originate from a genuine tau lepton, the hadronization of a quark or gluon, an electron, or a muon. We define a “loose” and a “tight” ID for  $\tau_h$  by choosing different working points of the DEEPTAU discriminant for genuine tau leptons. The rate of a jet to be misidentified as  $\tau_h$  by the DEEPTAU algorithm depends on the  $p_T$  and quark flavour of the jet. We estimate it in simulated events from W boson production in association with jets to be 0.43% for a genuine  $\tau_h$  identification efficiency of 70%. The misidentification rate for electrons (muons) is 2.6 (0.03)% for a genuine  $\tau_h$  identification efficiency of 80 (>99)%.

To avoid double counting of charged-particle candidates that pass both the electron and muon reconstruction, we remove reconstructed electrons that are within  $\Delta R < 0.05$  of any reconstructed muon. Furthermore, we require that  $\tau_h$  candidates be separated from any reconstructed electron or muon passing the tight working point by  $\Delta R > 0.5$ . Any jet that is within  $\Delta R < 0.4$  of any reconstructed electron or muon that passes the loose ID or within  $\Delta R < 0.5$  of a  $\tau_h$  candidate that passes the tight ID is removed as well.

## 5 Event selection and search strategy

We analyse events that were collected with various triggers that require the presence of one, two, or three light leptons, with  $p_T$  thresholds that depend on the data-taking year and the flavour combination of the reconstructed leptons, as listed in Table 1. The efficiency of the trigger selection is larger than 90% for three-lepton events everywhere, approaching 100% for events with large lepton  $p_T$ .

Table 1: Requirements on the light-lepton  $p_T$  values in the online and offline selections. The first two columns give the numbers of electrons and muons in the event ( $N_e$  and  $N_\mu$ ). The third column lists the  $p_T$  thresholds on the reconstructed electrons and muons in the online trigger selection. The fourth column lists the offline event selection requirements applied in addition to the baseline requirements of  $p_T(\ell_1) > 15$  GeV and  $p_T(\ell_{2,3}) > 10$  GeV. For the  $e\mu$  trigger, the requirements are given for the highest and second-highest  $p_T$  light lepton, referred to as  $l_1$  and  $l_2$ . The values in parentheses give the thresholds applied in 2017 and 2018, where they are different from 2016. All events are required to pass the conditions of at least one of the rows.

$N_e$	$N_\mu$	Online selection	Offline selection
$\geq 1$	—	$p_T(e_1) > 27$ (32) GeV	$p_T(e_1) > 30$ (35) GeV
—	$\geq 1$	$p_T(\mu_1) > 24$ GeV	$p_T(\mu_1) > 25$ GeV
$\geq 2$	—	$p_T(e_1) > 23$ GeV, $p_T(e_2) > 12$ GeV	$p_T(e_1) > 25$ GeV, $p_T(e_2) > 15$ GeV
—	$\geq 2$	$p_T(\mu_1) > 17$ GeV, $p_T(\mu_2) > 8$ GeV	$p_T(\mu_1) > 20$ GeV
$\geq 1$	$\geq 1$	$p_T(l_1) > 23$ GeV, $p_T(l_2) > 8$ (12) GeV	$p_T(l_1) > 25$ GeV, $p_T(l_2) > 10$ (15) GeV
$\geq 3$	—	$p_T(e_1) > 16$ GeV, $p_T(e_2) > 12$ GeV, $p_T(e_3) > 8$ GeV	$p_T(e_1) > 25$ GeV, $p_T(e_2) > 15$ GeV
$\geq 2$	$\geq 1$	$p_T(e_{1,2}) > 12$ GeV, $p_T(\mu_1) > 8$ GeV	$p_T(e_1) > 25$ GeV, $p_T(e_2) > 15$ GeV
$\geq 1$	$\geq 2$	$p_T(e_1) > 9$ GeV, $p_T(\mu_{1,2}) > 9$ GeV	—
—	$\geq 3$	$p_T(\mu_1) > 12$ (10) GeV, $p_T(\mu_2) > 10$ (5) GeV, $p_T(\mu_3) > 5$ GeV	—

We select events with exactly three leptons that pass the tight ID criteria. For a sideband enriched in events with nonprompt leptons, we retain events where at least one lepton fails the tight but passes the loose ID criteria. Events with additional loose leptons or with at least one b jet are removed, as well as events where all leptons have the same charge. The highest  $p_T$  (leading) lepton, referred to as  $\ell_1$ , is required to have  $p_T(\ell_1) > 15 \text{ GeV}$ . To ensure a high trigger efficiency, higher  $p_T$  thresholds are applied to the leading and second-highest  $p_T$  (sub-leading) light lepton depending on the lepton flavours present in the event, as summarized in Table 1. If OSSF lepton pairs are present in an event, they are required to have an invariant mass  $m(\ell^+\ell^-) > 5 \text{ GeV}$  to remove contributions from low-mass resonances. Additionally, we require  $|m(\ell^+\ell^-) - m_Z| > 15 \text{ GeV}$  for any OSSF lepton pair, where  $m_Z = 91.2 \text{ GeV}$  is the Z boson mass [107], to remove background events with Z bosons. While this removes HNL signal events with decays mediated by an on-shell Z boson, the SM Z boson background is overwhelming in this phase space and thus the loss of sensitivity incurred by this requirement is negligible. Finally, events with b jets are removed to suppress background contributions with top quarks.

Events are categorized by the flavour of the selected leptons. For events with only electrons and muons, this results in the four categories  $eee$ ,  $ee\mu$ ,  $e\mu\mu$ , and  $\mu\mu\mu$ . For events with exactly one  $\tau_h$ , we distinguish the three categories  $ee\tau_h$ ,  $e\mu\tau_h$ , and  $\mu\mu\tau_h$ . We do not select events with more than one  $\tau_h$ , since the typically smaller signal efficiency, higher background contamination, and lower resolution of the  $\tau_h$  reconstruction compared with those for electrons and muons result in a low signal acceptance and a significant background yield for these events.

For HNL models with  $m_N$  below the W boson mass  $m_W = 80.4 \text{ GeV}$  [107], the HNL decay proceeds via a virtual W or Z boson, resulting in typically low- $p_T$  leptons. In the case of  $m_N > m_W$ , the decay will first proceed to an on-shell W boson and a lepton, with a subsequent leptonic decay of the W boson, resulting in typically higher  $p_T$  for at least one of the leptons. Similarly for  $m_N > m_Z$ , the decay via an on-shell Z boson also results in events with leptons of typically higher  $p_T$ . Other kinematic properties of the final-state leptons will be significantly different as well for the cases of  $m_N < m_W$  (“low mass”) and  $> m_W$  (“high mass”). Thus, we define two orthogonal event selections to target the two separate mass ranges, by categorizing events with  $p_T(\ell_1) < 55 \text{ GeV}$  as low-mass and  $> 55 \text{ GeV}$  as high-mass events.

In the low-mass selection, events are further required to have  $p_T^{\text{miss}} < 75 \text{ GeV}$  to remove background contributions with SM neutrinos, such as  $t\bar{t}$  and diboson production, and to have a trilepton invariant mass  $m(3\ell) < 80 \text{ GeV}$  to remove  $Z\gamma$  photon conversion events. In the high-mass selection, the subleading lepton is required to have  $p_T(\ell_2) > 15 \text{ GeV}$  to reduce background contributions with nonprompt leptons, and events with an OSSF lepton pair and  $|m(3\ell) - m_Z| < 15 \text{ GeV}$  are removed to reduce  $Z\gamma$  photon conversion backgrounds. To remove background contributions with charge-misidentified electrons, events in the high-mass selection with two same-sign electrons and a muon are required to have consistent results between three independent charge measurements [108] for the two electrons and to have a dielectron mass more than  $15 \text{ GeV}$  away from  $m_Z$ . Although charge-misidentified electrons can also play a role in other final states, their contribution to the background is small in other flavour channels. Charge mismeasurement for muons is negligible [109, 110].

Following the strategy applied in Ref. [42], we define a number of orthogonal search regions (SRs) by classifying the events according to several kinematic variables that provide a good discrimination between signal and background contributions, as summarized in Table 2. Events are first sorted based on whether they have an OSSF lepton pair or not, since background processes with a Z boson contribute primarily to the OSSF events. In the low-mass region, the



Table 2: Definitions of the search regions (SRs) for events in the low-mass (upper part) and high-mass (lower part) selections.

OSSF pair	$p_T(\ell_1)$ (GeV)	$m(3\ell)$ (GeV)	$\min m(\ell^+\ell^-)$ (GeV)	$m_T$ (GeV)	SR name	
<i>Low-mass selection</i>						
No	<30	<80	<10	any	La1	
			10–20		La2	
			20–30		La3	
			>30		La4	
	30–55	<80	<10	any	La5	
			10–20		La6	
			20–30		La7	
			>30		La8	
Yes	<30	<80	<10	any	Lb1	
			10–20		Lb2	
			20–30		Lb3	
			>30		Lb4	
	30–55	<80	<10	any	Lb5	
			10–20		Lb6	
			20–30		Lb7	
			>30		Lb8	
<i>High-mass selection</i>						
No	>55	<100	any	<100	Ha1	
				>100	Ha2	
				>100	<100	Ha3
		>100	<100	any	100–150	Ha4
					150–250	Ha5
					>250	Ha6
	>200	<100	any	100–200	Ha7	
				>100	Ha8	
				any	Ha9	
Yes	>55	<75	any	<100	Hb1	
				100–200	Hb2	
				>200	Hb3	
		>105	<100	any	<100	Hb4
					100–200	Hb5
					200–300	Hb6
	>200	<100	any	300–400	Hb7	
				>400	Hb8	
				100–200	<100	Hb9
	>200	<100	any	100–200	Hb10	
				200–300	Hb11	
				>300	Hb12	
>200	<100	any	<100	Hb13		
			100–200	Hb14		
			200–300	Hb15		
>200	<100	any	>300	Hb16		

SRs are then defined in bins of  $p_T(\ell_1)$  and the smallest invariant mass of any opposite-sign (OS) lepton pair,  $\min m(\ell^+\ell^-)$ . The SRs with  $p_T(\ell_1) < 30$  GeV target HNL scenarios where  $m_N$  is close to  $m_W$ , such that both the lepton from the HNL production and the leptons from the HNL decay have low  $p_T$ . The SRs with  $30 < p_T(\ell_1) < 55$  GeV, on the other hand, target HNL scenarios with a smaller  $m_N$ , such that the lepton from the HNL production can have a large  $p_T$ . The  $\min m(\ell^+\ell^-)$  variable is bounded to be smaller than  $m_N$  for HNL signal events, and thus provides sensitivity to distinguish different HNL signal scenarios.

In the high-mass region, the SRs are defined in bins of  $\min m(\ell^+\ell^-)$ ,  $m(3\ell)$ , and the transverse mass  $m_T$  calculated with  $\vec{p}_T^{\text{miss}}$  and the lepton not used for  $\min m(\ell^+\ell^-)$ , defined as  $m_T = \sqrt{2p_T^{\text{miss}}p_T(\ell)(1 - \cos \Delta\phi)}$ , where  $\Delta\phi$  is the  $\phi$  angle between the lepton and  $\vec{p}_T^{\text{miss}}$ . The variable  $\min m(\ell^+\ell^-)$  again provides discriminating power between different HNL masses, whereas  $m_T$  is targeted at the reconstruction of a resonance decaying into the third lepton and an SM neutrino that causes the  $\vec{p}_T^{\text{miss}}$  in the events. Although the HNL signal events have no such resonance and thus are distributed towards high  $m_T$  values, SM background processes like WZ production with  $W \rightarrow \ell\nu$  decays will have a distribution of  $m_T$  mostly below  $m_W$ . Finally,  $m(3\ell)$  measures a lower bound on the energy of the  $s$ -channel resonance that produced the leptons in the event, with larger values as  $m_N$  increases due to the large partonic centre-of-mass energy required to produce high-mass HNLs, and a distribution at lower values for the SM backgrounds that generally have a lower production threshold.

To further improve the separation of signal and background events, we employ machine learning classifiers based on boosted decision trees (BDTs) as implemented in the TMVA package [111]. The classifiers are trained to distinguish HNL signal events from background events taken from simulated samples for the Z+jets,  $t\bar{t}$ , and WZ background processes, using both selected and sideband events to also train against nonprompt-lepton background events. We train separate BDTs for different HNL coupling scenarios and  $m_N$  ranges, using different event selections and categories, and label these trainings as “BDT( $m_N, \ell, i\tau_h$ )”. The first argument specifies one of the five  $m_N$  ranges (in GeV), where we use the low-mass (high-mass) selection for the ranges 10–40 and 50–75 GeV (85–150, 200–250, and 300–400 GeV). The second argument specifies the lepton flavour of the neutrino generation to which the HNL couples exclusively. The third argument specifies the event categories used in the training: for electron and muon neutrino couplings, the event categories without  $\tau_h$  are used, i.e.  $eee$ ,  $ee\mu$ ,  $e\mu\mu$ , and  $\mu\mu\mu$ , labelled as “ $0\tau_h$ ”. For tau neutrino couplings, separate trainings are performed for final states with no  $\tau_h$  at generator level, using the  $0\tau_h$  event categories, and for final states with at least one  $\tau_h$  at generator level, using the  $ee\tau_h$ ,  $e\mu\tau_h$ , and  $\mu\mu\tau_h$  event categories, labelled as “ $1\tau_h$ ”.

The input variables to the BDTs are the kinematic properties of the reconstructed leptons; invariant and transverse masses of different dilepton and trilepton systems; the number of jets; kinematic properties of the reconstructed jets;  $\Delta R$  between different lepton and lepton-jet pairs;  $p_T^{\text{miss}}$ ; and the sum of the  $p_T$  of all reconstructed jets (leptons), referred to as  $H_T$  ( $L_T$ ). Additional input variables to the BDTs trained with the low-mass selection are various  $\Delta\phi$  between  $\vec{p}_T^{\text{miss}}$  and leptons or jets. Furthermore, the BDTs trained with the low-mass selection in the  $0\tau_h$  categories have the flavours and charges of the reconstructed electrons and muons as additional input variables. A selection of the most discriminating variables used in the different trainings is shown in Figs. 2–4. It can be seen that the different distributions provide sensitivity to distinguish between HNL signal and background distributions, but also show differences in the expected distributions for different  $m_N$  values, which is the reason to train separate BDTs for different mass ranges. Generally good agreement is observed between data and background prediction.

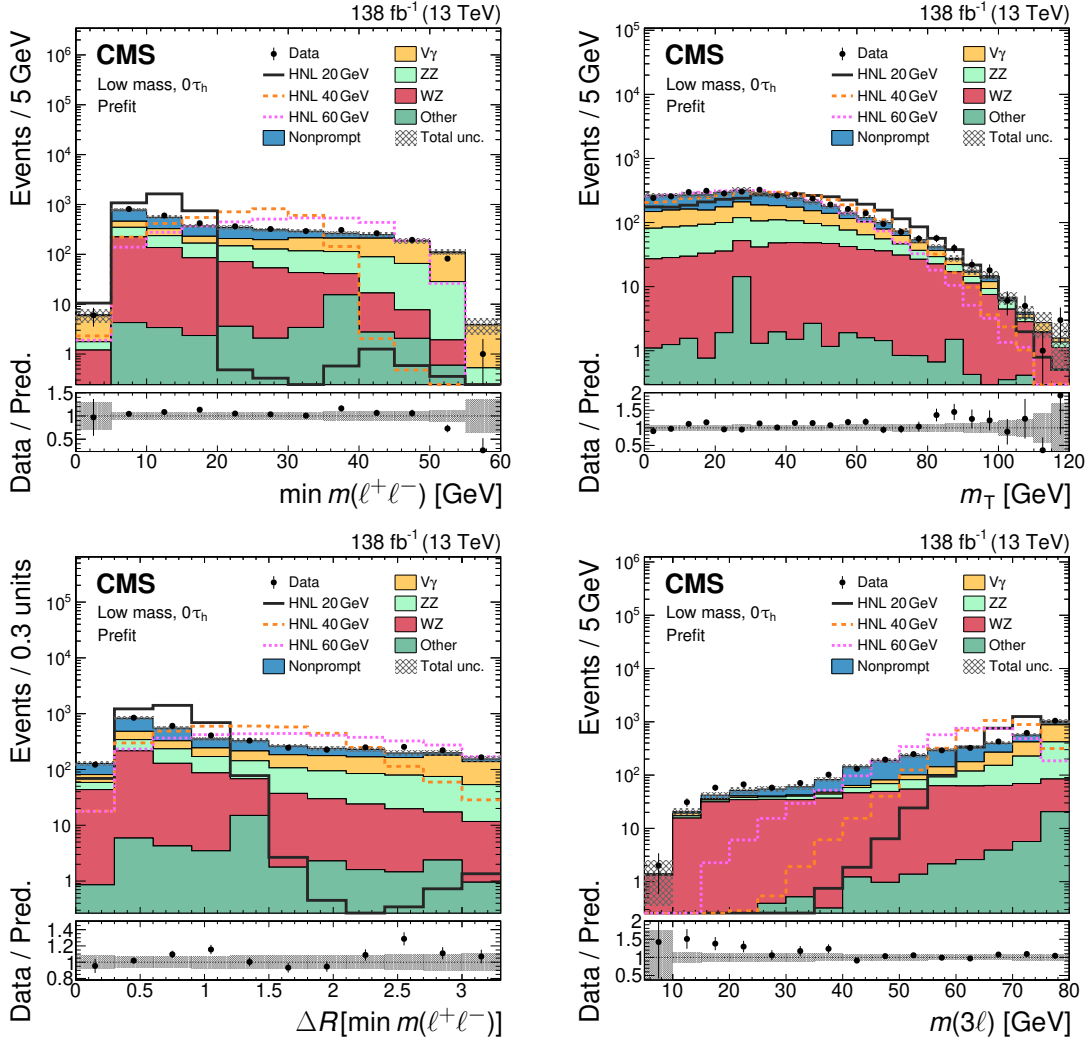


Figure 2: Comparison of observed (points) and predicted (coloured histograms) distributions in the low-mass selection for the  $0\tau_h$  categories combined. Important input variables to the BDT training are shown:  $\min m(\ell^+\ell^-)$  (upper left),  $m_T$  (upper right),  $\Delta R$  between the two leptons used for  $\min m(\ell^+\ell^-)$  ( $\Delta R[\min m(\ell^+\ell^-)]$ , lower left),  $m(3\ell)$  (lower right). The predicted background yields are shown before the fit to the data (“prefit”). The HNL predictions for three different  $m_N$  values with exclusive coupling to tau neutrinos are shown with coloured lines, and are normalized to the total background yield. The vertical bars on the points represent the statistical uncertainties in the data, and the hatched bands the total uncertainties in the predictions. The last bins include the overflow contributions. In the lower panels, the ratios of the event yield in data to the overall sum of the predictions are shown.

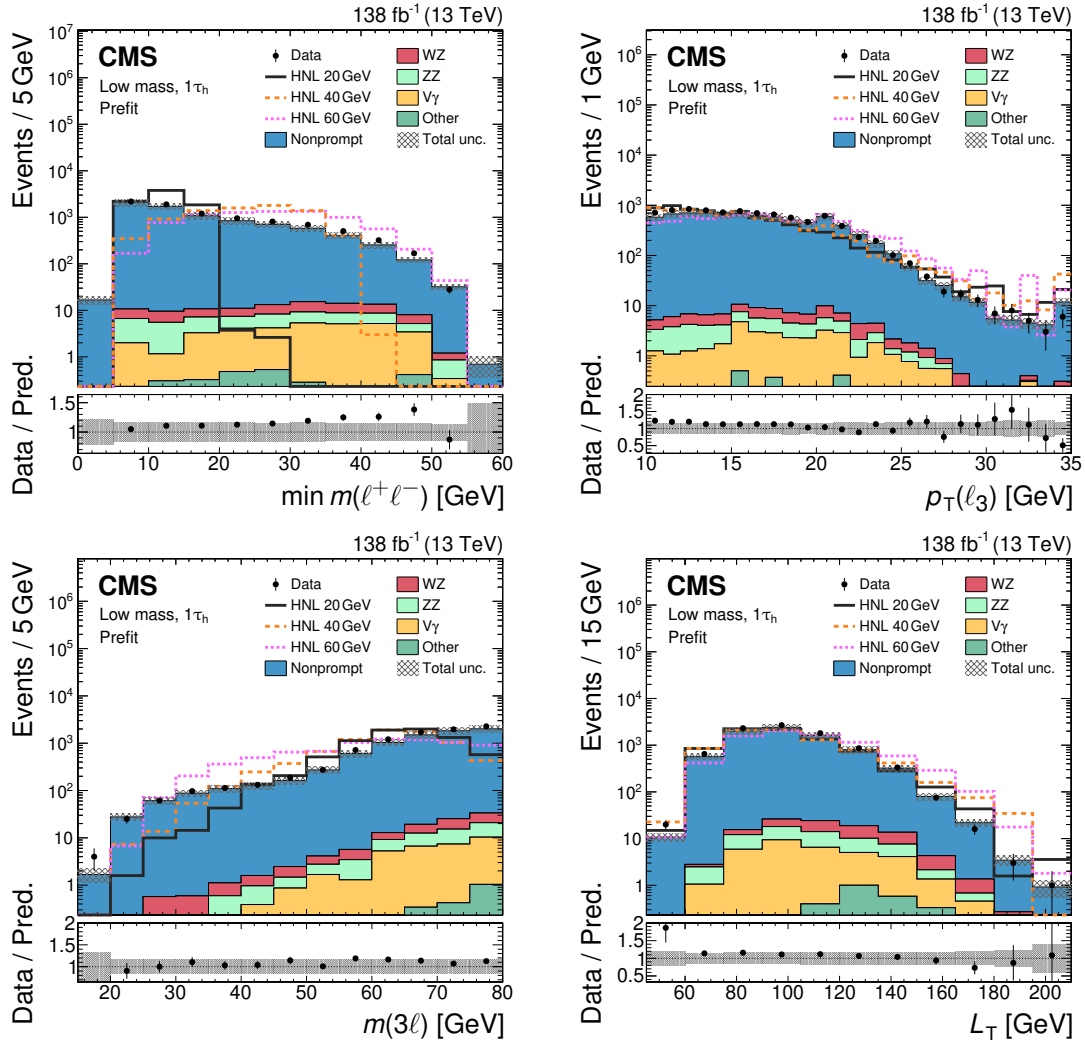


Figure 3: Comparison of observed (points) and predicted (coloured histograms) distributions in the low-mass selection for the  $1\tau_h$  categories combined. Important input variables to the BDT training are shown:  $\min m(\ell^+\ell^-)$  (upper left),  $p_T(\ell_3)$  (upper right),  $m(3\ell)$  (lower left),  $L_T$  (lower right). The predicted background yields are shown before the fit to the data (“prefit”). The HNL predictions for three different  $m_N$  values with exclusive coupling to tau neutrinos are shown with coloured lines, and are normalized to the total background yield. The vertical bars on the points represent the statistical uncertainties in the data, and the hatched bands the total uncertainties in the predictions. The last bins include the overflow contributions. In the lower panels, the ratios of the event yield in data to the overall sum of the predictions are shown.

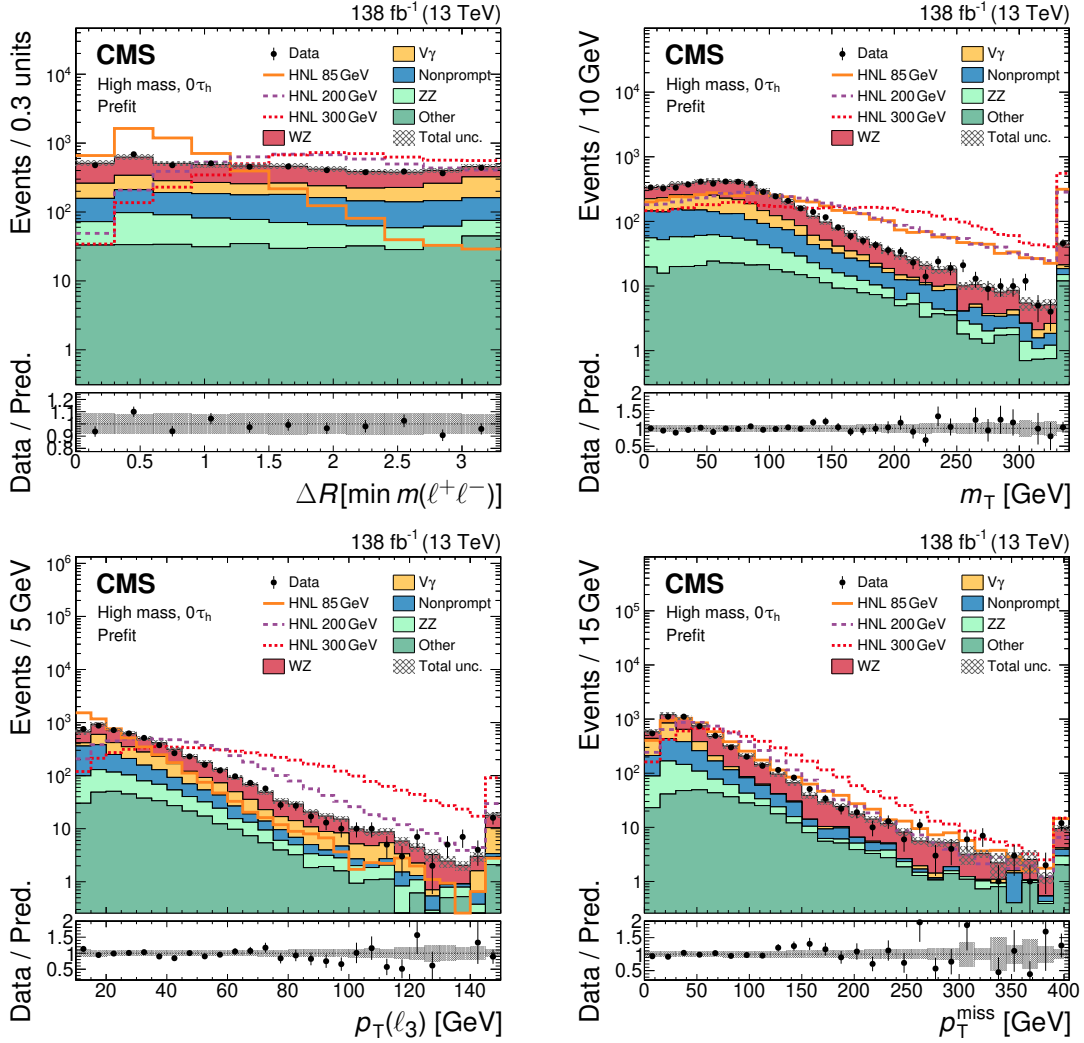


Figure 4: Comparison of observed (points) and predicted (coloured histograms) distributions in the high-mass selection for the  $0\tau_h$  categories combined. Important input variables to the BDT training are shown:  $\Delta R[\min m(\ell^+\ell^-)]$  (upper left),  $m_T$  (upper right),  $p_T(\ell_3)$  (lower left),  $p_T^{\text{miss}}$  (lower right). The predicted background yields are shown before the fit to the data (“prefit”). The HNL predictions for three different  $m_N$  values with exclusive coupling to tau neutrinos are shown with coloured lines, and are normalized to the total background yield. The vertical bars on the points represent the statistical uncertainties in the data, and the hatched bands the total uncertainties in the predictions. The last bins include the overflow contributions. In the lower panels, the ratios of the event yield in data to the overall sum of the predictions are shown.

The BDTs calculate event scores based on these input variables, and the score can be interpreted as a measure of how likely an event is to originate from the HNL signals used in the respective BDT training. The agreement between data and background prediction is validated for all BDT input variables and output scores in the control regions (CRs) defined in Section 6, and good agreement is found.

For the final results, we combine the approaches based on SRs and BDTs. In the low-mass selection, the background events used in the BDT training predominantly have an OSSF lepton pair, whereas the SRs with no OSSF pair have only small background yields and no significant separation between signal and background contributions is provided by the BDTs for these events. Thus, we analyse together the BDT score distributions for the combined SRs with an

OSSF pair (i.e. Lb1–8, as defined in Table 2) and the yields in the SRs without an OSSF pair (i.e. La1–8). In the high-mass selection, good sensitivity to the HNL signal is provided by the BDT scores for  $m_N$  up to 400 GeV for electron and muon neutrino couplings, whereas the low expected signal yields for larger  $m_N$  or exclusive couplings to tau neutrinos result in a loss of sensitivity for the BDT approach. Consequentially, we use the BDT score distributions for the combined SRs Ha1–9 and Hb1–16 when targeting  $m_N$  up to 400 GeV for electron or muon neutrino couplings, and the yields in these SRs otherwise.

## 6 Background estimation

Background contributions from SM processes are estimated with a combination of methods based on CRs in data and simulated event samples. We distinguish between background contributions where all three selected leptons are prompt and those that have at least one non-prompt lepton. For prompt-lepton backgrounds, we additionally treat processes separately that have a charge-misidentified electron (referred to as “charge misID”) or at least one lepton originating from the conversion of a prompt photon produced at the interaction point. Prompt-lepton backgrounds are estimated from the simulated event samples discussed in Section 3, and are dominated by WZ and ZZ diboson production, where the latter includes resonant contributions from  $H \rightarrow ZZ$  production. All other prompt-lepton background contributions, of which the largest is from associated top quark and triboson production, are grouped together with charge-misID contributions as “Other” in the figures.

To validate the modelling of the dominant diboson background contributions in the simulated event samples, we define three CRs that are orthogonal to the SRs by the requirement of an OSSF lepton pair consistent with  $m_Z$ . These CRs target WZ and ZZ production, as well as  $Z\gamma$  production with photon conversion. The total yield predicted by the SM backgrounds is compared with the observed data yield, and a correction factor is derived where necessary. Additionally, the distributions for several observables relevant in the SR definitions and the BDTs are compared to ensure that these background contributions are well modelled, and to derive uncertainties in the background normalizations.

The WZ CR is defined by selecting events with exactly three tight light leptons with  $p_T(\ell_1) > 25$  GeV and  $p_T(\ell_2) > 15$  GeV, where two leptons form an OSSF pair with  $|m(\ell^+\ell^-) - m_Z| < 15$  GeV. Events with b jets are excluded to reduce contributions from associated top quark production,  $p_T^{\text{miss}} > 50$  GeV is required to account for the SM neutrino from the W boson decay, and the requirement of  $|m(3\ell) - m_Z| > 15$  GeV removes contributions with photon conversions. More than 80% of the events in the CR originate from WZ production. Signal contributions to this CR are negligible, with predicted yields of signal processes not excluded by Ref. [42] less than 0.5% of the total background yield for all mass points in this analysis. The total yields observed in the data agree with the prediction. The comparison of the distributions for several observables in Fig. 5 demonstrates good agreement as well, with deviations smaller than 10% in most bins.

The ZZ CR is defined by selecting events with exactly four tight light leptons with  $p_T(\ell_1) > 15$  GeV, where the four leptons form two OSSF pairs with  $|m(\ell^+\ell^-) - m_Z| < 15$  GeV each. In the case of four leptons of the same flavour, the pairs are chosen such that the sum of the mass differences with respect to  $m_Z$  is minimized. The OSSF pair with the invariant mass further away from  $m_Z$  is labelled “Z<sub>2</sub>”. Events with b jets are removed to reduce contributions from associated top quark production, and  $m(\ell^+\ell^-) > 12$  GeV is required for every OS lepton pair to remove contributions from low-mass resonances. Contributions from background processes

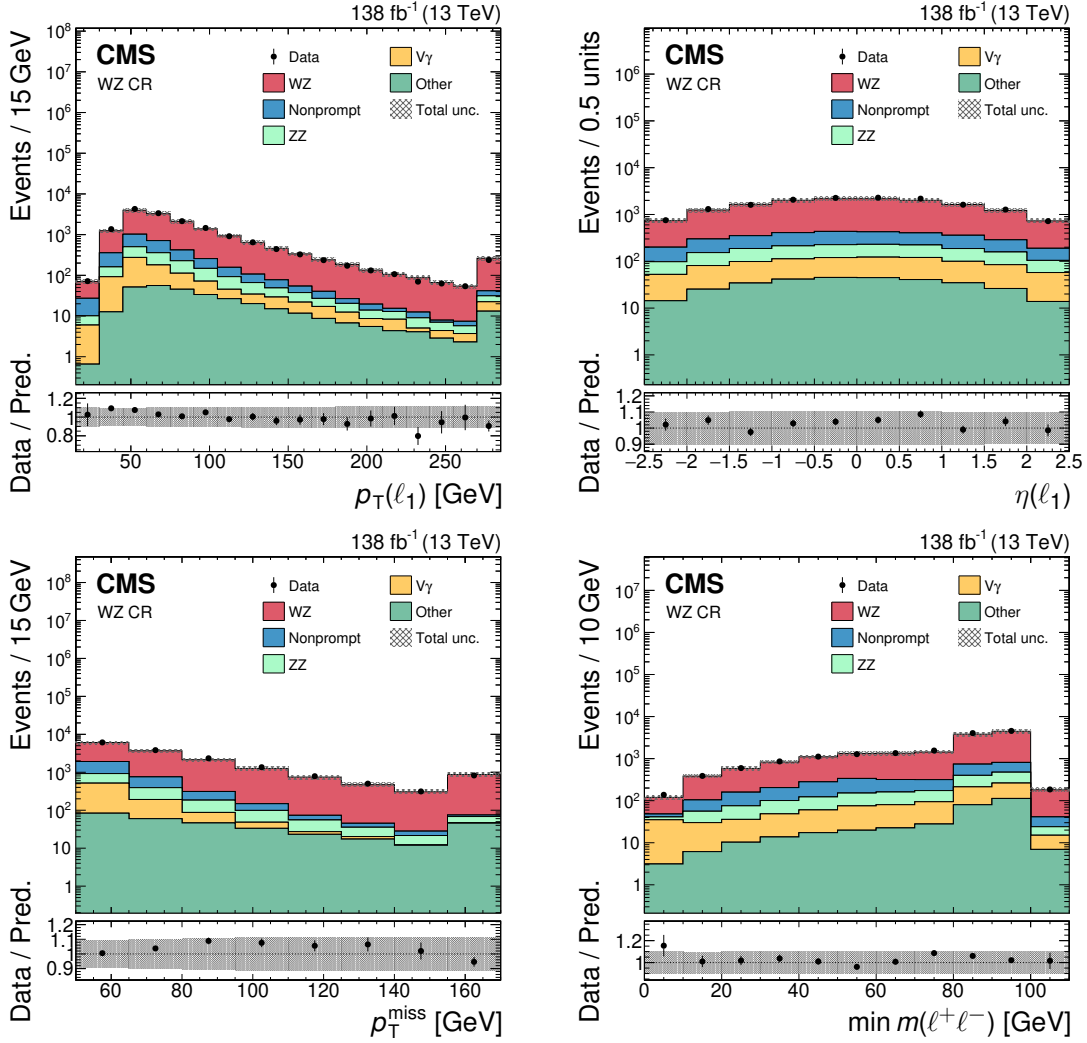


Figure 5: Comparison of observed (points) and predicted (coloured histograms) distributions in the WZ CR. The leading lepton  $p_T$  (upper left) and  $\eta$  (upper right), as well as  $p_T^{\text{miss}}$  (lower left) and  $\min m(\ell^+\ell^-)$  (lower right) are shown. The vertical bars on the points represent the statistical uncertainties in the data, and the hatched bands the total uncertainties in the predictions. The last bins include the overflow contributions. In the lower panels, the ratios of the event yield in data to the overall sum of the predictions are shown.

other than ZZ production or from signal contamination are negligible in this CR. We find the observed yields to be larger than the prediction, and assign a scale factor of 1.12 to the simulated ZZ samples to correct for the difference in the total yield. After applying the scale factor, good agreement between the prediction and the observation is found across several observables, some of which are shown in Fig. 6. Except for a few bins with lower statistical precision, the agreement is generally better than 10%.

Background contributions from processes with photon conversions are also estimated from simulated samples. The main photon conversion background arises from  $Z\gamma$  production, where the photon undergoes an asymmetric conversion into two leptons of which one has very low  $p_T$  and is not reconstructed. For the  $Z\gamma$  CR, events with exactly three tight light leptons with  $p_T(\ell_1) > 15$  GeV are selected. To select  $Z\gamma$  events where the photon is radiated from one of the leptons from the Z boson decay but at the same time remove contributions from Z+jets and WZ production, we require  $|m(3\ell) - m_Z| < 10$  GeV, as well as that two leptons

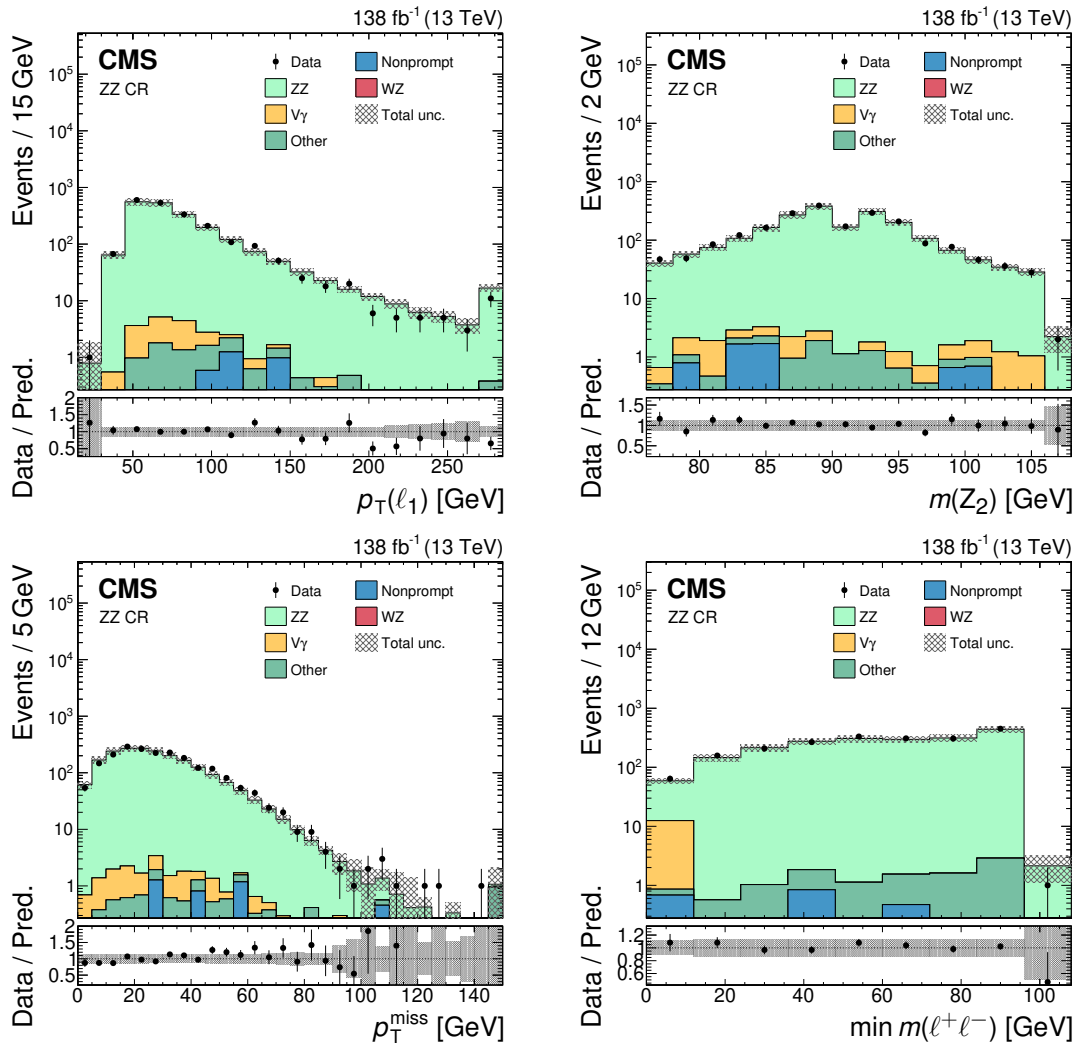


Figure 6: Comparison of observed (points) and predicted (coloured histograms) distributions in the ZZ CR. The leading lepton  $p_T$  (upper left),  $m(\ell^+\ell^-)$  of  $Z_2$  ( $m(Z_2)$ , upper right),  $p_T^{\text{miss}}$  (lower left), and  $\min m(\ell^+\ell^-)$  (lower right) are shown. The ZZ prediction is scaled with a normalization factor of 1.12, as discussed in the text. The vertical bars on the points represent the statistical uncertainties in the data, and the hatched bands the total uncertainties in the predictions. The last bins include the overflow contributions. In the lower panels, the ratios of the event yield in data to the overall sum of the predictions are shown.

form an OSSF pair with  $|m(\ell^+\ell^-) - m_Z| > 15$  GeV. Events with b jets are removed. In this CR, about 70% of the events originate from photon conversions. Expected signal yields for processes not excluded by Ref. [42] are below 0.5% of the total yield. To correct for differences in the total yield between data and prediction, we apply a scale factor of 1.11 to simulated  $Z\gamma$  samples. Figure 7 shows the data and predicted distributions for several observables, with the scale factor applied, and exhibits agreement that is typically better than 10%.

Simulated event samples are used to predict background contributions with charge-misID electrons. The misID rate in simulation depends strongly on the material included in the detector model, and is validated by dedicated measurements in data by comparing event yields with same- and opposite-sign electron pairs [97]. It is found that the misidentification rate is overestimated (underestimated) in 2016 (2017–2018) samples by about 10 (50)%, and we apply correction factors to the normalization of the charge-misID background correspondingly.



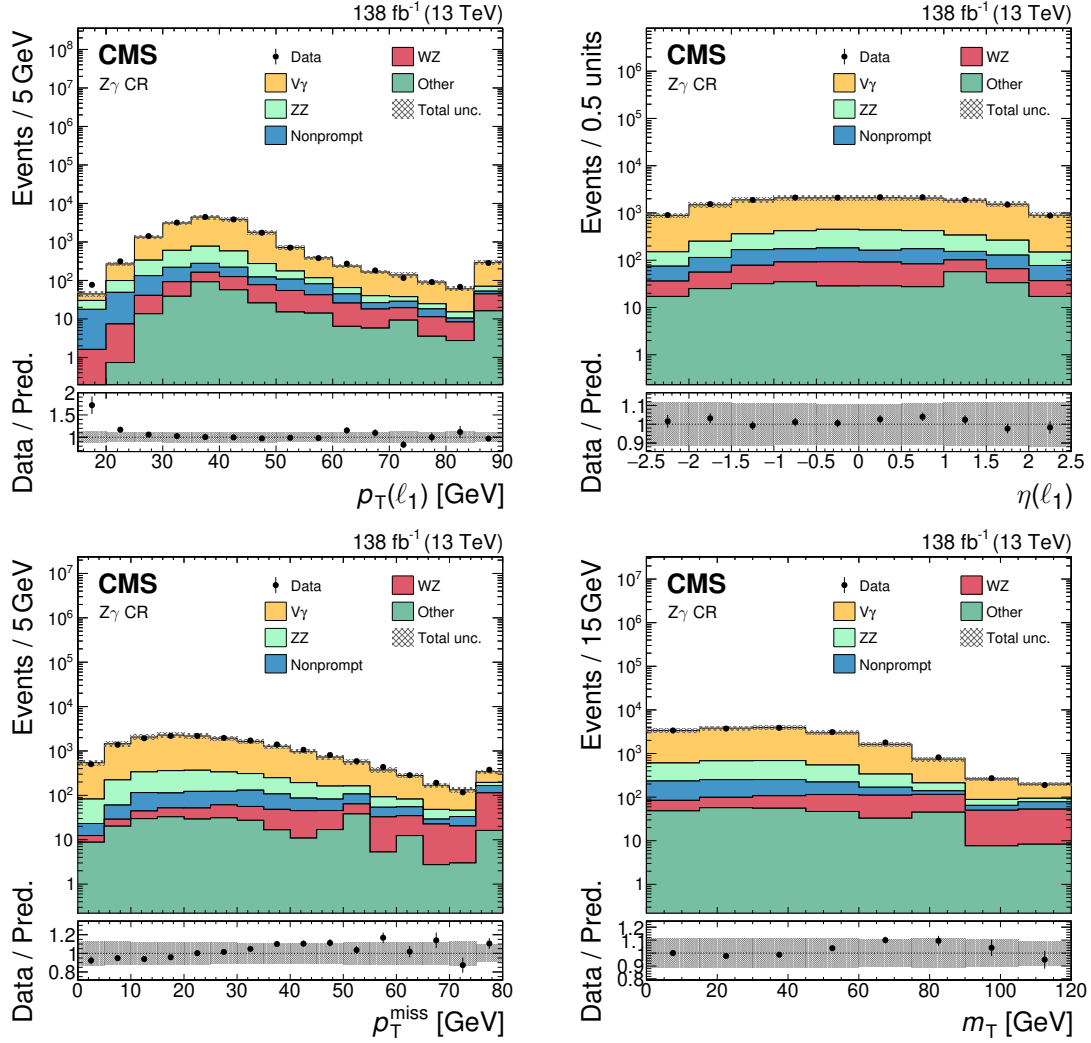


Figure 7: Comparison of observed (points) and predicted (coloured histograms) distributions in the  $Z\gamma$  CR. The leading lepton  $p_T$  (upper left) and  $\eta$  (upper right),  $p_T^{\text{miss}}$  (lower left), and  $m_T$  (lower right) are shown. The  $Z\gamma$  prediction is scaled with a normalization factor of 1.11, as discussed in the text. The vertical bars on the points represent the statistical uncertainties in the data, and the hatched bands the total uncertainties in the predictions. The last bins include the overflow contributions. In the lower panels, the ratios of the event yield in data to the overall sum of the predictions are shown.

Nonprompt-lepton background contributions arise mostly from  $t\bar{t}$  and  $Z$ +jets production with an additional nonprompt lepton. They are especially relevant in the  $1\tau_h$  categories. A “tight-to-loose” ratio method [100, 112, 113] is applied to estimate the nonprompt-lepton background contributions from control samples in data. The tight-to-loose ratio is defined as the probability  $f$  for a loose lepton to also satisfy the tight ID selection. It is evaluated separately for the different lepton flavours, and is measured as a function of  $p_T$  and  $|\eta|$ . For electrons and muons,  $f$  is measured in a sample enriched in SM events composed uniquely of jets produced through the strong interaction selected with nonisolated single-lepton triggers. For  $\tau_h$ ,  $f$  is measured in samples enriched in  $Z$ +jets and  $t\bar{t}$  events. The measured values of  $f$  are applied as weights to events that pass the SR selection but have one or more leptons that pass the loose and fail the tight selection. Both simulated events and data samples enriched in nonprompt leptons are used to validate the tight-to-loose ratio method for all lepton flavours. Good agreement of

better than 30% is found in these tests in the most relevant kinematic distributions, with larger deviations up to 50% only for nonprompt electrons with  $p_T > 55$  GeV.

## 7 Systematic uncertainties

Multiple sources of systematic uncertainty affect the signal prediction, the background event yields, and the distributions of the observables used for the signal extraction. The sources and their correlations between the data-taking years are described below, and their impact on the fits described in Section 9 is summarized in Table 3.

The integrated luminosities for the three data-taking years have individual uncertainties between 1.2 and 2.5% [114–116], and the overall uncertainty for the 2016–2018 period is 1.6%. This uncertainty affects the normalization of the background contributions from simulated event samples, as well as the extraction of cross section limits from the final estimate of the limit on the number of signal events.

The distribution of the number of additional pp interactions per event in simulation is matched to data by reweighting the profile of the true number of interactions to the one inferred from the instantaneous luminosity profile in data. The systematic uncertainty is estimated from a variation of the total inelastic cross section used for this reweighting by  $\pm 4.6\%$ , which is treated as correlated among the data-taking years.

The trigger selection efficiency is measured in data and simulation with independent trigger paths based on hadronic activity and  $p_T^{\text{miss}}$  signatures. The efficiencies in data and simulation agree within 3%, which is assigned as a systematic uncertainty that is correlated between the data-taking years. Additionally, the statistical uncertainty in the measured trigger efficiencies in data is considered, separately for each data-taking year.

Table 3: Relative impacts of the uncertainty sources in fits for six different fit models specified with  $m_N$  value and coupling scenario, where the relative impact is defined as the ratio between the uncertainty from the respective source and the total uncertainty in the HNL signal strength. The symbol “—” indicates that the corresponding uncertainty source is not applicable.

Uncertainty source	$m_N = 40$ GeV			$m_N = 200$ GeV		
	e	$\mu$	$\tau$	e	$\mu$	$\tau$
Luminosity, pileup reweighting	5.0%	2.6%	11.3%	5.8%	7.6%	4.4%
Trigger efficiency	2.4%	10.6%	26.4%	2.9%	6.9%	5.1%
Light-lepton selection efficiency & energy calibration	8.7%	15.5%	7.9%	10.4%	18.3%	1.2%
$\tau_h$ selection efficiency	—	—	2.7%	—	—	14.2%
Jet energy calibration, $p_T^{\text{miss}}$ , b tagging efficiency	10.6%	8.4%	34.4%	8.6%	12.4%	24.0%
WZ background normalization	1.1%	9.6%	7.4%	2.8%	5.4%	4.0%
ZZ background normalization	3.9%	9.9%	8.0%	4.1%	6.1%	6.5%
$Z\gamma$ background normalization	7.4%	8.3%	5.1%	1.9%	1.5%	12.1%
Other background normalization	1.4%	5.6%	1.6%	13.8%	6.3%	10.5%
Nonprompt light-lepton background	10.8%	16.0%	20.9%	15.6%	26.4%	9.1%
Nonprompt $\tau_h$ background	—	—	14.3%	—	—	66.7%
HNL cross section prediction	4.7%	3.5%	3.8%	3.7%	3.0%	2.1%
Total systematic	23.3%	25.5%	55.1%	27.7%	35.8%	75.5%
Statistical	96.8%	96.5%	83.4%	96.1%	93.3%	65.5%

During the 2016 and 2017 data-taking periods, a gradual shift in the timing of the inputs of the ECAL level-1 trigger in the region  $|\eta| > 2.0$  caused a specific trigger inefficiency [55]. For events containing an electron (a jet) with  $p_T > 50$  (100) GeV in the region  $2.5 < |\eta| < 3.0$  the efficiency loss is  $\approx 10$ – $20\%$ , depending on  $p_T$ ,  $\eta$ , and time. Correction factors are derived from data and applied to the acceptance evaluated by simulation, and the impact on our results is small.

The efficiency of the tight ID selection of light leptons is measured in data and simulation using a “tag-and-probe” method applied to  $Z \rightarrow \ell^+ \ell^-$  events [117]. Per-lepton corrections are derived separately for electrons, muons, and  $\tau_h$ . Statistical and systematic uncertainties in the correction factors are included, with the former (latter) treated as uncorrelated (correlated) between the data-taking years. Corrections for the differences in the electron energy scale and resolution between data and simulation are derived from  $Z \rightarrow ee$  events using only ECAL information [93], and systematic uncertainties are considered that are correlated between the data-taking years.

Uncertainties in the jet energy scale and resolution are evaluated from the  $p_T$  variations of the reconstructed jets in simulated events [61]. The variation due to the jet energy scale, as well as an additional variation to account for the uncertainty in the contribution from unclustered PF particles [63], is propagated to  $p_T^{\text{miss}}$ . The jet energy scale (jet energy resolution and unclustered energy) variation is treated as correlated (uncorrelated) between the data-taking years. Differences in the b tagging efficiency between data and simulation are corrected by applying scale factors to simulated events. Uncertainties in the scale factors are evaluated by separate variations for light- and heavy-flavour jets, where both correlated and uncorrelated variations between the three data-taking years are considered [64].

Several uncertainties are considered for the normalization of the background processes. For the dominant  $WZ$ ,  $ZZ$ , and  $Z\gamma$  contributions, we assign an uncertainty of 10% each, corresponding to the level of agreement in the CRs described in Section 6. The SM predictions for triboson production have a precision of about 10% [118–122], which is assigned as a normalization uncertainty to the triboson background. For associated top quark production, a normalization uncertainty of 10% is assigned, matching the experimental precision of the latest CMS measurements of the most important contributions [103, 113]. The uncertainty in the charge-misID contribution originates from the correction factors and is taken to be 15% [97]. For all remaining contributions in the “Other” category, we assign a normalization uncertainty of 20% corresponding to the experimental precision in the signal strength of H production in association with a vector boson [123].

The uncertainties in the nonprompt background contributions stem from the tight-to-loose ratio method. For nonprompt light leptons, a normalization uncertainty of 30% is applied when the leading nonprompt lepton is a muon, and a  $p_T$ -dependent uncertainty when it is an electron. In the latter case, the uncertainty is 15% for  $p_T < 35$  GeV of the electron, 30% for  $35 < p_T < 55$  GeV, and 50% for  $p_T > 55$  GeV. In the case of nonprompt  $\tau_h$  leptons, a normalization uncertainty of 30% is assigned to account for observed differences in the validation, separately for events with and without an OSSF lepton pair because of the different composition of sources of nonprompt  $\tau_h$  leptons in these two event selections.

The HNL signal samples for  $m_N < m_W$  are simulated at LO accuracy, and their normalization is scaled with the ratio between the SM cross sections of W boson production evaluated at next-to-NLO with the FEWZ v3.1 program [124–127] and at LO with MADGRAPH5\_aMC@NLO, using settings identical to those of the signal samples. The uncertainty in the signal cross section is then evaluated from the variations of the renormalization and factorization scale and of the

PDFs in the next-to-NLO calculation and amounts to 4% in total [46]. For the HNL signal samples with  $m_N > m_W$ , the simulation is done at NLO accuracy, and no additional scale factor is applied. From the evaluation of scale variations and the PDF choice, we find a signal cross section uncertainty of 3 (15)% for the DY (VBF) production mode.

## 8 Results

For each HNL signal scenario, a binned likelihood function  $L(r, \theta)$  is constructed from the product of Poisson probabilities to obtain the observed yields in the relevant distributions, given the HNL signal prediction scaled with a signal strength  $r$  and the SM background estimates. Additional terms are included to account for the systematic uncertainty sources, where  $\theta$  denotes the full set of corresponding nuisance parameters [128]. Statistical uncertainties in the predicted yields are implemented through a single nuisance parameter in each bin for all processes [129, 130]. We consider the cases of exclusive HNL couplings to electron, muon, and tau neutrinos separately, and use different distributions to construct  $L$  depending on the coupling scenario and  $m_N$ , as listed in Table 4. To obtain background-only fits, the maximum likelihood estimator of  $\theta$  with a fixed  $r = 0$  is evaluated for specific fit setups. In Fig. 8, the number of observed events in data is compared with the background predictions in the SRs, separately combined for the  $0\tau_h$  and  $1\tau_h$  categories, after simultaneous background-only fits to the SRs of all flavour channels. Furthermore, the distributions of the BDT output scores are compared between data and prediction in Figs. 9–11, after the background-only fits corresponding to the fit setups in Table 4 where the corresponding BDT is used. In all figures, the signal prediction for several HNL mass points is shown as well, with  $|V_{\ell N}|^2$  values chosen such that the predicted signal yield matches roughly the total background yield.

The number of observed events in data is in good agreement with the SM background expectations within the statistical and systematic uncertainties. No significant excess is found for any final state or in any SR.

## 9 Interpretation

To derive exclusion limits at 95% confidence level (CL) on HNL signal scenarios, we apply the modified frequentist  $CL_s$  approach [128, 131–133]. Distributions of the LHC test statistic [128], based on the profile likelihood method, are evaluated in the asymptotic approximation [133] and used to calculate the  $CL_s$  value [131, 132]. We exclude a signal scenario if the signal strength of  $r = 1$  is excluded at 95% CL or greater.

The limits are obtained under the assumption of a Majorana or a Dirac HNL, and are evaluated at a grid of points in the  $(m_N, |V_{\ell N}|^2)$  parameter space. For a Dirac HNL, the predicted signal yields are emulated from a subset of events in the simulated Majorana samples by selecting only events in which the leptons from the original W boson decay and from the direct HNL decay have opposite lepton number. For electron and muon neutrino couplings, masses of up to 1.5 TeV are considered, whereas tau neutrino couplings are evaluated only up to 1 TeV since the exclusion limit passes above  $|V_{\tau N}|^2 = 1$  already at this mass point. The results are shown in Fig. 12. The obtained limits are connected with straight lines between neighbouring mass points for which the same fit distributions are used. For  $m_N$  values at which the fit distributions change, the limits are evaluated for both strategies and shown separately. Since the BDTs are trained with nonoverlapping mass ranges, the sensitivity is generally different for two strategies evaluated at the same  $m_N$  value, and we thus obtain disjoint limit curves for several of these mass points. The expected and observed exclusion limits generally agree within

Table 4: Summary of the selections, categories, and distributions used in the maximum likelihood fits for the HNL signal points.

HNL model	Selection	Categories	OSSF	Fitted distributions
(10–40 GeV, e)	low mass	$0\tau_h$	no	La1–8
		$0\tau_h$	yes	BDT(10–40, e, $0\tau_h$ )
(40–75 GeV, e)	low mass	$0\tau_h$	no	La1–8
		$0\tau_h$	yes	BDT(50–75, e, $0\tau_h$ )
(85–125 GeV, e)	high mass	$0\tau_h$	any	BDT(85–150, e, $0\tau_h$ )
(125–250 GeV, e)	high mass	$0\tau_h$	any	BDT(200–250, e, $0\tau_h$ )
(250–400 GeV, e)	high mass	$0\tau_h$	any	BDT(300–400, e, $0\tau_h$ )
( $\geq 400$ GeV, e)	high mass	$0\tau_h$	any	Ha1–9, Hb1–16
(10–40 GeV, $\mu$ )	low mass	$0\tau_h$	no	La1–8
		$0\tau_h$	yes	BDT(10–40, $\mu$ , $0\tau_h$ )
(40–75 GeV, $\mu$ )	low mass	$0\tau_h$	no	La1–8
		$0\tau_h$	yes	BDT(50–75, $\mu$ , $0\tau_h$ )
(85–125 GeV, $\mu$ )	high mass	$0\tau_h$	any	BDT(85–150, $\mu$ , $0\tau_h$ )
(125–200 GeV, $\mu$ )	high mass	$0\tau_h$	any	BDT(200–250, $\mu$ , $0\tau_h$ )
(200–400 GeV, $\mu$ )	high mass	$0\tau_h$	any	BDT(300–400, $\mu$ , $0\tau_h$ )
( $\geq 400$ GeV, $\mu$ )	high mass	$0\tau_h$	any	Ha1–9, Hb1–16
(10–40 GeV, $\tau$ )	low mass	$0\tau_h$	no	La1–8
		$0\tau_h$	yes	BDT(10–40, $\tau$ , $0\tau_h$ )
		$1\tau_h$	no	La1–8
		$1\tau_h$	yes	BDT(10–40, $\tau$ , $1\tau_h$ )
(40–75 GeV, $\tau$ )	low mass	$0\tau_h$	no	La1–8
		$0\tau_h$	yes	BDT(50–75, $\tau$ , $0\tau_h$ )
		$1\tau_h$	no	La1–8
		$1\tau_h$	yes	BDT(50–75, $\tau$ , $1\tau_h$ )
( $\geq 85$ GeV, $\tau$ )	high mass	all	any	Ha1–9, Hb1–16

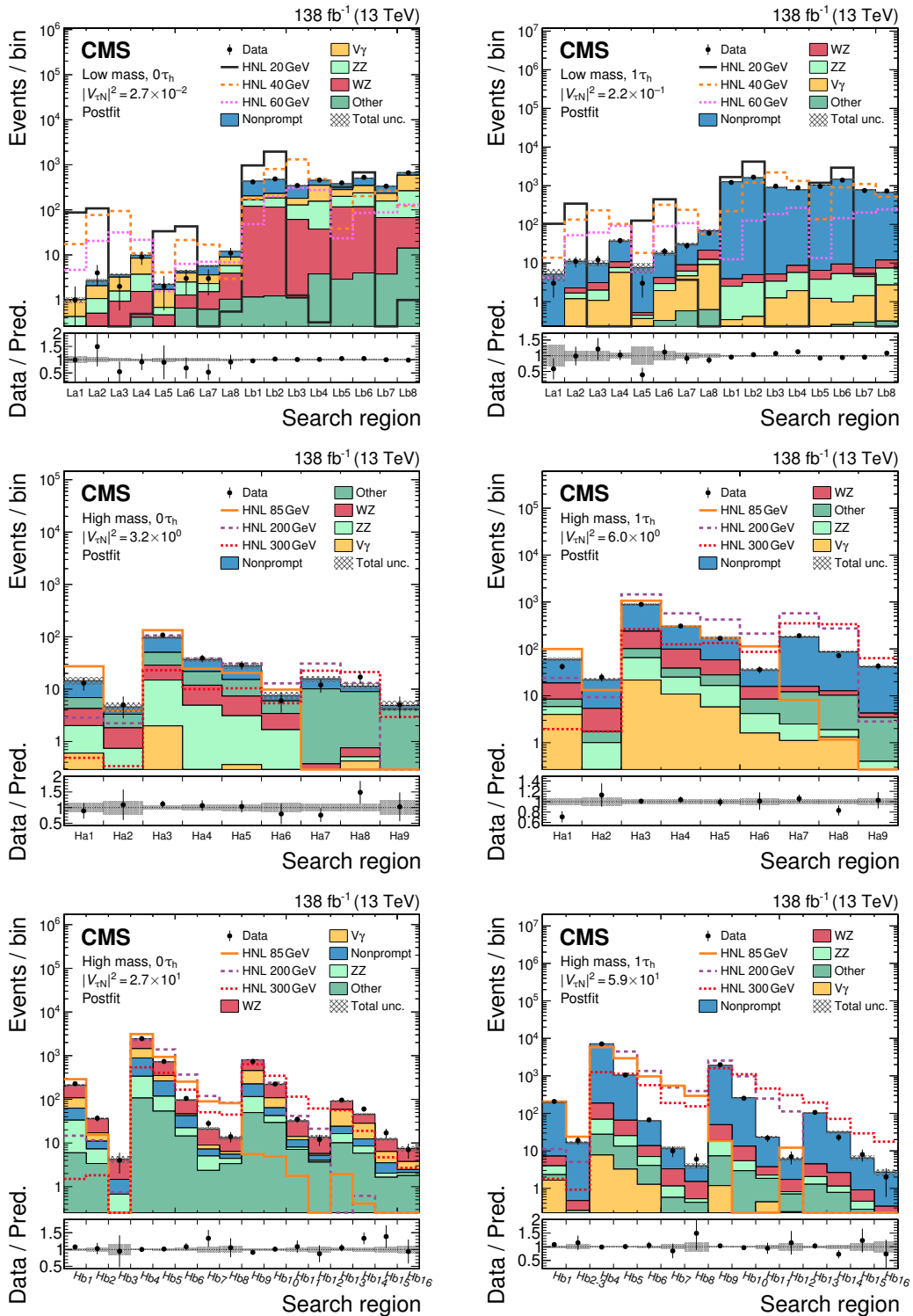
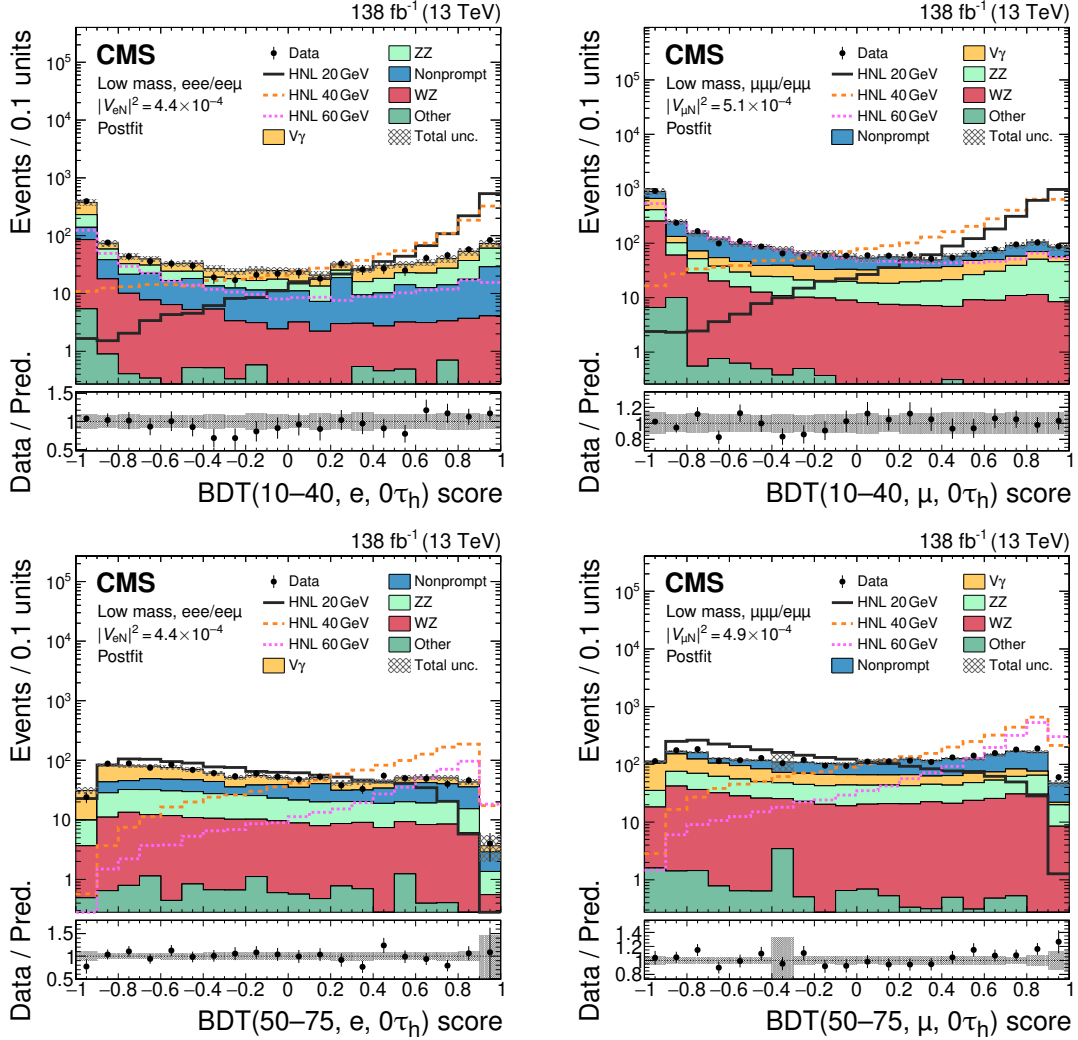


Figure 8: Comparison of the number of observed (points) and predicted (coloured histograms) events in the SR bins, shown for the  $0\tau_h$  (left column) and  $1\tau_h$  (right column) categories combined. The La1–8 and Lb1–8 (upper row), Ha1–Ha9 (middle row), and Hb1–16 (lower row) are displayed. The predicted background yields are shown with the values of the normalizations and nuisance parameters obtained in background-only fits applied (“postfit”). The HNL predictions for three different  $m_N$  values with exclusive coupling to tau neutrinos are shown with coloured lines. The vertical bars on the points represent the statistical uncertainties in the data, and the hatched bands the total uncertainties in the background predictions as obtained from the fits. In the lower panels, the ratios of the event yield in data to the overall sum of the background predictions are shown.



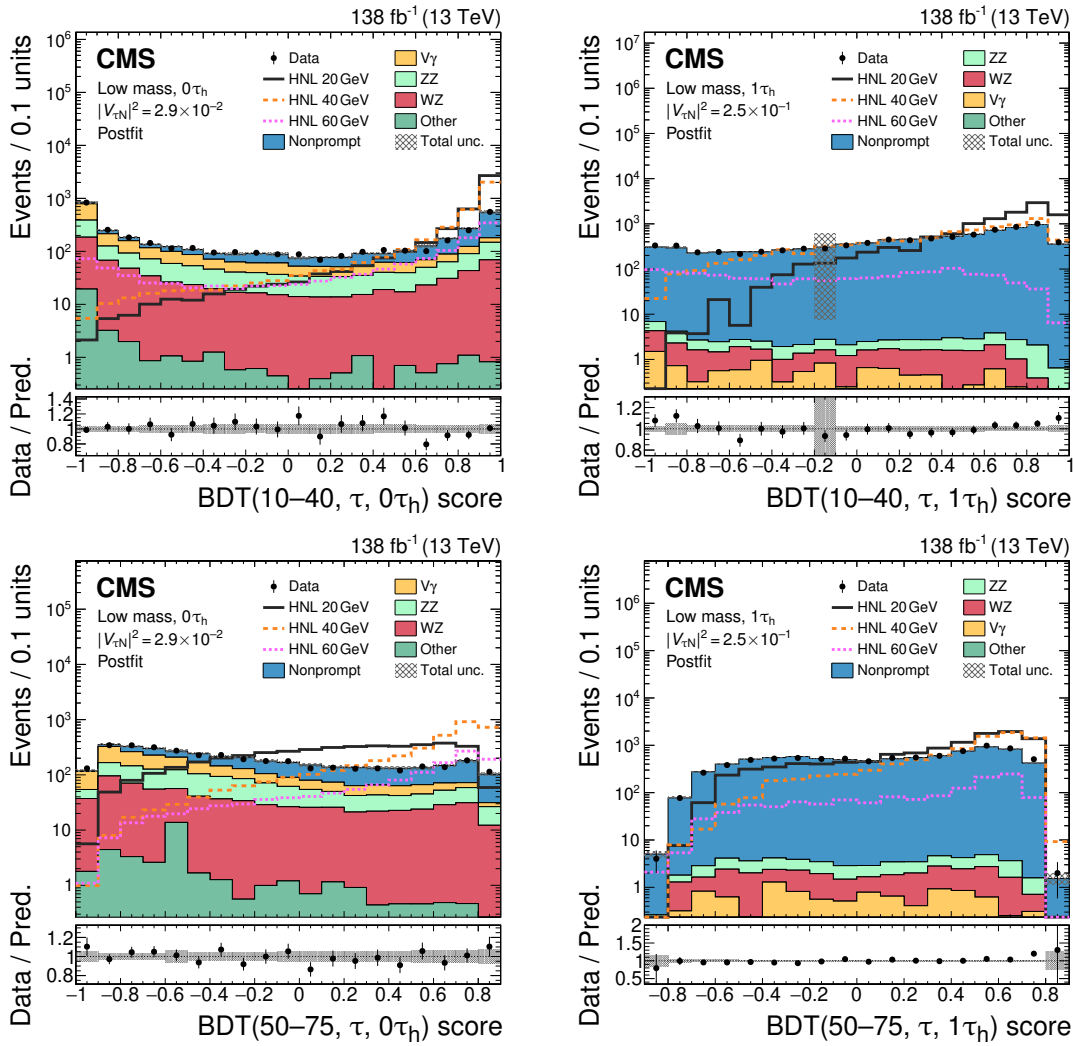


Figure 10: Comparison of the observed (points) and predicted (coloured histograms) BDT output distributions of the low-mass selection, shown for the  $0\tau_h$  channels combined (left column) and the  $1\tau_h$  channels combined (right column). The output scores  $\text{BDT}(10-40, \tau, 0\tau_h)$  (upper left),  $\text{BDT}(10-40, \tau, 1\tau_h)$  (upper right),  $\text{BDT}(50-75, \tau, 0\tau_h)$  (lower left), and  $\text{BDT}(50-75, \tau, 1\tau_h)$  (lower right) are displayed. The predicted background yields are shown with the values of the normalizations and nuisance parameters obtained in background-only fits applied (“postfit”). The HNL predictions for three different  $m_N$  values with exclusive coupling to tau neutrinos are shown with coloured lines. The vertical bars on the points represent the statistical uncertainties in the data, and the hatched bands the total uncertainties in the background predictions as obtained from the fits. In the lower panels, the ratios of the event yield in data to the overall sum of the background predictions are shown.



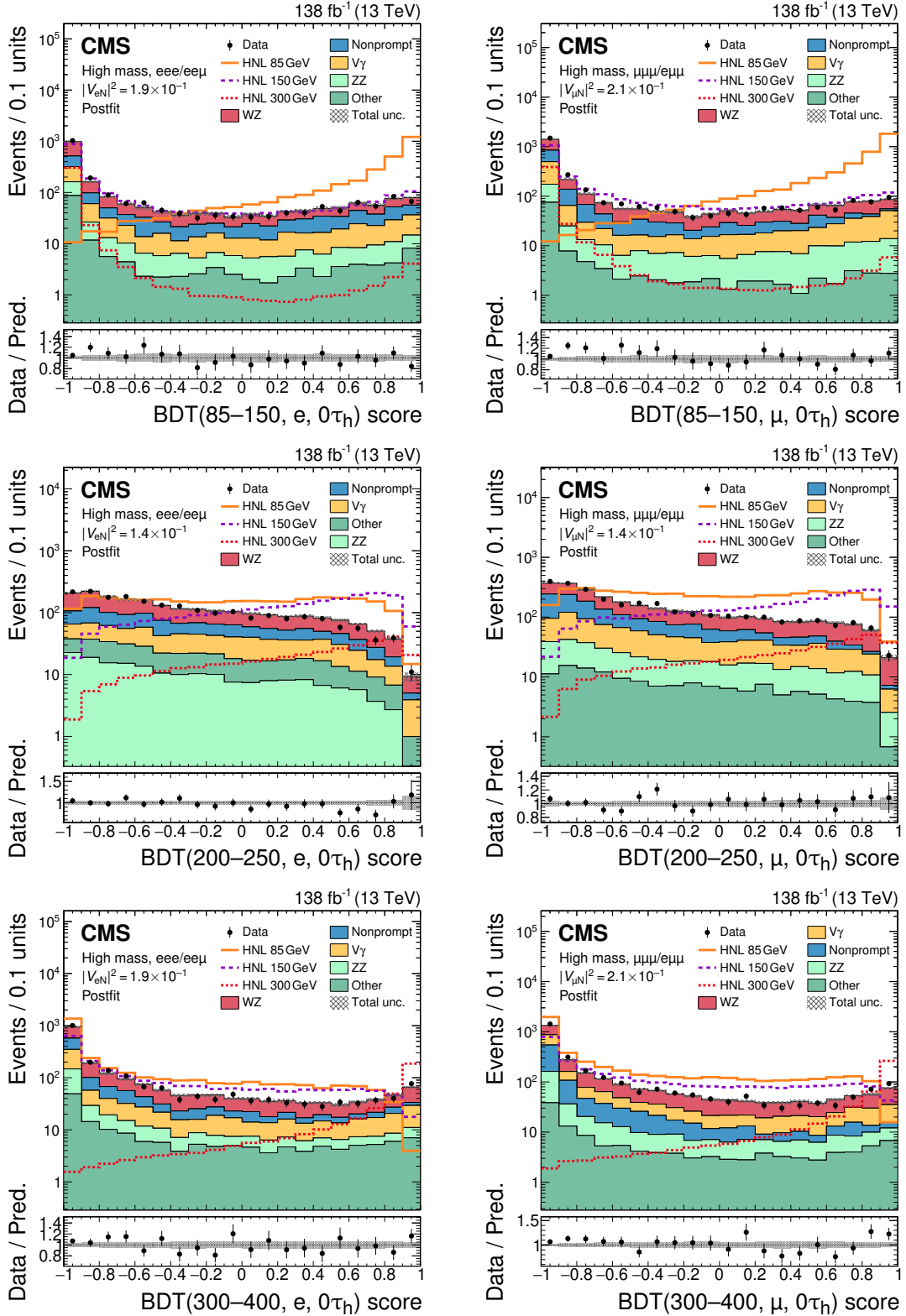


Figure 11: Comparison of the observed (points) and predicted (coloured histograms) BDT output distributions of the high-mass selection, shown for the  $eee$  and  $ee\mu$  channels combined (left column) and the  $e\mu\mu$  and  $\mu\mu\mu$  channels combined (right column). The output scores BDT(85–150,  $e, 0\tau_h$ ) (upper left), BDT(85–150,  $\mu, 0\tau_h$ ) (upper right), BDT(200–250,  $e, 0\tau_h$ ) (middle left), BDT(200–250,  $\mu, 0\tau_h$ ) (middle right), BDT(300–400,  $e, 0\tau_h$ ) (lower left), and BDT(300–400,  $\mu, 0\tau_h$ ) (lower right) are displayed. Notations as in Fig. 9.

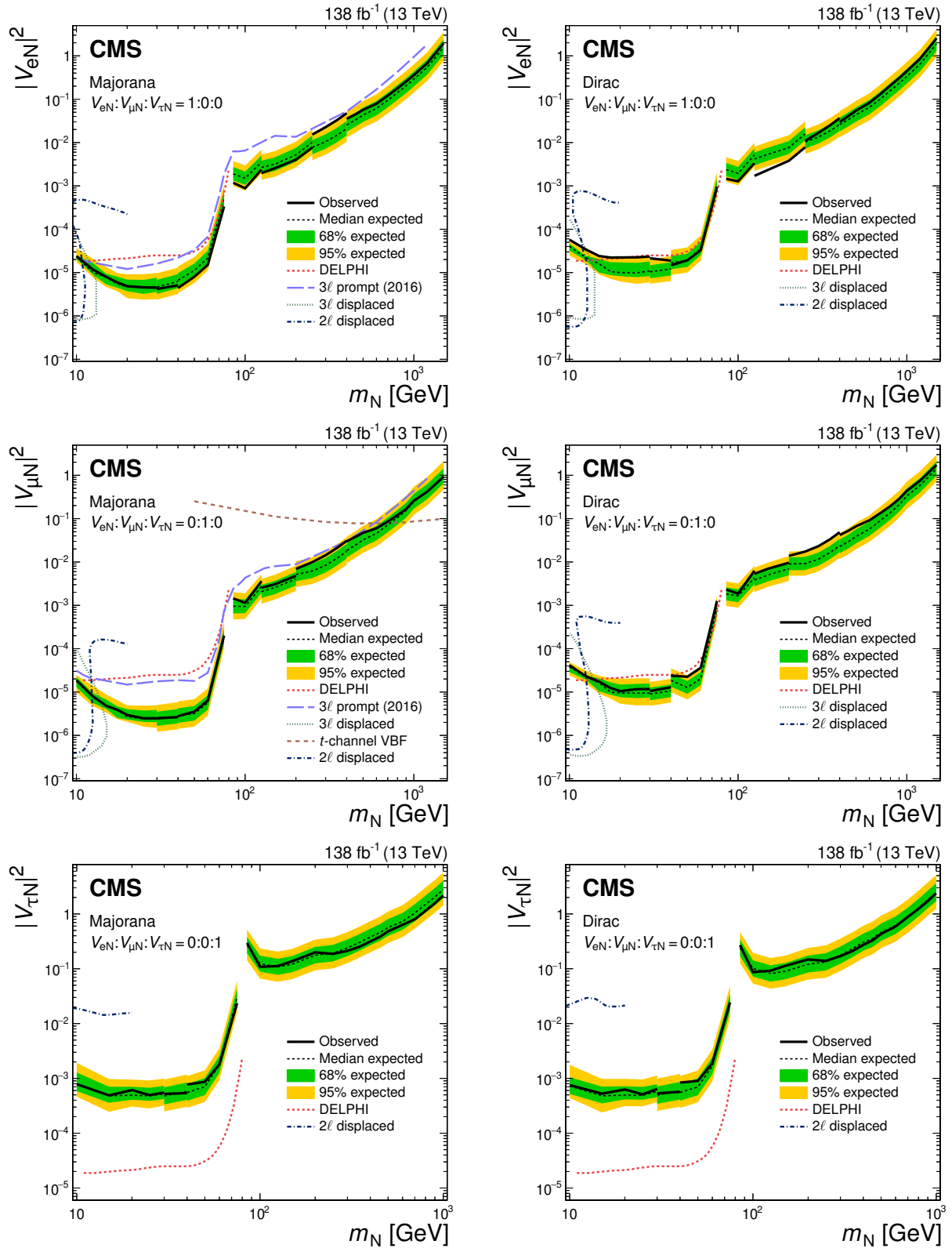


Figure 12: The 95% CL limits on  $|V_{eN}|^2$  (upper row),  $|V_{\mu N}|^2$  (middle row), and  $|V_{\tau N}|^2$  (lower row) as functions of  $m_N$  for a Majorana (left) and Dirac (right) HNL. The area above the solid (dashed) black curve indicates the observed (expected) exclusion region. Previous results from the DELPHI Collaboration [134] are shown for reference. The previous CMS result “3 $\ell$  prompt (2016)” [42] is shown to highlight the improvements achieved in our analysis, and the results “3 $\ell$  displaced” [46], “2 $\ell$  displaced” [48], and “ $t$ -channel VBF” [135] are shown to highlight the complementarity to other search strategies.

one standard deviation, with a few exceptions discussed in the following.

For exclusive couplings to electron neutrinos and  $m_N < m_W$ , we exclude  $|V_{eN}|^2$  values for Majorana (Dirac) HNL of  $4.8 \times 10^{-6}$  ( $2.23 \times 10^{-5}$ ) at a mass of 20 GeV, of  $1.5 \times 10^{-5}$  ( $3.3 \times 10^{-5}$ ) at 60 GeV, and of  $3.3 \times 10^{-4}$  ( $9.6 \times 10^{-4}$ ) at 75 GeV, which is the highest simulated mass point below  $m_W$ . For masses below 30 GeV, the HNLs become long-lived and have a reduced selection efficiency, with, e.g., 16 times less events selected at  $m_N = 10$  GeV and  $|V_{eN}|^2 = 10^{-5}$  compared with a prompt HNL of the same mass, resulting in less stringent limits. In the high-mass selection, we exclude  $|V_{eN}|^2$  values for Majorana (Dirac) HNL of  $1.2 \times 10^{-3}$  ( $1.5 \times 10^{-3}$ ) at 85 GeV, which is the lightest simulated mass point above  $m_W$ , of  $8.8 \times 10^{-4}$  ( $1.3 \times 10^{-3}$ ) at 100 GeV, and of  $7.8 \times 10^{-2}$  ( $8.2 \times 10^{-2}$ ) at 600 GeV. The most notable discrepancies between observed and expected limits are for HNL masses between 250 and 400 GeV (125 and 250 GeV) in the case of a Majorana (Dirac) HNL, caused by a small excess (deficit) in the last bin of the corresponding BDT score distribution. Similarly a discrepancy is observed at HNL masses below 40 GeV in case of a Dirac HNL. This is due to a small excess in the relevant BDT distribution, which leads the sensitivity in the Dirac requirement of an OSSF electron pair in the final selection. Compared with the results of the previous prompt HNL search presented in Ref. [42] for Majorana HNL, the limits improve by up to one order of magnitude. For masses below 20 GeV, we exclude short-lived HNL scenarios not excluded by the displaced HNL searches presented in Refs. [46, 48]. The exclusion limits obtained by the DELPHI Collaboration [134] for  $m_N < m_W$  are less stringent (similar) compared with our results for the case of Majorana (Dirac) HNL.

Using the low-mass selection and considering exclusive couplings to muon neutrinos, we find limits on  $|V_{\mu N}|^2$  for Majorana (Dirac) HNL of  $2.9 \times 10^{-6}$  ( $1.0 \times 10^{-5}$ ) at  $m_N = 20$  GeV, of  $6.3 \times 10^{-6}$  ( $3.6 \times 10^{-5}$ ) at 60 GeV, and of  $2.0 \times 10^{-4}$  ( $1.3 \times 10^{-3}$ ) at 75 GeV. Below 30 GeV, the limits are less stringent because of the impact of the long HNL lifetime, with 34 times fewer events selected at  $m_N = 10$  GeV and  $|V_{\mu N}|^2 = 10^{-5}$  compared with a prompt HNL. Above  $m_W$ , we exclude  $|V_{\mu N}|^2$  values for Majorana (Dirac) HNL of  $1.4 \times 10^{-3}$  ( $2.3 \times 10^{-3}$ ) at a mass of 85 GeV, of  $1.1 \times 10^{-3}$  ( $1.9 \times 10^{-3}$ ) at 100 GeV, and of  $6.0 \times 10^{-2}$  ( $9.1 \times 10^{-2}$ ) at 600 GeV. We improve the exclusion limits from the previous prompt HNL search [42] by up to one order of magnitude, and complement the limits from previous displaced HNL searches [46, 48] for short-lived HNLs below 20 GeV. For  $m_N < m_W$ , our exclusion limits are more stringent (similar) in the case of Majorana (Dirac) HNLs compared with the results of the DELPHI Collaboration [134]. Compared with a CMS result that searches for high-mass Majorana HNLs with muon neutrino couplings in  $t$ -channel VBF production [135], our results provide stricter exclusion limits up to  $m_N \approx 700$  GeV.

The case of HNLs at the GeV scale with exclusive tau neutrino couplings was probed before only by the DELPHI Collaboration for  $m_N < m_W$  [134], by the BaBar Collaboration for  $m_N < 1.3$  GeV [136], and recently by the CMS Collaboration in displaced HNL searches for  $m_N < 20$  GeV [48]. Using the low-mass selection, we exclude Majorana (Dirac) HNLs with  $|V_{\tau N}|^2$  values of  $6.1 \times 10^{-4}$  ( $6.3 \times 10^{-4}$ ) at a mass of 20 GeV, of  $1.8 \times 10^{-3}$  ( $1.9 \times 10^{-3}$ ) at 60 GeV, and of  $2.3 \times 10^{-2}$  ( $2.4 \times 10^{-2}$ ) at 75 GeV. The DELPHI limits for  $m_N < m_W$  are up to two orders of magnitude more stringent than our results. Above  $m_W$ , the tau neutrino couplings are probed for the first time, and we find limits for Majorana (Dirac) HNLs of  $3.0 \times 10^{-1}$  ( $2.7 \times 10^{-1}$ ) at 85 GeV,  $1.1 \times 10^{-1}$  ( $8.6 \times 10^{-2}$ ) at 100 GeV, and  $5.9 \times 10^{-1}$  ( $5.0 \times 10^{-2}$ ) at 600 GeV.

## 10 Summary

A search for heavy neutral leptons (HNLs) produced in proton-proton collisions at  $\sqrt{s} = 13$  TeV has been presented. The data were collected with the CMS experiment at the LHC and correspond to an integrated luminosity of  $138 \text{ fb}^{-1}$ . Events with three charged leptons (electrons, muons, and hadronically decaying tau leptons) are selected, and dedicated identification criteria based on machine learning techniques are applied to reduce the contribution from non-prompt leptons not originating from the hard scattering process. Remaining standard model (SM) background contributions with nonprompt leptons are estimated from control samples in data, whereas other SM contributions that mostly stem from diboson production are estimated from Monte Carlo event simulations. A combination of categorization by kinematic properties and machine learning discriminants achieves optimal separation of the predicted signal and SM background contributions.

No significant deviations from the SM predictions are observed. Exclusion limits at 95% confidence level are evaluated, assuming exclusive HNL couplings to a single generation of SM neutrinos in the mass range  $10 \text{ GeV} - 1.5 \text{ TeV}$ , for both Majorana and Dirac HNLs. These results exceed previous experimental constraints over large parts of the mass range. Constraints on tau neutrino couplings for HNL masses above the  $W$  boson mass are presented for the first time.

## Acknowledgments

We congratulate our colleagues in the CERN accelerator departments for the excellent performance of the LHC and thank the technical and administrative staffs at CERN and at other CMS institutes for their contributions to the success of the CMS effort. In addition, we gratefully acknowledge the computing centres and personnel of the Worldwide LHC Computing Grid and other centres for delivering so effectively the computing infrastructure essential to our analyses. Finally, we acknowledge the enduring support for the construction and operation of the LHC, the CMS detector, and the supporting computing infrastructure provided by the following funding agencies: SC (Armenia), BMBWF and FWF (Austria); FNRS and FWO (Belgium); CNPq, CAPES, FAPERJ, FAPERGS, and FAPESP (Brazil); MES and BNSF (Bulgaria); CERN; CAS, MoST, and NSFC (China); MINCIENCIAS (Colombia); MSES and CSF (Croatia); RIF (Cyprus); SENESCYT (Ecuador); ERC PRG, RVTT3 and MoER TK202 (Estonia); Academy of Finland, MEC, and HIP (Finland); CEA and CNRS/IN2P3 (France); SRNSF (Georgia); BMBF, DFG, and HGF (Germany); GSRI (Greece); NKFIH (Hungary); DAE and DST (India); IPM (Iran); SFI (Ireland); INFN (Italy); MSIP and NRF (Republic of Korea); MES (Latvia); LMTLT (Lithuania); MOE and UM (Malaysia); BUAP, CINVESTAV, CONACYT, LNS, SEP, and UASLP-FAI (Mexico); MOS (Montenegro); MBIE (New Zealand); PAEC (Pakistan); MES and NSC (Poland); FCT (Portugal); MESTD (Serbia); MCIN/AEI and PCTI (Spain); MOSTR (Sri Lanka); Swiss Funding Agencies (Switzerland); MST (Taipei); MHESI and NSTDA (Thailand); TUBITAK and TENMAK (Turkey); NASU (Ukraine); STFC (United Kingdom); DOE and NSF (USA).

Individuals have received support from the Marie-Curie programme and the European Research Council and Horizon 2020 Grant, contract Nos. 675440, 724704, 752730, 758316, 765710, 824093, 101115353, and COST Action CA16108 (European Union); the Leventis Foundation; the Alfred P. Sloan Foundation; the Alexander von Humboldt Foundation; the Science Committee, project no. 22r1-037 (Armenia); the Belgian Federal Science Policy Office; the Fonds pour la Formation à la Recherche dans l'Industrie et dans l'Agriculture (FRIA-Belgium); the Agentschap

voor Innovatie door Wetenschap en Technologie (IWT-Belgium); the F.R.S.-FNRS and FWO (Belgium) under the “Excellence of Science – EOS” – be.h project n. 30820817; the Beijing Municipal Science & Technology Commission, No. Z191100007219010 and Fundamental Research Funds for the Central Universities (China); the Ministry of Education, Youth and Sports (MEYS) of the Czech Republic; the Shota Rustaveli National Science Foundation, grant FR-22-985 (Georgia); the Deutsche Forschungsgemeinschaft (DFG), under Germany’s Excellence Strategy – EXC 2121 “Quantum Universe” – 390833306, and under project number 400140256 – GRK2497; the Hellenic Foundation for Research and Innovation (HFRI), Project Number 2288 (Greece); the Hungarian Academy of Sciences, the New National Excellence Program - ÚNKP, the NKFIH research grants K 124845, K 124850, K 128713, K 128786, K 129058, K 131991, K 133046, K 138136, K 143460, K 143477, 2020-2.2.1-ED-2021-00181, and TKP2021-NKTA-64 (Hungary); the Council of Science and Industrial Research, India; ICSC – National Research Centre for High Performance Computing, Big Data and Quantum Computing, funded by the EU NexGeneration program (Italy); the Latvian Council of Science; the Ministry of Education and Science, project no. 2022/WK/14, and the National Science Center, contracts Opus 2021/41/B/ST2/01369 and 2021/43/B/ST2/01552 (Poland); the Fundação para a Ciência e a Tecnologia, grant CEECIND/01334/2018 (Portugal); the National Priorities Research Program by Qatar National Research Fund; MCIN/AEI/10.13039/501100011033, ERDF “a way of making Europe”, and the Programa Estatal de Fomento de la Investigación Científica y Técnica de Excelencia María de Maeztu, grant MDM-2017-0765 and Programa Severo Ochoa del Principado de Asturias (Spain); the Chulalongkorn Academic into Its 2nd Century Project Advancement Project, and the National Science, Research and Innovation Fund via the Program Management Unit for Human Resources & Institutional Development, Research and Innovation, grant B37G660013 (Thailand); the Kavli Foundation; the Nvidia Corporation; the SuperMicro Corporation; the Welch Foundation, contract C-1845; and the Weston Havens Foundation (USA).

## References

- [1] Super-Kamiokande Collaboration, “Evidence for oscillation of atmospheric neutrinos”, *Phys. Rev. Lett.* **81** (1998) 1562, doi:10.1103/PhysRevLett.81.1562, arXiv:hep-ex/9807003.
- [2] SNO Collaboration, “Direct evidence for neutrino flavor transformation from neutral-current interactions in the Sudbury Neutrino Observatory”, *Phys. Rev. Lett.* **89** (2002) 011301, doi:10.1103/PhysRevLett.89.011301, arXiv:nucl-ex/0204008.
- [3] KamLAND Collaboration, “First results from KamLAND: Evidence for reactor antineutrino disappearance”, *Phys. Rev. Lett.* **90** (2003) 021802, doi:10.1103/PhysRevLett.90.021802, arXiv:hep-ex/0212021.
- [4] S. Bilenky, “Neutrino oscillations: From a historical perspective to the present status”, *Nucl. Phys. B* **908** (2016) 2, doi:10.1016/j.nuclphysb.2016.01.025, arXiv:1602.00170.
- [5] J. Formaggio, A. de Gouvêa, and R. Robertson, “Direct measurements of neutrino mass”, *Phys. Rept.* **914** (2021) 1, doi:10.1016/j.physrep.2021.02.002, arXiv:2102.00594.

- [6] KATRIN Collaboration, “Direct neutrino-mass measurement with sub-electronvolt sensitivity”, *Nature Phys.* **18** (2022) 160, doi:10.1038/s41567-021-01463-1, arXiv:2105.08533.
- [7] Planck Collaboration, “Planck 2018 results. VI. cosmological parameters”, *Astron. Astrophys.* **641** (2020) A6, doi:10.1051/0004-6361/201833910, arXiv:1807.06209. [Erratum: doi:10.1051/0004-6361/201833910e].
- [8] eBOSS Collaboration, “Completed SDSS-IV extended baryon oscillation spectroscopic survey: Cosmological implications from two decades of spectroscopic surveys at the Apache Point Observatory”, *Phys. Rev. D* **103** (2021) 083533, doi:10.1103/PhysRevD.103.083533, arXiv:2007.08991.
- [9] Z. Sakr, “A short review on the latest neutrinos mass and number constraints from cosmological observables”, *Universe* **8** (2022) 284, doi:10.3390/universe8050284.
- [10] P. Minkowski, “ $\mu \rightarrow e\gamma$  at a rate of one out of  $10^9$  muon decays?”, *Phys. Lett. B* **67** (1977) 421, doi:10.1016/0370-2693(77)90435-X.
- [11] T. Yanagida, “Horizontal gauge symmetry and masses of neutrinos”, in *Proc. Workshop on the Unified Theories and the Baryon Number in the Universe: Tsukuba, Japan, February 13–14, 1979*. 1979. [Conf. Proc. C 7902131 (1979) 95].
- [12] M. Gell-Mann, P. Ramond, and R. Slansky, “Complex spinors and unified theories”, in *Supergravity*, p. 315. North Holland Publishing, 1979. arXiv:1306.4669.
- [13] S. Glashow, “The future of elementary particle physics”, *NATO Sci. Ser. B* **61** (1980) 687, doi:10.1007/978-1-4684-7197-7\_15.
- [14] R. Mohapatra and G. Senjanović, “Neutrino mass and spontaneous parity nonconservation”, *Phys. Rev. Lett.* **44** (1980) 912, doi:10.1103/PhysRevLett.44.912.
- [15] J. Schechter and J. Valle, “Neutrino masses in  $SU(2) \otimes U(1)$  theories”, *Phys. Rev. D* **22** (1980) 2227, doi:10.1103/PhysRevD.22.2227.
- [16] R. Shrock, “General theory of weak leptonic and semileptonic decays. I. leptonic pseudoscalar meson decays, with associated tests for, and bounds on, neutrino masses and lepton mixing”, *Phys. Rev. D* **24** (1981) 1232, doi:10.1103/PhysRevD.24.1232.
- [17] Y. Cai, T. Han, T. Li, and R. Ruiz, “Lepton number violation: Seesaw models and their collider tests”, *Front. Phys.* **6** (2018) 40, doi:10.3389/fphy.2018.00040, arXiv:1711.02180.
- [18] S. Dodelson and L. Widrow, “Sterile neutrinos as dark matter”, *Phys. Rev. Lett.* **72** (1994) 17, doi:10.1103/PhysRevLett.72.17, arXiv:hep-ph/9303287.
- [19] A. Boyarsky et al., “Sterile neutrino dark matter”, *Prog. Part. Nucl. Phys.* **104** (2019) 1, doi:10.1016/j.pnpnp.2018.07.004, arXiv:1807.07938.
- [20] M. Fukugita and T. Yanagida, “Baryogenesis without grand unification”, *Phys. Lett. B* **174** (1986) 45, doi:10.1016/0370-2693(86)91126-3.
- [21] E. Chun et al., “Probing leptogenesis”, *Int. J. Mod. Phys. A* **33** (2018) 1842005, doi:10.1142/S0217751X18420058, arXiv:1711.02865.

- [22] M. Drewes, Y. Georis, and J. Klarić, “Mapping the viable parameter space for testable leptogenesis”, *Phys. Rev. Lett.* **128** (2022) 051801, doi:10.1103/PhysRevLett.128.051801, arXiv:2106.16226.
- [23] J. Beacham et al., “Physics beyond colliders at CERN: Beyond the standard model working group report”, *J. Phys. G* **47** (2020) 010501, doi:10.1088/1361-6471/ab4cd2, arXiv:1901.09966.
- [24] M. Drewes, J. Klarić, and J. López-Pavón, “New benchmark models for heavy neutral lepton searches”, *Eur. Phys. J. C* **82** (2022) 1176, doi:10.1140/epjc/s10052-022-11100-7, arXiv:2207.02742.
- [25] F. del Aguila and J. Aguilar-Saavedra, “Distinguishing seesaw models at LHC with multi-lepton signals”, *Nucl. Phys. B* **813** (2009) 22, doi:10.1016/j.nuclphysb.2008.12.029, arXiv:0808.2468.
- [26] A. Atre, T. Han, S. Pascoli, and B. Zhang, “The search for heavy Majorana neutrinos”, *JHEP* **05** (2009) 030, doi:10.1088/1126-6708/2009/05/030, arXiv:0901.3589.
- [27] V. Tello et al., “Left-right symmetry: from LHC to neutrinoless double beta decay”, *Phys. Rev. Lett.* **106** (2011) 151801, doi:10.1103/PhysRevLett.106.151801, arXiv:1011.3522.
- [28] F. Deppisch, P. Bhupal Dev, and A. Pilaftsis, “Neutrinos and collider physics”, *New J. Phys.* **17** (2015) 075019, doi:10.1088/1367-2630/17/7/075019, arXiv:1502.06541.
- [29] S. Pascoli, R. Ruiz, and C. Weiland, “Heavy neutrinos with dynamic jet vetoes: multilepton searches at  $\sqrt{s} = 14, 27, \text{ and } 100 \text{ TeV}$ ”, *JHEP* **06** (2019) 049, doi:10.1007/JHEP06(2019)049, arXiv:1812.08750.
- [30] A. Abdullahi et al., “The present and future status of heavy neutral leptons”, *J. Phys. G* **50** (2023) 020501, doi:10.1088/1361-6471/ac98f9, arXiv:2203.08039.
- [31] C. Antel et al., “Feebly interacting particles: FIPs 2022 workshop report”, *Eur. Phys. J. C* **83** (2023) 1122, doi:10.1140/epjc/s10052-023-12168-5, arXiv:2305.01715.
- [32] W.-Y. Keung and G. Senjanovic, “Majorana neutrinos and the production of the right-handed charged gauge boson”, *Phys. Rev. Lett.* **50** (1983) 1427, doi:10.1103/PhysRevLett.50.1427.
- [33] S. Petcov, “Possible signature for production of Majorana particles in  $e^+e^-$  and  $p\bar{p}$  collisions”, *Phys. Lett. B* **139** (1984) 421, doi:10.1016/0370-2693(84)91844-6.
- [34] A. Datta, M. Guchait, and A. Pilaftsis, “Probing lepton number violation via Majorana neutrinos at hadron supercolliders”, *Phys. Rev. D* **50** (1994) 3195, doi:10.1103/PhysRevD.50.3195, arXiv:hep-ph/9311257.
- [35] P. Bhupal Dev, A. Pilaftsis, and U.-k. Yang, “New production mechanism for heavy neutrinos at the LHC”, *Phys. Rev. Lett.* **112** (2014) 081801, doi:10.1103/PhysRevLett.112.081801, arXiv:1308.2209.
- [36] D. Alva, T. Han, and R. Ruiz, “Heavy Majorana neutrinos from  $W\gamma$  fusion at hadron colliders”, *JHEP* **02** (2015) 072, doi:10.1007/JHEP02(2015)072, arXiv:1411.7305.

- [37] C. Degrande, O. Mattelaer, R. Ruiz, and J. Turner, “Fully-automated precision predictions for heavy neutrino production mechanisms at hadron colliders”, *Phys. Rev. D* **94** (2016) 053002, doi:10.1103/PhysRevD.94.053002, arXiv:1602.06957.
- [38] CMS Collaboration, “Search for heavy Majorana neutrinos in  $\mu^\pm\mu^\pm + \text{jets}$  and  $e^\pm e^\pm + \text{jets}$  events in pp collisions at  $\sqrt{s} = 7 \text{ TeV}$ ”, *Phys. Lett. B* **717** (2012) 109, doi:10.1016/j.physletb.2012.09.012, arXiv:1207.6079.
- [39] CMS Collaboration, “Search for heavy Majorana neutrinos in  $\mu^\pm\mu^\pm + \text{jets}$  events in proton-proton collisions at  $\sqrt{s} = 8 \text{ TeV}$ ”, *Phys. Lett. B* **748** (2015) 144, doi:10.1016/j.physletb.2015.06.070, arXiv:1501.05566.
- [40] ATLAS Collaboration, “Search for heavy Majorana neutrinos with the ATLAS detector in pp collisions at  $\sqrt{s} = 8 \text{ TeV}$ ”, *JHEP* **07** (2015) 162, doi:10.1007/JHEP07(2015)162, arXiv:1506.06020.
- [41] CMS Collaboration, “Search for heavy Majorana neutrinos in  $e^\pm e^\pm + \text{jets}$  and  $e^\pm\mu^\pm + \text{jets}$  events in proton-proton collisions at  $\sqrt{s} = 8 \text{ TeV}$ ”, *JHEP* **04** (2016) 169, doi:10.1007/JHEP04(2016)169, arXiv:1603.02248.
- [42] CMS Collaboration, “Search for heavy neutral leptons in events with three charged leptons in proton-proton collisions at  $\sqrt{s} = 13 \text{ TeV}$ ”, *Phys. Rev. Lett.* **120** (2018) 221801, doi:10.1103/PhysRevLett.120.221801, arXiv:1802.02965.
- [43] CMS Collaboration, “Search for heavy Majorana neutrinos in same-sign dilepton channels in proton-proton collisions at  $\sqrt{s} = 13 \text{ TeV}$ ”, *JHEP* **01** (2019) 122, doi:10.1007/JHEP01(2019)122, arXiv:1806.10905.
- [44] ATLAS Collaboration, “Search for heavy neutral leptons in decays of W bosons produced in 13 TeV pp collisions using prompt and displaced signatures with the ATLAS detector”, *JHEP* **10** (2019) 265, doi:10.1007/JHEP10(2019)265, arXiv:1905.09787.
- [45] LHCb Collaboration, “Search for heavy neutral leptons in  $W^+ \rightarrow \mu^+\mu^\pm \text{jet}$  decays”, *Eur. Phys. J. C* **81** (2021) 248, doi:10.1140/epjc/s10052-021-08973-5, arXiv:2011.05263.
- [46] CMS Collaboration, “Search for long-lived heavy neutral leptons with displaced vertices in proton-proton collisions at  $\sqrt{s} = 13 \text{ TeV}$ ”, *JHEP* **07** (2022) 081, doi:10.1007/JHEP07(2022)081, arXiv:2201.05578.
- [47] ATLAS Collaboration, “Search for heavy neutral leptons in decays of W bosons using a dilepton displaced vertex in  $\sqrt{s} = 13 \text{ TeV}$  pp collisions with the ATLAS detector”, *Phys. Rev. Lett.* **131** (2023) 061803, doi:10.1103/PhysRevLett.131.061803, arXiv:2204.11988.
- [48] CMS Collaboration, “Search for long-lived heavy neutral leptons with lepton flavour conserving or violating decays to a jet and a charged lepton”, 2023. arXiv:2312.07484. Submitted to *JHEP*.
- [49] A. Abada, N. Bernal, M. Losada, and X. Marcano, “Inclusive displaced vertex searches for heavy neutral leptons at the LHC”, *JHEP* **01** (2019) 093, doi:10.1007/JHEP01(2019)093, arXiv:1807.10024.



- 
- [50] J.-L. Tastet, O. Ruchayskiy, and I. Timiryasov, “Reinterpreting the ATLAS bounds on heavy neutral leptons in a realistic neutrino oscillation model”, *JHEP* **12** (2021) 182, doi:10.1007/JHEP12(2021)182, arXiv:2107.12980.
- [51] HEPData record for this analysis, 2024. doi:10.17182/hepdata.146676.
- [52] T. Asaka, S. Blanchet, and M. Shaposhnikov, “The  $\nu$ MSM, dark matter and neutrino masses”, *Phys. Lett. B* **631** (2005) 151, doi:10.1016/j.physletb.2005.09.070, arXiv:hep-ph/0503065.
- [53] CMS Collaboration, “The CMS experiment at the CERN LHC”, *JINST* **3** (2008) S08004, doi:10.1088/1748-0221/3/08/S08004.
- [54] CMS Collaboration, “Development of the CMS detector for the CERN LHC Run 3”, 2023. arXiv:2309.05466. Accepted by *JINST*.
- [55] CMS Collaboration, “Performance of the CMS Level-1 trigger in proton-proton collisions at  $\sqrt{s} = 13$  TeV”, *JINST* **15** (2020) P10017, doi:10.1088/1748-0221/15/10/P10017, arXiv:2006.10165.
- [56] CMS Collaboration, “The CMS trigger system”, *JINST* **12** (2017) P01020, doi:10.1088/1748-0221/12/01/P01020, arXiv:1609.02366.
- [57] CMS Collaboration, “Particle-flow reconstruction and global event description with the CMS detector”, *JINST* **12** (2017) P10003, doi:10.1088/1748-0221/12/10/P10003, arXiv:1706.04965.
- [58] CMS Collaboration, “Technical proposal for the Phase-II upgrade of the Compact Muon Solenoid”, CMS Technical Proposal CERN-LHCC-2015-010, CMS-TDR-15-02, 2015.
- [59] M. Cacciari, G. P. Salam, and G. Soyez, “The anti- $k_T$  jet clustering algorithm”, *JHEP* **04** (2008) 063, doi:10.1088/1126-6708/2008/04/063, arXiv:0802.1189.
- [60] M. Cacciari, G. P. Salam, and G. Soyez, “FASTJET user manual”, *Eur. Phys. J. C* **72** (2012) 1896, doi:10.1140/epjc/s10052-012-1896-2, arXiv:1111.6097.
- [61] CMS Collaboration, “Jet energy scale and resolution in the CMS experiment in pp collisions at 8 TeV”, *JINST* **12** (2017) P02014, doi:10.1088/1748-0221/12/02/P02014, arXiv:1607.03663.
- [62] CMS Collaboration, “Jet algorithms performance in 13 TeV data”, CMS Physics Analysis Summary CMS-PAS-JME-16-003, 2017.
- [63] CMS Collaboration, “Performance of missing transverse momentum reconstruction in proton-proton collisions at  $\sqrt{s} = 13$  TeV using the CMS detector”, *JINST* **14** (2019) P07004, doi:10.1088/1748-0221/14/07/P07004, arXiv:1903.06078.
- [64] CMS Collaboration, “Identification of heavy-flavour jets with the CMS detector in pp collisions at 13 TeV”, *JINST* **13** (2018) P05011, doi:10.1088/1748-0221/13/05/P05011, arXiv:1712.07158.
- [65] E. Bols et al., “Jet flavour classification using DeepJet”, *JINST* **15** (2020) P12012, doi:10.1088/1748-0221/15/12/P12012, arXiv:2008.10519.

- [66] CMS Collaboration, “Performance summary of AK4 jet b tagging with data from proton-proton collisions at 13 TeV with the CMS detector”, CMS Detector Performance Note CMS-DP-2023-005, 2023.
- [67] GEANT4 Collaboration, “GEANT4—a simulation toolkit”, *Nucl. Instrum. Meth. A* **506** (2003) 250, doi:10.1016/S0168-9002(03)01368-8.
- [68] CMS Collaboration, “Pileup mitigation at CMS in 13 TeV data”, *JINST* **15** (2020) P09018, doi:10.1088/1748-0221/15/09/P09018, arXiv:2003.00503.
- [69] J. Alwall et al., “The automated computation of tree-level and next-to-leading order differential cross sections, and their matching to parton shower simulations”, *JHEP* **07** (2014) 079, doi:10.1007/JHEP07(2014)079, arXiv:1405.0301.
- [70] P. Artoisenet, R. Frederix, O. Mattelaer, and R. Rietkerk, “Automatic spin-entangled decays of heavy resonances in Monte Carlo simulations”, *JHEP* **03** (2013) 015, doi:10.1007/JHEP03(2013)015, arXiv:1212.3460.
- [71] NNPDF Collaboration, “Parton distributions from high-precision collider data”, *Eur. Phys. J. C* **77** (2017) 663, doi:10.1140/epjc/s10052-017-5199-5, arXiv:1706.00428.
- [72] A. Manohar, P. Nason, G. P. Salam, and G. Zanderighi, “How bright is the proton? A precise determination of the photon parton distribution function”, *Phys. Rev. Lett.* **117** (2016) 242002, doi:10.1103/PhysRevLett.117.242002, arXiv:1607.04266.
- [73] A. V. Manohar, P. Nason, G. P. Salam, and G. Zanderighi, “The photon content of the proton”, *JHEP* **12** (2017) 046, doi:10.1007/JHEP12(2017)046, arXiv:1708.01256.
- [74] NNPDF Collaboration, “Illuminating the photon content of the proton within a global PDF analysis”, *SciPost Phys.* **5** (2018) 008, doi:10.21468/SciPostPhys.5.1.008, arXiv:1712.07053.
- [75] K. Bondarenko, A. Boyarsky, D. Gorbunov, and O. Ruchayskiy, “Phenomenology of GeV-scale heavy neutral leptons”, *JHEP* **11** (2018) 032, doi:10.1007/JHEP11(2018)032, arXiv:1805.08567.
- [76] P. Nason, “A new method for combining NLO QCD with shower Monte Carlo algorithms”, *JHEP* **11** (2004) 040, doi:10.1088/1126-6708/2004/11/040, arXiv:hep-ph/0409146.
- [77] S. Frixione, G. Ridolfi, and P. Nason, “A positive-weight next-to-leading-order Monte Carlo for heavy flavour hadroproduction”, *JHEP* **09** (2007) 126, doi:10.1088/1126-6708/2007/09/126, arXiv:0707.3088.
- [78] S. Frixione, P. Nason, and C. Oleari, “Matching NLO QCD computations with parton shower simulations: the POWHEG method”, *JHEP* **11** (2007) 070, doi:10.1088/1126-6708/2007/11/070, arXiv:0709.2092.
- [79] S. Alioli, P. Nason, C. Oleari, and E. Re, “NLO single-top production matched with shower in POWHEG:  $s$ - and  $t$ -channel contributions”, *JHEP* **09** (2009) 111, doi:10.1088/1126-6708/2009/09/111, arXiv:0907.4076. [Erratum: doi:10.1007/JHEP02(2010)011].

- [80] P. Nason and C. Oleari, “NLO Higgs boson production via vector-boson fusion matched with shower in POWHEG”, *JHEP* **02** (2010) 037, doi:10.1007/JHEP02(2010)037, arXiv:0911.5299.
- [81] S. Alioli, P. Nason, C. Oleari, and E. Re, “A general framework for implementing NLO calculations in shower Monte Carlo programs: the POWHEG BOX”, *JHEP* **06** (2010) 043, doi:10.1007/JHEP06(2010)043, arXiv:1002.2581.
- [82] E. Re, “Single-top Wt-channel production matched with parton showers using the POWHEG method”, *Eur. Phys. J. C* **71** (2011) 1547, doi:10.1140/epjc/s10052-011-1547-z, arXiv:1009.2450.
- [83] E. Bagnaschi, G. Degrossi, P. Slavich, and A. Vicini, “Higgs production via gluon fusion in the POWHEG approach in the SM and in the MSSM”, *JHEP* **02** (2012) 088, doi:10.1007/JHEP02(2012)088, arXiv:1111.2854.
- [84] P. Nason and G. Zanderighi, “ $W^+W^-$ , WZ and ZZ production in the POWHEG-BOX-V2”, *Eur. Phys. J. C* **74** (2014) 2702, doi:10.1140/epjc/s10052-013-2702-5, arXiv:1311.1365.
- [85] J. M. Campbell and R. K. Ellis, “An update on vector boson pair production at hadron colliders”, *Phys. Rev. D* **60** (1999) 113006, doi:10.1103/PhysRevD.60.113006, arXiv:hep-ph/9905386.
- [86] J. M. Campbell, R. K. Ellis, and C. Williams, “Vector boson pair production at the LHC”, *JHEP* **07** (2011) 018, doi:10.1007/JHEP07(2011)018, arXiv:1105.0020.
- [87] J. M. Campbell, R. K. Ellis, and W. T. Giele, “A multi-threaded version of MCFM”, *Eur. Phys. J. C* **75** (2015) 246, doi:10.1140/epjc/s10052-015-3461-2, arXiv:1503.06182.
- [88] T. Sjöstrand et al., “An introduction to PYTHIA 8.2”, *Comput. Phys. Commun.* **191** (2015) 159, doi:10.1016/j.cpc.2015.01.024, arXiv:1410.3012.
- [89] CMS Collaboration, “Extraction and validation of a new set of CMS PYTHIA 8 tunes from underlying-event measurements”, *Eur. Phys. J. C* **80** (2020) 4, doi:10.1140/epjc/s10052-019-7499-4, arXiv:1903.12179.
- [90] J. Alwall et al., “Comparative study of various algorithms for the merging of parton showers and matrix elements in hadronic collisions”, *Eur. Phys. J. C* **53** (2008) 473, doi:10.1140/epjc/s10052-007-0490-5, arXiv:0706.2569.
- [91] R. Frederix and S. Frixione, “Merging meets matching in MC@NLO”, *JHEP* **12** (2012) 061, doi:10.1007/JHEP12(2012)061, arXiv:1209.6215.
- [92] S. Bolognesi et al., “On the spin and parity of a single-produced resonance at the LHC”, *Phys. Rev. D* **86** (2012) 095031, doi:10.1103/PhysRevD.86.095031, arXiv:1208.4018.
- [93] CMS Collaboration, “Electron and photon reconstruction and identification with the CMS experiment at the CERN LHC”, *JINST* **16** (2021) P05014, doi:10.1088/1748-0221/16/05/P05014, arXiv:2012.06888.
- [94] CMS Collaboration, “ECAL 2016 refined calibration and Run2 summary plots”, CMS Detector Performance Note CMS-DP-2020-021, 2020.

- [95] CMS Collaboration, “Performance of the CMS muon detector and muon reconstruction with proton-proton collisions at  $\sqrt{s} = 13$  TeV”, *JINST* **13** (2018) P06015, doi:10.1088/1748-0221/13/06/P06015, arXiv:1804.04528.
- [96] K. Rehermann and B. Tweedie, “Efficient identification of boosted semileptonic top quarks at the LHC”, *JHEP* **03** (2011) 059, doi:10.1007/JHEP03(2011)059, arXiv:1007.2221.
- [97] CMS Collaboration, “Observation of four top quark production in proton-proton collisions at  $\sqrt{s} = 13$  TeV”, *Phys. Lett. B* **847** (2023) 138290, doi:10.1016/j.physletb.2023.138290, arXiv:2305.13439.
- [98] CMS Collaboration, “Evidence for associated production of a Higgs boson with a top quark pair in final states with electrons, muons, and hadronically decaying  $\tau$  leptons at  $\sqrt{s} = 13$  TeV”, *JHEP* **08** (2018) 066, doi:10.1007/JHEP08(2018)066, arXiv:1803.05485.
- [99] CMS Collaboration, “Observation of single top quark production in association with a Z boson in proton-proton collisions at  $\sqrt{s} = 13$  TeV”, *Phys. Rev. Lett.* **122** (2019) 132003, doi:10.1103/PhysRevLett.122.132003, arXiv:1812.05900.
- [100] CMS Collaboration, “Measurement of the Higgs boson production rate in association with top quarks in final states with electrons, muons, and hadronically decaying tau leptons at  $\sqrt{s} = 13$  TeV”, *Eur. Phys. J. C* **81** (2021) 378, doi:10.1140/epjc/s10052-021-09014-x, arXiv:2011.03652.
- [101] CMS Collaboration, “Search for electroweak production of charginos and neutralinos in proton-proton collisions at  $\sqrt{s} = 13$  TeV”, *JHEP* **04** (2022) 147, doi:10.1007/JHEP04(2022)147, arXiv:2106.14246.
- [102] CMS Collaboration, “Measurements of the electroweak diboson production cross sections in proton-proton collisions at  $\sqrt{s} = 5.02$  TeV using leptonic decays”, *Phys. Rev. Lett.* **127** (2021) 191801, doi:10.1103/PhysRevLett.127.191801, arXiv:2107.01137.
- [103] CMS Collaboration, “Inclusive and differential cross section measurements of single top quark production in association with a Z boson in proton-proton collisions at  $\sqrt{s} = 13$  TeV”, *JHEP* **02** (2022) 107, doi:10.1007/JHEP02(2022)107, arXiv:2111.02860.
- [104] CMS Collaboration, “Muon identification using multivariate techniques in the CMS experiment in proton-proton collisions at  $\sqrt{s} = 13$  TeV”, 2023. arXiv:2310.03844. Accepted by *JINST*.
- [105] CMS Collaboration, “Performance of reconstruction and identification of  $\tau$  leptons decaying to hadrons and  $\nu_\tau$  in pp collisions at  $\sqrt{s} = 13$  TeV”, *JINST* **13** (2018) P10005, doi:10.1088/1748-0221/13/10/P10005, arXiv:1809.02816.
- [106] CMS Collaboration, “Identification of hadronic tau lepton decays using a deep neural network”, *JINST* **17** (2022) P07023, doi:10.1088/1748-0221/17/07/P07023, arXiv:2201.08458.
- [107] Particle Data Group, R. L. Workman et al., “Review of particle physics”, *Prog. Theor. Exp. Phys.* **2022** (2022) 083C01, doi:10.1093/ptep/ptac097.


- [108] CMS Collaboration, “Performance of electron reconstruction and selection with the CMS detector in proton-proton collisions at  $\sqrt{s} = 8$  TeV”, *JINST* **10** (2015) P06005, doi:10.1088/1748-0221/10/06/P06005, arXiv:1502.02701.
- [109] CMS Collaboration, “Performance of CMS muon reconstruction in cosmic-ray events”, *JINST* **5** (2010) T03022, doi:10.1088/1748-0221/5/03/T03022, arXiv:0911.4994.
- [110] CMS Collaboration, “Performance of the reconstruction and identification of high-momentum muons in proton-proton collisions at  $\sqrt{s} = 13$  TeV”, *JINST* **15** (2020) P02027, doi:10.1088/1748-0221/15/02/P02027, arXiv:1912.03516.
- [111] H. Voss, A. Höcker, J. Stelzer, and F. Tegenfeldt, “TMVA, the toolkit for multivariate data analysis with ROOT”, in *Proc. 11th Int. Workshop on Advanced Computing and Analysis Techniques in Phys. Research (ACAT 2017): Amsterdam, The Netherlands, April 23–27, 2007*. 2007. arXiv:physics/0703039. [PoS (ACAT2007) 040]. doi:10.22323/1.050.0040.
- [112] CMS Collaboration, “Search for new physics in same-sign dilepton events in proton-proton collisions at  $\sqrt{s} = 13$  TeV”, *Eur. Phys. J. C* **76** (2016) 439, doi:10.1140/epjc/s10052-016-4261-z, arXiv:1605.03171.
- [113] CMS Collaboration, “Measurement of the cross section of top quark-antiquark pair production in association with a W boson in proton-proton collisions at  $\sqrt{s} = 13$  TeV”, *JHEP* **07** (2023) 219, doi:10.1007/JHEP07(2023)219, arXiv:2208.06485.
- [114] CMS Collaboration, “Precision luminosity measurement in proton-proton collisions at  $\sqrt{s} = 13$  TeV in 2015 and 2016 at CMS”, *Eur. Phys. J. C* **81** (2021) 800, doi:10.1140/epjc/s10052-021-09538-2, arXiv:2104.01927.
- [115] CMS Collaboration, “CMS luminosity measurement for the 2017 data-taking period at  $\sqrt{s} = 13$  TeV”, CMS Physics Analysis Summary CMS-PAS-LUM-17-004, 2018.
- [116] CMS Collaboration, “CMS luminosity measurement for the 2018 data-taking period at  $\sqrt{s} = 13$  TeV”, CMS Physics Analysis Summary CMS-PAS-LUM-18-002, 2019.
- [117] CMS Collaboration, “Measurements of inclusive W and Z cross sections in pp collisions at  $\sqrt{s} = 7$  TeV”, *JHEP* **01** (2011) 080, doi:10.1007/JHEP01(2011)080, arXiv:1012.2466.
- [118] A. Lazopoulos, K. Melnikov, and F. Petriello, “QCD corrections to tri-boson production”, *Phys. Rev. D* **76** (2007) 014001, doi:10.1103/PhysRevD.76.014001, arXiv:hep-ph/0703273.
- [119] T. Binoth, G. Ossola, C. G. Papadopoulos, and R. Pittau, “NLO QCD corrections to tri-boson production”, *JHEP* **06** (2008) 082, doi:10.1088/1126-6708/2008/06/082, arXiv:0804.0350.
- [120] V. Hankele and D. Zeppenfeld, “QCD corrections to hadronic WWZ production with leptonic decays”, *Phys. Lett. B* **661** (2008) 103, doi:10.1016/j.physletb.2008.02.014, arXiv:0712.3544.
- [121] F. Campanario et al., “QCD corrections to charged triple vector boson production with leptonic decay”, *Phys. Rev. D* **78** (2008) 094012, doi:10.1103/PhysRevD.78.094012, arXiv:0809.0790.

- [122] S. Dittmaier, A. Huss, and G. Knippen, “Next-to-leading-order QCD and electroweak corrections to WWW production at proton-proton colliders”, *JHEP* **09** (2017) 034, doi:10.1007/JHEP09(2017)034, arXiv:1705.03722.
- [123] CMS Collaboration, “A portrait of the Higgs boson by the CMS experiment ten years after the discovery”, *Nature* **607** (2022) 60, doi:10.1038/s41586-022-04892-x, arXiv:2207.00043. [Author correction: doi:10.1038/s41586-023-06164-8].
- [124] K. Melnikov and F. Petriello, “Electroweak gauge boson production at hadron colliders through  $\mathcal{O}(\alpha_S^2)$ ”, *Phys. Rev. D* **74** (2006) 114017, doi:10.1103/PhysRevD.74.114017, arXiv:hep-ph/0609070.
- [125] R. Gavin, Y. Li, F. Petriello, and S. Quackenbush, “FEWZ 2.0: A code for hadronic Z production at next-to-next-to-leading order”, *Comput. Phys. Commun.* **182** (2011) 2388, doi:10.1016/j.cpc.2011.06.008, arXiv:1011.3540.
- [126] R. Gavin, Y. Li, F. Petriello, and S. Quackenbush, “W physics at the LHC with FEWZ 2.1”, *Comput. Phys. Commun.* **184** (2013) 208, doi:10.1016/j.cpc.2012.09.005, arXiv:1201.5896.
- [127] Y. Li and F. Petriello, “Combining QCD and electroweak corrections to dilepton production in FEWZ”, *Phys. Rev. D* **86** (2012) 094034, doi:10.1103/PhysRevD.86.094034, arXiv:1208.5967.
- [128] ATLAS and CMS Collaborations, and LHC Higgs Combination Group, “Procedure for the LHC Higgs boson search combination in Summer 2011”, Technical Report CMS-NOTE-2011-005, ATL-PHYS-PUB-2011-11, 2011.
- [129] R. Barlow and C. Beeston, “Fitting using finite Monte Carlo samples”, *Comput. Phys. Commun.* **77** (1993) 219, doi:10.1016/0010-4655(93)90005-w.
- [130] J. S. Conway, “Incorporating nuisance parameters in likelihoods for multisource spectra”, in *Proc. 2011 Workshop on Statistical Issues Related to Discovery Claims in Search Experiments and Unfolding (PHYSTAT 2011): Geneva, Switzerland, January 17–20, 2011*. 2011. arXiv:1103.0354. doi:10.5170/CERN-2011-006.115.
- [131] T. Junk, “Confidence level computation for combining searches with small statistics”, *Nucl. Instrum. Meth. A* **434** (1999) 435, doi:10.1016/S0168-9002(99)00498-2, arXiv:hep-ex/9902006.
- [132] A. L. Read, “Presentation of search results: The CL<sub>s</sub> technique”, *J. Phys. G* **28** (2002) 2693, doi:10.1088/0954-3899/28/10/313.
- [133] G. Cowan, K. Cranmer, E. Gross, and O. Vitells, “Asymptotic formulae for likelihood-based tests of new physics”, *Eur. Phys. J. C* **71** (2011) 1554, doi:10.1140/epjc/s10052-011-1554-0, arXiv:1007.1727. [Erratum: doi:10.1140/epjc/s10052-013-2501-z].
- [134] DELPHI Collaboration, “Search for neutral heavy leptons produced in Z decays”, *Z. Phys. C* **74** (1997) 57, doi:10.1007/s002880050370. [Erratum: doi:10.1007/BF03546181].






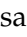


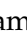


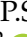


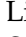
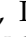


- [135] CMS Collaboration, “Probing heavy Majorana neutrinos and the Weinberg operator through vector boson fusion processes in proton-proton collisions at  $\sqrt{s} = 13$  TeV”, *Phys. Rev. Lett.* **131** (2023) 011803, doi:10.1103/PhysRevLett.131.011803, arXiv:2206.08956.
- [136] BaBar Collaboration, “Search for heavy neutral leptons using tau lepton decays at BaBar”, *Phys. Rev. D* **107** (2023) 052009, doi:10.1103/PhysRevD.107.052009, arXiv:2207.09575.

## A The CMS Collaboration




### Yerevan Physics Institute, Yerevan, Armenia

A. Hayrapetyan, A. Tumasyan<sup>1</sup> 






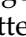







### Institut für Hochenergiephysik, Vienna, Austria

W. Adam , J.W. Andrejkovic, T. Bergauer , S. Chatterjee , K. Damanakis , M. Dragicevic , P.S. Hussain , M. Jeitler<sup>2</sup> , N. Krammer , A. Li , D. Liko , I. Mikulec , J. Schieck<sup>2</sup> , R. Schöfbeck , D. Schwarz , M. Sonawane , S. Templ , W. Waltenberger , C.-E. Wulz<sup>2</sup> 









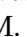


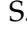
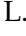

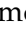
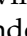
### Universiteit Antwerpen, Antwerpen, Belgium

M.R. Darwish<sup>3</sup> , T. Janssen , P. Van Mechelen 









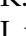

### Vrije Universiteit Brussel, Brussel, Belgium

E.S. Bols , N. Breugelmans, J. D'Hondt , S. Dansana , A. De Moor , M. Delcourt , F. Heyen, S. Lowette , I. Makarenko , D. Müller , S. Tavernier , M. Tytgat<sup>4</sup> , G.P. Van Onsem , S. Van Putte , D. Vannerom 









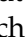

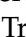

### Université Libre de Bruxelles, Bruxelles, Belgium

B. Clerbaux , A.K. Das, G. De Lentdecker , H. Evard , L. Favart , P. Gianneios , D. Hohov , J. Jaramillo , A. Khalilzadeh, F.A. Khan , K. Lee , M. Mahdavihorrani , A. Malara , S. Paredes , L. Thomas , M. Vanden Bemden , C. Vander Velde , P. Vanlaer 








### Ghent University, Ghent, Belgium

M. De Coen , D. Dobur , Y. Hong , J. Knolle , L. Lambrecht , G. Mestdach, K. Mota Amarilo , C. Rendón, A. Samalan, K. Skovpen , N. Van Den Bossche , J. van der Linden , L. Wezenbeek 








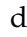






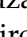

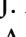

### Université Catholique de Louvain, Louvain-la-Neuve, Belgium

A. Benecke , A. Bethani , G. Bruno , C. Caputo , C. Delaere , I.S. Donertas , A. Giammanco , Sa. Jain , V. Lemaître, J. Lidrych , P. Mastrapasqua , T.T. Tran , S. Wertz 










### Centro Brasileiro de Pesquisas Físicas, Rio de Janeiro, Brazil

G.A. Alves , E. Coelho , C. Hensel , T. Menezes De Oliveira , A. Moraes , P. Rebello Teles , M. Soeiro, A. Vilela Pereira<sup>5</sup> 

### Universidade do Estado do Rio de Janeiro, Rio de Janeiro, Brazil

W.L. Aldá Júnior , M. Alves Gallo Pereira , M. Barroso Ferreira Filho , H. Brandao Malbouisson , W. Carvalho , J. Chinellato<sup>6</sup>, E.M. Da Costa , G.G. Da Silveira<sup>7</sup> , D. De Jesus Damiao , S. Fonseca De Souza , R. Gomes De Souza, M. Macedo , J. Martins<sup>8</sup> , C. Mora Herrera , L. Mundim , H. Nogima , J.P. Pinheiro , A. Santoro , A. Sznajder , M. Thiel 

### Universidade Estadual Paulista, Universidade Federal do ABC, São Paulo, Brazil

C.A. Bernardes<sup>7</sup> , L. Calligaris , T.R. Fernandez Perez Tomei , E.M. Gregores , I. Maitto Silverio , P.G. Mercadante , S.F. Novaes , B. Orzari , Sandra S. Padula 

### Institute for Nuclear Research and Nuclear Energy, Bulgarian Academy of Sciences, Sofia, Bulgaria

A. Aleksandrov , G. Antchev , R. Hadjiiska , P. Iaydjiev , M. Misheva , M. Shopova , G. Sultanov 






**University of Sofia, Sofia, Bulgaria**

A. Dimitrov , L. Litov , B. Pavlov , P. Petkov , A. Petrov , E. Shumka 



**Instituto De Alta Investigación, Universidad de Tarapacá, Casilla 7 D, Arica, Chile**

S. Keshri , S. Thakur 







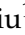




**Beihang University, Beijing, China**

T. Cheng , T. Javaid , L. Yuan 


**Department of Physics, Tsinghua University, Beijing, China**

Z. Hu , Z. Liang, J. Liu, K. Yi<sup>9,10</sup> 


**Institute of High Energy Physics, Beijing, China**

G.M. Chen<sup>11</sup> , H.S. Chen<sup>11</sup> , M. Chen<sup>11</sup> , F. Iemmi , C.H. Jiang, A. Kapoor<sup>12</sup> , H. Liao , Z.-A. Liu<sup>13</sup> , R. Sharma<sup>14</sup> , J.N. Song<sup>13</sup>, J. Tao , C. Wang<sup>11</sup>, J. Wang , Z. Wang<sup>11</sup>, H. Zhang 

**State Key Laboratory of Nuclear Physics and Technology, Peking University, Beijing, China**

A. Agapitos , Y. Ban , A. Levin , C. Li , Q. Li , Y. Mao, S. Qian, S.J. Qian , X. Sun , D. Wang , H. Yang, L. Zhang , Y. Zhao, C. Zhou 

**Sun Yat-Sen University, Guangzhou, China**

Z. You 

**University of Science and Technology of China, Hefei, China**

K. Jaffel , N. Lu 

**Nanjing Normal University, Nanjing, China**

G. Bauer<sup>15</sup>

**Institute of Modern Physics and Key Laboratory of Nuclear Physics and Ion-beam Application (MOE) - Fudan University, Shanghai, China**

X. Gao<sup>16</sup> 



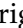
**Zhejiang University, Hangzhou, Zhejiang, China**

Z. Lin , C. Lu , M. Xiao 




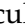
**Universidad de Los Andes, Bogota, Colombia**

C. Avila , D.A. Barbosa Trujillo, A. Cabrera , C. Florez , J. Fraga , J.A. Reyes Vega

**Universidad de Antioquia, Medellin, Colombia**

J. Mejia Guisao , F. Ramirez , M. Rodriguez , J.D. Ruiz Alvarez 

**University of Split, Faculty of Electrical Engineering, Mechanical Engineering and Naval Architecture, Split, Croatia**

D. Giljanovic , N. Godinovic , D. Lelas , A. Sculac 


**University of Split, Faculty of Science, Split, Croatia**




















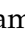
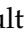


































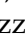


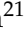

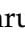





























M. Kovac , A. Petkovic, T. Sculac 





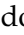














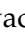





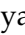















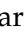



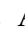


**Institute Rudjer Boskovic, Zagreb, Croatia**

P. Bargassa , V. Brigljevic , B.K. Chitroda , D. Ferencek , K. Jakovcic, S. Mishra , A. Starodumov<sup>17</sup> , T. Susa 

**University of Cyprus, Nicosia, Cyprus**

A. Attikis , K. Christoforou , A. Hadjiagapiou, C. Leonidou, J. Mousa , C. Nicolaou, L. Paizanos, F. Ptochos , P.A. Razis , H. Rykaczewski, H. Saka , A. Stepennov 

**Charles University, Prague, Czech Republic**M. Finger , M. Finger Jr. , A. Kveton **Escuela Politecnica Nacional, Quito, Ecuador**E. Ayala **Universidad San Francisco de Quito, Quito, Ecuador**E. Carrera Jarrin **Academy of Scientific Research and Technology of the Arab Republic of Egypt, Egyptian Network of High Energy Physics, Cairo, Egypt**Y. Assran<sup>18,19</sup>, S. Elgammal<sup>19</sup>**Center for High Energy Physics (CHEP-FU), Fayoum University, El-Fayoum, Egypt**M. Abdullah Al-Mashad , M.A. Mahmoud **National Institute of Chemical Physics and Biophysics, Tallinn, Estonia**K. Ehataht , M. Kadastik, T. Lange , S. Nandan , C. Nielsen , J. Pata , M. Raidal , L. Tani , C. Veelken **Department of Physics, University of Helsinki, Helsinki, Finland**H. Kirschenmann , K. Osterberg , M. Voutilainen **Helsinki Institute of Physics, Helsinki, Finland**S. Bharthuar , E. Brücken , F. Garcia , K.T.S. Kallonen , R. Kinnunen, T. Lampén , K. Lassila-Perini , S. Lehti , T. Lindén , L. Martikainen , M. Myllymäki , M.m. Rantanen , H. Siikonen , E. Tuominen , J. Tuominiemi **Lappeenranta-Lahti University of Technology, Lappeenranta, Finland**P. Luukka , H. Petrow **IRFU, CEA, Université Paris-Saclay, Gif-sur-Yvette, France**M. Besancon , F. Couderc , M. Dejardin , D. Denegri, J.L. Faure, F. Ferri , S. Ganjour , P. Gras , G. Hamel de Monchenault , V. Lohezic , J. Malcles , F. Orlandi , L. Portales , J. Rander, A. Rosowsky , M.Ö. Sahin , A. Savoy-Navarro<sup>20</sup> , P. Simkina , M. Titov , M. Tornago **Laboratoire Leprince-Ringuet, CNRS/IN2P3, Ecole Polytechnique, Institut Polytechnique de Paris, Palaiseau, France**F. Beaudette , A. Buchot Perraguin , P. Busson , A. Cappati , C. Charlot , M. Chiusi , F. Damas , O. Davignon , A. De Wit , I.T. Ehle , B.A. Fontana Santos Alves , S. Ghosh , A. Gilbert , R. Granier de Cassagnac , A. Hakimi , B. Harikrishnan , L. Kalipoliti , G. Liu , J. Motta , M. Nguyen , C. Ochando , R. Salerno , J.B. Sauvan , Y. Sirois , A. Tarabini , E. Vernazza , A. Zabi , A. Zghiche **Université de Strasbourg, CNRS, IPHC UMR 7178, Strasbourg, France**J.-L. Agram<sup>21</sup> , J. Andrea , D. Apparuu , D. Bloch , J.-M. Brom , E.C. Chabert , C. Collard , S. Falke , U. Goerlach , C. Grimault, R. Haeberle , A.-C. Le Bihan , M. Meena , G. Saha , M.A. Sessini , P. Van Hove **Institut de Physique des 2 Infinis de Lyon (IP2I ), Villeurbanne, France**D. Amram, S. Beauceron , B. Blancon , G. Boudoul , N. Chanon , D. Contardo , P. Depasse , C. Dozen<sup>22</sup> , H. El Mamouni, J. Fay , S. Gascon , M. Gouzevitch , C. Greenberg, G. Grenier , B. Ille , E. Jourdu'huy, I.B. Laktineh, M. Lethuillier , L. Mirabito, S. Perries, A. Purohit , M. Vander Donckt , P. Verdier , J. Xiao 

**Georgian Technical University, Tbilisi, Georgia**A. Khvedelidze<sup>17</sup> , I. Lomidze , Z. Tsamalaidze<sup>17</sup> **RWTH Aachen University, I. Physikalisches Institut, Aachen, Germany**V. Botta , L. Feld , K. Klein , M. Lipinski , D. Meuser , A. Pauls , N. Rówert , M. Teroerde **RWTH Aachen University, III. Physikalisches Institut A, Aachen, Germany**S. Diekmann , A. Dodonova , N. Eich , D. Eliseev , F. Engelke , J. Erdmann , M. Erdmann , P. Fackeldey , B. Fischer , T. Hebbeker , K. Hoepfner , F. Ivone , A. Jung , M.y. Lee , F. Mausolf , M. Merschmeyer , A. Meyer , S. Mukherjee , D. Noll , F. Nowotny, A. Pozdnyakov , Y. Rath, W. Redjeb , F. Rehm, H. Reithler , U. Sarkar , V. Sarkisovi , A. Schmidt , A. Sharma , J.L. Spah , A. Stein , F. Torres Da Silva De Araujo<sup>23</sup> , S. Wiedenbeck , S. Zaleski**RWTH Aachen University, III. Physikalisches Institut B, Aachen, Germany**C. Dziwok , G. Flügge , W. Haj Ahmad<sup>24</sup> , T. Kress , A. Nowack , O. Pooth , A. Stahl , T. Ziemons , A. Zotz **Deutsches Elektronen-Synchrotron, Hamburg, Germany**H. Aarup Petersen , M. Aldaya Martin , J. Alimena , S. Amoroso, Y. An , J. Bach , S. Baxter , M. Bayatmakou , H. Becerril Gonzalez , O. Behnke , A. Belvedere , S. Bhattacharya , F. Blekman<sup>25</sup> , K. Borrás<sup>26</sup> , A. Campbell , A. Cardini , C. Cheng, F. Colombina , S. Consuegra Rodríguez , G. Correia Silva , M. De Silva , G. Eckerlin, D. Eckstein , L.I. Estevez Banos , O. Filatov , E. Gallo<sup>25</sup> , A. Geiser , A. Giralardi , V. Guglielmi , M. Guthoff , A. Hinzmann , L. Jeppe , B. Kaech , M. Kasemann , C. Kleinwort , R. Kogler , M. Komm , D. Krücker , W. Lange, D. Leyva Pernia , K. Lipka<sup>27</sup> , W. Lohmann<sup>28</sup> , F. Lorkowski , R. Mankel , I.-A. Melzer-Pellmann , M. Mendizabal Morentin , A.B. Meyer , G. Milella , K. Moral Figueroa , A. Mussgiller , L.P. Nair , A. Nürnberg , Y. Otariid, J. Park , D. Pérez Adán , E. Ranken , A. Raspereza , D. Rastorguev , B. Ribeiro Lopes , J. Rübenach, L. Rygaard, A. Saggio , M. Scham<sup>29,26</sup> , S. Schnake<sup>26</sup> , P. Schütze , C. Schwanenberger<sup>25</sup> , D. Selivanova , K. Sharko , M. Shchedrolosiev , R.E. Sosa Ricardo , D. Stafford, F. Vazzoler , A. Ventura Barroso , R. Walsh , D. Wang , Q. Wang , Y. Wen , K. Wichmann, L. Wiens<sup>26</sup> , C. Wissing , Y. Yang , A. Zimmermann Castro Santos **University of Hamburg, Hamburg, Germany**A. Albrecht , S. Albrecht , M. Antonello , S. Bein , L. Benato , S. Bollweg, M. Bonanomi , P. Connor , K. El Morabit , Y. Fischer , E. Garutti , A. Grohsjean , J. Haller , H.R. Jabusch , G. Kasieczka , P. Keicher, R. Klanner , W. Korcar , T. Kramer , C.c. Kuo, V. Kutzner , F. Labe , J. Lange , A. Lobanov , C. Matthies , L. Moureaux , M. Mrowietz, A. Nigamova , Y. Nissan, A. Paasch , K.J. Pena Rodriguez , T. Quadfasel , B. Raciti , M. Rieger , D. Savoie , J. Schindler , P. Schleper , M. Schröder , J. Schwandt , M. Sommerhalder , H. Stadie , G. Steinbrück , A. Tews, M. Wolf **Karlsruher Institut fuer Technologie, Karlsruhe, Germany**S. Brommer , M. Burkart, E. Butz , T. Chwalek , A. Dierlamm , A. Droll, N. Faltermann , M. Giffels , A. Gottmann , F. Hartmann<sup>30</sup> , R. Hofsaess , M. Horzela , U. Husemann , J. Kieseler , M. Klute , R. Koppenhöfer , J.M. Lawhorn , M. Link, A. Lintuluoto , B. Maier , S. Maier , S. Mitra , M. Mormile , Th. Müller , M. Neukum, M. Oh , E. Pfeffer , M. Presilla , G. Quast , K. Rabbertz , B. Regnery , N. Shadskiy 

I. Shvetsov , H.J. Simonis , M. Toms , N. Trevisani , R.F. Von Cube , M. Wassmer ,  
S. Wieland , F. Wittig, R. Wolf , X. Zuo 





**Institute of Nuclear and Particle Physics (INPP), NCSR Demokritos, Aghia Paraskevi, Greece**

G. Anagnostou, G. Daskalakis , A. Kyriakis, A. Papadopoulos<sup>30</sup>, A. Stakia 

**National and Kapodistrian University of Athens, Athens, Greece**

P. Kontaxakis , G. Melachroinos, Z. Painesis , A. Panagiotou, I. Papavergou ,  
I. Paraskevas , N. Saoulidou , K. Theofilatos , E. Tziaferi , K. Vellidis , I. Zisopoulos 






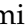
**National Technical University of Athens, Athens, Greece**

G. Bakas , T. Chatzistavrou, G. Karapostoli , K. Kousouris , I. Papakrivopoulos ,  
E. Siamarkou, G. Tsiopolitis, A. Zacharopoulou

**University of Ioánnina, Ioánnina, Greece**

K. Adamidis, I. Bestintzanos, I. Evangelou , C. Foudas, C. Kamtsikis, P. Katsoulis,  
P. Kokkas , P.G. Kosmoglou Kioseoglou , N. Manthos , I. Papadopoulos , J. Strologas 



**HUN-REN Wigner Research Centre for Physics, Budapest, Hungary**

M. Bartók<sup>31</sup> , C. Hajdu , D. Horvath<sup>32,33</sup> , K. Márton, A.J. Rádl<sup>34</sup> , F. Sikler ,  
V. Veszpremi 

**MTA-ELTE Lendület CMS Particle and Nuclear Physics Group, Eötvös Loránd University, Budapest, Hungary**

M. Csanád , K. Farkas , A. Fehérkuti<sup>35</sup> , M.M.A. Gadallah<sup>36</sup> , Á. Kadlecik ,  
P. Major , K. Mandal , G. Pásztor , G.I. Veres 




**Faculty of Informatics, University of Debrecen, Debrecen, Hungary**

P. Raics, B. Ujvari , G. Zilizi 






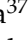


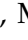





**Institute of Nuclear Research ATOMKI, Debrecen, Hungary**

G. Bencze, S. Czellar, J. Molnar, Z. Szillasi

**Karoly Robert Campus, MATE Institute of Technology, Gyongyos, Hungary**

T. Csorgo<sup>35</sup> , F. Nemes<sup>35</sup> , T. Novak 

**Panjab University, Chandigarh, India**

J. Babbar , S. Bansal , S.B. Beri, V. Bhatnagar , G. Chaudhary , S. Chauhan ,  
N. Dhingra<sup>37</sup> , A. Kaur , A. Kaur , H. Kaur , M. Kaur , S. Kumar , K. Sandeep ,  
T. Sheokand, J.B. Singh , A. Singla 
















**University of Delhi, Delhi, India**

A. Ahmed , A. Bhardwaj , A. Chhetri , B.C. Choudhary , A. Kumar , A. Kumar ,  
M. Naimuddin , K. Ranjan , S. Saumya 

**Saha Institute of Nuclear Physics, HBNI, Kolkata, India**

S. Baradia , S. Barman<sup>38</sup> , S. Bhattacharya , S. Das Gupta, S. Dutta , S. Dutta, S. Sarkar






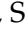




**Indian Institute of Technology Madras, Madras, India**

M.M. Ameen , P.K. Behera , S.C. Behera , S. Chatterjee , G. Dash , P. Jana ,  
P. Kalbhor , S. Kamble , J.R. Komaragiri<sup>39</sup> , D. Kumar<sup>39</sup> , P.R. Pujahari , N.R. Saha ,  
A. Sharma , A.K. Sikdar , R.K. Singh, P. Verma, S. Verma , A. Vijay












**Tata Institute of Fundamental Research-A, Mumbai, India**

S. Dugad, M. Kumar , G.B. Mohanty , M. Shelake, P. Suryadevara


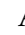







**Tata Institute of Fundamental Research-B, Mumbai, India**

A. Bala , S. Banerjee , R.M. Chatterjee, R.K. Dewanjee<sup>40</sup> , M. Guchait , Sh. Jain ,  
A. Jaiswal, S. Kumar , G. Majumder , K. Mazumdar , S. Parolia , A. Thachayath 

**National Institute of Science Education and Research, An OCC of Homi Bhabha National Institute, Bhubaneswar, Odisha, India**

S. Bahinipati<sup>41</sup> , C. Kar , D. Maity<sup>42</sup> , P. Mal , T. Mishra , V.K. Muraleedharan Nair Bindhu<sup>42</sup> , K. Naskar<sup>42</sup> , A. Nayak<sup>42</sup> , S. Nayak, P. Sadangi, S.K. Swain ,  
S. Varghese<sup>42</sup> , D. Vats<sup>42</sup> 

**Indian Institute of Science Education and Research (IISER), Pune, India**

S. Acharya<sup>43</sup> , A. Alpana , S. Dube , B. Gomber<sup>43</sup> , P. Hazarika , B. Kansal ,  
A. Laha , B. Sahu<sup>43</sup> , S. Sharma , K.Y. Vaish

**Isfahan University of Technology, Isfahan, Iran**

H. Bakhshiansohi<sup>44</sup> , A. Jafari<sup>45</sup> , M. Zeinali<sup>46</sup> 







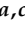
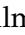







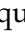



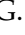

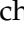
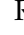

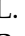

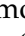


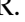
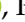

**Institute for Research in Fundamental Sciences (IPM), Tehran, Iran**

S. Bashiri, S. Chenarani<sup>47</sup> , S.M. Etesami , Y. Hosseini , M. Khakzad , E. Khazaie<sup>48</sup> ,  
M. Mohammadi Najafabadi , S. Tizchang 

**University College Dublin, Dublin, Ireland**

M. Grunewald 





**INFN Sezione di Bari<sup>a</sup>, Università di Bari<sup>b</sup>, Politecnico di Bari<sup>c</sup>, Bari, Italy**

M. Abbrescia<sup>a,b</sup> , R. Aly<sup>a,c,49</sup> , A. Colaleo<sup>a,b</sup> , D. Creanza<sup>a,c</sup> , B. D'Anzi<sup>a,b</sup> ,  
N. De Filippis<sup>a,c</sup> , M. De Palma<sup>a,b</sup> , A. Di Florio<sup>a,c</sup> , W. Elmetenawee<sup>a,b,49</sup> ,  
L. Fiore<sup>a</sup> , G. Iaselli<sup>a,c</sup> , M. Louka<sup>a,b</sup>, G. Maggi<sup>a,c</sup> , M. Maggi<sup>a</sup> , I. Margjeka<sup>a,b</sup> ,  
V. Mastrapasqua<sup>a,b</sup> , S. My<sup>a,b</sup> , S. Nuzzo<sup>a,b</sup> , A. Pellecchia<sup>a,b</sup> , A. Pompili<sup>a,b</sup> ,  
G. Pugliese<sup>a,c</sup> , R. Radogna<sup>a</sup> , G. Ramirez-Sanchez<sup>a,c</sup> , D. Ramos<sup>a</sup> , A. Ranieri<sup>a</sup> ,  
L. Silvestris<sup>a</sup> , F.M. Simone<sup>a,b</sup> , Ü. Sözbilir<sup>a</sup> , A. Stamerra<sup>a</sup> , D. Troiano<sup>a</sup> ,  
R. Venditti<sup>a</sup> , P. Verwilligen<sup>a</sup> , A. Zaza<sup>a,b</sup> 








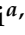





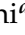



**INFN Sezione di Bologna<sup>a</sup>, Università di Bologna<sup>b</sup>, Bologna, Italy**

G. Abbiendi<sup>a</sup> , C. Battilana<sup>a,b</sup> , D. Bonacorsi<sup>a,b</sup> , L. Borgonovi<sup>a</sup> , P. Capiluppi<sup>a,b</sup> ,  
A. Castro<sup>a,b</sup> , F.R. Cavallo<sup>a</sup> , M. Cuffiani<sup>a,b</sup> , G.M. Dallavalle<sup>a</sup> , T. Diotallevi<sup>a,b</sup> ,  
F. Fabbri<sup>a</sup> , A. Fanfani<sup>a,b</sup> , D. Fasanella<sup>a,b</sup> , P. Giacomelli<sup>a</sup> , L. Giommi<sup>a,b</sup> ,  
C. Grandi<sup>a</sup> , L. Guiducci<sup>a,b</sup> , S. Lo Meo<sup>a,50</sup> , M. Lorusso<sup>a,b</sup> , L. Lunerti<sup>a,b</sup> ,  
S. Marcellini<sup>a</sup> , G. Masetti<sup>a</sup> , F.L. Navarria<sup>a,b</sup> , A. Perrotta<sup>a</sup> , F. Primavera<sup>a,b</sup> ,  
A.M. Rossi<sup>a,b</sup> , S. Rossi Tisbeni<sup>a,b</sup> , T. Rovelli<sup>a,b</sup> , G.P. Siroli<sup>a,b</sup> 

**INFN Sezione di Catania<sup>a</sup>, Università di Catania<sup>b</sup>, Catania, Italy**

S. Costa<sup>a,b,51</sup> , A. Di Mattia<sup>a</sup> , R. Potenza<sup>a,b</sup>, A. Tricomi<sup>a,b,51</sup> , C. Tuve<sup>a,b</sup> 

**INFN Sezione di Firenze<sup>a</sup>, Università di Firenze<sup>b</sup>, Firenze, Italy**

P. Assiouras<sup>a</sup> , G. Barbagli<sup>a</sup> , G. Bardelli<sup>a,b</sup> , B. Camaiani<sup>a,b</sup> , A. Cassese<sup>a</sup> ,  
R. Ceccarelli<sup>a</sup> , V. Ciulli<sup>a,b</sup> , C. Civinini<sup>a</sup> , R. D'Alessandro<sup>a,b</sup> , E. Focardi<sup>a,b</sup> ,  
T. Kello<sup>a</sup>, G. Latino<sup>a,b</sup> , P. Lenzi<sup>a,b</sup> , M. Lizzo<sup>a</sup> , M. Meschini<sup>a</sup> , S. Paoletti<sup>a</sup> ,  
A. Papanastassiou<sup>a,b</sup>, G. Sguazzoni<sup>a</sup> , L. Viliani<sup>a</sup> 

**INFN Laboratori Nazionali di Frascati, Frascati, Italy**




















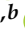



L. Benussi , S. Bianco , S. Meola<sup>52</sup> , D. Piccolo 

**INFN Sezione di Genova<sup>a</sup>, Università di Genova<sup>b</sup>, Genova, Italy**

P. Chatagnon<sup>a</sup> , F. Ferro<sup>a</sup> , E. Robutti<sup>a</sup> , S. Tosi<sup>a,b</sup> 










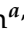

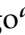


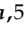

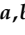




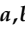


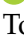

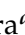


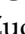

**INFN Sezione di Milano-Bicocca<sup>a</sup>, Università di Milano-Bicocca<sup>b</sup>, Milano, Italy**

A. Benaglia<sup>a</sup> , G. Boldrini<sup>a,b</sup> , F. Brivio<sup>a</sup> , F. Cetorelli<sup>a</sup> , F. De Guio<sup>a,b</sup> , M.E. Dinardo<sup>a,b</sup> , P. Dini<sup>a</sup> , S. Gennai<sup>a</sup> , R. Gerosa<sup>a,b</sup> , A. Ghezzi<sup>a,b</sup> , P. Govoni<sup>a,b</sup> , L. Guzzi<sup>a</sup> , M.T. Lucchini<sup>a,b</sup> , M. Malberti<sup>a</sup> , S. Malvezzi<sup>a</sup> , A. Massironi<sup>a</sup> , D. Menasce<sup>a</sup> , L. Moroni<sup>a</sup> , M. Paganoni<sup>a,b</sup> , S. Palluotto<sup>a,b</sup> , D. Pedrini<sup>a</sup> , B.S. Pinolini<sup>a</sup>, G. Pizzati<sup>a,b</sup>, S. Ragazzi<sup>a,b</sup> , T. Tabarelli de Fatis<sup>a,b</sup> 




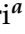





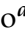

**INFN Sezione di Napoli<sup>a</sup>, Università di Napoli 'Federico II'<sup>b</sup>, Napoli, Italy; Università della Basilicata<sup>c</sup>, Potenza, Italy; Scuola Superiore Meridionale (SSM)<sup>d</sup>, Napoli, Italy**

S. Buontempo<sup>a</sup> , A. Cagnotta<sup>a,b</sup> , F. Carnevali<sup>a,b</sup>, N. Cavallo<sup>a,c</sup> , F. Fabozzi<sup>a,c</sup> , A.O.M. Iorio<sup>a,b</sup> , L. Lista<sup>a,b,53</sup> , P. Paolucci<sup>a,30</sup> , B. Rossi<sup>a</sup> , C. Sciacca<sup>a,b</sup> 







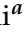
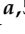




**INFN Sezione di Padova<sup>a</sup>, Università di Padova<sup>b</sup>, Padova, Italy; Università di Trento<sup>c</sup>, Trento, Italy**

R. Ardino<sup>a</sup> , P. Azzi<sup>a</sup> , N. Bacchetta<sup>a,54</sup> , D. Bisello<sup>a,b</sup> , P. Bortignon<sup>a</sup> , G. Bortolato<sup>a,b</sup>, A. Bragagnolo<sup>a,b</sup> , A.C.M. Bulla<sup>a</sup> , R. Carlin<sup>a,b</sup> , P. Checchia<sup>a</sup> , T. Dorigo<sup>a</sup> , F. Gasparini<sup>a,b</sup> , U. Gasparini<sup>a,b</sup> , M. Gulmini<sup>a,55</sup> , E. Lusiani<sup>a</sup> , M. Margoni<sup>a,b</sup> , F. Marini<sup>a</sup> , G. Maron<sup>a,55</sup> , M. Migliorini<sup>a,b</sup> , J. Pazzini<sup>a,b</sup> , P. Ronchese<sup>a,b</sup> , R. Rossin<sup>a,b</sup> , F. Simonetto<sup>a,b</sup> , G. Strong<sup>a</sup> , M. Tosi<sup>a,b</sup> , A. Triossi<sup>a,b</sup> , S. Ventura<sup>a</sup> , M. Zanetti<sup>a,b</sup> , P. Zotto<sup>a,b</sup> , A. Zucchetta<sup>a,b</sup> 



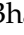









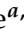
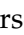
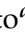







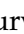
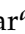

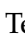

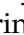
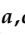



**INFN Sezione di Pavia<sup>a</sup>, Università di Pavia<sup>b</sup>, Pavia, Italy**

S. Abu Zeid<sup>a,56</sup> , C. Aimè<sup>a,b</sup> , A. Braghieri<sup>a</sup> , S. Calzaferri<sup>a</sup> , D. Fiorina<sup>a</sup> , P. Montagna<sup>a,b</sup> , V. Re<sup>a</sup> , C. Riccardi<sup>a,b</sup> , P. Salvini<sup>a</sup> , I. Vai<sup>a,b</sup> , P. Vitulo<sup>a,b</sup> 









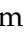
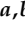



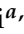
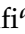




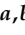

**INFN Sezione di Perugia<sup>a</sup>, Università di Perugia<sup>b</sup>, Perugia, Italy**

S. Ajmal<sup>a,b</sup> , M.E. Ascioti<sup>a,b</sup>, G.M. Bilei<sup>a</sup> , C. Carrivale<sup>a,b</sup>, D. Ciangottini<sup>a,b</sup> , L. Fanò<sup>a,b</sup> , M. Magherini<sup>a,b</sup> , V. Mariani<sup>a,b</sup> , M. Menichelli<sup>a</sup> , F. Moscatelli<sup>a,57</sup> , A. Rossi<sup>a,b</sup> , A. Santocchia<sup>a,b</sup> , D. Spiga<sup>a</sup> , T. Tedeschi<sup>a,b</sup> 


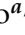
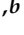
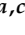





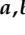





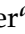






**INFN Sezione di Pisa<sup>a</sup>, Università di Pisa<sup>b</sup>, Scuola Normale Superiore di Pisa<sup>c</sup>, Pisa, Italy; Università di Siena<sup>d</sup>, Siena, Italy**








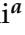










C.A. Alexe<sup>a,c</sup> , P. Asenov<sup>a,b</sup> , P. Azzurri<sup>a</sup> , G. Bagliesi<sup>a</sup> , R. Bhattacharya<sup>a</sup> , L. Bianchini<sup>a,b</sup> , T. Boccali<sup>a</sup> , E. Bossini<sup>a</sup> , D. Bruschini<sup>a,c</sup> , R. Castaldi<sup>a</sup> , M.A. Ciocci<sup>a,b</sup> , M. Cipriani<sup>a,b</sup> , V. D'Amante<sup>a,d</sup> , R. Dell'Orso<sup>a</sup> , S. Donato<sup>a</sup> , A. Giassi<sup>a</sup> , F. Ligabue<sup>a,c</sup> , D. Matos Figueiredo<sup>a</sup>, A. Messineo<sup>a,b</sup> , M. Musich<sup>a,b</sup> , F. Palla<sup>a</sup> , A. Rizzi<sup>a,b</sup> , G. Rolandi<sup>a,c</sup> , S. Roy Chowdhury<sup>a</sup> , T. Sarkar<sup>a</sup> , A. Scribano<sup>a</sup> , P. Spagnolo<sup>a</sup> , R. Tenchini<sup>a</sup> , G. Tonelli<sup>a,b</sup> , N. Turini<sup>a,d</sup> , F. Vaselli<sup>a,c</sup> , A. Venturi<sup>a</sup> , P.G. Verdini<sup>a</sup> 

**INFN Sezione di Roma<sup>a</sup>, Sapienza Università di Roma<sup>b</sup>, Roma, Italy**







C. Baldenegro Barrera<sup>a,b</sup> , P. Barria<sup>a</sup> , C. Basile<sup>a,b</sup> , M. Campana<sup>a,b</sup> , F. Cavallari<sup>a</sup> , L. Cunqueiro Mendez<sup>a,b</sup> , D. Del Re<sup>a,b</sup> , E. Di Marco<sup>a</sup> , M. Diemoz<sup>a</sup> , F. Errico<sup>a,b</sup> , E. Longo<sup>a,b</sup> , P. Meridiani<sup>a</sup> , J. Mijuskovic<sup>a,b</sup> , G. Organtini<sup>a,b</sup> , F. Pandolfi<sup>a</sup> , R. Paramatti<sup>a,b</sup> , C. Quaranta<sup>a,b</sup> , S. Rahatlou<sup>a,b</sup> , C. Rovelli<sup>a</sup> , F. Santanastasio<sup>a,b</sup> , L. Soffi<sup>a</sup> 

**INFN Sezione di Torino<sup>a</sup>, Università di Torino<sup>b</sup>, Torino, Italy; Università del Piemonte Orientale<sup>c</sup>, Novara, Italy**

N. Amapane<sup>a,b</sup> , R. Arcidiacono<sup>a,c</sup> , S. Argiro<sup>a,b</sup> , M. Arneodo<sup>a,c</sup> , N. Bartosik<sup>a</sup> , R. Bellan<sup>a,b</sup> , A. Bellora<sup>a,b</sup> , C. Biino<sup>a</sup> , C. Borca<sup>a,b</sup> , N. Cartiglia<sup>a</sup> , M. Costa<sup>a,b</sup> , R. Covarelli<sup>a,b</sup> , N. Demaria<sup>a</sup> , L. Finco<sup>a</sup> , M. Grippo<sup>a,b</sup> , B. Kiani<sup>a,b</sup> , F. Legger<sup>a</sup> , F. Luongo<sup>a,b</sup> , C. Mariotti<sup>a</sup> , L. Markovic<sup>a,b</sup> , S. Maselli<sup>a</sup> , A. Mecca<sup>a,b</sup> , L. Menzio<sup>a,b</sup>,

E. Migliore<sup>a,b</sup> , M. Monteno<sup>a</sup> , R. Mulargia<sup>a</sup> , M.M. Obertino<sup>a,b</sup> , G. Ortona<sup>a</sup> ,  
L. Pacher<sup>a,b</sup> , N. Pastrone<sup>a</sup> , M. Pelliccioni<sup>a</sup> , M. Ruspa<sup>a,c</sup> , F. Siviero<sup>a,b</sup> ,  
V. Sola<sup>a,b</sup> , A. Solano<sup>a,b</sup> , A. Staiano<sup>a</sup> , C. Tarricone<sup>a,b</sup> , D. Trocino<sup>a</sup> , G. Umoret<sup>a,b</sup> ,  
E. Vlasov<sup>a,b</sup> , R. White<sup>a,b</sup> 

**INFN Sezione di Trieste<sup>a</sup>, Università di Trieste<sup>b</sup>, Trieste, Italy**

S. Belforte<sup>a</sup> , V. Candelise<sup>a,b</sup> , M. Casarsa<sup>a</sup> , F. Cossutti<sup>a</sup> , K. De Leo<sup>a</sup> ,  
G. Della Ricca<sup>a,b</sup> 

**Kyungpook National University, Daegu, Korea**

S. Dogra , J. Hong , C. Huh , B. Kim , D.H. Kim , J. Kim, D. Lee, H. Lee, S.W. Lee ,  
C.S. Moon , Y.D. Oh , M.S. Ryu , S. Sekmen , B. Tae, Y.C. Yang 





**Department of Mathematics and Physics - GWNNU, Gangneung, Korea**

M.S. Kim 

**Chonnam National University, Institute for Universe and Elementary Particles, Kwangju, Korea**

G. Bak , P. Gwak , H. Kim , D.H. Moon 

**Hanyang University, Seoul, Korea**

E. Asilar , J. Choi , D. Kim , T.J. Kim , J.A. Merlin

**Korea University, Seoul, Korea**

S. Choi , S. Han, B. Hong , K. Lee, K.S. Lee , S. Lee , J. Park, S.K. Park, J. Yoo 




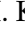

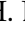

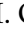


**Kyung Hee University, Department of Physics, Seoul, Korea**

J. Goh , S. Yang 




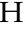
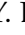
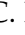

**Sejong University, Seoul, Korea**

H. S. Kim , Y. Kim, S. Lee



**Seoul National University, Seoul, Korea**

J. Almond, J.H. Bhyun, J. Choi , W. Jun , J. Kim , S. Ko , H. Kwon , H. Lee , J. Lee ,  
J. Lee , B.H. Oh , S.B. Oh , H. Seo , U.K. Yang, I. Yoon 

**University of Seoul, Seoul, Korea**

W. Jang , D.Y. Kang, Y. Kang , S. Kim , B. Ko, J.S.H. Lee , Y. Lee , I.C. Park , Y. Roh,  
I.J. Watson 

**Yonsei University, Department of Physics, Seoul, Korea**

S. Ha , H.D. Yoo 





**Sungkyunkwan University, Suwon, Korea**

M. Choi , M.R. Kim , H. Lee, Y. Lee , I. Yu 


**College of Engineering and Technology, American University of the Middle East (AUM),  
Dasman, Kuwait**

T. Beyrouthy

**Riga Technical University, Riga, Latvia**

K. Dreimanis , A. Gaile , G. Pikurs, A. Potrebko , M. Seidel 

**University of Latvia (LU), Riga, Latvia**

N.R. Strautnieks 




**Vilnius University, Vilnius, Lithuania**

M. Ambrozias , A. Juodagalvis , A. Rinkevicius , G. Tamulaitis 







**National Centre for Particle Physics, Universiti Malaya, Kuala Lumpur, Malaysia**

N. Bin Norjoharuddeen , I. Yusuff<sup>58</sup> , Z. Zolkapli

**Universidad de Sonora (UNISON), Hermosillo, Mexico**

J.F. Benitez , A. Castaneda Hernandez , H.A. Encinas Acosta, L.G. Gallegos Maríñez, M. León Coello , J.A. Murillo Quijada , A. Sehwat , L. Valencia Palomo 

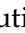



**Centro de Investigacion y de Estudios Avanzados del IPN, Mexico City, Mexico**

G. Ayala , H. Castilla-Valdez , H. Crotte Ledesma, E. De La Cruz-Burelo , I. Heredia-De La Cruz<sup>59</sup> , R. Lopez-Fernandez , C.A. Mondragon Herrera, A. Sánchez Hernández 


**Universidad Iberoamericana, Mexico City, Mexico**

C. Oropeza Barrera , M. Ramírez García 

**Benemerita Universidad Autonoma de Puebla, Puebla, Mexico**

I. Bautista , I. Pedraza , H.A. Salazar Ibarguen , C. Uribe Estrada 

**University of Montenegro, Podgorica, Montenegro**

I. Bujanja, N. Raicevic 

**University of Canterbury, Christchurch, New Zealand**

P.H. Butler 



**National Centre for Physics, Quaid-I-Azam University, Islamabad, Pakistan**

A. Ahmad , M.I. Asghar, A. Awais , M.I.M. Awan, H.R. Hoorani , W.A. Khan 







**AGH University of Krakow, Faculty of Computer Science, Electronics and Telecommunications, Krakow, Poland**

V. Avati, L. Grzanka , M. Malawski 

**National Centre for Nuclear Research, Swierk, Poland**

H. Bialkowska , M. Bluj , B. Boimska , M. Górski , M. Kazana , M. Szeper , P. Zalewski 
















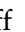
**Institute of Experimental Physics, Faculty of Physics, University of Warsaw, Warsaw, Poland**

K. Bunkowski , K. Doroba , A. Kalinowski , M. Konecki , J. Krolikowski , A. Muhammad 



**Warsaw University of Technology, Warsaw, Poland**

K. Pozniak , W. Zabolotny 

**Laboratório de Instrumentação e Física Experimental de Partículas, Lisboa, Portugal**

M. Araujo , D. Bastos , C. Beirão Da Cruz E Silva , A. Boletti , M. Bozzo , T. Camporesi , G. Da Molin , P. Faccioli , M. Gallinaro , J. Hollar , N. Leonardo , G.B. Marozzo, T. Niknejad , A. Petrilli , M. Pisano , J. Seixas , J. Varela , J.W. Wulff

**Faculty of Physics, University of Belgrade, Belgrade, Serbia**

P. Adzic , P. Milenovic 



















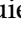






**VINCA Institute of Nuclear Sciences, University of Belgrade, Belgrade, Serbia**

M. Dordevic , J. Milosevic , V. Rekovic

**Centro de Investigaciones Energéticas Medioambientales y Tecnológicas (CIEMAT), Madrid, Spain**

M. Aguilar-Benitez, J. Alcaraz Maestre , Cristina F. Bedoya , Oliver M. Carretero 

















M. Cepeda , M. Cerrada , N. Colino , B. De La Cruz , A. Delgado Peris , A. Escalante Del Valle , D. Fernández Del Val , J.P. Fernández Ramos , J. Flix , M.C. Fouz , O. Gonzalez Lopez , S. Goy Lopez , J.M. Hernandez , M.I. Josa , D. Moran , C. M. Morcillo Perez , Á. Navarro Tobar , C. Perez Dengra , A. Pérez-Calero Yzquierdo , J. Puerta Pelayo , I. Redondo , D.D. Redondo Ferrero , L. Romero, S. Sánchez Navas , L. Urda Gómez , J. Vazquez Escobar , C. Willmott












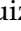







#### Universidad Autónoma de Madrid, Madrid, Spain

J.F. de Trocóniz 

#### Universidad de Oviedo, Instituto Universitario de Ciencias y Tecnologías Espaciales de Asturias (ICTEA), Oviedo, Spain

B. Alvarez Gonzalez , J. Cuevas , J. Fernandez Menendez , S. Folgueras , I. Gonzalez Caballero , J.R. González Fernández , P. Leguina , E. Palencia Cortezon , C. Ramón Álvarez , V. Rodríguez Bouza , A. Soto Rodríguez , A. Trapote , C. Vico Villalba , P. Vischia 


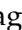
#### Instituto de Física de Cantabria (IFCA), CSIC-Universidad de Cantabria, Santander, Spain

S. Bhowmik , S. Blanco Fernández , J.A. Brochero Cifuentes , I.J. Cabrillo , A. Calderon , J. Duarte Campderros , M. Fernandez , G. Gomez , C. Lasaosa García , R. Lopez Ruiz , C. Martinez Rivero , P. Martinez Ruiz del Arbol , F. Matorras , P. Matorras Cuevas , E. Navarrete Ramos , J. Piedra Gomez , L. Scodellaro , I. Vila , J.M. Vizan Garcia 

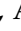








#### University of Colombo, Colombo, Sri Lanka

M.K. Jayananda , B. Kailasapathy<sup>60</sup> , D.U.J. Sonnadara , D.D.C. Wickramarathna 








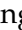
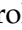



#### University of Ruhuna, Department of Physics, Matara, Sri Lanka

W.G.D. Dharmaratna<sup>61</sup> , K. Liyanage , N. Perera , N. Wickramage 





#### CERN, European Organization for Nuclear Research, Geneva, Switzerland


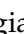
D. Abbaneo , C. Amendola , E. Auffray , G. Auzinger , J. Baechler, D. Barney , A. Bermúdez Martínez , M. Bianco , B. Bilin , A.A. Bin Anuar , A. Bocci , C. Botta , E. Brondolin , C. Caillol , G. Cerminara , N. Chernyavskaya , D. d'Enterria , A. Dabrowski , A. David , A. De Roeck , M.M. Defranchis , M. Deile , M. Dobson , L. Forthomme , G. Franzoni , W. Funk , S. Giani, D. Gigi, K. Gill , F. Glege , L. Gouskos , M. Haranko , J. Hegeman , B. Huber, V. Innocente , T. James , P. Janot , O. Kaluzinska , S. Laurila , P. Lecoq , E. Leutgeb , C. Lourenço , L. Malgeri , M. Mannelli , A.C. Marini , M. Matthewman, A. Mehta , F. Meijers , S. Mersi , E. Meschi , V. Milosevic , F. Monti , F. Moortgat , M. Mulders , I. Neutelings , S. Orfanelli, F. Pantaleo , G. Petrucciani , A. Pfeiffer , M. Pierini , D. Piparo , H. Qu , D. Rabaday , M. Rovere , H. Sakulin , S. Scarfi , C. Schwick, M. Selvaggi , A. Sharma , K. Shchelina , P. Silva , P. Sphicas<sup>62</sup> , A.G. Stahl Leitner , A. Steen , S. Summers , D. Treille , P. Tropea , A. Tsiros, D. Walter , J. Wanczyk<sup>63</sup> , J. Wang, S. Wuchterl , P. Zehetner , P. Zejdl , W.D. Zeuner

#### Paul Scherrer Institut, Villigen, Switzerland













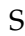



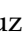



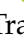
T. Bevilacqua<sup>64</sup> , L. Caminada<sup>64</sup> , A. Ebrahimi , W. Erdmann , R. Horisberger , Q. Ingram , H.C. Kaestli , D. Kotlinski , C. Lange , M. Missiroli<sup>64</sup> , L. Noehte<sup>64</sup> , T. Rohe 

#### ETH Zurich - Institute for Particle Physics and Astrophysics (IPA), Zurich, Switzerland




T.K. Aarrestad , K. Androsov<sup>63</sup> , M. Backhaus , G. Bonomelli, A. Calandri , C. Caz-

zaniga , K. Datta , P. De Bryas Dexmiers D'archiac<sup>63</sup> , A. De Cosa , G. Dissertori , M. Dittmar, M. Donegà , F. Eble , M. Galli , K. Gedia , F. Glessgen , C. Grab , N. Härringer , T.G. Harte, D. Hits , W. Lustermann , A.-M. Lyon , R.A. Manzoni , M. Marchegiani , L. Marchese , C. Martin Perez , A. Mascellani<sup>63</sup> , F. Nessi-Tedaldi , F. Pauss , V. Perovic , S. Pigazzini , C. Reissel , T. Reitenspiess , B. Ristic , F. Riti , R. Seidita , J. Steggemann<sup>63</sup> , D. Valsecchi , R. Wallny 













#### Universität Zürich, Zurich, Switzerland

C. Amsler<sup>65</sup> , P. Bärtshi , M.F. Canelli , K. Cormier , J.K. Heikkilä , M. Huwiler , W. Jin , A. Jofrehei , B. Kilminster , S. Leontsinis , S.P. Liechi , A. Macchiolo , P. Meiring , F. Meng , U. Molinatti , A. Reimers , P. Robmann, S. Sanchez Cruz , M. Senger , E. Shokr, F. Stäger , Y. Takahashi , R. Tramontano 




#### National Central University, Chung-Li, Taiwan

C. Adloff<sup>66</sup>, D. Bhowmik, C.M. Kuo, W. Lin, P.K. Rout , P.C. Tiwari<sup>39</sup> , S.S. Yu 




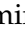

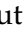

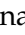

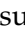



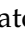


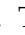


#### National Taiwan University (NTU), Taipei, Taiwan

L. Ceard, Y. Chao , K.F. Chen , P.s. Chen, Z.g. Chen, A. De Iorio , W.-S. Hou , T.h. Hsu, Y.w. Kao, S. Karmakar , R. Khurana, G. Kole , Y.y. Li , R.-S. Lu , E. Paganis , X.f. Su , J. Thomas-Wilsker , L.s. Tsai, H.y. Wu, E. Yazgan 


#### High Energy Physics Research Unit, Department of Physics, Faculty of Science, Chulalongkorn University, Bangkok, Thailand

C. Asawatangtrakuldee , N. Srimanobhas , V. Wachirapusanand 

#### Çukurova University, Physics Department, Science and Art Faculty, Adana, Turkey

D. Agyel , F. Boran , Z.S. Demiroglu , F. Dolek , I. Dumanoglu<sup>67</sup> , E. Eskut , Y. Guler<sup>68</sup> , E. Gurpinar Guler<sup>68</sup> , C. Isik , O. Kara, A. Kayis Topaksu , U. Kiminsu , G. Onengut , K. Ozdemir<sup>69</sup> , A. Polatoz , B. Tali<sup>70</sup> , U.G. Tok , S. Turkcapar , E. Uslan , I.S. Zorbakir 


#### Middle East Technical University, Physics Department, Ankara, Turkey

G. Sokmen, M. Yalvac<sup>71</sup> 


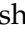


#### Bogazici University, Istanbul, Turkey

B. Akgun , I.O. Atakisi , E. Gülmez , M. Kaya<sup>72</sup> , O. Kaya<sup>73</sup> , S. Tekten<sup>74</sup> 



#### Istanbul Technical University, Istanbul, Turkey

A. Cakir , K. Cankocak<sup>67,75</sup> , G.G. Dincer<sup>67</sup> , Y. Komurcu , S. Sen<sup>76</sup> 

#### Istanbul University, Istanbul, Turkey

O. Aydilek<sup>24</sup> , S. Cerci<sup>70</sup> , V. Epshteyn , B. Haciasahinoglu , I. Hos<sup>77</sup> , B. Kaynak , S. Ozkorucuklu , O. Potok , H. Sert , C. Simsek , C. Zorbilmez 


#### Yildiz Technical University, Istanbul, Turkey

B. Isildak<sup>78</sup> , D. Sunar Cerci<sup>70</sup> 

#### Institute for Scintillation Materials of National Academy of Science of Ukraine, Kharkiv, Ukraine

A. Boyaryntsev , B. Grynyov 

#### National Science Centre, Kharkiv Institute of Physics and Technology, Kharkiv, Ukraine





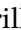





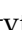






L. Levchuk 

#### University of Bristol, Bristol, United Kingdom

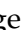


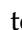


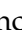


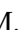


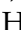




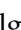

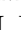


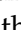





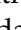





D. Anthony , J.J. Brooke , A. Bundock , F. Bury , E. Clement , D. Cussans 

H. Flacher , M. Glowacki, J. Goldstein , H.F. Heath , M.-L. Holmberg , L. Kreczko , S. Paramesvaran , L. Robertshaw, S. Seif El Nasr-Storey, V.J. Smith , N. Stylianou<sup>79</sup> , K. Walkingshaw Pass




#### **Rutherford Appleton Laboratory, Didcot, United Kingdom**

A.H. Ball, K.W. Bell , A. Belyaev<sup>80</sup> , C. Brew , R.M. Brown , D.J.A. Cockerill , C. Cooke , K.V. Ellis, K. Harder , S. Harper , J. Linacre , K. Manolopoulos, D.M. Newbold , E. Olaiya, D. Petyt , T. Reis , A.R. Sahasransu , G. Salvi , T. Schuh, C.H. Shepherd-Themistocleous , I.R. Tomalin , T. Williams 

#### **Imperial College, London, United Kingdom**

R. Bainbridge , P. Bloch , C.E. Brown , O. Buchmuller, V. Cacchio, C.A. Carrillo Montoya , G.S. Chahal<sup>81</sup> , D. Colling , J.S. Dancu, I. Das , P. Dauncey , G. Davies , J. Davies, M. Della Negra , S. Fayer, G. Fedi , G. Hall , M.H. Hassanshahi , A. Howard, G. Iles , M. Knight , J. Langford , J. León Holgado , L. Lyons , A.-M. Magnan , S. Malik, M. Mieskolainen , J. Nash<sup>82</sup> , M. Pesaresi , P.B. Pradeep, B.C. Radburn-Smith , A. Richards, A. Rose , K. Savva , C. Seez , R. Shukla , A. Tapper , K. Uchida , G.P. Uttley , L.H. Vage, T. Virdee<sup>30</sup> , M. Vojinovic , N. Wardle , D. Winterbottom 






#### **Brunel University, Uxbridge, United Kingdom**

K. Coldham, J.E. Cole , A. Khan, P. Kyberd , I.D. Reid 

#### **Baylor University, Waco, Texas, USA**

S. Abdullin , A. Brinkerhoff , B. Caraway , E. Collins , J. Dittmann , K. Hatakeyama , J. Hiltbrand , B. McMaster , J. Samudio , S. Sawant , C. Sutantawibul , J. Wilson 





















#### **Catholic University of America, Washington, DC, USA**

R. Bartek , A. Dominguez , C. Huerta Escamilla, A.E. Simsek , R. Uniyal , A.M. Vargas Hernandez 




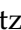









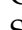



#### **The University of Alabama, Tuscaloosa, Alabama, USA**

B. Bam , R. Chudasama , S.I. Cooper , C. Crovella , S.V. Gleyzer , E. Pearson, C.U. Perez , P. Rumerio<sup>83</sup> , E. Usai , R. Yi 





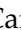





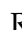








#### **Boston University, Boston, Massachusetts, USA**

A. Akpinar , D. Arcaro , C. Cosby , G. De Castro, Z. Demiragli , C. Erice , C. Fangmeier , C. Fernandez Madrazo , E. Fontanesi , D. Gastler , F. Golf , S. Jeon , I. Reed , J. Rohlf , K. Salyer , D. Sperka , D. Spitzbart , I. Suarez , A. Tsatsos , S. Yuan , A.G. Zecchinelli 











#### **Brown University, Providence, Rhode Island, USA**

G. Benelli , X. Coubez<sup>26</sup>, D. Cutts , M. Hadley , U. Heintz , J.M. Hogan<sup>84</sup> , T. Kwon , G. Landsberg , K.T. Lau , D. Li , J. Luo , S. Mondal , M. Narain<sup>†</sup> , N. Pervan , S. Sagir<sup>85</sup> , F. Simpson , M. Stamenkovic , N. Venkatasubramanian, X. Yan , W. Zhang

#### **University of California, Davis, Davis, California, USA**

S. Abbott , J. Bonilla , C. Brainerd , R. Breedon , H. Cai , M. Calderon De La Barca Sanchez , M. Chertok , M. Citron , J. Conway , P.T. Cox , R. Erbacher , F. Jensen , O. Kukral , G. Mocellin , M. Mulhearn , D. Pellett , W. Wei , Y. Yao , F. Zhang 




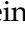

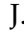









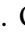








#### **University of California, Los Angeles, California, USA**

M. Bachtis , R. Cousins , A. Datta , G. Flores Avila, J. Hauser , M. Ignatenko , M.A. Iqbal , T. Lam , E. Manca , A. Nunez Del Prado, D. Saltzberg , V. Valuev 









**University of California, Riverside, Riverside, California, USA**

R. Clare , J.W. Gary , M. Gordon, G. Hanson , W. Si , S. Wimpenny<sup>†</sup> 

**University of California, San Diego, La Jolla, California, USA**

A. Aportela, A. Arora , J.G. Branson , S. Cittolin , S. Cooperstein , D. Diaz , J. Duarte , L. Giannini , Y. Gu, J. Guiang , R. Kansal , V. Krutelyov , R. Lee , J. Letts , M. Masciovecchio , F. Mokhtar , S. Mukherjee , M. Pieri , M. Quinnan , B.V. Sathia Narayanan , V. Sharma , M. Tadel , E. Vourliotis , F. Würthwein , Y. Xiang , A. Yagil 

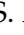

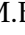












**University of California, Santa Barbara - Department of Physics, Santa Barbara, California, USA**

A. Barzdukas , L. Brennan , C. Campagnari , J. Incandela , J. Kim , A.J. Li , P. Masterson , H. Mei , J. Richman , U. Sarica , R. Schmitz , F. Setti , J. Sheplock , D. Stuart , T.Á. Vámi , S. Wang 




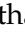
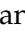



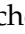


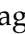


**California Institute of Technology, Pasadena, California, USA**

A. Bornheim , O. Cerri, A. Latorre, J. Mao , H.B. Newman , G. Reales Gutiérrez, M. Spiropulu , J.R. Vlimant , C. Wang , S. Xie , R.Y. Zhu 



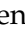
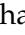






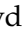




**Carnegie Mellon University, Pittsburgh, Pennsylvania, USA**

J. Alison , S. An , M.B. Andrews , P. Bryant , M. Cremonesi, V. Dutta , T. Ferguson , A. Harilal , A. Kallil Tharayil, C. Liu , T. Mudholkar , S. Murthy , P. Palit , K. Park, M. Paulini , A. Roberts , A. Sanchez , W. Terrill 








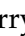

















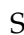









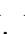

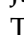

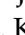
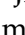

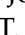


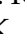






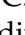

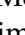


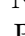
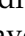
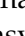

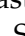

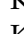
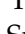
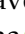

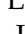
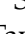

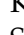
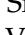


**University of Colorado Boulder, Boulder, Colorado, USA**

J.P. Cumalat , W.T. Ford , A. Hart , A. Hassani , G. Karathanasis , N. Manganelli , A. Perloff , C. Savard , N. Schonbeck , K. Stenson , K.A. Ulmer , S.R. Wagner , N. Zipper , D. Zuolo 





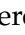




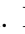





**Cornell University, Ithaca, New York, USA**

J. Alexander , S. Bright-Thonney , X. Chen , D.J. Cranshaw , J. Fan , X. Fan , S. Hogan , P. Kotamnives, J. Monroy , M. Oshiro , J.R. Patterson , M. Reid , A. Ryd , J. Thom , P. Wittich , R. Zou 

**Fermi National Accelerator Laboratory, Batavia, Illinois, USA**














M. Albrow , M. Alyari , O. Amram , G. Apollinari , A. Apresyan , L.A.T. Bauerdick , D. Berry , J. Berryhill , P.C. Bhat , K. Burkett , J.N. Butler , A. Canepa , G.B. Cerati , H.W.K. Cheung , F. Chlebana , G. Cummings , J. Dickinson , I. Dutta , V.D. Elvira , Y. Feng , J. Freeman , A. Gandrakota , Z. Gecse , L. Gray , D. Green, A. Grummer , S. Grünendahl , D. Guerrero , O. Gutsche , R.M. Harris , R. Heller , T.C. Herwig , J. Hirschauer , L. Horyn , B. Jayatilaka , S. Jindariani , M. Johnson , U. Joshi , T. Klijsma , B. Klima , K.H.M. Kwok , S. Lammel , D. Lincoln , R. Lipton , T. Liu , C. Madrid , K. Maeshima , C. Mantilla , D. Mason , P. McBride , P. Merkel , S. Mrenna , S. Nahn , J. Ngadiuba , D. Noonan , V. Papadimitriou , N. Pastika , K. Pedro , C. Pena<sup>86</sup> , F. Ravera , A. Reinsvold Hall<sup>87</sup> , L. Ristori , E. Sexton-Kennedy , N. Smith , A. Soha , L. Spiegel , S. Stoynev , J. Strait , L. Taylor , S. Tkaczyk , N.V. Tran , L. Uplegger , E.W. Vaandering , A. Whitbeck , I. Zoi 

**University of Florida, Gainesville, Florida, USA**






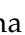
C. Aruta , P. Avery , D. Bourilkov , L. Cadamuro , P. Chang , V. Cherepanov , R.D. Field, E. Koenig , M. Kolosova , J. Konigsberg , A. Korytov , K. Matchev , N. Menendez , G. Mitselmakher , K. Mohrman , A. Muthirakalayil Madhu 

N. Rawal , D. Rosenzweig , S. Rosenzweig , J. Wang 





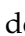








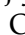



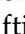





#### **Florida State University, Tallahassee, Florida, USA**

T. Adams , A. Al Kadhim , A. Askew , S. Bower , R. Habibullah , V. Hagopian , R. Hashmi , R.S. Kim , S. Kim , T. Kolberg , G. Martinez, H. Prosper , P.R. Prova, M. Wulansatiti , R. Yohay , J. Zhang












#### **Florida Institute of Technology, Melbourne, Florida, USA**

B. Alsufyani, M.M. Baarmand , S. Butalla , S. Das , T. Elkafrawy<sup>56</sup> , M. Hohlmann , R. Kumar Verma , M. Rahmani, E. Yanes







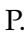




#### **University of Illinois Chicago, Chicago, USA, Chicago, USA**

M.R. Adams , A. Baty , C. Bennett, R. Cavanaugh , R. Escobar Franco , O. Evdokimov , C.E. Gerber , M. Hawksworth, A. Hingrajiya, D.J. Hofman , J.h. Lee , D. S. Lemos , A.H. Merrit , C. Mills , S. Nanda , G. Oh , B. Ozek , D. Pilipovic , R. Pradhan , E. Prifti, T. Roy , S. Rudrabhatla , M.B. Tonjes , N. Varelas , M.A. Wadud , Z. Ye , J. Yoo 









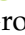







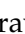





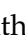

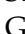
#### **The University of Iowa, Iowa City, Iowa, USA**

M. Alhousseini , D. Blend, K. Dilsiz<sup>88</sup> , L. Emediato , G. Karaman , O.K. Köseyan , J.-P. Merlo, A. Mestvirishvili<sup>89</sup> , J. Nachtman , O. Neogi, H. Ogul<sup>90</sup> , Y. Onel , A. Penzo , C. Snyder, E. Tiras<sup>91</sup> 










#### **Johns Hopkins University, Baltimore, Maryland, USA**

B. Blumenfeld , L. Corcodilos , J. Davis , A.V. Gritsan , L. Kang , S. Kyriacou , P. Maksimovic , M. Roguljic , J. Roskes , S. Sekhar , M. Swartz 

#### **The University of Kansas, Lawrence, Kansas, USA**

A. Abreu , L.F. Alcerro Alcerro , J. Anguiano , S. Arteaga Escatel , P. Baringer , A. Bean , Z. Flowers , D. Grove , J. King , G. Krintiras , M. Lazarovits , C. Le Mahieu , J. Marquez , N. Minafra , M. Murray , M. Nickel , M. Pitt , S. Popescu<sup>92</sup> , C. Rogan , C. Royon , R. Salvatico , S. Sanders , C. Smith , Q. Wang , G. Wilson 






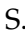









#### **Kansas State University, Manhattan, Kansas, USA**

B. Allmond , R. Gujju Gurunadha , A. Ivanov , K. Kaadze , A. Kalogeropoulos , Y. Maravin , J. Natoli , D. Roy , G. Sorrentino 




















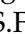

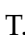
#### **Lawrence Livermore National Laboratory, Livermore, California, USA**

F. Rebassoo , D. Wright 

#### **University of Maryland, College Park, Maryland, USA**

A. Baden , A. Belloni , J. Bistany-riebman, Y.M. Chen , S.C. Eno , N.J. Hadley , S. Jabeen , R.G. Kellogg , T. Koeth , B. Kronheim, Y. Lai , S. Lascio , A.C. Mignerey , S. Nabili , C. Palmer , C. Papageorgakis , M.M. Paranjpe, L. Wang 

#### **Massachusetts Institute of Technology, Cambridge, Massachusetts, USA**

J. Bendavid , I.A. Cali , P.c. Chou , M. D'Alfonso , J. Eysermans , C. Freer , G. Gomez-Ceballos , M. Goncharov, G. Grosso, P. Harris, D. Hoang, D. Kovalskiy , J. Krupa , L. Lavezzo , Y.-J. Lee , K. Long , A. Novak , C. Paus , D. Rankin , C. Roland , G. Roland , S. Rothman , G.S.F. Stephans , Z. Wang , B. Wyslouch , T. J. Yang 

#### **University of Minnesota, Minneapolis, Minnesota, USA**

B. Crossman , B.M. Joshi , C. Kapsiak , M. Krohn , D. Mahon , J. Mans 















B. Marzocchi , S. Pandey , M. Revering , R. Rusack , R. Saradhy , N. Schroeder ,  
N. Strobbe 










**University of Mississippi, Oxford, Mississippi, USA**

L.M. Cremaldi 






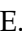

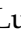


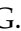




**University of Nebraska-Lincoln, Lincoln, Nebraska, USA**

K. Bloom , D.R. Claes , G. Haza , J. Hossain , C. Joo , I. Kravchenko , J.E. Siado ,  
W. Tabb , A. Vagnerini , A. Wightman , F. Yan , D. Yu 



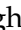
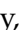




**State University of New York at Buffalo, Buffalo, New York, USA**

H. Bandyopadhyay , L. Hay , H.w. Hsia, I. Iashvili , A. Kharchilava , M. Morris ,  
D. Nguyen , S. Rappoccio , H. Rejeb Sfar, A. Williams , P. Young 


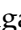
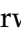
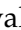









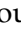




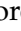

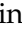



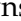

**Northeastern University, Boston, Massachusetts, USA**

G. Alverson , E. Barberis , J. Dervan, Y. Haddad , Y. Han , A. Krishna , J. Li ,  
M. Lu , G. Madigan , R. Mccarthy , D.M. Morse , V. Nguyen , T. Orimoto ,  
A. Parker , L. Skinnari , D. Wood 







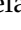

**Northwestern University, Evanston, Illinois, USA**

J. Bueghly, Z. Chen , S. Dittmer , K.A. Hahn , Y. Liu , Y. Miao , D.G. Monk ,  
M.H. Schmitt , A. Taliercio , M. Velasco








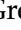








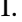
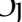
**University of Notre Dame, Notre Dame, Indiana, USA**

G. Agarwal , R. Band , R. Bucci, S. Castells , A. Das , R. Goldouzian , M. Hildreth ,  
K.W. Ho , K. Hurtado Anampa , T. Ivanov , C. Jessop , K. Lannon , J. Lawrence ,  
N. Loukas , L. Lutton , J. Mariano, N. Marinelli, I. Mcalister, T. McCauley , C. Mcgrady ,  
C. Moore , Y. Musienko<sup>17</sup> , H. Nelson , M. Osherson , A. Piccinelli , R. Ruchti ,  
A. Townsend , Y. Wan, M. Wayne , H. Yockey, M. Zarucki , L. Zygalá 

**The Ohio State University, Columbus, Ohio, USA**

A. Basnet , B. Bylsma, M. Carrigan , L.S. Durkin , C. Hill , M. Joyce , M. Nunez Ornelas ,  
K. Wei, B.L. Winer , B. R. Yates 











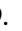

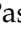



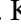


**Princeton University, Princeton, New Jersey, USA**

F.M. Addesa , H. Bouchamaoui , P. Das , G. Dezoort , P. Elmer , A. Frankenthal ,  
B. Greenberg , N. Haubrich , G. Kopp , S. Kwan , D. Lange , A. Loeliger ,  
D. Marlow , I. Ojalvo , J. Olsen , A. Shevelev , D. Stickland , C. Tully 




**University of Puerto Rico, Mayaguez, Puerto Rico, USA**

S. Malik 

**Purdue University, West Lafayette, Indiana, USA**

A.S. Bakshi , V.E. Barnes , S. Chandra , R. Chawla , A. Gu , L. Gutay, M. Jones ,  
A.W. Jung , D. Kondratyev , A.M. Koshy, M. Liu , G. Negro , N. Neumeister ,  
G. Paspalaki , S. Piperov , V. Scheurer, J.F. Schulte , M. Stojanovic , J. Thieman ,  
A. K. Viridi , F. Wang , W. Xie 

**Purdue University Northwest, Hammond, Indiana, USA**

J. Dolen , N. Parashar , A. Pathak 

**Rice University, Houston, Texas, USA**

D. Acosta , T. Carnahan , K.M. Ecklund , P.J. Fernández Manteca , S. Freed, P. Gardner,  
F.J.M. Geurts , W. Li , J. Lin , O. Miguel Colin , B.P. Padley , R. Redjimi, J. Rotter ,  
E. Yigitbasi , Y. Zhang 







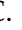



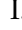
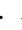








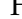
**University of Rochester, Rochester, New York, USA**

A. Bodek , P. de Barbaro , R. Demina , J.L. Dulemba , A. Garcia-Bellido , O. Hindrichs , A. Khukhunaishvili , N. Parmar, P. Parygin<sup>93</sup> , E. Popova<sup>93</sup> , R. Taus 

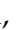

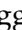



**The Rockefeller University, New York, New York, USA**

K. Goulianos 







**Rutgers, The State University of New Jersey, Piscataway, New Jersey, USA**

B. Chiarito, J.P. Chou , S.V. Clark , D. Gadkari , Y. Gershtein , E. Halkiadakis , M. Heindl , C. Houghton , D. Jaroslowski , O. Karacheban<sup>28</sup> , S. Konstantinou , I. Laflotte , A. Lath , R. Montalvo, K. Nash, J. Reichert , H. Routray , P. Saha , S. Salur , S. Schnetzer, S. Somalwar , R. Stone , S.A. Thayil , S. Thomas, J. Vora , H. Wang 

**University of Tennessee, Knoxville, Tennessee, USA**

H. Acharya, D. Ally , A.G. Delannoy , S. Fiorendi , S. Higginbotham , T. Holmes , A.R. Kanuganti , N. Karunarathna , L. Lee , E. Nibigira , S. Spanier 







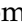


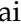

**Texas A&M University, College Station, Texas, USA**

D. Aebi , M. Ahmad , O. Bouhali<sup>94</sup> , R. Eusebi , J. Gilmore , T. Huang , T. Kamon<sup>95</sup> , H. Kim , S. Luo , R. Mueller , D. Overton , D. Rathjens , A. Safonov 








**Texas Tech University, Lubbock, Texas, USA**

N. Akchurin , J. Damgov , N. Gogate , V. Hegde , A. Hussain , Y. Kazhykarim, K. Lamichhane , S.W. Lee , A. Mankel , T. Peltola , I. Volobouev 

**Vanderbilt University, Nashville, Tennessee, USA**

E. Appelt , Y. Chen , S. Greene, A. Gurrola , W. Johns , R. Kunnawalkam Elayavalli , A. Melo , F. Romeo , P. Sheldon , S. Tuo , J. Velkovska , J. Viinikainen 

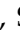









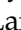

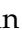









**University of Virginia, Charlottesville, Virginia, USA**

B. Cardwell , B. Cox , J. Hakala , R. Hirosky , A. Ledovskoy , C. Neu , C.E. Perez Lara 






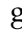







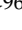

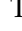


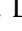


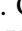
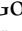
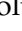
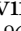





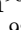
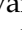
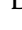









**Wayne State University, Detroit, Michigan, USA**
















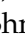





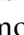









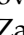




S. Bhattacharya , P.E. Karchin 

**University of Wisconsin - Madison, Madison, Wisconsin, USA**

A. Aravind, S. Banerjee , K. Black , T. Bose , S. Dasu , I. De Bruyn , P. Everaerts , C. Galloni, H. He , M. Herndon , A. Herve , C.K. Koraka , A. Lanaro, R. Loveless , J. Madhusudanan Sreekala , A. Mallampalli , A. Mohammadi , S. Mondal, G. Parida , L. Pétré , D. Pinna, A. Savin, V. Shang , V. Sharma , W.H. Smith , D. Teague, H.F. Tsoi , W. Vetens , A. Warden 

**Authors affiliated with an institute or an international laboratory covered by a cooperation agreement with CERN**

S. Afanasiev , V. Andreev , Yu. Andreev , T. Aushev , M. Azarkin , I. Azhgirey , A. Babaev , A. Belyaev , V. Blinov<sup>96</sup>, E. Boos , V. Borshch , D. Budkouski , V. Bunichev , V. Chekhovsky, R. Chistov<sup>96</sup> , M. Danilov<sup>96</sup> , A. Dermenev , T. Dimova<sup>96</sup> , D. Druzhin<sup>97</sup> , M. Dubinin<sup>86</sup> , L. Dudko , A. Ershov , G. Gavrilo , V. Gavrilo , S. Gninenko , V. Golovtcov , N. Golubev , I. Golutvin , I. Gorbunov , Y. Ivanov , V. Kachanov , V. Karjavine , A. Karneyeu , V. Kim<sup>96</sup> , M. Kirakosyan, D. Kirpichnikov , M. Kirsanov , V. Klyukhin , O. Kodolova<sup>98</sup> , D. Konstantinov , V. Korenkov , A. Kozyrev<sup>96</sup> , N. Krasnikov , A. Lanev , P. Levchenko<sup>99</sup> 

N. Lychkovskaya , V. Makarenko , A. Malakhov , V. Matveev<sup>96</sup> , V. Murzin , A. Nikitenko<sup>100,98</sup> , S. Obraztsov , V. Oreshkin , V. Palichik , V. Perelygin , M. Perfilov, S. Polikarpov<sup>96</sup> , V. Popov , O. Radchenko<sup>96</sup> , R. Ryutin, M. Savina , V. Savrin , V. Shalaev , S. Shmatov , S. Shulha , Y. Skovpen<sup>96</sup> , S. Slabospitskii , V. Smirnov , A. Snigirev , D. Sosnov , V. Sulimov , E. Tcherniaev , A. Terkulov , O. Teryaev , I. Tlisova , A. Toropin , L. Uvarov , A. Uzunian , A. Vorobyev<sup>†</sup>, G. Vorotnikov , N. Voytishin , B.S. Yuldashev<sup>101</sup>, A. Zarubin , I. Zhizhin , A. Zhokin 

†: Deceased

<sup>1</sup>Also at Yerevan State University, Yerevan, Armenia

<sup>2</sup>Also at TU Wien, Vienna, Austria

<sup>3</sup>Also at Institute of Basic and Applied Sciences, Faculty of Engineering, Arab Academy for Science, Technology and Maritime Transport, Alexandria, Egypt

<sup>4</sup>Also at Ghent University, Ghent, Belgium

<sup>5</sup>Also at Universidade do Estado do Rio de Janeiro, Rio de Janeiro, Brazil

<sup>6</sup>Also at Universidade Estadual de Campinas, Campinas, Brazil

<sup>7</sup>Also at Federal University of Rio Grande do Sul, Porto Alegre, Brazil

<sup>8</sup>Also at UFMS, Nova Andradina, Brazil

<sup>9</sup>Also at Nanjing Normal University, Nanjing, China

<sup>10</sup>Now at The University of Iowa, Iowa City, Iowa, USA

<sup>11</sup>Also at University of Chinese Academy of Sciences, Beijing, China

<sup>12</sup>Also at China Center of Advanced Science and Technology, Beijing, China

<sup>13</sup>Also at University of Chinese Academy of Sciences, Beijing, China

<sup>14</sup>Also at China Spallation Neutron Source, Guangdong, China

<sup>15</sup>Now at Henan Normal University, Xinxiang, China

<sup>16</sup>Also at Université Libre de Bruxelles, Bruxelles, Belgium

<sup>17</sup>Also at an institute or an international laboratory covered by a cooperation agreement with CERN

<sup>18</sup>Also at Suez University, Suez, Egypt

<sup>19</sup>Now at British University in Egypt, Cairo, Egypt

<sup>20</sup>Also at Purdue University, West Lafayette, Indiana, USA

<sup>21</sup>Also at Université de Haute Alsace, Mulhouse, France

<sup>22</sup>Also at Department of Physics, Tsinghua University, Beijing, China

<sup>23</sup>Also at The University of the State of Amazonas, Manaus, Brazil

<sup>24</sup>Also at Erzincan Binali Yildirim University, Erzincan, Turkey

<sup>25</sup>Also at University of Hamburg, Hamburg, Germany

<sup>26</sup>Also at RWTH Aachen University, III. Physikalisches Institut A, Aachen, Germany

<sup>27</sup>Also at Bergische University Wuppertal (BUW), Wuppertal, Germany

<sup>28</sup>Also at Brandenburg University of Technology, Cottbus, Germany

<sup>29</sup>Also at Forschungszentrum Jülich, Juelich, Germany

<sup>30</sup>Also at CERN, European Organization for Nuclear Research, Geneva, Switzerland

<sup>31</sup>Also at Institute of Physics, University of Debrecen, Debrecen, Hungary

<sup>32</sup>Also at Institute of Nuclear Research ATOMKI, Debrecen, Hungary

<sup>33</sup>Now at Universitatea Babeş-Bolyai - Facultatea de Fizica, Cluj-Napoca, Romania

<sup>34</sup>Also at MTA-ELTE Lendület CMS Particle and Nuclear Physics Group, Eötvös Loránd University, Budapest, Hungary

<sup>35</sup>Also at HUN-REN Wigner Research Centre for Physics, Budapest, Hungary

<sup>36</sup>Also at Physics Department, Faculty of Science, Assiut University, Assiut, Egypt

<sup>37</sup>Also at Punjab Agricultural University, Ludhiana, India

<sup>38</sup>Also at University of Visva-Bharati, Santiniketan, India



- <sup>39</sup>Also at Indian Institute of Science (IISc), Bangalore, India
- <sup>40</sup>Also at Birla Institute of Technology, Mesra, Mesra, India
- <sup>41</sup>Also at IIT Bhubaneswar, Bhubaneswar, India
- <sup>42</sup>Also at Institute of Physics, Bhubaneswar, India
- <sup>43</sup>Also at University of Hyderabad, Hyderabad, India
- <sup>44</sup>Also at Deutsches Elektronen-Synchrotron, Hamburg, Germany
- <sup>45</sup>Also at Isfahan University of Technology, Isfahan, Iran
- <sup>46</sup>Also at Sharif University of Technology, Tehran, Iran
- <sup>47</sup>Also at Department of Physics, University of Science and Technology of Mazandaran, Behshahr, Iran
- <sup>48</sup>Also at Department of Physics, Isfahan University of Technology, Isfahan, Iran
- <sup>49</sup>Also at Helwan University, Cairo, Egypt
- <sup>50</sup>Also at Italian National Agency for New Technologies, Energy and Sustainable Economic Development, Bologna, Italy
- <sup>51</sup>Also at Centro Siciliano di Fisica Nucleare e di Struttura Della Materia, Catania, Italy
- <sup>52</sup>Also at Università degli Studi Guglielmo Marconi, Roma, Italy
- <sup>53</sup>Also at Scuola Superiore Meridionale, Università di Napoli 'Federico II', Napoli, Italy
- <sup>54</sup>Also at Fermi National Accelerator Laboratory, Batavia, Illinois, USA
- <sup>55</sup>Also at Laboratori Nazionali di Legnaro dell'INFN, Legnaro, Italy
- <sup>56</sup>Also at Ain Shams University, Cairo, Egypt
- <sup>57</sup>Also at Consiglio Nazionale delle Ricerche - Istituto Officina dei Materiali, Perugia, Italy
- <sup>58</sup>Also at Department of Applied Physics, Faculty of Science and Technology, Universiti Kebangsaan Malaysia, Bangi, Malaysia
- <sup>59</sup>Also at Consejo Nacional de Ciencia y Tecnología, Mexico City, Mexico
- <sup>60</sup>Also at Trincomalee Campus, Eastern University, Sri Lanka, Nilaveli, Sri Lanka
- <sup>61</sup>Also at Saegis Campus, Nugegoda, Sri Lanka
- <sup>62</sup>Also at National and Kapodistrian University of Athens, Athens, Greece
- <sup>63</sup>Also at Ecole Polytechnique Fédérale Lausanne, Lausanne, Switzerland
- <sup>64</sup>Also at Universität Zürich, Zurich, Switzerland
- <sup>65</sup>Also at Stefan Meyer Institute for Subatomic Physics, Vienna, Austria
- <sup>66</sup>Also at Laboratoire d'Annecy-le-Vieux de Physique des Particules, IN2P3-CNRS, Annecy-le-Vieux, France
- <sup>67</sup>Also at Near East University, Research Center of Experimental Health Science, Mersin, Turkey
- <sup>68</sup>Also at Konya Technical University, Konya, Turkey
- <sup>69</sup>Also at Izmir Bakircay University, Izmir, Turkey
- <sup>70</sup>Also at Adiyaman University, Adiyaman, Turkey
- <sup>71</sup>Also at Bozok Universitetesi Rektörlüğü, Yozgat, Turkey
- <sup>72</sup>Also at Marmara University, Istanbul, Turkey
- <sup>73</sup>Also at Milli Savunma University, Istanbul, Turkey
- <sup>74</sup>Also at Kafkas University, Kars, Turkey
- <sup>75</sup>Now at Istanbul Okan University, Istanbul, Turkey
- <sup>76</sup>Also at Hacettepe University, Ankara, Turkey
- <sup>77</sup>Also at Istanbul University - Cerrahpasa, Faculty of Engineering, Istanbul, Turkey
- <sup>78</sup>Also at Yildiz Technical University, Istanbul, Turkey
- <sup>79</sup>Also at Vrije Universiteit Brussel, Brussel, Belgium
- <sup>80</sup>Also at School of Physics and Astronomy, University of Southampton, Southampton, United Kingdom
- <sup>81</sup>Also at IPPP Durham University, Durham, United Kingdom

---

<sup>82</sup>Also at Monash University, Faculty of Science, Clayton, Australia

<sup>83</sup>Also at Università di Torino, Torino, Italy

<sup>84</sup>Also at Bethel University, St. Paul, Minnesota, USA

<sup>85</sup>Also at Karamanoğlu Mehmetbey University, Karaman, Turkey

<sup>86</sup>Also at California Institute of Technology, Pasadena, California, USA

<sup>87</sup>Also at United States Naval Academy, Annapolis, Maryland, USA

<sup>88</sup>Also at Bingöl University, Bingöl, Turkey

<sup>89</sup>Also at Georgian Technical University, Tbilisi, Georgia

<sup>90</sup>Also at Sinop University, Sinop, Turkey

<sup>91</sup>Also at Erciyes University, Kayseri, Turkey

<sup>92</sup>Also at Horia Hulubei National Institute of Physics and Nuclear Engineering (IFIN-HH), Bucharest, Romania

<sup>93</sup>Now at an institute or an international laboratory covered by a cooperation agreement with CERN

<sup>94</sup>Also at Texas A&M University at Qatar, Doha, Qatar

<sup>95</sup>Also at Kyungpook National University, Daegu, Korea

<sup>96</sup>Also at another institute or international laboratory covered by a cooperation agreement with CERN

<sup>97</sup>Also at Universiteit Antwerpen, Antwerpen, Belgium

<sup>98</sup>Also at Yerevan Physics Institute, Yerevan, Armenia

<sup>99</sup>Also at Northeastern University, Boston, Massachusetts, USA

<sup>100</sup>Also at Imperial College, London, United Kingdom

<sup>101</sup>Also at Institute of Nuclear Physics of the Uzbekistan Academy of Sciences, Tashkent, Uzbekistan